Unsteady Aerodynamics, Aeroacoustics and Aeroelasticity of Turbomachines

Edited by

Kenneth C. Hall, Robert E. Kielb and Jeffrey P. Thomas

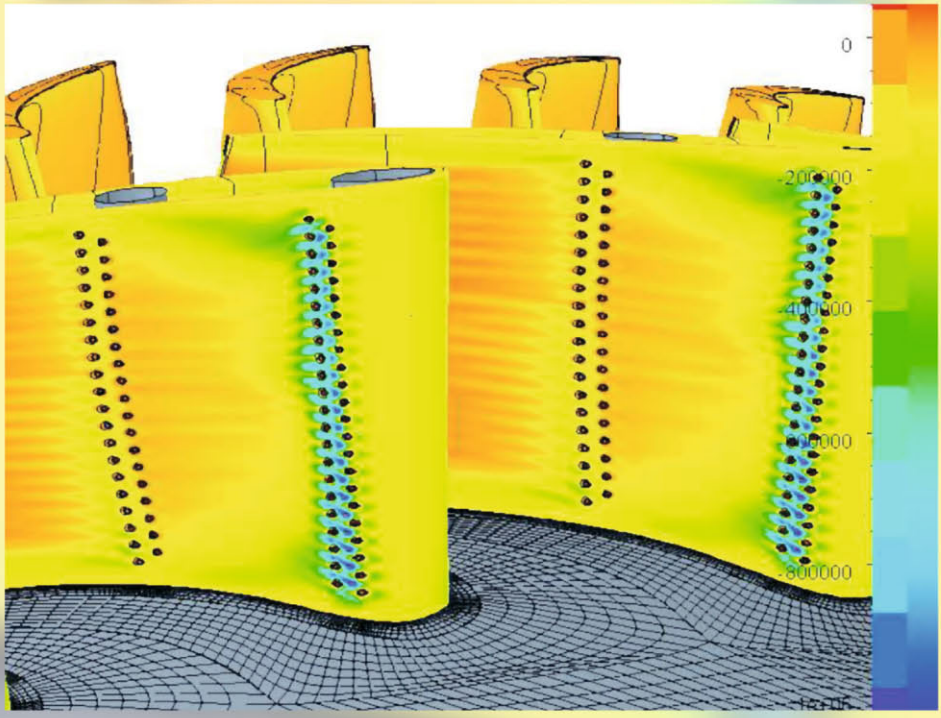

Springer

UNSTEADY AERODYNAMICS, AERODACOUSTICS AND AEROELASTICITY OF TURBOMACHINES

Unsteady Aerodynamics, Aeroacoustics and Aeroelasticity of Turbomachines

Edited by

KENNETH C. HALL
Duke University, Durham, North Carolina, U.S.A.

ROBERT E. KIELB
Duke University, Durham, North Carolina, U.S.A.

and

JEFFREY P. THOMAS
Duke University, Durham, North Carolina, U.S.A.

Springer

A C.I.P. Catalogue record for this book is available from the Library of Congress.

ISBN-10 1-4020-4267-1 (HB)
ISBN-13 978-1-4020-4267-6 (HB)

Published by Springer,
P.O. Box 17, 3300 AA Dordrecht, The Netherlands.

www.springer.com

Printed on acid-free paper

Printed in the Netherlands.

Contents

Preface

Over the past 30 years, leading experts in turbomachinery unsteady aerodynamics, aeroacoustics, and aeroelasticity from around the world have gathered to present and discuss recent advancements in the field. The first International Symposium on Unsteady Aerodynamics, Aeroacoustics, and Aeroelasticity of Turbomachines (ISUAAAT) was held in Paris, France in 1976. Since then, the symposium has been held in Lausanne, Switzerland (1980), Cambridge, England (1984), Aachen, Germany (1987), Beijing, China (1989), Notre Dame, Indiana (1991), Fukuoka, Japan (1994), Stockholm, Sweden (1997), and Lyon, France (2000). The Tenth ISUAAAT was held September 7-11, 2003 at Duke University in Durham, North Carolina. This volume contains an archival record of the papers presented at that meeting.

The ISUAAAT, held roughly every three years, is the premier meeting of specialists in turbomachinery aeroelasticity and unsteady aerodynamics. The Tenth ISUAAAT, like its predecessors, provided a forum for the presentation of leading–edge work in turbomachinery aeromechanics and aeroacoustics of turbomachinery. Not surprisingly, with the continued development of both computer algorithms and computer hardware, the meeting featured a number of papers detailing computational methods for predicting unsteady flows and the resulting aerodynamics loads. In addition, a number of papers describing interesting and very useful experimental studies were presented. In all, 44 papers from the meeting are published in this volume.

The Tenth ISUAAAT would not have been possible without the generous financial support of a number of organizations including GE Aircraft Engines, Rolls-Royce, Pratt and Whitney, Siemens-Westinghouse, Honeywell, the U.S. Air Forces Research Laboratory, the Lord Foundation of North Carolina, and the Pratt School of Engineering at Duke University. The organizers offer their sincere thanks for the financial support provided by these institutions. We would also like to thank the International Scientific Committee of the ISUAAAT for selecting Duke University to host the symposium, and for their assistance in its organization. Finally, the organizers thank Loraine Ashley of the Department of Mechanical Engineering and Materials Science for her Herculean efforts organizing the logistics, communications, and finances required to host the conference.

The Eleventh ISUAAAT will be held in Moscow, Russia, September 4–8, 2006, and will be hosted by the Central Institute of Aviation Motors. Dr. Viktor Saren, the hosting member of the International Scientific Committee, will serve as deputy chair of the symposium; Dr. Vladimir Skibin, the General Director of CIAM, will serve as chair.

Kenneth C. Hall
Robert E. Kielb
Jeffrey P. Thomas

Department of Mechanical Engineering and Materials Science
Pratt School of Engineeering

I

FLUTTER

FLUTTER BOUNDARIES FOR PAIRS OF LOW PRESSURE TURBINE BLADES

Roque Corral, [1,2] Nélida Cerezal, [2] and Cárlos Vasco [1]

[1] *Industria de Turbopropulsores SA*
Parque Empresarial San Fernando, 28830 Madrid
Spain
roque.corral@itp.es

[2] *School of Aeronautics, UPM*
Plaza Cardenal Cisneros 3, 28040 Madrid
Spain

Abstract The aerodynamic damping of a modern LPT airfoil is compared to the one obtained when pairs of blades are forced to vibrate as a rigid body to mimic the dynamics of welded-pair assemblies. The stabilizing effect of this configuration is shown by means of two-dimensional simulations.

The modal characteristics of three bladed-disk models that differ just in the boundary conditions of the shroud are compared. These models are representative of cantilever, interlock and welded-pair designs of rotating parts. The differences in terms of frequency and mode-shape of the three models are sketched. Finally their relative merits from a flutter point of view are discussed using the 2D aerodynamic damping characteristics.

Keywords: Flutter, Low Pressure Turbine, Stability Map

Introduction

Flutter has been a problem traditionally associated to compressor and fan blades. However the steady trend during the last decades to design high-lift, highly-loaded low pressure turbines (LPTs), with the final aim of reducing their cost and weight, while keeping the same efficiency, has lead to a reduction of the blade and disk thickness and an increase of the blade aspect ratio. Both factors tend to lower the stiffness of the bladed-disk assembly and therefore its natural frequencies.

As a result of the afore mentioned evolution vanes and rotor blades of the latter stages of modern LPTs of large commercial turbofan engines, which may

K.C. Hall et al.(eds.),
Unsteady Aerodynamics, Aeroacoustics and Aeroelasticity of Turbomachines, 3–16.

be designed with aspect ratios of up to six, may potentially flutter and undergo alternate stresses similar to the ones encountered in fans and compressors.

Vibration control of shrouded LPT blades may be accomplished using either cantilever, inter-lock or welded-pair configurations. Flat sided shrouds may vibrate freely even for very small clearances specially for low inter-blade phase angles (IBFA) and provide little control over the vibration characteristics of the bladed-disk. To remedy this deficiency z-shaped shrouds (interlocks) were designed with the aim of remaining tight during the whole flight envelope. This type of designs significantly modify the vibration characteristics of cantilever blades, however, the mode-shapes of a given family may significantly vary with the nodal diameter and induce bending-torsion coupling. Finally, pairs of blades welded in the tip-shroud, were devised as a practical alternative to control the vibration characteristics of LPT bladed-disks and may be seen in some turbofan engines. This latter configuration substantially modifies as well the mode-shapes and frequencies of the baseline (cantilever) and interlock solutions.

It is well known that flutter boundaries are very sensitive to blade mode-shapes and that the reduced frequency plays a secondary role. A comprehensive numerical study of the influence of both parameters for LPT airfoils was performed by Kielb & Panowski (2000) and supported by experimental work (Nowinski and Panovski, 2000). The aim of this work is to investigate the influence of pairing the blades in the aerodynamic damping of a typical LPT section and apply the results to a realistic configuration to elucidate the potential benefits of such configurations in the modal behaviour of bladed-disk assemblies.

Numerical Formulation

Linearized Euler Equations

A two-dimensional cascade of blades vibrating sinusoidally with a small amplitude, common angular frequency, ω, and common inter-blade phase-angle, σ, may be modeled within engineering accuracy by the linearized Euler equations if the flow remains attached along the airfoil.

The two-dimensional Euler equations in conservative form for an arbitrary control volume may be written as:

$$\frac{d}{dt}\int_{\Omega}\mathbf{U}d\Omega+\int_{\Sigma}\{(\mathbf{f},\mathbf{g})-\mathbf{UV}\}.d\mathbf{A}=0 \tag{1}$$

where $\mathbf{U}$ is the vector of conservative variables, $\mathbf{f}$ and $\mathbf{g}$ the inviscid fluxes, Ω the flow domain, Σ its boundary, $d\mathbf{A}$ the differential area pointing outward to the boundary and $\mathbf{V}$ the velocity of the boundary. Now we may decomposed the flow into two parts: a steady or mean background flow, plus a small but

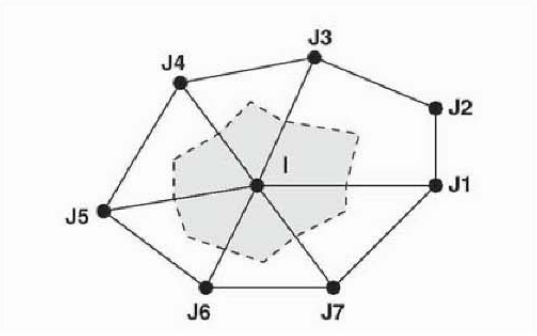

Figure 1. Typical hybrid-cell grid and associated dual mesh

periodic unsteady perturbation, which in turn may be expressed as a Fourier series in time. If we retain just the first harmonic any variable may be expressed as:

$$\mathbf{U}(\mathbf{x},t) = \mathbf{U}_0(\mathbf{x}) + \mathrm{Re}(\widehat{\mathbf{u}}(\mathbf{x})e^{i\omega t}) \tag{2}$$

where $\mathbf{U}_0$ represents the background flow and $\widehat{\mathbf{u}}$ is the complex perturbation. The Euler equations may then be linearized about the mean flow to obtain:

$$\begin{aligned}(\frac{d}{d\tau} + i\omega)\int_\Omega \widehat{\mathbf{u}}d\Omega \quad + \quad \int_\Sigma \left(\frac{\partial \mathbf{g}}{\partial \mathbf{U}}\widehat{\mathbf{u}}, \frac{\partial \mathbf{g}}{\partial \mathbf{U}}\widehat{\mathbf{u}}\right).d\mathbf{A} \quad = \quad i\omega\int_\Sigma \mathbf{U}_0\mathbf{x}'.d\mathbf{A} \\ i\omega\int_\Omega \mathbf{U}_0 d\Omega' \qquad + \qquad \int_\Sigma (\mathbf{f}_0, \mathbf{g}_0).d\mathbf{A}'\end{aligned} \tag{3}$$

which is a linear equation of complex coefficients and where the first term is an additional time-derivative added to solve the equations marching in the pseudo-time τ.

Spatial Discretization

The code known as $Mu^2s^2T - L$ solves the two-dimensional linearized Euler equations (3) in conservative form. The spatial discretization is obtained linearizing the discretized equations of the non-linear version of the code Mu^2s^2T (Corral and Gisbert, 2002), from which the background solution is obtained. The spatial domain is discretized using hybrid unstructured grids that may contain cells with an arbitrary number of faces and the solution vector is stored at the vertexes of the cells. The code uses an edge-based data structure, a typical grid is discretized by connecting the median dual of the cells surrounding an internal node (Figure 1). For the node i the semi-discrete form of Eq 3. can be written as

$$\frac{d\Omega_i \widehat{\mathbf{u}}_i}{d\tau} + \sum_{j=1}^{n_{edges}} \frac{1}{2} S_{ij} (\widehat{\mathbf{F}}_i + \widehat{\mathbf{F}}_j) - \widehat{\mathbf{D}}_{ij} = \widehat{\mathbf{S}}(\widehat{\mathbf{u}}_i) \tag{4}$$

where S_{ij} is the area associated to the edge ij, and n_{edges} the number of edges that surround node j. The resulting numerical scheme is cell-centered in the dual mesh and second-order accurate. It may be shown that for triangular grids the scheme is equivalent to a cell vertex finite volume scheme. A blend of second and fourth order artificial dissipation terms, $\widehat{\mathbf{D}}_{ij}$, is added to capture shock waves and prevent the appearance of high frequency modes in smooth flow regions respectively. The second order terms are activated in the vicinity of shock waves by means of a pressure-based sensor and locally the scheme reverts to first order in these regions. The artificial dissipation terms can be written as

$$\widehat{\mathbf{D}}_{ij} = |A_{ij}| \, S_{ij} \left[\mu_{ij}^{(2)} (\widehat{\mathbf{u}}_j - \widehat{\mathbf{u}}_i) - \mu_{ij}^{(4)} (L_j - L_i) \right] \tag{5}$$

where $\mu_{ij}^{(2)}$ and $\mu_{ij}^{(4)}$ are the average of the artificial viscosity coefficients in the nodes i and j, L is a pseudo-Laplacian operator:

$$L(\widehat{\mathbf{u}}_i) = \sum_{j=1}^{n_{edges}} (\widehat{\mathbf{u}}_j - \widehat{\mathbf{u}}_i) \simeq \frac{n_{edges}}{4} \left(\Delta x^2 \widehat{\mathbf{u}}_{xx} + \Delta y^2 \widehat{\mathbf{u}}_{yy} \right)_i \tag{6}$$

where the last approximation is only valid in regular grids and $|A_{ij}|$ is a 4×4 matrix that plays the role of a scaling factor. If $|A_{ij}| = (|u| + c)_{ij} I$, where I is the identity matrix, the standard scalar formulation of the numerical dissipation terms (Jameson et al., 1981) is recovered. When $|A_{ij}|$ is chosen as the Roe matrix (1981) the matricial form of the artificial viscosity (Swanson and Turkel, 1992) is obtained. The scalar version of the numerical diffusion terms has been used in this work since for the Mach numbers of interest in this work the differences between both approaches are negligible (Corral et al. 2000).

The exact, 2D, unsteady, non-reflecting boundary conditions (Giles, 1990) have been used at the inlet and outlet while the phase-shifted boundary conditions at the periodic boundaries are written in Fourier space as $\widehat{\mathbf{u}}(x, y + \text{pitch}) = \widehat{\mathbf{u}}(x, y) e^{i\sigma}$.
A more detailed description of the code as well as some validation examples may be found in Corral et al. (2003)

Analysis Methodology

Since one of the aims of this work was to study the influence of the torsion centre for different reduced frequencies and configurations it was decided to follow a simplified design approach (Panovski and Kielb, 2000). The basic

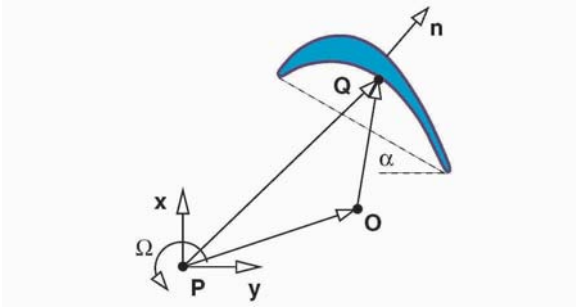

Figure 2. Description of the blade motion as a rigid body

idea is to assume that the main contribution to the aerodynamic damping is due to the actual blade and the two neighbouring blades. In this case the aerodynamic damping varies sinusoidally with the inter-blade phase angle and it may be computed with as few as three linear computations. The validity of such approach has been shown both experimentally (Nowinski and Panovski, 2000) and numerically (Panovski and Kielb, 2000).

Following the approach of Panovski and Kielb (2000) just the unsteady pressure field associated to the bending in the x and y direction and the torsion about a given point, P, for a reference displacement are computed. The unsteady pressure associated to the motion of the airfoil as a rigid body about an arbitrary torsion axis, O, is computed as a linear combination of three reference solutions. The velocity of an arbitrary point, $\mathbf{V}_Q$, of the airfoil is of the form:

$$\mathbf{V}_Q(t) = \mathbf{V}_P(t) + \Omega(t)\mathbf{k} \times \mathbf{PQ} \tag{7}$$

where Ω is the angular velocity of the airfoil, $\mathbf{k}$ is the unit vector perpendicular to the xy plane. Choosing $\mathbf{V}_P$ and Ω properly it is possible to make an arbitrary point O the torsion axis, this condition is

$$\mathbf{V}_O(t) = \mathbf{V}_P(t) + \Omega(t)\mathbf{k} \times \mathbf{PO} = 0 \tag{8}$$

and hence is enough to satisfy $\mathbf{V}_P = -\Omega\mathbf{k} \times \mathbf{PO}$ for an arbitrary Ω. We may write $\mathbf{V}_P = v_x\mathbf{i} + v_y\mathbf{j}$ where

$$v_x = \epsilon_x \omega \mathrm{Re}\left(i\widehat{h}_{x,ref}e^{i\omega t}\right) \quad \text{and} \quad v_y = \epsilon_y \omega \mathrm{Re}\left(i\widehat{h}_{y,ref}e^{i\omega t}\right) \tag{9}$$

and ϵ_x and ϵ_y are scaling factors of the actual displacements with respect the ones of reference $\widehat{h}_{x,ref}$ and $\widehat{h}_{y,ref}$. Analogously

$$\alpha = \epsilon_\Omega \mathrm{Re}\left(\widehat{\alpha}_{ref}e^{i\omega t}\right) \quad \text{and} \quad \Omega = \epsilon_\Omega \omega \mathrm{Re}\left(i\widehat{\alpha}_{ref}e^{i\omega t}\right). \tag{10}$$

The unsteady pressure perturbation, $p^{'}$, due to the motion of the airfoil as a rigid body is assumed to behave linearly and therefore it may be expressed as the sum of the unsteady pressure fields associated to bending in the x direction, p'_{v_x}, bending in the y direction, p'_{v_y}, and torsion about the point P, p'_{Ω}, i.e.:

$$p' = p'_{v_x} + p'_{v_y} + p'_{\Omega} = \epsilon_x p'_{v_x,ref} + \epsilon_y p'_{v_y,ref} + \epsilon_{\Omega} p'_{\Omega,ref}. \tag{11}$$

The work per cycle over the airfoil, W, is

$$W = \int_0^{2\pi/\omega} \int_{\Sigma_c} p' \mathbf{V}_q . d\mathbf{A} dt \tag{12}$$

where $\mathbf{V}_q$ is the velocity of the blade surface. $W > 0$ means that the blade motion is damped by the aerodynamics. Substituting equations 7 and 11 in 12 it is possible to obtain the following expression for W in non-dimensional form:

$$\Theta = \frac{W}{\rho_e U_e d_{max}^2 \omega c H} = \left\{ \begin{array}{ccc} \epsilon_x & \epsilon_y & \epsilon_{\Omega} \end{array} \right\} \left[\begin{array}{ccc} \overline{w}_{x,x} & \overline{w}_{x,y} & \overline{w}_{x,\Omega} \\ \overline{w}_{y,x} & \overline{w}_{y,y} & \overline{w}_{y,\Omega} \\ \overline{w}_{\Omega,x} & \overline{w}_{\Omega,y} & \overline{w}_{\Omega,\Omega} \end{array} \right]_{ref} \left\{ \begin{array}{c} \epsilon_x \\ \epsilon_y \\ \epsilon_{\Omega} \end{array} \right\}$$

where each element of work coefficient matrix represents the non-dimensional work obtained combining each unsteady pressure field with on the displacements of each mode (e.g. $\overline{w}_{x,\Omega}$ is the work perform by the unsteady pressure associated to the airfoil bending in x on the displacements due to the torsion about point P), ρ_e and U_e are, respectively, the density and velocity at the cascade exit, d_{max} is the maximum airfoil displacement in the reference cases and cH is an estimate for the airfoil surface.

The work coefficient matrix $[w]$ is calculated once for each IBFA of the fundamental modes. The general procedure is then to run the unsteady code in the three fundamental modes with a reference amplitude through the range of inter-blade phase angles. As few as three inter-blade phase angles per fundamental mode need to be used. The rest of IBFA are obtained assuming that $w = a + b\sin\sigma + c\cos\sigma$. The critical IBFA is computed then as the minimum of the previous expression.

In this work we have obtained the values of the damping coefficients for $\sigma = 0^{\circ}$ and $\sigma = \pm 90^{\circ}$ to estimate the whole range of inter-blade phase angles. The errors associated to this approximation may be seen in figure 3 where the damping coefficients for the edgewise, flap and torsion modes for different reduced frequencies are displayed. It may be appreciated that the damping coefficient curves of the edgewise and flap modes have a sinusoidal form. This is specially true for $k = 0.1$ while for $k = 0.4$ two spikes, corresponding to resonant conditions, are superimposed to the sine-like shape. This behaviour

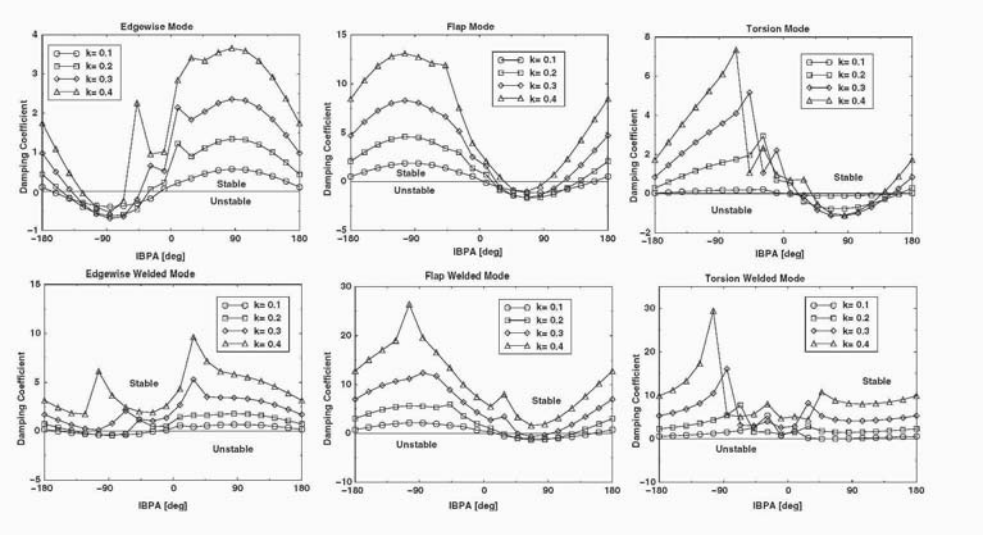

Figure 3. Damping as a function of IBPA for the three fundamental modes. Top: single blade configuration. Bottom: Welded-pair configuration

is as could be expected since it is well known that the relative influence of the adjacent blades to the reference one decreases when the reduced frequency is increased (see Corral & Gisbert (2002) for example). The deviations from the sinusoidal from of the torsion mode are larger, but in all the cases the critical interblade phase angle is still well predicted.

Flutter Stability Maps

Panovski and Kielb (2000) showed, using flutter stability maps, how the modeshape and the reduced frequency were the basic parameters that controlled the stability of a two-dimensional LPT section. In practice only the mode-shape is relevant from a design perspective since the possible range of variation of the reduced frequency is very limited. We have extended such analysis to pairs of airfoils moving as a rigid body. The aim is to mimic the mode shapes obtained when pairs of blades are welded to increase the aerodynamic damping of the bladed-disk assembly. The edgewise and flap modes are defined as bending modes along and perpendicular to the line that joins the leading and trailing edges, respectively. The center of torsion of the third fundamental mode is located at the l.e. of the airfoil, when pairs of blades are considered the pair is formed adding a new airfoil adjacent to the pressure side of the reference airfoil and the center of torsion of the fundamental node is kept at the l.e. of the reference section. The airfoil used in all the simulations

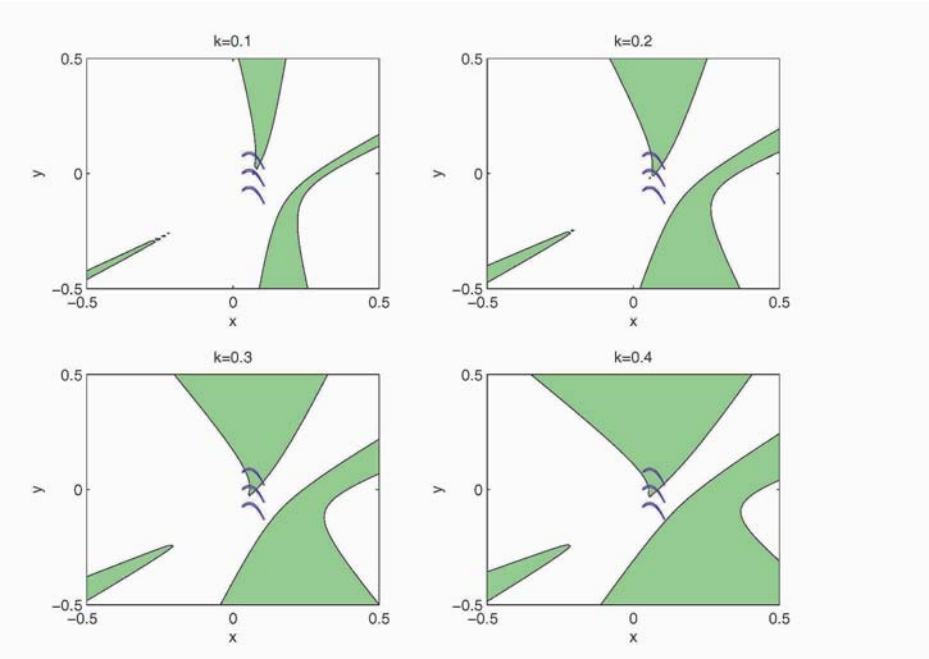

Figure 4. Flutter stability maps for the single blade configuration. The shadow regions represent the locus of the stable torsion centres

corresponds to the mid-section of a representative rotor blade ($\alpha_{inlet} = 37°$, $\alpha_{exit} = 64°$, $M_{is} = 0.76$).

Figure 3 displays the damping coefficient as a function of the IBFA for the different fundamental modes previously described. For both configurations it may be seen the stabilizing effect of the reduced frequency although for the single blade configuration there always exists a region of unstable IBPA for the computed range of reduced frequencies. The stabilizing effect of the welded-pair configuration may be clearly seen at the bottom of the same figure. In this case all the fundamental modes are stable for $k = 0.4$ being the flap mode the most critical one. The torsion mode is highly stabilised for the welded-pair configuration and becomes neutrally stable for $k = 0.1$.

The damping curves of the fundamental modes have been fitted to a sine curve and the methodology described in the previous section used to construct the stability maps for both configurations to conduct a complete study of mode shape in a practical and systematic manner.

Figure 4 shows the flutter stability maps for the single blade configuration, the middle section represents the reference section and the shadow regions the locus of the stable torsion centres. It may be appreciated firstly how the airfoil is intrinsically unstable in torsion and secondly how increasing the reduced

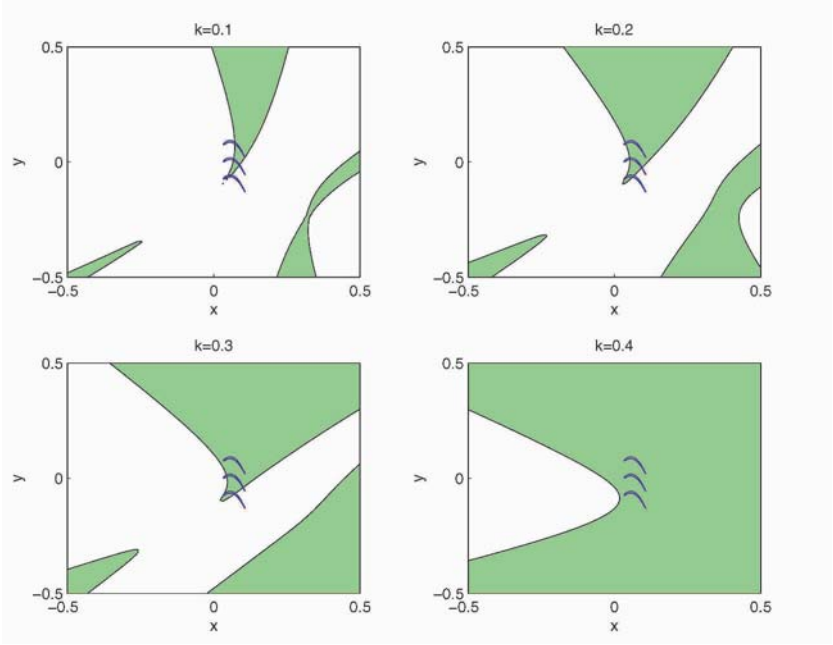

Figure 5. Flutter stability maps for the welded-pair configuration. The shadow regions represent the locus of the stable torsion centres

frequency the stable region is enlarged. It is worth noting as well that while the axial mode (bending in the x direction) is stable the flex mode (bending in the y direction) is unstable, this may inferred by realizing that a torsion axis at infinity ($y \to \infty$ for instance, which is a stable region) generates a pure axial bending stable mode.

Figure 5 shows the equivalent map for a pair of airfoils moving as a rigid body. The upper airfoil of the pair corresponds to the upper section of the figure. The increase of the aerodynamic damping with respect the single blade configuration is clearly seen and for $k = 0.4$ the airfoil is stable in torsion modes whose centre of torsion is in the vicinity of the blade and in a wide range of bending directions, the only unstable mode is the flex mode.

Only qualitative comparisons are possible with the results obtained by the research efforts of Panovski & Kielb (2000) since neither the geometry nor all the aerodynamic conditions are available, still it may be concluded that the basic steady aerodynamic conditions are comparable in first approximation and the stability map of both cases is similar as well confirming the idea that the sensitivity to the geometry and aerodynamic conditions is low.

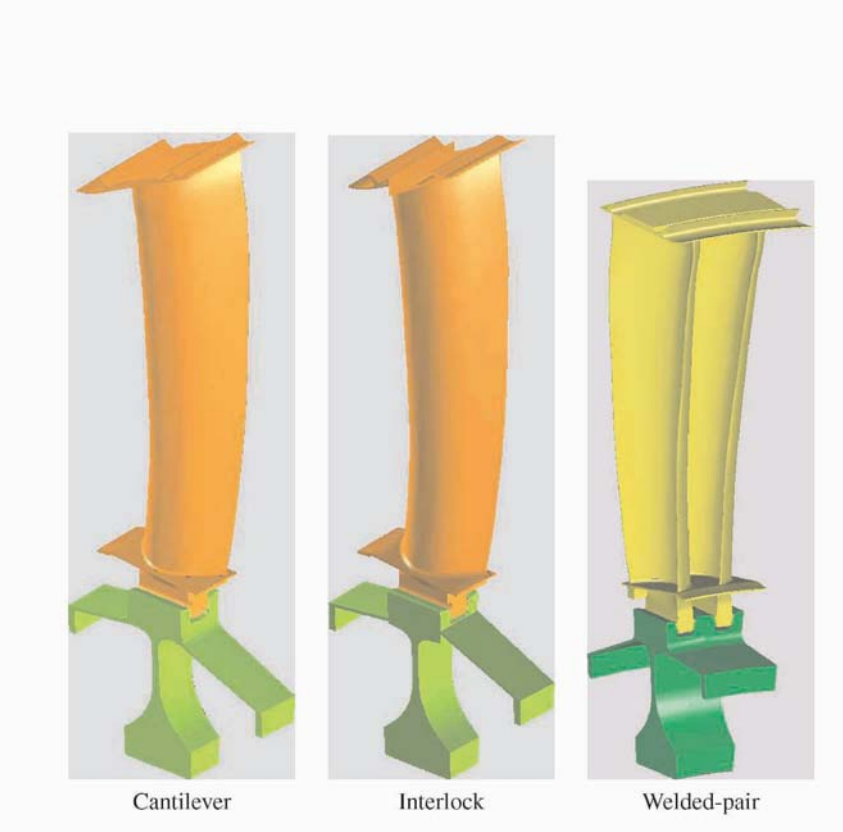

Figure 6. Global view of the the bladed-disk assembly configurations

Modal Characteristics of Bladed-Disks

The aim of this section is to elucidate in a qualitative manner how the previous results influence the stability of realistic bladed-disk configurations and in particular to discuss the relative merit of using cantilever, interlock or welded-pair configurations. Although there exists a big leap in moving from pure 2D to fully 3D mode shapes the simplicity of the approach makes the exercise still attractive.

The bladed-disk assembly considered in this study is representative of the first stages of modern LPTs. A global view of the whole assembly may be seen in figure 6. The vibration characteristics of the cantilever, interlock and welded-pair configurations has been obtained with the same grid. The boundary condition in the contact nodes between sliding parts, namely, between the disk and the blade in the attachment, and between the shroud contacts in the interlock configuration enforces that the displacements of these in both sides are identical. This simplifying hypothesis is made to avoid the generation of non-linear models where the concepts of natural frequency and mode-shape need to be re-interpreted.

Since only the first two families are usually relevant for flutter studies we have restricted ourselves to the lowest range of the frequency - nodal-diameter diagram. Two analysis were carried out, firstly at rest and ambient temperature and secondly at the operating sped with the associated temperatures. Only slight differences were seen in this particular case because the increase in stiffening due to the centrifugal force was compensated by the decrease in the Young's module due to the increase in the inlet temperature of the turbine at the operating conditions. Since both results were very similar and to avoid further complications, the results presented correspond to the ones obtained at rest. The figure 7 shows the frequency characteristics of the first families for the cantilever (top), welded-pair (middle) and interlock (bottom) configurations. Several conclusions may be drawn upon inspection of this figure and the mode-shapes, not shown here for the sake of brevity,

1 The disk is very stiff compared to the blades. This may be seen in the mode-shapes, that show very small displacements of the disk, and in the frequency nodal diameter diagram that displays a high number of modes with nearly the same frequency within the same family.

2 The welded-pair configuration has slightly higher frequencies than the cantilever one with the exception of the third family that corresponds to the first torsion (1F) mode whose frequency drops.

3 The interlock provides and effective means to raise the frequencies of the assembly. The lower nodal diameters of the first family correspond to shroud dominated modes.

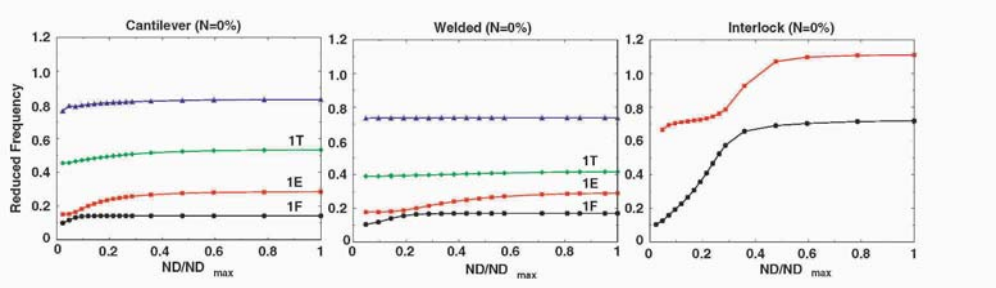

Figure 7. Modal characteristics of the bladed-disk assembly. Left: cantilever. Middle: Welded-pair. Right: Interlock

The baseline (cantilever) configuration is likely to be unstable since the reduced frequency of the first flap mode is too low, the first torsion mode is probably unstable a well. The welded-pair configuration is better from a flutter point of view than the cantilever one, the torsion mode will be stable in spite of having a lower reduced frequency, however, although the frequency of the 1^{st} flap mode is slightly higher than before, according with with the 2D inviscid results the mode is still unstable although the damping coefficient for the most unstable inter-blade phase angle has been reduced to one third of the original baseline configuration. This means that to predict absolute flutter boundaries three-dimensional and mistuning effects need to be retained.

The interlock configuration raises significantly the natural frequencies of the bladed-disk and hence is an effective mechanism as well to prevent flutter. A very similar interlock configuration was analyzed by Sayma et al. (1998), they found that the 6-12 nodal diameters, which corresponds in figure 7 (bottom) to 20% of the maximum nodal diameter, were unstable confirming previous engine testing. A plausible explanation may be found by noting that the modes corresponding to the low diameter nodes of the interlock configuration are edgewise modes, which are stable, while the modes corresponding to the high diameter nodes are torsion modes, whose stability depends on the reduced frequency but that figure 3 (right) shows that is stable. The instability is concentrated in the region where the edgewise modes become torsion modes and the reduced frequency is not high enough to ensure their stability.

Concluding Remarks

LPT blades are sometimes welded in pairs to increase their flutter characteristics. It has been shown by means of two-dimensional simulations that the aerodynamic damping welded-pairs is larger than the one of single blades. This specially true for torsion modes and bending modes whose flapping direction is aligned with the tangential direction of the cascade. A more in depth dis-

cussion of the theoretical benefits of using such configurations requires taking into account the frequency and three-dimensional mode shape modification.

The frequency characteristics of three bladed-disk configurations have been presented. The three assemblies differ just in the boundary conditions of the tip-shroud. It has been observed that the frequency characteristics of the welded-pair configuration are essentially the same that the cantilever configuration while the interlock changes dramatically the overall behaviour of the assembly. The prediction of the stability or not of the welded-pair configuration requires to account for three-dimensional and mistuning effects. The stability of the interlock is compromised by the transition between edgewise and torsion modes with the nodal diameter of the first family. It is believed that the torsion modes with low reduced frequency, that the 2D simulations show are unstable, are responsible of the instability, this is consistent with the results of other researchers.

Acknowledgments

The authors wish to thank ITP for the permission to publish this paper and for its support during the project. This work has been partially funded by the Spanish Minister of Science and Technology under the PROFIT grant FIT-100300-2002-4 to the School of Aeronautics of the UPM.

References

Corral, R., Burgos, M.A., and García, A., "Influence of the Artificial Dissipation Model on the propagation of Acoustic and Entropy Waves", ASME Paper 2000-GT-563, 2000.

Corral, R., Escribano, A., Gisbert, F., Serrano, A., and Vasco, V., "Validation of a Linear Multigrid Accelerated Unstructured Navier-Stokes Solver for the Computation of Turbine Blades on Hybrid Grids", AIAA Paper 2003-3326, 2003.

Corral, R., and Gisbert, F., "A Numerical Investigation on the Influence of Lateral Boundaries in Linear Vibrating Cascades", ASME Paper 2002-GT-30451, 2002.

Giles, M.B., "Non-reflecting Boundary Conditions for Euler Equation Calculations", AIAA Journal, Vol. 28, No. 12, pp. 2050-2057, 1990.

Jameson, A., Schmidt, W., and Turkel, E., "Numerical Solution of the Euler Equations by Finite Volume Techniques using Runge-Kutta Time Stepping Schemes", AIAA Paper 81-1259,1991.

Nowinski, M., and Panovsky, J., "Flutter Mechanisms in Low Pressure Turbine Blades", Journal of Engineering for Gas Turbines and Power, Vol. 122, pp. 82-88, 2000

Panovski, J., and Kielb, R.E., "A Design Method to Prevent Low Pressure Turbine Blade Flutter", Journal of Engineering for Gas Turbines and Power, Vol. 122, pp. 89-98, 2000

Roe, P., "Approximate Riemman Solvers, Parameters, Vectors and Difference Schemes", Journal of Computational Physics, Vol. 43, pp. 357-372, 1981.

Sayma, A.I., Vahdati M., Green, J.S., and Imregun, M., "Whole-Assembly Flutter Analysis of a Low Pressure Turbine Blade", in Proceedings of the 8th International Symposium in Unsteady Aerodynamics and Aeroelasticity of Turbomachines, pp. 347-359, Edited by T.H., Fransson, 1998

Swanson, R.C., and Turkel, E., "On Central-Difference and Upwinding Schemes" Journal of Computational Physics, Vol. 101, pp. 292-306, 1992.

INFLUENCE OF A VIBRATION AMPLITUDE DISTRIBUTION ON THE AERODYNAMIC STABILITY OF A LOW-PRESSURE TURBINE SECTORED VANE

Olga V. Chernysheva,[1] Torsten H. Fransson,[1] Robert E. Kielb,[2] and John Barter[3]

[1]*Royal Institute of Technology*
S-100 44 Stockholm, Sweden
olga@egi.kth.se
fransson@egi.kth.se

[2]*Duke University*
Durham, NC 27708-0300, USA
rkielb@duke.edu

[3]*GE Aircraft Engines,*
Cincinnati, OH 45215-1988, USA
john.Barter@ae.ge.com

Abstract A parametrical analysis summarizing the effect of the reduced frequency and sector mode shape is carried out for a low-pressure sectored vane cascade for different vibration amplitude distributions between the airfoils in sector as well as the numbers of the airfoils in sector. Critical reduced frequency maps are provided for torsion- and bending-dominated sector mode shapes.

Despite the different absolute values of the average aerodynamic work between four-, five- and six-airfoil sectors a high risk for instability still exists in the neighborhood of realistic reduced frequencies of modern low-pressure turbine. Based on the cases studied it is observed that a sectored vane mode shape with the edge airfoils in the sector dominant provides the most unstable critical reduced frequency map.

Keywords: Flutter, sectored vane, sector mode shape, vibration amplitude distribution, critical reduced frequency.

K.C. Hall et al. (eds.),
Unsteady Aerodynamics, Aeroacoustics and Aeroelasticity of Turbomachines, 17–29.

Nomenclature

c	chord length	[m]
k	reduced frequency based on half-chord and outlet fbw velocity, $\omega c/(2V_2)$	[-]
M	Mach number	[-]
V	fbw velocity	[m/s]
X	cascade axial co-ordinate	[-]
Y	cascade tangential co-ordinate	[-]
Greek		
β	absolute fbw angle	[deg]
ω	circular frequency	[rad/s]
Subscripts		
IS	isentropic	
1	inlet	
2	outlet	

1. Introduction

In order to eliminate or reduce blade vibration problems in turbomachines, the adjacent airfoils around the wheel are often mechanically connected together with either lacing wires, tip shrouds or part-span shrouds in a number of identical sectors. Such mechanical connections make the vibratory mode shapes much more complex. At the same time it allows a significant improvement in the stability margin of the design.

Numerical (see, for example, [1-3]) and experimental aerodynamic analysis has demonstrated the stabilizing effect. The numerical studies for sectored vanes presented in [1-2] were conducted with all blades in the sector vibrating with the same frequency and amplitude and at different real mode shapes. The method used in [1] utilized the possibility of superposition for a linear system, the approach in [2] required calculations on a domain that covered as many passages as airfoils belonging to one sector. The findings were illustrated for selected sets of sectored vane modes for five- and six-airfoil low-pressure steam turbine sectored vanes in [1] and for three-airfoil low-pressure turbine sectored vane in [2]. Nevertheless, even though the sectored vanes benefited by the mechanical connection between vanes, flutter was still predicted for certain ranges of inter-sector phase angles.

According to structural analysis of a sectored vane displacement the blades in the sector might have different amplitudes, mode shapes and vibration frequencies which obviously affect the aerodynamic stability of the sectored vane. An important contribution of the blade mode shape into the aerodynamic stability of the cascade has been already demonstrated in [4] for a freestanding low-pressure turbine blade with a real rigid-body mode shape. During the aeroelastic design phase, it was recommended to also study mode shape rather than only the reduced frequency of a blade. Further investigation, conducted in

[5] for a wide range of physical and aerodynamic blade parameters confirmed the findings and made it more general.

The approach presented in [3] employed, similarly to [1], the superposition assumption and, unlike [1], allowed a complex rigid-body mode shape with non-uniform amplitude distribution between the blades in a sector. The effect of real rigid-body sector mode shape variation on the aerodynamic stability of a low-pressure six-airfoil sectored vane was shown when all blades in sector were vibrating with identical amplitude. Although it was confirmed that tying blades together in a sector drastically improved the stability of the cascade, for some mode shapes sectored vane still remained unstable at relevant reduced frequencies.

2. Objectives

The present paper aims to investigate further the sensitivity of the critical (flutter) reduced frequency versus mode shape maps for the sectored vane, namely towards an non-uniform distribution in the amplitudes between the blades in the sector. The influence of the number of the airfoils in the sectored vane will be demonstrated.

3. Method of attack

The method for investigation of flutter appearance in a cascade, where blades are connected together in a number of identical sectors is presented in [3] and can be shortly described as follows:

- The aerodynamic response of a sectored vane is calculated based on the aerodynamic work influence coefficient representation of a freestanding bladed cascade.

- There is a possibility to consider different vibration amplitudes and any inter-blade phase angles for the blades in the sector, while the inter-sector phase angles follow the Lane's criteria [6] and all blades have the same vibration frequency.

- Assuming a rigid-body motion allows to define the blade mode shape entirely by its pitching axis position. Thus, at a selected reduced frequency and given pitching axis positions for the blades in sector the aerodynamic work for the sector is calculated as a function of the inter-sector phase angle as well as amplitude and phase angle distributions between the airfoils in the sector. The absolute maximum of the work is then calculated and the algorithm is continued for another pitching axis position until the whole range of the mode shapes is covered.

- Afterwards, the results for a number of reduced frequencies are overlaid to produce a plot of critical reduced frequency versus pitching axis position for the reference sectored vane. This determines the value of reduced frequency for which each torsion axis locations of the blades in the sector becomes unstable.

For the practical applications shown in this paper the following restrictions are applied in the algorithm:

- Mode shape of the sectored vane is considered to be real, i.e. the blades in sector can only have 0 and/or 180 degree inter-blade phase angle between each other.
- All the blades in the sector have the same relative pitching axis location.

In the present paper the method is applied for a number of different vibration amplitude distributions for the airfoils belonging to the same sector as well as for different numbers of airfoils in the sector.

4. Sectored vane geometry and calculations in traveling wave domain

The stability analysis is performed for a sectored low-pressure gas-turbine vane cascade (Fig. 1) consisting of 15 sectors.

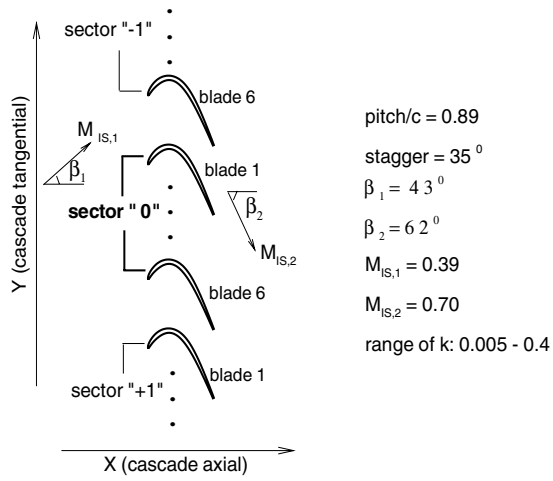

Figure 1. Sectored vane geometry and parameters for the profile

Steady and unsteady calculations are performed with the linearized inviscid flow solver NOVAK [7]. An overview of physical and aerodynamic parame-

ters for the aeroengine profile used for the calculations in the traveling wave domain is presented in Fig. 1. The basic calculations in the traveling wave domain are performed at 10 different inter-blade phase angles for the three fundamental modes, bending in two orthogonal directions and torsion.

5. Results and discussion

The vibration amplitude distributions between the airfoils in sector are chosen as for the following three cases:

1. Uniform: all blades in sector vibrating with the same amplitude.
2. Edge blades dominated: vibration amplitude of the edge blades is 1 while the amplitude of the inner blades is 0.5.
3. Internal blades dominated: vibration amplitude of the edge blades is 0.5 while the amplitude of the inner blades is 1.

The number of airfoils in a sector has been selected as four, five or six. While varying the real sector mode shape it is assumed that the mode shapes of the airfoils belonging to the same sector are changing in an identical manner.

The maps in Figures 2 to 8 show the values of the critical reduced frequencies. Each contour line in the critical reduced frequency map corresponds to the value of reduced frequency for which the reference vane is neutrally stable. The reference vane is in the center of the diagram and identified with a thicker line.

The discussion of the results is divided into two parts, for the torsion axis location varied in the near field of the reference vane (torsion dominated modes) and for torsion axis location approaching infinity (bending dominated modes).

A comparison of the aerodynamic behavior of the multiple airfoils sectored vanes is made against a freestanding blade cascade. In the freestanding blade cascade the blades vibrate with identical mode shapes as well as amplitudes and have a constant inter-blade phase angle between each other. The critical reduced frequency maps for the freestanding blade cascade are shown in Fig. 2a (torsion-dominated mode shapes) and in Fig. 2b (bending-dominated mode shapes) as a reference towards the four-, five- and six-airfoil sectored vanes to be shown later.

Near field domain

Comparing the present investigation with the findings for the freestanding blade (Fig. 2a), it is concluded from Figures 3 to 5 that the overall stability behavior of a sectored vane cascade of four, five or six blades, as well as the main directions, for the most stable and unstable regions, remains the same. These directions are also not affected by the different amplitude distributions

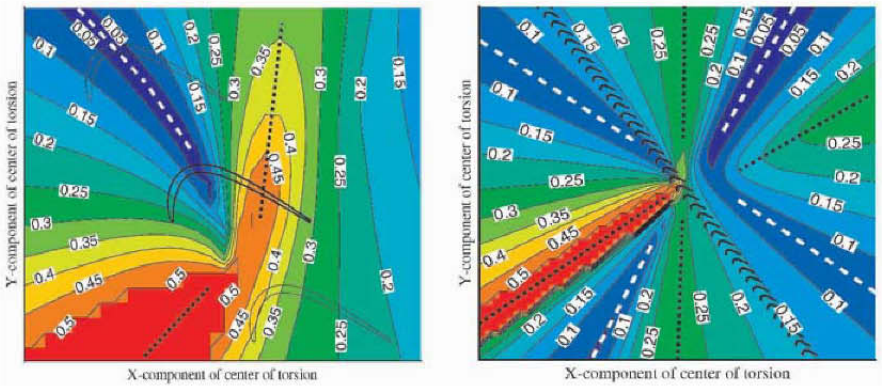

(a) Torsion-dominated mode shapes (b) Bending dominated mode shapes

Figure 2. Freestanding blade cascade

from cases 1, 2, and 3. In all cases the stability of the reference sectored vane is more sensitive to a change in the pitching axis location along, rather than normal to, the surfaces of the airfoils.

The region of the most stable pitching axis locations begins slightly below the reference vane, passes its high curvature region and extends upwards along the pitch-wise direction of the cascade (see dashed line in Figs. 2a and 3-5). The most unstable direction (see dotted line in Figs. 2a and 3-5) of the pitching axis locations also begins below the reference vane and has two branches. One corresponding to a higher instability level is orientated upstream of the cascade approximately perpendicular to the cascade tangential direction. Another one with a lower level of instability passes the reference vane at approximately 60% true chord and is directed outside of the cascade normal to the aft part of the vane.

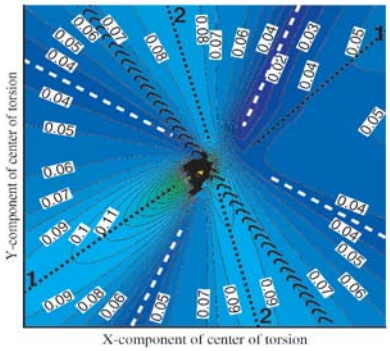

(a) Four-airfoil sectored vane

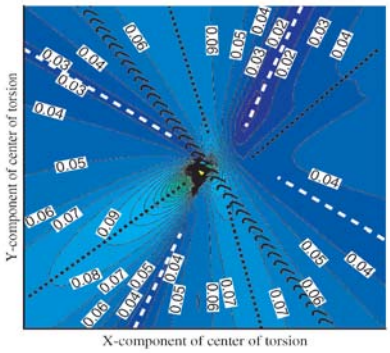

(b) Five-airfoil sectored vane

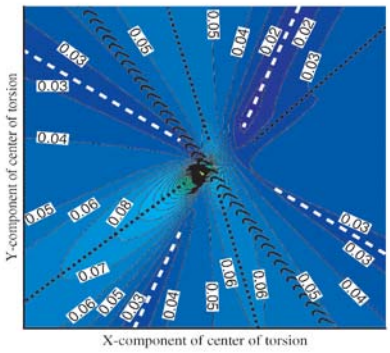

(c) Six-airfoil sectored vane

Figure 3. Case 1 vibration amplitude distribution (far field domain)

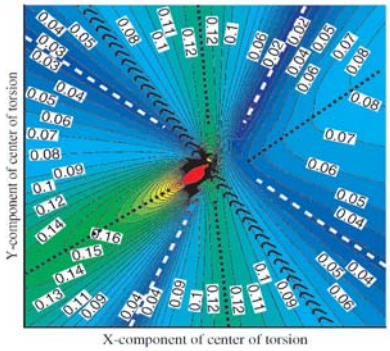

(a) Four-airfoil sectored vane

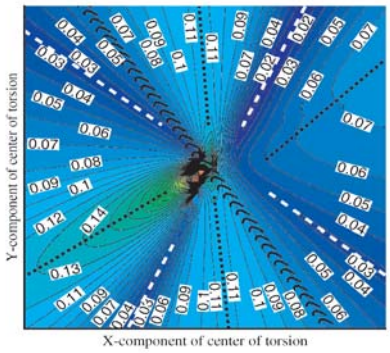

(b) Five-airfoil sectored vane

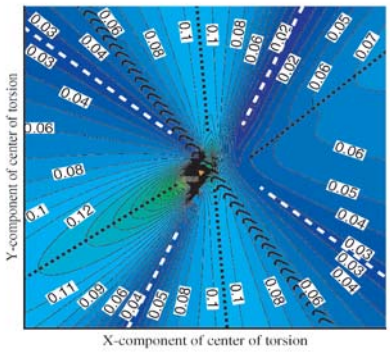

(c) Six-airfoil sectored vane

Figure 4. Case 2 vibration amplitude distribution (far field domain)

However, the absolute value of the average aerodynamic work is fairly different between the freestanding blade and multiple-airfoil sectored vanes. None of the four-, five- or six-airfoil sectored vane has a region of as high gradients in critical reduced frequency along the mid-section of the reference vane as the freestanding blade. Furthermore, the stability increase for a sectored vane is clearly seen: the shape of the domain with unstable pitching axis locations that the multiple-airfoil sectored vanes have at k=0.25 (for Case 1 amplitude distribution, Fig. 3), at k=0.35 (for Case 2 amplitude distribution, Fig. 4) or at k=0.2 (for Case 3 amplitude distribution, Fig. 5) is achieved for the freestanding blade already at much higher reduced frequency of k=0.5 (Fig. 2a).

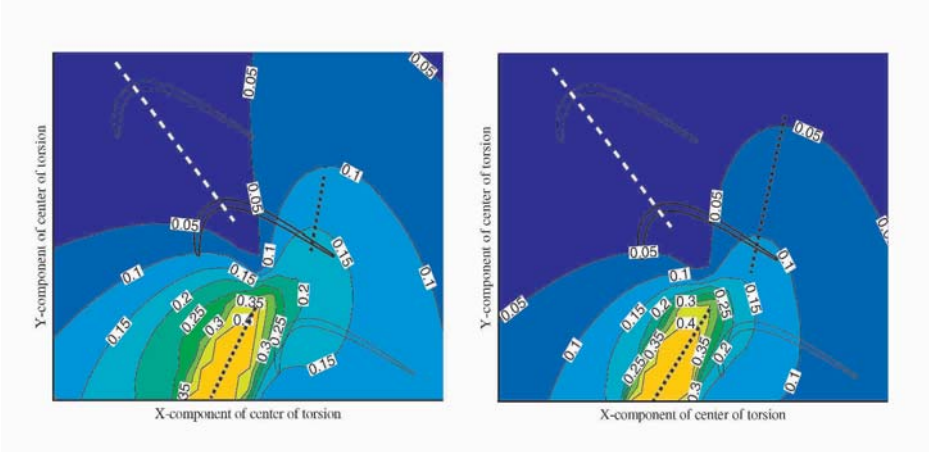

(a) Four-airfoil sectored vane

(b) Six-airfoil sectored vane

Figure 5. Case 3 vibration amplitude distribution (near field domain)

Increasing the number of airfoils in a sector clearly affects the absolute value of the average aerodynamic work of the sectored vane with uniform (Figs. 3a-c) or internal blade dominated (Figs. 5a-b) vibration amplitude distribution. For similar curved contour lines the values of the critical reduced frequency corresponding to these lines are higher for the sectored vane with a lower number of airfoils in sector. In the domain near the aft part of the suction surface of the reference vane an increase in the number of blades from four to six leads to a decrease of 0.05 in the critical reduced frequency values. The size of the domain corresponding to the critical reduced frequency less than 0.05 is significantly larger for the six- than for the four-airfoil sectored vane. For the sectored vane displacement with the edge blades dominated (Figs. 4a-c) the influence on the absolute value of the average aerodynamic work of the number of airfoils in the sector is much less.

A comparison of Figures 3 to 5 shows the effect of a vibration amplitude ratio between the edge and internal blades of the sector on the aerodynamic stability of the sectored vane. A change in the vibration amplitude distribution from the uniform to the internal blades dominant stabilizes the sectored vane. While choosing the vibration amplitude with the edge airfoils dominant decreases the stability (Figs. 4a-c). The size of the domain with the critical reduced frequency less than 0.05 becomes smaller. While near the aft part of the reference vane suction surface the maximum of the critical reduced frequency values increases.

Far field domain

The descriptions of the results are given here with respect to the torsion axis location. This means that the torsion axis location approaching infinity along the chord-wise direction corresponds to a translation of the reference vane in the normal to the chord-wise direction. Similarly, a torsion axis location approaching infinity in the normal-to-chord direction is equivalent to a chord-wise bending. Thus, symmetry at infinity in the critical reduced frequency map about the reference vane is expected (Figs. 6-7). Furthermore, the stability prediction for bending-dominated modes become a complementary tool for clarification of the trends observed for the torsion-dominated modes.

As for freestanding blade cascades (Fig. 2b) the critical reduced frequency maps for the four-, five- and six-airfoil sectored vanes (Figs. 5-6) have two most stable and two most unstable regions. The directions of these regions are somewhat similar to the freestanding blades despite the vibration amplitude distribution between the airfoils in the sector (Figs. 6-7). The number of airfoils in the sector does not, in general, affect the directions of the two most stable and two most unstable regions (Figs. 6a-c and 7a-c). The two most stable regions are perpendicular to each other (see dashed line in Figs. 6-7). The first unstable region (which is also the largest of the two unstable regions found) is orientated almost normal to the pitch-wise direction of the cascade (dotted line 1). The second region of lower stability lies somewhere parallel to the throat line of the reference vane (dotted line 2). As expected, the aerodynamic damping level of the sectored vanes with the edge blade dominated (Figs. 7a-c) are higher than for the sectored vanes with the uniform vibration amplitude distribution (Figs. 6a-c). The critical reduced frequency values for the Case 2 amplitude distribution are varying between 0.03 and 0.17, while for the Case 1 those values are lying between 0.02 and 0.11.

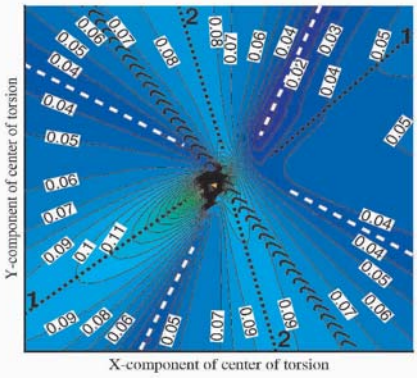

(a) Four-airfoil sectored vane

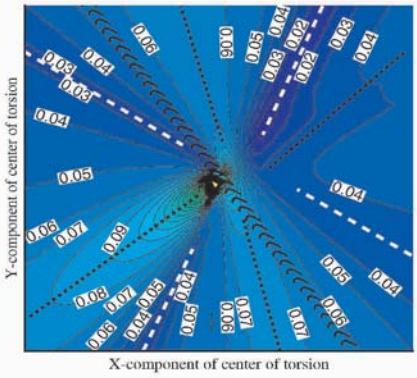

(b) Five-airfoil sectored vane

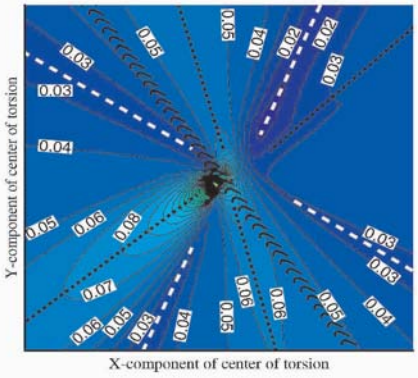

(c) Six-airfoil sectored vane

Figure 6. Case 1 vibration amplitude distribution (far field domain)

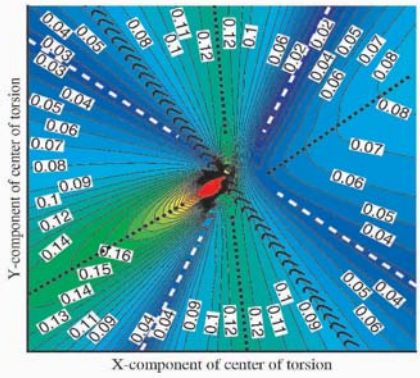

(a) Four-airfoil sectored vane

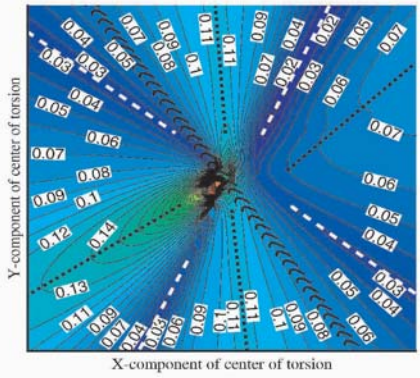

(b) Five-airfoil sectored vane

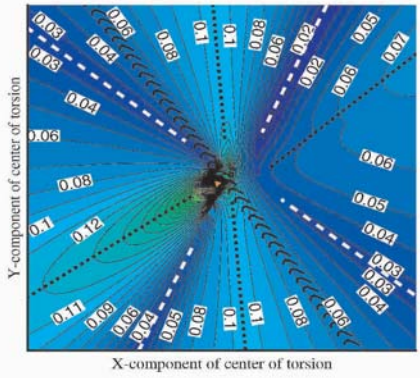

(c) Six-airfoil sectored vane

Figure 7. Case 2 vibration amplitude distribution (far field domain)

This is still much lower than the freestanding blade cascade which has critical reduced frequency values between 0.05 and 0.5 (Fig. 2b).

Soldier modes. Structural analysis shows that a vibration pattern with identical amplitude and zero inter-blade phase angle is a typical mode shape for a sectored vane cascade at low reduced frequencies. The critical reduced frequency maps for the four-, five- and six-airfoil sectored vanes for this so-called "soldier mode" are shown in Figures 8a, 8b and 8c, respectively.

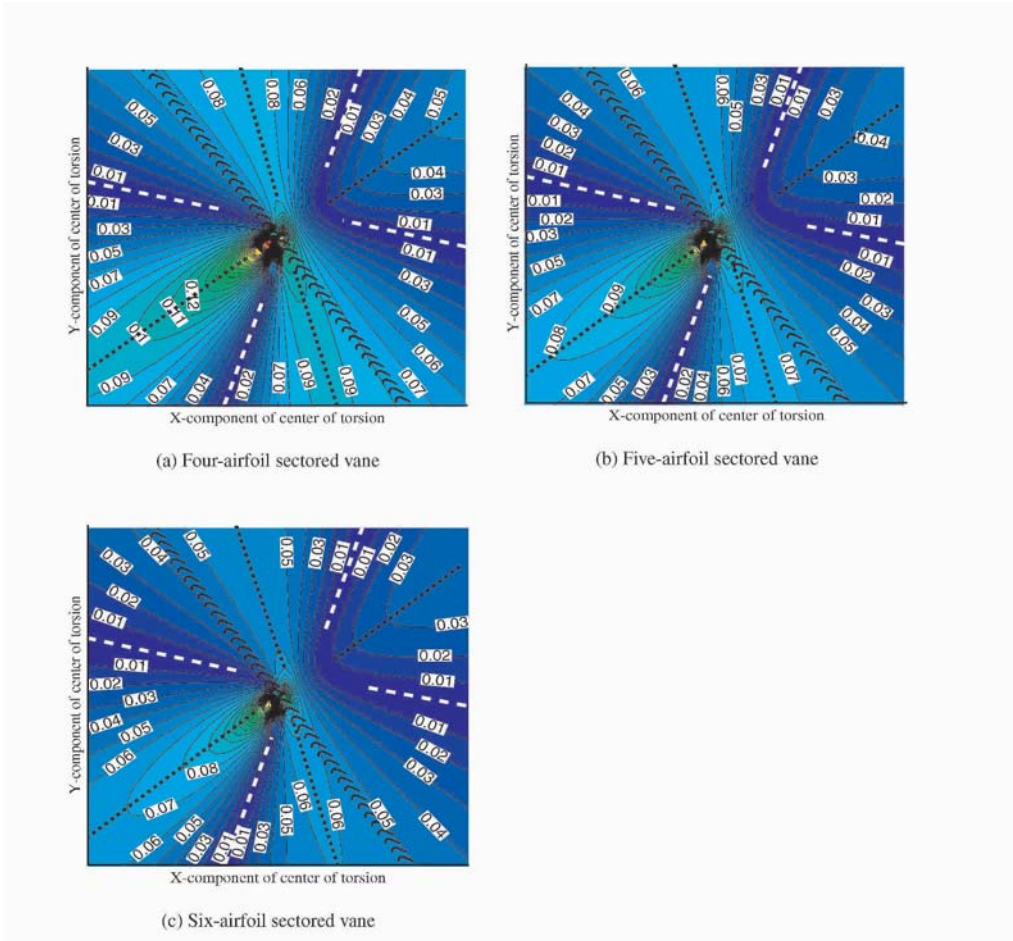

Figure 8. Soldier mode (far field domain)

As for a more general case of real sector mode shapes (far-field domain, Case 1 amplitude distribution, referred to Figs. 6a-c) a presence of the two most stable and two most unstable regions is observed. The absence of the out-phase motions of the blades within the sector, that characterizes the soldier modes, does not affect the directions of the second region of stability and the two instability regions (Figs. 8a-c). While the angle between the largest stable region and the pitch-wise direction of the cascade increases up to 45 degrees.

As expected, the sectored vanes undergoing solder modes become even more stable, in comparison to a more general case of real sector mode shapes, with the range of the critical reduced frequencies between 0.01-0.11.

Thus, also for bending-dominated modes the similarity between the main stability and instability directions for the four-, five- and six-airfoil sectored vanes are observed. The differences in the level of aerodynamic damping are defined by the number of the airfoils in the corresponding sectored vane. As expected, increasing the number of airfoils in sector from four to six increases the aerodynamic stability of the cascade.

6. Conclusions

A model for performing a stability analysis towards a reduced frequency and sector mode shape variation has been applied to a low-pressure turbine sectored vane. A parametrical study summarizing the effect of the reduced frequency and sector mode shape has been carried out varying the vibration amplitude distribution between the airfoils in sector as well as the number of airfoils in sector. The main assumption is that the flow is isentropic and two-dimensional. Critical reduced frequency maps have been provided for torsion- and bending-dominated sector mode shapes and the following conclusions have been drawn.

Even though the absolute value of the average aerodynamic work is rather different between four-, five- and six-airfoil sectors a high risk for instability still exists in the neighborhood of realistic reduced frequencies of modern low-pressure turbine (critical reduced frequency between 0.2 and 0.3 for torsion-dominated modes, between 0.01 and 0.05 for bending-dominated modes).

For the cases studied it is observed that the sectored vane displacement with the edge airfoils in the sector dominating provides the most unstable critical reduced frequency map.

Increasing the number of blades in the sector decreases the risk for a sectored vane to be unstable for uniform or internal blades dominated amplitude distributions. The stability of the sectored vane with edge blades dominated amplitude distribution is not affected much by the number of blades in the sector.

7. Future work

To generalize the findings, similar parametric studies should be performed for another sectored vane geometry and for other flow conditions.

An extension from single to multiple frequency modes can be introduced in the present algorithm. It would take into account the mode coalescence, i.e. even though every single frequency mode by itself can be stable, their cross products may make the multiple frequency mode to be unstable.

Acknowledgments

The authors wish to thank GE Aircraft Engines for the provision of NOVAK (2D Version 6.0), for financial support and for the permission to publish the findings. Thanks also to the Swedish Energy Authority for partial financial support of the first author.

References

[1] Whitehead, D. S., and Evans, D. H., 1992, "Flutter of grouped turbine blades", 92-GT-227, *ASME Gas Turbine and Aeroengine Congress and Exposition*, Cologne, Germany.

[2] Kahl, G., 1995, "Application of the time linearized Euler method to flutter and forced response calculations", ASME paper 95-GT-123.

[3] Chernysheva, O. V., Fransson, T. H., Kielb, R., E., and Barter, J., 2003, "Effect of sector mode shape variation on the aerodynamic stability of a low-pressure turbine sectored vane", GT2003-38632, *ASME/IGTI Turbo Expo*, Atlanta, Georgia, USA.

[4] Panovsky, J., and Kielb, R., E., 1998, "A design method to prevent low-pressure turbine blade flutter", 98-GT-575, *ASME Gas Turbine Conference and Exhibition*, Stockholm, Sweden.

[5] Tchernysheva, O. V., Fransson, T. H., Kielb, R., E., and Barter, J., 2001, "Comparative analysis of blade mode shape influence on flutter of two-dimensional turbine blades", ISABE-2001-1243, *XV ISOABE Conference*, Bangalore, India.

[6] Lane, F., 1956, "System mode shapes in the flutter of compressor blade rows", *Journal of the Aeronautical Science*, Jan., pp. 54-66.

[7] Holmes, D.,G., and, Chuang, H.A., 1991, "2D linearized harmonic Euler flow analysis for flutter and forced response", *Unsteady Aerodynamics Aeroacoustics and Aeroelasticity of Turbomachines and Propellers*, Springer Verlag, New York, pp. 213-230.

A METHOD TO ASSESS FLUTTER STABILITY OF COMPLEX MODES

Andrea Arnone[1], Francesco Poli[1], and Claudia Schipani[2]

[1] *"Sergio Stecco" Department of Energy Engineering*
University of Florence
Via S. Marta, 3 - 50139 Florence, ITALY

[2] *Avio - R&D*
Via Nizza, 312 - 10127 Turin, ITALY

Abstract A method to quickly predict aeroelastic stability or instability of blade row complex vibration modes is described. The computational approach is based on a time-linearized Navier-Stokes aeroelastic solver, and a specifically developed program. Time is saved by doing a few fundamental solver computations and then superposing the solutions to analyze each complex mode.
Test results on two low pressure turbines are presented.

Keywords: Flutter screening, complex modes, preliminary design, time-linearized, aeroelasticity

1. Introduction

Nowadays, important goals in the aero-engine design are weight and cost reduction, as well as reliability increase. These goals are reached by reducing the number of mechanical parts and by adopting thin and highly loaded blades. These trends increase the relevance of blade row vibration phenomena (flutter and forced response) that are recognized as a major cause of high cycle fatigue (HCF) failure in rotating as well as static components.

In recent years the attention of aero-engine industry has been focused on the development of advanced computational tools, that, combining CFD and structural dynamic analysis, —more or less accurately— model the fluid-structure interaction, and, in particular, enable the assessment of flutter stability [Marshall and Imregun, 1996]. However these tools are computationally very expensive and require detailed input data: thus their application is usually limited to the design validation phase, while they are not suitable for sensitivity and parameter studies, that are often needed during the preliminary design.

K.C. Hall et al. (eds.),
Unsteady Aerodynamics, Aeroacoustics and Aeroelasticity of Turbomachines, 31–40.

Less significant advances have been made for the development of design methods, that, adopting a simplified approach to the fluid-structure interaction modeling, but still relying on specifically developed computational tools, may be applied in the preliminary design, without loosing representativeness of the blade design under investigation.

The recent work by Panovsky and Kielb, proposing a design method to prevent LP turbine blade flutter [Panovsky and Kielb, 2000], is a well-known attempt in this direction. This method (P-K method) is based on the finding that flutter stability of a turbine blade vibration mode is not only depending on the mode frequency and blade aerodynamic operating condition, but also on the blade modeshape.
The flutter stability is still assessed by comparing the actual to critical reduced frequency, making the new method easily applicable. The critical reduced frequency, traditionally constant for a given mode typology (torsion or bending), is derived from the blade torsion axis location —or bending direction—, while the actual reduced frequency is computed through the traditional formula, based on mode frequency and blade aerodynamic operating condition: $k = \omega c/(2v_{out})$, where ω is the angular frequency, c is the chord and v_{out} is the outlet flow velocity.

On the other side the proposed method is limited to real modes in traveling waves. Real modes are single harmonic component modes: all points belonging to the same blade vibrate in phase (or antiphase) with each other.
This hypothesis is acceptable for elastically suspended uncoupled blades, but essentially excludes blade row assembly modes to be properly described.
This is the case for shrouded rotor rows, where the blade mechanical coupling generates the so-called complex modes, that can be seen as a superposition of two real modes in quadrature.

2. Computational method

Aim of this paper is to present a method to assess flutter stability of complex modes. As in the P-K method, the blade modeshape is approximated to a rigid motion and the row vibrates in traveling wave mode. Additionally, as in P-K, a single section of the blade (e.g. the one with the greatest displacements) is used to represent the blade 3D vibration mode.

Aeroelastic solver

During our research on Computational Aeroelasticity (CA) at the Department of Energy Engineering (University of Florence), we developed an aeroelastic solver, designed to work together with the steady/unsteady flow solver TRAF [Arnone, 1994].
This aeroelastic solver (named LARS, time-Linearized Aeroelastic Response

Solver) is based on the uncoupled energy approach: the blade harmonic oscillation is prescribed in terms of frequency and modeshape, and flutter stability is assessed through a work per period calculation. Quasi-three-dimensional fluid motion equations (Euler, thin shear layer or Navier-Stokes) are time-linearized about a steady solution [Hall and Clark, 1993]; this steady solution, representing the mean flow, is computed by TRAF in steady mode, while its harmonic perturbation, representing the flow field unsteadiness generated by blade harmonic motion, is calculated by LARS.

Numerical stability is guaranteed through the introduction of appropriate artificial dissipation, derived from TRAF definition through frozen coefficient linearization. In order to speed up convergence, local time stepping, multigrid acceleration and residual smoothing techniques have been implemented in a way similar to that adopted for TRAF. Non-reflecting boundary conditions are used on inlet and outlet boundaries [Giles, 1988].

The solver implements both traveling wave mode and influence coefficient technique; in this work the traveling wave mode has been applied.

LARS was previously validated for turbine blades applications on International Standard Configuration turbine experimental data [Fransson and Verdon, 1991], in particular STCF4 (see figures 1a, 1b).

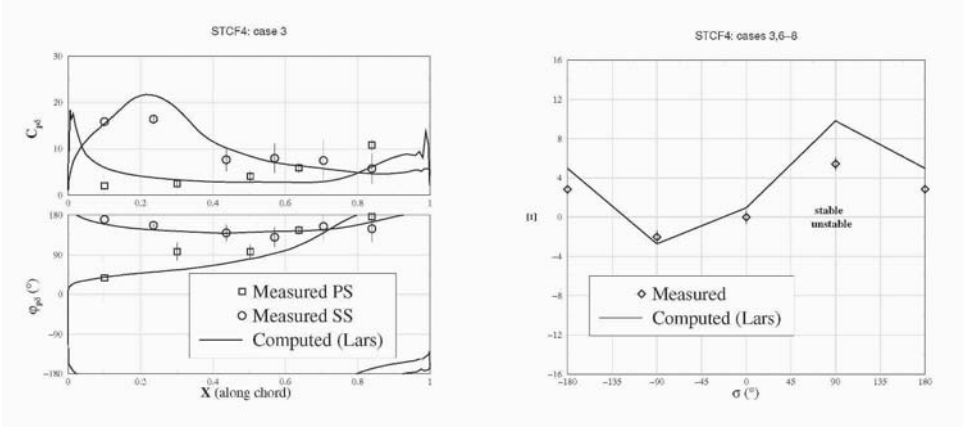

Figure 1a. 4^{th} standard configuration, case 3. Comparison of computed and experimental pressure perturbation coefficient (magnitude and phase)

Figure 1b. 4^{th} standard configuration, cases 3, 6, 7, 8. Comparison of computed and experimental aerodamping coefficient

Flutter screening for real modes

Before applying flutter screening to complex modes, real mode screening has been implemented, through the integration of LARS with a specific pro-

gram developed at Department of Energy Engineering (University of Florence). This program is called INDIAN (INtegrated & DIstributed ANswer).

A detailed description of real mode flutter screening is not the aim of this paper, but the procedure will be briefly reviewed, because it represents the baseline scheme in the development of complex mode flutter screening.

An arbitrary real rigid vibration mode can be described as a real coefficient linear combination of three fundamental real modes, and the aerodynamic work can be expressed as a quadratic form of these coefficients. Once the 3×3 work matrix has been derived, the evaluation of the aerodynamic work for any real mode is straightforward and very efficient.
The aerodynamic work is then normalized to obtain the aerodynamic damping coefficient. This normalization is defined through a (squared) vibration amplitude, identified in such a way to achieve consistency with the traditional definitions of damping coefficient in the two particular cases of pure bending and pure torsion. In the appendix a fully consistent normalization is derived, alternative to that proposed by Panovsky and Kielb [Panovsky and Kielb, 2000].

In the LARS-INDIAN based screening procedure:

1 aeroelastic calculations are carried out on two pure bending modes along orthogonal directions and one pure torsion mode, selected as fundamental modes, at prescribed interblade phase angles (IBPAs) and vibration frequencies, covering the respective ranges of variation;

2 fundamental perturbations are combined, so that the work and aerodynamic damping for any arbitrary torsion axis location can be derived;

3 the generation of several flutter maps, applicable in real mode flutter screening, is allowed, namely:

- aerodamping maps, providing the aerodynamic damping coefficient as a function of torsion axis location —or bending direction— for a given IBPA and vibration frequency,
- stability maps, providing the stability parameter (defined as the minimum of the aerodynamic damping sinusoidal approximation over the range of IBPA variation) as a function of torsion axis location —or bending direction— for a given frequency,
- critical reduced frequency maps, providing the reduced frequency below which the stability parameter becomes negative as a function of torsion axis location —or bending direction—.

Flutter screening for complex modes

In applying flutter screening to complex modes, a similar approach is followed.

The rigid complex mode is described as a complex —instead of real— coefficient linear combination of the same three fundamental modes: the pressure perturbation on a generic complex mode (at a given IBPA and frequency) is derived by linearly superposing the three fundamental real perturbations solved for the generation of real mode flutter maps.

Note that the generic complex mode is assigned as the sum of two real modes in quadrature with a specified amplitude ratio. This non-unique description of the mode is converted into a unique complex coefficient linear combination of the three fundamental modes, and the complex mode pressure perturbation and the aerodynamic work are consequently derived. The aerodynamic work normalization is consistently extended from real to complex modes, through an appropriate "complex mode amplitude" (see appendix).

In the above described approach to complex mode screening no simplifying assumptions are introduced [Kielb et al., 2003]: all contributions to the aerodynamic work are taken into account (those combining the unsteady pressures generated by one harmonic component to the displacements of the same harmonic component, those combing the unsteady pressures generated by one harmonic component to the displacements of the other harmonic component, as well as the mean pressure contribution).

Moreover, since a complex mode is specified through four real parameters (two complex coefficient ratios) rather than two (two real coefficient ratios), a two-dimensional flutter map is not suitable for complex mode flutter stability assessment.

Hence, when dealing with complex modes, mode-specific outputs are generated. In particular, for each prescribed complex mode:

1 the aerodynamic damping coefficient (at each IBPA and frequency for which input data have been provided),

2 the stability parameter (at each frequency for which input data have been provided),

3 the critical reduced frequency,

4 the aerodynamic damping coefficient at a specified IBPA (at each frequency for which input data have been provided), obtained by exploiting the aerodamp sinusoidal approximation,

5 the critical reduced frequency at a specified IBPA.

3. Results

The application of the method to two low pressure turbine rotor bladerows is presented; the two testcases are jointly defined with Duke University, and will be labeled AT and BT.

Complex flutter screening results, obtained through the present method, are compared with the results of a similar method based on CYCLOPS [Kielb and Barter, 2003]; for validation purposes, they are also compared with the aerodamping solution of TACOMA 3D Navier-Stokes time-linearized analysis [Holmes et al., 1997], performed on 3D flexible modeshapes.

Since overall flutter stability behavior remain rather similar for similar geometries and aerodynamic conditions of LPT blades with pure subsonic flow [Tchernycheva et al., 2001], it is possible to perform the aeroelastic calculations on a blade and then extend the results to another one, for preliminary design purposes.

In this paper, LARS calculations have been carried out on one section of the BT bladerow, and then used for both AT and BT complex flutter screening.

In figures 2a and 2b, the critical reduced frequency maps obtained on the BT selected section are presented.

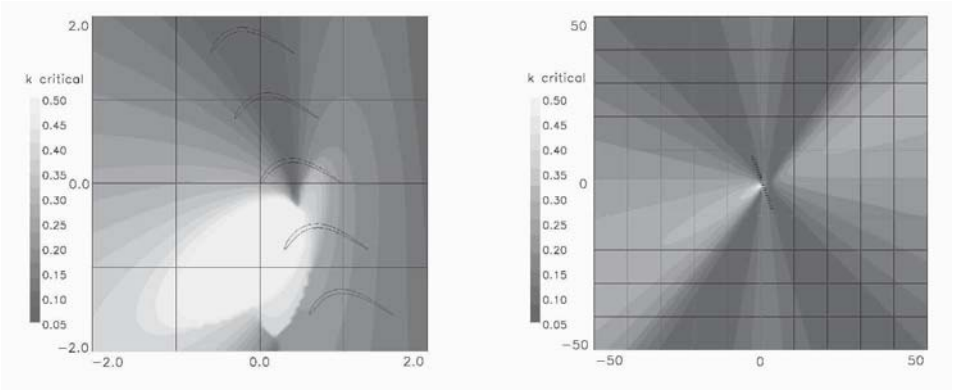

Figure 2a. BT bladerow: nearfield critical reduced frequency map

Figure 2b. BT bladerow: farfield critical reduced frequency map

For each testcase, two complex mode families have been analyzed: the first will be referred to as m1, the second as m2.

In figure 3a the aerodynamic damping coefficient is plotted versus the number of nodal diameters for the AT m1 mode family. The two INDIAN results are based on Navier-Stokes and Euler aeroelastic calculations: the adopted aerodynamic work normalization is the one described in the appendix. It can be seen that viscous effects do not have much influence on the blade flutter stability.

For comparison purposes, results are also presented in terms of the so-called "critical damping ratio", based on the energy normalization described in [Kielb et al., 2003]: in figure 3b INDIAN results are plotted together with CYCLOPS and TACOMA 3D solutions. The two CYCLOPS curves are derived from Euler aeroelastic calculations performed on two different LPT blades; in par-

ticular "Cyclops B" is based on the BT blade, while the reference configuration for "Cyclops E" is the one presented in [Panovsky and Kielb, 2000]. INDIAN results compare well with CYCLOPS ones, especially with "Cyclops E"; the trend of TACOMA solution is also captured: the agreement is better on backward traveling waves, while INDIAN solution overpredicts stability for low positive nodal diameters.

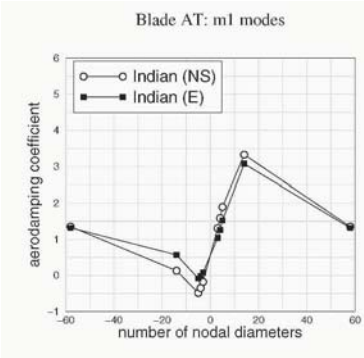

Figure 3a. AT m1 modes: aerodamping coefficient

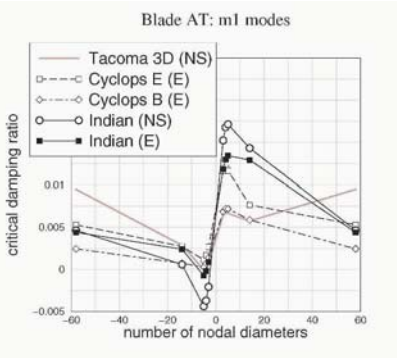

Figure 3b. AT m1 modes: critical damping ratio

In figures 4a and 4b, the same plots are presented for AT m2 modes. Again viscous effects seem to be not very important and INDIAN results agree well with CYCLOPS, especially with the "Cyclops E" curve. For low (positive and negative) nodal diameters the agreement is fairly good with TACOMA 3D results, as well.

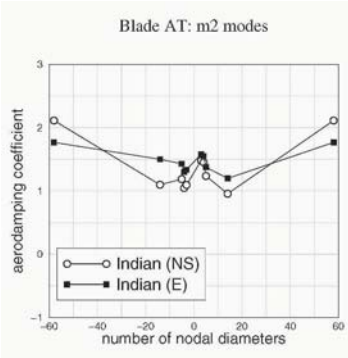

Figure 4a. AT m2 modes: aerodamping coefficient

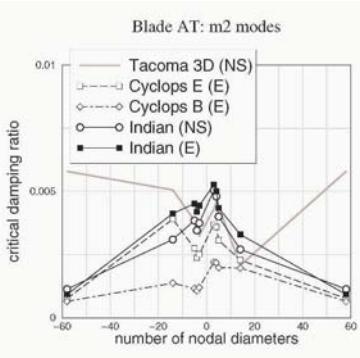

Figure 4b. AT m2 modes: critical damping ratio

In figures 5a and 5b, results for BT m1 mode family are shown. For this blade, only Navier-Stokes based INDIAN results are presented. A generally good agreement is obtained between INDIAN, CYCLOPS and TACOMA;

again the agreement is better for backward traveling waves, and INDIAN tends to overestimate stability for positive nodal diameters.

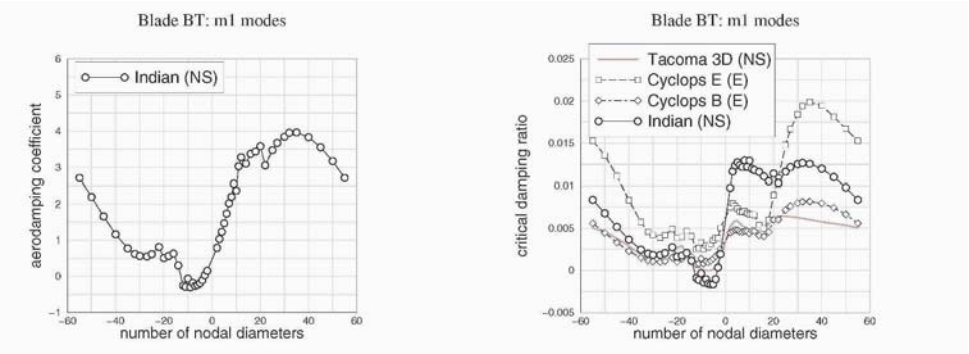

Figure 5a. BT m1 modes: aerodamping coefficient

Figure 5b. BT m1 modes: critical damping ratio

Finally, results for BT m2 modes are presented in figures 6a and 6b. Here agreement is satisfactory between INDIAN and CYCLOPS results. Compared with TACOMA solution, the trend is captured in the low nodal diameter region, but the two flutter screening methods consistently over- or underpredict stability in the other regions.

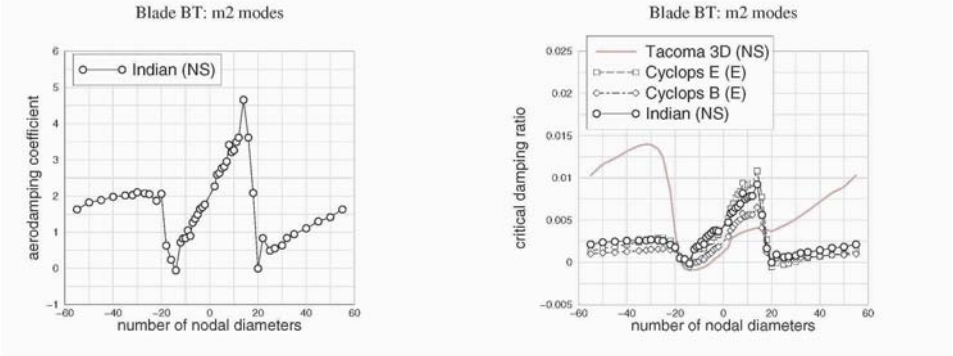

Figure 6a. BT m2 modes: aerodamping coefficient

Figure 6b. BT m2 modes: critical damping ratio

4. Conclusions

A computational method for efficient complex mode flutter screening was described.

This approach exploits a set of aeroelastic time-linearized calculations in order to predict flutter stability of any specified complex mode of the analyzed bladerow and of similar ones. The method was developed for turbomachinery

bladerow design and was applied to two low pressure turbine rotor rows, for test and comparison purposes. From these results it was concluded that the method agrees well with the similar one described in [Kielb and Barter, 2003] for the majority of the examined modes. Both methods were also compared with a 3D time-linearized direct analysis: since they sometimes overestimate aeroelastic stability, flutter screening methods are not always conservative, so they are suitable for preliminary design, but further and more accurate analysis is required during design refinement. Additionally it was found that viscous effects are not very influent on flutter stability.

Future work is needed to understand if disagreement between flutter screening and 3D calculations is caused by the approximation method adopted to reduce 3D flexible modeshapes to 2D rigid ones.

Acknowledgments

The authors wish to acknowledge Avio for the financial support and the permission to publish. Special thanks to Prof. E. Carnevale (University of Florence) for encouraging this work. The authors wish also to express their gratitude to Prof. R.E. Kielb (Duke University) and J. Barter (GE) for providing testcase data and for some useful suggestions.

Appendix: Normalization for work

Let c_w be the aerodynamic work coefficient (that is, the aerodynamic work per unit span divided by mean inlet dynamic pressure and by squared chord).
The aerodamping coefficient is

$$\Xi = -\frac{c_w}{\pi A^2} \tag{A.1}$$

where A represents the vibration non-dimensional 'amplitude'.

In the traditional definition (see [Bölcs and Fransson, 1986]) A is the angular amplitude (in radians) for pure torsion or the translational amplitude (divided by the chord) for pure bending. When we deal with arbitrary rigid modes, we must define A in such a way to be consistent with the two mentioned extreme cases, while remaining smooth in the whole range of possible modes. We define

$$A = f^{-\frac{1}{2}} |h_\psi| \tag{A.2}$$

where h_ψ is the torsional coefficient in the linear combination that defines the mode under examination and f is an appropriate correction factor.

For real modes f must be continuous and positive real (so that it cannot affect the sign of the aerodamping), must tend to one when the torsion axis location Q gets near the airfoil and must tend to zero when Q gets infinitely far from the airfoil in such a way that $f D_Q^2 \to 1$ where D_Q is the distance of Q from the airfoil, normalized by the chord.

The correction factor proposed by Panovsky and Kielb [Panovsky and Kielb, 2000] is

$$f_{PK} = \left(\sqrt{{x_Q^N}^2 + {y_Q^N}^2} + \sqrt{(x_Q^N - 1)^2 + {y_Q^N}^2} \right)^{-2} \tag{A.3}$$

where x^N and y^N are two normalized coordinates such that the airfoil LE and TE are placed in $(0,0)$ and $(1,0)$, respectively. With this factor the desired goal of consistency is not quite reached, since $f_{PK}\, D_Q^2 \rightarrow 1/4$.

An alternative, fully consistent, correction factor is given by

$$f_{43} = \frac{4}{3 + f_{PK}^{-1}} \tag{A.4}$$

For complex modes f must be again continuous and positive real and must tend to real mode f when the complex mode degenerates to a real one. For real modes x_Q^N and y_Q^N were of course real and derived from the three linear combination real coefficients that describe the vibration mode (h_x, h_y and h_ψ). In order to extend the correction factor definition to complex modes, we can derive two complex quantities ($\hat{x}_Q^N$ and $\hat{y}_Q^N$) in a formally identical way, exploiting h_x, h_y and h_ψ (that are now complex). These two quantities are not coordinates of a point, since they are complex, but their moduli can be used in the previous formulae to compute generalized correction factors.

References

Arnone, A. (1994). Viscous analysis of three-dimensional rotor flow using a multigrid method. *Journal of turbomachinery*, 116:435–445.

Bölcs, A. and Fransson, T.H. (1986). *Aeroelasticity in turbomachines Comparison of theoretical and experimental cascade results*. Number 13 in Communication du laboratoire de thermique appliquée et de turbomachines de l'école polytechnique fédérale de Lausanne. EPFL.

Fransson, T.H. and Verdon, J.M. (1991). Updated report on "standard configurations for unsteady flow through vibrating axial-flow turbomachine-cascades". <http://www.egi.kth.se/proj/Projects/Markus%20joecker/STCF/STCF1to10/Documents/SC2110.92update.pdf>.

Giles, M. (1988). Non-reflecting boundary conditions for the euler equations. <http://web.comlab.ox.ac.uk/oucl/work/mike.giles/psfiles/bcs.ps.gz>.

Hall, K.C. and Clark, W.S. (1993). Linearized euler predictions of unsteady aerodynamic loads in cascades. *AIAA Journal*, 31:540–550.

Holmes, D.G., Mitchell, B.E., and Lorence, C.B. (1997). Three dimensional linearized navier-stokes calculations for flutter and forced response. In 8^{th} *International Symposium on Unsteady Aerodynamics and Aeroelasticity in Turbomachines*.

Kielb, R.E. and Barter, J. (2003). Flutter design of lpt blades with cyclic symmetry modes - complicating effects. Submitted to ISUAAAT 2003 Conference.

Kielb, R.E., Barter, J., Chernysheva, O., and Fransson, T.H. (2003). Flutter of low pressure turbine blades with cyclic symmetric modes - a preliminary design method. In *IGTI ASME Turbo Expo*.

Marshall, J.G. and Imregun, M. (1996). A review of aeroelasticity methods with emphasis on turbomachinery applications. *Journal of fluids and structures*, 10:237–267.

Panovsky, J. and Kielb, R.E. (2000). A design method to prevent low pressure turbine blade flutter. *Journal of engineering for gas turbines and power*, 122:89–98.

Tchernycheva, O.V., Fransson, T.H., Kielb, R.E., and Barter, J. (2001). Comparative analysis of blade mode shape influence on flutter of two-dimensional turbine blades. In *XV ISOABE conference*.

FLUTTER DESIGN OF LOW PRESSURE TURBINE BLADES WITH CYCLIC SYMMETRIC MODES

Robert Kielb
Duke University
rkielb@duke.edu

John Barter
GE Aircraft Engines

Olga Chernysheva and Torsten Fransson
Swedish Royal Institute of Technology

Abstract This paper describes a new preliminary design method to conduct flutter screening of LPT blades with cyclic symmetry mode shapes. As in the method for real mode shapes, baseline unsteady aerodynamic analyses must be performed for the 3 fundamental motions, two translations and a rotation. Unlike the current method work matrices must be saved for a range of reduced frequencies and interblade phase angles. These work matrices are used to generate the total work for the complex mode shape. Since it only requires knowledge of the reduced frequency and mode shape (complex), this new method is still very quick and easy to use. Theory and example applications are presented and compared with the results of full three-dimensional viscous CFD analyses. Reasonable agreement is found. The interaction effects of the cosine and sine modes and the work associated with the steady pressure are shown to generally be significant.

Keywords: Flutter, Cyclic Symmetry, Preliminary Design, Low Pressure Turbines

K.C. Hall et al. (eds.),
Unsteady Aerodynamics, Aeroacoustics and Aeroelasticity of Turbomachines, 41–52.

1. Introduction

Panovsky and Kielb (1998) presented a method to conduct preliminary flutter design analysis for LPT blades. The study identified the blade mode shape as the most important contributor determining blade stability. Each mode shape is represented by three rigid body motions (two translations and one rotation) at the spanwise location of maximum displacement. These three motions can be described by a "pitching axis". The critical value of reduced frequency is determined solely by this pitching axis location. By comparing this critical value with the actual reduced frequency, the stability is determined. Further investigation using the same approach (Chernycheva et al, 2001) has shown that the overall stability behavior, as well as identification of the most stable and the most unstable regions as a function of blade mode shape remain remarkably similar for a rather wide range of physical and aerodynamic parameters of LPT blades with pure subsonic flow. This method has been shown to be valuable in screening preliminary designs and identifying a minimal set of unsteady CFD analysis for final designs.

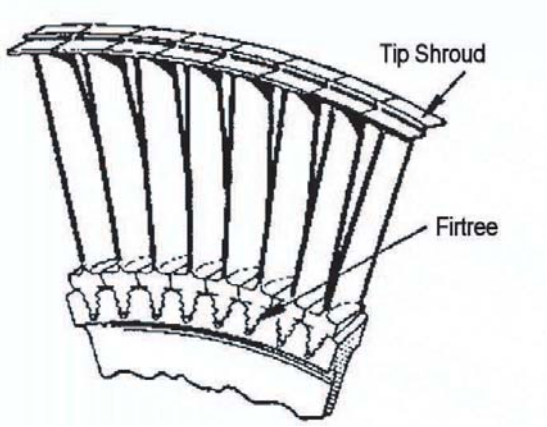

Figure 1. Local Blade Surface Velocity and Normal Vector

Many low pressure turbine (LPT) blade designs include a tip shroud (as shown in Fig. 1), that mechanically connects the blades together in a structure exhibiting cyclic symmetry. Since this arrangement is cyclically symmetric, each eigenvalue has a complex mode shape that can be represented by two real mode shapes that are commonly called the cosine and sine modes. The Panovsky-Kielb method results in two pitching axis locations for each eigenvalue. Although this can easily be done, experience has shown that it is ultra-conservative. That is, virtually all designs are judged to be unstable. This is shown in Kielb et al. (2003). This paper also describes an approach to extend the Panovsky-Kielb method to consider these complex mode shapes. As

in the Panovsky-Kielb method, baseline unsteady aerodynamic analyses must be performed for the 3 fundamental motions, two translations and a rotation. Unlike the current method work matrices must be saved for a range of reduced frequencies and interblade phase angles. These work matrices are used to generate the total work for the complex mode shape. Since it only requires knowledge of the reduced frequency and mode shape (complex), this new method is still very quick and easy to use. This paper describes the complete theory for extension of the Panovsky-Kielb method, gives example results, discusses the importance of the interaction effects of the cosine and sine modes, and discusses the contribution to work associated with the steady pressure.

2. Work for General Complex Mode Shapes

Work per cycle can be calculated by integrating the dot product of the local velocity vector with the local force vector over one cycle of vibration and the entire airfoil surface.

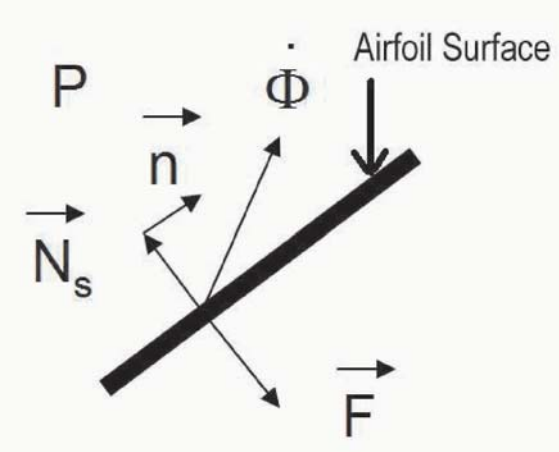

Figure 2. Coordinate Systems

$$W_{cyc} = \int_A \int_0^T -\left(\dot{\vec{\Phi}} \cdot \vec{N} P\right) dt dA$$

where

$\dot{\vec{\Phi}} =$ velocity

$\vec{N} =$ normal vector

$P =$ surface pressure

For harmonic motion the displacement, normal vector and surface pressure can be written as (the bar over the variables indicates the complex conjugate)

$$\vec{\Phi} = \frac{1}{2}\left(\vec{\phi}e^{-i\omega t} + \bar{\vec{\phi}}e^{i\omega t}\right)$$
$$\vec{N} = \vec{N}_s + \frac{1}{2}\left(\vec{n}e^{-i\omega t} + \bar{\vec{n}}e^{i\omega t}\right)$$
$$P = P_s + \frac{1}{2}\left(pe^{-i\omega t} + \bar{p}e^{i\omega t}\right)$$

The work per cycle then becomes

$$W_{cyc} = \frac{i\pi}{2}\int_A \left[P_s\left(\vec{\phi}\cdot\bar{\vec{n}} - \bar{\vec{\phi}}\cdot\vec{n}\right) + \vec{N}_s\cdot\left(\vec{\phi}\bar{p} - \bar{\vec{\phi}}p\right)\right]dA$$

For real mode shapes the work per cycle reduces to the familiar expression

$$W_{cyc}(\phi \text{ is real}) = \pi\int_A \left[\vec{N}_s\cdot\vec{\phi}p_{imag}\right]dA$$

Thus the steady pressure term does not contribute to the work when the mode shape is real. As will be shown, this is not the case when the mode shape is complex.

3. Work for Cyclic Symmetry Mode Shapes

For cyclic symmetry eigensolutions the mode shapes are complex. For a forward traveling wave

$\vec{\phi} = (\vec{a}_c - i\vec{a}_s)$
$\vec{n} = \vec{n}_c - i\vec{n}_s$
Where $\vec{a}_c$ and $\vec{a}_s$ are commonly referred to as the cosine and sine modes.
The work per cycle becomes
$W_{cyc} = \pi\int_A \left[\vec{N}_s\cdot(\vec{a}_c p_{imag} + \vec{a}_s p_{real}) - P_s\left(\vec{a}_c\cdot\vec{n}_s - \vec{a}_s\cdot\vec{n}_c\right)\right]dA$

Thus, the work has a component associated with the unsteady pressure and a component associated with the steady pressure.

$$W_{cyc} = W_{up} + W_{Ps}$$

4. Work Associated with Unsteady Pressure

The unsteady pressure can be decomposed into contributions from the cosine and sine components of the complex mode shape. For a forward traveling wave

$$p_{real} = p_{cr} + p_{si}$$
$$p_{imag} = p_{ci} - p_{sr}$$
$$W_{up} = \pi \int_A (\vec{a}_c (p_{ci} - p_{sr}) + \vec{a}_s (p_{cr} + p_{si})) \cdot \vec{n} dA$$
$$W_{up} = \pi \int_A (\vec{a}_c p_{ci}) \cdot \vec{n} dA + \pi \int_A (\vec{a}_s p_{si}) \cdot \vec{n} dA - \pi \int_A (\vec{a}_c p_{sr}) \cdot \vec{n} dA + \pi \int_A (\vec{a}_s p_{cr}) \cdot \vec{n} dA$$
$$W_{up}(\text{forward traveling wave}) = W_{cc} + W_{ss} - W_{cs} + W_{sc}$$

As can be seen W_{cc} and W_{ss} (diagonal terms) represent the work due to the unsteady pressure acting on the mode shape producing that unsteady pressure. The W_{cs} and W_{sc} terms (off-diagonal) represent the interaction terms. That is, the work caused by the unsteady pressure due to the sine mode acting upon the mode shape due to the cosine mode, and vice versa.

5. Rigid Body Mode Shapes

As in Panovsky and Kielb (1998) the three dimensional mode shapes are reduced to a two dimensional rigid body mode shape consisting of two translations and one rotation about the leading edge (See Figure 2).

$$\{a_{lc}\} = \begin{Bmatrix} h_{\xi lc} \\ h_{\eta lc} \\ \alpha_{lc} \end{Bmatrix} \text{ and } \{a_{ls}\} = \begin{Bmatrix} h_{\xi ls} \\ h_{\eta ls} \\ \alpha_{ls} \end{Bmatrix}$$

The l subscript defines the nodal diameter, and determines the interblade phase angle, of the mode.

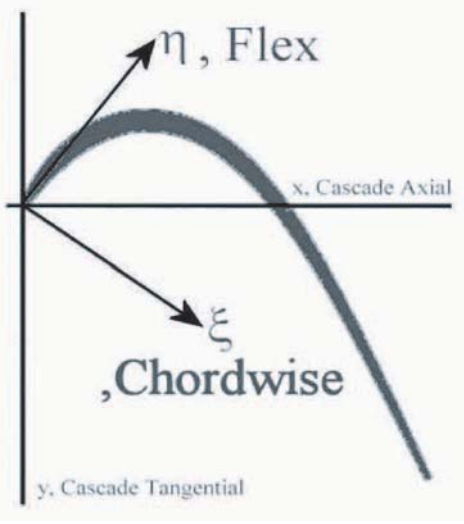

Figure 3. Aerodynamic Damping for Blade BT Mode 1

Now consider the term, W_{cc}.

$$W_{cc} = \pi \int_A (\vec{a}_c p_{ci}) \cdot \vec{n} dA$$
$$\vec{a}_c = h_{\xi c}\vec{\phi}_\xi + h_{\eta c}\vec{\phi}_\eta + \alpha_c \vec{\phi}_\alpha$$
$\vec{\phi}_\xi, \vec{\phi}_\eta$ are unit vectors in the ξ and η directions, respectively
$\vec{\phi}_\alpha$ is a vector in the η direction with an amplitude equal to the distance from the leading edge
$$p_{ci} = h_{\xi c} C_{\xi i} + h_{\eta c} C_{\eta i} + \alpha_c C_{\alpha i}$$

The C_i terms are the imaginary parts of the linearized unsteady aerodynamic coefficients. As in Panovsky and Kielb (1998) the work term can then be written as

$$W_{cc} = \left\{ \begin{array}{ccc} h_{\xi c} & h_{\eta c} & \alpha_c \end{array} \right\} \left[\begin{array}{ccc} w_{\xi\xi} & w_{\xi\eta} & w_{\xi\alpha} \\ w_{\eta\xi} & w_{\eta\eta} & w_{\eta\alpha} \\ w_{\alpha\xi} & w_{\alpha\eta} & w_{\alpha\alpha} \end{array} \right] \left\{ \begin{array}{c} h_{\xi c} \\ h_{\eta c} \\ \alpha_c \end{array} \right\}$$
$$where$$
$$w_{ab} = \pi \int_A \left(\left(\vec{\phi}_a C_{bi} \right) \cdot \vec{n} \right) dA$$

By similarity

$$W_{ss} = \left\{ \begin{array}{ccc} h_{\xi s} & h_{\eta s} & \alpha_s \end{array} \right\} \left[\begin{array}{ccc} w_{\xi\xi} & w_{\xi\eta} & w_{\xi\alpha} \\ w_{\eta\xi} & w_{\eta\eta} & w_{\eta\alpha} \\ w_{\alpha\xi} & w_{\alpha\eta} & w_{\alpha\alpha} \end{array} \right] \left\{ \begin{array}{c} h_{\xi s} \\ h_{\eta s} \\ \alpha_s \end{array} \right\}$$

The interaction terms can also be shown to be of the form

$$W_{cs} = \left\{ \begin{array}{ccc} h_{\xi c} & h_{\eta c} & \alpha_c \end{array} \right\} \left[\begin{array}{ccc} \tilde{w}_{\xi\xi} & \tilde{w}_{\xi\eta} & \tilde{w}_{\xi\alpha} \\ \tilde{w}_{\eta\xi} & \tilde{w}_{\eta\eta} & \tilde{w}_{\eta\alpha} \\ \tilde{w}_{\alpha\xi} & \tilde{w}_{\alpha\eta} & \tilde{w}_{\alpha\alpha} \end{array} \right] \left\{ \begin{array}{c} h_{\xi s} \\ h_{\eta s} \\ \alpha_s \end{array} \right\}$$
$$\tilde{w}_{ab} = \pi \int_A \left(\left(\vec{\phi}_a C_{br} \right) \cdot \vec{n} \right) dA$$

The C_r terms are the real parts of the unsteady aerodynamic coefficients. To get the W_{sc} terms simply interchange the c and s subscripts. In the new method presented herein, these three-by-three work matrices must be generated for a baseline airfoil for a range of interblade phase angles and reduced frequencies. These matrices can then used for a wide range of LPT blade designs.

6. Steady Pressure Term

Now consider the work due to the steady pressure for the same rigid body mode shapes. It can be shown that for the forward traveling wave.

$$W_{Ps} = -\pi \int_A \left[P_s \left(\vec{a}_c \cdot \vec{n}_s - \vec{a}_s \cdot \vec{n}_c\right)\right] dA =$$
$$-\pi \left(\left(\alpha_s h_{c,\xi} - \alpha_c h_{s,\xi}\right) \int_A P_s \cos\left(\theta_N\left(A\right)\right) dA + \left(\alpha_c h_{s,\eta} - \alpha_s h_{c,\eta}\right) \int_A P_s \sin\left(\theta_N\left(A\right)\right) dA \right)$$

The term θ_N is the local angle between the surface normal and the chord line. Therefore the first integration term is the steady lift and the second is the steady drag. In general the work associated with the steady pressure is nonzero for airfoils producing lift and drag, and having both translational and rotational motion.

7. Backward Traveling Waves

For backward traveling waves the interblade phase angle changes sign and the mode shape is

$\phi = \vec{a}_c + i\vec{a}_s$
The work associated with the unsteady pressure then becomes
W_{up}(backward traveling waves) $= W_{cc} + W_{ss} + W_{cs} - W_{sc}$

Thus, the sign of the interaction terms is negative of that for the forward traveling waves. Note that all of these individual work terms are different from those of the forward traveling waves because the interblade phase angle is also switched in sign. The work associated with the unsteady pressure, W_{Ps}, is the negative of that shown above for the forward traveling wave.

8. Example Problems

A finite element cyclic symmetry analysis was performed on a LPT turbine rotor (Blade BT). For the first 20 nodal diameter mode the reduced frequency is 0.23 and the mode shapes for the forward traveling wave are

$$\{a_{20c}\} = \left\{ \begin{array}{c} -0.260 \\ -0.036 \\ -0.638 \end{array} \right\} \text{ and } \{a_{20s}\} = \left\{ \begin{array}{c} -0.072 \\ -0.059 \\ 0.149 \end{array} \right\}$$

Since 92.1% of the kinetic energy is in cosine mode, this mode is expected to dominate. The cosine mode has a pitching axis at (ξ=-0.056, η=0.407). For this location the traditional P-K method plot gives a critical reduced frequency of approximately 0.1. The sine mode has a pitching axis at (ξ=0.396, η=-0.482) for which the critical reduced frequency is approximately 0.5. Therefore, the traditional method judges the cosine mode to be stable and the sine mode to be unstable.

This case was run using the method described herein with using the blade described in Reference 1 for the baseline work matrices. The results are given in Table 1. As can be seen the total work is dominated by W_{cc} with a significant contribution from the interaction terms, W_{cs} and W_{sc}. This interaction terms results in a stabilizing effect for the forward traveling wave and a destabilizing effect for the backward traveling wave. The work associated with the steady pressure has a relatively small effect on the total work. The critical damping ratio, ζ, is given for both the current method and a that of a full 3D, viscous, CFD method. Both modes are judged to be stable and there is relatively good agreement between methods.

The above analysis was performed for additional nodal diameters and the results are shown in Figure 4.

Table 1. Work and Damping for Blade BT, Mode 1, 20 Nodal Diameters

Work Component	Forward Traveling Wave	Backward Traveling Wave
W_{cc}	-61.6	-40.2
W_{ss}	-0.3	0.3
W_{cs}	14.5	10.4
W_{sc}	5.7	4.1
W_{Ps}	-2.2	2.2
W_{cyc}	-72.9	-31.4
ζ	0.89%	0.39%
ζ (CFD Method)	0.62%	0.27%

The results labeled Cyclops E were obtained using the current method with the baseline work matrices for the blade described in Reference 1 using a 2D inviscid code. Those labeled Cyclops B were obtained using work matrices obtained from a midspan section of blade BT, also using a 2D inviscid code. In addition results labeled Indian NS (Navier-Stokes) and Indian Euler are from a similar method developed at the University of Florence [Arnone et al., 2003]. The Indian results were based on baseline aerodynamics for blade BT. Similar results for the second mode of blade BT are shown in Figure 5. For both modes the current method predicts the trends of damping versus nodal diameter reasonably well. With respect to using the current method as a preliminary design screening method, the overall stability is predicted correctly for these two modes (for both baseline work cases).

Blade AT was also analyzed with the new cyclic symmetry method and compared with CFD. These comparisons are shown in Figures 6 and 7.

Although not shown, similar comparisons have been made for three modes of two additional blades. For a total of 10 cases the overall stability agrees with the full 3D CFD method in all cases except one, where the current predicts

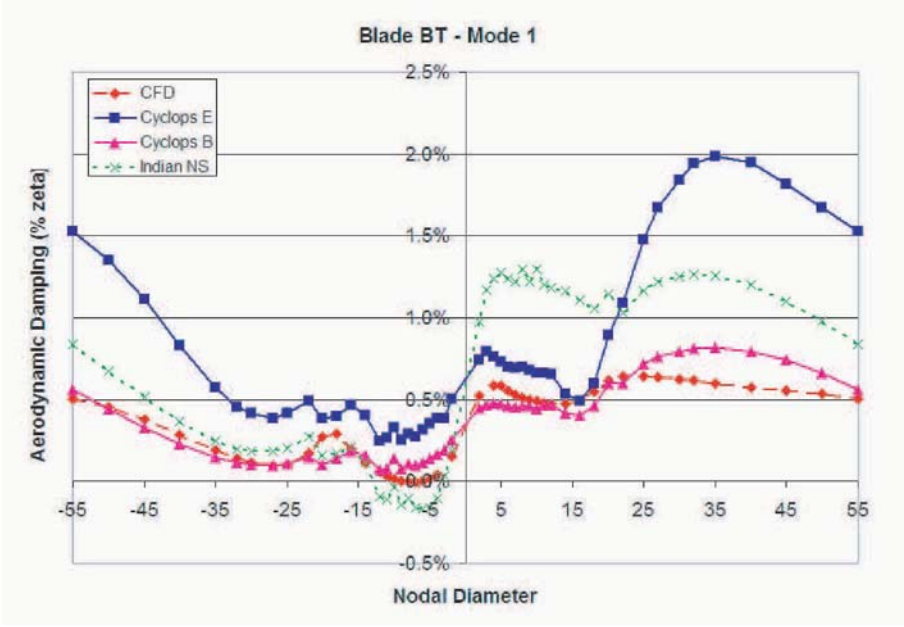

Figure 4. Aerodynamic Damping for Blade BT Mode 1

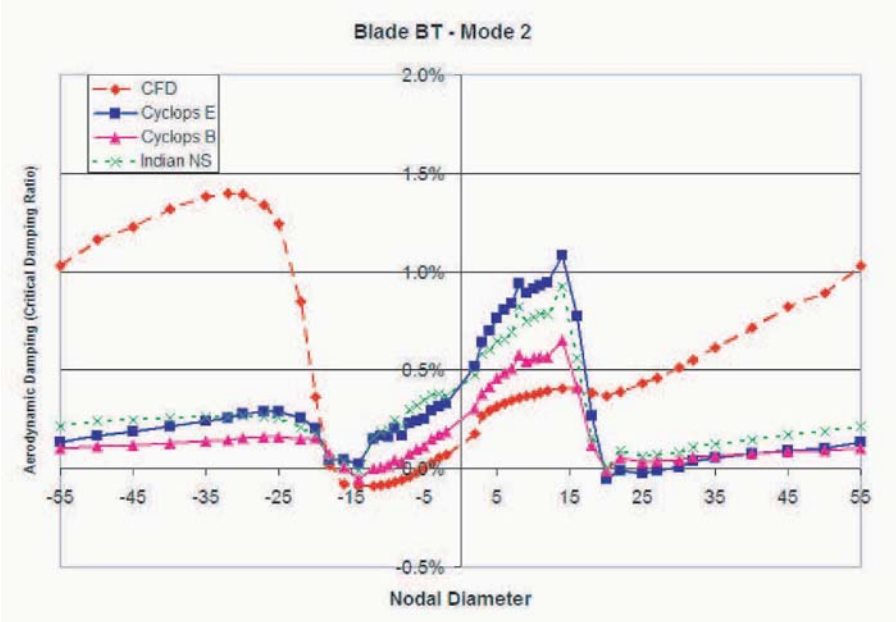

Figure 5. Aerodynamic Damping for Blade BT Mode 2

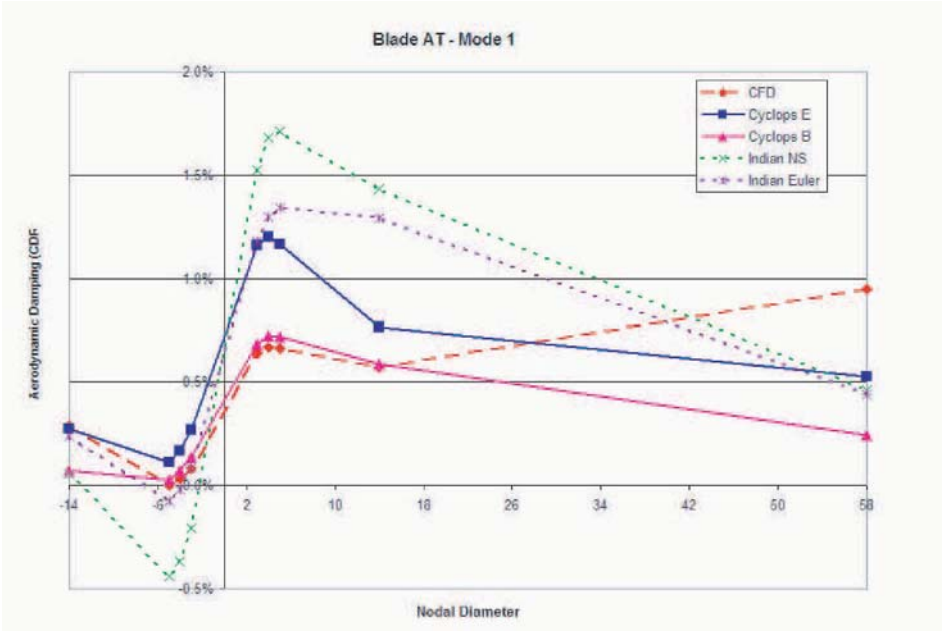

Figure 6. Blade AT Mode 1 Damping Contributions

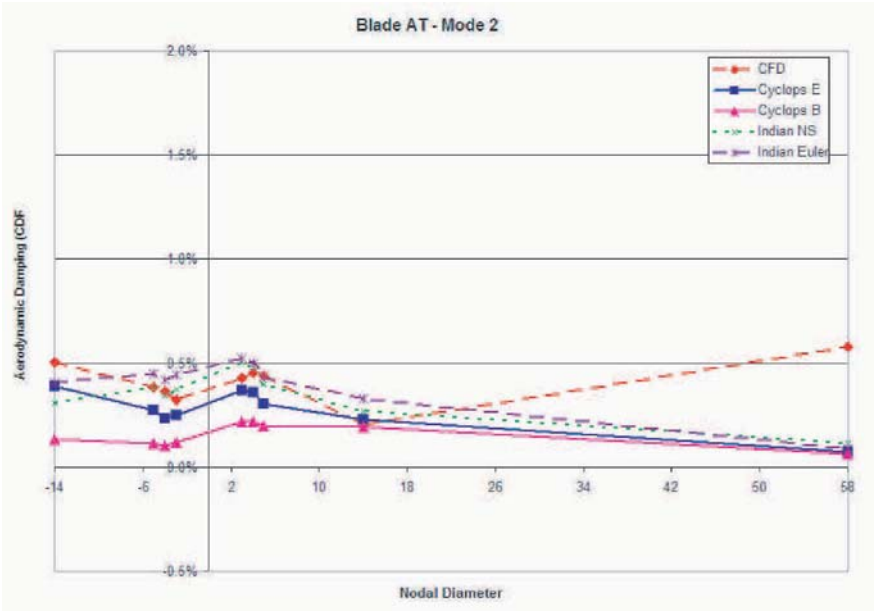

Figure 7. Blade AT Mode 2 Damping Contributions

instability and the 3D CFD method predicting stability. This type of error is preferred for a preliminary design screening tool.

The results for Blade BT were further examined to determine the contributions to total damping from the individual work terms. Four representative nodal diameters were selected for study. The 2 nodal diameter mode is nearly a pure sine mode (99.2% of total energy). The 5 nodal diameter mode is predominately a sine mode (90.8% of total energy). The 20 nodal diameter mode is predominately a cosine mode (92.1% of total energy). The 50 nodal diameter mode is nearly a pure cosine mode (99.9% of total energy). Figure 5 shows the damping contributions (critical damping ratio) from the W_{cc}, W_{ss}, W_{cs}, $W_{sc,}$ and W_{Ps} work terms. That is, the individual work terms are divided by 4π times the total energy. A positive number represents a stabilizing contribution.

The 2 nodal diameter results show that contribution of the interaction terms can be significant for nearly pure real modes. That is, the W_{sc} contribution is approximately half of the contribution of the W_{ss}. The 5 nodal diameter forward traveling wave results show that the interaction term can be the dominant contributor. The effect of the steady pressure terms is anti-symmetric about zero nodal diameters. At 5 nodal diameters the contribution of the steady pressure term is larger than that of W_{cc} and W_{ss}. In this case the contribution of the steady pressure term decreases as the number of nodal diameters is increased.

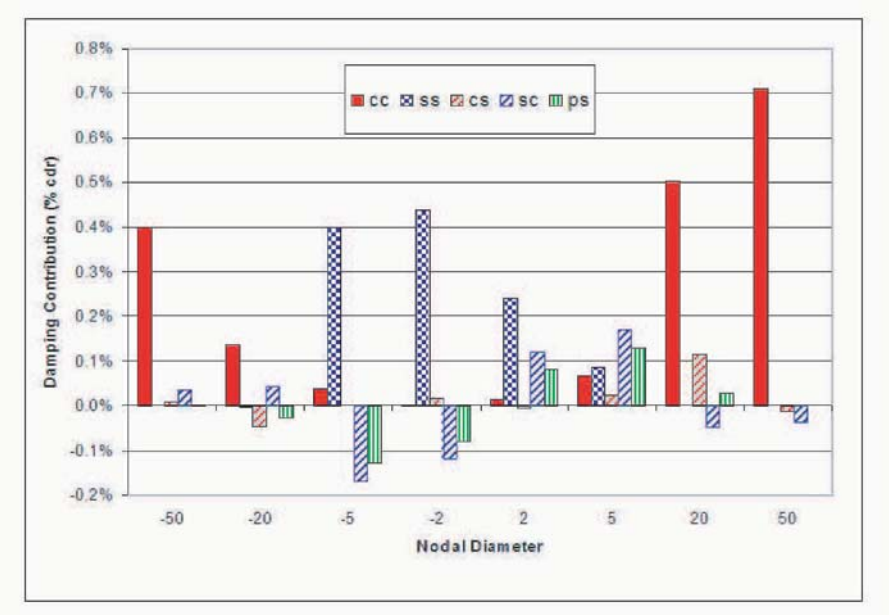

Figure 8. Damping Contributions

9. Summary & Conclusions

This paper presents an extension to the traditional Panovsky-Kielb for flutter analysis of LPT blades that considers the cyclic symmetry mode shapes. As demonstrated in the example problems this new cyclic symmetry method produces aerodynamic damping results that are in reasonable agreement with those of complete three-dimensional viscous CFD method. It does not require any additional input information or CFD analysis. The work due to the interaction effects of the cosine and sine modes was generally found to be significant, even for some nearly pure real modes. In addition, the work associated with the steady pressure was also found to be significant.

Acknowledgement

The authors wish to acknowledge GE Aircraft Engines for financial support and for the permission to publish this work. The authors also express gratitude to Francesco Poli (University of Florence) and Claudia Schipani (Fiat Avio) for their cooperation on the test cases.

References

[1] Arnone, A, Poli, F., and Shipani, C., 2003, A Method to Assess Flutter Stability of Complex Modes, Accepted for Presentation at the 10^{th} ISUAAAT, Duke University, September 2003

[2] Chernycheva, O. V., Fransson, T. H., Kielb, R. E., and Barter, J., 2001, "Comparative analysis of blade mode shape influence on flutter of two-dimensional turbine blades", *ISABE-2001-1243, XV ISOABE conference, September 2-7,* Bangalore, India

[3] Kielb, R. E., and Barter, J., Chernycheva, O. V., and Fransson , T. H., 2003, "Flutter of Low Pressure Turbine Blades with Cyclic Symmetric Modes – A Preliminary Design Method", *presented at ASME Turbo Expo 2003, June 2003, Atlanta, Georgia*, accepted for publication in the *ASME Journal of Turbomachinery*.

[4] Panovsky J., and Kielb R. E., 1998, "A Design Method to Prevent Low Pressure Turbine Blade Flutter", 98-GT-575, *ASME Gas Turbine Conference and Exhibition*, Stockholm, Sweden

EXPERIMENTAL AND NUMERICAL INVESTIGATION OF 2D PALISADE FLUTTER FOR THE HARMONIC OSCILLATIONS

Vladymir Tsimbalyuk, Anatoly Zinkovskii
Institute for Problems of Strength, Ukrainian National Academy of Sciences
Ukrainian National Academy of Sciences, 2 Timiriazevskaia str., 01014 Kiev, Ukraine
tsymb@yahoo.com

Vitaly Gnesin
Department of Aerohydromechanics, Institute for Problems in Machinery
Ukrainian National Academy of Sciences, 2/10 Pozharsky st., Kharkov 310046, Ukraine
gnesin@ipmach.kharkov.ua

Romuald Rzadkowski, Jacek Sokolowski
Institute of Fluid-Flow Machinery, Polish Academy of Sciences
80-952 Gdansk, ul. Fiszera 14, Polish Naval Academy
z3@imp.gda.pl

Abstract The verification of the computational models for unsteady flows through the oscillating blade row becomes more difficult, because the experimental data for three-dimensional flows are currently hardly available in the published literature. Therefore comparisons between numerical methods and experimental ones for simple cascade geometry at inviscid flow conditions must play an essential role in validation of the three -dimensional unsteady solution methods. In this study the numerical calculations were performed to compare the theoretical results with experiments for the harmonic motion. The calculations were carried out for the torsional and bending oscillations of the compressor cascade. The comparison of the calculated and experimental results for different conditions of the cascade oscillations has shown the good quantitative and qualitative agreement.

Keywords: flutter, inviscid, blades

K.C. Hall et al. (eds.),
Unsteady Aerodynamics, Aeroacoustics and Aeroelasticity of Turbomachines, 53–63.

1. Introduction

Cases of flutter-type instability are sometime encountered in the course of developing new gas turbine engines. Costly testing is necessary to eliminate this problem. One of the main problems in predicting flutter at the engine design stage is determining the transient aerodynamic loads that develop during the vibrations of blades. This problem is particularly important in the case of separated flow, when theoretical methods of determining the transient aerodynamic loads are not yet sufficiently reliable. Thus, in this study, we use an experimental method of determinate the transient aerodynamic loads on the vibrating blades of turbine engine.

It is quite difficult to measure the aerodynamic loads along the blades during rotation of the blading ring. Thus, with allowance for the three-dimensional nature of the air flow about the ring, the cylindrical sections of the ring are often modeled as vane cascades. When such a cascade is placed in a wind tunnel, the flow parameters, geometric characteristics, and vibration parameters should be constant along the vanes.

The aeroelastic results of bending vibrations of 2D linear cascade in subsonic flow were published by Kaminier and Stel'makh 1996 and torsional Kaminier et al. 1988. The experimental results of aero-damping and dynamic stability of compressor cascades under bending-torsional vibrations were presented in Len et al. 1986.

Useful benchmark data, which became a de facto standard for unsteady cascade flows, can be found in Bölcs and Fransson 1986 for the EPFL series of Standard configurations.

Aerodynamic loads are measured indirectly either through the aerodynamic damping of bladed vibrations by Kaminier and Nastenko 1973 or the distribution of transient pressures on the blade surfaces Tanaka et al. 1984. They are measured directly with an extensometric dynamometer Kimura and Nomiyama 1988 or on the basis of the forces developed by vibrators Kaminier at el. 1988.

In the Institute for Problem of Strength of NAS of Ukraine the proper 2D experimental bench was developed to measure simultaneously unsteady aerodynamic force and moment with arbitrary combinations of motions y and a of airfoil cascades in the subsonic flow. Description of such test bench is given in paper Tsimbalyuk et al. 2002.

2. Test Stand

To realize flow about the vane cascade with prescribed velocities and angles of attack, the cascade was placed in a wind tunnel (Figures 1, 2) in which Mach numbers up to 0.7 could be attained. The four central vanes in the cascade were secured to individual vibration units and could undergo prescribed vibrations with two degrees of freedom. Since there was some mechanical

coupling even with vibration-proofing elements between the units, it was necessary to keep the vibrations in all of the units steady (whether there was a flow or not) in order to prevent this coupling from affecting the measurement results. Proceeding on the basis of this requirement, we employed an eight-channel feedback system to automatically control the vibrations of the vanes (vibration units). The system also controls the voltages and, thus, the forces on the vibrator coils so as to reduce the difference between the signal of the master oscillator and the vane vibration signal obtained in each channel (the equipment used was described in more detail in Tsymaluk 1996).

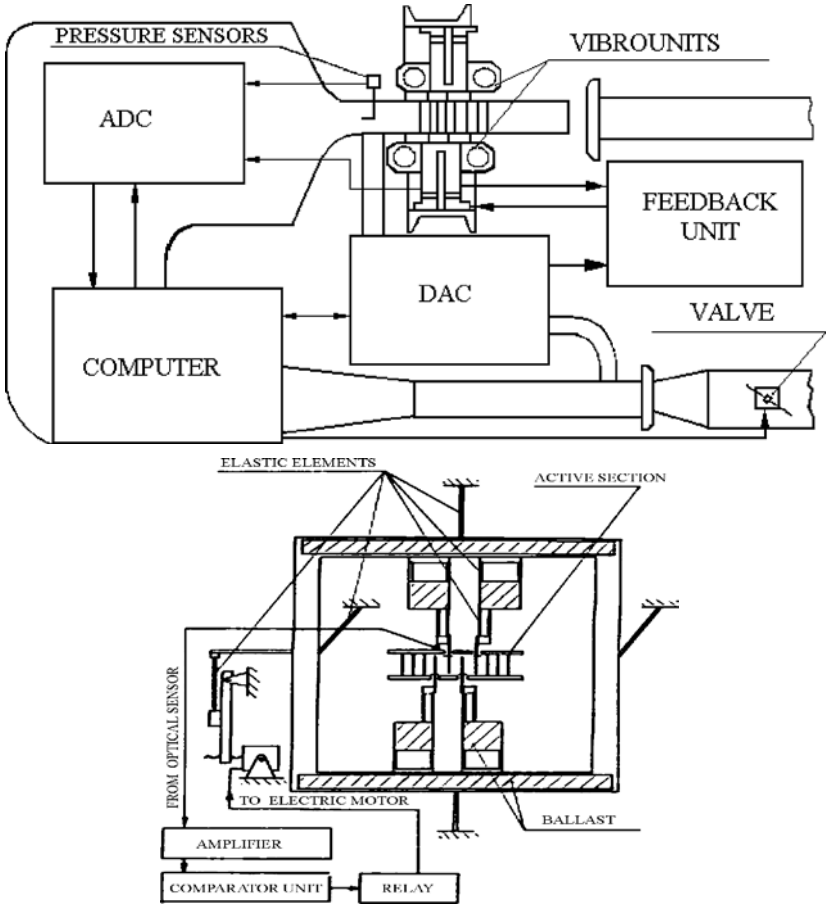

Figure 1. Test stand

The considered cascade consists of 9 airfoils. The central three were fastened cantilever on the individual vibro-unit (see Figure 3), they could accomplish assigned displacements, aerodynamic loads were measured on them. Such airfoils are called active. An elastic suspension was designed for vanes that has two elastic elements of different widths. The auxiliary (narrow) elas-

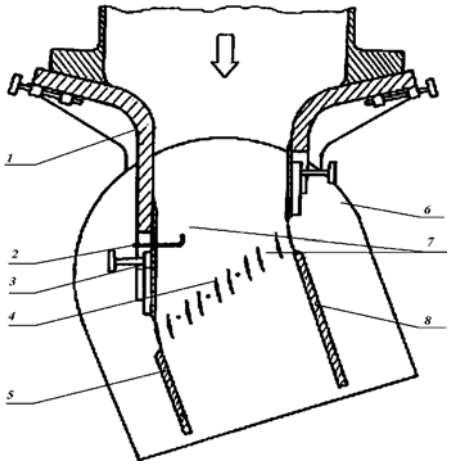

Figure 2. Linear Test Facility, 1 - nuzzle wall; 2 - Pito tube; 3 - blade; 4 - airfoil; 5,8 - outlet rotary screens; 6 - rotary disk; 7 - openings for static pressure release

tic element does not impede the twisting of the main (wide) element about its own longitudinal axis, and during flexural vibrations the two elements form an elastic parallelogram. This setup ensures constant vibration parameters along the vane. The unit just described also makes it possible to change the natural frequencies of the suspension by using replaceable main elements differing only in thickness.

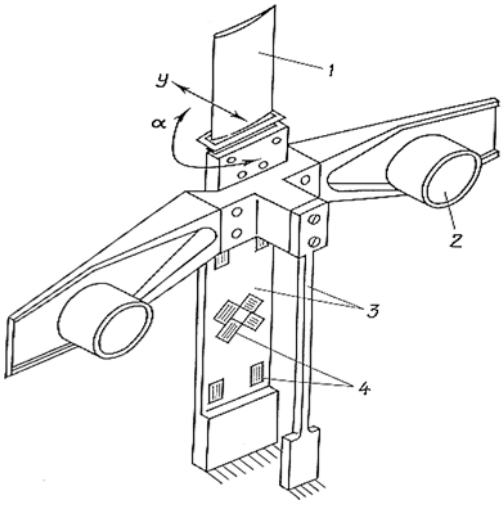

Figure 3. Structure of the airfoil flexible suspension 1 - airfoil; 2 - voice coil of the vibrator; 3 - elastic elements; 4 - strain gages

There were used three active airfoils to asset aerodynamic loads on initial airfoil (n=0), which were induced by vibration of airfoils -2, using designed experimental workbench. This could be accounted for periodicity of influence of airfoil n = -1 on n = 1 one to be the same as for n = -2 on n = 0, influence of n = 1 airfoil on n = -1 - the same as for n = 2 on n = 0 airfoil.

In accordance with developed method, the required vibrations were induced for every active airfoil. The first harmonic of the unsteady aerodynamic force and moment was measured on them. It should be noted, that determined unsteady aerodynamic forces and moments, and thus aerodynamic influence coefficients (AIC) were related to the center of airfoil chord, about which its angular displacement occurred.

The geometrical characteristics of the compressor cascade and oscillation regimes are presented by Tsimbalyuk et al. 2002. The blade length L=0.069 m, the chord length b= 0.05 m, the circular camber 10^o, the thickness-to chord ration 0.07, the stager angle 60 deg., pitch-to -chord ration 0.78, the inlet Mach number 0.12 -0.35, the vibration amplitude ho =0.0007 m, α_o =0.0084 rad. The cross-section of the blade is presented in Figure 4.

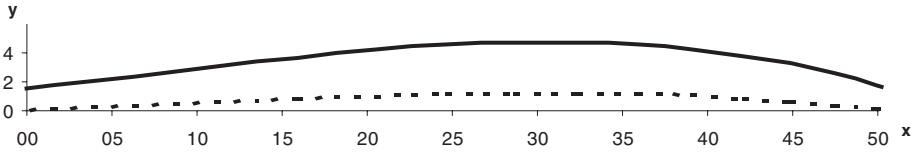

Figure 4. Airfoil coordinates, solid line-suction side, dashed line -pressire side

In order to calculate the AIC the vibrations of airfoils were induced by turns. The vibration amplitude of the blade was almost invariable along its length and equal to ω = 85.85 Hz, which is equal to the natural frequency of the system.

3. Aeroelastic Model

Let assume that the blades are non-twisted with a constant cross-sectional area along the blade length. The centre of shear and gravity of the blade cross-sections coincide. Let us consider the motion of nth blade as plane motion of the solid body with two degrees of freedom. The transverse displacements of the nth blade in x, y directions (h_{x_n},h_{y_n}) are described as:

$$h_{x_n}(t) = h_{x_0} \sin[\omega_n t + (n-1)\delta],$$

$$h_{y_n}(t) = h_{y_0} \sin[\omega_n t + (n-1)\delta],$$

and angular displacements of the nth blade $\alpha_n(t)$:

$$\alpha_n(t) = \alpha_0 \sin[\omega_n t + (n-1)\delta]. \tag{1}$$

Here h_{x_0},h_{y_0},α_0 are the amplitudes of oscillations the same for all blades; ω_n is oscillation angular frequency of the nth blade; δ is the constant interblade phase angle; n is the blade number.

The equations of motion are reduced to set of three ordinary linear differential equations of first order for only torsion (α_n) and bending(h_{xn}, h_{yn}). For a constant force $\mathbf{F}_o$ acting during a period Δt one obtains the linear differential equations of second order with the constant coefficients for n-th blade:

$$\ddot{h}_{xn} + 2n_n \dot{h}_{xn} + \omega_n^2 h_{xn} = \frac{f_{xn}}{m_n}, \tag{2}$$

$$\ddot{h}_{yn} + 2n_n \dot{h}_{yn} + \omega_n^2 h_{yn} = \frac{f_{yn}}{m_n}, \tag{3}$$

$$\ddot{\alpha_n} + 2n_n \dot{\alpha_n} + \omega_n^2 \alpha_n = \frac{M_{sn}}{m_n}, \tag{4}$$

where n_n is a damping parameters.

The 3D unsteady transonic fbw of an ideal gas is described by the Euler equations, represented as conservation laws in an arbitrary Cartesian coordinate system, rotating with the constant angular velocity ω (see Gnesin and Rzadkowski 2000):

$$\frac{\partial}{\partial t} \int\limits_{\Omega} \mathbf{f} \mathrm{d}\Omega + \oint\limits_{\sigma} \mathbf{F} \cdot \mathbf{n} \mathrm{d}\sigma + \int\limits_{\Omega} \mathbf{H} \mathrm{d}\Omega = 0,$$

$$\mathbf{f} = \begin{bmatrix} \rho \\ \rho v_1 \\ \rho v_2 \\ \rho v_3 \\ E \end{bmatrix}; \mathbf{F} = \begin{bmatrix} \rho \mathbf{v} \\ \rho v_1 \mathbf{v} + \delta_{1i} p \\ \rho v_2 \mathbf{v} + \delta_{2i} p \\ \rho v_3 \mathbf{v} + \delta_{3i} p \\ (E+p)\mathbf{v} \end{bmatrix}; \mathbf{H} = \begin{bmatrix} 0 \\ \rho a_{e1} - 2\rho\omega v_2 \\ \rho a_{e2} - 2\rho\omega v_1 \\ 0 \\ 0 \end{bmatrix}; \delta_{ji} = \begin{cases} 1 j = i \\ 0 j \neq i \end{cases} \tag{3}$$

Here p and ρ are the pressure and density; v_1, v_2, v_3 are the velocity components; a_{e1} and a_{e2} are the transfer acceleration projections; $E = \rho\left(\varepsilon + \frac{v_1^2+v_2^2+v_3^2-r^2\omega^2}{2}\right)$ is the total energy of volume unit; ε is an internal energy of mass unit; r is the distance from the rotation axis.

The above system of equations is completed by the perfect gas state equation

$$p = \varepsilon(\chi - 1),$$

where χ denotes the ratio of the fluid specific heats.

The spatial solution domain is discretized using linear hexahedral elements.

The 3D Euler equations are integrated on moving H-H (or H-O) - type grid with use of explicit monotonous second - order accuracy Godunov - Kolgan difference scheme.

4. Numerical and Experimantal Results

The aeroelastic behavior of the system "flow-cascade" without taking into account the mechanical damping is defined by a the work coefficient value which is equal to the work performed by aerodynamic forces during one cycle of oscillations:

$$W = \int_0^{\frac{1}{\nu}} M \frac{d\alpha}{dt} dt, \tag{5}$$

where c is the length of blade chord, α_0 is oscillation amplitude, M is aerodynamical moment, W is the aerodynamic work during one cycle of oscillation for torsional oscillations, and

$$W = \int_0^{\frac{1}{\nu}} -\mathbf{F} \cdot \mathbf{v}\, dt, \tag{6}$$

for bending oscillations.

The work coefficients versus interblade phase angle (IBPA) for different flow regimes and modes of oscillations are presented in Figures 5-7.

Figure 5 shows the work coefficient as function of IBPA for bending oscillations under incidence flow angle which is equal to zero. The light squares (circles) correspond to the experimental data, the black squares (circles) correspond to numerical results. The negative values of work coefficient demonstrate the dissipation of an oscillating blade energy to the flow (aerodamping), the positive values - to the transfer of the energy from the main flow to the blade (flutter).

The strong influence of both IBPA and Strouhal number on the aerodynamic stability of tune modes is seen in Figure 5. With decreasing of Strouhal number (increasing of the inlet flow velocity) the stability decreases.

It should be noted that the work coefficient in dependence of IBPA has a typical sinusoidal form. At the IBPA equal to 180 deg the maximal aerodamping is observed, at the IBPA near 0 deg the minimal aerodamping is found.

The quantitative and qualitative agreement between predicted and measured values is satisfactory.

In Figure 6 the variation of work coefficient versus IBPA for torsional oscillations under i = 0 and Sh = 0.616 is shown. The agreement between theoretical

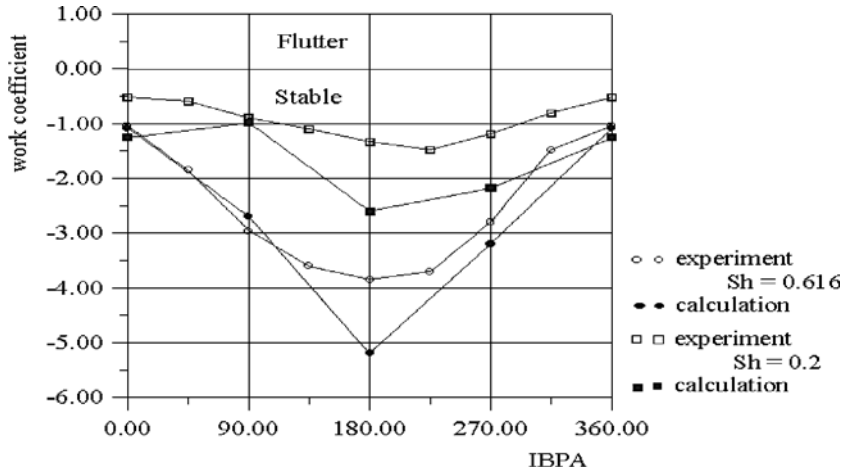

Figure 5. The aerodynamic work coefficient in dependence of IBPA for the bending vibration (i = 0ř, Strouhal Number - Sh = 0.2 - 0.616)

and experimental results is good. For torsional oscillations in the range of 0 deg. $<$ IBPA $<$ 180 deg. the work coefficients have positive value that corresponds to the transfer of energy from the flow to the oscillating blade. The maximal excitation occurs near δ = +90 deg.

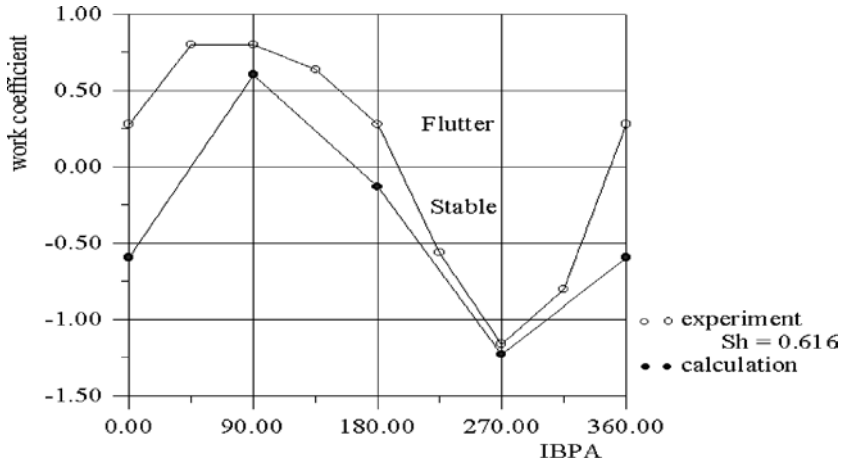

Figure 6. The aerodynamic work coefficient in dependence of IBPA for torsion vibration (I = 0ř, Strouhal Number - Sh = 0.616)

The aeroelastic characteristics at the bending vibration for the attack flow angle of 16 deg is presented in Figure 7. The agreement between the exper-

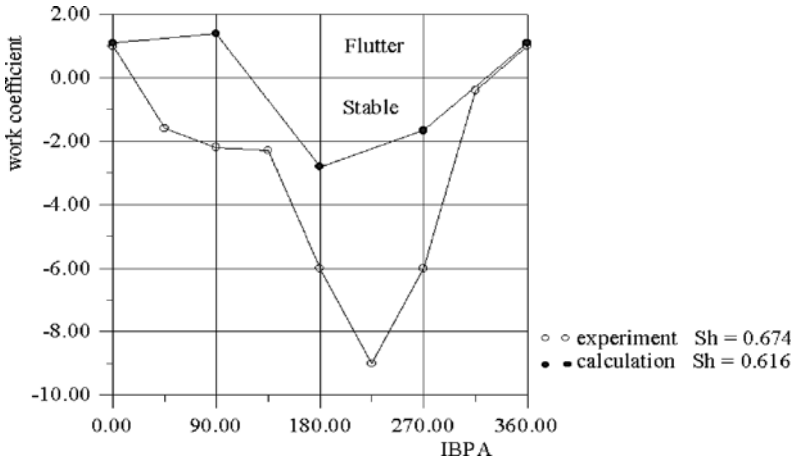

Figure 7. Aerodynamic work coefficient in dependence of IBPA for the bending vibration (i = 16ř, Strouhal Number - Sh = 0.616)

imental and numerical results near the IBPA of 0 deg is seen although some discrepancy for IBPA of 180 deg is found.

In Figures 8, 9 and 10 the calculated and measured amplitude of unsteady forces at the bending oscillations, for different incidence angles were shown. The calculation of the unsteady amplitude by using the aerodynamic influence coefficients were done taking into account only four neighbouring blades ($-1 \leq n \leq 1$) and two neighbouring blades ($-2 \leq n \leq 2$). From results presented in these Figures it is seen that for considered flow regime taking into account only two neighbouring blades give the satisfactory agreement with numerical calculations.

5. Conclusions

1. A partially - integrated method based on the solution of the coupled aerodynamic-structure problem is used for calculation of unsteady 3D flow through an oscillating blade row to determine the critical conditions of flutter initiation.

2. The numerical investigation has been performed to calculate aeroelastic response of the compressor cascade at the different flow regimes and laws of oscillations.

3. The comparison of calculated and experimental results for bending and torsional oscillations has shown a satisfactory quantitative and qualitative agreement.

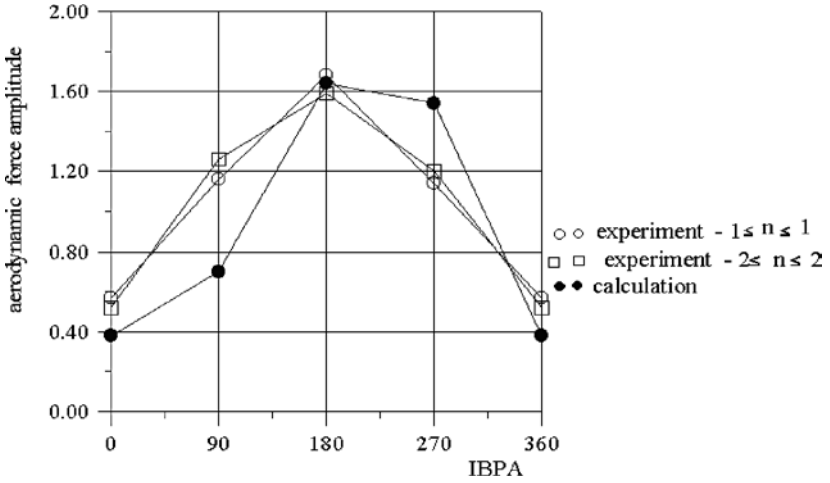

Figure 8. Amplitude of unsteady aerodynamic force at the bending oscillations

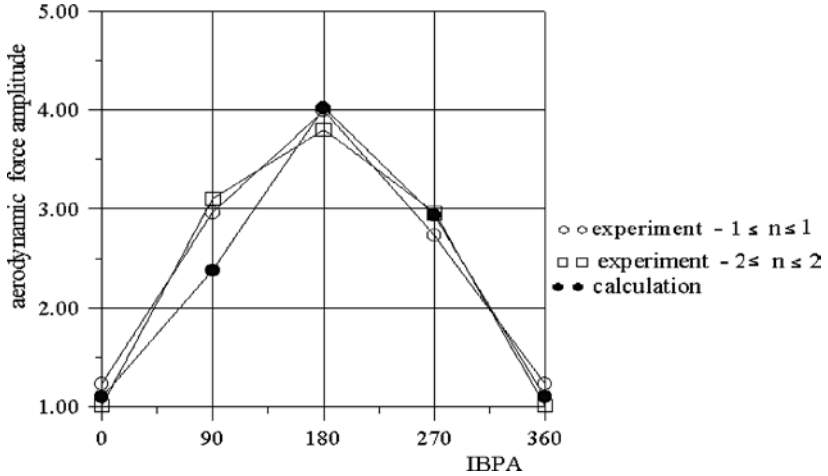

Figure 9. Amplitude of unsteady aerodynamic force at the bending oscillations i = 0, Sh = 0.616

References

Bölcs A., Fransson T.H. (1986) Aeroelasticity in Turbomachines Comparison of Theoretical and Experimental Cascade Results, Communication du Laboratoire de Thermique Appliquée et Turbomachines, Nr.13. Lusanne, Epfel.

Bölcs A., and Fransson T.H. (1986). Aeroelasticity in Turbomachines Comparison of Theoretical and Experimental Cascade Results, Communication du Laboratoire de Thermique Appliquée et Turbomachines, Nr.13, Appendix A5 All Experimental and Theoretical Results for the 9 Standard Configurations, Lusanne, Epfel.

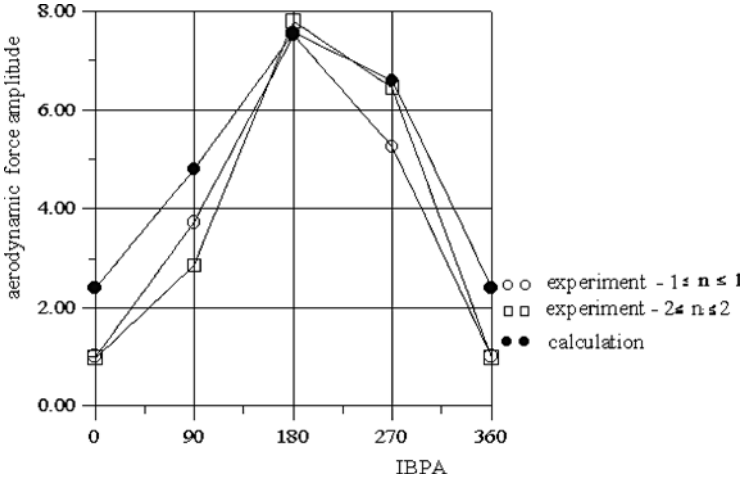

Figure 10. Amplitude of unsteady aerodynamic force at the bending oscillations i = 16, Sh = 0.616

Stel'makh A.L., Kaminer A.A. (1981). Effect of the geometrical parameters of a compressor cascade on the limit of bending self-oscillations of blades caused by cascade flutter, Strength of Materials, 15, 1, 104-109.

Kaminer A.A., Stel'makh A.L. (1996). Effect of the aerodynamic connectedly between blades of the aerodynamic damping of their vibrations, and origin of cascade flutter, Strength of Materials, 14, 12, 1667-1672.

Kaminer A.A., Chervonenko A.G., and Tsymbalyuk V.A. (1988). Method for Studying Unsteady Aerodynamic Characteristics of Airfoil Cascades vibrating in a Three-Dimensional Flow. Preprint. Institute for Problems of Strength, Ac. Sci. of the Ukr.SSR, Kiev 1988 (in Russian).

Len A.D.,Kaminer A.A., Stel'makh A.L., Balalaev V.A. (1986). Loss of dynamic stability of torsional vibrations of blades due to cascade flutter, Strength of Materials, 18, 1, 76-80.

Gnesin V., and Rzadkowski R. (2000). The theoretical model of 3D flutter in subsonic, transonic and supersonic inviscid flow, Transactions of the Institute of Fluid-Flow Machinery, No. 106, 45-68.

Gnesin V., Rzadkowski R. (2002). A Coupled Fluid-Structure Analysis for 3D Inviscid Flutter of IV Standard Configuration, Journal of Sound and Vibration, 251(2), 315-327.

Gnesin V., Rzadkowski R. and Kolodyazhnaya, L., V. (2000). A coupled fluid-structure analysis for 3D flutter in turbomachines, ASME paper 2000-GT-0380.

Rzadkowski R., Gnesin V. (2000). The numerical and experimental verification of the 3D inviscid code, Transactions of the Institute of Fluid-Flow Machinery, No. 106, 2000, 69-95.

Rzadkowski R. (1998). Dynamics of steam turbine blading. Part two: Bladed discs, Ossolineum, WrocŠaw-Warszawa.

Tsimbalyuk V.A. (1996). Method of measuring transient aerodynamic forces and moments on vibrating cascade , Strength of Materials, 28, 2, 150-157.

Tsimbalyuk V.A., Zinkovski A.P and Rzadkowski R. (2002). Experimental Investigation of Palisade Flutter for the Harmonic Oscillations, *Proc. of the XV Conference of Flow Mechanics*, Augustow, Poland

POSSIBILITY OF ACTIVE CASCADE FLUTTER CONTROL WITH SMART STRUCTURE IN TRANSONIC FLOW CONDITION

Junichi Kazawa
Toshinori Watanabe
Department of Aeronautics and Astronautics, University of Tokyo
7-3-1 Hongo Bunkyo-ku, Tokyo 113-8656, Japan
Phone : +81 3 5841-6624 Fax : +81 3 5841-6622
kazawa@aero.t.u-tokyo.ac.jp

Abstract To study the possibility of active cascade flutter control by application of smart structure, numerical analyses were performed under transonic flow conditions with passage shock waves by a developed flow-structure coupled method. In the flow condition of the present study, the unsteady aerodynamic force induced by the shock oscillation was dominant for instability of blade vibration. The direction of blade movement during oscillation was first adopted as the control parameter, because it was known to be a quite influential factor for vibration instability of blades in the transonic flows. The method could decrease the passage shock movement near the blade surface and effectively suppress the blade vibration, though it was not effective when the blade stiffness was small. For more effective control, the method in which the trailing edge of blade was actively vibrated was sought to control the passage shock oscillation. The trailing edge oscillation might be realized by, for instance, application of piezo-electric device. The method was revealed to change the unsteady aerodynamic force acted on the blade from exciting to damping force if the phase of trailing edge oscillation was properly selected. The suppressing effect of the control method came from its effect on passage shock movement, which was confirmed by developed flow-structure coupled method.

1. Introduction

Active control of surge and rotating stall has been successfully studied in the last decade [1] including phenomenological description of the onset of instability and control mechanism. Concerning the cascade flutter problem, some active control techniques have also been reported, in which acoustic waves are introduced to suppress the flutter [2], or the acoustic impedance on casing wall is actively controlled to reduce the exciting energy of the oscillating blade [3].

K.C. Hall et al.(eds.),
Unsteady Aerodynamics, Aeroacoustics and Aeroelasticity of Turbomachines, 65–76.

On the other hand, the study of "smart structure" has been advanced in the research field of structures and materials. The smart materials can deform themselves reacting to electric signals. Active control techniques, in which the smart materials are applied to the flap of the aircraft wing or fuselage panel, have been proposed so far [4] to prevent flutter instability of them. If the characteristics of smart materials are properly utilized for the active control of cascade flutter, an effective and reliable control method can be realized since such materials directly change the structural characteristics of the vibrating materials, or can give flexible deformation of the blades.

The authors have studied some methods of cascade flutter control by use of the developed flow-structure coupled method. For example, flutter suppression was found to be possible by changing natural frequency of blade in the subsonic flow condition [5]. The control can be realized by the application of Shape Memory Alloy.

In the present study, two methods of the cascade flutter control were analyzed for suppression of vibration instability in transonic flow conditions with passage shock waves. In the studied flow condition, it is well known that the unsteady aerodynamic force induced by the movement of passage shock wave is dominant for blade vibration instability. It is also known that the direction of blade movement during oscillation is a quite influential factor for flutter instability.

Based on the knowledge above, the possibility of flutter suppression by changing the oscillation direction of blades was investigated first. The change in the direction can be carried out with, for instance, some kind of shape memory alloy. The second method was to give forced oscillation on the trailing edge section of blades. It was thought that the occurrence of cascade flutter could be suppressed through the change in the oscillatory motion of shock waves impinged to the blade surfaces. The forced vibration of the trailing edge section can be realized with piezo-electric devices.

The results of these numerical studies are reported in the present paper.

2. Numerical Argorithm

A numerical flow-structure coupled method has been developed in the course of the present study [5]. Figure 1 shows the procedure of the method. The computed unsteady aerodynamic force in the flow calculation is introduced into the structural calculation in which the equation of motion of the blade is solved to obtain the blade displacement. The computed blade displacement is used for generation of the new grid coordinates in the next time step of flow calculation.

The flow calculation is based on the two-dimensional nonlinear Euler equation, that is solved through a second order upwind TVD scheme. LU-ADI

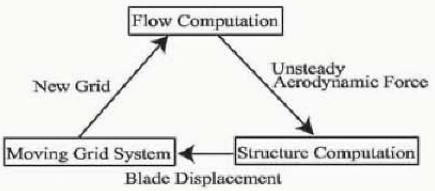

Figure 1. Procedure of Flow Structure Coupled Method

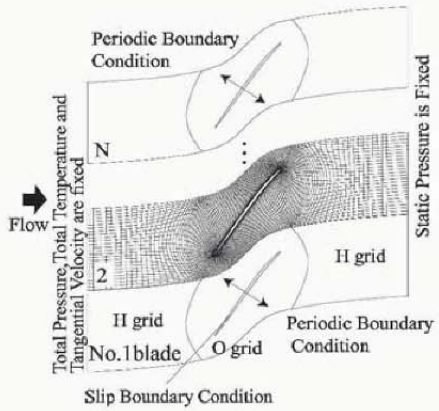

Figure 2. Computational Domain, Grid, Boundary Conditions

factorization algorithm coupled with Newtonian iterations is used as the time-marching scheme. Figure 2 shows computational domain, grid, and boundary conditions. The number of flow channel, N, can be arbitrarily selected in the computation, and the inter blade phase angles of 360n/N (n=1,2, ..., N) can exist in N flow channels. Periodic boundary conditions were imposed on the upper and lower side of the computational domain, that is, physical values at the lower boundary of No. 1 flow region and those at upper boundary of No. N flow region were set to be same. At the inlet boundary, total pressure, total temperature, and rotational speed (tangential velocity) were fixed. Non-reflecting boundary condition was used on the inlet boundary to prevent reflection of the wave induced by the blade vibration. Static pressure was specified at the outlet boundary, and the blade surfaces were treated as slip boundaries. H+O+H grid was adopted for computation. O grid was used around the blades to achieve good orthogonality, and H-grids were generated in upstream and downstream regions in order to make inlet and outlet boundaries distant from the blades.

Figure 3 shows structural model of blades in one-degree of freedom. The direction of blade movement, indicated by the angle Ψ in Fig.3, can be arbitrarily selected. The equation of motion of structural model as shown in Fig.3 is written by the following equation (1);

$$M\frac{d^2h}{dt^2} + D\frac{dh}{dt} + Kh = L \tag{1}$$

where M is blade mass, h is blade displacement, D is structural damping, K is blade stiffness, and L is unsteady aerodynamic force acted on blade. This equation was solved through Runge-Kutta-Gill scheme. The structural

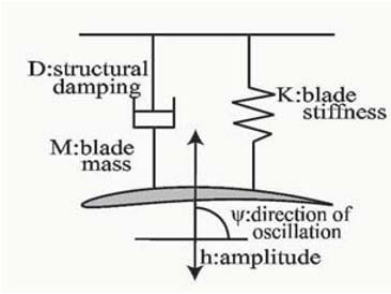

Figure 3. Structural Model

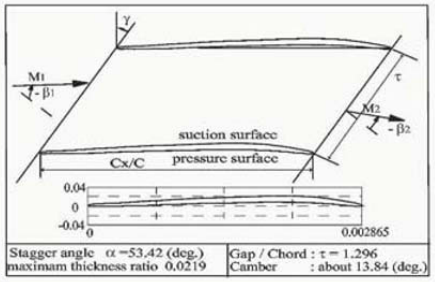

Figure 4. Cascade Model (Tip Section of Quiet Fan B)

damping, D, was neglected in the present analysis to concentrate our focus on the aerodynamic damping effect in the flow-structure coupled situation.

3. An Analysis of Blade Vibration Instability

The tip section of Quiet Fan B in NASA Quiet Engine Program [6], shown in Fig.4, was adopted as the cascade model for the present analysis. Figure 5 shows the computed steady Mach contours in the case when inlet Mach number is 1.25, and the static pressure ratio (po/pi, i;inlet, o;outlet) is 1.7. A passage shock wave generated at the trailing edge of each blade can be clearly seen in flow channels. Concerning vibration instability of this cascade model, the oscillation of the passage shock wave is known to be the most influential factor. An oblique shock is generated at the leading edge of each blade, and impinges to the suction surface of the adjacent blade.

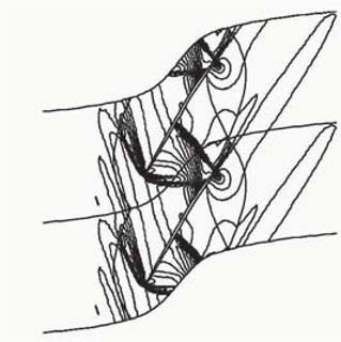

Figure 5. Mach contour

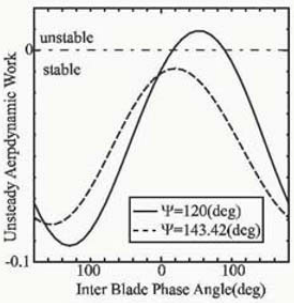

Figure 6. Unsteady Aerodynamic Work

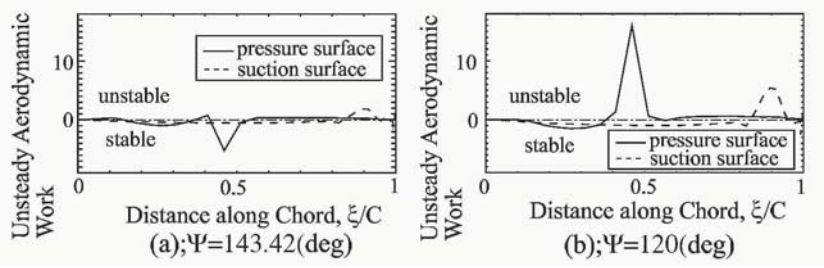

Figure 7. Unsteady Aerodynamic Work Distribution on the Blade Surface

The blade vibration instability was investigated in the above flow field. The blade was forced to oscillate with the reduced frequency of 0.084. The direction of blade motion, Ψ, was 143.42 degrees (case 1) and 120 degrees (case 2). Since a realistic blade is designed in a three-dimensional manner, the stagger angle is different in the spanwise direction. The difference of stagger angle results in the change in the direction of blade oscillation at each spanwise section of the blade. It is reported that the oscillation direction plays an important role for the blade vibration instability in the transonic flow condition [7].

The influence coefficient method [8] was used for analysis of blade vibration instability. Figure 6 shows the result of instability analysis by this method when the reduced frequency is 0.084. The horizontal axis is the inter blade phase angle, while the vertical axis corresponds to the unsteady aerodynamic work on a blade. Blade vibration is unstable when the aerodynamic work is positive. As shown in Fig.6, blade vibration was always stable in the case 1. In the results of the case 2, on the other hand, the blade oscillation was unstable around 90 degrees of inter blade phase angle.

Figure 7 shows the chordwise unsteady aerodynamic work distribution on the blade surface when all blades were forced to oscillate with 90 degrees of inter blade phase angle. Figure 7(a) shows the results of the case 1, while Fig. 7(b) shows those of the case 2. At the part where the unsteady aerodynamic work is positive, the unsteady aerodynamic force acts as exciting force. In the results of Fig. 7(a), a negative peak can be seen at around 50% chord position on the pressure surface. The peak is caused by the oscillation of passage shock. In the result of the case 2, Fig. 7(b), the peak is observed to be positive, which means that the unsteady aerodynamic work induced by passage shock movement becomes exciting one. The characteristics of unsteady aerodynamic force thus differ depending on the blade oscillation direction. The unsteady aerodynamic work due to the shock oscillation is revealed to be dominant for blade vibration instability in the result, because the value of the peak is larger than that at another position on the blade surface. On the suction surface, on the

other hand, a positive peak is observed at around 90% chord position both in the case 1 and case 2. The peak is caused by the oscillation of the oblique shock impinges there from the leading edge of the neighboring blade.

4. Flutter Suppression by Changing Direction of Blade Oscillation

The control by changing the oscillation direction of blade was numerically analyzed. The control method is thought possible by application of a kind of shape memory alloy.

To study the effectiveness of the control, the case in which all blades were forced to oscillate were analyzed in 4 flow channels with 90 degrees of inter blade phase angle as shown in Fig. 8. The oscillation directions of No.1 and No.3 blades were set to be 143.42 degrees, while those of No.2 and No.4 blades were 120 degrees. Figure 8 shows the chordwise unsteady aerodynamic work distribution on the blade surface. Solid line is the result of the case with control, while dotted line is that of the case without control. Figure 8(a) is the result of No.1 blade (Ψ =143.42 deg.), and Fig. 8(b) is that of No.2 blade (Ψ =120 deg.). From Fig. 8(a), it is seen that the result of the controlled case is almost the same as that of the case without control for No. 1 blade. For the No. 2 blade, however, the peak at 50% chord position on the pressure surface changes from positive one to negative one by the control as shown in Fig. 8(b). Alteration of the blade oscillation direction should change the movement of passage shock, and the induced unsteady aerodynamic work should thereby be changed into, possibly, stable direction.

Based on the previous results, the control method of changing oscillation direction of blade was analyzed by the flow-structure coupled method. Initial velocity of $0.01C\omega$ (C:chord length, ω:angular frequency of blade) was given to No.1 blade, and $-0.01C\omega$ to No.3 blade. No.2 and No.4 blade were set

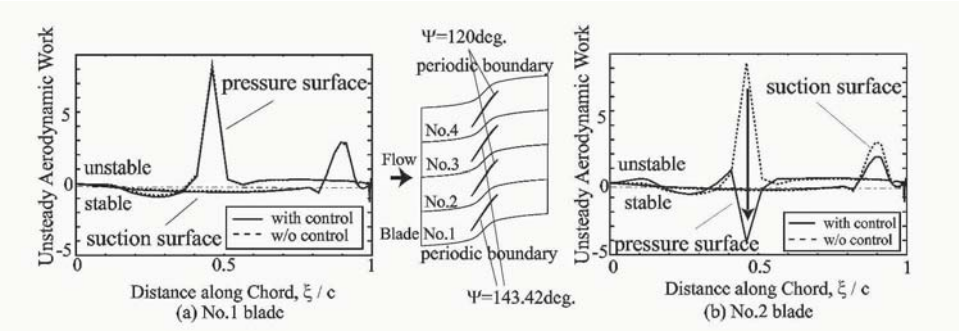

Figure 8. Variation of Unsteady Aerodynamic Work Distribution on the Blade Surface due to the Direction of Oscillation

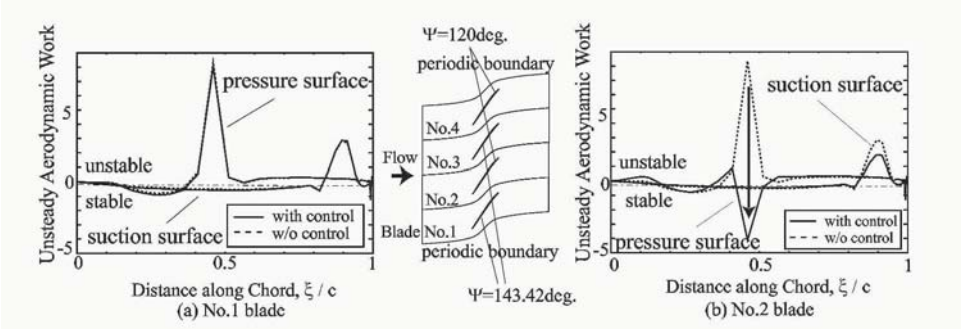

Figure 9. Time History of the Blade Displacement and the Unsteady Aerodynamic Force (with Control of Oscillation Direction)

stationary at the initial state. The angle of blade motion, Ψ, of all blades was initially 120 degrees. The angle Ψ of No.1 and No.3 blades was impulsively changed to 143.42 degrees from 120 degrees at the time when the displacement of the blades started to increase.

Figure 9 shows the time history of the displacements of No.1 and No.2 blades as well as the unsteady aerodynamic force on these blades. The dotted line indicates the result when Ψ of all blades are kept 120 degrees for comparison. As shown in Fig.9, the increase in displacement was effectively suppressed by changing oscillation direction. The phase of the unsteady aerodynamic force is observed to delay compared with that of the blade displacement after the start of the control. In this situation, the unsteady aerodynamic force acts as a damping force on the blade. As for the No.2 blade, the result corresponds to that of the previous result shown in Fig. 8. The displacement of No.1 blade was decreased probably because of the influence of the decrease in the displacement of No.2 blade.

5. Analysis of Flutter suppression by Trailing Edge Oscillaton

From the results of detailed analysis, the control method by changing oscillation direction was found not effective when the blade stiffness was small. As a more general control method effective for transonic cascades, the active vibration of blade trailing edge was found to have great potential. Figure 10 illustrates the method of the trailing edge oscillation. The region of flapping oscillation extends about 30% chord length from the trailing edge. The angular displacement of the oscillation is ϕ. The active vibration of trailing edge oscillation can be realized by, for instance, piezo-electric device. The active trailing edge oscillation is expected to provide desirable change in the oscillatory motion of passage shock wave as shown in the previous case.

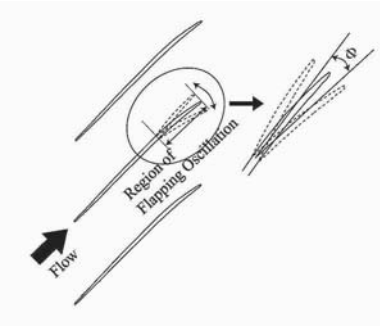

Figure 10. Oscillation of Blade Trailing Edge

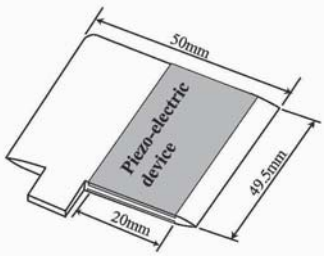

Figure 11. Flat Plate equipped with Piezo-Electric Device

As a test case, a piezo-electric device was mounted on a flat plate as shown in Fig.11, and the active vibration of the plate was observed. Figure 12 shows the sketch of the trailing edge oscillation. The displacement of the trailing edge was measured from the photograph, and a displacement of the trailing edge by around 0.2mm was found.

5.1 Analysis in the case when all blades are forced to oscillate

The phase difference between blade vibration and trailing edge oscillation, denoted as δ, was found to be important in the present analysis. δ is positive when the phase of trailing edge oscillation advances compared with that of the blade vibration. Eight cases of δ, δ = -135, -90, -45, 0, 45, 90, 135, 180 (deg.), were analyzed in the study, and two characteristic results of δ = 45 and δ = -135 (deg.) cases are reported here.

For the feasibility study of the method, the case in which all blades were forced to oscillate with 90 degrees of inter blade phase angle were analyzed first. The trailing edges of No.1 and No.3 blades were oscillated and those of No.2 and No.4 blades were not oscillated.

Figure 13 shows the time history of the displacement and the unsteady aerodynamic force of the No.1 and No.2 blades when δ = 45 (deg.). In Fig.13, dot-

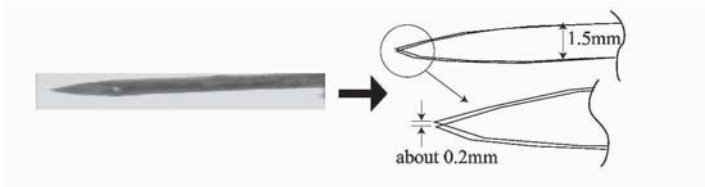

Figure 12. Amplitude of Trailing Edge

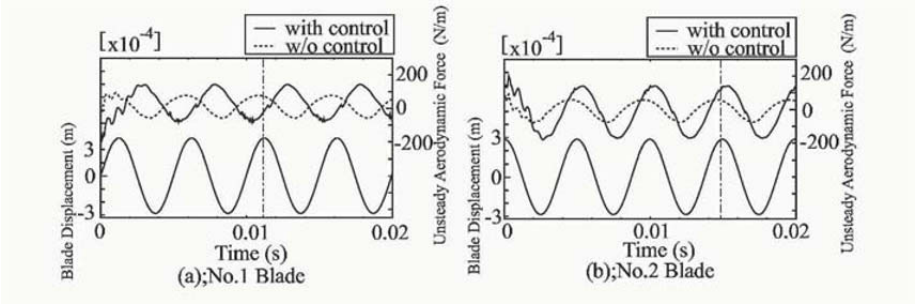

Figure 13. Time History of the Blade Displacement and the Unsteady Aerodynamic Force (δ = 45 degrees)

ted line indicates the results of the case without control (trailing edges of the blades are not oscillated). In the controlled case, the blade with trailing edge oscillation (in this case, No.1 and No.3 blades) is called "controlled blade", while the blade without trailing edge oscillation (No.2 and No.4 blades) is called "non-controlled blade." In the results of the case without control (dotted line) shown in Fig.13, the phase of the unsteady aerodynamic force advanced compared with that of the blade displacement. In this situation, the unsteady aerodynamic force acts on blade as an exciting force, so that the blade vibration is unstable. On the other hand, in the case with trailing edge oscillation (δ = 45 deg.), the phase of the unsteady aerodynamic force delays compared with that of blade displacement on both controlled and non-controlled blades. In this situation, the unsteady aerodynamic force acts on the blade as a damping force. From the result, it is found that the trailing edge oscillation can change the unsteady aerodynamic force from exciting to damping force when δ is 45 degrees.

Figure 14 shows the unsteady aerodynamic work distribution on No.1 and No.2 blades when δ = 45 deg. The peak around 50% chord position on the

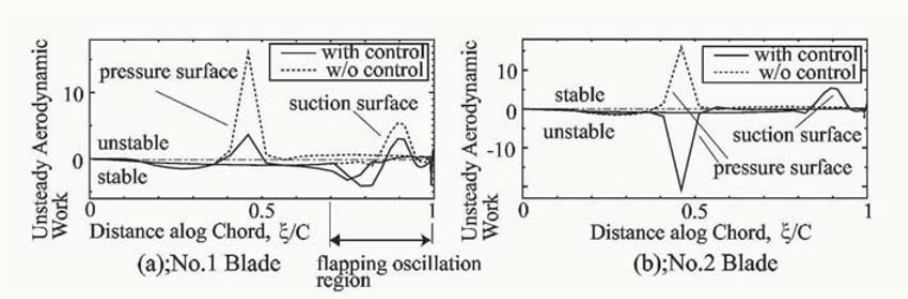

Figure 14. Unsteady Aerodynamic Work Distribution on Blade Surface (δ = 45 degrees)

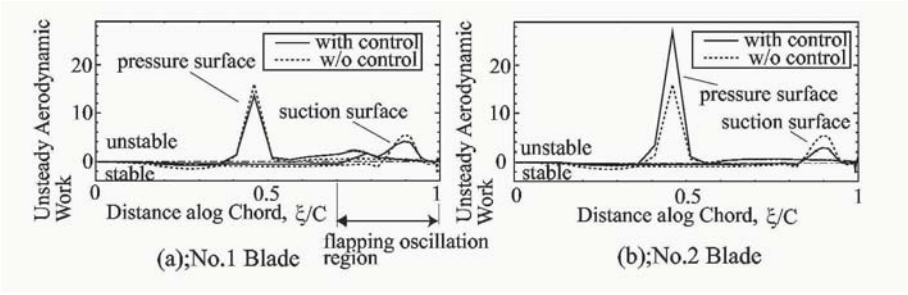

Figure 15. Unsteady Aerodynamic Work Distribution on Blade Surface (δ = -135 degrees)

pressure surface of controlled blade is seen to become low by trailing edge oscillation. Since the passage shock movement induces this peak, it can be said that the trailing edge oscillation alters the passage shock oscillation. The unsteady aerodynamic work around the flapping oscillation region is different from that of the case without trailing edge oscillation, which is also caused by the trailing edge oscillation. Through the integration of the chordwise distribution of unsteady aerodynamic work shown in Fig. 14(a), the total value of unsteady aerodynamic work was found to shift from positive one to negative one. From Fig. 14(b), the results of non-controlled blade, the positive peak around 50% chord in the pressure surface changes to negative one.

Figure 15 shows the unsteady aerodynamic work distribution on No.1 and No.2 blades when δ = -135 degrees. The peak level around 50% chord in the pressure surface of controlled blade was same as that in the case without control. On the other hand, the unsteady aerodynamic work on the flapping oscillation region was increased by this control. In the results of non-controlled blade as shown in Fig. 15(b), the unsteady aerodynamic work induced by passage shock movement is observed to increase in the case with control. When δ = -135 degrees, therefore, the trailing edge oscillation increases the exciting force on the blades compared with that in the case without control.

In the present control method with trailing edge oscillation, the phase difference δ is a quite influential factor for instability. The proper selection of δ is very important.

5.2 Suppression of unstable vibration by the trailing edge oscillation

To confirm the effectiveness of the control method with trailing edge oscillation, the case of δ = 45 degrees was analyzed by the flow-structure coupled method. The initial velocity of V_0=0.01$C\omega$ was given to No.1 blade, and that of -V_0 was given to No.3 blade. No.2 and No.4 blades had the initial displacement (No.2 blade; h_0=0.01C, and No.4 blade; -h_0) to simulate the case when

all blades oscillate with 90 degrees of inter blade phase angles at the initial state of computation. The trailing edges of No.1 and No.3 blades were actively oscillated. Since the blade oscillation frequency is an implicit parameter in the fbw-structure coupled method, the blade oscillation frequency is calculated in the present study by the Fourier transfer of blade displacement to obtain ω the angular frequency. The blade displacement h' and ϕ are calculated from the following equations;

$$h' = \sin(\omega t + \theta) \, where, \theta = \arctan\left(\frac{Im\{h\}}{Re\{h\}}\right) \tag{2}$$

$$\phi = B \sin(\omega t + \theta + \delta) \tag{3}$$

Figure 16 shows the time history of the blade displacement and the unsteady aerodynamic force when δ is about 45 degrees. The result of the case without control is also indicated by the dotted line for comparison. As shown in Fig.16, the increase in the displacement of all blades is effectively suppressed by the trailing edge oscillation. In the controlled case, the phase of the unsteady aerodynamic force delays compared with that of the blade displacement.

From the analysis by fbw structure coupled method, it can be concluded that the method of active trailing edge oscillation can effectively suppress the cascade flutter in transonic fbw regime.

6. Conclusions

Possibility of active cascade flutter control under transonic fbw condition with passage shock waves was numerically studied. Two methods of flutter

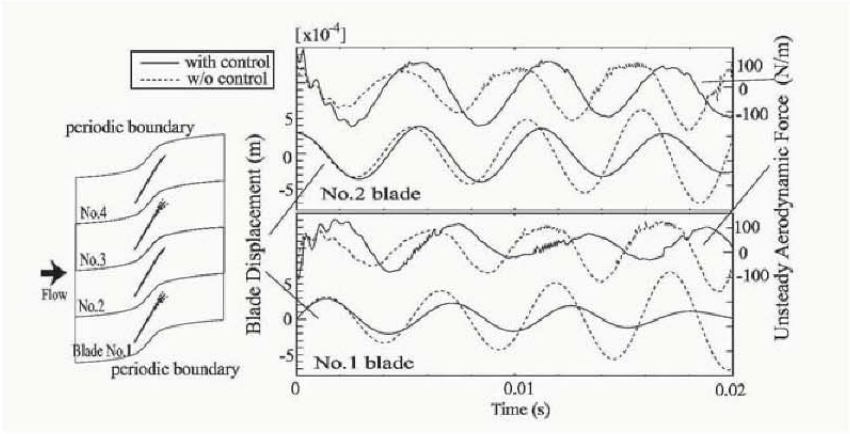

Figure 16. Time History of the Blade Displacement and the Unsteady Aerodynamic Force (with Trailing Edge Oscillation)

control were analyzed by the developed numerical code. In the first method, the direction of the oscillatory motion of blades was actively changed. The method can be realized with some kind of shape memory alloy. The second control method gives active oscillation to the blade trailing edge with a flap-like manner. The active vibration can be realized with piezo-electric devices.

The conclusions are summarized as follows.

1 In the adopted cascade model, the unsteady aerodynamic force induced by passage shock movement was dominant for instability of blade vibration.

2 The control method with changing oscillation direction can control the passage shock movement near the blade surface, and change the unsteady aerodynamic force induced by the passage shock from exciting to damping one.

3 By the method of active trailing edge vibration, the unsteady aerodynamic force induced by the passage shock oscillation can be changed from exciting to damping force if the phase of the trailing edge vibration is properly selected compared with that of blade oscillation. The cascade flutter can be effectively suppressed in the case. At an improper phase, on the contrary, the control increases the exciting force on the blade.

References

[1] A. H. Epstein, J. E. Ffowcs Williams, and E. M. Greitzer, "Active Suppression of Aerodynamic Instabilities in Turbomachines", Journal of Propulsion and Power, Vol. 5, No.2, 1989, pp. 204-211.

[2] Nagai, K. and Namba, M., "Effect of Acoustic Control on the Flutter Boundaries of Supersonic Cascade", Unsteady Aerodynamics and Aeroelasticity of Turbomachines, Fransson, T. H. ed., Kluwer Academic Publishers, 1998, pp.165-179.

[3] Xiaofeng Sun, Xiaodong Jing, and Hongwu Zhao, "Control of Blade Flutter by Smart-Casing Treatment", J.of Propulsion and Power, Vol.17, No.2, 2001, pp248-255.

[4] For Example, L. B. Scherer, C. A. Martin, M. West, J. P. Florance, C. D. Wiesman, A. W. Burner, and G. A. Fleming, "DARPA/AFRL/ NASA Smart Wing Second Tunnel Test Results", SPIE Vol.3674, pp.249-259.

[5] Kazawa, J. and Watanabe, T. , "Numerical Analysis toward Active Control of Cascade Flutter with Smart Structure", 38th AIAA/ASME/SAE/ASEE Joint Propulsion Conference and Exhibit, 7-10 July 2002, Indianapolis, Indiana. AIAA Paper 2002-4079.

[6] "Experimental Quiet Engine Program," contract No.NAS3-12430, March 1970.

[7] Shibata, T. and Kaji, S. , "Role of Shock Structures in Transonic Fan Roter Flutter", Proc of the 8th International Symposium: Unsteady Aerodynamics of Turbomachines and Propellers, Fransson, T. H. ed, Sept. 1997, pp.733-747.

[8] Hanamura, Y., Tanaka, H., and Yamaguchi, K., "A Simplified Method to Measure Unsteady Forces Acting on the Vibrating Blades in Cascade", Bulletin of JSME, 1980, Vol.23, No.180, pp.880-887.

EXPERIMENTAL FLUTTER INVESTIGATIONS OF AN ANNULAR COMPRESSOR CASCADE: INFLUENCE OF REDUCED FREQUENCY ON STABILITY

Joachim Belz and Holger Hennings
DLR – Institute of Aeroelasticity
Bunsenstrasse 10
D-37073 Göttingen, Germany
joachim.belz@dlr.de
holger.hennings@dlr.de

Abstract Due to the trend of increasing power and reducing weight, the fan and compressor bladings of turbomachinery might be more sensitive to flutter, which must strictly be avoided already in the design process. In order to increase our understanding of the flutter phenomena for fan and compressor cascades, aeroelastic investigations are essential.

This paper presents the achievements and results of experimental flutter investigations with a compressor cascade in the test facility of non-rotating annular cascades at EPFL. Flow conditions such as those that occur in rotating cascades are simulated by generating a spiral flow in the upstream. The construction of the cascade which takes into account the structural properties necessary to perform flutter experiments is described. For the simulation of elastic torsional vibrations of a two-dimensional blade section, the cascade consists of 20 blades (NACA3506 profile) mounted on elastic spring suspensions which allows for torsional motion about the midchord.

In order to investigate the influence of the reduced frequency on the global stability of the cascade and its local contibutions, experiments were performed for two different reduced frequencies. At the higher reduced frequency the cascade remains aerodynamically stable, however, at the lower reduced frequency and transonic flow conditions, some of the interblade phase angles appear to be aerodynamically unstable.

Keywords: Flutter, Reduced Frequency, Experiments, Annular Cascade

K.C. Hall et al.(eds.),
Unsteady Aerodynamics, Aeroacoustics and Aeroelasticity of Turbomachines, 77–91.

Introduction

The demand for a decrease in engine weight and a reduction in fuel consumption has, among other things, led to engines that contain a decreased number of compressor stages and slender fan or compressor blades. This results in both more flexible blades and in higher pressure ratios at each stage with a higher flow velocity around the blades. The variations of these parameters influence the aeroelastic stability of the blade assembly and can lead to flutter, i.e. self-excited blade vibrations due to an interaction with the motion-induced unsteady aerodynamic forces. For this reason, aeroelastic investigations are essential to provide detailed knowledge about flutter phenomena, especially for compressor cascades in transonic flow. Experimental data of unsteady aerodynamic and flutter tests are required for the validation of theoretical results as well.

In the past years, the increasing number of theoretical investigations has been accompanied by several experiments on vibrating cascades. Széchényi et al. (1980), Carta (1982), Buffum et al. (1998), and Lepicovski et al. (2002) have obtained unsteady aerodynamic data by harmonic torsional oscillations of one blade or all blades of their linear compressor cascades. Carta particularly showed the influence of the interblade phase angle on stability at low Mach numbers, whereas Széchényi and Buffum concentrated their investigations on the influence of large incidence angles on stability. Körbächer (1996) investigated the bending motion of the blades of a compressor cascade in an annular wind tunnel. A cascade with the same geometry was used by Hennings and Belz (1999, 2000) to examine the aerodynamic damping by forced pitching motions of the blades with respect to shock movements. The results were compared with theoretical investigations by Carstens and Schmitt (1999) as well as Kahl and Hennings (2000), who took into account leakage flow effects.

The experimental investigations presented here were performed in the wind tunnel for annular cascades at the École Polytechnique Fédérale de Lausanne (EPFL). This wind tunnel has been used by several other researchers for the measuring of unsteady pressure distributions due to blade vibrations for aerodynamic stability investigations of compressor and turbine cascades or upstream generated aerodynamics gusts for forced response investigations. The following investigations performed are cited as examples: Körbächer and Bölcs (1996), Körbächer (1996), Nowinski and Panovsky (1998)), Rottmeier (2003).

The aim of the investigation presented here was to investigate the influence of reduced frequencies on the cascade's aerodynamic and aeroelastic behavior at transonic flow. Two reduced frequencies were chosen in such a manner, that in one case self-excited cascade vibration (flutter) occured and in the other case the cascade remained aerodynamically stable. In order to realize cascade flutter the structural damping had to be minimized by redesigning the elastic

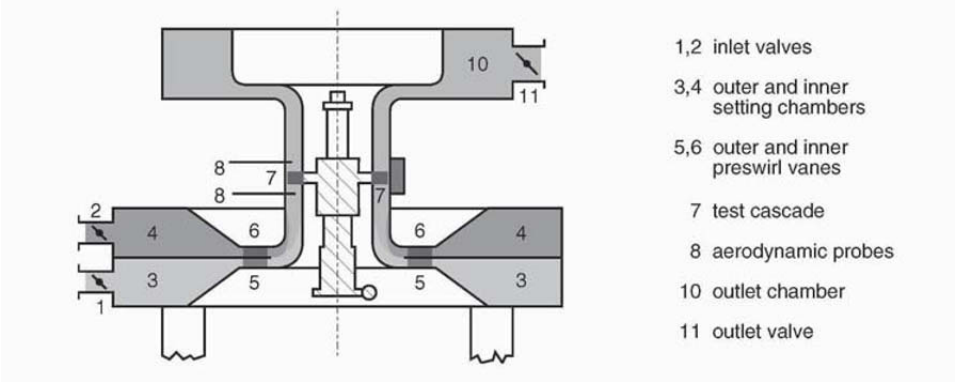

Figure 1. Schematic cross-section of the annular cascade tunnel; Bölcs (1983)

spring suspensions. The unsteady pressure distribution, the influence of the shock impulse at transonic flow conditions, and the local and global stability measured for the two reduced frequencies are compared.

1. Annular Test Facility

1.1 Annular Wind Tunnel

The experimental investigations presented here were performed in the wind tunnel for annular cascades at the EPFL. The annular cascade tunnel was developed for a research project between BBC and the EPFL to investigated the steady and unsteady flow in annular cascades without having to rotate them; Bölcs (1983). A spiral flow is generated in order to simulate real inflow angles such as those that would occur in a rotating cascade. Figure 1 shows the cross-section of the wind tunnel. The advantage of an annular cascade such as circumferential flow periodicity is combined with the advantage of a fixed cascade in respect of data aquisition and data transfer. Steady flow conditions are measured by aerodynamic probes in the upstream and downstream sections and by pressure taps on the blades' surfaces. The aerodynamic probes were calibrated to obtain the total pressure p_{t_1} and p_{t_2}, the steady pressures p_1 and p_2, the flow angles β_1 and β_2, and the Mach numbers Ma_1 and Ma_2 from the measured pressure data.

1.2 Cascade

The compressor cascade used here is composed of 20 blades with a NACA 3506 profile of $c = 80\,\mathrm{mm}$ in nominal chord length, a stagger angle of $\beta_g = 40°$, and a pitch at midspan of $s = 56.5\,\mathrm{mm}$ (Fig. 2). The profiles were shortened to a $c_{\mathrm{red}} = 77.5\,\mathrm{mm}$ chord length with a round trailing edge (see

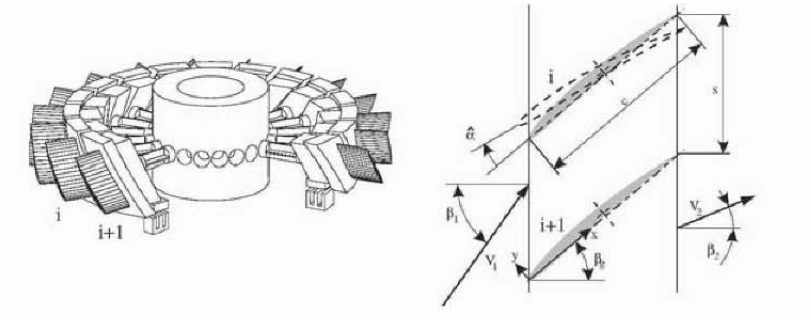

Figure 2. Components and geometry of the cascade

also Fig. 5 and 6). The blades are mounted via elastic spring suspensions which allow a torsional motion around midchord.

A NACA3506 profile was chosen for the investigations of tuned bending vibrations by Körbächer (1996). The fact that pitching motions of this profile should be more critical in aeroelastic stability – mainly for transonic flow conditions – was the reason why investigations of the aerodynamic damping using excited pitching vibrations were carried out by Hennings and Belz (1999, 2000). For the flutter measurements the blades are tuned to lower eigenfrequencies in order to reach an aerodynamically as well as aeroelastically unstable case. For the latter one the aerodynamic self-excitation has to surpass the structural damping of the cascade, namely of the elastic spring suspension.

For experimental investigations concerning the aerodynamic damping, the blades are driven by electromagnetic exciters such that their motions represent a traveling wave modes with one of the possible interblade phase angles

$$\sigma_k = \frac{2\pi}{N}(k-1) \quad , \quad k = 1...N \; , \tag{1}$$

given by the number of $N = 20$ blades. The unsteady pitching motions

$$\alpha_i(t) = \hat{\alpha} \cdot \cos(\Omega t - i\,\sigma_k) \tag{2}$$

of the blades are controlled in both their amplitudes $\hat{\alpha}$ and interblade phase angles σ_k. In order to reach appropriate amplitudes, the inertia of each blade and the vibrating part of the inner wall of the wind tunnel had to be reduced and the blades had to be excited near resonance (Figure 3 shows the assembly of the cascade). Lowering the eigenfrequencies by a minor mass moment of inertia, the torsional stiffness had to be reduced as well. So, the demand of both lower torsional stiffness (in presence of a high transversal stiffness to avoid a heaving motion) and lower structural damping led to a new one-piece spring suspension.

The spring suspension was made out a cylindrical part by cutting sections out using electrical discharge machining. The remaining section consists of

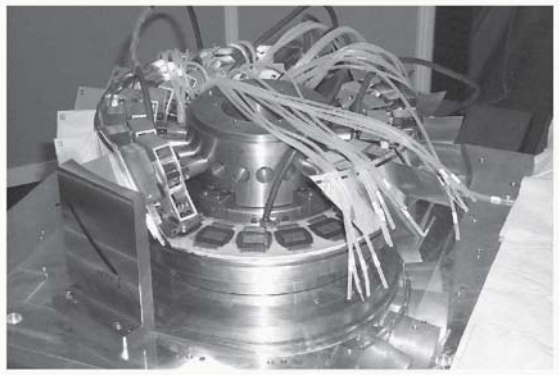

Figure 3. Annular cascade with some blades removed

Figure 4. Elastic spring suspension

eight rectangular beams orientated such that the torsional stiffness is low and the transverse stiffness is high. The use of electrical discharge machining made it possible to manufacture the spring suspension out of one part, which results in a very low structural damping (see Figure 4).

2. Experimental Investigations

As blade flutter in axial turbomachines is caused by an interaction of the blade motions and the motion-induced unsteady aerodynamic forces, the main parameters for flutter beside the cascade's geometry and structural properties are the flow conditions and the damping properties of the structure. Hence, two different approaches for experimental flutter investigations are possible: in the so-called "aerodynamic approach" a certain level of structural damping is needed for the blades to prevent self-excited vibrations if the cascade

is aerodynamically unstable. In order to determine the aerodynamic damping the blades are forced into controlled harmonic vibrations in each traveling wave mode successively and the motion induced unsteady pressure distributions is measured. The analysis of this data — in particular the out-of-phase unsteady harmonic pressure — leads to an estimation of the aerodynamic stability of each traveling wave mode. In a so-called "aeroelastic approach" the aerodynamic instability can overcome for the structural damping and the cascade starts to flutter. With the use of some safety devices (like hydaulic flutter brakes), the blade vibrations and the unsteady pressure distributions can be measured at the onset of flutter.

In order to drive the cascade into flutter each blade was tuned to a lower eigenfrequency of 183 Hz by increasing the mass moment of inertia. This cascade was mounted in the annular wind tunnel. Steady flow conditions were achieved by adjusting the inlet total pressure, the inlet inflow angle, and the back pressure. A hydraulic brake prevented blade vibrations during the adjustment of the steady flow. These flow conditions were surveyed by probe measurements of upstream and downstream flow field and by measuring the steady pressure distribution on the blades.

At the up- and down-stream flow field an aerodynamic probe was used to scan one pitch of the cascade by taking small steps in the radial and circumferential directions. The measured probe pressures were used to compute mass flow averaged in- and out-flow values such as p_{t_1}, p_{t_2}, p_1, p_2, etc. (Table 1). The steady pressure distribution the blades were measured with pressure taps on the pressure and suction surface at nine equidistant chordwise positions and the three radial positions $z/h = 0.2$, 0.5, and 0.8 on several blades. They were transformed to steady pressure coefficients

$$C_p = \frac{p - p_1}{p_{t_1} - p_1} \tag{3}$$

using the mass flow averaged values of the inflow total and steady pressure p_{t_1} and p_1, respectively (Fig. 5).

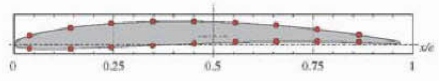

Figure 5. Location of the pressure taps

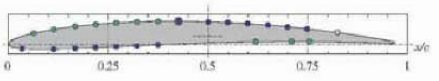

Figure 6. Location of the piezoelectric pressure transducers

Afterwards, the hydaulic brake was released to set the blade assembly to controlled pitching oscillations for the performance of the unsteady measurements ("aerodynamic approach") or to allow self-excited vibrations for the performance of the flutter experiments ("aeroelastic approach"). The unsteady pressure distribution was measured by 25 piezoelectric transducers, 15 of which

are mounted on the suction side and 10 on the pressure side of the blades. The transducers were distributed in blocks on only four blades. In each block, the transducers are located close together in order to resolve the unsteady pressure distribution near possible shock positions (Fig. 6).

The blade vibrations were measured by an eddy-current displacement sensor for each blade.

2.1 Investigated Flow Cases

The aim of the experiments was to investigate the behavior of a cascade running into flutter. In order to decrease the reduced frequency

$$\omega^* = 2\pi \frac{f\, c_{\mathrm{red}}}{v_1} \tag{4}$$

with respect to the same inflow velocity v_1 the cascade was tuned to a lower torsional blade eigenfrequency. So it was possible to investigate an unstable aeroelastic condition at a transonic flow case, which had been previously investigated.

Table 1. Steady upstream and downstream flow parameters

	Transonic Reference Case		Flutter Case	
ω^*	0.362		0.289	
	Upstream:	Downstream:	Upstream:	Downstream:
Ma	0.87	0.72	0.90	0.75
β	50.3 °	41.5 °	50.4 °	40.1 °
p_t	1323 mbar	1254 mbar	1397 mbar	1311 mbar
p	814 mbar	854 mbar	836 mbar	834 mbar

The transonic flow condition is characterized by the occurrence of a front shock at $x/c \approx 0.25...0.35$ and a channel shock at $x/c \approx 0.65...0.85$ on the suction side and at $x/c \approx 0.25...0.35$ on the pressure side (Fig. 7b). In- and out-flow parameters are mentioned in Table 1. Releasing the hydraulic brake at this flow condition, it was possible to set the blade assembly to controlled pitching oscillations around midchord for each interblade phase angle and to measure the unsteady pressure distribution up to a pitching amplitude of approximate $0.1°$ in order to determine the aerodynamic damping following the "aerodynamic approach". The excitation frequency of $177\,\mathrm{Hz}$ was choosen slighly below the eigenfrequency of the blades in order to distuinguish forced and free vibrations in the frequency range. This excitation frequency corresponds to a reduced frequency $\omega^* = 0.289$. Exceeding this amplitude the cascade starts to vibrate with a frequency of $182\,\mathrm{Hz}$ ("Flutter Case" Table 1).

With the same cascade, an aerodynamic damping investigations was performed following the "aerodynamic approach" with each blade tuned to a higher eigenfrequency and excited at 215 Hz ($\omega^* = 0.362$). Here the cascade remained aerodynamically and aeroelastically stable ("Transonic Reference Case" Table 1).

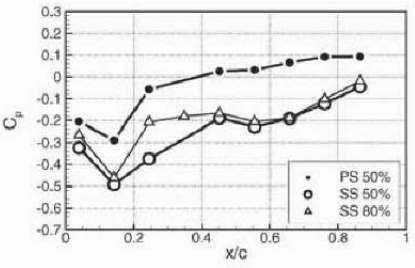

Figure 7a. Steady pressure distribution (C_p) of the transonic ref. case ($\omega^* = 0.362$)

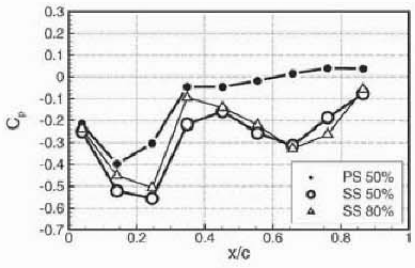

Figure 7b. Steady pressure distribution (C_p) of the flutter case ($\omega^* = 0.289$)

2.2 Evaluation of the Aerodynamic Damping

Due to the fact that the cascade in the "flutter case" remains aeroelastically stable for very small pitching amplitudes (below $0.2°$) it was possible to obtain unsteady pressure distributions caused by forced pitching vibrations of the blades in each traveling wave mode — in the same manner as the larger amplitudes in the "transonic reference case".

Following the "aerodynamic aproach" the measured unsteady pressure values and vibration signals were recorded. A Fourier transformation yields the first harmonic of the pressure which is related to the pitching motion of that blade i according to eq. (2) by

$$p(t) = \hat{p}\ \cos(\Omega t - i\,\sigma_k + \Phi)\ . \tag{5}$$

The unsteady pressure coefficient is defined as

$$\tilde{C}_p = \frac{\tilde{p}}{\hat{\alpha}\,(p_{t_1} - p_1)} \tag{6}$$

where $\tilde{p} = \hat{p}\exp(j\Phi)$ is the first harmonic of the unsteady pressure. The $\tilde{C}_p$-distribution for the interblade phase angle (IBPA) $\sigma_k = 72°$ is shown in Figure 8a for the "transonic reference case" and in Figure 8b for the "flutter case". In order to avoid numerical inaccuracies due to the discrete Fourier transformation, the sinusoidal vibration signals were Fourier transformed as

$\omega^* = 0.362$

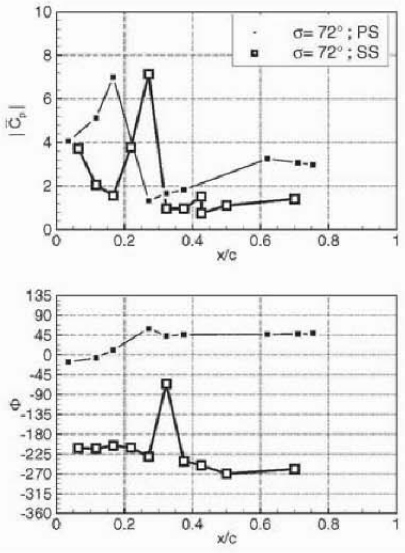

Figure 8a. Unsteady pressure coefficient $\tilde{C}_p$ for the IBPA $\sigma_k = 72°$ of the transonic reference case (magnitude at the top, phase at the bottom)

$\omega^* = 0.289$

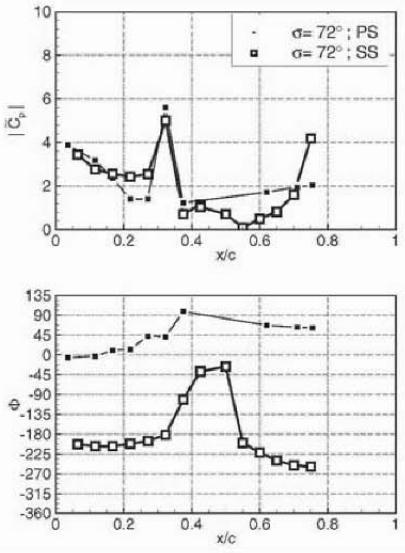

Figure 8b. Unsteady pressure coefficient $\tilde{C}_p$ for the IBPA $\sigma_k = 72°$ of the flutter case (magnitude at the top, phase at the bottom)

well. Arranging the $\tilde{C}_p$-distributions of each IBPA side by side, Figures 9a and 9b are obtained.

It can be seen from the pressure distribution of both cases, that the impulse response of the front shock is visible on the suction side at $x/c \approx 0.28$ in the "transonic reference case" and at $x/c \approx 0.32$ in the "flutter case". Comparing the channel shock of the "transonic reference case" with the "flutter case", the impulse response on the pressure side is visible at $x/c \approx 0.17$ in the "transonic reference case" and at $x/c \approx 0.32$ in the "flutter case". The impulse response of the channel shock is only visible at the suction side at $x/c > 0.75$ for the "flutter case".

The contribution of the locally acting aerodynamic forces due to the unsteady pressure to the aerodynamic damping of the cascade is given by the local work coefficient, i.e. the dimensionless work per unit arc length performed by the fluid on the blades. It is obtained by the integration with respect to time t over one period T of the pitching motion $\alpha(t)$ and yields

$$w^*(\xi) = \int_0^T \tilde{C}_p(\xi, t) \frac{\dot{\alpha}(t)}{\hat{\alpha}} \left[(\vec{r}(\xi) - \vec{r}_0) \times \vec{n}(\xi) \right]_3 \mathrm{d}t \tag{7}$$

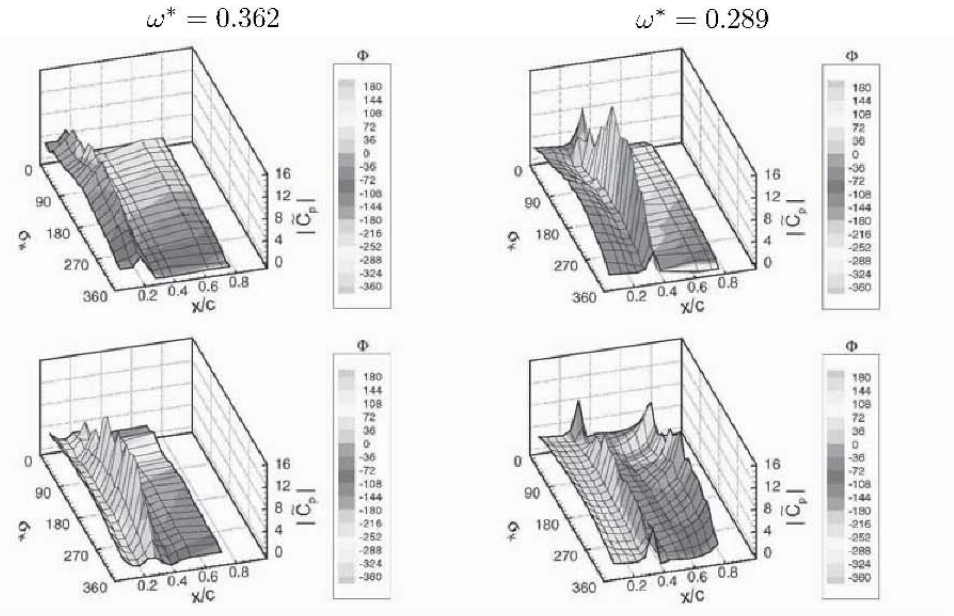

Figure 9a. Unsteady pressure coefficient $\tilde{C}_p$ for all IBPAs of the transonic ref. case (top: pressure side, bottom: suction side)

Figure 9b. Unsteady pressure coefficient $\tilde{C}_p$ for all IBPAs of the flutter case (top: pressure side, bottom: suction side)

where $(\vec{r}(\xi) - \vec{r}_0)$ is the dimensionless vector from the pitching axis to a surface point at the dimensionless arc length ξ and $\vec{n}(\xi)$ as the outward normal vector on that surface point. The subscript "3" denotes the radial component of the cross product. For the pitching motions of rigid blades in a given traveling wave mode, the local work coefficient is dependend on the amplitude of the aerodynamic moment due to the first harmonic of the unsteady pressure on a surface location, the (harmonic) pitching motion of that blade, and the phase between them to a local stability parameter. It is negative for stable and positive for unstable aerodynamic conditions.

In order to assess the aerodynamic stability of the two transonic cases in detail, the local work coefficient $w^*(\xi)$ is used to acquire an insight into the local contributions of the unsteady pressure at each measuring location — especially at locations, where considerable pressure fluctuations appear due to the shock movement, which is caused by the blade vibration. Regarding Figure 10a for the "transonic reference case" and Figure 10b for the "flutter case", the following aspects are recognizable:

- The contribution of the high unsteady pressure level on the leading edge stabilizes the pitching motion of the blade for all traveling wave modes. On the suction side, the local work coefficient is nearly constant, on

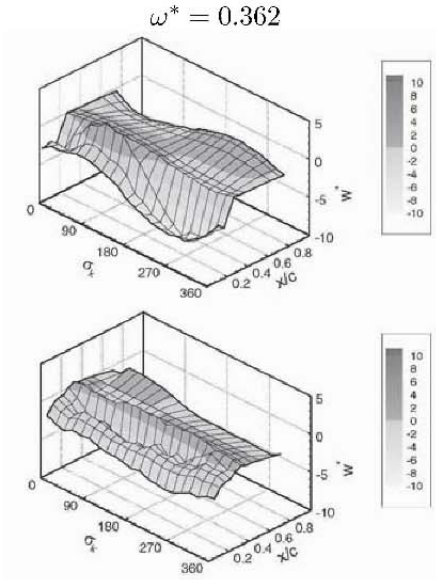

Figure 10a. Local work coefficient for all IBPAs of the transonic reference case (top: pressure side, bottom: suction side)

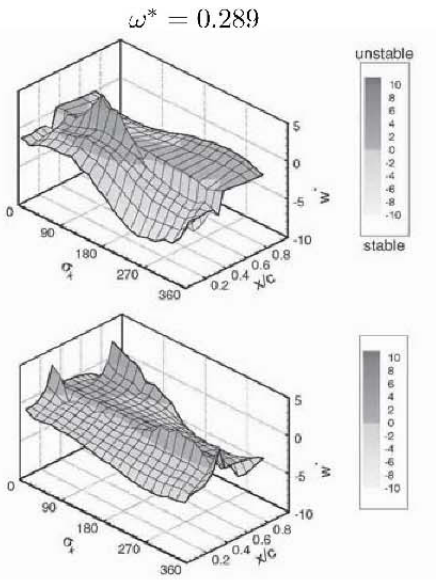

Figure 10b. Local work coefficient for all IBPAs of the flutter case (top: pressure side, bottom: suction side)

the pressure side, the stabilizing effect of the leadling edge for traveling wave modes with an IBPA between $180°$ and $360°$ is higher then for IBPA between $0°$ and $180°$.

- The high unsteady pressure level due to the front shock is stabilizing the motion in all travelling wave modes except for those with an IBPA between $288°$ and $360°$ for the "transonic reference case". Here the local work coefficient is near zero, that means no significant contribution to stability or instability. In contrast to that, the shock impulse of the front shock stabilizes only for the IBPA between $36°$ and $180°$ in the "flutter case" — for the other traveling wave modes it destabilizes.

- Comparing the channel shock impulse on the pressure side, in both cases the largest contribution to instability occurs in the vicinity of an IBPA of $126°$, but at a higher level for the "flutter case" Regarding the contribution of the front shock impulse on the suction side, this effects may cancel each other out.

- The most significant difference between the two cases is the strong channel shock impulse on the suction side in the "flutter case". Due to its

position near trailing edge and the large moment arm, its contribution is very strong:

- to the stability for the IBPAs between $180°$ and $360°$ and between $0°$ and $18°$
- and to the instability for the IBPAs between $36°$ and $162°$ with a strong jump between stability at $18°$ and instability at $36°$.

In order to assess how these contributions affect the flutter behavior of the cascade, a global damping parameter was evaluated as follows: With the definition of the unsteady pressure coefficient according to eq. (6), the unsteady moment coefficient $\tilde{C}_M$ is calculated. Using the imaginary part, the global damping coefficient is defined as

$$\Xi = -\operatorname{Im}\{\tilde{C}_M\} = +\operatorname{Im}\left\{\int_0^{S/c} \tilde{C}_p(\xi)\left[(\vec{r}(\xi)-\vec{r}_0)\times\vec{n}(\xi)\right]_3 \mathrm{d}s\right\} . \quad (8)$$

A positive value of Ξ represents stability with damped oscillations; negative values indicate instability.

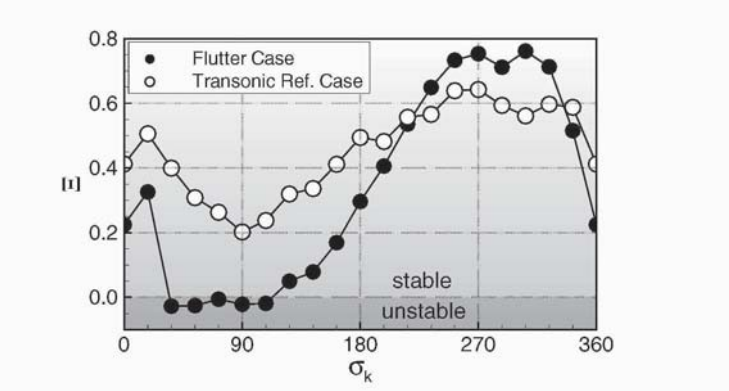

Figure 11. Global damping coefficient Ξ of the "flutter case" (black) and the "transonic referece case" (white)

It can be seen, that in both cases the traveling wave modes with the lowest aerodynamic damping occur at IBPA near $90°$. Especially for the flutter case, the aerodynamic damping for IBPA between $36°$ and $108°$ is negative, i.e. if the structural damping could not compensate this aerodynamic instability, the cascade starts to flutter.

2.3 Flutter Measurements

Increasing the vibration amplitude beyond a certain level in the "flutter case" the cascade starts with self-excited vibrations. Figure 12 plots the amplitude

of some blades versus time when the cascade was excited at a frequency of $177\,\mathrm{Hz}$. After reaching a certain amplitude, the cascade start to vibrate at its eigenfrequency of $182\,\mathrm{Hz}$. Then the excitation was turned down. While the cascade was vibrating in its eigenfrequency and was simultaneously excited, beats are clearly visible. A Fourier analysis performed every $100\,\mathrm{ms}$

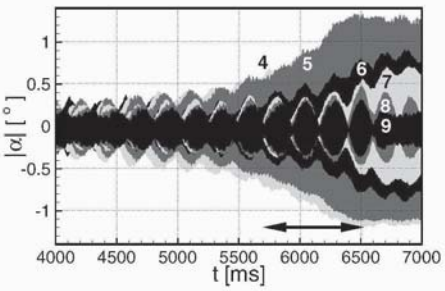

Figure 12. Increasing amplitudes of the blades 4 ... 9 of the flutter case

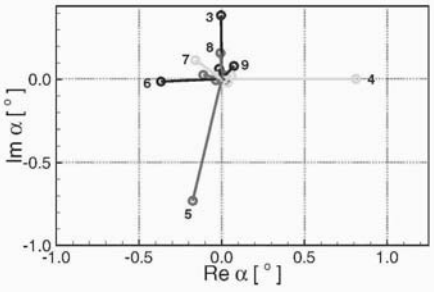

Figure 13. Amplitudes and phases of the blade deflections at $t = 5700\,\mathrm{ms}$

for sections of $819\,\mathrm{ms}$ (8192 time samples) leads to the complex amplitudes (amplitude and phase) and gives an insight into the vibration mode. (Figure 13 shows the results of a Fourier analysis started at $5700\,\mathrm{ms}$.)

It is visible, that only some blades — namely blade 3 to 9 — were vibrating with a significant amplitude. The phase between these blades remained constant over time, but there is no equal interblade phase angle between all blades visible. This may be caused by the cascades's mistuning due to blades equiped with pressure taps and tubes as well as blades with unsteady pressure transducers.

3. Summary

Measurements of aerodynamic damping were performed for nearly identical transonic flow cases, but for different reduced frequencies. For the lower reduced frequency the cascade was proven to be aerodynamically unstable. Besides the front shock impulse and pressure side's channel shock impulse this unstable case was characterized by a strong channel shock impulse near suction side's trailing edge. While the effects of the front shock impulse and pressure side's channel shock impulse canceled out each other, the impulse of the channel shock near the trailing edge on the suction side had a significant influence on stability. Increasing the forced vibration amplitude, the cascade started with self-excited vibrations.

Acknowledgments

The investigations were carried out as part of a joint research project of the MTU Aero Engines GmbH and the DLR Institute of Aeroelasticity. The authors would like to acknowledge the authorization for publishing the results here. They would also like to extend their thanks to Prof. Bölcs (EPFL) for the possibility of using the annular wind tunnel. Finally, the technical support by Mr. Beretta, Dr. Ott, and Dr. Rottmeier is gratefully acknowledged.

References

Belz, J., Hennings, H. (2000). *Aerodynamic Stability Investigations of an Annular Compressor Cascade Based on Unsteady Pressure Measurements,* Proceedings of the 9th International Symposium on Unsteady Aerodynamics, Aeroacustics and Aeroelasticity of Turbomachines (ISUAAAT), 4–8 Sept 2000, Lyon, France, pp. 280–295

Bölcs, A. (1983). *A Test Facility for the Investigation of Steady and Unsteady Transonic Flows in Annular Cascades,* ASME Paper 83-GT-34

Buffum, D.H., Capece, V.R., King, A.J., and El-Aini, Y.M. (1998). *Oscillating Cascade Aerodynamics at Large Mean Incidence,* ASME Journal of Turbomachinery, Vol. 120, pp. 122–130

Carta, F.O. (1982). *An Experimental Investigation of Gapwise Periodicity and Unsteady Aerodynamic Response in an Oscillating Cascade. I – Experimental and Theoretical Results,* NASA Contractor Rep., CR-3513

Carstens, V. and Schmitt, S. (1999). *Comparison of Theoretical and Experimental Data for an Oscillating Transonic Compressor Cascade,* ASME Paper 99-GT-408

Hennings, H. and Belz, J. (1999). *Experimental Investigation of the Aerodynamic Stability of an Annular Compressor Cascade Performing Tuned Pitching Oscillations in Transonic Flow,* ASME Paper 99-GT-407

Kahl, G. and Hennings, H. (2000). *Computational Investigation of an Oscillating Compressor Cascade Experiment,* Proceedings of the 9th International Symposium on Unsteady Aerodynamics, Aeroacustics and Aeroelasticity of Turbomachines (ISUAAAT), 4–8 Sept 2000, Lyon, France, pp. 819–829

Körbächer, H. and Bölcs, A. (1996). *Steady-State and Time-Dependent Experimental Results of a NACA-3506 Cascade in an Annular Channel,* ASME Paper 96-GT-334

Körbächer, H. (1996). *Experimental Investigation of the Unsteady Flow in an Oscillating Annular Compressor Cascade,* Ph.D. Thesis, Swiss Federal Institute of Technology, Lausanne, Switzerland

Lepicovsky, J., MacFarland, E.R., Capece, V.R., and Hayden, J. (2002). *Unsteady Pressures in a Transonic Fan Cascade Due To a Single Oscillating Airfoil,* ASME Paper GT-2002-30312

Nowinski, M., and Panovsky, J. (1998). *Flutter Mechanisms in Low Pressure Turbine Blades,* ASME Paper 98-GT-573

Rottmeier, F. (2003). *Experimental Investigation of a Vibrating Axial Turbine Cascade in Presence of Upstream Generated Aerodynamic Guests,* Ph.D. Thesis, École Polytechnique Fédérale de Lausanne, Switzerland

Széchényi, E., and Girault, J.P. (1980). *A Study of Compressor Blade Stall Flutter in a Straight Cascade Wind-tunnel,* Symposium on Aeroelasticity in Turbomachines, Lausanne, Switzerland

Whitehead, D.S. (1987). *Classical Two-Dimensional Methods,* AGARD Manual on Aeroelasticity in Axial-Flow Turbomachines, AGARD-AG-298, Vol. 1, Chapter 3: Unsteady Turbomachinery Aerodynamics, M.F. Platzer and F.O. Carta, eds.

II

FORCED RESPONSE

UNSTEADY GUST RESPONSE IN THE FREQUENCY DOMAIN

A. Filippone
UMIST
Department of Mechanical, Aerospace, Manufacturing Engineering
Manchester M60 1QD
United Kingdom
a.filippone@umist.ac.uk

Abstract A theory has been derived to describe the unsteady response of arbitrary two-dimensional bodies in the frequency domain. The theory provides the values of the admittance for side force and yawing moment under sinusoidal gust conditions. This approach provides indirectly the power spectra density (PSD), which is often used to characterize systems in unsteady periodic conditions (Filippone and Siquier, 2003, Filippone, 2003). The flow model is inviscid, with the assumption of small perturbations. Results are shown for a squared, a triangular, and a circular plate, as well as some road vehicles. The existence of critical damping is discussed for some cases.

1. Introduction

Lateral gusts have been known to affect the handling of many road vehicles, including large Sport Utility Vehicles (UV). Another example is vehicle passing: at some speeds, this creates a destabilizing wave that can be attributed to a gust-like phenomenon. The destabilizing effect is a function of both the relative speed and the relative size and inertial mass of the vehicles. A high speed train encountering a gust at the exit of a tunnel is another case considered critical (Schetz, 2001). However, some gust events are outright violent. Recently (May 8, 2003), the US National Weather Service reported that straight-line winds were suspected of causing a freight train to derail in Kansas.

Laboratory experiments in this area of aerodynamics are scarce due to the intrinsic difficulty of creating gust conditions in the wind tunnel. In fact, lateral unsteady flows of fixed frequency, shape and speed must be created along with the main wind tunnel flow. However, a limited number of studies exist. Bearman and Mullarkey, 1994, studied the lateral gust response of a family of bluff

K.C. Hall et al.(eds.),
Unsteady Aerodynamics, Aeroacoustics and Aeroelasticity of Turbomachines, 95–106.

bodies resembling road vehicles. These bodies are characterized by different after-body scant angles, from zero to 40 degrees.

Earlier on, Bearman, 1971a, and Bearman, 1971b, performed important experiments on flat plates and circular disks in turbulent and laminar flow, and calculated the admittance for the drag force (or side force, in the present nomenclature) of these bodies. The systems were placed in a wind tunnel in a position normal to the incoming flow. These plates were a particular case of bluff bodies, for which flow separation plays a major role. Bearman's paper discusses a number of fundamental issues, such as the general behavior of the admittance in turbulent flow, and the theory used to correlate the wind tunnel data (Vickery, 1965). Vickery's experimental and theoretical work led to a semi-empirical relationship for the admittance of flat plates in normal turbulent flow. This correlation is sometimes used to predict the admittance in wind engineering applications.

Howell and Everitt, 1983, considered a high speed train with two degrees-of-freedom (pitch and yaw), in order to identify the risk of a train overturning in high cross winds, and the effects associated to track-side structures and passengers. Larose et al., 1999, have performed wind tunnel experiments to derive the frequency response of very large ships at sea. This study was aimed at providing controls to large vessels at port. Data for aerospace systems could not be found in the technical literature, perhaps because wing controls are considered in terms of *effectiveness*, rather than admittance.

We will use a development based on an indicial approach, which, in spite of some underlying simplifications, is fast and powerful. This paper will discuss the properties of the admittance functions and their practical meaning.

The theory originates from a mathematical treatment of the results determined by Drischler and Diederich, 1957, who considered sharp-edged traveling gusts past two-dimensional wings in a wide range of speeds. The theory allows the calculation of the admittance for the lift force (or side force, if the system is non lifting) and for the pitching moment (or yawing moment, respectively). This analysis does not take into account the structural inertia of the system.

Classical analyses in the frequency domain are due to von Kármán and Sears, 1938 for the sinusoidal gust on the two-dimensional airfoil. However, it is more common to find analyses in the time domain, for example the classical works of Küssner, 1936, and Wagner, 1925, who derived basic transfer functions for the abrupt change in angle of attack (Küssner) and the response to a fixed sharp-edged gust (Wagner). See Leishman, 2000, for a full review.

2. Theoretical Model

The systems discussed will have one degree-of-freedom. They consist of a rigid body, whose position can be described by a single coordinate. The body has a length distribution $b(z)$ in the streamwise coordinate x, as shown in Fig. 1.

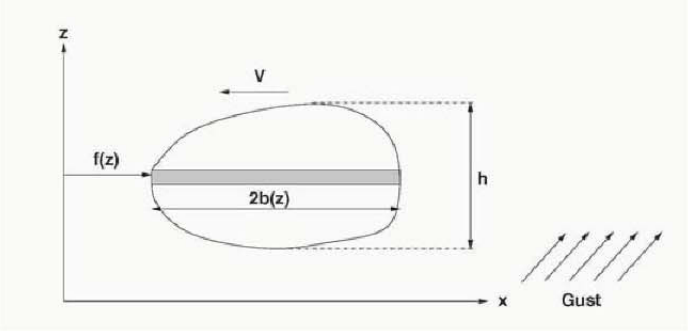

Figure 1. Reference system

The height of the system is h; $f(z)$ is the local position of the leading edge line. The gust is applied in a direction normal to the plane $\{x, z\}$. The flow model will be potential, with a free stream velocity V in the x-direction. The flow will be inviscid, subject to small perturbations, created by oscillatory gusts of reduced frequency k.

The gust response will be modeled in the frequency domain by the admittance, that we indicate with $H(k)$. In wind engineering, this quantity is often indicated by χ^2. For a more detailed discussion, see Filippone and Siquier, 2003, Filippone, 2003.

For complete clarity, the admittance is a transfer function defined as the ratio between the loads under unsteady forcing of finite frequency k and the quasi steady loads, e.g. loads with infinitely large wavelength:

$$H(k) = \frac{F(k)}{F(k \to 0)} \tag{1}$$

where F is a generic load (lift, side force, yaw moment, etc.). With the definition Eq. 1 we have $H \to 1$ as $k \to 0$. This definition is coherent with that given originally by Davenport (1961). A result not conforming with this limiting value will not be considered correct. The definition of Eq. 1 is important, also because it is related in a straightforward way to the power spectra density:

$$PSD(k) \sim 2H^2(k) \tag{2}$$

which does not require the Fourier transform of the system's response in the time domain.

In an earlier study (Filippone and Siquier, 2003), we proved that under the above conditions the admittance for side force (or lifting force) can be described by the following equation:

$$H(k) = \frac{1}{h}\int_h r(z) H_\lambda[r(z)k]\, e^{-i\varphi(z)k} dz \tag{3}$$

where

$$H_\lambda = e^{-i\lambda k}\left\{\Big[\, J_0(\lambda k) - iJ_1(\lambda k)\Big]\, C(k) + \frac{1}{\lambda} iJ_1(\lambda k)\right\} \tag{4}$$

is the admittance for the infinite swept lifting surface; $C(k)$ is a complex function describing the indicial response of an inviscid oscillatory flow (Theodorsen function; Theodorsen, 1935):

$$C(k) = F(k) + iG(k). \tag{5}$$

The quantities J_0, J_1 are Bessel functions of the first and second kind in the reduced frequency k

$$J_n(k) = \sum_{p=0}^{\infty} \frac{(-1)^p (k/2)^{n+2p}}{p\,!\,\Gamma(n+p+1)} \tag{6}$$

and Γ is the gamma function; λ is the gust speed ratio, defined as

$$\lambda = \frac{V}{V + V_g} = \frac{1}{1 + V_g/V} \tag{7}$$

where V_g is the gust velocity in a frame of reference fixed with the ground, V is the velocity of the body. All the values of λ can be considered, except the singular value obtained for $V = -V_g$ (e.g. when the gust and the body are traveling in opposite directions with the same speed). The value $\lambda = 1$ corresponds to a stationary gust, e.g. $V_g = 0$; $\lambda = 0$ is a limit value obtained with $V_g/V \to \pm\infty$, which is possible with a stationary body (e.g. $V = 0$) and a moving gust. Values of $0 < \lambda < 1$ are the most common in practical applications.

Finally, two functions, appearing in Eq. 3 are two functions of the local body length

$$r(z) = \frac{b(z)}{\overline{b}} \tag{8}$$

$$\varphi(z) = \frac{f(z)}{\overline{b}} \tag{9}$$

where $\overline{b}$ is the average body length.

Properties of the Admittance

Eq. 4 is the basic transfer function for the infinite lifting surface. Eq. 3 is an integral form of $H_\lambda(k)$ obtained from the concept of strip theory; $H_\lambda(k)$ must be calculated only once, and can be used for an arbitrary body. The strip theory is based on the assumption that the downwash velocity at one spanwise location does not affect the downwash at a nearby position. It is evident that

$$\lim_{k\to 0} H_\lambda(k) = 1, \tag{10}$$

which is coherent with the definition of admittance, Eq. 1. There exist values of the gust speed ratio that yield values of the admittance larger than the unity, though $H_\lambda(k)$ is always finite. When the forcing frequency is significantly lower that the natural frequency of the aerodynamic system, the transfer function is equal to unity.

Eq. 3 shows that at a given frequency the admittance is inversely proportional to the profile width. The leading edge is invariant to yawing or stretching. This can also be inferred from the transfer function.

Integration of the equations is generally done numerically, but for a limited number of cases there exist closed-form solutions.

Admittance for the Moment

The yawing moment can be calculated around any axis a (Filippone and Siquier, 2003), and is written as:

$$\begin{aligned} H_\lambda^M(k) = & \left(a+\frac{1}{2}\right)\left[J_0(\lambda k) - iJ_1(\lambda k)\right] C(k) \\ & -\frac{i}{2\lambda}(\lambda+2a)J_1(\lambda k) - \frac{1-\lambda}{2\lambda}J_2(\lambda k) \end{aligned} \tag{11}$$

where J_2 is a Bessel function of order 2. A number of simplifications can be made from Eq. 11. First, consider a body pitching or yawing around an axis $a = -1/2$. In this case, Eq. 11 can be simplified in at least two cases: If $a = -1/2$, then

$$H_\lambda^M(k) = \frac{\lambda-1}{2\lambda}\Big[\, J_2(\lambda k) - iJ_1(\lambda k)\Big]. \tag{12}$$

If $\lambda = 1$ (stationary gust), then

$$H_{\lambda=1}^M(k) = \left(a+\frac{1}{2}\right) H_{\lambda=1}(k). \tag{13}$$

Therefore, the admittance for the yawing moment is proportional to the admittance for the side force, and the two functions are in phase at all frequencies.

The latter equation can be normalized so as to have a unit value at $k \sim 1$. Also note that if $a = -1/2$ then the body is neutral at all frequencies with respect to the pitching moment.

Side Force and Yawing Moment Coefficients

A further development of the theory leads to an explicit expression for the side force coefficient:

$$\overline{C_S}^2 = \left[2\pi^2 p_g \int_0^\infty \frac{|H_\lambda(k)|^2 f(k,k_0)}{\phi(0)}\, dk\right] \overline{\left(\frac{w}{V}\right)}^2 \tag{14}$$

where $|H(k)|$ is the magnitude of the transfer function $H_\lambda(k)$; $p_g = L_{ref}/2\overline{b}$ is the gust parameter; w/V is the gust amplitude; $f(k,k_o)$ is an oscillatory function quickly damped on both sides of the frequency k_o. Finally,

$$\phi(\tau) = \frac{1}{2T}(T-\tau)\cos(\omega_0\tau) - \frac{1}{2T}\left(\frac{\sin(\omega_0(2T-\tau)) - \sin(\omega_0\tau)}{2\omega_0}\right) \tag{15}$$

is the gust auto-correlation function evaluated at $\tau = 0$. In Eq. 15, T is the time needed by the gust to travel the reference length with the speed V; ω_o is the frequency associated to k_o.

The integral term in Eq. 14 depends on the admittance over the whole spectrum of frequencies and on the reference frequency k_o. The integral is a constant with respect to the gust amplitude. Hence $\sqrt{\overline{C_S}^2}$ varies linearly with the root mean square gust angle $\sqrt{\overline{\alpha}^2}$. This linear dependence is also valid for the yawing moment coefficient, C_Y. In the latter case, replace the admittance for the moment, Eq. 11, into Eq. 14 to obtain the coefficient of proportionality. Results from this theory are compared in Fig. 2 with the experimental data of Bearman & Mullarkey for the road vehicle BA20 (scant angle 20 degrees). The figure shows both the side force coefficient C_Y and the pitching moment coefficient C_S as a function of the RMS of the gust angle. The correlation is quite satisfactory.

3. Critical Damping

Critical damping occurs when the system's response decays to a very small number: At a certain frequency the system is able to dissipate all the energy from the external forcing. MacDonald, 1975, defines the critical damping as 1% of the steady state load response.

It is generally suggested that the decreasing admittance with the increasing frequency is due to the fact that the smaller turbulent eddies have a higher frequency, e.g. shorter wavelengths. However, we prove that this is also the

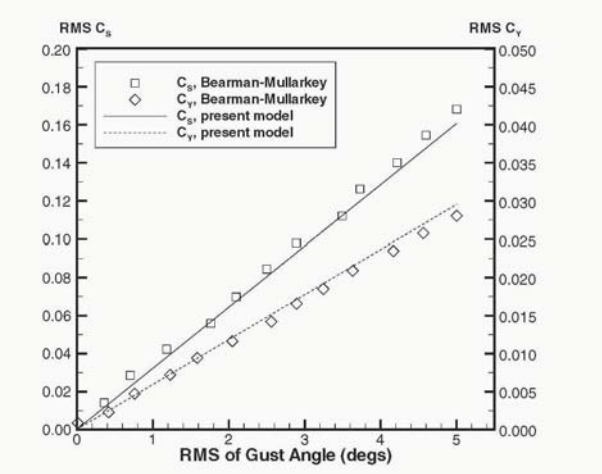

Figure 2. RMS of the side force and pitching moment coefficients for the road vehicle BA20, compared with Bearman-Mullarkey's experimental data (Bearman and Mullarkey, 1994).

case for a *laminar inviscid flow*. A number of other events seem to occur. Past a critical damping frequency the transfer function increases again, and may reach several other minima. We have found no experimental data to substantiate this conclusion.

The existence of critical damping in this model is associated to a combination of increasingly oscillatory Bessel functions. The first critical damping frequencies are $k_c \sim 5.13$ for the circular plate and $k_c \sim 2.13$ for the square plate, both with a gust speed ratio $\lambda = 1$.

This result shows that the square plate is more effective in reducing the response from an unsteady forcing. For non-analytical bodies, critical frequencies may not exist.

With the assumption of small perturbations, critical damping will be associated to a pressure wave of wavelength equal to the gust wavelength. When the latter one is a multiple of the plate's chord, also the pressure distribution will have the same wavelength (with a time lag). When the gust wavelength λ_g is equal to the chord $c = 2b$ the following relationships hold:

$$k = \frac{\omega b}{V} = \frac{\omega c}{2V} = \frac{2\pi f c}{2V} = \frac{\pi f \lambda_g}{V} = \frac{\pi f}{V}\frac{V_g}{f} = \pi\frac{V_g}{V} = \pi\frac{1-\lambda}{\lambda} \qquad (16)$$

having assumed that the gust wavelength is related to its frequency by $\lambda_g = V_g/f$. If there are n wavelength over the chord of the plate, the critical frequency is estimated from

$$k_c \sim n\pi \frac{1-\lambda}{\lambda} \tag{17}$$

If we plot the calculated data from Eq. 3 and the estimate, Eq. 16, we find a similar trend, although the values are not quite right, Fig. 3.

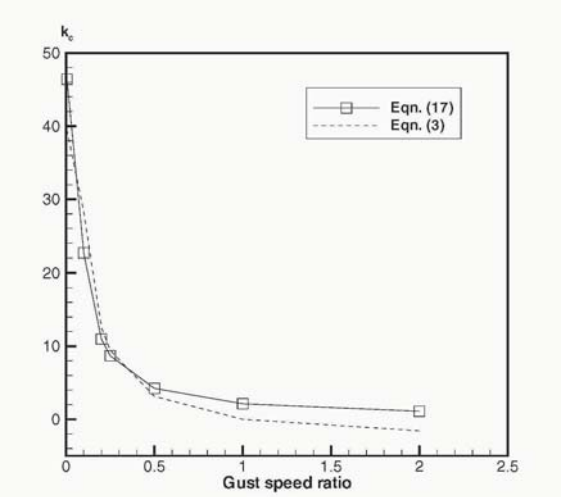

Figure 3. Estimate of the first frequency for critical damping, squared plate in laminar small perturbation flow, as function of the gust speed ratio

Bearman's experiments (Bearman, 1971a), and Vickery's theoretical correlations (Vickery, 1965) both refer to plates in normal turbulent flow. These authors seem to imply that critical damping does exist in normal flow conditions, at frequencies that are not discordant with the present ones ($k < 10$).

One key point evidenced by the experiments of Bearman et al. in turbulent flow is the fact that the admittance does not tend to one at the very long wavelengths.

4. Analytical Solutions

A number of closed-form solutions of Eq. 3 are possible. We will consider here only the case of the squared and the triangular plate. We leave to the reader the integration of other simple geometrical forms.

A solution for the squared plate is given by Eq. 4. Fig. 4 shows the map of the admittance in the imaginary plane for different gust speed ratios for a squared figure. With increasing λ the system tends tends asymptotically to a closed loop. The range of the reduced frequency is $k = 1 - 10$.

The case of the circular plate is somewhat more complicated, since the admittance contains trigonometric functions in implicit form. Therefore this case was solved using a numerical method, as described in Filippone, 2003.

For a generic triangular plate with a sweep angle α and height h, the geometrical functions are:

$$r(z) = 2\left(1 - 2\frac{|z|}{h}\right), \qquad \varphi(z) = 8\frac{|z|}{h}. \tag{18}$$

Therefore, the admittance becomes

$$H = \frac{1}{h}\int_{-h/2}^{h/2} r(z) H_\lambda[r(z)k]\; e^{-i\lambda k\varphi(z)}\, dz. \tag{19}$$

By operating a change of variables $z_1 = \dfrac{z}{h/2}$ we find

$$H = \frac{1}{2}\int_{-1}^{1} 2(1-|z_1|)\, H_\lambda\left[2k(1-|z_1|)\right]\; e^{-i\lambda k 4|z_1|}\, dz. \tag{20}$$

Therefore, *H does not depend on the sweep angle*. Similar conclusion is found for the pitching moment. We plotted the admittance for the triangular plate at $\lambda = 1$ in Fig. 5 and we compared with the admittance of squared plate $H_1(k)$ for frequencies up to $k = 10$. The oscillations of the admittance have smaller amplitude and show no critical damping.

5. Other Applications

Applications to road vehicles have been attempted, and Fig. 2 showed good results for the RMS of the side force and pitching moment. As an extension

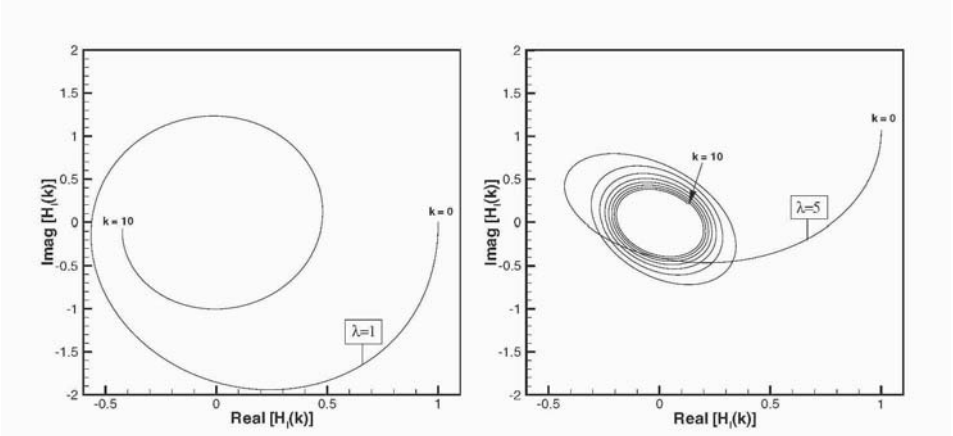

Figure 4. Admittance behavior for a squared plate as a function of the gust speed ratio. The data show the critical damping frequencies

of the theory, we have tried to simulate the gust response of a SUV (Range Rover), as shown in Fig. 6.

6. Conclusions

A theory for the simulation of small perturbation potential flows under sinusoidal gust conditions has been derived and applied via the strip theory to

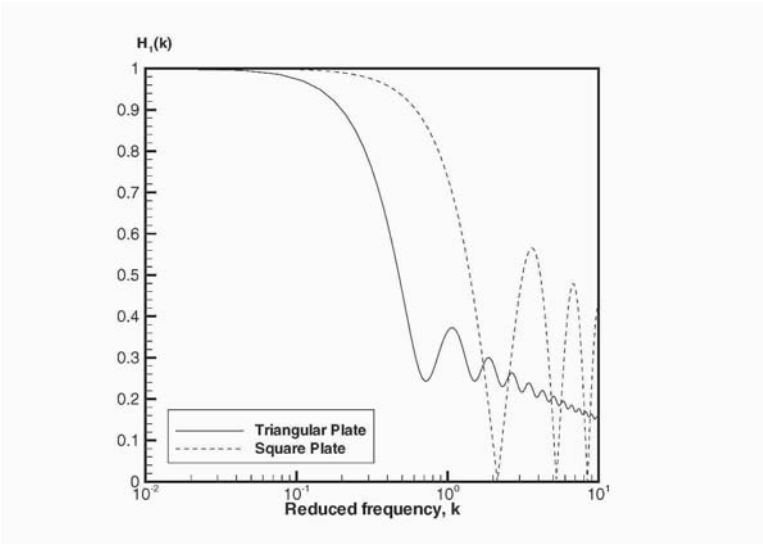

Figure 5. Side force admittance for a triangular plate compared with a square plate, $\lambda = 1$

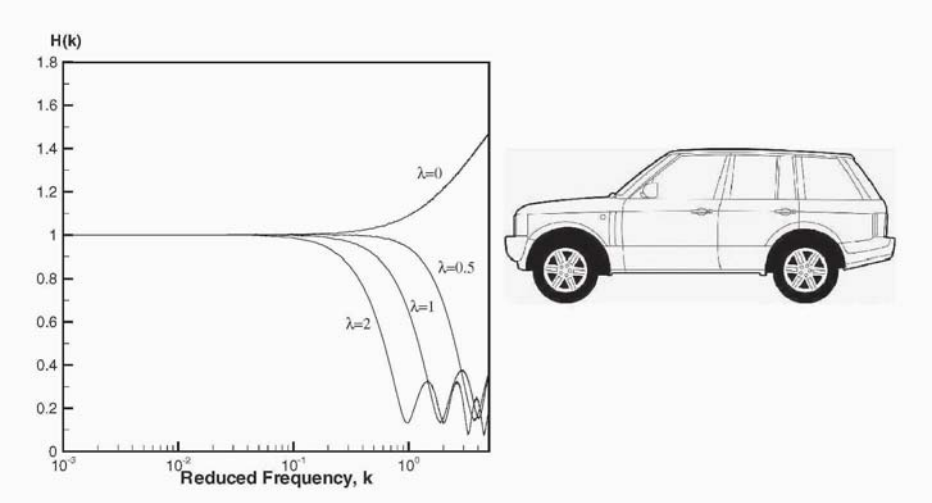

Figure 6. Gust response of a Range Rover, model shown on the right

a number of analytical and generic two-dimensional plates. The analysis was carried out in the frequency domain. An extension of the theory can be done as to include road vehicles (cars and high speed trains), and neglecting secondary effects in the third dimension. Results obtained for these bodies are reasonable and compare well with existing experimental data. The model does not allow for the simulation of yawed flow conditions and for the effects of turbulence.

Possibilities exist to extend the theory to calculate the drag response in the frequency domain, and to treat systems with more than one degree-of-freedom.

References

Bearman, PW (1971a). An investigation of the forces on flat plates normal to a turbulent flow. *J. Fluid Mech*, 46(1), pp. 177–198.

Bearman, PW (1971b). Wind loads on structures in turbulent flow. In *The Modern Design of Wind-Sensitive Structures*. National Physical Lab, UK.

Bearman, P.W. and Mullarkey, S.P. (1994). Aerodynamic forces on road vehicles due to steady side winds and gusts. In *Road Vehicle Aerodynamics*, pp. 4.1–4.12, Loughborough University, UK. Royal Aeronautical Society Conference.

Drischler, J.A. and Diederich, F.W. (1957). Lift and moment responses to penetration of sharp-edged travelling vertical gusts, with application to penetration of weak blast waves. NACA Report TN 3956.

Filippone, A (accepted for publication, 2003). Unsteady gust response of road vehicles. *ASME J. Fluids Eng.*

Filippone, A and Siquier, J. Aerodynamic admittance of two-dimensional bodies. *J. Royal Aero. Soc.*, Vol 107, Issue 1075, pp. 404-418, July 2003.

Howell, J.P. and Everitt, K.W. (1983). Gust response of a high speed train model. In *Annual Meeting of the ASME – Aerodynamics of Transportation* (Morel, T. and Miller, J. editors), Vol. 7, pp. 81–89, Boston, MA.

Küssner, HG (1936). Zusammenfassender bericht über den instationären auftreib von flügeln. *Luftfahrtforschung*, 13(12), pp. 410–424.

Larose, GL, Agdrup, K, and Larsen, SV (1999). Direct measurements of the aerodynamic admittance of large ships. In *10th International conference on wind engineering*, Copenhagen, Denmark.

Leishman, GJ. (2000). *Principles of Helicopter Aerodynamics*, Chapter 8, *Cambridge Aerospace Series*. Cambridge University Press.

MacDonald, AJ (1975). *Wind Loading on Buildings*. Applied Sciences Publ., London.

Schetz, JA (2001). Aerodynamics of high-speed trains. *Ann. Rev. Fluid Mech.*, 33, pp. 371–414.

Theodorsen, T. (1935). General theory of aerodynamic instability and the mechanism of flutter. NACA Report 496.

Vickery, BJ (1965). On the flow behind the coarse grid and its use as a model of atmospheric turbulence in studies related to wind loads on buildings. Report Aero 1143, Nat. Phys. Lab. Aero, Middlesex, UK.

von Kármán, T. and Sears, W.R. (1938). Airfoil theory for non-uniform motion. *J. Aeronaut. Sci.*, 5(10), pp. 379–390.

Wagner, H (1925). Über die Entstahung des dynamischen Auftriebes von Tragflügeln. *Zeitschrift für Angewandte Mathematik und Mechanik*, 5(1), pp. 17–35.

Main Symbols

a	=	position of the rotation axis
b	=	half-length of the body
$\overline{b}$	=	mean value of the chord
$C(k)$	=	Theodorsen's function, Eq. 5
C_S	=	Side force coefficient
C_Y	=	Yawing moment coefficient
f	=	gust frequency
$F(k)$	=	indicial lift force in Theodorsen's function
$G(k)$	=	indicial phase lag in lift response (Theodorsen)
i	=	imaginary unit
$H_\lambda(k)$	=	aerodynamic admittance 2D body
$H_\lambda^M(k)$	=	yawing moment admittance of 2D body
$J_n(k)$	=	Bessel function of order n
k	=	reduced frequency
L_{ref}	=	reference length
n	=	number of wavelengths
p_g	=	gust parameter $p_g = L_{ref}/2\overline{b}$
$r(z)$	=	defined by Eq. 8
T	=	reference time in Eq. 15
V	=	velocity in the coordinate system of the ground
V_g	=	gust velocity in the coordinate system of the ground

Greek Symbols

α	=	gust angle
λ	=	gust speed parameter, Eq. 7
λ_g	=	gust wavelength
$\phi(s)$	=	gust auto correlation function
$\varphi(z)$	=	defined by Eq. 9
ω	=	pulsation

Underscripts/Overscripts

$()_g$	=	gust
$()_\lambda$	=	gust speed ratio λ as a parameter
$\overline{()^2}$	=	mean square value over full oscillation
$()_c$	=	critical value

AXIAL TURBINE BLADE VIBRATIONS INDUCED BY THE STATOR FLOW

Comparison of Calculations and Experiment

M. B. Schmitz, O. Schäfer, J. Szwedowicz, T. Secall-Wimmel
ABB Turbo Systems Ltd
Thermal Machinery Lab
CH-5401 Baden
Switzerland
michael.schmitz@ch.abb.com

T. P. Sommer
ALSTOM (Switzerland) Ltd
CH-5401 Baden
Switzerland
thomas.sommer@power.alstom.com

Abstract The forced excitation of the rotor blades of a single-stage turbine due to rotor-stator interaction is calculated with an in-house unsteady flow solver and a general purpose finite element code. A scaled configuration is used in order to reduce the amount of computational effort. The unsteady flow solution is obtained on three blade-to-blade cuts. The time dependent static pressure on the blade surface is Fourier transformed with respect to the vane passing frequency and the relevant Fourier modi of the original three blade profile cuts are interpolated to the overall blade height. This Fourier transformed flow solution is transferred to the finite element model where the blade excitation is obtained. Two reduced geometrical rotor-stator configurations are investigated and compared with respect to the flow field and the resulting blade excitation.

Keywords: Forced Response, Rotor-Stator Interaction, Unsteady Flow Computation

1. Introduction

Even today, with computing power available rather cheaply, an unsteady flow simulation comprising the full annulus of merely a single stage is impractical for routine engineering use. A reduced model is required to lower computing time to an acceptable level, allowing unsteady simulations to have

K.C. Hall et al. (eds.),
Unsteady Aerodynamics, Aeroacoustics and Aeroelasticity of Turbomachines, 107–118.

an impact on the design of a turbine. So called single passage methods such as the inclined time plane approach by Giles [12], the direct store method by Erdos [2], or the harmonic balance method of Dewhurst and He [1] have been developed over the last decade. However, these methods have often not made it into design codes, yet. If a single passage method is not available, the computational effort can be reduced by simulating only a fraction of the full annulus. Ideally, this is achieved by dividing the number of blades for each blade row by the highest common factor. Often, as is the case for the turbine stage under investigation, it is not possible to achieve a small computational domain with an integer blade count ratio by this approach. Here, the stage consists of 43 vanes and 64 blades, rather close to a ratio of two vanes per three blades. The closest numbers of vanes and blades corresponding to exactly a ratio of two to three are 42 vanes and 63 blades, with a highest common factor of 21. For practical reasons, then, the choice was made to modify the problem from 43/64 to 42/63 and to calculate only $(1/21)^{th}$ of the annulus.

A modification of this kind while retaining the original blade shape would change the throat area for both vane and blade, and thus the flow capacity, the reaction, the flow angles, and so on. In order to retain the original stage properties, the geometry has to be modified, as well. Two approaches could be taken: To restagger or reskew the airfoils, or to scale them. In the case of a restagger, the throat to pitch ratio is set to be equal to the original, and the curvature and trailing edge thickness is kept constant. The pitch to chord ratio, on the other hand is changed, as well as the inlet metal angle of the blade, and thus the incidence. With the scaling approach, the throat to pitch ratio is again set equal to the original, and the pitch to chord ratio, as well as the inlet metal angle, are retained, but the trailing edge thickness and the curvature is changed. In the present investigation, the scaling approach is used in order to minimize any incidence effect on the blade.

When the computational problem is simplified in this manner, it is clear that the unsteady flow will also change. The obvious and most important difference is that a change in vane count will also alter the vane passing frequency that each rotor blade sees. We will argue here that, at least for a case with a vane pitch that is much larger than the blade pitch, the only significant change occurs in the frequency of the disturbances. The idea behind this simplification is that disturbances such as wakes are sufficiently separated in the sense that with either original or modified vane count, there will never be two wakes inside a single blade passage. Thus it could be argued that each disturbance is seen by the blades as an independent entity.

The computed unsteady blade pressure will be applied to the mechanical blade model that represents the original geometry. The transfer of the unsteady pressure is done in Fourier space, conserving the complex amplitudes but prescribing the real vane passing frequency instead of that of the CFD model.

The present paper tries to answer the question if the above simplifications lead to significant errors in both the detailed unsteady flow field and the computed blade response.

2. Test Rig

A description of the test rig and the measurements are given in [5]. From the two measured operation points, the high-pressure ratio operation point is selected for the current study. The total pressure ratio of 2.72 causes a transonic flow through the turbine stage.

The unsteady flow measurements were performed on a rigid rotor at constant speed. The forced response experiments, on the other hand, were done on a rotor with flexible blades with resonant frequencies close to the vane passing frequency. This rotor was accelerated through the resonance of interest, and the blade vibration amplitudes were measured using strain gauges. The eigenfrequencies and the mode shapes were also determined in a clamped block. The measured torsional eigenfrequencies of the 64 blades for clamped conditions vary between -6.8% up to $+1.8\%$ with respect to the mean frequency indicating significant mistuning [5], [10].

The analysis of Seinturier [10] shows that the mean of the amplitudes of the mistuned system is only 89% of that of the equivalent tuned system.

3. CFD-Method

The numerical approach is a time marching method, solving the Navier-Stokes equations with a Baldwin-Lomax turbulence model on a structured multiblock grid [8], [9]. The spatial discretization is performed with a cell centered finite volume method. The fluxes are computed with a central scheme and Jameson's artificial viscosity [Jameson, 1991]. The time discretization is a dual time stepping method [Melson et al., 1993] with a multi stage Runge Kutta scheme. Chimera interpolation is used at the rotor stator interface (Fig. 1).

The equations are transformed to a local blade to blade coordinate system m'/ϕ where the streamwise coordinate is defined as $m' = \int \frac{dm}{r}$, with the meridional coordinate $dm = \sqrt{dx^2 + dr^2}$ and ϕ, x, r are circumferential angle, axial and radial coordinate, respectively. This transformation is angle-preserving and also valid for pure radial streamsheets.

Two configurations (equivalent to 40/60 and 42/63) were generated using scaled airfoils and maintaining the axial gap. The complete computational domain in the m'/ϕ plane is shown in Fig. 1. Each block is discretized on a structured curvilinear H-type mesh with 64×192 and 48×192 cells for stator and rotor, respectively. The unsteady flow is calculated on three blade to blade sections at $20\%, 50\%$ and 80% span. The streamsheet thicknesses are taken from a steady through-flow calculation.

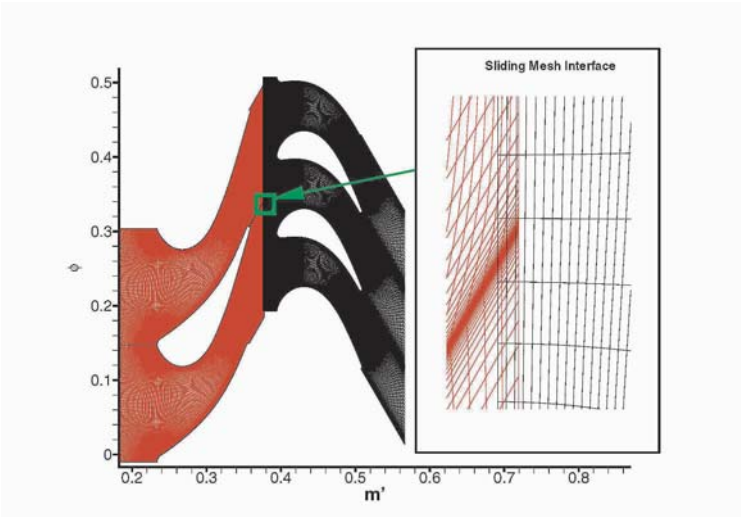

Figure 1. Computational mesh and overlapping region with sliding mesh cells

3.1 Unsteady flow results

At each blade surface node, the unsteady pressure history for two vane passing periods is Fourier decomposed. Consequently, the second Fourier mode represents the vane passing frequency. For comparison with measured pressures, the resulting amplitudes are used, while the forced response method uses the equivalent complex components.

The resulting Fourier amplitudes at leading (white bars) and trailing edge (black bars) of the midspan profile are shown in Fig. 2. At leading edge the dominant amplitude is caused by the vane passing frequency and it's multiples while at the trailing edge, the vortex shedding at Strouhal frequency becomes visible. The snapshot of the entropy contours of the unsteady flow confirms that the vortex shedding is well resolved. The calculated shedding frequency is in good agreement to the expected value for a Strouhal number of 0.2 and the given trailing edge thickness.

For both scaled stage configurations, the calculated static pressures at mid span of the rotor blades are shown in comparison with experimental data in Figs. 3 and 4. The time averaged blade pressures are very similar for both numerical configurations, while in the time dependent results, some differences can be observed.

Good agreement with the measurements is observed for the first harmonic of the 42/63 configuration, except at the leading edge. Here, the numerical amplitudes are higher than the experimental ones. The largest differences in the

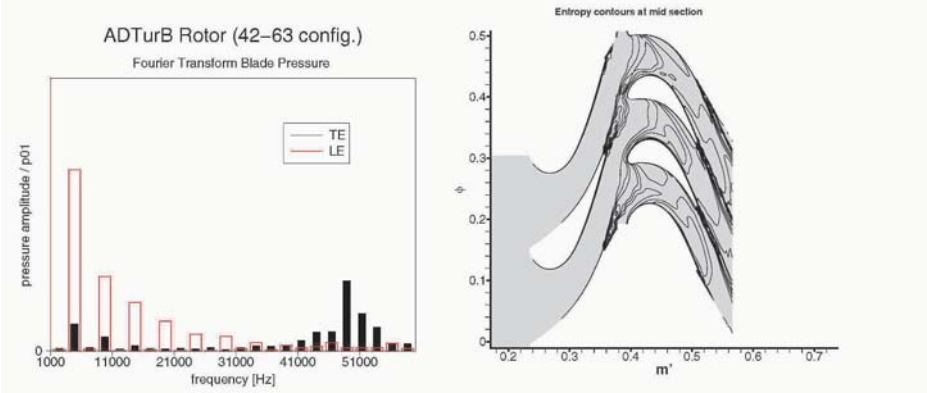

Figure 2. Fourier modi of the static pressure at leading and trailing edge (left) and Entropy contours of the unsteady flow field (right)

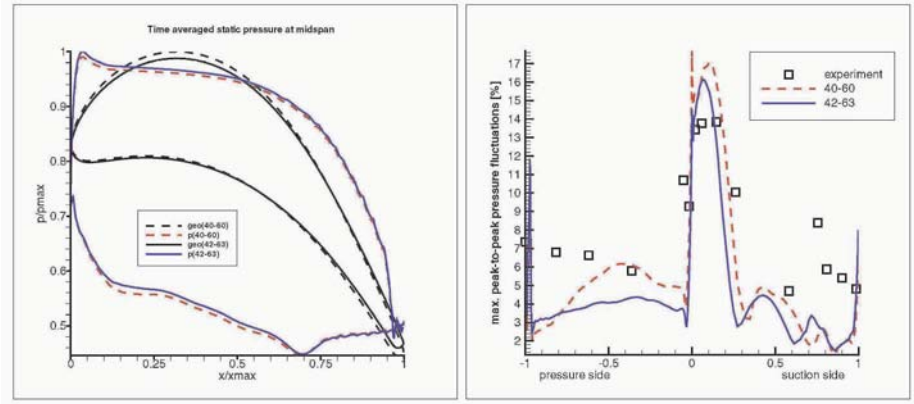

Figure 3. Time-averaged (left) and maximum pressure fluctuations (right)

unsteady results occur at the blade pressure side for the second harmonic. This might be related to scaling effects. Differences in vane spacing and blade count affect the circumferential position where a particular vane wake hits the rotor. The scaling of the trailing edge changes the wake thickness. Shape and size of the wake is expected to have a larger impact on the higher harmonics. The first harmonic drives the results of the forced response analysis of the rotor. Therefore, from the good agreement with experiments for both CFD models, reasonable forced response results can be expected with little difference between the two cases.

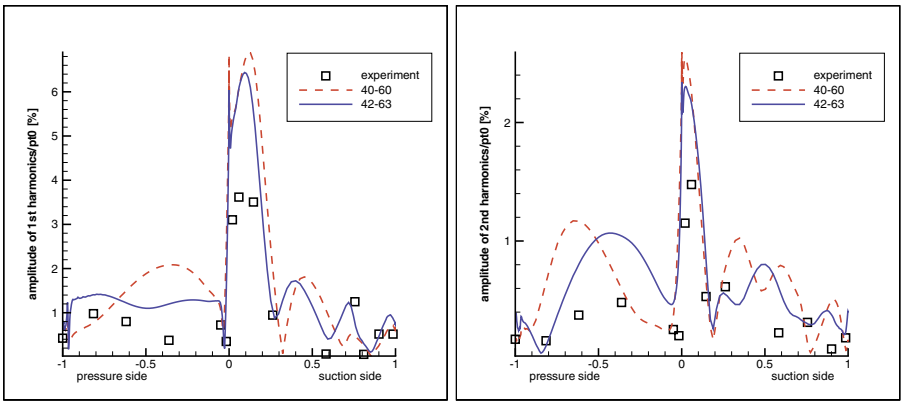

Figure 4. Pressure fluctuation at midspan of first and second harmonic of the vane passing frequency

4. Mechanical model

The rotor blade is represented by 3D 10-node quadratic tetrahedron finite elements with hourglass control (Fig. 5). The rotating turbine disc assembly is represented by a cyclic parabolic finite element model. Neglecting the frictional slip at the blade root due to high centrifugal stresses, the blade is rigidly attached to the rotor by a fir tree (Fig. 5). This model is used to simulate the vibration of the entire disc. All FE analyses are performed with a commercial general purpose finite element solver.

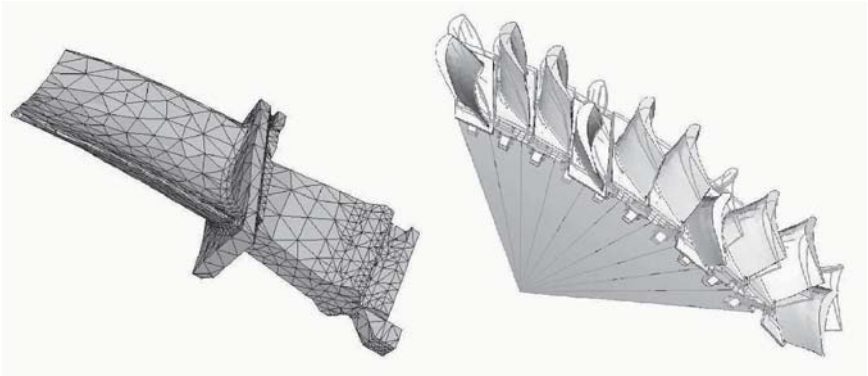

Figure 5. Rotor blade finite element model

The free vibration FE analysis is performed at a rotational speed of 6957 RPM. The eigenfrequencies $f_{i,n} = \omega_{i,n}/2\pi$ (where $\omega_{i,n}$ denotes angular eigen-

frequency) of the disc assembly are obtained from

$$([K(\Omega, n)] - \omega^2{}_{i,n}[M(n)])\{\phi_{i,n}\}^{(l)} = 0 \tag{1}$$

where the blade complex matrices of mass $[M(n)]$ and stiffness $[K(\Omega, n)]$ depend on nodal diameter number $n = 0, 1, ..., N/2$ for even N or $(N-1)/2$ if N is an odd number of blades [11]. The stiffening effect caused by the rotation is included in the matrix $[K(\Omega, n)]$. For each mode i with nodal diameter n (except for $n = 0$ and $n = N/2$), two identical eigenfrequencies $\{\phi_{i,n}\}^{(l)}$ are computed from Eq. 1 which correspond to two possible mode shapes of the cyclic sector.

The computed nodal diameter diagram and torsional mode shapes of interest are presented in Fig. 6. The calculated eigenfrequencies vary slightly from

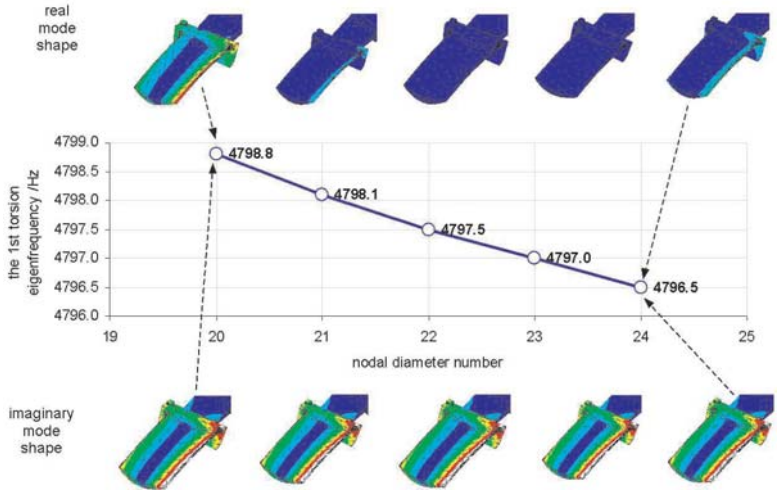

Figure 6. Calculated torsional eigenfrequencies in the excitation region due to a stator excitation of 43 vanes

4798.8 Hz to 4796.6 Hz for increasing nodal diameters from 20 up to 24. For 43 vanes and 63 blades, the 21^{st} nodal diameter will be predominantly excited. From the rig test, accelerating the rotor through the resonance [4], [5], a resonance frequency at 4800 RPM was determined. The calculated eigenfrequency is in good agreement with these observations.

5. Transferring CFD pressure to the FE model

The complex pressure amplitudes of the Fourier mode corresponding to the vane passing frequency are interpolated and extrapolated from the three profile sections onto a fine transfer mesh, covering the entire blade surface (Fig. 7). In a second step, the complex pressure results are transferred from the fine intermediate mesh to the much coarser surface mesh of the FE model.

Each FE surface element face is assigned the pressure of a single point on the transfer mesh. This point is found using a growing tolerance sphere around the center of the FE-element, truncated by two restricting planes parallel to the finite element surface (Fig. 8). This method automatically detects the correct blade surface.

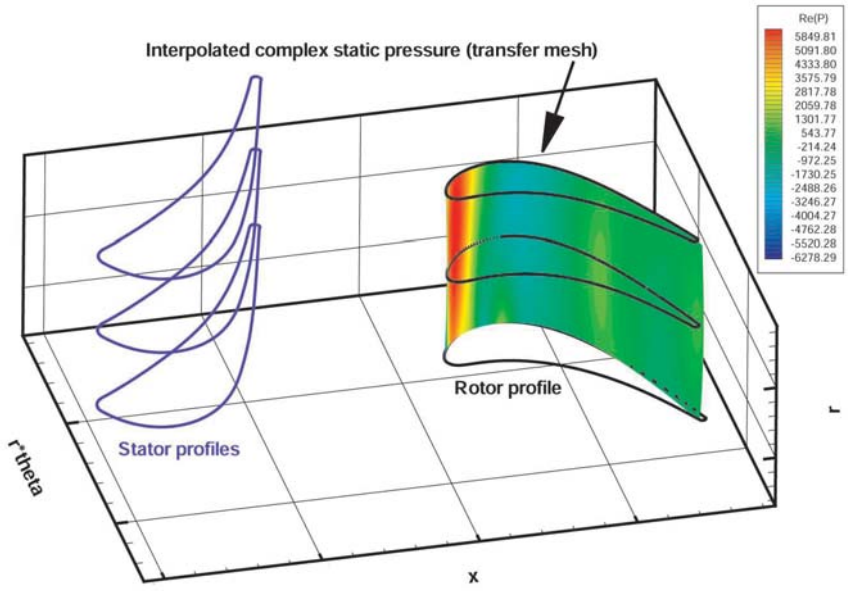

Figure 7. Interpolation of the Q3D complex blade pressure (real part shown) to the blade

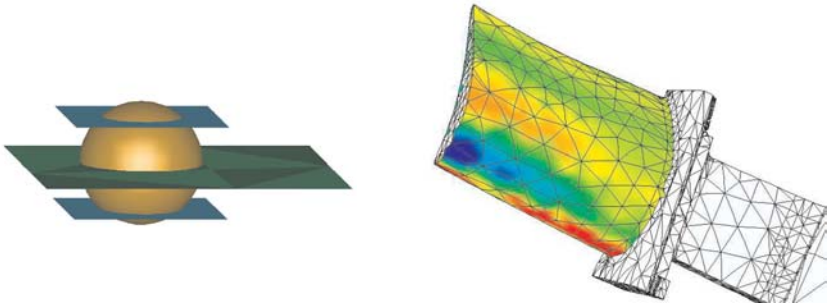

Figure 8. Definition of the tolerance sphere to transfer the CFD results to the FE-model (left) and real part of the pressure load on the FE-model (right)

6. Forced response analysis

In the FE response analysis, the real and imaginary pressure results acting on each contour node are used as excitation loads for the 1^{st} torsional mode of the blade vibrating with the 21^{st} nodal diameter [11].

$$F_{\delta,\chi}^{(real,blade)} = P_{k,\chi}[cos(k\alpha_\delta - \beta_{k,\chi}) + jsin(k\alpha_\delta - \beta_{k,\chi})]$$
$$F_{\delta,\chi}^{(img,blade)} = P_{k,\chi}[sin(k\alpha_\delta - \beta_{k,\chi}) - jcos(k\alpha_\delta - \beta_{k,\chi})]$$

where $j = \sqrt{-1}$ and χ refers either to the circumferential or to the axial direction, α_d is the circumferential position of node δ, and β denotes the phase delay ($P_k = \sqrt{(P_{k,im}^2 + P_{k,real}^2)}$; $\beta = arctan(P_{k,im}/P_{k,real}$)).

Since the resonance is at the 43^{rd} engine order, the frequency shift due to the scaling of the CFD model is corrected implicitly. The CFD results are read across from the steady calculation at the speed, close to the resonance speed, of the steady state rig tests.

The resonance steady-state response of the rotor blade is computed by using a commercial general purpose FE-solver that solves

$$m_{i,n}\ddot{q}_{i,n} + 2\omega_{i,n}\zeta - i\dot{q}_{i,n} + k_{i,n}q_{i,n} = \{\phi\}_{i,n}^T\{P_k\}e^{j(k\alpha_\delta - \beta_k)}e^{j(k\Omega t)}$$

where $k = 1, 2, ..., \infty$ the Fourier mode of the excitation, $i = 1, 2, 3$ indicates the number of the mode shape and α_δ denotes the circumferential position of the excited node of the cyclic FE model [11]. $m_{i,n} = \{\phi\}_{i,n}^T[M(n)]\{\phi\}_{i,n}$ and $k_{i,n} = \{\phi\}_{i,n}^T[K(\omega, n)]\{\phi\}_{i,n}$ are the modal mass and stiffness of the cyclic FE model, respectively. $\{\phi\}_{i,n}^T$ is the conjugate transposed vector of the disc eigenform $\{\phi\}_{i,n}$.

From calibration bench tests with a rigidly clamped blade root, a damping of 0.17% was obtained. In the real disk assembly, the blades are not per-

fectly clamped and the disk contributes to the overall damping. Consequently, a damping value of 0.3% was used for the forced response calculations, in line with [10]. Using $\varpi = \omega(1-\xi^2)^{1/2}$, a damping ratio of 0.3% will give a resonance frequency that is virtually identical to the natural frequency of 4798.10 Hz determined in the free vibration analysis.

The resonance amplitudes and the von Mises stresses are shown in Fig. 9. The maximum response occurs at the tip trailing edge, and the maximum von Mises stress occurs at the shank of the blade.

Figure 10 shows the calculated tip amplitudes compared to the test results. The amplitudes are normalized with respect to the averaged blade displacement from the mistuned disk, and the range of individual blade responses is indicated by the vertical line. The line on the averaged experimental displacement value

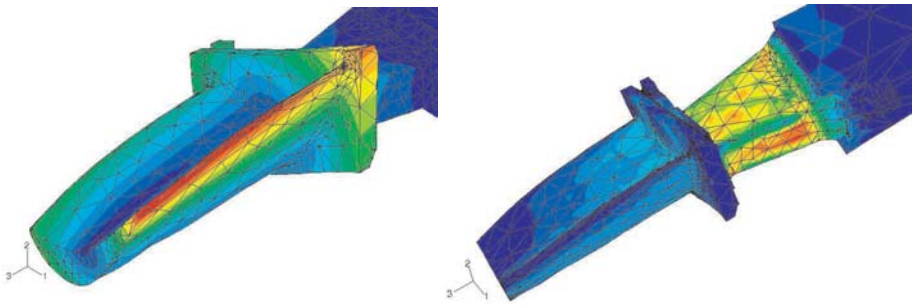

Figure 9. FE results: Displacements (left) and stresses (right)

indicates the range of amplitudes in the mistuned system.

The agreement between calculation and experiments is good and only small differences are observed between the two cases.

7. Summary and Conclusion

For this single stage turbine, the chosen unsteady Q3D approach and the applied 2-3 scaling give good results with respect to the overall blade displacement.

The scaling procedure of the CFD model causes only small differences in the unsteady pressure, especially for the 1^{st} harmonic. Both numerical configurations are in good agreement to the unsteady pressure measurements, and the resulting blade excitations are in good agreement with the experimentally obtained data. As for the CFD calculations, the forced response results are close together for both applied flow pressures.

The differences in the unsteady effects due to the scaling are small compared to other effects like the coarsening of the flow data in radial direction due to

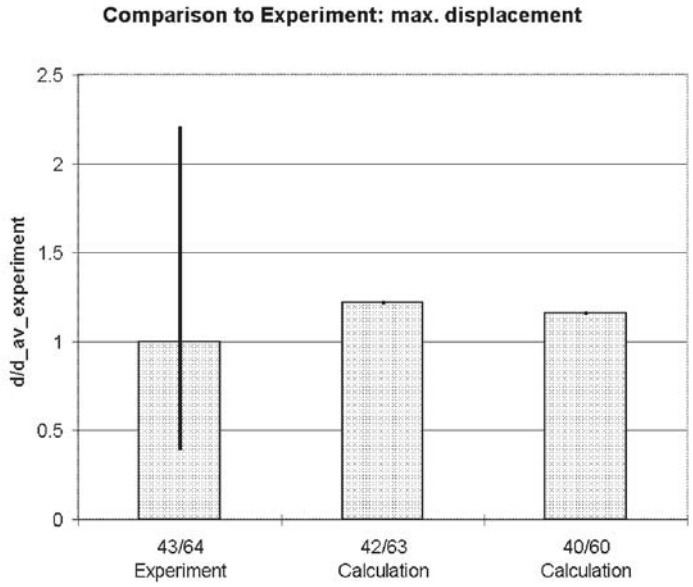

Figure 10. Comparison to experiments: Max. displacements

the interpolation from three profile cuts to the whole blade height or due to the transfer from the intermediate CFD mesh to the coarse FE surface elements. The applied extrapolation procedure from several blade-to-blade CFD planes can be more adequate for the bending mode shapes of the lowest blade eigenfrequencies, whose excitability increases successively to the highest value from the platform towards the airfoil tip.

The effects of mistuning are reflected by the broad data range in the experimentally obtained displacement values. It is difficult to quantify damping, especially damping of a mistuned system, and to define from this a representative value for the tuned disk calculation. To quantify the displacements correctly however, it is important to have a good assumption of the mechanical damping of the disk assembly.

It is assumed that the observed small effects due to the scaling cannot be generalized to more complex configurations. In multi-stage turbomachines, higher harmonics will systematically be generated by e.g. wakes or blade-wake interactions from former stages.

Acknowledgments

The authors wish to thank ALSTOM (Switzerland) Ltd for their support of the work and for the permission to publish the results. The experimental data used in this paper was acquired in the research programme ADTurB, funded

by the European Community under the Industrial and Material Technologies Programme (BriteEuram III), contract no. BPR-CT95-0124.

References

[1] Dewhust S., He L., (2000). Unsteady Flow Calculations Through Turbomachinery Stages Using Single-Passage Domain with Shape-Correction Method, *Proceedings of* 9^{th} *Symposium on Unsteady Aerodynamics, Aeroacoustics and Aeroelasticity*, Lyon, France, pages 338-350.

[2] Erdos J. L., Alzner E., McNally W. (1977). Numerical Solution of Periodic Transonic Flow Through a Fan Stage, *AIAA Journal*, Vol 15, No. 11.

[3] Giles M. B., (1988). Calculation of Unsteady Wake Rotor Interaction, *Journal of Propulsion and Power*, Vol. 4, No. 4, pages 356-362.

[4] Green J. S., (2001), An Overview of a European Collaborative Programme for Forced Response. Proceedings of 6^{th} National Turbine Engine High Cycle Fatigue Conference, Jacksonville, USA.

[5] Hennings H., Elliott, R., (2002). Forced Response Experiments in a High Pressure Turbine Stage, ASME Turbo Expo 2002, Amsterdam, The Netherlands, paper No. GT-2002-30453.

[6] Jameson, A., Schmidt, W., and Turkel, E., (1981). *Numerical Solutions of the Euler Equations by Finite Volume Methods using Runge-Kutta-Time-Stepping Schemes*, AIAA paper 81-1259.

[7] Melson N.D., Sanetrik M. D., Atkins H. L., Time-accurate Navier-Stokes Calculations with Multigrid Acceleration, 6th Copper Mountain Conference on Multigrid Methods, pages 423-439, 1993.

[8] Schäfer, O. (2002). Simulation of Unsteady Compressible Flow in Turbomachinery. *Progress in Computational Fluid Dynamics*, Vol.2, No.1, pp.1-8.

[9] Schäfer, O., Phillipsen, B., and Breuhaus, B., (1998). Last Advances in Numerical Simulation of Aerodynamic Forces on Turbine Blades of Turbochargers for Pulse Charged Engines, CIMAC Congress, pp.1705-1719, Copenhagen.

[10] Seinturier E., Lombard J.-P., Berthillier, M., Sgarzi, O., (2002). Numerical Method for Mistuned Bladed Disk Forced Response, ASME Turbo Expo 2002, Amsterdam, The Netherlands, paper No. GT-2002-30424.

[11] Szwedowicz, J., Sextro, W., Visser, R. and Masserey, P.A., (2003), On Forced Vibration of Shrouded Turbine Blades. Proceedings of ASME Turbo Expo 2003, ASME Paper GT-2003-38808.

MISTUNING AND COUPLING EFFECTS IN TURBOMACHINERY BLADINGS

Gerhard Kahl
MTU Aero Engines
Munich, Germany
Gerhard.Kahl@muc.mtu.de

Abstract A numerical method has been developed to study the effects of structural mistuning on the aeroelastic behavior of turbomachinery cascades. The approach used is the combination of a modal reduction technique, where the structural properties of each blade are represented by only a few eigenmodes, with a linearized Euler method for the aerodynamic calculations. The method is validated and applied to two test cases, comprising of a high pressure turbine rotor and a transonic compressor rotor. Both are representative of modern turbomachinery designs. The results of the validation confirm the ability of the present method to accurately capture the dominant effects that influence the aeroelastic behavior of the cascades. Further case studies are performed to assess the influence of alternating and random mistuning on the resonant response amplitudes and on the aeroelastic stability.

1. Introduction

Analysis of the aeroelastic behavior of turbomachinery cascades in many cases still rely on the assumption of a perfectly symmetric structure, where all blades are structurally and aerodynamically identical. In practice small differences between the individual airfoils of a cascade are unavoidable. The resulting small variations in the structural characteristics of the individual airfoils can cause dramatic effects. For example, strain gauge tests of complete rotors often show a spread in the measured response amplitudes of the different blades of a factor of more than two. Given the fact that mostly only a few blades are instrumented, this leads to the question of what the true maximum amplitude of all blades might be, since this is what the design of the blade has to take into account. Furthermore, the question arises at to what the effect of the small structural variations on the aeroelastic stability may be, which can often not be measured as readily as the forced response amplitudes.

K.C. Hall et al.(eds.),
Unsteady Aerodynamics, Aeroacoustics and Aeroelasticity of Turbomachines, 119–131.

A wide range of publications exists that assess effects of structural mistuning. However, many of these neglect the aerodynamic damping and coupling altogether (e.g. [1], [2], [9], [14] [11]), or use simplified methods, allowing only for two-dimensional rigid motions of the blade sections [7]. In other instances, the aerodynamic interaction between different structural modes is neglected [13]. The present work puts more emphasis on the aerodynamic damping and coupling effects, while using a simple structural model. The approach presented is intended to allow the consideration of multiple modes for each blade and is capable of dealing with sub- and transonic flow situations. Its main goal is the applicability for design use, meaning that it has to supply results quickly for a large number of configurations.

2. Aeroelastic Model

The starting point of this analysis are the fundamental equations of motion in physical space and in the time domain for a discretized system of coupled blades, for example conforming to a FEM approach. For a linear elastic system, these can be formally written as:

$$\tilde{\mathbf{M}}\ddot{\tilde{\vec{x}}} + \tilde{\mathbf{D}}\dot{\tilde{\vec{x}}} + \tilde{\mathbf{K}}\tilde{\vec{x}} + \tilde{\vec{F}}_c = \tilde{\vec{F}}. \tag{1}$$

Here $\tilde{\mathbf{M}}$, $\tilde{\mathbf{D}}$ and $\tilde{\mathbf{K}}$ are the mass, damping and stiffness matrices, respectively, while $\tilde{\vec{F}}_c$ introduces the aerodynamic coupling between the blades and is dependent on the deflection and velocity of the blades. The damping is assumed to be of viscous type, i.e. the damping forces are proportional to the velocity. The right hand side, $\tilde{\vec{F}}$, contains the external forces acting on the structure, while the vector $\tilde{\vec{x}}$ holds the displacement degrees-of-freedom for the finite elements of the complete model. For an accurate representation of the vibratory behavior, the number of degrees-of-freedom (DOF) for a typical cascade will have to be on the order of more than 10,000 times the number of blades. In the present method, a number of assumptions are introduced to arrive at a formulation that is at the same time accurate enough to give a good representation of the true aeroelastic behavior of the structure while still being simple enough to allow rapid analysis of a large number of configurations with variations in the dominant parameters.

The first assumption is that we are dealing with harmonic oscillations of the structure, so that the motion of each blade can be expressed using a complex exponential approach. Furthermore, in order to reduce the number of DOF, a modal approach is employed. It uses a small number n_{modes} of in-vacuo modeshapes $\vec{\Phi}$ of the individual blades as generalized coordinates. Thus, each blade of the cascade retains only a few degrees-of-freedom, which are characterized by the amplitudes $a_{b,m}$ of the respective modeshapes. While the amplitudes can differ between the individual blades, the underlying modeshapes are as-

sumed to be identical for all blades of the cascade under consideration. The motion $\tilde{\vec{x}}_b$ of an arbitrary blade b is then approximated by

$$\tilde{\vec{x}}_b(r,\Phi,z,t) = \vec{x}_b(r,\Phi,z)e^{i\lambda t} = \sum_{m=1}^{n_{modes}} a_{b,m}\vec{\Phi}_m e^{i\lambda t} \tag{2}$$

with

$$\lambda = \omega + i\gamma \tag{3}$$

Here, the complex exponent λ consists of a real part ω that represents the angular frequency of oscillation and an imaginary part γ that characterizes the evolution of the amplitude with time, representative of the effective damping present in the system under consideration. In this respect, a positive value of γ implies an exponentially decaying oscillation amplitude, hence positive damping, while a negative value of γ consequently yields exponentially growing amplitudes, corresponding to negative damping, as in the case of a flutter instability. Accordingly, Eq. 1 can be approximated using a reduced set of eigenmodes as

$$[-\lambda^2\mathbf{M} + i\lambda\mathbf{D} + (\mathbf{K} + \mathbf{C})]\vec{a} = \vec{F}. \tag{4}$$

In this equation, only generalized quantities are used. The vector $\vec{a}$ contains the complex amplitudes for all modes retained for the complete set of blades, hence for an annular cascade consisting of n_{blades} individual blades, each of which retains n_{modes} modeshapes, the number of degrees-of-freedom in this reduced set of equations is $n_{blades} \cdot n_{modes}$. The matrix $\mathbf{D}$ holds the modal damping values that, just like the generalized masses and stiffnesses, can be assigned to each blade and mode individually. While the matrices $\mathbf{M}$ and $\mathbf{D}$ are diagonal, the stiffness matrix $\mathbf{K}$ can contain off-diagonal elements that are used to model mechanical coupling between the individual blades, as it is present through the disk on which the blades are mounted. The vector $\vec{F}$ in Eq. 4 contains the generalized external forces on the individual blades and modes that result from the projection of the physical forces $\tilde{\vec{F}}$ on the eigenmodes $\mathbf{\Phi}$ by

$$\vec{F} = \mathbf{\Phi}^*\tilde{\vec{F}}. \tag{5}$$

Here, the $\mathbf{\Phi}^*$ denotes the hermitian (conjugate-transpose) of the eigenvector matrix $\mathbf{\Phi}$. Similarly, the aerodynamic coupling forces have been transformed into the modal domain, additionally assuming that a linear aerodynamic approach is valid. Then the modal forces due to the aerodynamic interactions $\tilde{\vec{F}}_c$ can be written as the product of the complex aerodynamic influence coefficient matrix $\mathbf{C}$ and the modal amplitudes $\vec{a}$:

$$\tilde{\vec{F}}_c = \mathbf{C}\vec{a} = \mathbf{\Phi}^*\tilde{\vec{F}}_c. \tag{6}$$

The matrix $\mathbf{C}$, in contrast to the other matrices, is usually fully populated. It contains the aerodynamic influence coefficients that couple all blades and all modes of the cascade. In the present method, these influence are calculated using a 3D linearized Euler solver that is an extension of the method described in [5], for further details refer to [6]. Using this reduced model, blade-to-blade variations can be readily introduced into the system by changing the generalized properties mass, stiffness or damping assigned to any of the individual blade modes. Additionally, it is possible to add individually varying or constant mechanical coupling stiffness between different blades.

Eigenvalue Analysis

In the absence of external forces, the prime interest is on the eigenmodes and eigenvalues of the cascade, describing the flutter stability and the free vibration behavior of the cascade. For this purpose, Eq. 4 can be reformulated as

$$[\mathbf{M}^{-1}(\mathbf{K}+\mathbf{C}) + i\mathbf{M}^{-1}\mathbf{D}\lambda - \mathbf{E}\lambda^2]\vec{a} = \vec{0}. \tag{7}$$

Being a non-linear eigenvalue problem, this is fairly inconvenient to solve numerically. To overcome this, it is assumed that the aeroelastic eigenvalues λ do not differ much from the in-vacuo eigenvalues λ_0. Then we can approximate Eq. 7 as

$$[\mathbf{M}^{-1}(\mathbf{K}+\mathbf{C}) + i\mathbf{M}^{-1}\mathbf{D}\lambda_0 - \mathbf{E}\lambda^2]\vec{a} = \vec{0}. \tag{8}$$

In this approach, no assumption concerning the distribution of damping in the cascade is made, so that also the effect of damping mistuning can be studied. On the other hand, the approach can only be expected to yield valid results as long as the computed eigenvalues are similar to the in-vacuo eigenvalues of the individual blades. For practical purposes, this condition is usually well met, as discussed in more detail in [6]. To evaluate the aeroelastic stability of a cascade in the presence of aerodynamic and structural coupling as well as structural mistuning, we thus have to solve a linear eigenvalue problem of $n_{blades} \cdot n_{modes}$ DOF, which can be done very quickly and efficiently with standard numerical solvers even for a large number of mistuned configurations.

Forced Response Analysis

If external forces are present, then the forced response of the oscillation system is of interest, namely the amplitudes and phases of all the blades after the transients have decayed. For this reason, it is sufficient to set $\lambda = \omega$ in Eq. 4, because ω is now known in advance to be the frequency of the excitation force $\vec{F}$ and hence is also the oscillation frequency in which the coupled aeroelastic system responds. The resulting linear system of equations

$$[-\omega^2\mathbf{M} + i\omega\mathbf{D} + (\mathbf{K}+\mathbf{C})]\vec{a} = \vec{F} \tag{9}$$

can then be directly solved. In doing so, the appropriate dynamic properties of the individual blades and modes are inserted in the corresponding matrices for any prescribed value of the excitation frequency ω.

3. Validation: High Pressure Turbine Rotor

The present method was validated using a single stage turbine rig, representative of a modern high-pressure turbine stage. It was designed in the course of the IMT Area 3 turbine project [12] and was used as a cornerstone in various European research programs [8]. In the ADTurB, and in the currently running ADTurBII program [4], the main emphasis is on aeroelastic effects. In the ADTurB program, the excitation of the rotor due to the stator wakes was studied, with a special focus on the influence of mechanical mistuning of the rotor blades. The resonant crossing of the 43rd engine order, corresponding to the excitation by the stator wakes, with the 1st torsional eigenmode was studied experimentally in this program. The data gathered in this effort will be used in the following to validate the current method for forced response calculations under mistuned conditions.

The operating point of the test vehicle is slightly transonic with exit Mach numbers just exceeding unity in the stator as well as in the rotor. The eigenfrequencies of all rotor blades were determined by experimental modal analysis with the blades clamped to a massive supporting root block device. It was found that most blades 1T eigenfrequencies clustered around a mean value to within +/- 1.5%, while seven blades exhibited significantly lower eigenfrequencies, deviating in excess of 5%. This large deviation was due to the fact that the blades were manufactured in different batches, which resulted in variations of the geometric tolerances and possibly in the properties of the raw material used. As a consequence of this finding, these seven rogue blades were not included to calculate the mean frequency f_{mean} that is used in the following analysis. The resulting mistuning parameter $\epsilon = f/f_{mean} - 1$ is shown in Fig. 1 for every blade, highlighting the severe mistuning of blades 5, 11, 17, 42 and 55 to 57. In the rig experiment, the blades are mounted on a disc, which adds significantly more flexibility to the blade root than the clamping device of the modal analysis. Furthermore, the disc introduces mechanical coupling between the individual blades. To account for these effects, the generalized stiffness used in the analysis is assumed to be 11% lower than the value resulting from the single blade FE calculation, and a coupling stiffness of 0.9% between each two neighboring blades is introduced into the system. These values were deduced from the resonant frequencies measured in the rig test, i.e. after completion of the tests.

Sweeping the excitation frequency through the whole range of interest, the maximum response amplitudes of all blades were computed. A similar proce-

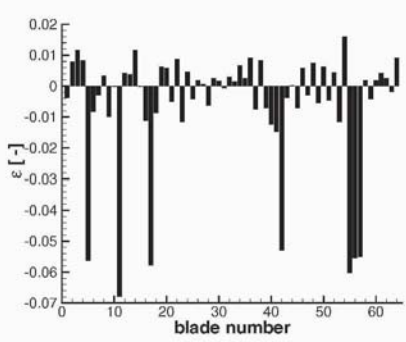

Figure 1. ADTurB rotor 1T mistuning pattern

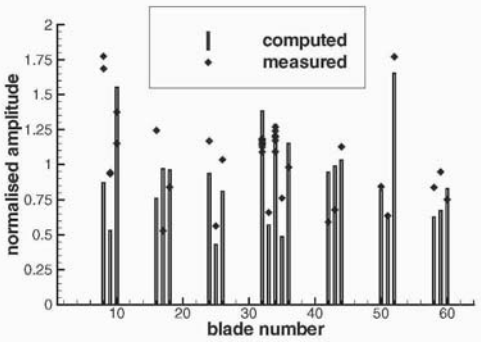

Figure 2. Comparison of computed and measured maximum ADTurB rotor 1T / 43rd EO blade amplitudes

dure was used in the experiment, where the variation of excitation frequency was achieved by speeding up the rotor. This was done sufficiently slowly, so that the influence of transient processes can be neglected. Experimentally determined blade amplitudes are available for 23 of the 64 rotor blades. Figure 2 shows the comparison of the resulting measured and computed maximum response amplitudes for all the blades that have experimental data available. The response amplitudes have been normalized using the mean value of the measured peak amplitudes of all blades.

The measured data for the various blades was taken from a number of different test runs, so that data from more than one run is available for a few of the blades. All the available data is included in this figure, so that the spread of the values for one blade, e.g. blade 32, gives an indication of the repeatability and measurement uncertainty of the experimental data. The figure indicates that the agreement between measured and computed data is quite acceptable. Not only is the mean response amplitude over the whole cascade matched well by the computation, but also the spread between the minimum and the maximum response of any blade is reproduced with good accuracy. Furthermore, in many instances the distribution of the amplitudes to the individual blades is shown by the computation in much the same manner as by the experiments.

To further evaluate the ability of the current method to model the dominant effects of mistuning in this cascade, the amplitude distribution for the complete frequency sweep is compared to experimental values in Fig. 3. Here, the blades 32 through 34 and 36 are chosen for comparison, since the corresponding measured values on these blades were measured simultaneously in a single run, making them particularly well suited for such a comparison. The dashed

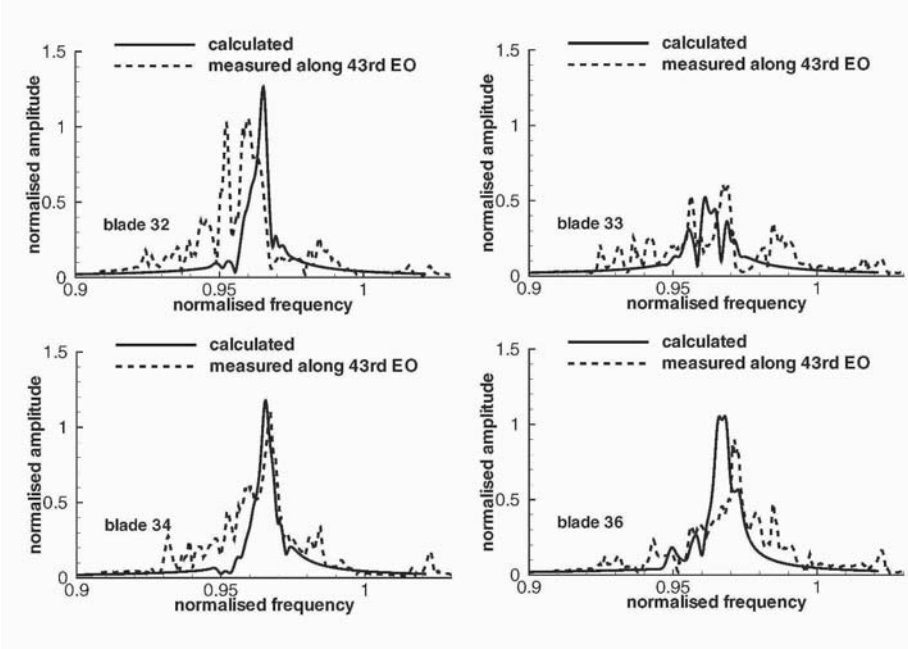

Figure 3. Comparison of computed and measured ADTurB rotor blade 32 to 36 response amplitudes

lines in Fig. 3 indicate the measured values, while the solid lines denote the computed results. The rotor speeds in this figure are non-dimensionalized using the mean measured frequency that was used to determine the values of ϵ in Fig. 1.

Comparing the different graphs confirms the good agreement between the computed and the measured maximum amplitudes. Furthermore, the frequency at which this maximum occurs is also well met by the computation. Nevertheless, some significant differences are also visible between the measured and the computed results. First, the computed distributions show much smoother curves than the measurements. It is not clear at this point if this behavior can be attributed to stochastic effects in the experiment or if there are deterministic phenomena at work that are not modeled by the current method. Secondly, especially blade number 32 shows two distinct maxima of almost equal magnitude, a fact that is not captured by the computation. In total, it can be concluded that the present method is capable of capturing the essential features of the mistuned cascade and is able to adequately reproduce the dynamic behavior in terms of resonant amplitudes.

4. Case Study: High Pressure Turbine Rotor

In the experimental set-up, only a single arrangement of the blades with their given individual mistuning on the rotor circumference could be studied. From these experiments alone, it is thus not possible to differentiate between the influence of individual blade mistuning and the influence of blade arrangement on the rotor. It remains unclear, whether the specific experimental configuration represents a typical case or - by mere chance - is a rare one with extraordinary high or low amplitudes. Furthermore, from the single configuration studied experimentally, it cannot be shown conclusively whether some correlation between resonant amplitude and mistuning strength exists. To acquire more information on these topics, a further analytical study was performed. Here, 1500 cases were studied, where for each of these, the blades were randomly rearranged on the rotor. Each configuration was then analyzed using the same procedure as described above for the experimental configuration. In Fig. 4, the resulting amplitude values are displayed. Here, the individual maximum blade amplitudes are shown as an interval, where the maximum and minimum for each blade have been marked with the solid gradient and delta symbols, respectively. Note that the blade numbers given here refer to the blades themselves, not to the blade position on the rotor. Each blade number hence corresponds to a single mistuning strength ϵ. Further symbols shown in the figure are the solid squares, denoting the median of blade amplitudes for each blade, and the open diamonds, showing the computational results for the experimental configuration, as in Fig. 2. The figure shows that the blade relative positioning

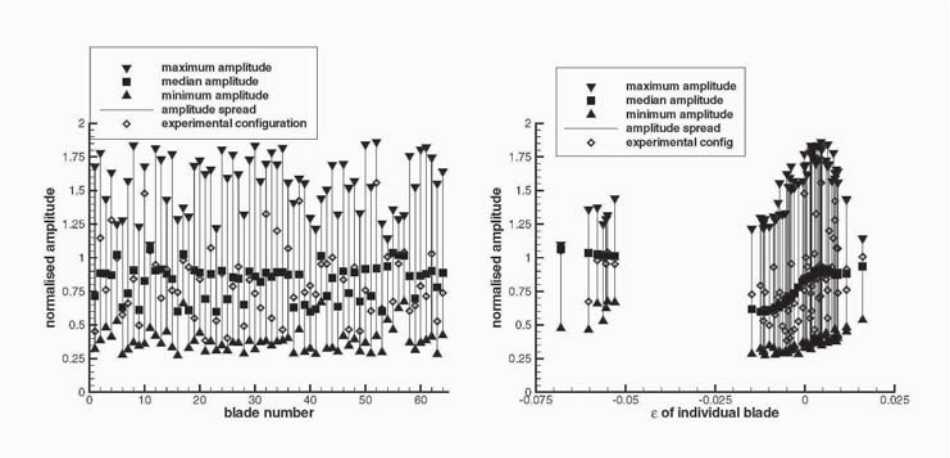

Figure 4. ADTurB rotor 1T / 43rd EO blade amplitudes of each blade over blade number for 1500 configurations of random rearrangement

Figure 5. As Fig. 4, but plotted over mistuning parameter ϵ

around the rotor circumference has a large influence on the response amplitudes. For some blades, the maximum and minimum amplitudes are more than a factor of 5 apart. The median values, representing the highest probability of the amplitudes, however, are restricted to a much smaller band, ranging from normalized amplitude values of approximately 0.6 to 1.1. The values taken from the experimental configuration blend into the range given, covering most of the amplitude region. Furthermore, the distribution of the median values close to normalized amplitudes of one indicates that the average of the experimentally observed amplitudes, which was taken as the reference value, is very representative of a typical configuration. Arranging the same data points over the individual blade mistuning parameter ϵ results in the graph shown in Fig. 5. Here a certain dependence of the minimum, maximum and median amplitude values on the blade mistuning is apparent. Obviously, the spread of minimum and maximum amplitudes is highest for small positive values of ϵ, while it is lower for large negative or positive ϵ. The median amplitudes are highest for the blades with large negative mistuning, then drop to significantly lower amplitudes for small negative values of ϵ and rise again sharply with small positive ϵ. However, the relative positioning of the blades has a much larger influence on the amplitudes than the individual mistuning strength.

5. Case Study: Transonic Compressor Rotor

The second test case studied here is the rotor of a single stage transonic compressor rig [3], representative of a modern HP compressor front stage. It consists of 16 carbon-fiber reinforced rotor blades mounted on a titanium disk, and of 29 stator vanes. The tip diameter is 0.38m, maximum relative rotor inlet Mach numbers reach $Ma_1 = 1.4$ at the tip. At the design speed of 20,000 RPM, the FEM analysis yields the frequencies of 762 Hz for the 1F eigenmode, and 1505 Hz for the 1T eigenmode. The aerodynamic influence coefficients for the rotor were calculated for these two modes, and the aeroelastic eigenvalues were deduced from Eq. 6, assuming a constant mechanical damping (logarithmic decrement) for each mode of $\delta_{mech} = 0.01$. The results for a perfectly tuned case are shown in Fig. 6, with the 1F-related eigenvalues on the left, and the 1T related ones on the right hand side. The eigenvalues are shown as damping (log. dec.) over frequency ratio $\eta = f/f_0$ with f_0 being the in-vacu eigenfrequency of the respective modes. For the tuned cascade, the eigenvectors are the well known traveling wave modes with constant interblade phase angle, which is indicated by the inset labels in Fig. 6. The results show that the cascade is aeroelastically stable, all damping values are greater than zero. The damping is in all cases significantly larger than the mechanical damping of $\delta_{mech} = 0.01$, indicating that the vibrational behavior of the cascade is dominated by the aerodynamic damping and coupling. Finally, Fig. 6 shows that

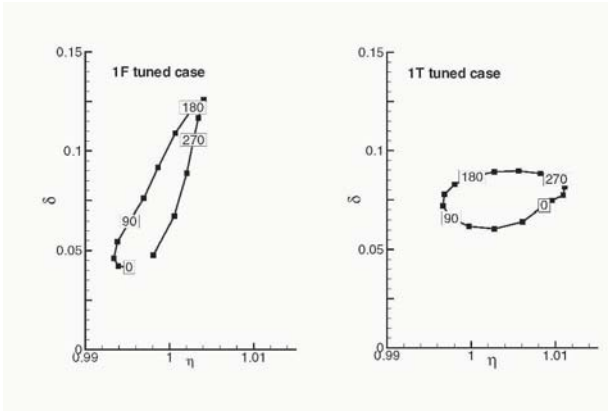

Figure 6. 1T and 1F aeroelastic eigenvalues of the tuned transonic compressor rotor

the eigenfrequencies of the cascade differ up to approximately 1% from the in-vacuo eigenfrequency due to the unsteady aerodynamic forces.

In the following, the effects of frequency mistuning are studied on the 1T eigenmode. First, alternating frequency mistuning is introduced, i.e. the generalized stiffnesses are decreased for the odd numbered blades and increased for the even numbered ones. Figure 7 shows the aeroelastic eigenvalues for the 1T mode. The circles correspond to the tuned configuration, while the triangles denote the mistuned configuration with a mistuning parameter of $\epsilon = \pm 0.02$. Furthermore, the trajectories of the eigenvalues for the values between $\epsilon = 0$ and $\epsilon = \pm 0.02$ are indicated by the lines. The results show that the damping values converge towards the mean of the tuned configuration values, so that the damping of the least stable eigenvalue is increased, i.e. the cascade is aeroelastically more stable. The alternating mistuning separates the eigenvalues into two distinct clusters, each forming a small ovoid similar to the one of the tuned configuration. This indicates that the blades of equal in-vacuo resonant frequencies are coupled through the unsteady aerodynamic influence coefficients spanning two blade passages, while the immediate neighbors are increasingly decoupled from one another due to their differing structural parameters. When using the same mistuning pattern and applying external excitation forces, the resonant amplitudes arise as shown in Fig. 8. In this figure, the triangles show the situation for a four engine order (EO) excitation, the circles denote the response amplitudes for an 18 EO excitation, while open and solid symbols denote the response of the odd and even numbered blades, respectively. A first observation from this plot is that the responses for the tuned configuration strongly depend on the EO of the excitation - which is due to the difference in aerodynamic damping, as found in Fig. 6. Furthermore, the resonant responses for the 18 EO excitation decrease with increasing alternating mistuning, while those for the 4 EO excitation increase, at least for

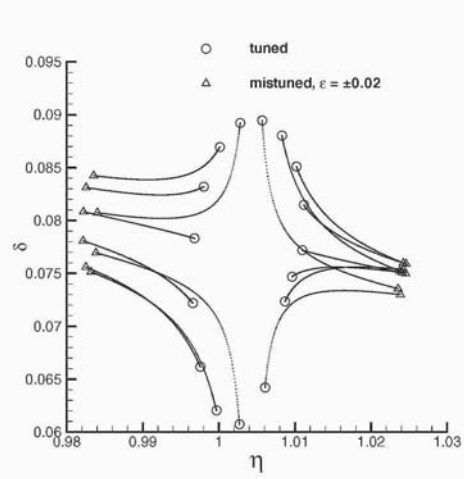

Figure 7. 1T aeroelastic eigenvalues of the transonic compressor rotor under alternating mistuning

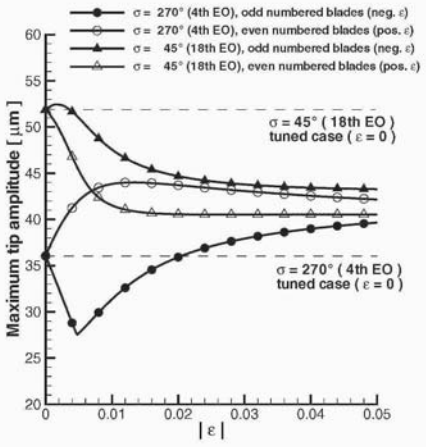

Figure 8. 1T resonant amplitudes under alternating mistuning with 4 and 18 EO excitations

the even numbered blades, which show the higher amplitudes. This result implies that, in certain cases, deterministic mistuning can be used to decrease the response amplitudes in comparison to the tuned configuration. Finally, the influence of random mistuning on the resonant response has been studied. 500 cases of randomly generated frequency distributions with the mistuning ranging from $\epsilon = 0$ to $\epsilon = \pm 0.25$ have been generated and analyzed for excitation EOs between 0 and 16, corresponding to interblade phase angles of $\sigma = 0°$ to $\sigma = 360°$. In Fig. 9, the resulting maximum response amplitudes are plotted. The figure shows that for excitation interblade phase angles of $\sigma > 90°$, all

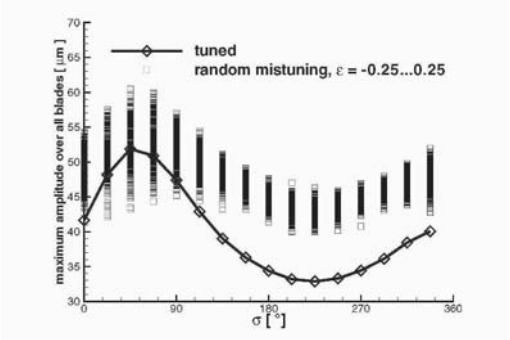

Figure 9. 1T transonic compressor amplitudes under random mistuning

randomly selected distributions result in larger maximum amplitudes than for the tuned case, while for $\sigma = 0^\circ$ to $\sigma = 90^\circ$, some configurations exist with resulting maximum amplitudes that are lower than for the tuned configuration. The majority of the configurations nevertheless yield higher amplitudes than in the tuned case, and in the worst mistuned case, exceeding the tuned amplitude by more than 40%. It can be observed that the largest relative increase occurs for the excitation interblade phase angle with small tuned response amplitudes and that the spread of the resulting mistuned maximum amplitudes corresponds to the tuned amplitudes for each excitation interblade phase angle: It is small for the cases with small tuned amplitude, and large for cases with large tuned amplitudes. Given the fact that the actual configuration of the stochastic mistuning in a real machine cannot be controlled or predicted, it is obvious that the predictions from a tuned cascade model do not yield a conservative value for the resulting maximum amplitudes, but generally produce too low values.

6. Summary and Conclusions

A numerical method has been presented that can be used to study the effects of structural mistuning on the aeroelastic behavior of turbomachinery cascades. The method has been validated using data from a recent high pressure turbine experiment and has proven to yield acceptable results in describing the magnitude and distribution of mistuned resonant response amplitudes on the turbine rotor blades. Further case studies on the same turbine rig and on a transonic compressor rig rotor have been performed to demonstrate the multitude of phenomena that can be observed in mistuned aeroelastic systems.

The method presented here has been successfully applied to the modeling of some of these phenomena. Owing to its formulation with only a few degrees-of-freedom, it is very fast and thus well suited to perform parametric variations or stochastic "Monte-Carlo" - simulations.

Acknowledgments

Part of the experimental data used in this thesis was acquired in the research program ADTurB, funded by the European Community under the Industrial and Material Technologies Program (BriteEuRam III), contract no. BPR-CT95-0124. The permission to publish is gratefully acknowledged.

References

[1] Afolabi, D.: The Frequency Response of Mistuned Bladed Disk Assemblies, in: *Kielb, R.E. (ed.): Vibrations of Blades and Bladed Disk Assemblies*, pp. 15-22, ASME, 1985.

[2] Bladh, R.; Castanier, R.; Pierre, C.: Reduced Order Modelling and Vibration Analysis of Mistuned Bladed Disk Assemblies with Shrouds, *Journal of Engineering for Gas Turbines and Power*, Vol. 121, pp. 515-522, 1999.

[3] Blaha, C.; Kablitz, S.; Hennecke, D.K.; Schmidt-Eisenlohr, U.; Pirker, K.; Haselhoff, S.: Numerical Investigation of the Flow in an Aft-Swept Transonic Compressor Rotor, *ASME-GT-0490*, May 2000

[4] Hennings, H.; Elliot, R.: Forced Response Experiments in a High Pressure Turbine Stage, ASME-GT-2002-30453, 2002

[5] Kahl, G.: Application of a Time Linearized Euler Solver to Aeroelastic Problems in Turbomachinery, ASME 95-GT-123, 1995.

[6] Kahl, G.: Aeroelastic Effects of Mistuning and Coupling in Turbomachinery Bladings, *Communication du Laboratoire Thermique Apliquée et de Turbomachines de l' Ecole Polytechnique Federale de Lausanne*, No. 36, Lausanne, 2002.

[7] Kielb, R.E.; Kaza, K.R.V.: Effects of Structural Coupling on Mistuned Cascade Flutter and Response, *Trans. ASME J. Eng. Gas Turbines and Power*, Vol. 106, pp. 17-24, Jan. 1984.

[8] Kost, F.; Hummel, F.; Tiedemann, T.: Investigation of the Unsteady Rotor Flow Field in a Single Stage HP Turbine Stage, ASME-2000-GT-432, 2000.

[9] Moyroud, F.; Fransson, T.; Jaquet-Richardet, G.: A Comparison of Two Finite Element Reduction Techniques for Mistuned Blades, ASME-2000-GT-0362, 2000.

[10] Pierre, C.; Murthy, D.V.: Aeroelastic Modal Characteristics of Mistuned Blade Assemblies: Mode Localization and Loss of Eigenstructure. *AIAA Journal*, Vol. 30, No. 10, pp. 2483-2496, 1992.

[11] Rivas-Guerra, A.; Mignolet, M.: Local / Global Effects of Mistuning in the Forced Response of Bladed Disks, ASME-2001-GT-0289, 2001.

[12] Santoriello, G.; Colella, A.; Colantuoni, S.: Rotor Blade Aerodynamic Design, Alfa Romeo Avio, IMT Area 3 turbine project technical report, AER2-CT92-0044, 1993.

[13] Seinturier, E.; Lombard, J.-P.; Berthillier, M.; Sgarzi, O.: Turbine Mistuned Forced Response Prediction: Comparison with Experimental Results, ASME-2002-GT-30424, 2002.

[14] Yang, M.-T.; Griffin, J.: A Reduced Order Model of Mistuning Using a Subset of Nominal System Modes, ASME 99-GT-288, 1999.

EVALUATION OF THE PRINCIPLE OF AERODYNAMIC SUPERPOSITION IN FORCED RESPONSE CALCULATIONS

Stefan Schmitt
German Aerospace Center
Institute of Propulsion Technology
Cologne, Germany
stefan.schmitt@dlr.de

Dirk Nürnberger
German Aerospace Center
Institute of Propulsion Technology
Cologne, Germany
dirk.nuernberger@dlr.de

Volker Carstens
German Aerospace Center
Institute of Aeroelasticity
Göttingen, Germany
volker.carstens@dlr.de

Abstract The validity of the principle of superposition for forced response analysis is evaluated by its application to a research propfan stage. The counter-rotating propfan features transonic flow conditions and aerodynamic interaction between the blade rows. The computed unsteady aerodynamics are verified by comparison with rig measurements. A forced response analysis based on the principle of superposition is conducted, similar to the current practice in turbomachinery design. For reference, a fully coupled simulation of the propfan forced response is undertaken. This simulation does not rely on the principle of superposition, and the model can also resolve non-linear interaction effects beyond the validity of the linear superposition principle. The comparison shows a full validity of the superposition principle for the present case: Computed blade vibration amplitudes, as well as the unsteady aerodynamics inside the blade passages, are correct, even in quantitative terms. This supports the application of the superposition principle for forced response analysis within the industrial design process.

K.C. Hall et al. (eds.),
Unsteady Aerodynamics, Aeroacoustics and Aeroelasticity of Turbomachines, 133–144.

Introduction

Important goals in today's aeroengine design are the reduction of fuel consumption, engine weight and production effort. A contribution to lower weight and production costs is a reduction of the number of blades, and a closer axial spacing of the blade rows. The use of less blades leads to an increase in blade loading, while the reduced axial spacing increases the amount of interaction between adjacent blade rows. The aerodynamic interaction between the blades can excite the blades to vibrate causing a forced response problem.

The forced response problem is characterized by the interference of the external aerodynamic forces arising from up- or downstream excitation on the one hand, and the aerodynamic damping forces of the oscillating blades on the other hand. Current methods mostly rely on a linear superposition of these forces (Chiang and Kielb, 1993, Green and Marshall, 1999), where the response amplitudes are computed from the balance of excitation and damping forces.

The use of a non-linear aeroelastic method using fluid-structure coupling in the time domain enables a computation of the blade response amplitudes without the application of the rather restrictive superposition principle. Some directly coupled forced response calculations on turbomachinery stages have been presented in recent years: Wakeley and Potts calculated the excitation of a steam turbine stage due to partial admission (Wakeley and Potts, 1996). He calculated the forced response in a two-stage-compressor (He, 1999). Gottfried and Fleeter investigated an inlet-guide-vane/rotor research fan stage combination (Gottfried and Fleeter, 2000). The research group at Imperial College presented forced response calculations of a low pressure turbine (Sayma et al, 1998), a high pressure turbine, as well as a fan stage (Vahdati et al, 2000).

Unfortunately the results of the computations mentioned above do not yield definite information about the dependence of the numerical data on the use of either a coupled or a linear method. The authors conclude that at present it is not sufficiently clear in which cases fluid-structure coupling methods are necessary for forced response predictions.

1. Numerical Method

For the investigation, a time-domain aeroelastic method that incorporates fluid-structure coupling is used (DLR's TRACE-code: Nürnberger et al, 2001; Schmitt et al, 2001). The method consists of a non-linear Navier-Stokes solver for the aerodynamic part, and a linear modal model for the structural dynamics part. Some details of this method working in the time-domain are given as follows.

The aerodynamic part solves the three-dimensional Reynolds-Averaged Navier-Stokes equations in the relative frame of reference. The Spalart-Allmaras

one-equation turbulence model (Spalart and Allmaras, 1992) in combination with wall functions is used here for turbulence closure. The system of equation is discretized around the centers of the cells of the structured mesh in a blended finite-volume/finite-difference approach. For the convective terms, Roe's upwind scheme is used (Roe, 1981) in combination with van Leer's MUSCL-extrapolation (van Leer, 1979). The viscous terms are discretized by central differences. At entry and exit, non-reflecting boundary conditions based on a harmonic approach are applied (Giles, 1990). The coupling of multiple blade rows is realized here using the "sheared cells" approach (Giles, 1991). The time-accurate integration of the aerodynamic conservation laws uses a dual-time-stepping algorithm where the solution at the pseudo-time-levels is computed by an implicit solver. The computations are carried out on structured multi-block meshes. The blade vibration is taken into account by an algebraic mesh deformation. For the computations here, the blade count ratio is taken into account by meshing the geometry segment under consideration (the so called multi-passage approach). Parallel computing based on domain decomposition is applied.

The structural part uses a linear modal model. The mode shapes are taken from a real eigenvalue analysis done beforehand and are interpolated on the aerodynamic mesh. The mode shapes are constant during the aeroelastic simulation. Each mode shape of each blade is one degree of freedom in the linear structural model. The system of equations of motion for the structure is integrated in time using the Newmark method (Newmark, 1959). The coupling between fluid and structure is done by exchanging the modal forces and the displacements. The fluid-structure coupling exchanges information as well as updating the structural solution at every pseudo-time-subiteration of the aerodynamic solver. This iterative improvement of the coupled solution leads to a diminishing coupling error between fluid and structure. It gives a quasi-implicit character to the solution of the coupled problem.

Validation and prior applications of the aeroelastic method have been reported previously (Schmitt et al, 2001).

2. Configuration

A research propfan stage is used for the investigation (Wallscheid et al, 1998). The configuration is presented in Fig. 1 together with some tabulated key data. The propfan stage is a scaled rig stage. It consists of two counter-rotating rotors and no vanes. The design operating point is investigated where the flow is transonic for both rotors (see Fig. 1). The simulation is three-dimensional and viscous, and also considers the tip gap between the rotors and the casing. For the simulation, the original blade count of 10:12 is reduced

to 5:6. This leaves the blade count ratio, the operating point, and the interblade phase angle unchanged.

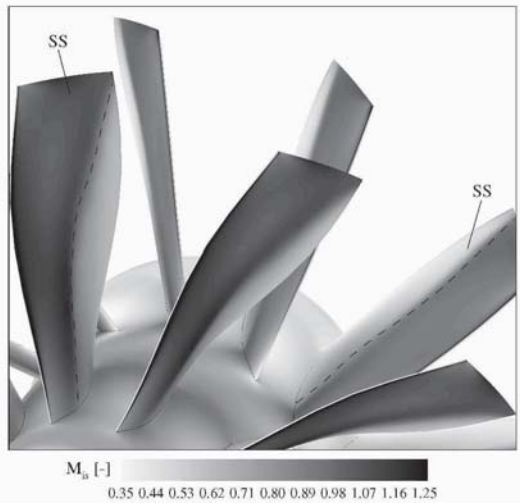

no. blades Rotor-I	10
no. blades Rotor-II	12
RPM Rotor-I	-4980
RPM Rotor-II	4316
Total Pressure Ratio	1.24
Entry Mach number	0.7-0.75
Exit Mach number	0.65-0.68
Outer Diameter	1m
Reynolds-Number	2.3 mill.

Figure 1. Research Propfan stage: Isentropic Mach-number on blade and hub surfaces and tabulated key data

The aerodynamic interactions between the blades - mainly the upstream running shock and the downstream convected wake - excite the rotor blades to vibration. This forced-response-excitation that appears at the blade passing frequency is investigated in the current aeroelastic study. For each rotor blade, the eigenmodes of vibration with an eigenfrequency close to the excitation frequency are sensitive to this excitation. Here, the excitations of the first and second rotor are investigated at the same time in one common simulation. For each rotor, one eigenmode of blade vibration is considered, the eigenmode with its eigenfrequency closest to the exciting blade passing frequency (remember the Campbell diagram). The original three-dimensional blade vibration mode shapes are used (Fig. 2). The mode shapes of interest feature a highly three-dimensional pattern due to the high excitation frequency of the blade row interaction. This is fully taken into consideration in the current three-dimensional simulation. In order to have a high level of excitation in the numerical study, the blade eigenfrequencies are adapted to the excitation frequency. The study neglects structural damping, i.e. only the aerodynamic damping of the blades balances the excitation of the blade passing.

With the fluid-structure coupled method, the full aeroelastic propfan configuration is simulated. The simulation includes at the same time the blade passing and the induced blade vibrations.

The results from the fluid-structure coupled aeroelastic computation are compared with results obtained from a linear forced response analysis. The lat-

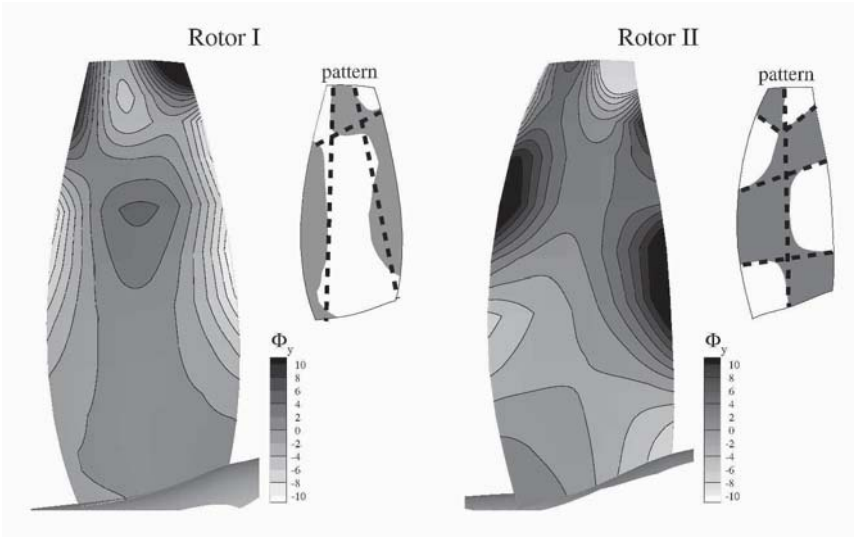

Figure 2. Eigenmodes (No. 12 for Rotor-I, No. 10 for Rotor-II)

ter uses aerodynamic solutions that are computed on the same meshes and by the same non-linear aerodynamic method as before. A simulation of the blade-row-interaction of the stage with stiff blades yields the aerodynamic forcing. The aerodynamic damping is computed from further non-linear aerodynamic simulations of each rotor alone where the blade vibration is prescribed as harmonic motion in the eigenmode under investigation. The solution of the forced response problem is then obtained by the combination of both results. This procedure makes use of the aerodynamic superposition principle and is typical of the analysis procedure currently applied within industry. This decoupled approach will be referred to as the linear solution to the forced-response-problem. It uses the aerodynamic solutions of a non-linear aerodynamic method. A linearized aerodynamic method (a frequency domain solver) was not used in the current study.

3. Results

The calculated unsteady aerodynamics agree very well with the unsteady Laser-2-Focus measurement data from the rig test (the time-averaged absolute velocity is presented in Fig. 3, the amplitude of the 1st harmonic of the absolute velocity in Fig. 4). As the (optical) vibration control system of the rig test monitored only low frequency excitations during running up, and no strain gauge measurements were taken, the comparison with the unsteady aerodynamic measurement data is the only possible comparison with experimental data here. The following aeroelastic investigation is based on these qualified unsteady aerodynamics, but of a numerical nature only.

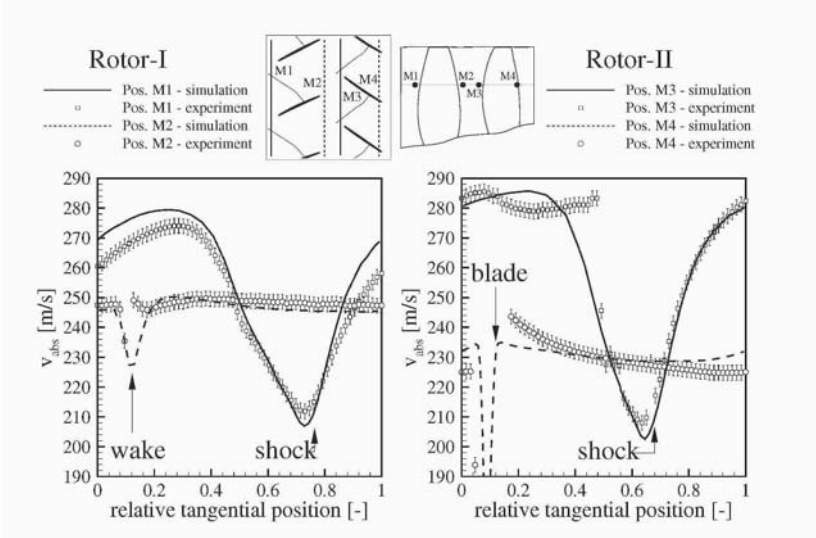

Figure 3. Computed time-averaged absolute velocity compared with measurement data

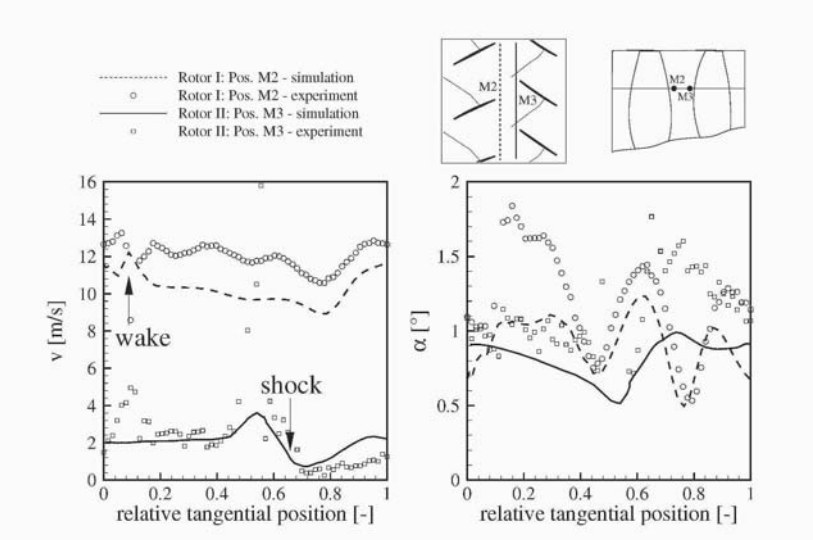

Figure 4. Computed amplitude of velocity and flow angle fluctuations between the rotors compared with measurement data

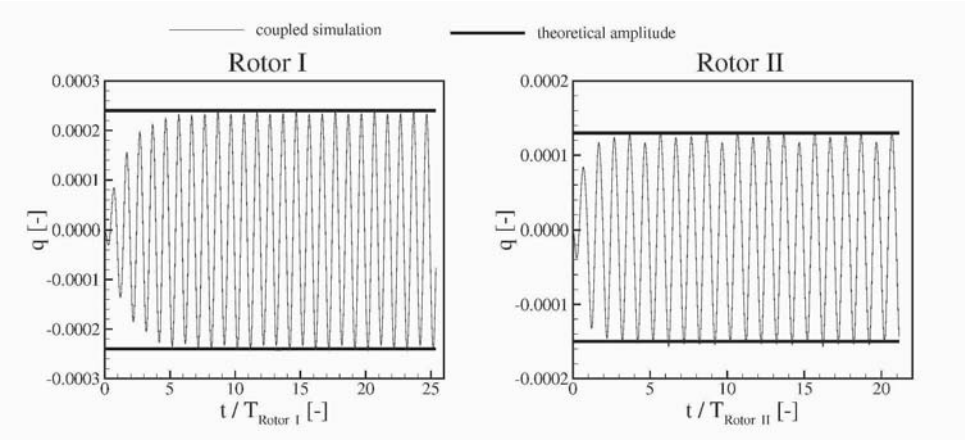

Figure 5. Temporal development of blade displacements in their eigenmodes

The vibration amplitudes obtained from the time development of the fully coupled aeroelastic simulation are the same as those predicted by the linear approach (Fig. 5). The absolute vibration amplitudes are moderate: The maximum displacements at the tip trailing edges are 36% of the trailing edge thickness for the first rotor, and 20% for the second rotor. Only small amplitudes would have been expected here for two reasons: 1. The excitation of higher order mode shapes is in general small as a complex mode shape is unlikely to by severely excited (the exciting aerodynamic pattern has to fit the mode shape for which the chances are low for complex mode shapes). 2. The investigated configuration is an existing rig stage that does not feature any severe forced response problem. Severe problems would have been avoided already in the design phase of the rig. The very good agreement between the coupled simulation and the linear solution is astonishing here as the coupled calculation computes the blade displacements of the first and the second rotor in one common simulation. So the coupled simulation allows each vibrating blade to change the aerodynamics in the stage, and therefore to change the aerodynamic disturbance (or "gust") on the other blade. The linear model on the other hand computes the displacements separately, and it suppresses any influence of the vibrating blade to the other blade. The linear model computes the solution to the forced response problem with one stiff (exciting) blade and one elastic (excited) blade.

The comparison of the coupled aeroelastic simulation with the linear solution is extended to the unsteady flow fields in the blade passages. In a post-processing step, the unsteady aerodynamic solutions from the decoupled calculations of the aerodynamic damping (each rotor alone) and the aerodynamic forcing (stage with stiff blades) are combined to a "superposed" aerodynamic

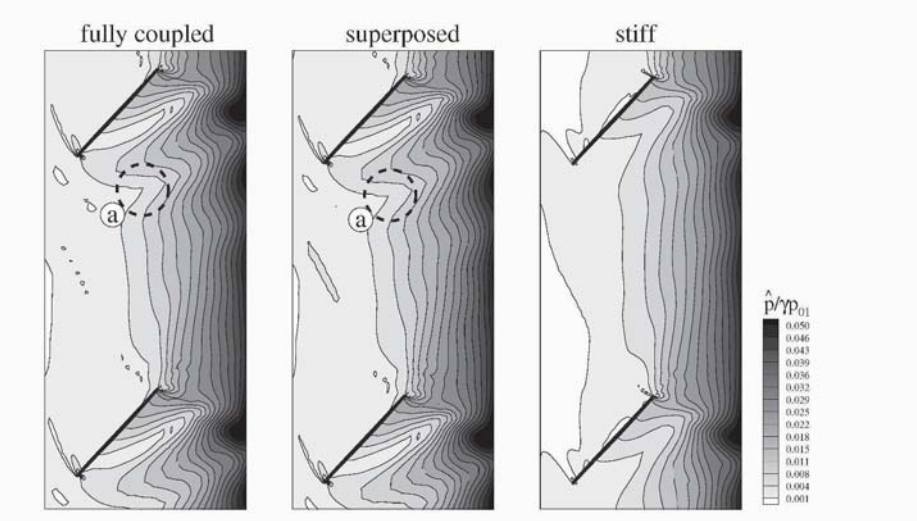

Figure 6. Amplitude of pressure fluctuations in the passage of the 1st rotor near tip

solution. This is an aerodynamic solution taking into account the vibrating blades by the use of the principle of superposition. "Superposed" and "fully coupled" solutions show identical unsteady aerodynamics inside the blade passages. Figure 6 shows the amplitude of perturbation pressure in the passage of the first rotor near the tip. The source of the pressure amplitudes visible in the exit plane of the rotor, and decaying when running upstream, is the not shown downstream second rotor that excites the first one. The two solutions taking into account the blade vibration (the "coupled" and "superposed" solution) differ (Fig. 6: "a") from the aerodynamic solution with "stiff" blades that neglects the blade vibration . The example shows the first rotor's tip section, but the same result was found for the full span as well as the second rotor. The agreement between "coupled" and "superposed" solutions, and disparity with the "stiff" solution, for the amplitudes, was also evident for the phases. Figure 7 presents the unsteady pressure distributions on the blade surfaces, here exemplarily for the second rotor. The agreement between the "superposed" and "fully coupled" solution is very good even in quantitative terms. The results from the "stiff" calculation deviate as the blade vibration is not incorporated there at all.

Both the blade row interaction and the blade vibration generate unsteady pressure fluctuations on the blade. If the blade row interaction and the blade vibration are computed separately, the local aerodynamic forcing as well as the local aerodynamic damping can be computed by a projection of the blade surface pressure amplitudes onto the blade eigenmodes (often referred to as local aerodynamic work coefficient). This was applied to the separate computations

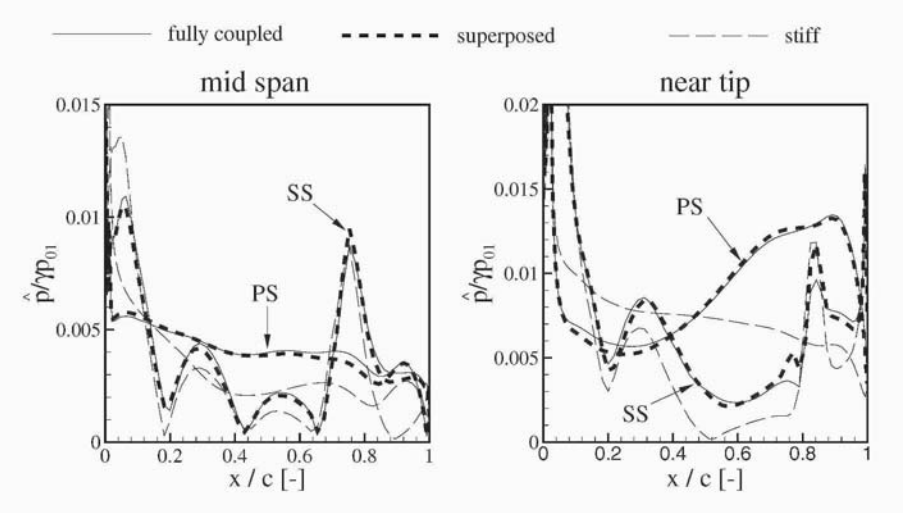

Figure 7. Amplitude of blade surface pressure of the 2nd rotor

of forcing and damping and yielded in a straight-forward manner the excitation mechanisms due to the more or less matching of the three-dimensional pattern of the pressure fluctuations on the one hand and the mode shape of the blade vibration on the other hand. The integral of this local contribution over the blade surface yields the integral modal forcing and damping respectively. For the fully coupled solution at resonance, the integral modal forcing is expected to be zero. That is the damping counterbalances the forcing. An analysis of the frequency spectrum of the integral modal force taken from the coupled simulation showed as expected a vanishing contribution of the harmonic at excitation frequency. Figure 8 shows the local contribution to the integral excitation from the "coupled" simulation for the pressure sides of both rotors. Parts of the blade surface contribute to the excitation (positive values), others to damping (negative values). The integral of the local forcing contribution over the blade surface is zero as already mentioned. The diagrams in the center compare the local excitation contribution to the result computed with stiff blades, which features of course a significant and positive integral modal forcing when integrated over the blade surface. The comparison shows for the "coupled" simulation as compared with the "stiff" solution, a reduction of the excitation in exciting blade surface areas ("a" and "c"), as well as at the same time an increase of damping in the damping areas of the blade surfaces ("b" and "d"). This is in full agreement with the anticipation based on a point of view that the pressure fluctuation generated by the vibrating blades are looked upon as additional fluctuations to the already present fluctuations from blade row interaction. The additional fluctuations from the blade vibration then change

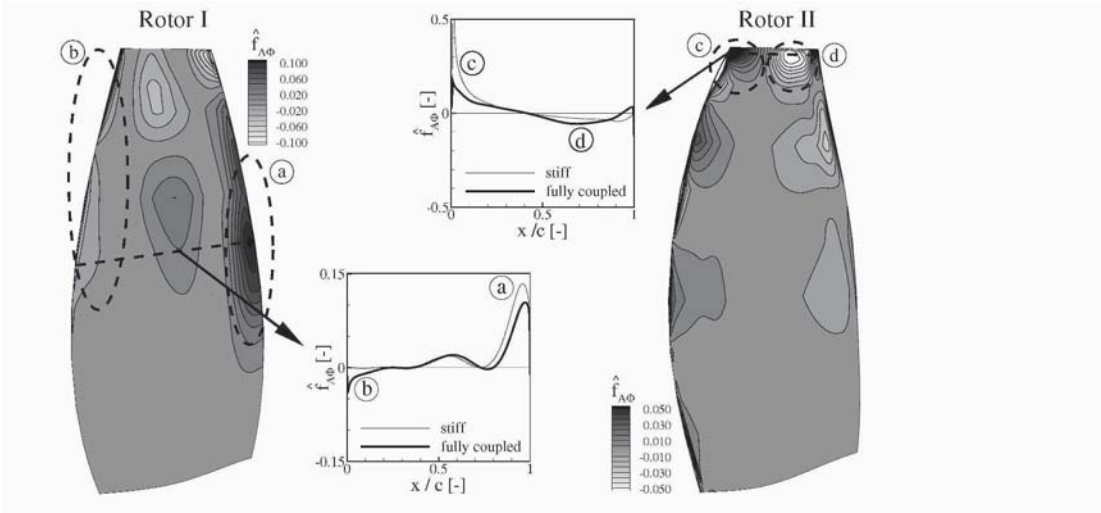

Figure 8. Local contribution $\underline{f_{A\Phi}}$ to the integral modal excitation on both rotors pressure sides

the sum pressure fluctuation pattern in such a manner that the integral over the surface becomes zero, so neither exciting nor damping. This corresponds to a blade vibration with a constant amplitude.

4. Conclusions

The numerical investigation shows a full agreement of the fully coupled solution with the solution obtained from the superposition of the decoupled simulations: This does not only hold for the vibration amplitudes, but even for the unsteady pressure distributions qualitatively as well as quantitatively. For the case under consideration, this confirms the validity of the superposition principle for the aerodynamics in cases of forced response.

The very good agreement between the coupled and the linear solution can be also looked upon from another point of view: For the present case, apparently the computed aerodynamic damping is not significantly influenced by the blade row interaction (the theoretical influence of blade row interference on flutter and forced response is described in Buffum, 1995).

The proven validity of the principle of superposition supports the forced response analysis currently applied within industry. There remain two advantages for the coupled analysis over the linear approach: 1. Only one coupled simulation is required for the full analysis of the system. The linear approach requires an increasing number of separate evaluations of the aerodynamic damping for complex configurations featuring multiple eigenmodes and frequencies (50 to 100 aerodynamic damping coefficients may be required

depending on the system's complexity). 2. The decoupled analysis requires the rotor alone computations for the evaluation of the aerodynamic damping to have the same time-average operating point as the multi-stage configuration. This was the case for the current configuration. Multi-stage compressors and turbines with high loading and small axial gaps between blades can feature blade rows where the operating point in the multi-stage configuration cannot be reached in a single blade row computation. Reasons for this are steady or even unsteady multi-stage effects. As the required aerodynamic damping cannot not be evaluated correctly in these cases, the principle of superposition cannot be applied. But forced response investigations are very likely required in these cases with strong blade row interference. The coupled approach can still be applied without any restriction, and so remains the means to analyze the forced response in such a system.

Acknowledgements

The authors would like to thank MTU Aero Engines for their support of the current work. Special thanks to Dr. Paul Petrie-Repar from DLR Göttingen for his efforts in carefully proofreading the manuscript.

References

D.H. Buffum. Blade Row Interaction Effects on Flutter and Forced Response. *AIAA Journal of Propulsion and Power*, 11(2):205–212, 1995.

H.-W.D. Chiang and R.E. Kielb. An Analysis System for Blade Forced Response. *ASME Journal of Turbomachinery*, 115:762–770, 1993.

M.B. Giles. Nonreflecting Boundary Conditions for Euler Equation Calculations. *AIAA Journal*, 28(12):2050–2058, 1990.

M.B. Giles. UNSFLO: A Numerical Method For The Calculation Of Unsteady Flow In Turbomachinery. Gas Turbine Laboratory Report, No. 205, MIT, Cambridge, Massachusetts, 1991.

D.A. Gottfried and S. Fleeter. Fluid-Structure Interaction Analysis of Blade Row Unsteady Aerodynamics and High Cycle Fatigue. In *Proceedings of the 9th International Symposium on Unsteady Aerodynamics, Aeroacoustics and Aeroelasticity of Turbomachines*, Lyon, France, 2000.

J.S. Green and J.G. Marshall. Forced Response Prediction within the Design Process. IMechE C557/067/99. In *Proceedings of the 3rd European Conference on Turbomachinery Fluid Dynamics and Thermodynamics*, pages 377–391, London, 1999.

L. He. 2-Dimensional Aero-Structure Coupling in Multi-bladerow Environment. In: T. Fransson and C.H. Sieverding (Eds.) *Aeroelasticity in Axial Flow Turbomachines*, von Karman Institute for Fluid Dynamics Lecture Series 1999-05, Rhode Saint Genèse, Belgium, 1999.

B. van Leer. Towards the Ultimate Conservative Difference Scheme. V. A Second-Order Sequel to Godunov's Method. *Journal of Computational Physics*, 32:101–136, 1979.

N.M. Newmark. A Method of Computation for Structural Dynamics. *ASCE Journal of the Engineering Mechanics Division*, 85(EM 3):67–94, 1959.

D. Nürnberger, F. Eulitz, S. Schmitt, A. Zachcial. Recent Progress in the Numerical Simulation of Unsteady Viscous Multistage Turbomachinery Flow. ISABE-2001-1081. In *Proceedings of the 15th International Symposium on Air Breathing Engines*, Bangalore, India, 2001.

P.L. Roe. Approximate Riemann Solvers, Parameter Vectors, and Difference Schemes. *Journal of Computational Physics*, 43:357–372, 1981.

A.I. Sayma, M. Vahdati, M. Imregun. Forced Response Analysis of an Intermediate Pressure Turbine Blade Using a Nonlinear Aeroelasticity Model. AIAA 98-3718. 34th AIAA/ASME/SAE/ASEE Joint Propulsion Conference & Exhibit, Cleveland, Ohio, 1998.

S. Schmitt, F. Eulitz, D. Nürnberger, V. Carstens, J. Belz. Simulation of Propfan Forced Response using a Direct Fluid-Structure Coupling Method. In *Proceedings of the 4th European Conference on Turbomachinery Fluid Dynamics and Thermodynamics*, pages 1023–1033, Florence, Italy, 2001.

P.R. Spalart and S.R. Allmaras. A One-Equation Turbulence Model for Aerodynamic Flows. AIAA 92-0439. AIAA 30th Aerospace Sciences Meeting & Exhibit, Reno, Nevada, 1992.

M. Vahdati, A.I. Sayma, M. Imregun. An Integrated Nonlinear Approach for Turbomachinery Forced Response Prediction. Part II: Case Studies. *Journal of Fluids and Structures*, 14:103–125, 2000.

G.R. Wakeley and I. Potts. Unsteady Flow Phenomena in Partially-Admitted Steam Turbine Control Stages. IMechE S461/006/96. In *Latest Advances in the Aerodynamics of Turbomachinery with Special Emphasis on Unsteady Flows*, ImechE Seminar Publication 1996-21, 1996.

L. Wallscheid, F. Eulitz, R. Heinecke. Investigation of Unsteady Flow Phenomena in a Counterrotating Ducted Propfan. ASME-98-GT-251. ASME International Gas Turbine and Aeroengine Congress and Exhibition, Stockholm, Sweden, 1998.

COMPARISON OF MODELS TO PREDICT LOW ENGINE ORDER EXCITATION IN A HIGH PRESSURE TURBINE STAGE

Markus Jöcker,[1] Alexandros Kessar,[1] Torsten H. Fransson,[1] Gerhard Kahl,[2] Hans-Jürgen Rehder[3]

[1]*Royal Institute of Technology*
S-100 44 Stockholm, Sweden
markus@egi.kth.se
alex@egi.kth.se
fransson@egi.kth.se

[2]*MTU Aero Engines*
D-80995 Munich, Germany
Gerhard.Kahl@muc.mtu.de

[3]*German Aerospace Center*
D-37073 Göttingen, Germany
hans-juergen.rehder@dlr.de

Abstract The paper compares three numerical strategies to predict the aerodynamic rotor excitation sources of "Low Engine Order" (LEO) in a high-pressure turbine stage. Main focus is laid on methods to compute the stator exit flow. The aim is to evaluate computationally cheap approaches to avoid modeling the whole circumference of the stator. A single passage viscous strategy, a single passage inviscid linear blade movement strategy, and a viscous multi-passage sector strategy are compared and evaluated. The assessment of the prediction quality is made by comparison of the computed stator exit flow to experimental data. The main result is that only the global behavior of the stator exit flow is estimated right, both the level and amplitude of Mach number and pressure are computed with poor agreement to experiments. Future evaluations of the resulting rotor excitation pressure are needed to estimate the level of necessary agreement to give acceptable predictions of the low engine order forced response.

Keywords: Forced Response, Low Engine Order Excitation, High Pressure Turbine, Stator Non-Uniformity

K.C. Hall et al. (eds.),
Unsteady Aerodynamics, Aeroacoustics and Aeroelasticity of Turbomachines, 145–159.

Nomenclatrue

A	Area	[m^2]
h/H	Relative blade height	[-]
m	Passage number	[-]
M	Mach number	[-]
N	Number of stator passages	[-]
ϕ_{norm}	Circumferential coordinate normalized with nominal pitch angle	[-]

Subscripts

ax	Axial
t	Throat
t	Total value

Abbreviations

2D	Two-dimensional (constant radius)
CFD	Computational Fluid Dynamics
DLR	German Aerospace Center
(L)EO	(Low) Engine Order
L2F	Laser Two Focus Anemometry
SP	Single passage model
MP	Multi passage model

1. Introduction

Forced vibrations are characterized by aerodynamic excitation sources, which are flow disturbances acting periodically on the blades and originate from upstream and/or downstream obstacles. The time-periodic excitation is in all cases caused by the relative rotational motion of excitation source and the excited structure, which leads to excitation frequencies multiples of the rotation frequency. A common way to identify forced response regions of a blade row is the "Campbell Diagram", a typical example for a turbine rotor is shown in Fig. 1, which is a key plot in the unsteady design process. The diagram shows crossings of excitation frequencies due to upstream and downstream vanes, as well as burner cans, with the eigenfrequencies of the blades. At these crossings, the risk of resonant excitation of the structure exists. Practically, in high-pressure turbines, vane passing does not excite the 1^{st} flex mode because of its low eigenfrequency (typical frequencies correspond to 8 to 10 excitations per revolution in the operating range). To the original figure presented in Ref. [1], an additional line was added indicating another excitation of low frequency, named the "Low Engine Order" (LEO) excitation. Such can be caused by non-uniformities on the stator blade row due to manufacturing variations and wear (for example vane erosion or burnout). The excitations can induce vibrations in fundamental blade modes such as the first bending or torsion mode, characterized by low frequency and possibly high vibration amplitudes. The severity is increased due to occurrence at high load operating conditions.

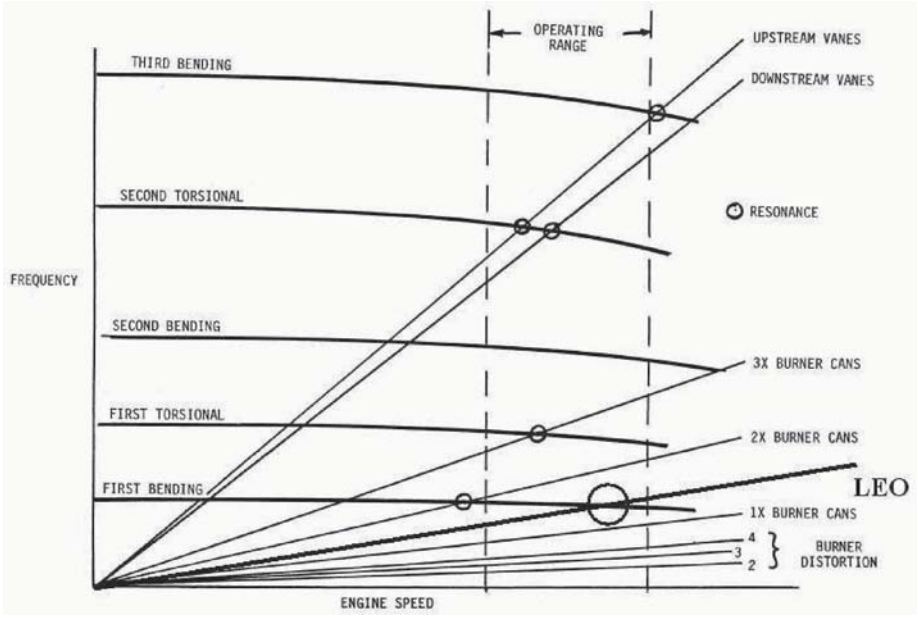

Figure 1. Example of a typical turbine Campbell diagram indicating Low Engine Order resonance

During the last decade intensive research and development activities have focused on the computation of wake passing frequency excitation in turbomachinery stages. The goal was to benchmark the capabilities of computational tools for further application during engine design. Furthermore, the investigation of unsteady flow physics was addressed aiming at widening the understanding of the mechanisms of aerodynamic blade vibration excitation, for example in [2].

Only little work has been published on the computation and understanding of low engine order excitations. These are more difficult to predict than vane passing excitations due to the following reasons:

- The frequency and magnitude of the low engine order excitation is not known a priori, because it is caused by unknown variations in the vane geometry due to manufacturing tolerances or wear on the vanes during operation.

- The periodicity of the excitation is often not known a priori. The spatial periodicity of the stator exit flow must be assumed to be over the whole circumference.

For a low-pressure turbine rotor, [3] investigated the 2^{nd} engine order temperature variations, which emanated from the combustor. The excitation was modeled with help of measured data. A full annulus analysis was presented by [4] indicating LEO excitations due to throat width variations in the stator. [5] showed a systematic study of low engine order forced response considering the effects of throat width variation in the stator and temperature distortion. A typical sector of the stage was modeled to compute the aerodynamic excitation. In [6], linear inviscid flow and non-linear viscous flow models for the unsteady flow in the ADLARF fan rotor are compared, LEO boundary conditions were derived from experiments. All these investigations derived the unsteady boundary conditions either from full annulus or sector vane computations, or calculated them from measured data.

This paper investigates the LEO excitation in a high-pressure turbine with transonic flow, for which a companion experimental program prescribes the excitation source. The objective is to assess different modeling options to compute the unsteady inlet boundary conditions due to a given distortion in the stator geometry. Instead of modeling the coupled stator-rotor domain, the computationally cheaper but more modeling intensive approach of de-coupling the stator and rotor computation is chosen, because the overall goal is to find approaches suitable for design. The stator flow analysis is the first critical step in the de-coupled approach. Unsteady pressure response on the rotor can presently not be evaluated due to the lack of experimental data.

The stator configuration is given by a sinusoidal variation of stator throat area, both a 5^{th} engine order variation and a 7^{th} engine order variation is available with two amplitudes of throat area variation each 2% and 4%. To limit the study on the modeling evaluation, the 5^{th} engine order case with 4% variation was chosen (see also Fig. 2). Three modeling strategies are evaluated and compared.

2. Experimental data and boundary conditions

Experiments

High quality experiments were set up and performed at the cold flow wind tunnel for rotating cascades (RGG) at DLR in Göttingen, Germany. The aim of the experiments was to simulate the effects of Low Engine Order excitation in a high pressure turbine stage. Therefore, the stator was modified to provide well defined configurations of distorted stators. One modification comprised a 5^{th} engine order variation of the stator pitch, which is shown in Fig. 2. In a similar way, a 7^{th} engine order variation was established.

The stator exit flow was measured first without and then with the rotor behind the stator. Table 1 presents data that was measured to provide and evaluate boundary conditions for CFD simulations. Additionally, stator inlet flow mea-

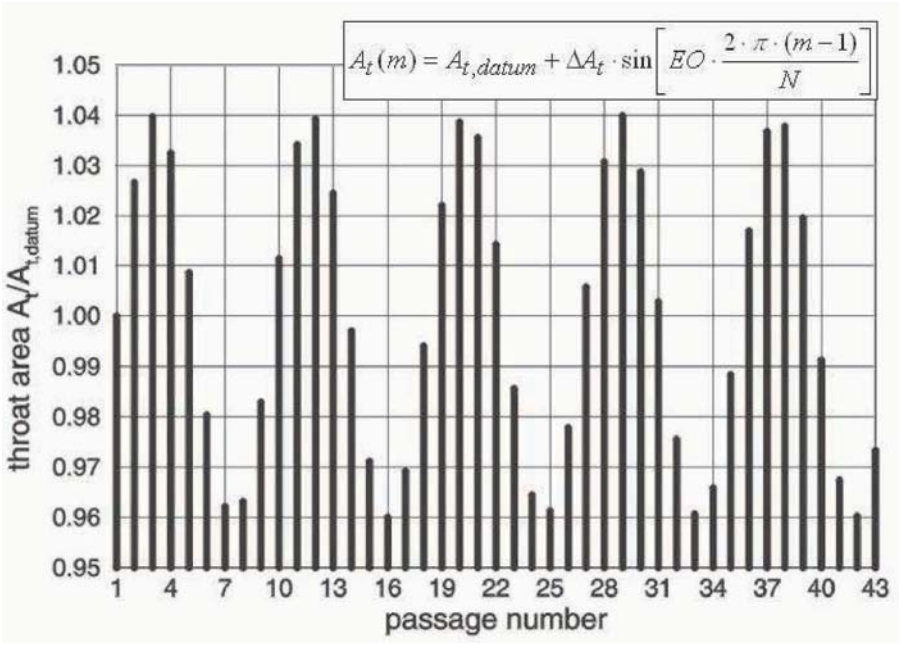

Figure 2. 5^{th} engine order throat area variation designed for experiments at DLR

Table 1. Overview of available measured data.

Technique	Stator only	Stage
Probe	Stator exit: -Total pressure	Stator exit: - Rotor exit: -Total pressure
L2F	Stator exit: -2D velocity vectors -2D turbulence level	Stator exit: -2D velocity vectors -2D turbulence level Rotor exit: -2D velocity vectors -2D turbulence level

surements were available including an assessment of the hub and tip end wall boundary layer status in front of the stator, see [7]. The operating point under consideration leads to transonic flow both in the stator and in the rotor, and a stator trailing edge shock contributes significantly to the stator exit flow. The

effective exit Mach number is averaged to slightly above one, which makes the analysis relatively sensitive regarding the resulting rotor excitation. The averaged rotor exit flow Mach number is well below one, but inside the passage, local transonic regions are expected. The rotational speed is adjusted such that a resonance condition, as computed in a structural analysis of the rotor, is met. Planned experiments will assess the unsteady pressure and the vibration characteristics of the rotor blades under these forced response conditions. However, such data is not available for the present evaluation of the numerical results.

Boundary conditions

Experimental stator only results of the exit flow are different to the stage results due to not completely matching conditions of the experiment in the two test runs. In the stator only tests the average exit Mach number at 128% $c_{ax,stator}$ was 1.00. In the stage experiments, the corresponding Mach number was 1.05. These small differences can be significant for the aerodynamic rotor excitation in the studied transonic flow. In all computations, beside one (TRACE) the stage results have been used for setting up the computations, because it is assumed that the boundary conditions from the stage experiments will lead to better agreement to the unsteady flow in the stage than the stator only computations. A Fourier analysis of the stator exit harmonics at midspan indicates that the low engine order harmonic content is only slightly influenced by the stator exit flow difference of the single passages. Closer to the end walls (at 20% and 9% of blade height), the differences between stator only and stage experiments are however remarkable. This can be seen in Figs. 4 and 5 when comparing the relative differences between stator only and stage result of the vane passing frequency (and multiples) to the ones in the low engine order frequency.

The mixed out flow parameters behind each passage of the stator are different, which is most probably caused by the geometric variation of the stator. To define a boundary condition for the computation, an arithmetic average of the mixed out flow parameters of each passage was specified.

3. Modeling Approaches

For the low engine order analysis, it is necessary to compute the aerodynamic excitation due to a spatial stator exit flow variation, which has a larger period than the vane pitch. In the present case of the 5^{th} EO modification, this variation has a spatial period of exactly 43/5 of the vane pitch, where 43 is the number of vane passages of the stator. If the unsteady computation is chosen to follow a linearized approach, the rotor inlet boundary condition needs to consist of an amplitude and a phase shift of this spatial flow distribution at the stator exit. The form is by definition of the linearized approach assumed to

be sinusoidal. Therefore, the following modeling approaches will focus on the estimation of the LEO harmonic of the excitation, but where available, other harmonics will be included in the discussion.

Strategy 1: Viscous single passage flow assembly. The simplest method would be to compute just one single passage, and "shift" the resulting stator wakes according to the positions of the stator trailing edges. In a pre-study, it has been found that this method is not suitable to reproduce the variations behind the real stator. The next approximation is to only compute the minimum and maximum spacing vane passage with single passage computations, and use these to calculate the amplitude of the low engine order excitation. This approach assumes that the relation between throat area and stator exit flow, in terms of 1^{st} harmonic spatial distribution, is linear. For simplicity, the passages are computed with the same average exit boundary conditions. The evaluation is done by computing the absolute difference between the 1^{st} harmonic amplitudes of the minimum and maximum spacing results. A closer look at the differences between the two exit flows confirmed that they are mainly in the 1^{st} harmonic. But it should be remarked that at 90% blade height, the difference in mean value was largest, which indicates that other physical effects are probably involved (see further results discussion). The computational tool VolSol, provided by Volvo Aero Corporation, Sweden, is used for the computations. For the present investigation, the standard k-ϵ turbulence model, with an extension by Kato and Launder [8], and standard wall functions were applied. The numerical method [9, 10] is an explicit three stage Runge-Kutta, time marching finite volume approach. The convective fluxes are calculated with a 3^{rd} order upwind biased scheme, the viscous fluxes are computed with a 2^{nd} order centered scheme. The code applies structured multi block H-type and O-type meshes and can be used for two- and three-dimensional computations. The farfield boundary conditions are partly non-reflecting.

Strategy 2: Inviscid quasi steady linear flutter computation. The three-dimensional linearized method SliQ [11, 12] allows the computation of the unsteady flow due to a blade movement flow perturbation. The method is foreseen for blade cascade flutter analysis, and hence allows the specification of an inter-blade phase angle between the motions of adjacent blades. The present strategy sets this inter-blade phase angle between the modeled vanes of the stator to a value corresponding to the throat variation in the stator, which must be sinusoidal to allow this approach. The frequency of the blade movement is however set to zero, which is the major difference to a usual flutter computation. The computation leads to a quasi-steady result of the unsteady flow to be evaluated at "a time" corresponding to the investigated stator configuration. A disadvantage of the method is that viscous effects cannot be regarded correctly.

The advantage of the strategy is that stator exit flows due to different orders of distortion may be calculated with very quick and simple computations. This makes it suitable for design approaches, where eventually many different configurations need to be computed. The evaluation as follows will give some insight on the applicability of this approach.

Strategy 3: Viscous computation of a sector of several vane passages. The number of NGVs (43) is not an integer multiple of the engine order under consideration. For an exact CFD analysis of this configuration, the whole annulus would have to be modeled. To reduce the computational effort, a sector of the stator is modeled, which violates the real geometry with an assumption of periodicity. Two approaches are presented:

1. A modified configuration with a scaled stator is modeled, where the throat width pattern repeats after an integer number of vanes. The NGVs are scaled so that the pitch/chord ratio and hence the vane loading remains identical to the original configuration. In the present case, this implies that the stator is scaled from 43 to 45 vanes on the circumference, each vane reduced in size by a factor 43/45. A sector of 9 passages is modeled to represent a periodic domain for the 5^{th} engine order excitation, resulting in a mesh of approximately 1.9 million points. The inlet total pressure, total temperature, and flow angle distribution was taken from traverse measurements taken from an earlier measurement campaign. These were scaled to the correct mean total pressure and total temperature levels. The exit boundary condition used here sets the mid-span circumferentially averaged pressure, thus allowing radial variations, according to the radial equilibrium condition, and circumferential variations due to the re-distribution of the flow according to the varying stator spacing. The computations are performed with the TRACE code, developed in cooperation between the DLR Institute of Propulsion Technology and MTU Aero Engines [13]. The block-structured code uses a cell-centered explicit finite-volume to solve the Reynolds-averaged Navier-Stokes equations formulated in relative Cartesian coordinates. It employs a time-marching Runge-Kutta scheme along with matrix dissipation to minimize corruption of solutions by numerical smoothing. For the current analysis, a k-ω turbulence model was employed in combination with wall functions on the blade, hub and tip surfaces.

2. The stator is not scaled, but the nearest number of passages representing a periodic sector are modeled. In the present case, 9 passages are modeled, which results in a domain that is slightly larger than the 5^{th} engine order domain of 43/5 passages. Without scaling of the vanes, this represents the exact geometry of the 9 passages measured in the experi-

mental program. The modeling error is introduced by assuming a periodic continuation of the domain, i.e. that passages 10 to 18 are identical to the modeled passages 1 to 9. The computations are performed with VolSol with similar computational parameters as for the single passage approach described in the previous strategy (Strategy 1).

4. Results

Space resolved data

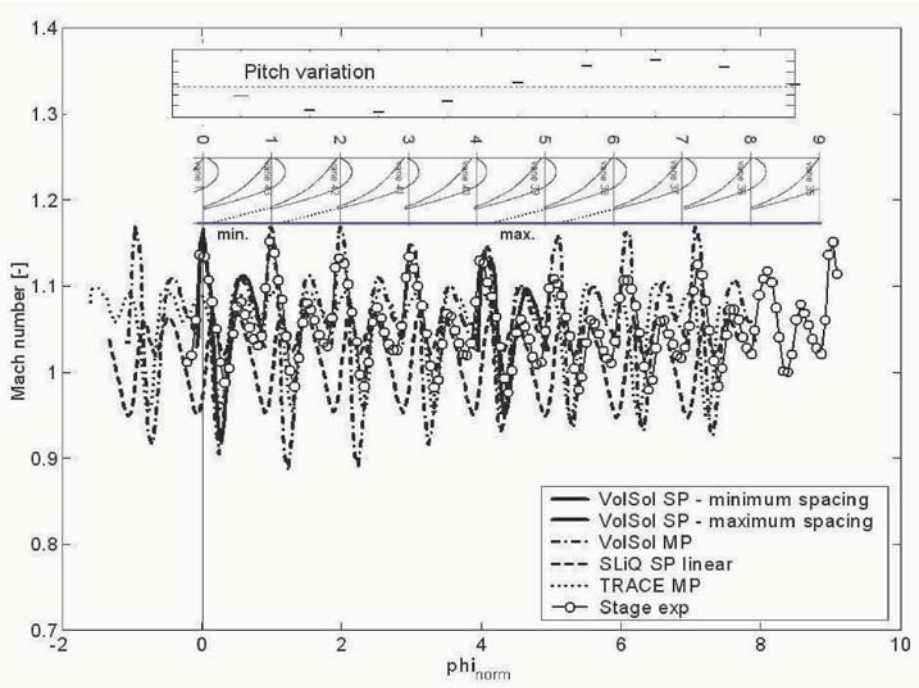

Figure 3. Space resolved stator exit Mach number at midspan at 128% of $c_{ax,stator}$

Figure 3 shows the space resolved stator exit flow behind nine passages. The Mach number has been chosen to represent the data because it is a direct measured result, whereas the pressure is a derived result with more uncertainty. Also illustrated is the variation of the corresponding vane pitches. It is obvious that a comparison of the data sets in this form is difficult. The measured and computed domain are not exactly the same, so that the 9 passage period is only partly overlapping. The single passage approach with VolSol is of course only represented in one passage each, the result of minimum and maximum spacing shown at the corresponding locations. Each passage exit flow goes through

two Mach number deficits, which have been described and discussed in detail in earlier work, for example Ref. [7], and (from left to right) identified as a wake and a shock deficit. This pattern is found in all of the curves. The global behavior found by all methods, and in the experiments, is that Mach number level and deficit amplitude decrease with increasing spacing. Obviously, the larger pitch leads to less acceleration of the flow and hence reduced deficits due to the wake and shock. The VolSol single and multi-passage results fit well but small differences indicate that the exit flow variation is not purely controlled by the single passage aerodynamics. Compared to experiments, the Mach number deficits by VolSol are too large. The TRACE computation is performed with slightly different boundary conditions (stator only boundary conditions, see above) and hence the Mach number result is at a lower level, and also, the wake and shock deficits are less than computed with VolSol, and hence fall better into the range of the experiments. The inviscid linear code SliQ overestimates the shock deficit and gives a too small wake deficit. The code was not expected to predict the correct viscous flow behavior.

So, beside the global behavior, none of the methods give a good representation of the measured data.

Harmonic decomposition

The important results from the stator computations with regard to the intended unsteady linearized rotor computations are the 5^{th} harmonic Fourier coefficients of the stator exit flow. These are compared below for the Mach number (Fig. 4) and for the pressure (Fig. 5). As all the results are available behind 9 passages only, the Fourier coefficients for the whole circumference were computed from an assembled result built from 5 times the 9 passages. Therefore, the vane passing frequency appears as the 45^{th} EO (see also Strategy 3 description above). An evaluation of the error introduced by this will be possible when full annulus computations are available.

The largest coefficients are at vane passing frequency for the pressure and at two times vane passing frequency for the Mach number. The latter one is due to the Mach number double deficit (wake and shock) as described above. Differences in these harmonics are related to the passage computation differences described in the space resolved data above. For example, the over prediction of Mach number deficits with VolSol gives too large amplitudes at one and two times vane passing frequency. The multi-passage computations by VolSol and TRACE give remarkably similar results in the 5^{th} harmonic both at midspan and close to the endwalls despite the observed differences in the global result. Both give much too small 5^{th} EO amplitudes. For the single passage method result, only the 5^{th} EO is included in the figures, which indicate a large over prediction both in Mach number and in pressure at 20% blade height and at

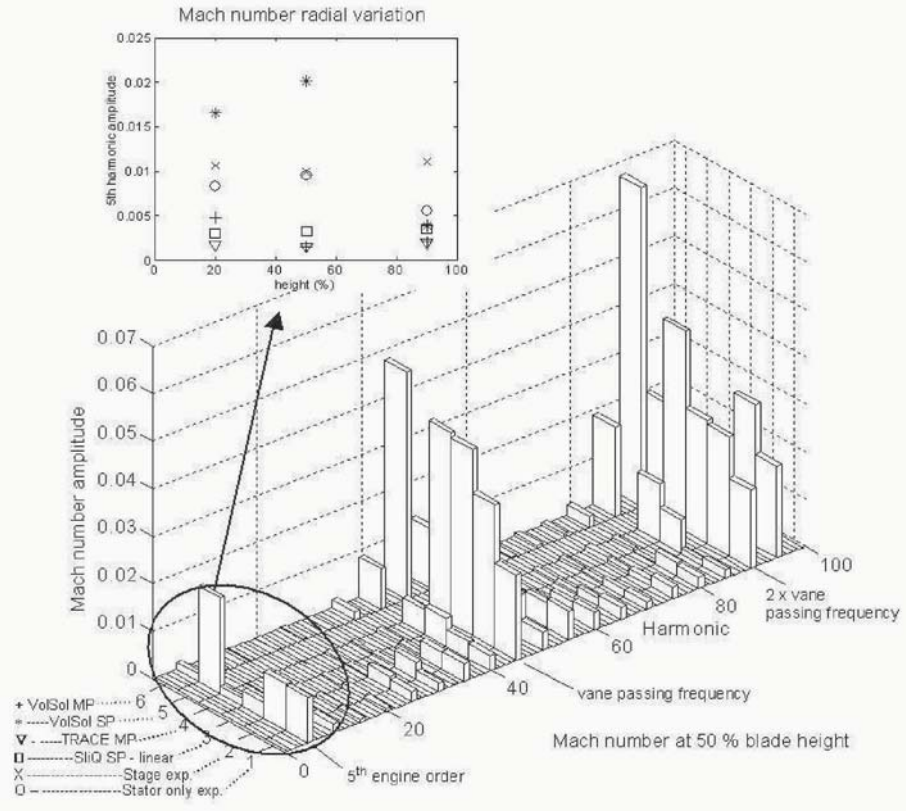

Figure 4. Mach number harmonics at 128% of $c_{ax,stator}$

midspan. At 90% blade height, this result falls in the same range as the other viscous results. Some error can be introduced as only the 1^{st} harmonic variation is considered (see Strategy 1 description). The inviscid linearized method SliQ gives a reasonable result for the Mach number compared to the other computations, but over predicts strongly the 5^{th} EO pressure variation. However, the good Mach number result is not regarded a reliable result because the code is not capable to compute the viscous effects. It is planned to extend the study and base the linearized SliQ computation on a steady viscous base flow.

At 90% blade height large variations in the stator exit flow are observed in the experiments, which are not computed by any of the methods. The analysis of the experiments shows that in this region, high secondary flow field effects occur (arising from a horse shoe vortex due to the inlet tip boundary layer, and a passage vortex due to the high flow deflection through the stator), causing large variations in the 5^{th} engine order exit flow harmonic. As pointed out in

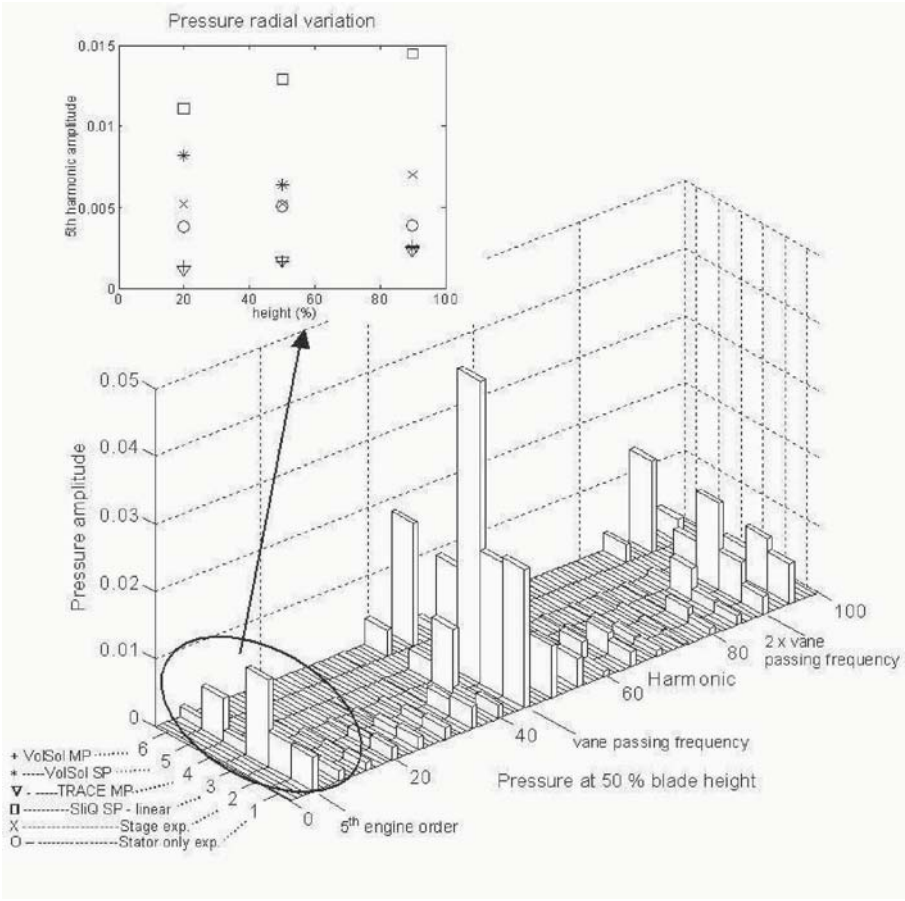

Figure 5. Pressure harmonics at 128% of $c_{ax,stator}$

the description of Strategy 1, the single passage analysis indicates that 5^{th} EO type of variation seems to change close to the tip, as the 1^{st} harmonic variation decreases, and instead the mean value variation increases. This information is not included in the harmonic analysis in Figs. 4 and 5.

5. Conclusions and Future Work

1. At midspan, the differences in the stator exit flow boundary conditions between stage and stator only experiments are more significant for the vane passing frequency than in the Low Engine Order frequency. Closer to the endwalls, the differences become remarkable.

2. None of the modeling approaches match the measured low engine order exit flow. Only the global behavior is represented by the computations.

3. The single passage models of minimum and maximum spacing overestimate the exit flow variation at 20% and 50% of blade height. At 90% of blade height, the shift of significance from 1^{st} harmonic to the spatial average indicate the different physical effect causing the low engine order.

4. The linearized method overestimates the variation of stator exit flow. The correct prediction of viscous effects as the wake deficit can not be expected, and a reasonable applicability is only granted when viscous effects are negligible for the rotor blade excitation. Future investigations will clarify this.

5. Both multi passage viscous methods give similar results even though the codes and the modeling approaches have been different. This gives confidence in the results of this type. Nevertheless, the calculated 5^{th} EO amplitudes are significantly smaller over the whole span than those of the experimental data. The reason for this discrepancy is not yet clear - Since different scaling approaches, different meshes, and different solvers were used and still very similar results were achieved, these parameters do not seem to have a large influence on the results. Possible reasons could be connected to the large differences observed in the predicted and measured secondary flows.

6. The largest differences between the models and the experiments have been detected at 90% span. Future modeling refinements will investigate if and how these flow variations can be computed, and what influence they have on the low engine order excitation of the rotor.

7. From the present analysis it is concluded that the physical effect causing the low engine order variation is probably the higher flow acceleration in a smaller pitch passage. At 90% span, the tip secondary flow seems to be affected by the pitch variation causing large changes in the stator exit flow field. Future analyses of the flow field will clarify this.

8. The computed harmonics will be used for unsteady rotor computations to estimate the unsteady rotor blade pressure, which will be compared to measured data as soon as available. The importance of different physical effects on the low engine order excitation will be estimated.

Acknowledgments

This work was initiated and supported by the European Community under the "Competitive and Sustainable Growth" Programme (1998 - 2002) in the Project "Aeroelastic Design of Turbine Blades II" (ADTurBII), contract number G4RD-CT- 2000-00189.

The opportunity to use the codes SliQ provided by Rolls-Royce plc and VolSol provided by Volvo Aero Corporation, Sweden is gratefully acknowledged. We also want to thank all collaborators who contributed to the present work, especially Jeff Green and Robert Elliott from Rolls-Royce plc for their project management and support with ideas and Christian Lenherr from ETH Zurich for the multi passage VolSol computations during his student project.

References

[1] Jay, R. L., Fleeter, S., Unsteady Aerodynamic Measurements in Forced Vibration Research, *AGARD Manual on Aeroelasticity in Axial Flow Turbomachines*, AGARD-AG-298, ISBN 92-835-0467-4, edited by Platzer, M. F., Carta F. O., 1988.

[2] Jöcker, M., Freudenreich, K., Rehder, H. J., Fransson, T. H., Parametric Studies of the Aerodynamic Excitation in High Pressure Turbines, *Proceedings of 9th International Symposium on Unsteady Aerodynamics, Aeroacoustics and Aeroelasticity of Turbomachines*, Lyon, France, 2000, ISBN: 2 7061 1052 X.

[3] Manwaring, S. R., Kirkeng, K. L., Forced Response Vibrations of a LP Turbine Due to Circumferential Temperature Distortions, *Proceedings of the 8th International Symposium on Unsteady Aerodynamics, Aeroacoustics and Aeroelasticity of Turbomachines*, Stockholm, Sweden, 1997, Kluwer Academic Publishers, ISBN: 0-7923-5040-5.

[4] Vahdati, M., Sayma, A., Imregun, M., Prediction of High and Low Engine Order Forced Responses for an LP Turbine Blade, AIAA Paper AIAA-98-3719, 1998.

[5] Bréard, C., Imregun, M., Green, J., Elliott, R., A Study of Low Engine Order Excitation in Turbomachines, *Proceedings of 9th International Symposium on Unsteady Aerodynamics, Aeroacoustics and Aeroelasticity of Turbomachines*, Lyon, France, 2000, ISBN: 2 7061 1052 X.

[6] Marshall, J.G., Chew, J.W., Xu, L., Denton, J., Prediction of Low Engine Order Inlet Distortion Driven Resonance in a Low Aspect Ratio Fan, ASME paper 2000-GT-0374, 2000.

[7] Freudenreich, K., Jöcker, M., Rehder, H.-J., Höhn, W., Fransson, T. H., Aerodynamic Performance of Two Isolated Turbine Stators in Transonic Annular Cascade Flow, 3rd European Conference on Turbomachinery - Fluid Dynamics and Thermodynamics, London, 2-5 March, 1999.

[8] Kato, M., Launder, D., The Modeling of Turbulent Flow Around Stationary and Vibrating Square Cylinders, 9th Symposium on Turbulent Shear Flows, August 16-18, 1993.

[9] Eriksson, L. E., A Third Order Accurate Upwind-Biased Finite Volume Scheme for Unsteady Compressible Flow, *VFA report 9370-154*, Volvo Aero Corporation, Trollhättan, Sweden, 1990.

[10] Eriksson, L. E., Development and Validation of Highly Modular Flow Solver Versions in G2DFLOW and G3DFLOW Series for Compressible Viscous Reacting Flow, *Technical Report 9970-1162*, Volvo Aero Corporation, Sweden, 1995.

[11] Giles, M., An Approach for Multi-Stage Calculations Incorporating Unsteadiness, ASME paper No. 92-GT-282, 1992.

[12] Marshall, J. G., Giles, M. B., Some Applications of a Time-Linearized Euler Method to Flutter and Forced Response in Turbomachinery, *Proceedings of the 8th International Symposium on Unsteady Aerodynamics, Aeroacoustics and Aeroelasticity of Turbomachines*, Stockholm, Sweden, 1997, Kluwer Academic Publishers, ISBN0-7923-5040-5.

[13] Fritsch, G., Hoeger, M., Blaha, C., Bauer, D., Viscous 3D Compressor Simulations in Parallel Architectures - Design Tool Development and Application to a Transonic Compressor Stage, AIAA-paper 97-2876, 1997.

EXPERIMENTAL REDUCTION OF TRANSONIC FAN FORCED RESPONSE BY IGV FLOW CONTROL

S. Todd Bailie, Wing F. Ng,
Department of Mechanical Engineering
Virginia Polytechnic Institute & State University
Blacksburg, Virginia

William W. Copenhaver
U.S. Air Force Research Lab
Propulsion Directorate
Wright-Patterson AFB, Ohio

Abstract The main contributor to the high-cycle fatigue of compressor blades is the response to aerodynamic forcing functions generated by an upstream row of stators or inlet guide vanes. Resonant response to engine order excitation at certain rotor speeds is especially damaging. Studies have shown that flow control by trailing edge blowing (TEB) can reduce stator wake strength and the amplitude of the downstream rotor blade vibrations generated by the unsteady stator-rotor interaction. In the present study, the effectiveness of TEB to reduce forced blade vibrations was evaluated in a modern single-stage transonic compressor rig. A row of wake generator (WG) vanes with TEB capability was installed upstream of the fan blisk, the blades of which were instrumented with strain gauges. Data was collected for varied TEB conditions over a range of rotor speed including one fundamental and multiple harmonic resonance crossings. Sensitivity of resonant response amplitude to full-span TEB flowrate, as well as optimal TEB flowrates, are documented for multiple modes. Resonant response sensitivity was generally characterized by a robust region of substantial attenuation, such that less-than-optimal TEB flowrates could prove to be an appropriate design tradeoff. For TEB flowrates beyond the optimal region, attenuation decreased due to over-filling of the wake deficit. The fundamental crossing amplitude of the first torsion mode was reduced by as much as 85% with full-span TEB at 1.1% of the total rig flow at that speed. Similar reductions were achieved for the various harmonic crossings, including as much as 94% reduction of the second leading edge bending mode resonant response using 0.74% of the rig flow for full-span TEB. Thus the results demonstrate the effectiveness of the TEB technique for reducing rotor vibrations in the complex flow environment of a modern, closely-spaced transonic stage row.

K.C. Hall et al. (eds.),
Unsteady Aerodynamics, Aeroacoustics and Aeroelasticity of Turbomachines, 161–173.

1. Introduction

The occurrence of high cycle fatigue (HCF) failures in military turbine engines has increased dramatically in the past 25 years. HCF has been cited as the cause of 56% of USAF engine-related Class-A failures between 1982 and 1996. Additionally, HCF-related maintenance costs are estimated at more than 400 million dollars per year [1]. In response to this alarming trend, many recent research efforts have focused on understanding and mitigating HCF problems in turbine engines.

Compressor and turbine rotor blades are particularly prone to HCF damage, as they experience continuous forced excitation. This excitation is primarily the result of unsteady flow interactions with neighboring blade rows [2, 3]. As rotor blades pass through the wakes shed by upstream stator vanes, they experience highly unsteady aerodynamic loading, inducing forced blade vibrations. Because potential flow interactions present an additional forcing function, downstream vanes can also excite rotor blade vibration. Both of these aerodynamic excitations occur at the fundamental vane passing frequency (VPF) and its harmonics, thus corresponding to fixed engine orders.

Operation at a resonance crossing, where the rotor speed is such that an engine order excitation coincides with a blade natural frequency, can be especially damaging. Because load cycles are rapidly accumulated at the high rotational speeds typical in turbomachinery, high-amplitude resonant vibrations can quickly lead to fatigue failure. Thus it is a standard, and often iterative, design practice to try to locate blade modes such that resonance crossings do not occur near the intended steady operating speed(s) of the rotor. However, rotor blades will experience multiple resonance crossings during engine run-up and run-down [2]. Accumulation of damage is consequently inevitable and, in the event that this damage exceeds material limits, a failure will occur.

Accordingly, a specific objective of the National HCF Science & Technology Program has been to damp resonant stress by 60% in fans [1]. There are two basic approaches to alter a system's forced response: either the system itself (that is, in this case, the fan blades) or the input to the system (the forcing functions) can be modified. While simply thickening the rotor blades can increase damage tolerance, the associated weight and dynamic load penalties are often unacceptable. Many research efforts have attempted to modify the system by adding damping, in various forms, to the rotor blades. While this approach has produced promising results, implementation without reducing the structural integrity of the rotor remains a challenge [4].

The forcing function can be modified in several ways. One such method, employed by von Flotow et al. [4], is to selectively impose an additional forcing function, out of phase with the original modal excitation, to produce a canceling effect. This technique can be highly effective, but must be calibrated to

target specific modes, and as such would generally be implemented only after a fatigue problem has been diagnosed. Also, to produce and control the additional forcing function, engine system complexity and performance penalties are typically increased.

An alternate method, which can be implemented without a priori knowledge of the critical resonance crossings, is to attempt to reduce the amplitude of the dominant forcing function, which is the set of wakes shed by the upstream vane row. Waitz et al. [5] discussed the feasibility of various flow control techniques for wake-reduction on curved airfoil shapes. The study concluded that the trailing edge blowing (TEB) technique should be more effective than boundary layer suction for reduction of viscous wakes. In this technique, air is ejected from the trailing edge of the wake source to reduce the mean velocity deficit and turbulent velocity fluctuations in the wake region. Morris et al. [6] studied TEB effects in a linear cascade of stator vanes, and subsequently in a 17-inch (43.2 cm) scaled fan rig, which had a rotor instrumented with strain gauges. Rotor blade stress reductions of as much as 90% were reported with TEB massflow for twenty vanes at 1.4% of the total rig flow. However, shock interaction was not present, as the rotor was operated at subsonic conditions [7].

The present study applies the TEB technique in a modern compressor rig. The compressor is a highly loaded transonic design with close stage row spacings. Thus strong shock-wake interactions are present, which have been observed to substantially increase wake depth [8]. The effects of full- and part-span IGV trailing edge blowing on rotor blade forced response have been evaluated. The present paper discusses findings from the full-span TEB experiments.

2. Description of Experiment

Stage Matching Investigation Rig

Experiments were conducted in the Stage Matching Investigation (SMI) transonic compressor rig at the Air Force Research Lab (AFRL). The rig consists of a high-speed, highly loaded rotor followed by a row of stator vanes. A row of wake generators (WGs), similar to inlet guide vanes (IGVs), is installed upstream of the rotor to simulate an embedded stage. The rig was originally designed to investigate upstream wake influences on stage flow matching [9]. However, with the adjustability of the WG forcing function and the addition of rotor-mounted strain gauges, the rig has recently proven useful for forced response experiments.

A schematic of the SMI rig flowpath with WGs installed is provided in Fig. 5. The fan is a 19-in (48.3 cm) diameter integrally bladed disk (or blisk) with 28 blades of 0.916 average aspect ratio. The rotor has a design speed

of 16,400 RPM, with hub and tip relative Mach numbers of 1.10 and 1.39, respectively. The stator row is composed of 49 vanes with 0.824 average aspect ratio. Design flow capacity is 34.5 lbm/s (15.6 kg/s), and design pressure ratio for the stage is 2.13. Additional details concerning the SMI rig design are provided in Ref. [9].

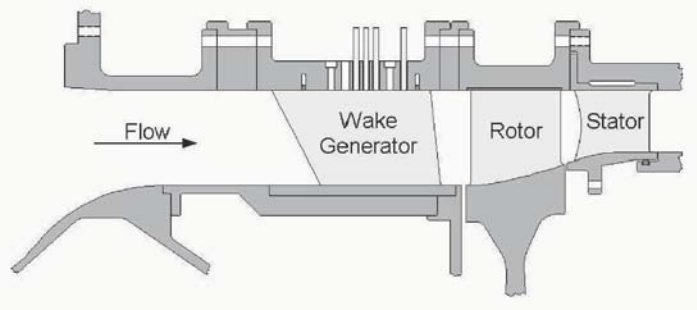

Figure 1. Cross-section of SMI transonic compressor rig

Wake Generators

The wake generators, which provide the aerodynamic forcing function in the present work, are symmetric airfoils without camber. They have a blunt trailing edge and are intended to produce wakes that are representative of the wakes shed from modern, highly loaded, low-aspect-ratio front stages. Such wakes are stronger and decay more slowly than those shed by high-aspect-ratio stages [10]. WG vane counts of 0 (clean inlet), 12, 24, or 40 may be chosen. In addition, the axial distance between the WG row and the rotor can be adjusted, via interchangeable spacers, to 12%, 26%, or 56% of the mean WG chord, which is 3.5 in (89 mm).

In the present study, the 26% chord spacing was chosen as being representative of axial gaps found in typical fans and compressors [10]. Figure 5 illustrates this spacing. To minimize the complexity of the TEB system plumbing and external compressed air consumption, the 12 WG configuration was selected. The WGs thus produce an aerodynamic gust forcing function at the twelfth engine-order (12E) and higher harmonics (24E, 36E, etc.).

Trailing Edge Blowing System

The TEB design was developed from a series of experiments in a small transonic blowdown wind tunnel at Virginia Tech. Steady velocity field measurements were taken downstream of the WG to assess the influence of discrete TEB hole size, shape, and pitchwise spacing on the wake-filling effectiveness. The tests were conducted at an inlet Mach number of 0.6. These experiments

confirmed the feasibility of TEB at high subsonic speeds and close axial distances, and led to selection of a final TEB hole configuration for the subsequent compressor rig experiments.

In order to minimize unsteady rotor blade loading, it is desirable to promote as much circumferential flowfield uniformity as possible. As such it was deemed unnecessary, even undesirable, to place TEB holes within the endwall boundary layers, which are present for the entire circumference. The selected TEB design consisted of seven blowing holes per WG, with both TE thickness-to-diameter and hole pitch-to-diameter ratios of 2.5, which provided effective coverage for almost the entire span between the endwall boundary layers.

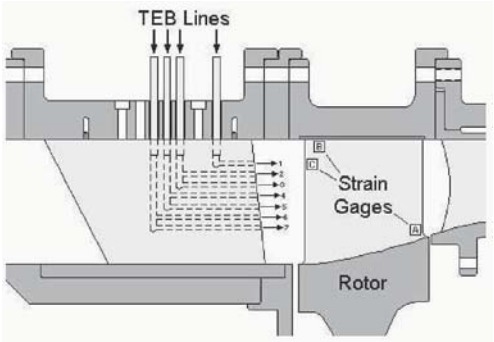

Figure 2. Detail of SMI rig showing approximate strain gauge locations and trailing edge blowing configuration.

While complete wake-filling would maximize circumferential flowfield uniformity, the compressor bleed air requirement to achieve this may be prohibitively costly to overall engine performance. It was desired to characterize the sensitivity of the forced response to the flowrate of TEB air and its spanwise distribution. Thus the TEB plumbing was designed to permit independent adjustment of flow to different spanwise sectors of holes. As shown in Fig. 5, four independent lines supplied the seven holes. One supply line fed a single tip hole, while the remaining three lines each supplied a pair of TEB holes. Maximum flow variation between paired holes was estimated to be 5%.

Because the single-stage compressor rig did not have sufficient pressure ratio to feed the flow control system by bleed recirculation, high-pressure air was supplied for TEB from external storage tanks. The flow was throttled to a typical settling tank pressure of 100 psi (690 kPa) and then independently regulated to four rig-mounted plenums, as shown in Fig. 5. Each plenum, with a typical pressure of 60 psig (414 kPa), distributed flow evenly to the same radial sector of TEB holes of all 12 WGs. Because the plumbing was designed for installation ease and experimental flexibility rather than for minimizing pressure losses, it should be noted that this high TEB supply pressure is not

representative of requirements for engine implementation. A pressure ratio of 2-3, typically achieved within two high-speed stages, should be adequate for implementing an efficient TEB design.

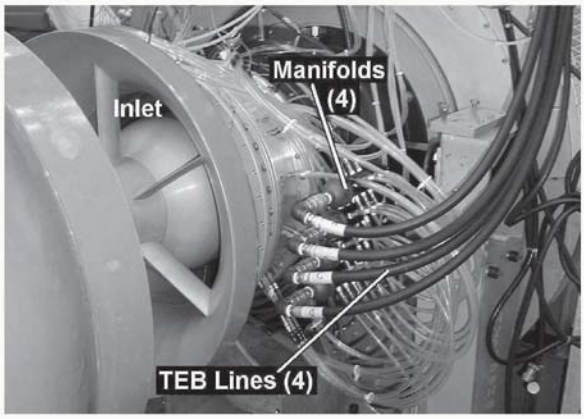

Figure 3. SMI rig assembly with TEB manifolds and tubing installed

Measurements and Data Analysis

As documented by Cheatham and Tyner [9], critical blade modes and their natural frequencies were identified by NASTRAN finite element analysis, impact testing, and holography. Stress Pattern Analysis using Thermal Emissions (SPATE) was also employed to identify areas of maximum vibratory stress for modes of interest. Three gauge locations, which offered sufficient sensitivity to the expected critical modes, were selected for vibration monitoring during subsequent rig tests.

Strain gauges were surface mounted on the pressure side of nine rotor blades at each of the three locations, which are depicted in Fig. 5. The strain gauge bridge circuitry was zero balanced and calibrated for 10 ksi (69 MPa) per signal volt. As required to maintain effective resolution of the dynamic signals while avoiding saturation due to high steady loading, the gauges were rebalanced at 80% rotor speed. The strain signals were extracted from the rotor via a slipring. These and other dynamic signals, such as a once-per-revolution key-phaser, were simultaneously recorded with a high-speed 28-channel analog tape recorder.

Several resonance crossings were identified from the Campbell diagram, shown in Fig. 5, as being potential HCF drivers for the 12-WG configuration. The fundamental 12E crossing of the first torsional mode (1T/12E) near 12,800 RPM was known to be particularly severe. Harmonic crossings were also of interest, including those of the second leading-edge bending mode (LE2B/24E)

near 13,600 RPM and the second chordwise bending mode (2C/36E) near 11,600 RPM. These crossings, as well as a pair of Mode 7 crossings, are indicated by circles in the figure. To encompass these and higher order modal crossings, a test range from 11,000 RPM to 16,000 RPM (67 - 97% of design speed) was selected.

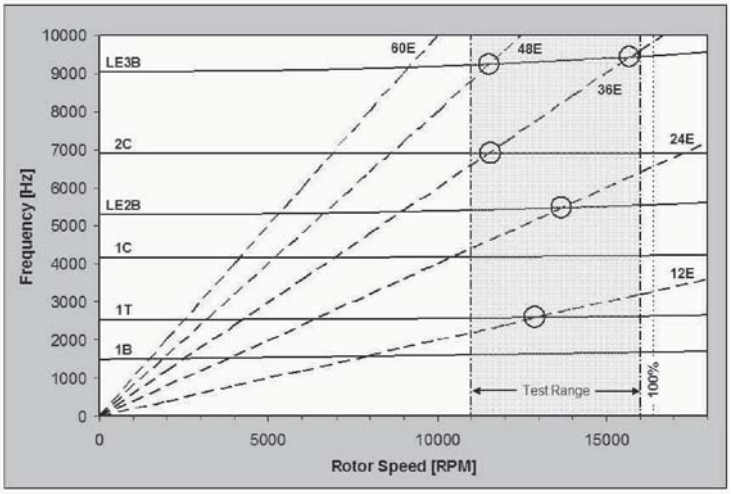

Figure 4. SMI fan Campbell diagram showing 12-WG harmonic excitations (dashed), test range (shaded) and resonance crossings (circled) within the test range

Rotor speed sweeps were conducted for a range of full- and part-span TEB fbwrates. The present discussion includes only the full-span TEB results, which correspond to uniform fbw to all 7 holes on each WG, with fbwrates ranging from 0.3% to 1.0% of the rig design fbw capacity. For each test case, data was recorded for a 45 second period, during which the rotor speed was gradually increased through the test range.

Rotor forced response data were then digitized and post-processed using an in-house engine-order tracking program. Using the key-phaser to establish the position of the rotor, the original time-sampled data were resampled at fixed rotor angle steps. As such, the resampled data always includes the same number of points per revolution, regardless of rotor speed. Upon subsequent FFT-analysis, spectral lines correspond to fixed engine-orders, or multiples of the shaft rotational frequency. Thus the effective sampling frequency, and hence the frequency associated with each spectral line, is scaled linearly with the rotational frequency. This order analysis approach has the advantage of providing precise amplitude and phase tracking of the response to known engine-order excitations (i.e. the WG wakes), as well as their higher harmonics. A detailed discussion of the computed order tracking technique is provided by Fyfe and Munck [11].

3. Results

The effectiveness of the order tracking technique for measurement of synchronous vibrations is demonstrated in Fig. 5. The various lines in the figure represent selected order components, corresponding to known aerodynamic forcing functions, from a single strain gauge signal during a single speed run-up at baseline (no TEB) conditions. As is the case for all forced response data presented here, stage loading was set by an exit flow throttle to represent a design operating line. Multiple resonance crossings are clearly characterized in the figure. In conjunction with the predicted Campbell diagram and order phase tracking, modes could be readily identified, as labeled in the figure. Additionally, with data from multiple rotor blades, scatter in blade response could be quantified, and appropriate adjustments could be made to the predicted Campbell diagram.

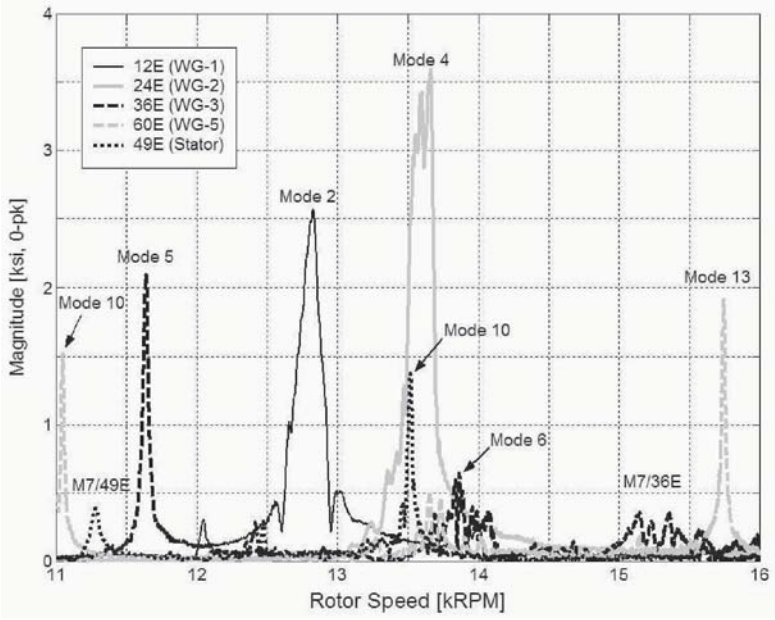

Figure 5. Baseline order tracks, showing multiple modal resonances due to upstream WG and downstream stator excitations

Basic measurement accuracy was very high, and errors added from the computed order tracking technique were found to be minimal. Measured order track amplitudes at resonance crossings from multiple gauges on the same blade, when normalized by the baseline response at that location, were found to be quite consistent with one another over the entire TEB range. This gauge-to-gauge comparison consistently yielded an error of less than one percent of the baseline response amplitude, confirming the high measurement accuracy.

Repeatability errors proved to be more significant than instrumentation errors. Thus repeatability in resonance crossing amplitude was used to quantify overall uncertainty in the rotor stress measurements. Considering multiple rotor speed sweeps, both upwards and downwards, and including widely varying sweep rates, resonance crossing amplitude was found to be repeatable within $\pm$ 3 percent for back-to-back data. However, day-to-day variability in crossing response amplitude was found to be as much as 10 percent. Since aerodynamic damping is much stronger than structural damping for the rotor blisk, variations in the atmospheric conditions and stage loading, due to poor repeatability of the throttle position, are believed to account for the increased variability. Thus, to minimize uncertainty, all data presented are from a back-to-back series of runs.

By stacking 12E order tracks for successive TEB flowrates against the baseline data, as shown in Fig. 6, the strong effect of flow control on resonant response is demonstrated. The surface plot at right provides an overview of the entire test domain, with the baseline 1T/12E resonance dominating in the foreground. The line plot at left compares selected slices of the same data to provide a more detailed view of the local effects at resonance. Data in the figure is taken from the most responsive of the measured blades, with a peak baseline response of 39.7 ksi (274 MPa) peak-to-peak (p-p), well above the design scope limit (from [9]) for that gauge location.

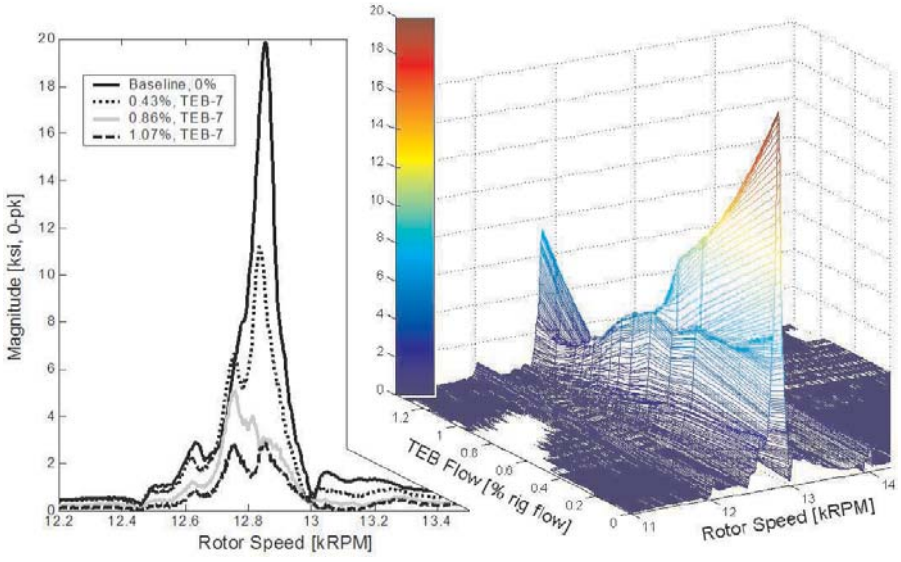

Figure 6. Effect of TEB on critical blade response at the 1T/12E resonance crossing

Application of increasing TEB flowrate is shown to progressively attenuate the first torsion response. Using a total of 1.07% of the rig inlet flow at the

crossing speed, the 1T response was limited to 5.8 ksi (40MPa) p-p on this blade, a reduction of 85%.

A secondary peak is also seen to emerge when TEB is applied. This peak is also attenuated, though not as sharply as the primary peak for the critical blade. A similar multi-peak characteristic was often observed for other blades and at other modal crossings, such as the labeled Modes 4 and 7/36E in Fig. 5 for a different blade. In some cases, more than two distinct peaks were noted at a crossing. This behavior, as well as the large blade-to-blade variability observed in maximum crossing amplitude, is believed to be caused by the complex coupled interaction between neighboring mistuned blades.

Resonant amplitude data from four blades were normalized and averaged for the 1T/12E and LE2B/24E crossings, as presented in Figs. 5 and 5, respectively. Amplitudes are normalized by the baseline crossing amplitude for each respective gauge used in the average, while TEB flowrates are normalized by the corrected rig inlet flow for the speed at which the respective crossing occurs. In addition to the four-blade-average data, the data from the blade with the highest baseline response is shown. Bars are included to illustrate the range of responses for the measured blades. It is noted that the maximum attenuation occurs on the critical blade for both crossings.

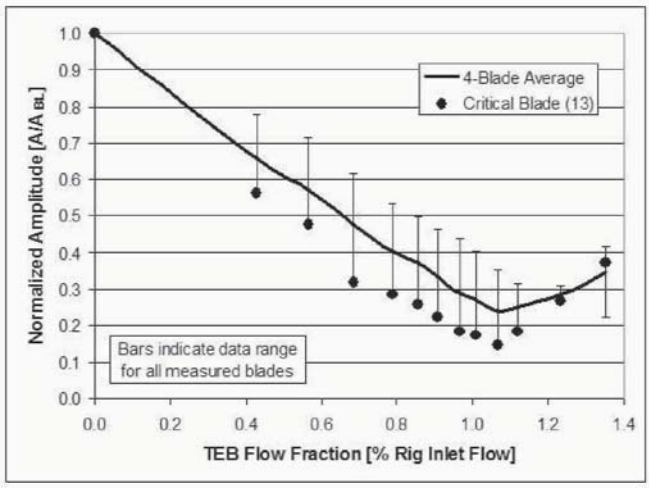

Figure 7. Effect of full-span TEB flowrate on first-torsion resonant response

As clearly illustrated in Figs. 6-5, the resonant response amplitude exhibits a saddle-type trend over the range of TEB flowrate. For increasing TEB flow, resonant response is attenuated until a minimum crossing response is achieved, at what is considered the optimal flowrate for that particular resonance crossing. If flow is further increased beyond this saddle point, referred to as overblow-

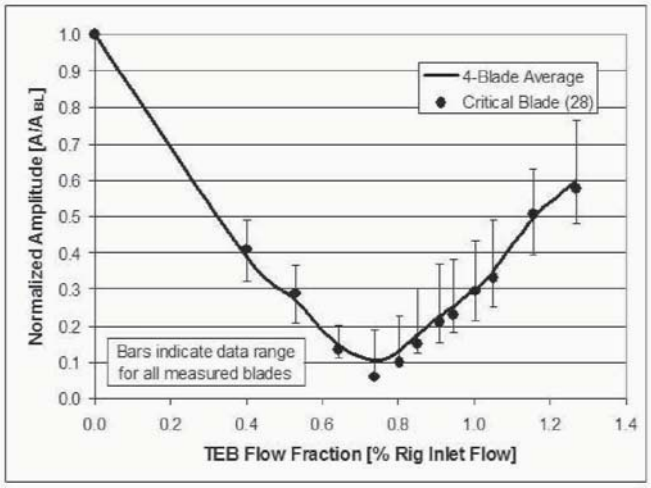

Figure 8. Effect of full-span TEB flowrate on LE2B/24E resonant response

ing, the crossing response begins to increase. In the event of substantial overblowing, the response can exceed that of the baseline case.

This inflection behavior, which was generally noted for all the measured crossings, is expected. The saddle point occurs when the offending forcing function harmonic passes through a minimum amplitude. Here the forcing function harmonic experiences a phase reversal, which corresponds conceptually to the original wake velocity deficit being replaced with a surplus. A phase reversal is accordingly noted in the harmonic response, which, like the forcing function harmonic, begins to increase in amplitude for overblowing.

It is noted that substantial attenuation in resonant amplitude, roughly proportional to the TEB flowrate, is achieved at less-than-optimal flowrates. This point should not be lost on the designer seeking an appropriate compromise between forced response mitigation and engine performance.

Based on the four-blade-average data, the maximum attenuation at the 1T/12E crossing was 76% using 1.07% of the rig flow for TEB. A maximum average attenuation of 89% was achieved at the LE2B/24E crossing using 0.74% of the rig flow. Table 1 summarizes the maximum reductions from the critical blade at these and other resonance crossings. In most cases, the 60% attenuation goal established for the National HCF Program [1] was exceeded.

Significant TEB sensitivity is only expected for resonance crossings involving excitation orders associated with the wake forcing function directly modified by TEB. Correspondingly, resonance amplitudes from crossings of the 49E order, an excitation produced by potential interaction with the 49 downstream stator vanes, were not significantly affected by the application of TEB. While

Table 1. Summary of maximum reductions in modal resonance amplitude by TEB.

Blade Mode		Excitation	Crossing	Critical Blade Response		TEB Flowrate
Number	Name	Order	RPM	Base [ksi, p-p]	Reduction [%]	[% rig flow]
2	1T	12E	12854	39.7	85	1.07
4	LE2B	24E	13568	11.0	94	0.74
5	2C	36E	11602	4.6	82	0.64
7	LE3B	36E	15392	18.0	53	0.46
7	LE3B	48E	11456	2.0	85	0.49
10	TE2B	48E	13594	5.1	90	0.73
12	LE4B	60E	13446	3.9	62	0.85

this forcing function could not be attenuated by TEB, it is worth noting that the 49E potential excitation is very weak in comparison to the viscous excitation originating upstream of the rotor. It was found that the blade response to the fundamental stator excitation was generally so small as to only be comparable to that produced by the fourth (48E) or fifth (60E) harmonics of the WG excitation.

Despite close blade row spacing and the presence of strong rotor bow shocks, substantial stress reductions were achieved at multiple resonance crossings in the present study. These results also compare favorably to those previously documented. Morris et al. [6] reported stress reductions on a high-subsonic rotor of 90% for chordwise bending (1C), and 43% for the third leading edge bending mode (LE3B). While the total TEB-to-rig massfbw ratio for the Morris experiments was greater than the optimal fbwrates determined in the present study, the fbw ratio was similar on a per-vane basis.

4. Conclusions

The TEB fbw control technique was implemented in row of wake generator (WG) vanes, placed just upstream of a modern highly loaded transonic fan stage. The WGs produced fundamental and harmonic engine order excitations that caused numerous resonance crossings in the tested range of the compressor. Rotor stress measurements confirmed that the TEB technique can be quite effective for reducing resonant rotor response, even with close blade row spacing and strong rotor bow shocks sweeping the WG trailing edge.

In most cases, the National HCF Program's goal of 60 percent reduction in resonant response was exceeded. Reductions of as much as 85% and 94% were achieved by TEB for the first torsion and second LE bending modes, respectively, while reductions at higher modal crossings were also substantial. While resonant response sensitivity to TEB fbwrate was shown to have

a saddle behavior, the characteristic was approximately linear for sub-optimal flowrates, which may provide an appropriate design tradeoff with respect to overall system-level performance.

Acknowledgments

The authors gratefully acknowledge the support of Mr. Oral Mehmed and NASA Glenn Research Center (GRC). The authors are especially indebted to the entire staff of the Compressor Aero Research Lab for their many useful suggestions as well as patient assistance provided during experiments. The support afforded the primary author by an NSF Graduate Research Fellowship is also duly acknowledged.

References

[1] Garrison, B., Editor. High Cycle Fatigue (HCF) Science and Technology Program 2000 Annual Report. Technical Report AFRL-PR-WP-TR-2001-2010, Air Force Research Lab, WPAFB, OH, 2001.

[2] Rao, J. S. *Turbomachine Blade Vibration*. Wiley Eastern Limited, New Delhi, India, 1991.

[3] Manwaring, S. R. and Wisler, D. C. Unsteady Aerodynamic and Gust Response in Compressors and Turbines. *ASME J. of Turbomachinery*, 115:724–40, 1993.

[4] von Flotow, A., Tappert, P., and Mercadal, M. HCF Active Control: An Active Wake Management Implementation Manual. In *The 6th National Turbine Engine High Cycle Fatigue (HCF) Conference*, Jacksonville, FL, 2001.

[5] Waitz, I. A., Brookfield, J. M., Sell, J., and Hayden, B. J. Preliminary Assessment of Wake Management Strategies for Reduction of Turbomachinery Fan Noise. *AIAA J. of Propulsion and Power*, 12(5):958–66, 1996.

[6] Morris, R. J., Benedict, B. K., and Cowles, B. A. Active Structural Control for Gas Turbine Engines. ASME Paper 98-GT-514, 1998.

[7] Benedict, B. K. Personal communication, 2001.

[8] Kozak, J. D. *Steady and Unsteady Aerodynamic Investigation of Inlet Guide Vane Trailing-Edge Blowing Flow Control in a F109 Turbofan Engine*. PhD thesis, Virginia Polytechnic Institute & State University, Blacksburg, Virginia, 2000.

[9] Cheatham, J. G. and Tyner, T. M. Stage Matching Investigation. Technical Report WL-TR-91-2098, Aero Propulsion and Power Directorate, Wright Laboratory, WPAFB, OH, 1992.

[10] Gorrell, S. E., Copenhaver, W. W., and Chriss, R. M. Upstream Wake Influences on the Measured Performance of a Transonic Compressor Stage. *AIAA J. of Propulsion and Power*, 17(1):43–8, 2001.

[11] Fyfe, K. R. and Munck, E. D. S. Analysis of Computed Order Tracking. *Mechanical Systems and Signal Processing*, 11(2):187–205, 1997.

III

MULTISTAGE EFFECTS

UNSTEADY AERODYNAMIC WORK ON OSCILLATING ANNULAR CASCADES IN COUNTER ROTATION

Combination of Supersonic and Subsonic Cascades

M. Namba
Sojo University
Ikeda, Kumamoto, 860-0082, Japan
namba@arsp.sojo-u.ac.jp

K. Nanba
Sojo University
nanba@arsp.sojo-u.ac.jp

Abstract The paper studies the effect of neighboring blade rows on unsteady aerodynamic force due to blade vibration and on flutter characteristics of cascading blades. For this purpose the computation program to calculate the unsteady blade loading based on the unsteady lifting surface theory for contra-rotating annular cascades was formulated and coded. Numerical examples of unsteady aerodynamic works for various combinations of cascades, i.e., subsonic-subsonic, supersonic-supersonic, and subsonic-supersonic cascades, are presented. It is clearly shown that the difference in the unsteady aerodynamic work on vibrating blades between the case of the decoupled cascade and the case of the aerodynamically coupled cascades is large when the neighbor cascade is supersonic. A computation program to solve the coupled bending-torsion flutter equation for the contra-rotating annular cascades was also developed. Some results of the flutter analysis are presented. The presence of the neighboring blade row gives rise to significant change in the critical flutter fluid velocity for the subsonic cascade when the main acoustic duct mode is of cut-on state.

Keywords: Cascade Flutter, Multiple Blade Rows, Unsteady Aerodynamics, Aeroelasticity

Introduction

The unsteady aerodynamic force on oscillating blades in a cascade is heavily dependent on the interblade phase angle. This implies that the aerodynamic coupling among blades plays a critical role on the cascade flutter characteris-

K.C. Hall et al. (eds.),
Unsteady Aerodynamics, Aeroacoustics and Aeroelasticity of Turbomachines, 177–188.

tics. From this standpoint neighboring blade rows, e.g., a neighboring rotor or stator or contra-rotating fan cascade, also will have a considerable influence on the unsteady aerodynamic force because blade rows are closely placed in actual turbomachines.

There are available a few published papers dealing with the influence of neighboring blade rows on the unsteady aerodynamic response of oscillating blades. The theoretical study based on the semi-actuator disk model by Tanida [1] and the experiments and the linear cascade theory by Kobayashi et al. [2, 3] should be cited as the earliest works. Their theories assume incompressible flows and therefore can not deal with aeroacoustic interaction between blade rows via cut-on acoustic duct modes. Butenko and Osipov [4] developed a theory for subsonic linear cascades in relative motion. Recently Hall and Silkowski [5] presented an analysis based on two-dimensional subsonic multiple blade rows, and Namba et al. [6] developed a three-dimensional theory for oscillating subsonic contra-rotating annular cascades. Those studies for subsonic flows indicate that the influence of aeroacoustic coupling among blade rows on the aerodynamic damping force is significant in particular when the main acoustic duct mode generated from the oscillating blade row is cut-on. It suggests that in the case of supersonic cascades, where oscillation of blades generates an infinite number of cut-on modes, neighboring blade rows will be much more influential.

The author [7] extended his study to supersonic contra-rotating annular cascades, where relative mean fluid velocities for both cascades are supersonic, and gave numerical results showing a cruicial difference in unsteady aerodynamic work on oscillating blades between aerodynamically decoupled and coupled cascades. However some bugs which result in exaggeration of the difference were later found in the computation codes.

The program has been improved and further extended so that it can deal with the combination of supersonic and subsonic cascades, for instance, a supersonic rotor cascade and a subsonic stator cascade. This paper gives some numerical results and investigates the influence of a neighboring blade row on unsteady aerodynamic work on vibrating blades for various combinations of cascades.

The present computation program based on the unsteady lifting surface theory [8, 9] is able to provide aerodynamic forces on oscillating blades as functions of the frequency. The compuation speed is remarkably high, so that it can be a very efficient tool to calculate aerodynamic force terms of the flutter equations. A computation program to solve the coupled bending-torsion flutter equation for the contra-rotating annular cascades was also formulated and coded. This paper presents some results of the flutter analysis demonstrating the significant influence of the neighboring blade row on the flutter boundaries.

1. Outline of the Analytical Method

1.1 Model Description

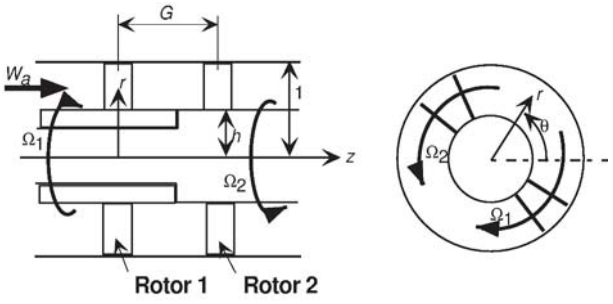

Figure 1. Contra-rotating annular cascades

We consider a pair of annular cascades in an annular duct of infinite axial extent with the outer duct radius r_T^* and the boss ratio h as shown in Figure 1. The undisturbed flow is a uniform axial flow of axial velocity W_a^*, static pressure p_0^* and fluid density ρ_0^*. In the following unstarred symbols denote dimensionless quantities, where lengths, velocities, pressures and times are scaled with respect to r_T^*, W_a^*, $\rho_0^* W_a^{*2}$ and r_T^*/W_a^*, respectively. Let subscripts 1 and 2 denote the upstream rotor 1 and the downstream rotor 2. Further following notations are used: N_{B1} and N_{B2}: numbers of blades, $\Omega_1 = \Omega_1^* r_T^*/W_a^* (\geq 0$, clockwise looking from a downstream station) and $\Omega_2 (\leq 0$, anti-clockwise): rotational angular velocities of the rotors, C_{a1} and C_{a2}: axial chord length assumed constant along the span, (r, θ, z), (r, θ_1, z_1) and (r, θ_2, z_2): cylindrical coordinates fixed to the duct, rotor 1 and rotor 2 respectively. The angle coordinates and axial coordinates of different frames are related to each other by

$$\theta = \theta_1 - \Omega_1 t = \theta_2 - \Omega_2 t, \quad z = z_1 = z_2 + G. \tag{1}$$

Here t denotes the time coordinate and G denotes the axial distance between the centers of rotor 1 and rotor 2.

We assume that the steady blade loading is zero, i.e., the time mean flow is uniform, and that the unsteady disturbances induced by blade vibrations are small. Therefore the unsteady flow is governed by linearized equations.

1.2 Multiplication of Blade Loading Frequency

Assume that the blades of rotor 1 are vibrating with a single frequency ω_{10} and an inter-blade phase angle $2\pi\sigma_{10}/N_{B1}$, so that the displacement normal to

the blade chord of the m-th blade is given by

$$a_1(r,z)e^{i\omega_{10}t+i2\pi\sigma_{10}m/N_{B1}} : \ m=0,1,...,N_{B1}-1. \tag{2}$$

Here σ_{10} is an integer between $-N_{B1}/2$ and $N_{B1}/2$.

Then as described in details in references [6, 7], aeroacoustic coupling between the rotors in mutual motion produces flow disturbances of multiple frequencies, resulting in blade loading of multiple frequencies. Thus we can describe the unsteady blade loading (pressure difference between upper and lower surfaces of blades) on the m-th blade of each rotor as summations of multiple frequency components:

$$\begin{gathered}\sum_{\nu=-\infty}^{\infty}\Delta p_{1-1,(\nu)}(r,z_1)e^{i\omega_{1\nu}t+i2\pi\sigma_{1\nu}m/N_{B1}} \\ \text{and} \\ \sum_{\mu=-\infty}^{\infty}\Delta p_{2-1,(\mu)}(r,z_2)e^{i\omega_{2\mu}t+i2\pi\sigma_{2\mu}m/N_{B2}},\end{gathered} \tag{3}$$

where

$$\omega_{1\nu}=\omega_{10}-\nu N_{B2}(\Omega_1-\Omega_2), \quad \sigma_{1\nu}=\nu N_{B2}+\sigma_{10}, \tag{4}$$

$$\omega_{2\mu}=\omega_{10}+(\mu N_{B1}+\sigma_{10})(\Omega_1-\Omega_2), \quad \sigma_{2\mu}=\mu N_{B1}+\sigma_{10}. \tag{5}$$

Further subscripts 1-1 and 2-1 imply the loading on rotor 1 blades due to vibration of rotor 1 blades themselves and the loading on rotor 2 blades due to vibration of rotor 1 blades respectively. It is worth emphasizing that all frequency components are coupled with each other and can not be determined independently.

In the case of blade vibration of rotor 2 with displacement normal to blade surface given by

$$a_2(r,z_2)e^{i\omega_{20}t+i2\pi\sigma_{20}m/N_{B2}} : \ m=0,1,...,N_{B2}-1, \tag{6}$$

similar formulations can be made, and the blade loadings may be written as

$$\begin{gathered}\sum_{\nu=-\infty}^{\infty}\Delta p_{2-2,(\nu)}(r,z_2)e^{i\omega_{2\nu}t+i2\pi\sigma_{2\nu}m/N_{B2}} \\ \text{and} \\ \sum_{\mu=-\infty}^{\infty}\Delta p_{1-2,(\mu)}(r,z_1)e^{i\omega_{1\mu}t+i2\pi\sigma_{1\mu}m/N_{B1}},\end{gathered} \tag{7}$$

where

$$\omega_{2\nu}=\omega_{20}-\nu N_{B1}(\Omega_2-\Omega_1), \quad \sigma_{2\nu}=\nu N_{B1}+\sigma_{20}, \tag{8}$$

$$\omega_{1\mu}=\omega_{20}+(\mu N_{B2}+\sigma_{20})(\Omega_2-\Omega_1), \quad \sigma_{1\mu}=\mu N_{B2}+\sigma_{20}. \tag{9}$$

1.3 Acoustic Modes and Frequencies

In the present problem disturbances are composed of multiple frequencies and multiple acoustic duct modes. The frequencies $\omega_{\nu,\mu}$ viewed in the frame fixed to the duct, i.e., (r, θ, z) system, and corresponding circumferential wave numbers $n_{\mu,\nu}$ of the duct modes are given in Table 1. Hereafter we denote the

Table 1. Frequencies and circumferential wave numbers of duct modes

Case	Frequency $\omega_{\mu,\nu}$	Wave number $n_{\mu,\nu}$
Vibration of rotor 1	$\omega_{10} + \mu N_{B1}\Omega_1 + \nu N_{B2}\Omega_2 + \sigma_{10}\Omega_1$	$\mu N_{B1} + \nu N_{B2} + \sigma_{10}$
Vibration of rotor 2	$\omega_{20} + \mu N_{B2}\Omega_2 + \nu N_{B1}\Omega_1 + \sigma_{20}\Omega_2$	$\mu N_{B2} + \nu N_{B1} + \sigma_{20}$

acoustic duct mode of $(n_{\mu,\nu}, \ell)$ by $(\mu, \nu;\ \ell)$, where ℓ denotes the radial order. A mode $(\mu, \nu;\ \ell)$ is cut-on if

$$\left(k_\ell^{(n_{\mu,\nu})}\right)^2 - \omega_{\mu,\nu}^2 M_a^2/(1 - M_a^2) < 0, \tag{10}$$

where $k_\ell^{(n)}$ denotes the radial eigenvalue [7].

Under this notation we can state that vibrating blades directly generate$^{(\mu,0;\ell)}$ modes. If all of these modes are cut-off and if the rotors are remotely separated, the influence of the neighboring blade row will not be substantial. We should note, however, that vortical disturbances are convected without decaying. Therefore in the case of vibration of rotor 1, the vortical disturbances from rotor 1 always exert a finite influence on rotor 2 even if all original modes $(\mu, 0;\ \ell)$ are cut-off and however large the rotor-to-rotor distance G may be. Further, any of the modes of $\nu \neq 0$ resulting from the interaction can be cut-on, giving backward reaction to rotor 1. The previous studies [6] indicate, however, that the vortical disturbances play only a minor role in the aerodynamic interaction between the blade rows.

Note that $\Omega_1\Omega_2 < 0$ in the case of contra-rotating cascades. Therefore duct modes of $\mu\nu > 0$ are of high frequency and low circumferential wave number, and are likely to satisfy the cut-on condition (10).

1.4 Solution Philosophy

The lifting surface theory represents the disturbance flow field as summation of disturbances induced by unsteady blade loadings of both rotors. The disturbance flow quantities are mathematically expressed in integral forms involving blade loading functions $\Delta p_{1-1,(\nu)}(r, z)$, etc. Once the blade loading functions are determined, the disturbance flow quantities are obtained by straightforward computation of the integrals.

In the present problem the blade loading functions are not prescribed but are unknown functions to be determined. The flow tangency condition at the blade surfaces gives a set of simultaneous integral equations for the unsteady blade loading functions $\Delta p_{1-1,(\nu)}(r,z)\ :\ \nu = 0, \pm 1, \pm 2, ...$ and $\Delta p_{2-1,(\mu)}(r,z)\ :\ \mu = 0, \pm 1, \pm 2, ...$ (the case of rotor 1 vibration), or $\Delta p_{1-2,(\mu)}(r,z)\ :\ \mu = 0, \pm 1, \pm 2, ...$ and $\Delta p_{2-2,(\nu)}(r,z)\ :\ \nu = 0, \pm 1, \pm 2, ...$ (the case of rotor 2 vibration) [6, 7]. There are available various methods to solve the equations numerically. A method based on combination of Galerkin formulation and expansion of blade loading functions in terms of double mode function series is applied to the present study. Details are omitted to save space.

1.5 Unsteady Aerodynamic Force and Work

In order to evaluate the frequency components of unsteady blade loadings, we use 'complex' work coefficients defined by

$$CW_{j-k,(\mu)} = \pi \int_h^1 \sqrt{1+\Omega_j^2 r^2} \times \int_{-C_{aj}/2}^{C_{aj}/2} \Delta p_{j-k,(\mu)}(r,z_j)\overline{a_j(r,z_j)}dz_j, \tag{11}$$

where an overlined symbol denotes the complex conjugate.

Then the aerodynamic work per cycle on the vibrating blades of rotor 1 or rotor 2 is given by the imaginary part of $CW_{1-1.(0)}$ or $CW_{2-2,(0)}$ respectively. Therefore If $\Im[CW_{1-1,(0)}] > 0$ or $\Im[CW_{2-2,(0)}] > 0$, the vibration is aerodynamically excited.

1.6 Coupled Bending-Torsion Flutter Analysis

The mathematical formulations of the coupled bending-torsion flutter analysis for the contra-rotating annular cascades are essentially same as conventional formulations for a single airfoil model except the aerodynamic force terms which include not only blade-to-blade aerodynamic coupling effects but also the effects of aerodynamic interaction between blade rows. The final form of the flutter equation can be written as

$$\left[\boldsymbol{K} - \lambda^2(\boldsymbol{M}+\boldsymbol{S}) - \boldsymbol{A}\right]\boldsymbol{q} = 0. \tag{12}$$

Here $\boldsymbol{M}$, $\boldsymbol{S}$, $\boldsymbol{K}$ and $\boldsymbol{A}$ are generalized mass, static mass moment, stiffness and aerodynamic force matrices respectively, and $\boldsymbol{q}$ is a column matrix of the modal displacement amplitudes. Further λ is the reduced frequency defined by

$$\lambda = \frac{\omega C_a}{W_a}. \tag{13}$$

Note that the generalized aerodynamic force matrix $\boldsymbol{A}$ is complex.

In the present study equation (12) is further rearranged into the form

$$[\boldsymbol{C} - X\boldsymbol{I}]\,\boldsymbol{q} = 0. \tag{14}$$

Here $\boldsymbol{C}$ is a complex matrix and $\boldsymbol{I}$ is a unit matrix. Further

$$X = \frac{\omega_{B1}^2}{\omega^2}, \tag{15}$$

and ω_{B1} denotes the natural circular frequency for the first order bending mode. Then X and $\boldsymbol{q}$ can be determined as eigenvalues and eigenvectors of the matrix $\boldsymbol{C}$.

Let all elastic and aerodynamic parameters other than λ be specified. Then the eigenvalues $X^{(m)}(\lambda):\ (m = 1, 2, \ldots)$ are functions of λ. Put

$$\frac{1}{\sqrt{X^{(m)}(\lambda)}} = f^{(m)}(\lambda) + ig^{(m)}(\lambda). \tag{16}$$

Then the m-th flutter mode is critical at the reduced frequency $\lambda = \lambda_F^{(m)}$ that satisfies

$$g^{(m)}(\lambda_F^{(m)}) = 0. \tag{17}$$

The m-th mode flutter velocity and flutter frequency are given by

$$W_{aF}^{(m)} = C_a \omega_{B1} \frac{f^{(m)}(\lambda_F^{(m)})}{\lambda_F^{(m)}}, \tag{18}$$

$$\omega_F^{(m)} = \omega_{B1} f^{(m)}(\lambda_F^{(m)}). \tag{19}$$

Note that to search the condition (17) we should compute the aerodynamic force terms for various values of λ. To this end computation by CFD may be too time-consuming. On the other hand the present analytical method is a very useful aerodynamic tool, which can provide numerical values of aerodynamic force terms for a specified reduced frequency within a few seconds on a modern personal computor.

2. Numerical Results and Discussion

2.1 Unsteady aerodynamic Work on Oscillating Blades

The results presented in this paper are restricted to cases where blades of rotor 1 (located upstream) are vibrating in a bending mode. The blade displacement function is assumed as

$$a_1(r, z_1) = H_1 C_{a1} h_1(r) / \sqrt{1 + \Omega_1^2 r^2}, \tag{20}$$

where $h_1(r)$ denotes the mode shape of bending displacement of order 1 of a uniform canti-lever beam. In all cases the axial Mach number and the boss ratio are fixed to $M_a = 0.6$ and $h = 0.7$ respectively. Further four cases shown in Table 2 are dealt with. Note that the relative flow velocity for the rotor blades is supersonic along the whole span for $|\Omega_1| = 3.0$ or $|\Omega_2| = 3.0$, and subsonic along the whole span for $|\Omega_1| = 1.0$ or $|\Omega_2| = 1.0$. In all cases the distance between the blade raw centers is fixed to $G = 2.0C_a$, where $C_a = (C_{a1} + C_{a2})/2$.

Table 2. Specified conditions

Case	N_{B1}	Ω_1	C_{a1}	N_{B2}	Ω_2	C_{a2}
sub-sub	40	1.0	0.1	40	-1.0	0.1
sub-sup	40	1.0	0.1	30	-3.0	0.0633
sup-sub	30	3.0	0.0633	40	-1.0	0.1
sup-sup	30	3.0	0.0633	30	-3.0	0.0633

Figures 2 - 5 demonstrate unsteady aerodynamic work coefficient $\Im[CW_{1-1,(0)}]$ as a function of the interblade phase parameter σ_{10} at a reduced frequency $\omega C_{a1} = 0.5$. In each figure comparison with the aerodynamically decoupled case (an isolated rotor cascade) is shown. Cut-on or cut-off regions of relevant duct modes are also indicated in the figures. First of all it should

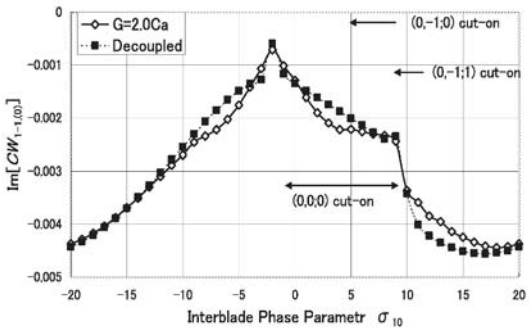

Figure 2. Case sub-sub. Modes $(1, -1;\ \ell)$ and $(-1, 1;\ \ell)$ of $\ell = 0,\ 1$ are cut-on everywhere

be pointed out that duct modes $(-1, 1; \ell)$ and $(1, -1; \ell)$ of $\ell = 0$ and $\ell = 1$ are cut-on in the whole region of σ_{10} in all cases. As a phenomenon common to both cases sub-sub (Figure 2) and sub-sup (Figure 3) the influence of the neighboring blade row, i.e., the difference in the aerodynamic work between the case of decoupled blade row and the case of coupled blade rows, is large

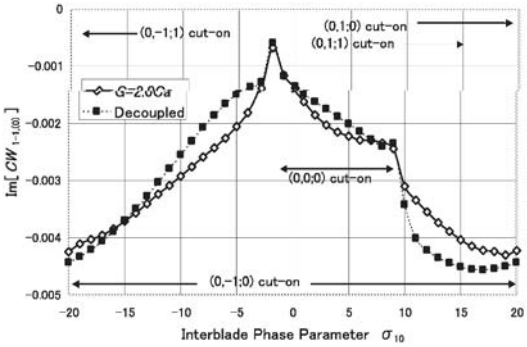

Figure 3. Case sub-sup. Modes $(1, -1;\ \ell)$ and $(-1, 1;\ \ell)$ of $\ell = 0,\ 1$ are cut-on everywhere

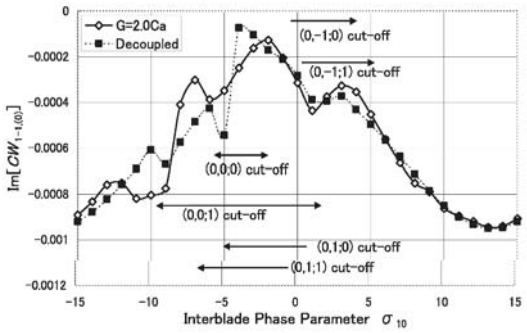

Figure 4. Case sup-sub

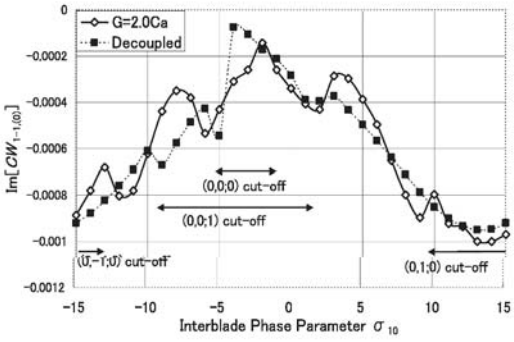

Figure 5. Case sup-sup

in the region where the main duct mode $(0,0;0)$ generated from rotor 1 is of cut-on state. Note that in the case of the decoupled blade row, this mode is one and only one cut-on duct mode at the specified reduced frequency. In addition strong influence is also seen in the regions where duct modes $(0,\nu,\ell)$ of $\nu = 1$ or $\nu = -1$ regenerated from rotor 2 are cut-on. In case sub-sup (Figure 3) where rotor 2 cascade is supersonic, a large number of duct modes are of cut-on state, and on the whole the influence of the neighboring blade row is higher than in case sub-sub (Figure 2). It would be worth emphasizing that at the resonance points of the duct mode $(0,0;0)$ the curves of the aerodynamic work show sharp bends, but the difference between the decoupled cascade and the coupled cascades is remarkably small.

In cases sup-sub (Fihure 4) and sup-sup (Figure 5) where rotor 1 cascade is supersonic most of the duct modes are cut-on and the number of cut-off duct modes is small. Near the resonance points of duct modes $(0,0;0)$ and $(0,0;1)$ which are originally generated from rotor 1 cascade the curves of the aerodynamic work show humps, but in contrast to cases of subsonic rotor 1 cascade (Figure 2 and 3) no coincidence in the aerodynamic work between the decoupled blade row and the coupled blade rows is observed at resonance points, and the difference is rather large around the resonance points. The curves for the coupled blade rows show more complicated variation with σ_{10} than those for the decoupled blade row because of appearance of resonance points of duct modes $(0,\nu;\ell)$ with $\nu \neq 0$ which are regenerated from rotor 2 cascades.

2.2 Critical Flutter Velocity

In the present flutter analysis the elastic properties of blades are assumed uniform along the span and natural mode shapes are assumed same as those for the uniform flat plate. Vibration modes of the first and second bending orders with the natural frequencies ω_{B1} and ω_{B2} and the first and second torsion orders with the natural frequencies ω_{T1} and ω_{T2} are taken into account. The specified values are as follows; the mass ratio $M_b/(\pi\rho_0 b_a^2 r_T(1-h)) = 120$, the normalized distance between the center of gravity and the elastic axis $x_{eg}/b_a = 0.141$, the normalized radius of gyration $r_e/b_a = \sqrt{0.6}$, the elastic axis position $z_e/C_a = -0.075$, and the natural frequency ratios $\omega_{T1}/\omega_{B1} = 6.0$, $\omega_{B2}/\omega_{B1} = 6.3$, $\omega_{T2}/\omega_{B1} = 18.0$. Here M_b is the mass of a blade, and $b_a = C_a/2$.

Figure 6 shows the dimensionless critical axial flow velocity at the flutter boundary dependent on interblade phase parameter σ_{10} . The aerodynamic and geometrical conditions are same as those of case sub-sub in Table 2 except the blade row distance $G = 1.1C_a$. We can observe that the flutter velocity of

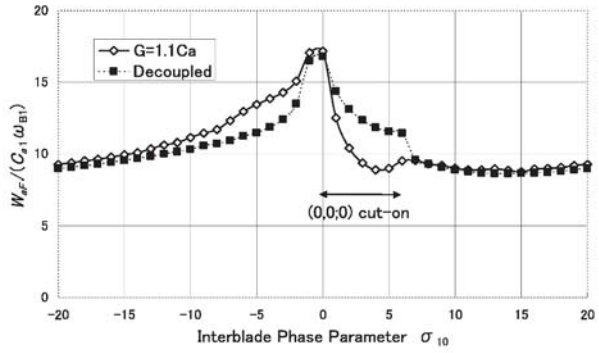

Figure 6. Critical axial flow velocity for coupled bending-torsion flutter in case sub-sub

the coupled blade rows is significantly lower than that of the decoupled blade row in the region where the duct mode $(0, 0; 0)$ is cut-on.

3. Conclusions

(1) The effect of the neighboring blade row on the unsteady blade (loading is closely related to the state (cut-on, cut-off, near (resonance) of acoustic duct modes.

2) In the case of vibrating (subsonic cascade the supersonic neighbor cascade gives stronger (influence on the unsteady aerodynamic work than the subsonic neighbor (cascade because of generation of a larger number of cut-on duct modes (due to interaction between cascades.

3) In the case of vibrating (supersonic cascade the aerodynamic work is significantly modified (around the resonance points of duct modes generated from aerodynamic (interaction with the neighboring cascade.

4) The critical flutter (condition can be significantly modified by the presence of the (neighboring cascade.

References

[1] Tanida,Y., "Effect of Blade Row Interference on Cascade Flutter," *Transactions of Japan Society for Aeronautical and Space Sciences*, **Vol. 9, No. 15**, 1966, pp.100-108.

[2] Kobayashi, H., Tanaka, H. and Maruta, H., "Effect of Rotor-Stator Interaction on Cascade Flutter, 1st Report: Experimantal Study on Pure Bending Mode of Compressor Cascade," *Transactions of Japan Society for Mechanical Engineers*, **Vol. 40, No. 334**, 1974, pp.1615-1626.

[3] Kobayashi, H., Tanaka, H. and Hanamura, Y., "Effect of Rotor-Stator Interaction on Cascade Flutter, 2nd Report: Theoretical Study on Pure Bending Mode," *Transactions of Japan Society for Mechanical Engineers*, **Vol. 41, No. 346**, 1975, pp.1770-1780.

[4] Butenko, K.K. and Osipov, A.A., "Unsteady Subsonic Flow Past Two Relatively Moving Flat Cascades of Thin Weakly Loaded Oscillating Blades," *Fluid Dynamics*, **Vol. 22**, 0015-4628/88/2304-0620, Plenum Publishing Corporation, New York, 1989, pp.620-625.

[5] Hall, K.C. and Silkowski, P.D., "The Influence of Neighboring Blade Rows on the Unsteady Aerodynamic Response of Cascades", *ASME J. of Turbomachinery*, **Vol. 119**, 1997, pp.85–93.

[6] Namba, M., Yamasaki, N. and Nishimura, S., "Unsteady Aerodynamic Force on Oscillating Blades of Counter-Rotating Annular Cascades," Proceedings of 9th International Symposium on Unsteady Aerodynamics, Aeroacoustics and Aeroelasticity of Turbomachines, to be published, 2001.

[7] Namba, M., "Unsteady Aerodynamic Response of Oscillating Supersonic Annular Cascades in Counter Rotation", *AIAA Meeting Papers on Disk*, Vol.6, No.3, 37th AIAA/ASME/SAE Joint Propulsion Conference, AIAA Paper No. 2001-3741, 2001.

[8] Namba, M. and Ishikawa, A., "Three-Dimensional Aerodynamic Characteristics of Oscillating Supersonic and Transonic Annular Cascades," *ASME J. of Engineering for Power*, **Vol. 105**, 1983, pp.138-146.

[9] Namba, M., "Three-Dimensional Flows," *AGARD Manual on Aeroelasticity in Axial Flow Turbomachines, Vol. 1, Unsteady Turbomachinery Aerodynamics*, **AGARD-AG-298**, M.F. Platzer and F.O. Carta, eds., Neuilly sur Seine, France, 1987.

STRUCTURE OF UNSTEADY VORTICAL WAKES BEHIND BLADES OF MUTUAL-MOVING ROWS OF AN AXIAL TURBOMACHINE

V.E. Saren, S.A. Smirnov
The Central Institute of Aviation Motors
Aviamotornaya st. 2, Moscow, 111116, Russia *

Abstract At research of effects of mutual circumferential shift of stators in system of rows stator-rotor-stator of an axial turbomachine (clocking effects, [1-3]) significant periodic velocity pulsations were found out in the field of turbulent vortical wakes behind rotor blades [3]. The basic frequency of these pulsations is equal to stators vanes passing frequency past rotor blade, and the amplitude of velocity pulsations essentially depends from stators clocking position. According to the Thomson theorem it is necessary to expect that the specified pulsations are caused by the free vortexes, descending from rotor blades owing to change on them of flow velocity circulation at interaction of rows. Clearly, that presence in vortical wakes of progressing waves of vorticity causes acoustic disturbances and additional aerodynamical losses owing to energy dissipation. As dissipative function depends on distribution of vorticity, for an estimation of the losses, caused a rotor-stator interaction, the description of vortical wakes structure at presence in them of free vortexes is necessary.

This paper contains results of free vorticity measurements in relative flow behind a rotor at its interaction with next stators. For the description of experimental results the semiempirical theory, based on model of linear isotropic turbulent diffusion at presence of a velocity gradient, caused by stationary (time-averaged) vortical wakes, is offered.

Keywords: Unsteady vortical wakes, mutual-moving rows

1. Experimental results

Measurements were carried out on large-dimensional (the external diameter 1,2m) low-speed (frequency of rotation 2000rev/min) the axial compressor,

*Work is executed at financial support of International scientific and technical centre (ISTC), the grant number 672.2.

K.C. Hall et al. (eds.),
Unsteady Aerodynamics, Aeroacoustics and Aeroelasticity of Turbomachines, 189–201.

containing system of rows stator (IGV) - a rotor (R) - stator (S), and in detail described in [4]. Numbers of stators vanes are identical, and axial gaps are determined so that clocking effect were significant. The velocity field was measured two-component laser anemometer on various radiuses in various axial sections between R and S.

On Fig.1 cascades of airfoils on mean radius and the line LL along which measurements were carried out are shown. At the fixed point of measurement registration of two velocity components (axial and tangential) is carried out on the PC in 129 moments of time in regular intervals allocated on the R blade passing period $T = h_r/u$, where h_r and u, accordingly, are a pitch and linear speed of R blade. During data recording the information on velocity components for each of 129 moments of time are collected. Common time of registration and sampling of representative data were determined by total number of the data (3000) for everyone velocity component.

Let $W = W(r, x, y, t)$ is a velocity vector, determined in the R system of reference, where r, x, y is, accordingly, radial, axial and tangential (along front) coordinates, and t is time. To investigate change W along front, it is necessary to execute measurements in points with tangential coordinates $y_n(n = 0, 1, 2, \ldots, N), y_N = y_0 + h_r$. In experiments measurements were carried out in the S system of reference (r, x, y_0, t_0). Thus coordinate y_0 is fixed, and velocity W is described as a variable on time t_0 with period T and conformity of coordinates is

$$y = y_0 + ut_0, t = t_0 \tag{1}$$

In each of the considered systems of reference obvious kinematic ratio take place

$$\begin{array}{cc} W(y, t + T_0) = W(y, t) & W(y + h_r, t) = W(y, t - T) \\ W(y_0, t_0 + T) = W(y_0, t_0) & W(y_0 + h_s, t_0) = W(y_0, t_0 - T_0), \end{array} \tag{2}$$

where $T_0 = h_s/u$ and h_s is a S pitch. From (2) follows that flow velocity in R system of reference may be presented by Fourier series

$$W(r, x, y, t) = \sum_k \sum_l W_{kl}(r, x) \cdot e^{i2\pi l\, y/h_r} \cdot e^{i2\pi k\, y/h_s} \cdot e^{-i2\pi k\, t/T_0}\, i = \sqrt{-1} \tag{3}$$

where summation on indexes k and l is carried out from $-\infty$ up to $+\infty$. It is possible to notice, that replacements of variables

$$y = \overline{y}, \quad t = \overline{t} + \overline{y}/u; \quad y_0 = \overline{y}_0, \quad t_0 = \overline{t}_0 - \overline{y}_0/u$$

result in two equivalent representations of W, expressed in systems of reference R or S

$$W = \sum_k \sum_l W_{kl} e^{i2\pi l\,\overline{y}/h_r} \cdot e^{i2\pi k\,\overline{t}/T_0} = \sum_k \sum_l W_{kl} e^{i2\pi k\,\overline{y}_0/hs} \cdot e^{i2\pi l\overline{t}_0/T}$$

with the following conformity of systems of reference

$$\overline{y} = u\overline{t}_0 \quad , \quad \overline{t} = -\overline{y}_0/u.$$

From here coefficients of expansion (3) may be calculated from equality

$$W_{kl} = \frac{u}{h_s h_r} \int_0^{h_s} \int_0^{h_r/u} W(r, x, \overline{y}_0, \overline{t}_0) e^{-i2\pi \ln \overline{t}_0/h_r} \cdot e^{-i2\pi k\,\overline{y}_0/h_s}\, d\overline{t}_0 d\overline{y}_0$$

Thus, the stated technique allows to receive a relative flow velocity in the R system of reference according to measurements in the S system (i.e. in a motionless point) at sufficient number N of measurement points on a S pitch h_s in $M = 129$ points of measurements on period T.

Let the projection of instant relative velocity behind R $W = W(r, x, y, t)$ on averaged on period T_0 and a pitch hr velocity W_{00} is presented as

$$\frac{(W \cdot W_{00})}{|W_{00}|^2} = w_0(r, x, y) + w(r, x, y, t),$$

where W_{00} is a zero member of expansion (3), and w_0 is averaged on period T_0 the velocity, referred to $|W_{00}|$. Then distribution $w_0 = w_0(r, x, y)$ along a line LL on a pitch hr describes time-averaged flow behind a R in a core of a flow and in the field of a vortical wake.

The value w_0 is presented on Fig.2 for section LL, distant from the R trailing front on distance of $\Delta = 8,75mm$ on mean radius of a flowing path. The full axial gap between R and S made thus $\Delta_{23} = 20,5mm$. Coefficients of expansion 3) were calculated according to the measurements executed for $N = 10$ and $M = 129$. It allows to determine 20 harmonics on coordinate y and no more than 2 harmonics on time t. It is hereinafter supposed that coordinates x and y are referred to a R pitch hr, and time to period T_0.

For comparison on Fig.2 values w_0 are put, received under the theory of an automodelling vortical wake [5]. Apparently, experimental data well are coordinated to the theoretical values, received for value of profile losses $\zeta = 0,051$. Design velocity $|W_{00}| = 91,5m/s$ at exit flow angle $\beta = 42^\circ$ (see Fig.1). The appropriate values, received in experiment, are equal: $|W_{00}| = 91,1m/s$; $\beta = 41,9^\circ$. Thus vector W_{00} does not depend from clocking position of IGV and S [8].

The value $w = w(r, x, y, t)$ describes distribution along a line LL of the pulsation part of flow velocity, referred to $|W_{00}|$. Examples of w distributions

are presented on Fig.3, where the data are received for two values of parameter $\nu = n/N$ $(n = 0, 1, \ldots, N)$, equal referred to h_s shift of IGV be relative S in a positive direction of axis Oy (against R rotation). The chosen values $\nu = 0,2$ and $0,6$ correspond to clocking positions of stators, providing the greatest and least levels of velocity pulsations behind a R. The moments of time $t = 0,5$ and $t = 0,8$ correspond to a situation, when velocity pulsations are in an antiphase.

Apparently from the received distributions w, periodic velocity pulsations are rather small in a fbw core and rather significant in a zone of a vortical wake and essentially depend on interaction of rows. It testifies to existence in the field of vortical wakes behind R blades significant fbw vorticity, which periodically varied in time and in space. Specified vorticity may be approximately determined, if the expansion (3) is received for sections LL, distant on various distances x from R trailing front. In this case vorticity may be presented as

$$\Omega = \sum_l \sum_k \Omega_{kl}(r,x) e^{i2\pi(l+k\frac{h_r}{h_s})y} \cdot e^{-i2\pi kt} \tag{4}$$

where $\Omega_{kl} = \frac{1}{2}\left[\frac{\partial W_{ykl}}{\partial x} - i2\pi\left(l + k\frac{h_r}{h_s}\right)W_{xkl}\right]$; W_{xkl}, W_{ykl} are, accordingly, axial and tangential components of velocity vector W_{kl}. The derivative $\frac{\partial W_{ykl}}{\partial x}$ may be approximately calculated on the measured values W_{ykl}, received on various, close located lines LL.

As illustration on Fig.4 distributions $|\Omega_1|$ in a zone of a vortical wake along a line LL, located on distance of 10mm from R trailing front on mean radius of a fbwing path, are presented. Here value

$$\Omega_1(r,x,y) = \sum_{l=-20}^{20} \Omega_{1l}(r,x)\ e^{i2\pi(l+\frac{h_r}{h_s})y}$$

corresponds to 1-st harmonic on time of the expansion (4), and values $\partial W_{ykl}/\partial x$ are received as a half-sum of the left and right relations of finite differences according to measurements on lines LL1 and LL2, located, accordingly, on distances $\Delta = 9mm$ and $\Delta = 11mm$ from R leading front. All values $|\Omega_1|$ on Fig.4 are referred to $|\Omega_1|_0$, received on an axis of a vortical wake $y = y_0$. The data are presented for various values of parameter $\nu = 0,2; 0,4; 0,6$.

Prominent feature of the received distribution is its nonmonotonic change at removal from an axis of a vortical wake that in a fbw core values of $|\Omega\ _1|$, as a rule, do not exceed$0,1\,|\Omega_1|_0$. Results of experiment allow to conclude that periodic vortexes behind a R, drifted by a fbw, intensively diffuse in a zone of vortical wakes behind blades. However, as against classical diffusion with

monotonous decrease (as an exponent) at removal from a source, diffusion of free vortexes has nonmonotonic character of distribution across a layer.

2. Model of free vortexes diffusion

Here the description of free vortexes diffusion in a vortical layer, in which distribution of time-averaged flow velocity is known, is offered. It is supposed that diffusion occurs due to turbulent pulsations of time-averaged velocity across a layer, i.e. periodic (free) vortexes remain passive. It The initial layer of free vortexes in a vicinity of an airfoil trailing edge ($x_1 = 0$) is supposed a line of contact discontinuity of velocity, in which linear intensity of vortexes may be determined by the formula, following from the Thomson theorem at absence of difference of static pressure across a layer

$$\Omega(r, 0, y_1, t) = \gamma(0, t) \cdot \delta(y_1) = -\frac{1}{|W_{00}|} \frac{\partial \Gamma}{\partial t} \cdot \delta(y_1) \tag{5}$$

Here γ is discontinuity of velocity on a line of contact discontinuity; $\delta(y_1)$ is delta function; $\Gamma(t) = \sum\limits_k \Gamma_k \cdot e^{-2\pi k t}$ is periodic (with period T_0) velocity circulation on the R blade. The system of coordinates (x_1, y_1) is used with the beginning in the R airfoil trailing edge and an axis Ox, directed along an axis of a vortical wake behind an airfoil.

The equation of turbulent diffusion in neglect viscosity in a considered case looks like

$$\frac{\partial \Omega}{\partial t} + w_0 \frac{\partial \Omega}{\partial x_1} = \frac{\partial}{\partial y} \left(D \cdot \frac{\partial \Omega}{\partial y} \right), \tag{6}$$

where w_0 is velocity of free vortexes drift, $D = const$ is diffusion constant. The value of w_0 is equal to velocity of time-averaged flow in a vortical wake behind R blade

$$w_0 = w_{00} \left[1 - u_1 \left(x_1, y_1 \right) \right],$$

where w_{00} is velocity in a flow core, and u $_1$ is additional velocity in a wake.

According to the semiempirical theory of turbulent vortical wakes behind airfoils u_1 may be presented in the form

$$u_1 = \frac{\chi}{\sqrt{x_1}} \overline{u}_1 \left(\eta \right) \quad , \quad \eta = y_1 / \sqrt{x_1} \quad , \quad \overline{u}_1 \left(0 \right) = 1,$$

where rather small value $\chi \approx 0,1$ is uniquely determined by factor of profile losses. From here the equation (6) becomes

$$\frac{1}{q}\,\frac{\partial\overline{\Omega}}{\partial t}+\frac{\partial\overline{\Omega}}{\partial x_1}-d\,\frac{\partial^2\overline{\Omega}}{\partial y_1^2}=\frac{\chi}{\sqrt{x_1}}\overline{u}_1\cdot\frac{\partial\overline{\Omega}}{\partial\dot{x}_1}\quad d=\frac{D}{w_0\cdot h_2},\,\overline{\Omega}=\frac{\Omega h_2}{w_{00}^{,}}\quad q=\frac{h_2}{T_0\cdot w_{00}} \tag{7}$$

To within of precision of value χ terms the particular solution of the equation (7), satisfying the initial condition (5), to conditions of symmetry and attenuation at $y\to\pm\infty$, is

$$\overline{\Omega}=\frac{1}{\sqrt{x_1}}e^{-\frac{1}{4d}\eta^2}\sum_{k\neq 0}A_k\left[1+\frac{\chi}{\sqrt{x_1}}f_1(\eta)+i2\pi kq\chi\sqrt{x_1}f_2(\eta)\right]e^{-i2\pi k(t-qx_1)}, \tag{8}$$

$$f_1(\eta)=\frac{\eta}{d}\int\limits_{\eta}^{\infty}\frac{1}{\eta_1^2}e^{\frac{1}{4d}\eta_1^2}\int\limits_{\eta_1}^{\infty}\left(\frac{1}{2}-\frac{\eta_2^2}{4d}\right)\eta_2\overline{u}_1(\eta_2)\,e^{-\frac{1}{4d}\eta_2^2}d\eta_2 d\eta_1,$$

$$f_2(\eta)=\frac{1}{d}e^{\frac{1}{4d}\eta^2}\int\limits_{\eta}^{\infty}e^{-\frac{1}{4d}\eta_1^2}\int\limits_{0}^{\eta_1}\overline{u}_1(\eta_2)\,d\eta_2 d\eta_1.$$

Apparently, the received solution essentially differs from a case $\chi=0$ ($w_0=const$) that the particles, forming at some moment of time a line, normal to an axis of a vortical wake, at the subsequent moments of time are bent. Free vortexes, diffused to the layers more removed from an axis of a wake, are transferred to the velocity, exceeding velocity of vortexes, located on an axis. As shows the analysis, it in particular results to that for the fixed value y_1 the amplitude of vorticity at increase of x_1 aspires to finite ($\neq 0$) value, and the axial density of total vorticity across a layer is increased as $\sqrt{x_1}$.

Prominent feature of the solution (8) is also dependence of distribution across a layer of amplitude function from number of a time harmonic k.

For a determination of connection between coefficients A_k of the series (8) it is possible to take advantage of a condition of total vorticity preservation in a flow for all time of free vortexes formation. At steady-state flow (i.e. proceeding indefinitely long) this condition gives a ratio

$$\lim_{x_1\to\infty}\frac{d}{dt}\left[\Gamma(t)+I(x_1,t)\right]=0,$$

where $I(x_1,t)=\int\limits_0^{x_1}\int\limits_{-\infty}^{+\infty}\Omega(x_1,y_1)\,dy_1dx_1$. From here after calculations follows

$$A_k \left[2\sqrt{\pi d} - \chi (1+i) \sqrt{\frac{\pi}{4\pi kq}} (\Phi_1 - i\pi kq\Phi_2) \right] = 2\pi kqi\overline{\Gamma}_k, \qquad (9)$$

$$\overline{\Gamma}_k = \frac{\Gamma_k}{h_2 w_{00}}, \quad k = \pm 1,\ \pm 2, \ldots$$

$$\Phi_1 = \int\limits_{-\infty}^{+\infty} e^{-\frac{1}{4d}\eta^2} \cdot f_1(\eta)\, d\eta, \quad \Phi_2 = \int\limits_{-\infty}^{+\infty} e^{-\frac{1}{4d}\eta^2} f_2(\eta)\, d\eta$$

It is necessary to notice that for $\chi = 0$ coefficient A_k unrestrictedly grows at $d \to 0$. In this case the layer of diffusion passes in a line of contact discontinuity, vorticity is described by δ-function and coefficients of the series, appropriate to decomposition (8), are determined by the formula

$$A_k = 2\pi kqi\overline{\Gamma}_k.$$

Equality (9), obviously, may be used both for a calculated estimation of the decomposition (8) coefficients, if value $\Gamma(t)$ is known, and for definition of the coefficients Γ_k, if A_k are determined experimentally.

3. Comparison of experimental and theoretical results

More detailed, than presented above, measurements of flow velocity behind R were executed on 75% of height of a flowing path in the same assembly of the compressor. The axial gap between R and S in the specified cylindrical section made 23mm, and lines LL settled down on distances $\Delta = 6, 8, 10, 12, 14, 16mm$ from trailing front of a R. The mutual circumferential position of stators was fixed ($\nu = 0$), and measurements were carried out in N=20 in regular intervals located points on the S pitch. At definition of value $\partial W_{ykl}/\partial x$ in the series (4) spline-approximation of the second order on points õ was used. As one would expect parameters of time-averaged vortical wake for extreme points $\Delta = 6mm$ and $\Delta = 16mm$ appreciablly differed from their values on interval $\Delta = 8 \div 14mm$. The profile losses coefficient, received on an mean part of an axial gap, is equal $\zeta = 0,063$ and was accepted further for the theoretical description.

As illustration of experimental data on Fig.5 dependences from a variable η of values are presented

$$\omega_1(x,y) = \frac{\Omega_1(r,x,y-y_0)}{\Omega_1(r,x,0)}, \qquad (10)$$

where complex amplitude Ω_1 of the first harmonic of the series (4) is determined in item 1, and y_0 is the ordinate of stationary vortical wake axes behind

the R blade, counted along a line LL. Dependences from $\Delta y = y - y_0$ of values Re ω_1 and Im ω_1 are presented on Fig.5 for values $\Delta = 8, 10, 12mm$.

Apparently from the received data, marked above the nonmonotonic change of free vorticity intensity at removal from an axis of a vortical wake is clearly shown in the presented experiments. It is necessary to note that the area of essential change of ω_1 in a vicinity of an vortical wake axis is much less than zone of a stationary vortical wake. It specifies rather small value of experimental diffusion constant of free vortexes.

For the theoretical description of dependence $\overline{\Omega}_1 = \overline{\Omega}_1(\Delta y)$ the formula (8) was used, where the value of loss of the averaged velocity in a wake $\overline{u}_1$ was accepted in the usual form for turbomachines [5]

$$\overline{u}_1(\eta) = \begin{cases} \cos^2(\pi k_0 \eta) \ , \ |\eta| \le \frac{1}{2k_0} \\ 0 \ , \ |\eta| > \frac{1}{2k_0} \end{cases} \quad , \quad k_0 = Const$$

In according to the determined factor of profile losses ($\zeta = 0,063$), the constants χ and k_0 were accepted equal: $\chi = 0,131$; $k_0 = 3,3$. Thus, theoretical values of $\overline{\Omega}_1$ were determined under formulas

$$\overline{\Omega}_1(r, x_1, \eta) = \frac{1}{\sqrt{x_1}} e^{-\frac{1}{4d}\eta^2} A_1 \cdot e^{i2\pi q x_1} \left[1 + \frac{\chi}{\sqrt{x_1}} f_1(r) + i2\pi q \chi \sqrt{x_1} \cdot f_2(r) \right] \tag{11}$$

$$f_1(\eta) = \frac{\eta}{d} \int\limits_{\eta}^{1/2k_0} \frac{1}{\eta_1^2} e^{\frac{1}{4d}\eta_1^2} \int\limits_{\eta_1}^{1/2k_0} \left(\frac{1}{2} - \frac{\eta_2^2}{4d} \right) \eta_2 \cos^2(\pi k_0 \eta_2) \, e^{-\frac{1}{4d}\eta_2^2} d\eta_2 d\eta_1$$

$$f_2(\eta) = \frac{1}{d} e^{\frac{1}{4d}\eta^2} \int\limits_{\eta}^{1/2k_0} e^{-\frac{1}{4d}\eta_1^2} \int\limits_{0}^{\eta_1} \cos^2(\pi k_0 \eta_2) \, d\eta_2 d\eta_1,$$

where χ and k_0 are the given values.

On Fig.6 dependences from η_1 of values Re ω_1 and Im ω_1 are presented, calculated under formulas (10) and (11) for the following values of parameters: $d* = k_0\sqrt{d} = 0,045; 0,050; 0,055; 0,060$ and $x_1 = 0,08; 0,17; 0,26$. On an abscissa axis on Fig.6 the value $\eta_1 = 2k_0 y_1 / \sqrt{x_1}$ is put, equal to distance y_1 from an axis of the vortical wake referred to it half-width.

Apparently from Fig.6, distribution of free vorticity at the given parameters of a stationary vortical wake in considered model of diffusion essentially depends on dimensionless diffusion constant d, which for the presented examples changes in limits $d = (4,2 \div 7,4) \cdot 10^{-4}$. As a whole character of change ω_1 across a vortical wake qualitatively is coordinated to the features, which have

been found out in experiments. It allows to hope that the offered model of diffusion, limited to the first approach on powers of parameter χ, allows to describe evolution of the first harmonic of free vortexes. As have shown similar calculations, for the second harmonic on time results are less satisfactory, that probably specifies necessity of the account of the subsequent approaches on powers χ.

Calculation of function $\omega_1 = \omega_1(\Delta y)$ has shown that at $d = 4.6 \cdot 10^{-4}$ values Re ω_1 and $|\omega_1|$ well are coordinated to the experimental data presented on Fig.5 on character of non-monotony. However thus the calculated width of a diffusion layer appeared essentially (in $1,5$ times) less, than in experiment. It is possible to assume that it is caused by application of the theory to the field of the measurements, close located to trailing edges of the R blades. Actually character of free vortexes formation in the field of trailing edges, where thickness of a boundary layer is significant, may differ from the line of contact discontinuity, accepted in the theory.

According to the specified assumption at calculation of ω_1 the distance from the R trailing front was put equal to $x = \Delta + 0,13$, that corresponds to presence in a trailing edge initial, $\neq 0$ thickness of a layer of free vortexes. The received calculated data in comparison to experiment are presented by continuous lines on Fig.5 and Fig.7.

Apparently calculation well enough describes results of measurements in a vicinity of an vortical wake axis on values Re ω_1 and $|\omega_1|$. The greatest differences of the theory and experiment are observed in rather small value Im ω_1, that may be connected both with measurement errors, and with more essential influence on Im ω_1 of the subsequent approaches on powers χ.

4. Conclusion

1 As have shown the executed in work experiments on measurement of unsteady flow velocity behind a rotor at its interaction with next stators the periodic free vortexes appear in a flow, caused by change of velocity circulation on the rotor blades.

2 For the description of structure of the vortical wake, containing free vortexes, the linear model of the isotropic turbulent diffusion is offered, taking into account change of velocity of free vortexes drift owing to loss of time-averaged flow velocity in a vortical wake.

3 Comparison of experiment to the results of calculation, executed as a first approximation concerning intensity of a stationary vortical wake, shows that the offered model of diffusion of free vortexes correctly describes its mechanism. It is possible to expect that development of the model will allow to construct the semiempirical theory, describing evolu-

tion of unsttady vortical wakes, caused aerodynamic interaction of rows in an axial turbomachine.

References

[1] Saren V.E., Savin N.M., Krupa V.G. (2000) Experimental and Computional Research of a Flow Structure in a Stator-Rotor-Stator System of an Axial Compressor, *The 9th International Symposium on Unsteady Aerodynamics, Aeroacoustics and Aeroelasticity of Turbomachines (ISUAAAT)*, Lyon, France, September 4-8, pp 494-502.

[2] Saren V.E., Savin N.M., Krupa V.G., Petrovitchev A.M. (2001) Influence of a rotor-stator interaction on the steady and unsteady characteristics of the axial compressor, *The report is adopted on XI International Symposium ISOABE*, Bangalore, INDIA, September 2-7.

[3] Saren V.E. and Smirnov S.A. (2003) Unsteady Vortical Wakes behind Mutually Moving Rows of Axial Turbomachine, *Thermophysics and Aerodynamics*, Vol.10, No.2.

[4] Savin N.M. and Saren V.E (2003) Stator Clocking Effect in a System of Rows Stator-Rotor-Stator of the Subsonic Axial Compressor, *10th Intern. Sump. on Unsteady Aerodynamics, Aeroacoustics and Aeroelasticity of Turbomachines (ISUAAAT)*, Durham, North Carolina, USA, Sept. 7-11.

[5] Samoilovich G.S. (1975) Excitation of Oscillation in Turbomachine Blades, *Mashinostroenie*, Moscow.

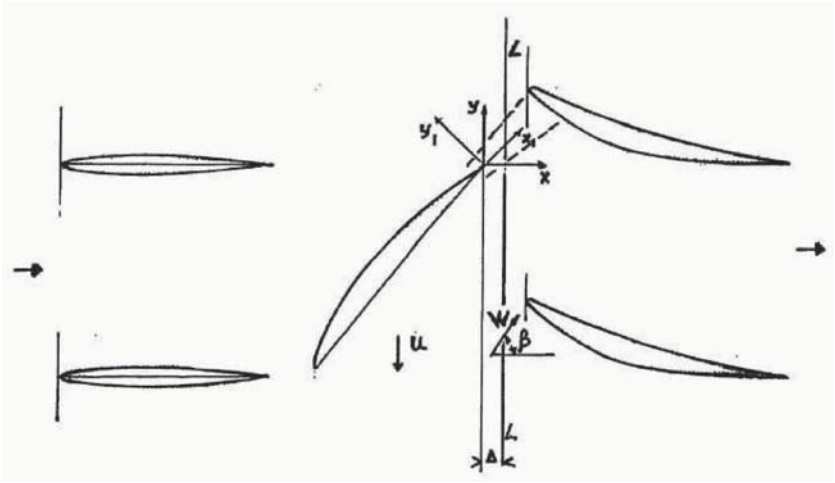

Figure 1.

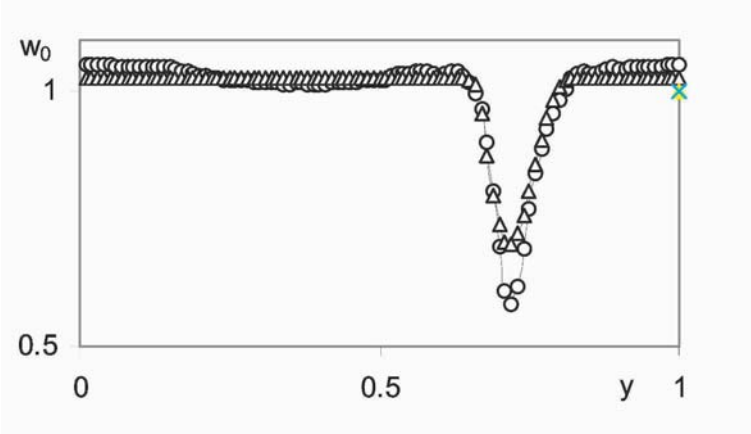

Figure 2. o-experimental distribution $W_0(y)$, Δ-automodelling distribution

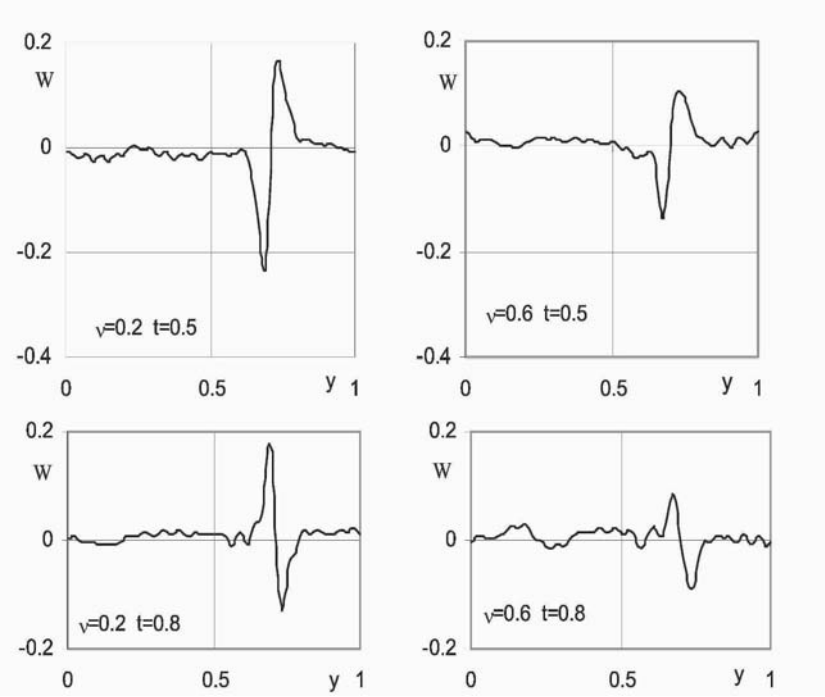

Figure 3. Experimental distributions W(y) for different values ν and t,

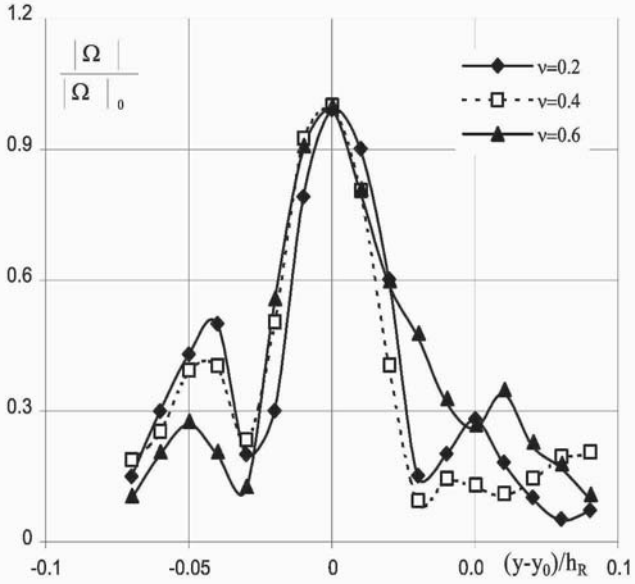

Figure 4. Pitch - wise distributions of the 1-st harmonic of vorticity near vortlcal wake axls Δ =10mm

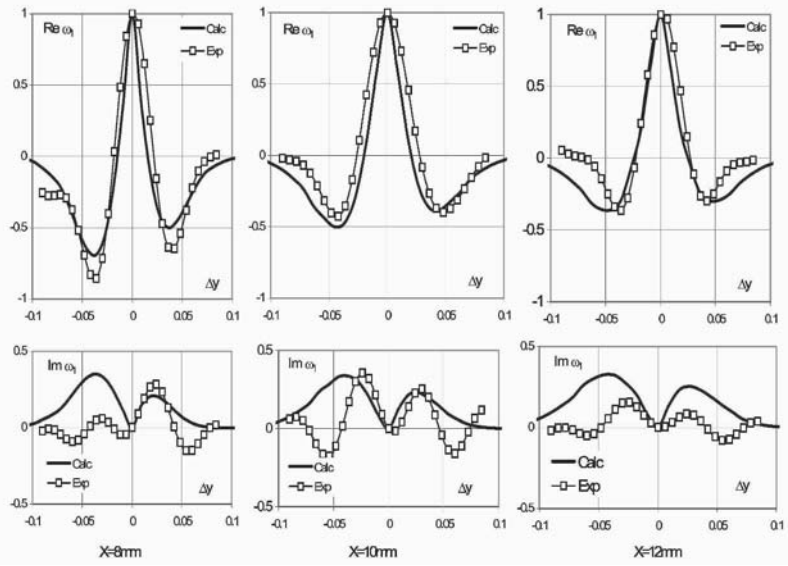

Figure 5. Distribution of the 1-st harmonic of free vortexes intensity along parallel front line

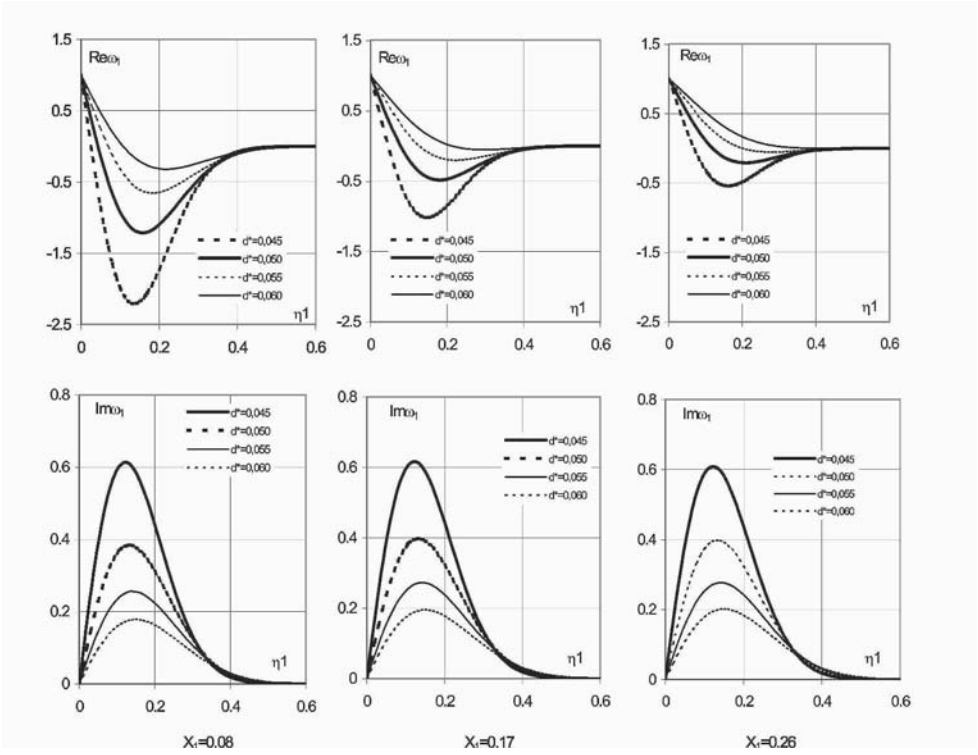

Figure 6. Teoretical distribution across vortical wake of the 1-st harmonic of free vortrxes intensity

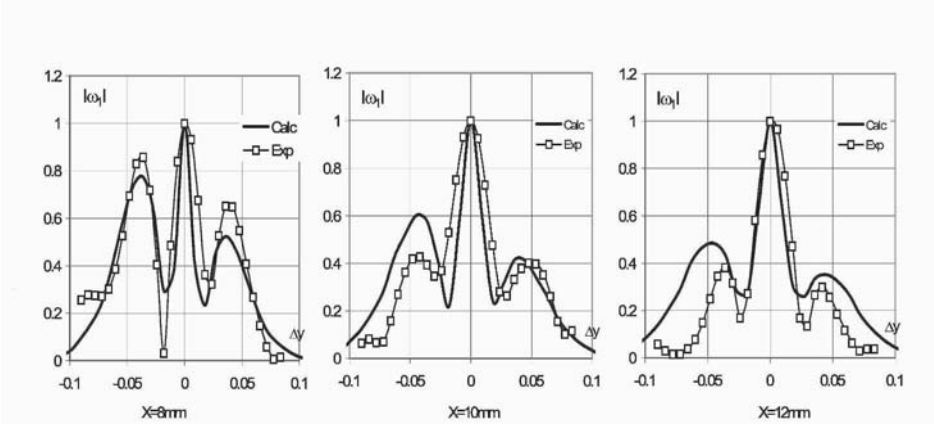

Figure 7. Distribution of amplitude of the 1-st harmonic of free vortexses intensity along parallel front line

THE EFFECT OF MACH NUMBER ON LP TURBINE WAKE-BLADE INTERACTION

M. Vera, H. P. Hodson
Whittle Laboratory
University of Cambridge, UK
R. Vazquez
ITP, Industria de Turbo Propul sores
Madrid, SPAIN

Abstract The techniques employed in high speed linear cascade testing to simulate the effect of unsteadiness are presented and compared with low speed counterparts. Results are obtained from a high speed cascade and a low speed cascade. Both are models of an existing (conventional) low pressure turbine blade. They are compared under steady and unsteady flow conditions. The results show that the same quantitative values of losses are obtained, proving the validity of the low speed approach for profiles with an exit Mach number of the order of 0.64. The range of validity of the conclusions is extended by reference to a profile designed using current low pressure turbine design practice. Wake traverses using pneumatic probes reveal that the unsteadiness reduced the profile losses up to Mach numbers of 0.9

1. Introduction

The development of the low pressure turbine (LPT) has reached a stage where rises in efficiency are difficult to obtain. Furthermore, the LPT could represent one third of the total engine weight. Therefore, one of the current trends that designers have adopted is to improve the overall performance of the LPT by reducing its weight. This new philosophy leads to fewer blades each of which carries a greater aerodynamic load.

The LPT operates at the lowest Reynolds number in the whole engine. This means that the development of the boundary layers will be determined by the transition from laminar to turbulent flow. Increasing the aerodynamic load increases the diffusion on the rear part of the blade and thus the risk of separation. In fact, the resulting blade usually features a large separation bubble in steady flow conditions. This can be partially or totally suppressed by transition to turbulent flow being caused by the wakes coming from an upstream row of blades. Due to the ability of the wakes shed by an upstream row to promote transition

K.C. Hall et al. (eds.),
Unsteady Aerodynamics, Aeroacoustics and Aeroelasticity of Turbomachines, 203–216.

in the neighborhood of separation, the study of wake-boundary interactions is of primary interest in the LPT environment. The large aspect ratio of the LPT blades (typically between 3 and 7) makes them appropriate for linear cascade testing.

Previous studies on wake induced transition phenomena for high speed flows have been carried out by others researchers (Brunner et. al, 2000 and Coton et. al, 2002) but still, very little is known about the topic. This fact together with the current limitations of the CFD tools (Vilmin et at, 2003) suggests that experimental studies of blade-wake interaction phenomena in high speed flows are needed. Even though the experimental techniques used in high speed testing are conceptually the same as those used in low speed, the problems encountered tend to be magnified at high speed. In addition, new challenges arise. Therefore, we should question when it is worth doing high speed cascade testing.

This paper aims to answer this question. It examines the extent to which the results from the low speed approach are meaningful. This paper follows previous comparisons between high speed and low speed testing, (Wisler, 1984), (Hodson and Dominy, 1993), by presenting a comparison between high speed and low speed testing of LPT linear cascades. In the main part of this paper, two profiles are compared. These profiles are not identical but they both are intended to model an existing LPT blade in the cascade environment at low speed or at high speed. Facilities and instrumentation will also be compared. Finally, results from a modern LPT blade will be presented to demonstrate the extent to which the conclusions are valid. To conclude, the behavior of this blade is presented up to exit Mach numbers of 0.9.

2. Design Process

In using high speed cascades, few compromises are needed to achieve a model of the real blade in the turbomachine. Indeed, true similarity can be obtained sometimes. In the case of low speed cascades, more compromises are required and the shape of the resulting low speed blade usually differs greatly from the real blade to be modelled. Typical sizes of the resulting LPT blades for both high and low speed cascade testing at the Whittle laboratory are shown in Table 1.

2.1 Choosing the bars

To achieve a realistic simulation of the rotor-stator interaction, several similarity parameters must be correctly matched. The method used to choose the size and the pitch of the bars is the same in low and high speed cascade testing and it is presented below. Only by following this procedure is a good simulation of the rotor-stator interaction situation achieved.

To reproduce the kinematics of the wake-blade interaction, the flow angle β_1 in the bar relative frame of reference, is matched to that of the upstream bladerow in the LPT. The relative and absolute inlet flow angles and the inlet axial velocity to the cascade, V_{x1}, then give the speed of the bars, U, from the velocity triangles at the inlet of the cascade.

The reduced frequency of the machine not only sets the ratio of the convection time scale to the wake passing time scale, but it also sets the ratio of the viscous diffusion time scale to the wake passing time scale. Therefore, it must be matched if a realistic rotor-stator interaction is to be achieved. The reduced frequency, F, and the bar passing frequency, f, are related according to the expression

$$F \equiv fC/V_2 = U/s_{bar} \cdot C/V_2 \propto f \cdot x/U \tag{1}$$

where C is the chord of the airfoil. Equation 1 provides the bar passing frequency and the pitch of the bars, s_{bar}. The reduced frequency is defined in terms of the exit velocity of the cascade, V_2. This is because the most important wake-blade interactions tend to occur in the latter half of the blade passage. Typical values of the bar passing frequencies for high speed and low speed cascades are given in Table 1.

Pfeil and Eifler (1976) showed that the structure of the far wake of an airfoil and that of a cylindrical body of the same drag is almost the same. If an estimation of the stagnation pressure losses of the blade row to be simulated is known, Y_p, the diameter of the bars, d, can be obtained according to

$$Y_p = d \cdot C_d/(s_{bar} \cdot Cos\beta_1) \tag{2}$$

which is exact for low speed flows. An estimation of the drag coefficient of the bars, C_d, at the relative conditions that Y_p represents, must be known. Typical dimensions of the resulting diameters of the bars are given in Table 1. These values are of the same order than the trailing edge thickness of the upstream blade row.

Once all the previous values are fixed, the ratio between the pitch of the cascade, s, and the pitch of the bars is known. Also, the flow coefficient of the bars, ϕ, is given by

$$\phi = V_{x1}/U \tag{3}$$

and this is fixed by the inlet angle in the cascade frame of reference.

Table 1. Typical dimensions of blades and bars in low speed and high speed cascades at the Whittle laboratory.

	High speed	Low speed
Chord (mm)	50	200
Bar diameter (mm)	0.41	2
Bar passing frequency	3 kHz	60 Hz

3. Test Facilities and Instrumentation

For the present work, two linear cascade facilities have been used. The description of the low speed passing bar linear cascade facility was previously documented by Banieghbal et. al, (1995). It is the aim of this paper to describe the high speed rotating bar linear cascade facility and to compare it with its low speed counterpart.

3.1 Transonic cascade facility

The high speed experiments were carried out in the transonic cascade facility at the Whittle laboratory. This is a continuous flow, closed-circuit variable density wind tunnel where Reynolds and Mach number can be fixed independently. Two vacuum pumps, working in parallel, are used to achieve sub-atmospheric pressures. A compressor is used to control the pressure ratio and thus the Mach number of the flow within the circuit. To control the humidity of the air, some of the air is passed through a dryer. The temperature variation can be limited by adjusting the cooling system. Before entering the cascade, the air passes through a honeycomb and screen in order to filter the air and to break up any large scale structures that may exist in the flow. At the entry to the cascade, the flow is accelerated in a convergent nozzle. At the exit, it is discharged into the large exit plenum that contains the test section.

3.2 Wake generators

The presence of the wakes shed from an upstream blade row is simulated using a wake generator. At the Whittle laboratory, the low speed cascades, the wake generator consists of bars fitted between two belts placed on either side of the side walls. The wake generator is driven by a motor by means of mechanism of belts and pulleys and provides linear motion to the bars.

In high-speed flows, the matching of similarity parameters demands a higher speed from the bars. For mechanical reasons this cannot be achieved with the type of bar passing wake generator typical of low speed rigs. Instead, the high speed bar wake generator consists of a number of metal bars equally spaced at the outer periphery of a disk that rotates in a plane parallel to the leading edge plane of the cascade. In this way the circumferential speed of the bars can be increased to the levels that are required in the cascade experiments. A cover encloses the rotating disk and bar assembly thus creating a sealed chamber containing the bars. This sealed cavity is needed to prevent the leakage that would occur if the cavity were opened to the plenum, i.e., to exit conditions. Low speed cascade testing tends to suffer from this sort of leakage. Therefore, controlling the inlet periodicity is easier in high speed due to the sealed chamber that contains the bars. The cover has a rectangular opening aligned with

the exit of the convergent nozzle over which the cascade is mounted. A similar configuration has successfully been used in Oxford (Doorly, 1984).

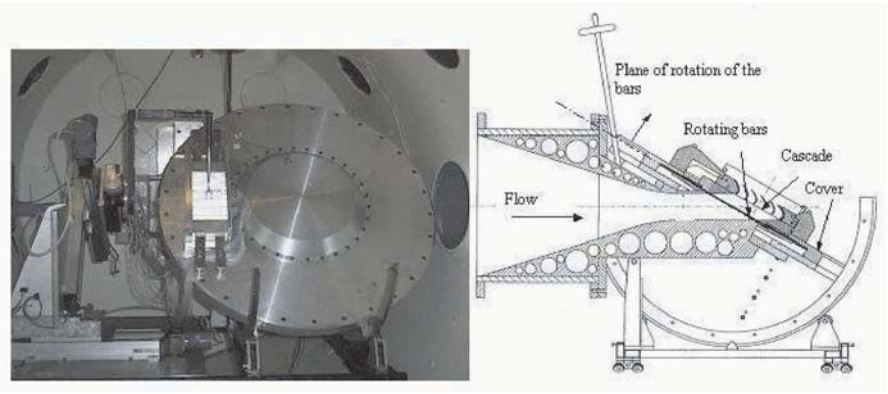

Figure 1. High speed rotating bar rig, frontal view (left) and cross section (right)

The bars move across the front of the cascade, thus simulating the upstream blade row. In the high speed rotating bar rig the bars are made of hypodermic tube. They are fitted at the outer periphery of the rotating disk. When the bars cross the test section, they are subjected to a transverse aerodynamic loading. This loading deflects the bars and thus limits their performance. The deflection, δ, must be smaller than the distance between the bars and the cover [1].

The bars are also subjected to an axial loading due to centrifugal effects. The axial tension tends to straighten the bars and thus reduces their deflection. The deflection is reduced, for a given diameter of the bars, by placing a weight on the tip of the bars. Additionally, when the bars leave the test section, the aerodynamic loading ceases. This transient leads to forced vibrations of the bars. By placing the weight on the tip of the bars, these vibrations are also reduced. The maximum mass that can be used is given by the maximum strength of the material.

The above discussion shows how to avoid some the mechanical constraints limiting the performance of the bars. These limitations must be taken into consideration when fixing the scale of the cascade. Only in this way can a realistic simulation of the blade-wake interaction phenomena be achieved.

[1]This distance is shorter than the axial gap between the bars and the leading edges of the cascade

3.3 Instrumentation

The instrumentation for high speed measurements is conceptually the same as that used for low speed testing. This instrumentation is described by Banieghbal et. al, (1995). The differences between the acquisition of data in low speed and high speed flows are due to the different scales of the values to be measured. This influences the quality of the measurements by influencing the resolution of the output of the signal and the resolution of the characteristic time.

The response frequency of conventional hot films and hot wires is of the order of 25 to 50kHz. The scale of the boundary layers and the freestream velocity indicates that the lowest turbulent frequencies are expected to be of the order of 3kHz and 100kHz for the low speed and high speed blades respectively. Therefore, the lowest turbulent frequencies can be characterized only for low speed flows. Additionally, Table 1 presents the typical value of the bar passing frequency in high speed cascade testing. This is of the order of 3kHz. Thus, for a given the response frequency of the anemometers, a poorer resolution of the bar passing period is obtained for high speed cascades.

4. Results

4.1 Inlet conditions to the cascade

The time mean conditions at inlet to the cascade are affected by the bars. These effects are due to the creation of entropy by the bars and work done by the component of the drag force of the bars in the direction of movement of the bars. In the ideal case, the time mean conditions at the inlet of the cascade can be measured by placing probes downstream of the bars. However, the distance between the bars and the leading edges of the cascade is usually small (25-50% of the chord). Therefore, access is difficult, especially in small scale, high speed cascades. Furthermore, the flow is unsteady. This can result in false readings from conventional instrumentation. Also, due to the presence of the blades, the time-mean inlet stagnation conditions may not be pitchwise uniform in the unsteady flows (Hodson and Dawes, 1996). To avoid these problems, a calculation procedure is used to determine the (mixed out) conditions downstream of the bars.

A control volume representing the flow through the row of bars, in the relative frame of reference, is shown in figure 2. The drag force, $\underline{D}$, represents the force produced by the bars on the fluid. It is taken to act against a direction averaged with both inlet an exit directions. This model is a modified version of the model proposed by Schulte and Hodson (1996). In their model an incompressible analysis of the same control volume is made, assuming that $\underline{D}$ acts in the same direction as the flow entering in the control volume. The validation

of this method for incompressible flow can be found in Schulte (1995). The validation for compressible flow is presented below.

The drag coefficient of the bars, C_d, is defined by

$$C_d = D/(d \cdot (P_{00,rel} - P_{s0})) \tag{4}$$

and

$$tan\beta_m = (tan\beta_0 + tan\beta_1)/2 \tag{5}$$

defines the direction against which the drag force acts.

On surfaces S_b and S_d, periodic boundary conditions apply and no net flow crosses these surfaces. Flow enters the control volume with a uniform velocity through surface S_a and leaves the control volume through surface S_c. It is assumed that mixed out conditions are already reached at surface S_c. The continuity, momentum and energy equations form an implicit system of equations that have to be solved for each inlet condition.

The solution to the system of equations depends, amongst others, on the drag coefficient of the bars, C_d. The value of C_d depends on the conditions at plane 0. Therefore, in order to solve the system of equations, the value of C_d has to be known for the range of Reynolds numbers and Mach numbers found in the measurements.

For the determination of C_d, the drag force produced by the bars, $\underline{D}$, must be known. To measure $\underline{D}$, the wake of one single stationary bar was traversed. Knowing the drag force, the drag coefficient of the bar can be calculated using (4). The value of C_d was measured for the entire range of Reynolds and Mach numbers covered by the measurements. By knowing the value of C_d, the implicit system of equations can be solved for a given value of the conditions upstream the bars and flow angle. Thus, the mixed out conditions downstream the bars can be determined.

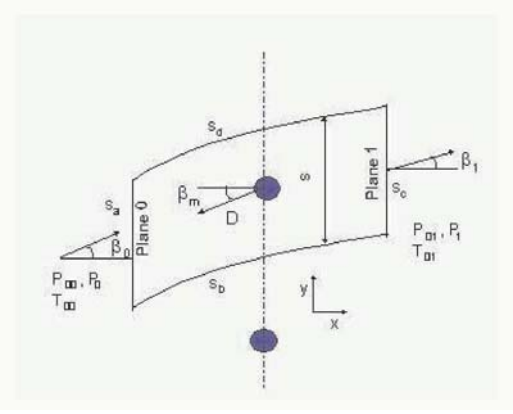

Figure 2. Control volume. Frame of reference fixed to the bars

The calculation of the conditions downstream of the moving bars will be now validated with experimental results. The measurements were performed in the high speed rotating bar rig. The cascade was removed and a pneumatic probe was placed downstream of the bars. The probe was placed in the plane where the leading edges of the cascade would have been. The conditions upstream the bars corresponded to the design inlet conditions of the cascade.

Downstream of the bars, the probe was traversed in the pitchwise direction at three different spanwise positions. The measured upstream conditions are used to calculate the conditions downstream of the bars by means of the calculation procedure described above. A comparison between the downstream measurements and the calculated values is shown in figure 3. The abscissa represents the radius of the bars at each measurement point. This value is non-dimensionalised by the radius of the bars at 50% of the span and at a pitchwise position that would correspond to the centre of the cascade. The ordinate represents the reduction in stagnation pressure through the row of bars expressed as a fraction of the equivalent exit dynamic pressure of the datum high speed cascade at design conditions. At $r/r_{50\%span}$ equal to 1, the differences between prediction and experiments are less than 0.1% of the cascade exit dynamic pressure. A good agreement between the calculation procedure and the measurements is found, thus validating the method.

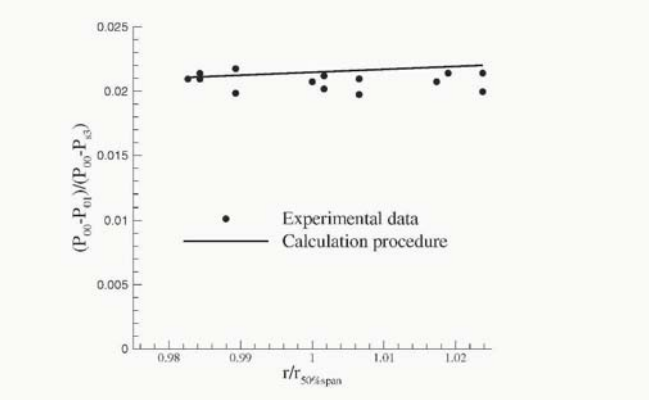

Figure 3. Comparison of experimental data and calculations for the loss of stagnation pressure across the bars at design conditions of the cascade, $Re_3 = 1.9 \times 10^5$, $Ma_3 = 0.64$

4.2 Datum Profiles

In this section, the results from a high speed and a low speed cascade both being the model of an existing LPT blade are compared for steady and unsteady

flow conditions. The comparison includes Mach number (velocity) distributions, profile loss measurements and surface mounted hot-film measurements.

4.2.1 Mach number distribution. Figure 4 shows a plot of the distribution of isentropic Mach number for the high speed and low speed cascades under steady flow conditions. The values are non-dimensionalised by the exit isentropic Mach number. The suction peak occurs at 55% of the suction surface length for both blades. The ratio of the maximum surface isentropic Mach number to the exit isentropic Mach number is about 1.15 for both profiles. The flow separates at about 75% of the suction surface length for both cases. Differences are seen in the region covered by the suction side separation bubble. For a similar length of bubble in both blades, the acceleration due to the blockage of the bubble is bigger in the case of the high speed profile. This is due to compressibility effects. For both profiles, the flow is attached to the blade surface at the trailing edge.

According to Banieghbal et. al, 1995, a pressure side separation bubble occurs on both blades. The Mach number distributions show differences in this region. These could be due to errors in the measurements of the very low velocities associated to the bubble on the low speed profile.The length of the bubble is the same for t he high speed and the low speed profile. The bubble extends up to 50% of the pressure surface length. From this position, the flow accelerates towards the exit value.

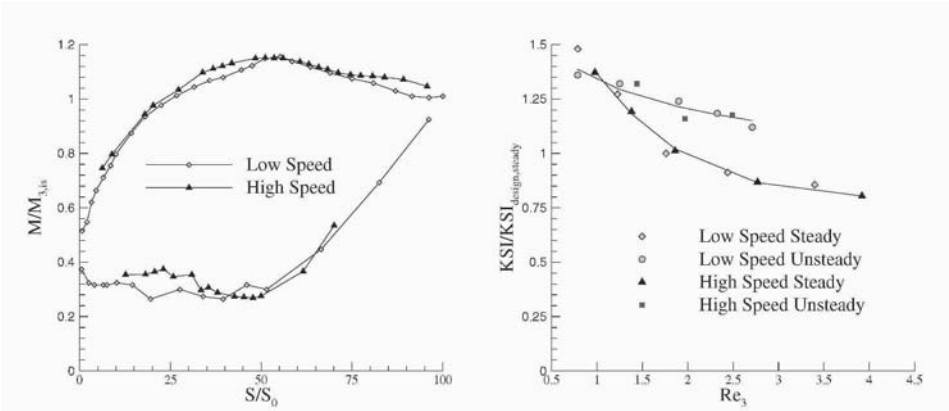

Figure 4. Mach number distribution around the low speed and the high speed profile under steady inflow. $Re_3 = 1.9 \times 10^5$

Figure 5. Kinetic Energy (profile) Loss Coefficient KSI versus Reynolds number

4.2.2 Cascade losses. Pitchwise traverses were performed at midspan behind the high speed and low speed cascade in order to measure the profile loss. Figure 5 shows a plot of the profile losses against Reynolds number for steady and unsteady inflow conditions for both cascades. The design exit Mach number of the high speed blade is 0.64. The kinetic energy loss coefficient KSI is used for the high speed cascade to allow a comparison to be made with the low speed cascade. This is because it is equal to the stagnation pressure loss coefficient when the flow is incompressible. It is seen in the figure that the same trends and the same absolute levels of losses are found for the low speed and high speed cascades. This is true for both steady and unsteady inflow conditions. Figure 5, on its own, answers the question regarding the validity of the low speed approach for the case under consideration.

The LPT blade that both cascades model was designed without considering the effect of unsteady inflow. At $Re_3 = 1.90 \times 10^5$, a small suction side separation bubble features on the blade under steady inflow. When wakes are present, wake induced transition always happens near the separation point. The suppression of this small bubble does not produce any benefit. Instead a penalty occurs because more surface is covered by turbulent flow thus increasing the losses. At $Re_3 = 0.88 \times 10^5$, the size of the separation bubble increases, being more detrimental in terms of losses. Therefore, the suppression of the separation bubble by the unsteadiness at this condition produces a benefit in terms of losses. The curve of unsteady inflow conditions crosses the one for steady inflow at about $Re_3 = 1.00 \times 10^5$.

4.2.3 Hot films results. Up to this point, the comparison between the high speed and the low speed cascade has been made on the bases of profile loss measurements and Mach number distributions. A comparison of the state of the boundary layer along both profiles is also needed. Multi-element hot film anemometers were used to study the development of the blade surface boundary layer. The description of the technique and the description of the presentation of the data can be extensively found in literature (e.g. Banieghbal et. al, 1995).

The anemometers were fitted at the mid-span of the suction surface of the blade in the central passage Figure 6 and figure 7 present distance-time, ST, diagrams of quasi-shear stress from one of the ensembles of the anemometer data, i.e., raw data. Both figures show data obtained at the design conditions. The same behavior can be identified in both cases. In the results obtained with steady inflow at the design point (not shown here), separation was seen to occur between 75% and 80% of the suction surface. The latter is true for the low speed and the high speed cascade. Figure 6 and 7 show that the onset of transition is moved upstream periodically due to the wake passing effect. Along the wake induced path, the onset of transition occurs near to the point

of steady separation. From the onset of transition onwards, the typical wedge shape proper of wake induced transition is seen (Schulte, 1995). This wedge shape is caused by the dissimilar velocity convections of the different characteristic trajectories of the leading and trailing edges of the turbulent spots. Between the wake trajectories, the flow is still separated. Along these paths, transition occurs within the shear layer existing between the free stream and the separation bubble.

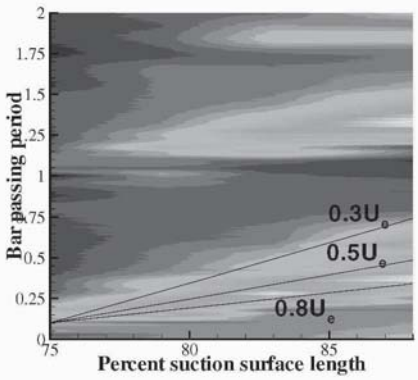

Figure 6. Quasi-shear stress. Design point. Low speed cascade , $Re_3 = 1.9 \times 10^5$, (Banieghbal et al, 1995)

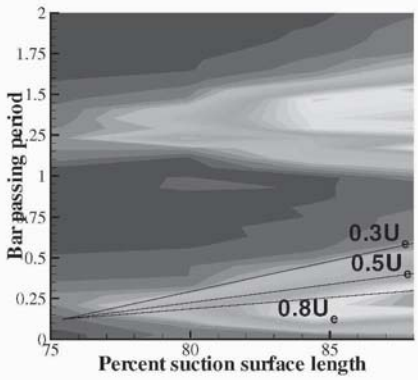

Figure 7. Quasi-shear stress. Design point. High speed cascade. $Re_3 = 1.9 \times 10^5$, $Ma_3 = 0.64$

4.3 CLT2 Profile

The conclusions drawn in the previous section are valid for a conventional profile. Nowadays, the new profiles tend to have an increased lift coefficient and/or loading in order to reduce either number of blades per stage and/or a full stage of the LPT (Vazquez et al. 2003). These authors argued that lift coefficients higher than 1.2 and mean stage loading parameters higher than 3 were required to achieve a reduction of the number of components of the LPT. With the conventional technology, these new values would lead to an important efficiency penalty associated in part with increased profile losses.

The profile that will be presented next is a blade designed by ITP and it is representative of these new trends. This blade, CLT2, is a high turning profile designed to take account of unsteady inflow conditions. A large suction side separation bubble side occurs on the blade under steady inflow conditions. This bubble is suppressed in the presence of the wakes coming from an upstream blade row during a certain fraction of the wake passing period. Due

to compressibility effects, any suppression of a bubble is expected to be more beneficial in high speed flows because of the reduction of blockage. Figure 8 presents the kinetic energy loss coefficient against Mach number under steady and unsteady inflow conditions. The results are shown for the design Reynolds numbers.

For the case under steady inflow, no dependency on Mach number is seen up to $M_3 = 0.76$, from where the losses start to increase. According to Denton (1994), the losses associated with a passage shock wave are generally small unless the shock wave boundary layer interaction produces an earlier separation and therefore, an increase in the losses. For the current case, the first shock waves appear in the passage around $Ma_3 = 0.83$. The increase of losses with Mach number is seen to appear at this Mach number because of the presence of the separation bubble and its increasing size.

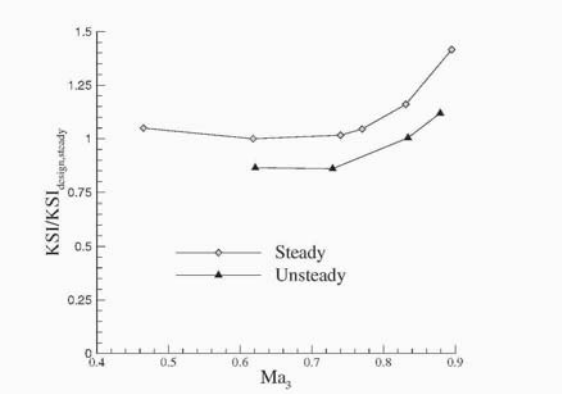

Figure 8. KSI loss coefficient versus Mach number at design Reynolds number (2.0×10^5) for the CLT2 cascade

For the case of unsteady inflow, the losses seem to remain at a constant level at least up to Mach 0.76. The decrease in losses produced by the unsteadiness remains approximately constant for the range of Mach numbers under consideration. It is equivalent to approximately 14% of the steady loss. A benefit is therefore obtained up to $Ma_3 = 0.88$, well within the transonic region.

It should be noticed that these experiments were carried out while keeping constant the rotational speed of the bars. So, the reduced frequency decreases when increasing the Mach number. Therefore, it might be expected that the curve of unsteady inflow conditions approaches that of steady inflow conditions when the Mach number increases. Instead, an approximately constant benefit is obtained for the entire range of Mach numbers under consideration. This is consistent with the suppression of a larger separation bubble at higher Mach numbers but lower reduced frequencies.

5. Conclusions

The techniques employed in the simulation of unsteadiness in high speed linear cascade testing have been presented and compared to the techniques involved in the low speed tests. Results from a high speed and a low speed cascade, both being models of an existing LPT blade have been compared for steady and unsteady flow conditions. The results have shown that the same quantitative values of losses are obtained, showing the validity of the low speed approach for profiles with an exit Mach number of the order of 0.64.

The previous affirmation has been extended to a high turning profile designed following current design practices. Measurements of the losses have shown that there is no dependency on Mach number up to $Ma_3 = 0.76$. A benefit coming from the wakes is achieved up to an exit Mach number of at least 0.9.

Acknowledgments

The authors would like to thank T. Chandler for his work on the high speed rotating bar rig. The authors would also like to thank ITP, for the funding of the project and the permission to publish this paper.

References

[1] Banieghbal, M.R., Curtis, E.M., Denton, J.D., Hodson, H.P., Huntsman, I., Schulte, V., Harvey, N. W., Steele, A. B., "Wake Passing in LP Turbines Blades", presented at the AGARD conference, Derby, UK, May 8-12, 1995

[2] Brunner, S., Fottner, L., Schiffer, H, "Comparison of Two Highly Loaded Low Pressure Turbine Cascades under the influence of Wake-Induced Transition " ASME 2000-GT-268, 2000

[3] Coton, T.,Arts, T., Lefebvre, M., Liamis, N, "Unsteady and calming effects investigation on a very high lift LPT blade", ASME GT-2002-30227, 2002.

[4] Denton, J.D., "Loss Mechanism in Turbomachines". IGTI Gas Turbine Scholar Lecture 1994. ASME J Turbomachinery, Oct. 1994.

[5] Doorly, D.J., "A Study of the effect of wake passing on Turbine Blades", PhD Thesis, Oxford University, 1984.

[6] Hodson, H.P., Dawes, W.N., "On the Interpretation of Measured Profile Losses in Unsteady Wake-Turbine Blade Interaction Studies", 1996.

[7] Hodson, HP, and Dominy, RG, "Annular Cascade Testing", AGARDograph 328 Advanced Methods for Cascade Testing, AGARD, 1993

[8] Schulte, V., "Unsteady Separated Boundary Layers in Axial Flow Turbomachinery", PhD Thesis, Cambridge University, 1995.

[9] Schulte, V., Hodson. H.P, "Unsteady Wake-Induced Boundary Layer Transition in High Lift LP Turbines", Journal of Turbomachinery, Vol.120, 1996.

[10] Stieger, R.D "The Effects of Wakes on Separating Boundary Layers in Low Pressure Turbines", PhD Thesis, Cambridge University, 2002.

[11] Vazquez, R., Cadrecha, D., Torre, D., "High Stage Loading Low Pressure Turbines. A New Proposal for an Efficiency Chart"

[12] Wisler, D.C, "Loss Reduction in Axial-Flow Compressors through Low-Speed Model Testing" ASME 84-GT-184, 1984.

MULTISTAGE COUPLING FOR UNSTEADY FLOWS IN TURBOMACHINERY

Kenneth C. Hall, Kivanc Ekici and Dmytro M. Voytovych
Department of Mechanical Engineering and Materials Science, Duke University, Durham, NC, 27708-0300

Abstract In this paper, we present the a three-dimensional time-linearized unsteady Euler solver for computing unsteady flows in multistage turbomachines. Using this approach, each blade row is modeled with a computational grid spanning a single blade passage. Within each blade passage, several time-linearized unsteady solutions are computed, one for each of several "spinning modes" retained in the model. Each spinning mode has its own frequency and interblade phase angle. These various solutions are coupled together at the inter-row boundaries between the blade rows. Results are presented for several geometries, and demonstrate the accuracy and efficiency of the method, as well as the importance of multistage effects. In particular, we show that multistage effects can strongly affect the aerodynamic loads acting on a given blade row. Furthermore, the method presented is highly efficient. For example, to perform a flutter calculation requires only about three times the CPU time of one steady flow computation for each interblade phase angle and frequency considered.

1. Introduction

Unsteady fluid motion is essential to gas turbine engine operation. Only through unsteady flow processes can a machine do work on a fluid to increase its total enthalpy. This unsteadiness is provided in compressors and turbines by relative motion of adjacent stators and rotors. Unfortunately, this motion also produces undesirable aeroacoustic and aeroelastic phenomena, i.e. tonal noise and forced blade vibrations induced by rotor/stator interactions. Furthermore, the aeroelastic (flutter) stability of a rotor can be profoundly influenced by the presence of nearby stators and rotors.

Most current unsteady aerodynamic theories model a single blade row in an infinitely long duct, ignoring potentially important multistage effects. However, unsteady flows are made up of acoustic, vortical, and entropic waves.

K.C. Hall et al. (eds.),
Unsteady Aerodynamics, Aeroacoustics and Aeroelasticity of Turbomachines, 217–229.

These waves provide a mechanism for the rotors and stators of multistage machines to communicate with one another.

Recently, a number of investigators have begun to examine the importance of multistage effects on flutter and forced response of cascades, see e.g. Buffum, 1993, Hall and Silkowski, 1997, Silkowski, 1996, and Silkowski and Hall, 1998. Silkowski & Hall have developed a 'Coupled Mode' analysis, an elegant and computationally efficient method for modelling neighboring blade row effects in realistic two-dimensional compressors. Using this approach, the coupling between blade rows is modelled using a subset of the so-called 'spinning modes,' pressure and vorticity waves that propagate between the blade rows. The blade rows themselves are represented by reflection and transmission coefficients. These coefficients describe how spinning modes interact with, and are scattered by, a given blade row. The coefficients can be calculated using any standard isolated blade row model. In particular, Hall & Silkowski used a linearized full potential flow model together with rapid distortion theory to account for incident vortical gusts. The isolated blade row reflection and transmission coefficients, inter-row coupling relationships, and appropriate boundary conditions are all assembled into a small sparse linear system of equations that describes the unsteady flow in a multistage machine arising from a prescribed blade vibration of one of the blade rows.

Using the Coupled Mode analysis, two important observation were made. First, the aerodynamic damping of a blade row that is part of a multistage machine will, in general, be significantly different than that predicted using an isolated blade row model. This is an important result since virtually all unsteady aerodynamic theories currently used in industry assume that the blade row can be modelled as isolated in an infinitely long duct. Second, a good estimate of the aerodynamic damping can be obtained using just a few spinning modes in the model. In fact, most of the unsteady aerodynamic coupling between blade rows occurs in the fundamental spinning mode, that is, the spinning mode associated with the original disturbance. Scattered modes are relatively less important.

2. Theory

To motivate the present method, consider a stator/rotor configuration as shown in Fig. 1, where the rotor blades vibrate with a frequency ω_0 and nodal diameter k_0. When the blades vibrate, the system responds aerodynamically producing acoustical, vortical, and entropic waves that will propagate away from the rotor. Some of the upstream propagating pressure waves will impinge on the stator blades. The stator will, in turn, respond aerodynamically, which will generate new waves and travel away from the stator. Some of these waves will later impinge on the rotor blades, and the process will repeat. Because of

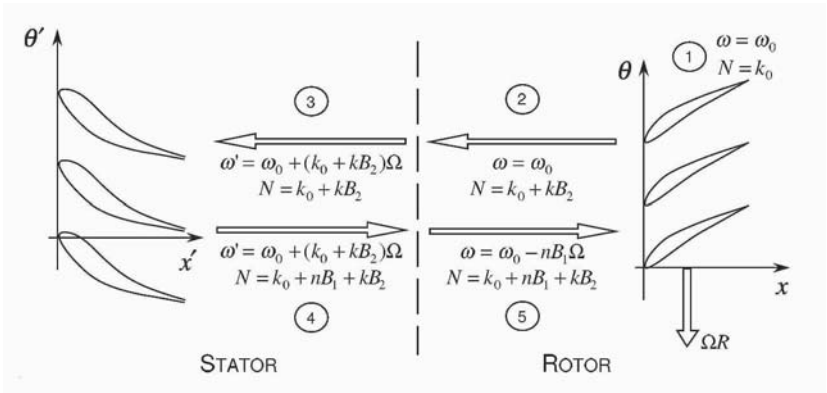

Figure 1. Kinematics of mode scattering and frequency shifting in a multistage machine

the relative motion of the rows, the frequency and the interblade phase angle of the waves in one row will be different when viewed in the frame of reference of the other rows, thus the initial unsteady excitation will scatter and shift into different modes.

The "Coupled Mode" analysis of Hall & Silkowski has demonstrated the importance of multistage coupling on the aeroelastic behavior of multistage machines. Nevertheless, without modification, the new method cannot be efficiently used for more more complex flow models, e.g. the two and three-dimensional Euler equations. In the case where a potential flow model is used to compute the unsteady aerodynamic reflection/transmission coefficients that describe how spinning modes interact with blade rows, many of the coefficients can be computed with a single LU (lower-upper) matrix decomposition. However, the discretized time-linearized Euler equations are generally solved iteratively using pseudo time marching. Only a handful of reflection/transmission coefficient can be computed using a single time-linearized calculation. Thus, the computational advantage of the original Coupled Mode analysis is somewhat diminished for complex flows.

In this paper, we present an alternative approach for solving the multistage problem. To motivate this technique, suppose that the machine to be analyzed has five blade rows with B_1, B_2, ..., B_5 blades per blade row, respectively (see Fig. 1). Suppose that rows 2 and 4 are stators, whereas rows 1, 3, and 5 are rotors. Next, blade row 3 (the middle rotor) is prescribed to vibrate in a traveling wave motion with frequency ω_0 and n_0 nodal diameters corresponding to a fixed interblade phase angle σ_0. Then, between the blade rows, the unsteady flow will be composed of "waves" with N nodal diameters, where

$$N = n_0 + n_1 B_1 + n_2 B_2 + n_3 B_3 + n_4 B_4 + n_5 B_5 \tag{1}$$

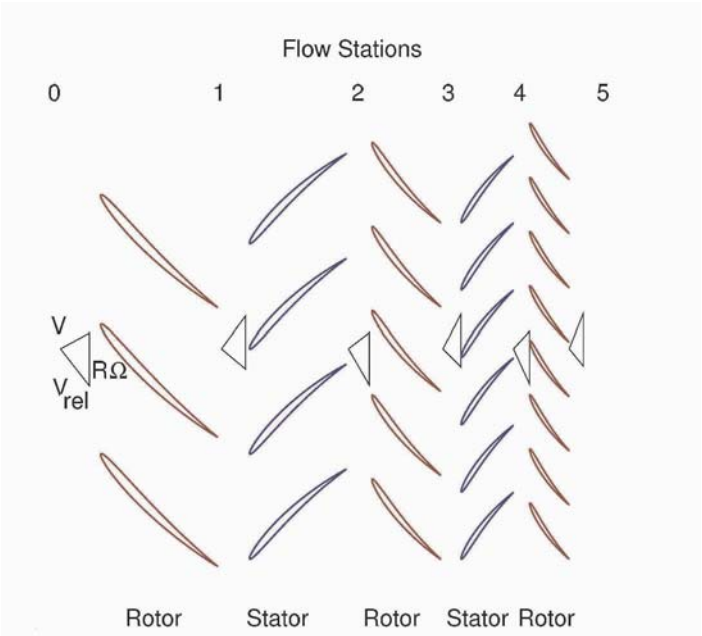

Figure 2. A two-dimensional, two and one-half stage compressor with rows of NACA four digit airfoils

and n_1, n_2, ..., n_5 can take on all integer values. In the rotor frame of reference, the temporal frequency of the waves will be

$$\omega = \omega_0 + (n_2 B_2 + n_4 B_4)\,\Omega \tag{2}$$

where Ω is the rotational rate of the rotor. Similarly, in the stator frame of reference, the frequency is

$$\omega' = \omega_0 - (n_1 B_1 + n_3 B_3 + n_5 B_5)\,\Omega \tag{3}$$

In practice, only a few of the many possible modes, i.e. $(n_1, n_2, \ldots, n_5)$ combinations, contribute significantly to the row to row coupling. This suggests the following strategy, which is the one used in this paper. For each blade row, computational grids for a single passage are generated, and the steady Euler equations are solved on these grids. Then, for the unsteady problem, multiple time-linearized solutions are solved simultaneously on each of the three grids. On each grid, several time-linearized solutions are computed, one for each frequency and interblade phase angle associated with the $(n_1, n_2, \ldots, n_5)$ modes retained in the model. At each iteration of the pseudo time-marching scheme, the unsteady solution at the boundaries between the rotor and stators are Fourier transformed in the circumferential direction to determine how much of each $(n_1, n_2, \ldots, n_5)$ mode is present. This information is then passed

between the stator and the rotor grids allowing acoustic, vortical, and entropic waves to pass from one frame of reference to the other.

This approach has a number of advantages over a direct nonlinear time-simulation of multistage flow. First, in the time-linearized (frequency domain) multistage flow solver, one blade passage is required for each blade row. For a nonlinear time simulation, enough passages must be retained in each blade row so that the computational domain is periodic in the circumferential direction. So for example, a rotor/stator geometry with 22 and 30 blades can be reduced to 11 and 15 blades, but no further. Furthermore, the time-simulation must be computed time-accurately. This makes such calculations extremely expensive. Using the time-linearized approach, on the other hand, one can use local time stepping, multigrid acceleration, and other acceleration techniques commonly used in steady flow calculations,

In the present analysis, we use an explicit Lax-Wendroff scheme to compute both the steady and time-linearized unsteady flow solutions (Hall and Clark, 1993). In both the steady and unsteady flow solvers, we use local time stepping and multigrid acceleration to speed convergence. A conservative smoothing algorithm is used to capture shocks and shock impulses.

3. Numerical Results

Two-Dimensional Results

In this section, the numerical results for a two-dimensional case, Configuration B (see Hall and Silkowski, 1997), will be generated using the multistage solver developed here. To simulate the two-dimensional flow, we solve a three-dimensional linear cascade where there is no radial variation in the steady and the unsteady solutions.

Configuration B is composed of three rows (stator/rotor/stator) of flat plates. The details of this configuration are given in Table 1. The axial gap between the neighboring row is 0.2 times the blade chord. For the case considered here, the steady flow is aligned with the airfoils, i.e., their is no turning of the flow. For the unsteady flow problem, the rotor blades plunge with a reduced frequency $\omega_0 c/U$ of 1.0. The interblade phase angle of the vibration varies between -180° and 180°. For each interblade phase angle, we compute the unsteady lift coefficient C_L using the method outlined above, where

$$C_L = \frac{L}{\rho U \dot{h}_0 c} \tag{4}$$

In Eq. (4), L is the total lift on the airfoil, and $\dot{h}_0$ is the amplitude of the plunging velocity. Shown in Fig. 3 is the real and imaginary parts of the computed unsteady lift when a single mode (the fundamental mode) is used for inter-row coupling. Also plotted on the same figures are the results obtained using the

Table 1. Parameters for Configuration B

		Stator	Rotor	Stator
Number of Blades	B	72	72	72
Chord	c	1.0	1.0	1.0
Gap-to-Chord Ratio	G	0.75	0.75	0.75
Stagger Angle	Θ	45^o	45^o	45^o
Relative Velocity	U	1.0	1.0	1.0
Relative Mach	M	0.7	0.7	0.7
Excitation Freq.	ω_0		1.0	
Excitation IBPA	σ_0		$-180^o \leq 0 \leq 180^o$	
Rotational Speed	ΩR	0.0	1.414	0.0

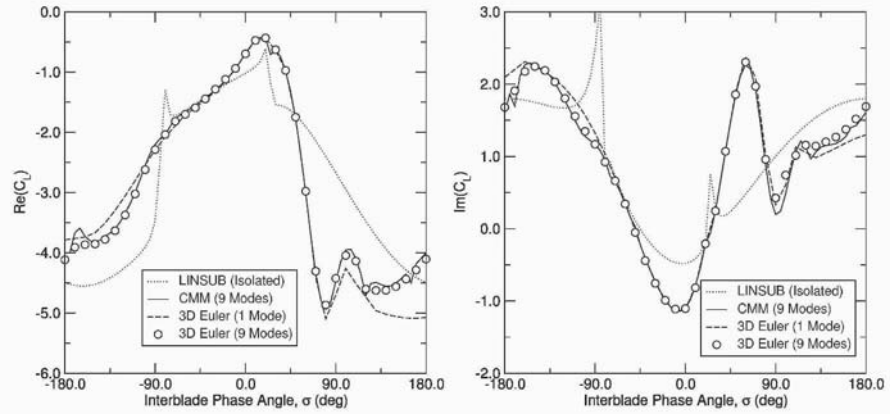

Figure 3. Comparison of the real part of C_L using a single mode

two-dimensional multistage solver (CMM) developed by Hall and Silkowski, 1997. The isolated row results are obtained using Whitehead's semi-analytical LINSUB code (see Whitehead, 1987). As one can see, the overall agreement between the CMM solver and the present solver is excellent. Furthermore, comparing the multistage analyses to the isolated blade row analysis, one sees that multistage influences are significant, that is, the unsteady forces computed are substantially different with and without the influence of neighboring blade rows.

Also shown in Fig. 3 is the computed lift using nine spinning modes to couple the blade rows. Note the very good agreement with one-mode solution, with only minor differences seen at interblade phase angles near $\pm 180^\circ$. These results, and previous results (Hall and Silkowski, 1997, Silkowski, 1996, Silkowski and Hall, 1998) imply that although multistage effects are indeed

Table 2. Parameters for Two-Row Helical Blade Configuration

		Rotor	Stator
Number of Blades	B	38	50
Axial Chord	c	0.11203	0.12566
Radius (Tip)	r_{tip}	1.0	1.0
Radius (Hub)	r_{hub}	0.5	0.5
Stagger Angle(Tip)	Θ	60^o	0^o
Stagger Angle(Hub)	Θ	40.89^o	0^o
Axial Velocity	U	1.0	1.0
Axial Mach Number	M	0.35	0.35
Excitation Freq.	ω_0	1.0	
Excitation IBPA	σ_0	$-180^o \leq \sigma_0 \leq 180^o$	
Rotational Speed	Ω	1.73205	0.0

important, one can obtain accurate results to the unsteady multistage problem using as few as one spinning mode in the solution procedure. The implication is that the cost of performing accurate multistage calculation scales with the number of blade rows.

Three-Dimensional Results (Bending)

To further validate the method, we compare computed three-dimensional results to the unsteady semi-analytical analysis of Namba et al., 2000. The configuration considered here is composed of two rows (rotor/stator) of blades. The upstream rotor has helical surfaces with zero steady pressure loading. The downstream rotor blades are flat untwisted plates aligned with flow that in the nonrotating frame of reference is uniform and axial. The details of this configuration are given in Table 2. The axial gap between the neighboring rows is 0.058973. In this case the rotor blades plunge with a reduced frequency ω_0 of 1.0 based on the local chord and the local axial velocity. The displacement of the blade is normal to the local blade chord. The amplitude of the displacement as a function of the radius is given by

$$a(r) = \frac{c_1 h_1(r)}{\sqrt{1 + \Omega^2 r^2}} \tag{5}$$

where $h_1(r)$ is the radial distribution of the amplitude of a canti-lever beam for the first bending mode.

As an example, the unsteady solution was obtained for an interblade phase angle of 94.7° using nine spinning modes. Figure 4 compares the real and the imaginary parts of the first harmonic of the unsteady pressure difference across the blade computed using the present method to the results obtained using the semi-analytical analysis of Namba et al., 2000. It can be seen that

Table 3. Parameters for Seven-Row Helical Blade Configuration

		Stator	Rotor	Stator	Rotor	Stator	Rotor	Stator
Number of Blades	B	17	22	29	38	50	65	85
Axial Chord	c	0.3696	0.1904	0.2167	0.1120	0.1257	0.06443	0.07392
Radius (Tip)	r_{tip}	1.0	1.0	1.0	1.0	1.0	1.0	1.0
Radius (Hub)	r_{hub}	0.5	0.5	0.5	0.5	0.5	0.5	0.5
Stagger Angle(Tip)	Θ	0^o	60^o	0^o	60^o	0^o	60^o	0^o
Stagger Angle(Hub)	Θ	0^o	40.89^o	0^o	40.89^o	0^o	40.89^o	0^o
Axial Velocity	U	1.0	1.0	1.0	1.0	1.0	1.0	1.0
Axial Mach Number	M	0.35	0.35	0.35	0.35	0.35	0.35	0.35
Rotational Speed	Ω	0.0	1.73205	0.0	1.73205	0.0	1.73205	0.0

the agreement between the two theories is excellent. These results indicate that the present method is "mode-converged" using just nine spinning modes.

Next, the interblade phase angle was varied between -180^o and 180^o and the unsteady lift coefficients was computed. Figure 5 shows the computed unsteady sectional lift coefficients at the mid-span station. The overall agreement over the full range of the possible interblade phase angles is very good. Also, one can easily see the effect of multistage coupling in the same figure.

Three-Dimensional Results (Torsion)

Next, we examine the effect of the number of blade rows in a multistage solution. The configuration used in the previous section is extended to seven rows (stator/rotor/stator/rotor/stator/rotor/stator). Again, the rotors are helical surfaces with zero steady pressure loading, and the stators are flat untwisted plates aligned with the axial steady flow. The details of this configuration are given in Table 3. The axial gap between two neighboring rows is given by $0.25 \times (c_1 + c_2)$. The fourth row of rotor blades are assumed to pitch around the mid-chord position with a reduced frequency ω_0 of 1.0 based on the local chord and the local axial velocity. The displacement of the blade is normal to the local blade chord. The amplitude of the displacement as a function of the radius is given by

$$a(r) = \theta_1(r)(x - x_e)\sqrt{1 + \Omega^2 r^2} \tag{6}$$

where $\theta_1(r)$ is the radial distribution of the amplitude of a canti-lever beam for the first torsion mode and x_e is the position of the torsion axis. In all of the solutions, the interblade phase angle is varied between -180^o and 180^o and the generalized force on the middle blade row is computed. Figure 6 compares solutions for the isolated rotor with a three-row and a seven-row configuration.

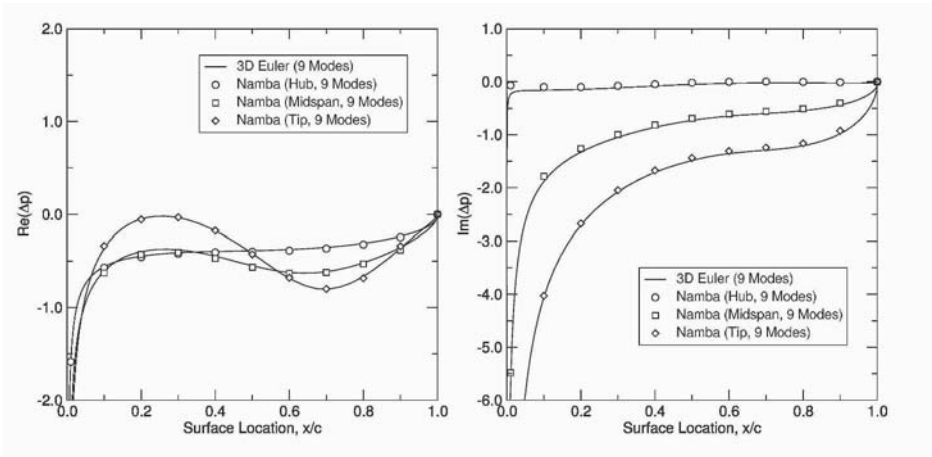

Figure 4. Comparison of the real part of Δp using 9 modes

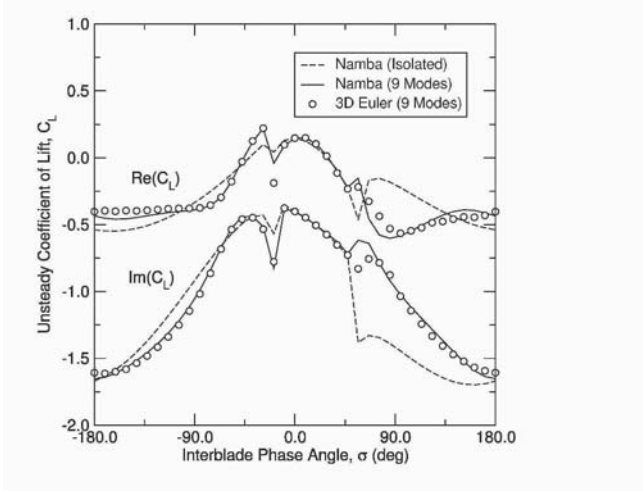

Figure 5. Comparison of C_L at the midspan for coupled and isolated solutions

Note that while the forces computed using three rows are significantly different than those computed using an isolated blade row, the three and seven row results are essentially identical. This implies that the two nearest neighbors have a strong influence on the aerodynamic response of a vibrating blade row, but more distant blade roes do not.

Modern Front Stage Compressor

As an example of the method applied to a realistic geometry, consider the case of the front stage of a modern compressor. This three-dimensional con-

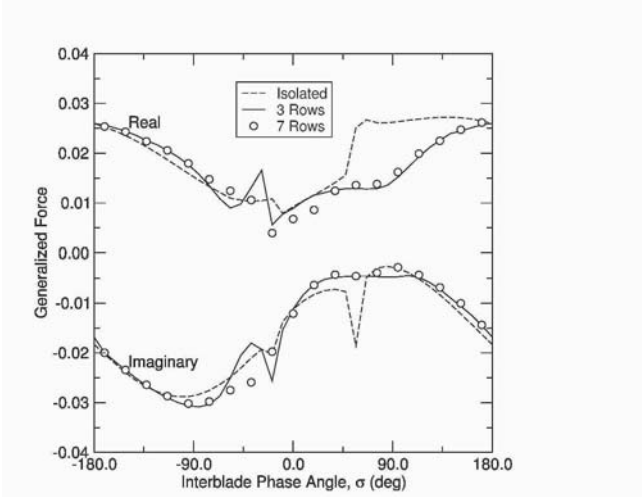

Figure 6. Comparison of Generalized Force for different number of blade rows

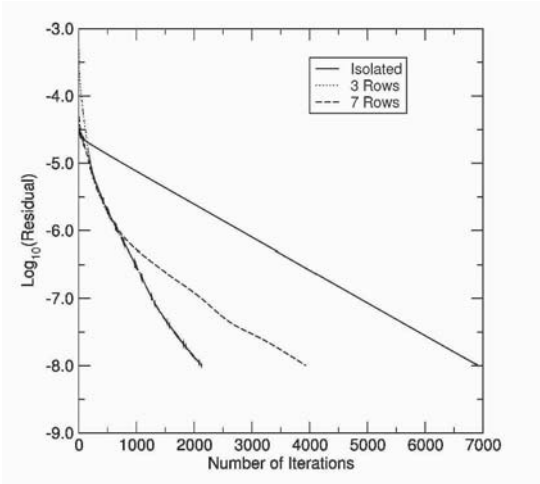

Figure 7. Convergence history for multistage calculations with various number of blade rows

figuration consists of three blade rows (IGV/rotor/stator). Figure 8 shows the static pressure distribution near the midspan location computed using a steady Euler multistage flow solver. Note, that the contours at the inter-row boundaries are not continuous since the only the circumferential averages of the flows in each blade row match at the boundaries.

Next, the middle blade row (rotor) is assumed to vibrate in its first bending mode and frequency. Figure 9 shows the real and the imaginary parts of the unsteady pressure on the rotor row for an interblade phase angle of -30. deg. The multistage solution was computed using one and eight spinning modes in

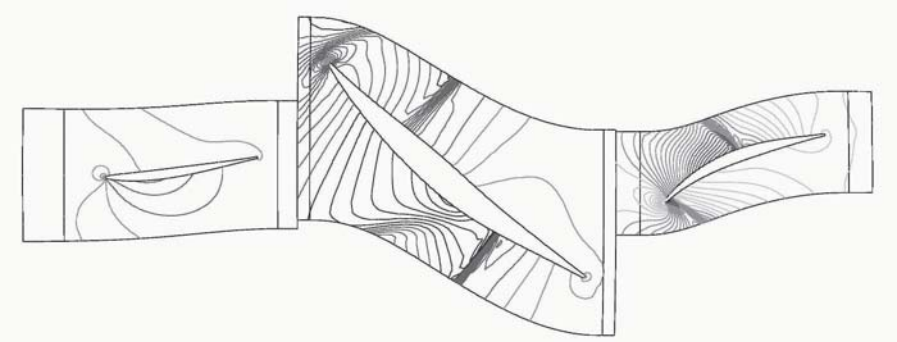

Figure 8. Pressure contours at the midspan of a front stage compressor

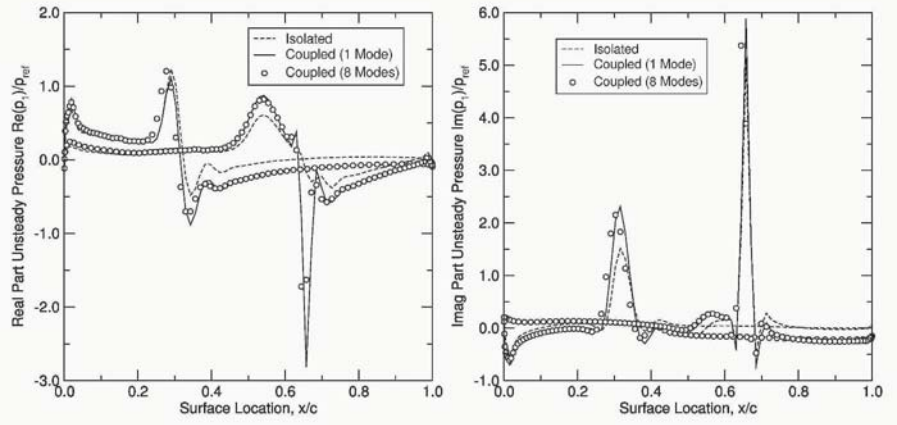

Figure 9. Unsteady pressure distribution on the surface of rotor blades vibrating in first bending with $\sigma = -30^o$

the coupling procedure. One can see that there is significant difference between the isolated and coupled (multistage) computations.

The unsteady pressure distribution can be integrated to obtain the unsteady modal force acting on the rotor blades due to their vibration. Figure 10 shows the real and imaginary parts of the computed generalized forces on the rotor blades as a function of interblade phase angle. Note the significant difference between the forces computed using a single blade row (the rotor) and three blade rows (the rotor and the upstream IGV and downstream stator). Clearly, multistage effects are important. However, the generalized force computed using just one spinning mode is in very good agreement with the force computed using eight spinning modes, indicating the dominant coupling is in the fundamental mode.

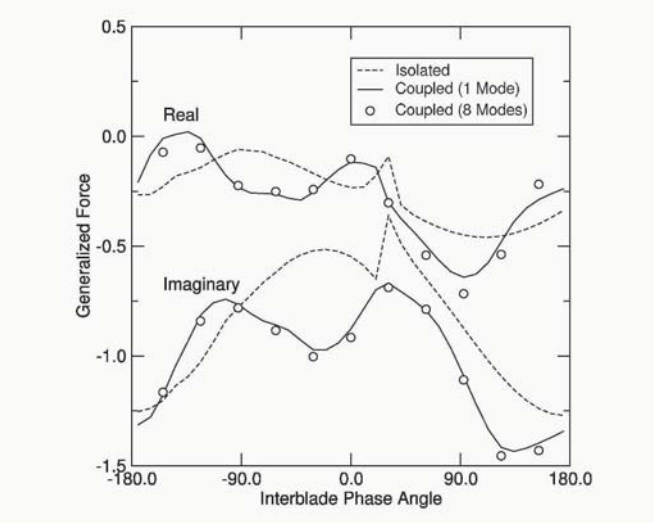

Figure 10. Generalized force acting on rotor blades vibrating in first bending

These results, and earlier two-dimensional results produced by Silkowski and Hall, 1998, Hall and Silkowski, 1997, Silkowski, 1996, confirm that the aerodynamic damping of a blade row that is part of a multistage machine can be significantly different than that predicted using an isolated blade row model. This is an important result since most unsteady aerodynamic theories currently used in industry assume that the blade row can be modeled as isolated in an infinitely long duct. However, a good estimate of the aerodynamic damping can be obtained using just a few spinning modes in the model. In fact, most of the unsteady aerodynamic coupling between blade rows occurs in the fundamental spinning mode, that is, the spinning mode associated with the original disturbance. Scattered modes are relatively less important.

4. Conclusions

In this paper, we have presented a new technique for computing unsteady flows in turbomachinery. The method, which is particularly well suited for the computation of the aerodynamic forces the produce flutter and forced response in turbomachinery, is computationally very efficient, requiring the same order of magnitude of CPU time as a comparable steady flow calculation. In addition, we have shown by numerical example that multistage influences can be quite pronounced. The authors' recommendation is that multistage effects be modeled in all unsteady aerodynamic calculations associated with flutter and forced response. Finally, we note that the predominant coupled among blade rows in a multistage machine is through a single spinning mode (the funda-

mental mode), and it appears that only the nearest two neighboring blade rows have a significant influence on an embedded blade row.

Acknowledgments

This work was supported in part through a grant from NASA Glenn Research Center (NAG3-2627). The authors would also like to thank Professor Namba for providing numerical results from his multistage analysis, to which we compared our results, and which appear in this article.

References

Buffum, D. H. (1993). Blade row interaction effects on flutter and forced response. AIAA Paper 93-2084.

Hall, K. C. and Clark, W. S. (1993). Linearized euler prediction of unsteady aerodynamic loads in cascades. *AIAA Journal*, 31(3):540–550.

Hall, Kenneth C. and Silkowski, Peter D. (1997). The influence of neighboring blade rows on the unsteady aerodynamic response of cascades. *Journal of Turbomachinery*, 119(1):83–95.

Namba, M, Yamasaki, N, and Nishimura, S (2000). Unsteady aerodynamic force on oscillating blades of contra-rotating annular cascades. *Proceedings of the 9th ISUAAAT Conference*.

Silkowski, P. D. and Hall, K. C. (1998). A coupled mode analysis of unsteady multistage flows in turbomachinery. *Journal of Turbomachinery*, 120(3):410–421.

Silkowski, Peter D. (1996). *A Coupled Mode Method for Multistage Aeroelastic and Aeroacoustic Analysis of Turbomachinery*. PhD thesis, Duke University, Durham, NC.

Whitehead, D. S. (1987). Classical two-dimensional methods. *AGARD Manual on Aeroelasticity in Axial Flow Turbomachines, Vol. 1, Unsteady Turbomachinery Aerodynamics (AG-298)*.

IV

AEROACOUSTICS

PASSIVE NOISE CONTROL BY VANE LEAN AND SWEEP

B. Elhadidi
University of Notre Dame
Notre Dame, IN 46556, USA

Abstract A model is developed for modelling the interaction of unsteady three-dimensional incident disturbances with an annular cascade of unloaded swept and leaned vanes. It is shown that the effectiveness of lean or sweep depends on the number of propagating modes and their radial distribution. Results show that vane lean and sweep can be used effectively for certain design configurations to reduce the radiated sound power. However, vane lean and sweep are not effective for all design configurations and for certain cases, they may result in increased radiated sound power.

Keywords: Turbomachinery noise, noise control, sweep, lean.

1. Introduction

Engine noise at approach or take-off, is one of the most critical components of total aircraft noise. For modern day large by-pass turbofan, the major noise contributor is that generated by the interaction of rotor wake with the stator vanes, known as fan noise. There are two major noise reduction techniques: active and passive noise reduction. Active suppression, such as boundary layer suction, has been successful, however, it implies delicate and expensive control systems. Passive suppression are relatively simple since they are incorporated in the fan design.

All passive noise reduction techniques rely on design experience. Classically the number of rotor blades and stator vanes are selected such that the dominant propagating mode is cut-off for the first blade harmonic (Tyler and Sofrin, 1962). Also, duct liners can be used to reduce the noise, by attenuating the propagating modes. However, duct splices used to connect the liners together, increases the number of attenuated propagating modes in the duct, reducing the liner efficiency considerably (McAlpine et al., 2003). Experimental evidence suggests that increased rotor/stator spacing is an effective noise reduction mechanism (Gliebe, 1993, Groeneweg et al., 1991). However, the excess engine weight penalty, and extra external aerodynamic drag may af-

K.C. Hall et al. (eds.),
Unsteady Aerodynamics, Aeroacoustics and Aeroelasticity of Turbomachines, 233–245.

fect the overall reduction gains. Furthermore, the authors have shown (to be published), that increasing the rotor/stator spacing will result in noise reduction only if the swirling mean flow is hydro-dynamically stable. Vane lean and/or sweep are other effective techniques in noise reduction (Woodward R. and Berton, 1999, Envia and Nallasamy, 1999). More recently, rotor blade sweep has been experimentally examined as a means for noise reduction (Heidelberg, 2003).

In this paper we investigate noise reduction by stator vane lean or sweep for the case of a constant uniform axial mean flow. Previously, investigators calculated the unsteady vane response to incident vortical disturbances using a lifting surface formulation (Schulten, 1982, Schulten, 1997), or strip-theory coupled to duct propagation codes (Envia and Nallasamy, 1999). Schulten concluded that lean is not effective whereas Envia and Nallassamy showed results where lean is effective, if it is applied in the opposite direction to the rotor rotation. Also, Schulten predicted that vane sweep is effective for large sweep angles, whereas, Envia and Nallassamy concluded that any sweep angle will be effective. We attempt to examine the previous conclusions, by examining the modal composition of the propagating sound.

In the present paper we develop a three-dimensional numerical analysis to examine the effects of lean or sweep. We begin by formulating the problem. Results are then presented examining the efficiency of lean or sweep in reducing the propagating sound power, and then conclude the paper.

2. Problem Formulation

Governing Equations

We apply the linearized Euler equations in this study. We also assume that the mean flow is isentropic. The flow variables, velocity $\mathbf{U}$, pressure p and density ρ, are considered to be the sum of their mean values $\mathbf{U}_o$, p_o and ρ_o, and their disturbances $\mathbf{u}$, p', ρ'. For this investigation, we assume that the mean flow is uniform and of the form, $\mathbf{U} = U_x \mathbf{e}_x$, where U_x is the constant axial mean flow component, and $\mathbf{e}_x$ is the unit vector along the machine axis.

It is convenient to represent the unsteady velocity disturbance as the sum of a vortical component $\mathbf{u}^R$ and an irrotational component $\nabla\phi$,

$$\mathbf{u}(\mathbf{x}, t) = \mathbf{u}^R + \nabla\phi. \tag{1}$$

For uniform mean flow the vortical component is divergence free, and is purely convected, and the governing equations reduce to (Goldstein, 1976, Atassi,

1994),

$$\frac{D_o \mathbf{u}^R}{Dt} = 0, \tag{2}$$

$$\left(\frac{1}{c_o^2}\frac{D_o^2}{Dt^2} - \nabla^2\right)\phi = 0, \tag{3}$$

where c_o is the mean flow speed of sound, $\frac{D_o}{Dt} = \frac{\partial}{\partial t} + U_x\frac{\partial}{\partial x}$ is the material derivative associated with the mean flow. The pressure is defined as,

$$p' \equiv -\rho_o \frac{D_o \phi}{Dt}. \tag{4}$$

Without loss of generality an incoming vortical gust can be represented as,

$$\mathbf{u}^R(\mathbf{x}, t) = \int_\omega \sum_{m_g=-\infty}^{\infty} \mathbf{a}_{m_g}(r) e^{i(k_x x + m_g\theta - \omega t)} d\omega, \tag{5}$$

where m_g is the azimuthal mode number for the vortical disturbance, and $\mathbf{a}_{m_g}$ represents the gust Fourier modes. ω is the gust angular frequency and $k_x = \frac{\omega}{U_x}$ is the axial wave number. For rotor/stator interaction problems, $\omega = m_g\Omega$, where Ω is the shaft rotational speed. The gust azimuthal mode $m_g = pB$, B is the number of upstream rotor blades, and p is an integer that represents the blade passing frequency (BPF). For this study we only consider the first BPF, $p = 1$. At incidence, we neglect the disturbance radial component, thus the incident vortical disturbance is of the form,

$$\mathbf{a}_{m_g} = \left(-\frac{m_g U_x}{r\omega}, 0, 1\right) a_\theta, \tag{6}$$

where a_θ is the blade up-wash. The mean flow velocity and density are normalized with respect to c_o, and ρ_o, respectively. The unsteady pressure, p' is normalized with respect to $\rho_o c_o a_\theta$. All length scales are normalized with respect to the mean radius, r_m, and the reduced frequency $\tilde{\omega} = \frac{\omega r_m}{c_o}$. The reduced frequency can be related to the rotor tip Mach number, M_t, by the relation, $\tilde{\omega} = pBM_t\frac{r_m}{r_t}$, where r_t is the tip radius.

We consider a single Fourier component of (5) and take $\phi = \tilde{\phi}e^{-i\omega t}$. Equation (3) is an elliptic equation and will be solved numerically.

Numerical Domain and Boundary Conditions

The computational domain is limited to a single vane passage by two surfaces as shown in Figure 1. There are three types of boundary conditions to be imposed. At the hub and tip radii, and vane surfaces we have solid surfaces, along which we apply the impermeability conditions, $\mathbf{u} \cdot \mathbf{n} = 0$. Along

the free surfaces (upstream and downstream of vane section), we impose the quasi-periodicity conditions for the pressure and the normal velocity component, $\{p', \mathbf{u}\cdot\mathbf{n}\}(x,r,\vartheta) = \{p', \mathbf{u}\cdot\mathbf{n}\}(x,r,0)e^{i\sigma}$. Here $\vartheta = \frac{2\pi}{V}$ is the angular vane spacing, V is the number of stator vanes, and $\sigma = \frac{2pB\pi}{V}$ is the inter-blade phase angle. At inflow and outflow non-reflecting boundary condi-

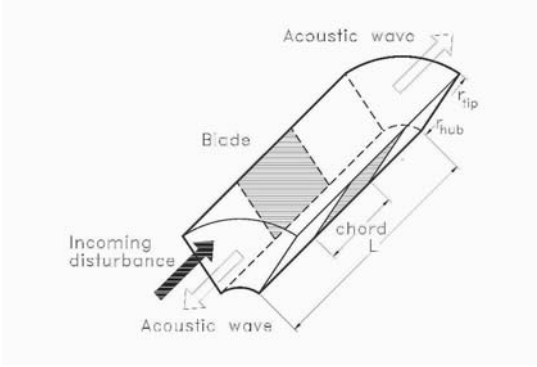

Figure 1. Schematic of the computational domain

tions are implemented. We seek a relationship between the values of p' at an outgoing section, x_1, to those inside the numerical domain, x_2, of the form, $p'(x_1, r, \theta) = \mathcal{M}p'(x_2, r, \theta)$. Here $\mathcal{M}$ is a mapping function. This mapping function has been developed and tested by Elhadidi, 2002.

Numerical Procedure

The harmonic wave equation (3) is solved using a second order finite difference scheme. The algebraic system of equations is solved using an iterative BiConjugate Gradient Stabilized technique and incomplete LU factorization included in PETSc (Balay S. and S., 2000) software.

The model is computationally efficient and results for a single frequency can be obtained in minutes on a single processor SunBlade 1000 computer. Extensive code convergence tests and validation with the benchmark aeroacoustics rotor/stator interaction problem proposed by Hanson, 1999, has been presented in Elhadidi, 2002.

3. Results

We investigate the effect of vane lean or sweep in this section for two test geometries. In one case, we consider the geometry proposed by Hanson, 1999, for the benchmark aeroacoustic problem. In this case, $B = 16$, $V = 24$, $r_t = 1.0$, and the hub radius, $r_h = 0.5$. In the second case we modify the number of rotor blades, $B = 23$ to match the results calculated by Schulten, 1982. The chord, $c = \frac{2\pi r_t}{V}$, and the computational domain length, $L = 3c$.

The axial Mach number, $M_x = 0.5$, and reduced frequency $\tilde{\omega} = 3\pi$, for all test cases. This corresponds to a rotor tip Mach number, $M_t = 0.79$.

We express the outgoing unsteady pressure in terms of the propagating and decaying pressure eigenfunctions which represent the unsteady pressure in the far-field (Golubev and Atassi, 1998),

$$p'(\mathbf{x}) = \sum_{m \in S_m} \sum_{n=1}^{\infty} c_{mn} \mathcal{P}_{mn}(r) e^{i(k_{mn}x + m\theta)}, \tag{7}$$

where m and n are the azimuthal and radial mode numbers for the acoustic modes. S_m is the set of all values of m, which are determined from the Tyler-Sofrin (Tyler and Sofrin, 1962) condition for tonal noise calculations. k_{mn} and $\mathcal{P}_{mn}$ are the axial eigenvalue and corresponding eigenfunction of the mode mn. $\mathcal{P}_{mn}$ is normalized such that the maximum is equal to unity, and the coefficient c_{mn} represents the magnitude of the unsteady pressure for mode mn.

To express the efficiency of noise reduction for lean or sweep, we calculate the relative acoustic power change (RAPC)to the case of zero lean and sweep,

$$\text{Relative power change} = RAPC = 100 \times \frac{P - P_{\alpha=\beta=0}}{P_{\alpha=\beta=0}}, \tag{8}$$

where $P_{\alpha=\beta=0}$ is the acoustic power at zero lean and sweep, α and β are the vane sweep and lean angles respectively. The acoustic sound power, P is calculated from, (Morfey, 1971),

$$P = \sum_{mn=\in S_{mn}} 2\pi \frac{1}{\rho_o c_o} \frac{\omega k_{mn}}{\Lambda_{mn}^2} \left(1 - M\frac{\Lambda_{mn}}{k_{mn}}\right) |c_{mn}|^2, \tag{9}$$

where P is the sound power and S_{mn} is the set of propagating modes. Efficient designs should have a negative RAPC.

Figure 2 shows the real component of the unsteady pressure difference across the stator vane span, for the first test case, with zero lean and sweep. The unsteady pressure difference exhibits a three-dimensional pressure distribution, where it is maximum at the leading edge and drops much faster at the hub as we move towards the trailing edge. This confirms the importance of three-dimensional calculations over the strip-theory approach.

Noise Control by Vane Lean

Lean is defined as the azimuthal displacement, β, of the vane leading edge from its baseline radial position, as shown in Figure 2. The positive lean angle, is in the counter clockwise direction. With this definition, positive lean corresponds to the direction of propagation of the upstream disturbances considered

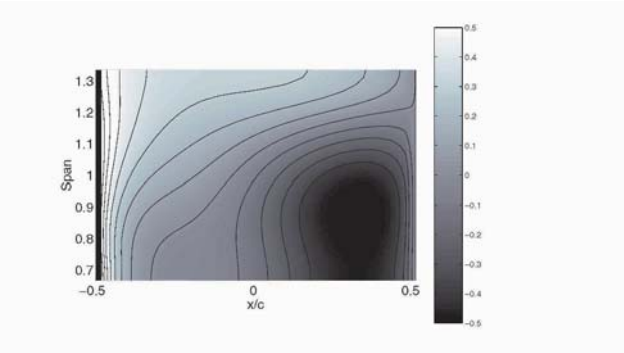

Figure 2. Real component of unsteady pressure difference across vane span for zero lean and sweep, $\tilde{\omega} = 3\pi$, $M_x = 0.5$

in the present work. Spanwise phase variation of the disturbance up-wash will depend on the lean angle. This phase variation is responsible for the noise reduction or amplification. Classically, for a single airfoil, an incident gust with spanwise phase variations reduces the unsteady blade loading and propagating sound (Atassi, 1994). Thus we may argue that increasing vane lean, which increases the incident disturbance spanwise phase variation, will also reduce the perceived noise levels. However, this is not the case. Schulten, 1982, has demonstrated that vane lean increases the noise level, and the quietest configuration was for zero vane lean. On the other hand, Envia and Nallasamy, 1999, have concluded that lean is always effective in the negative direction. In this section we examine the results found in the previous studies, and attempt to resolve the differing conclusions.

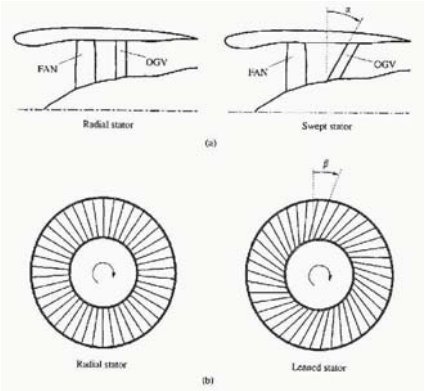

We consider two test geometries, and an incident disturbance with a reduced frequency $\tilde{\omega} = 3\pi$. For the first geometry, $B = 23$, $V = 24$, and there are three propagating acoustic modes ($c_{-1,0}, c_{-1,1}, c_{-1,2}$). This case is similar to

that studied by Schulten, 1982. For the second geometry, $B = 16$, $V = 24$, which is a more relevant case for a real engine configuration. For that case there are two propagating modes ($c_{-8,0}, c_{-8,1}$). Both studies are carried out to (i) compare and validate results with those of Schulten and (ii) examine the effectiveness of vane lean for realistic fans.

Validation Case: $B = 23, V = 24$. For this test case the number of rotor blades and stator vanes are chosen such that the propagating modes have an azimuthal mode number $m = -1$. Figure 3a shows the RAPC versus the lean angle. It is clear that lean is totally ineffective for this rotor/stator configuration with a significant power increase for any lean angle. These results are in agreement with calculations performed by Schulten for a similar geometry.

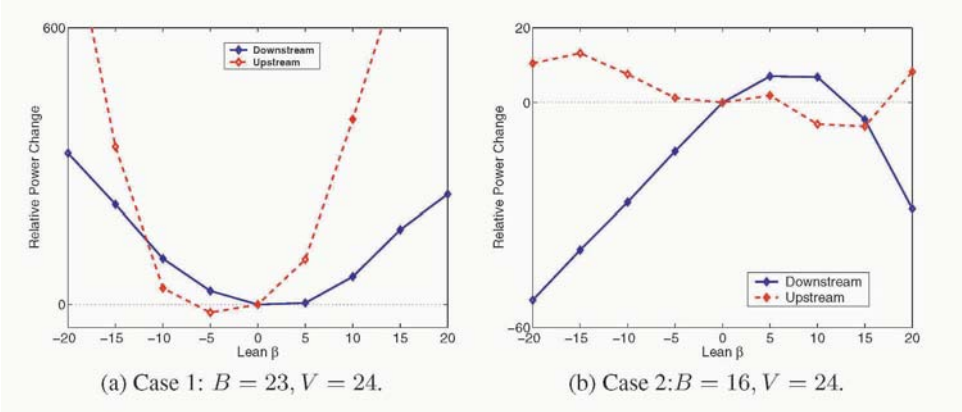

(a) Case 1: $B = 23, V = 24$. (b) Case 2:$B = 16, V = 24$.

Figure 3. Relative power change for downstream and upstream sound power levels for different lean angles. Solid lines represent downstream, and dashed lines upstream sound power change

Benchmark Case: $B = 16, V = 24$. For the benchmark test case the number of rotor blades and stator vanes are chosen such that the propagating modes have an azimuthal mode number $m = -8$. Figure 3b shows the RAPC versus the lean angle. The downstream sound power is significantly reduced for negative and for large positive lean angles. Lean is not effective for the upstream sound power, as also found by the previous investigators. This is attributed to the smaller wavelength of the upstream propagating waves.

Analysis of Lean Effectiveness. Figure 3 indicates that vane lean can be effective or ineffective depending on the rotor/stator geometry. This seems to counter classical results mentioned earlier, than an oblique gust increases the unsteady spanwise pressure distribution, reducing the unsteady lift and propagating sound power (Atassi, 1994). In order to understand and explain the

results of Figure 3, we examine the modal composition of the propagating modes.

Lean generates a spanwise phase variation of the disturbance up-wash on the vane surface. For uniform flow this phase variation is proportional to $e^{\,im_g\beta}$. The larger the lean angle, β, the stronger the phase variation. As shown in Elhadidi, 2002, Atassi et al., 200x, radial gust variations excite and couple with higher order propagating modes. Because of the spanwise phase variation caused by vane lean, the amplitude of the first propagating mode will reduce, whereas, the amplitude of the higher order modes may increase. As a result, for lean to be effective the power reduction contributed from the first mode must be larger than the power increase contributed from the higher order modes. Figure 4 compares the real component of the propagating pressure eigenmodes, $\Re\left(c_{mn}\mathcal{P}_{mn}\right)$, for the zero lean case, and Figure 5 compares the amplitudes of the downstream acoustic modes, $|c_{mn}|$, for various lean angles.

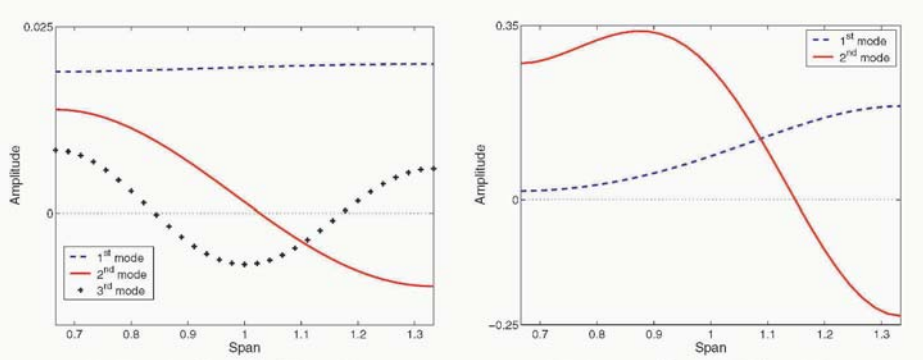

(a) Case 1: $B = 23, V = 24$. (b) Case 2: $B = 16, V = 24$.

Figure 4. Spanwise variation of the real part of the unsteady pressure of the acoustic propagating modes for the two test cases at zero lean $\tilde{\omega} = 3\pi, M_x = 0.5$

For the validation test case, the first propagating acoustic mode is almost a plane wave, and the amplitude of the downstream acoustic pressure decreases as lean is varied from its zero position as seen in Figure 5a. However, the second and third modes amplify at a faster rate than the reduction of the first mode. This accounts for the relative power increase with lean and explains the conclusions of Schulten, that lean is ineffective.

For the second test case, the amplitude of the first mode is reducing for all lean angles, as seen in Figure 5b. For negative lean angles there is an initial increase in the amplitude of the second mode, then a reduction. The increase in the second mode at negative lean angles is smaller than the reduction of the first mode thus reducing the overall sound power. Similarly as the amplitude of the second mode decreases for large positive lean angles, positive lean becomes efficient in the overall sound power reduction.

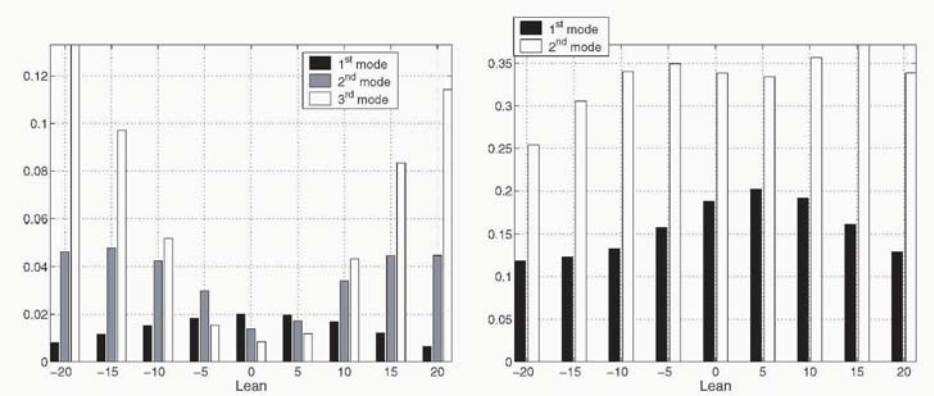

(a) Case 1: $B = 23, V = 24$. (b) Case 2: $B = 16, V = 24$.

Figure 5. Comparison of downstream acoustic pressure intensity for a reduced frequency $\tilde{\omega} = 3\pi$, $M_x = 0.5$ for different lean angles

Schulten suggested that the azimuthal mode number m of the propagating modes is not likely responsible for the increase in the sound power as shown in Figure 3. Rather he attributed this rise to the radial force component acting on the vanes as a result of the lean. We note that Schulten built his conclusions on a single case where $m = -1$. Our results for $m = -8$, show a significant reduction in the acoustic power, thus indicating the importance of the modal composition and the coupling of the cascade response with the gust radial variations.

Lean Effectiveness at Different Reduced Frequencies. The reduced frequency mainly affects the number of propagating modes in the duct. As a result lean effectiveness strongly depends on the reduced frequency. Figure 6 compares the RAPC for different lean angles at different reduced frequencies, for the geometry proposed by Hanson, 1999. For the first two frequencies $\tilde{\omega} = 2\pi, 2.5\pi$ there is one propagating mode, the sound power is significantly reduced for negative lean. For the third and fourth cases there are two propagating modes and the effectiveness of lean is reduced. This is due to the relative increase in amplitude of the second mode over the reduction of the first mode. For the last two test frequencies $\tilde{\omega} = 4\pi, 4.5\pi$ there are four propagating modes ($c_{-8,0}$, $c_{-8,1}$, $c_{-8,2}$, $c_{16,0}$) and lean becomes even less effective. For $\tilde{\omega} = 4\pi$, the reduction of the first mode no longer overcomes the increase of the higher order modes.

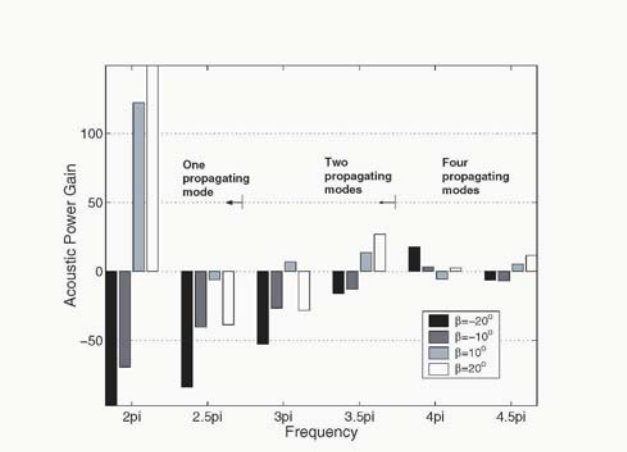

Figure 6. Comparison of RAPC for different stator lean angles and frequencies in uniform flow with $M_x = 0.5, r_h/r_t = 0.5, \tilde{\omega} = 3\pi$. Negative change indicated reduction in sound power levels

Noise Control by Vane Sweep

Sweep as lean is another noise reduction mechanism. Positive sweep is defined as the axial displacement of the vane leading edge from its baseline radial position, as shown in Figure 2. Vane sweep modifies the spanwise phase variation of the incident gust as does lean. For the case of a uniform flow, the disturbance up-wash phase variation is proportional to $e^{i\left(\frac{\omega}{U_x}\Delta r \tan\alpha\right)}$. Increasing the sweep angle will increase the wake intersections with the vane leading edge.

As for the case of lean, numerical calculations are validated by comparing them to results of Schulten, 1997 and, Envia and Nallasamy, 1999. Schulten has concluded that for high Mach number sweep is only effective for large positive sweep angles. For low positive sweep angles sweep is ineffective and there may be an increase in the noise level. It was also indicated that sweep is more effective for reducing upstream noise levels than for downstream noise levels. Envia and Nallasamy have presented experimental evidence showing sweep effectiveness for high positive angles, and numerical results which concluded that positive sweep is always effective and negative sweep is always ineffective. In what follows we attempt to resolve the differing conclusions.

Case Study: $B = 16, V = 24$. Figure 7 compares the upstream and downstream RAPC versus the sweep angle α. The upstream acoustic power level is reduced for both positive and negative sweep. On the other hand, there is a reduction in the downstream sound power for negative sweep, and an initial increase for small positive sweep angles, confirming results calculated by Schulten, 1997. The downstream sound power decreases for sweep angles

larger than 12.5^o. Also, the rate of sound power reduction is larger for sound propagating upstream than downstream. The stronger reduction is attributed to the difference in the axial wavelength. The upstream axial wavelength is smaller than the downstream wavelength, thus variations in vane sweep cause more phase differences. These results are in good agreement with those of Schulten for the same geometry and Mach number. In fact, Schulten predicts the angle of effective sweep to be about 12^o, and that the reduction rate in the upstream sound power is much larger than the downstream sound power.

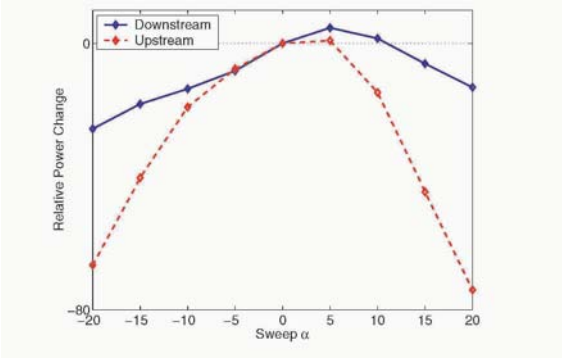

Figure 7. Relative power change for downstream and upstream power levels for different sweep angles

Numerical results indicate that sweep is effective for negative angles. Envia and Nallasamy, 1999 used a combined analytical/numerical technique which concluded that sweep was only effective for positive sweep. The differences between the present results and theirs are attributed to two factors: (i) In their model the wake decay was accounted for and thus the up-wash of the wake is different for positive and negative sweep. In our model we do not account for wake decay, and we beleive it is unlikely to introduce such significant changes. (ii) Our computations are three-dimensional which are different at high frequency from the strip-theory approach used by Envia and Nallasamy.

To demonstrate that the vane sweep introduces spanwise phase variations, the unsteady pressure difference along the vane span for four cases is shown in Figure 8. The first two plots (a) and (b) are for negative sweep, and the plots (c) and (d) are for positive sweep. There is significant spanwise radial loading, associated with vane sweep, compared to the case of zero lean and sweep in Figure 2. Clearly this can not be modeled using strip-theory.

4. Summary for Noise Control

Noise reduction by passive means is possible and simple to apply. It is found from this study that implementation of vane lean or sweep may reduce the sound levels for the tonal noise components. It is important to note that

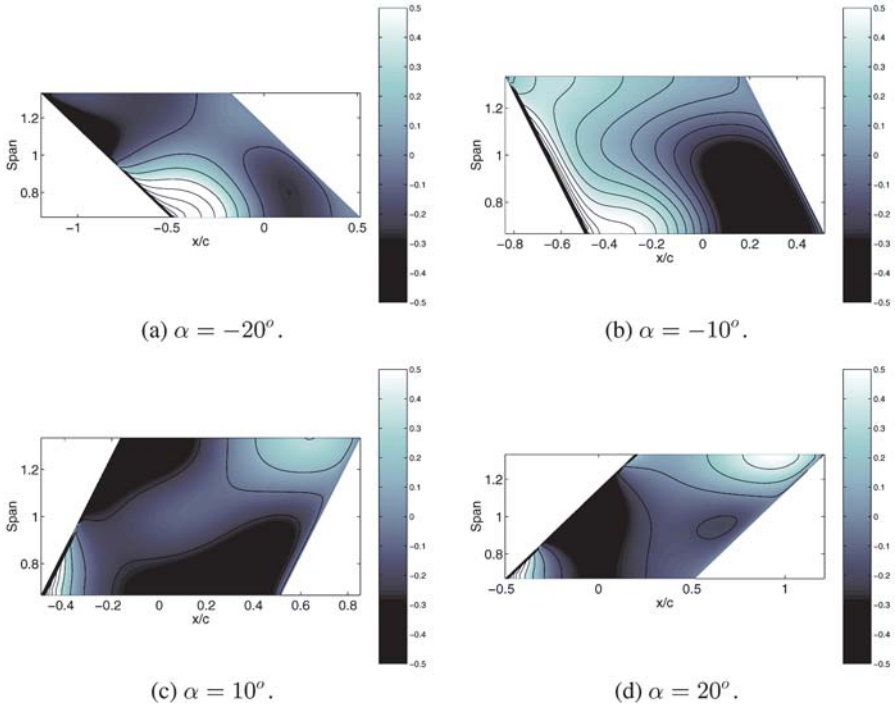

Figure 8. Unsteady pressure difference across vane for different sweep angles and $\acute{\omega} = 3\pi, M_x = 0.5$.

vane lean is dependent on a specific rotor/stator design, tip-hub ratio, and Mach number. Caution should be taken when specifying the lean angle, as a rule of thumb negative lean angles may be more beneficial, however, it is *crucial* to check the results numerically at the design phase. Vane sweep is efficient for large positive sweep angles. Negative sweep angles, even-though unconventional, may show promise to future sound reduction mechanisms. Both lean or sweep effectiveness depends on the number of propagating modes. For a single frequency (tonal noise), the vanes can be designed optimally to reduced the propagating sound power, however, for a frequency spectrum (broadband noise), the number of propagating modes is large, thus vane lean or sweep may not be beneficial.

References

Atassi, H. (1994). *In Aerodynamics and Aeroacoustics,* chapter Unsteady Aerodynamics of Vortical Flows: Early and Recent Developments, pages 121-172. World Scientific.

Atassi, H., Ali, A., and Atassi, O. (200x). Scattering of incident disturbances by an annular cascade in a swirling fbw. *Under consideration for publication in Journal of Fluid Mechanics.*

Balay S., Gropp W., M. L. and S., B. (2000). Petsc users manual. ANL-95/11-Revision 2.1.0, Argonne National Laboratory.

Elhadidi, B. (2002). *Sound Generation and Propagation in Annular Cascades with Swirling Flows*. PhD thesis, University of Notre Dame.

Envia, E. and Nallasamy, M. (1999). Design selection and analysis of a swept and leaned stator concept. *Journal of Sound and Vibration*, 228:793–836.

Gliebe, P. (1993). *Aeroacoustics in Turbomachines and Propellers-Future Research Needs. In Unsteady Aerodynamics, Aeroacoustics, and Aeroelasticity of Turbomachines and Propellers*, pages 621–642. Ed. Atassi, H. M. Springer-Verlag.

Goldstein, M. (1976). *Aeroacoustics*. McGraw-Hill International Book Company.

Golubev, V. and Atassi, H. (1998). Acoustic-vorticity waves in swirling flows. *Journal of Sound and Vibration*, 209(2):203–222.

Groeneweg, J., Sofrin, T., Rice, E., and Gliebe, P. (1991). *Aeroacoustics of Flight Vehicles:Theory and Practice. Volume 1: Noise Sources*, chapter Turbomachinery Noise, pages 151–209. Acoustical Society of America. NASA RP-1258.

Hanson, D. (1999). Fan stator with harmonic excitation by rotor wake. Third CAA Workshop on Benchmark Problems, Category 4.

Heidelberg, L. (2003). Comparison of tone mode measurements for a forward swept and baseline rotor fan. In *9th AIAA/CEAS Aeroacoustics Conference*.

McAlpine, A., Wright, M., Batard, H., and Thezelais, S. (2003). Finite/boundary element assessment of a turbofan splice intake liner at supersonic fan operating conditions. In *9th AIAA/CEAS Aeroacoustics Conference*.

Morfey, C. (1971). Acoustic energy in non-uniform flows. *Journal of Sound and Vibration*, 14(2):159–170.

Schulten, J. (1982). Sound generated by rotor wakes interacting with a leaned vane stator. *AIAA Journal*, 20:1352–1358.

Schulten, J. (1997). Vane sweep effects on rotor/stator interaction noise. *AIAA Journal*, 35:945–951.

Tyler, J. and Sofrin, T. (1962). Axial flow compressor noise studies. *SAE Transactions*, 70:309–332.

Woodward R., Elliot D., H. C. and Berton, J. (1999). Benefits of swept and leaned stators for fan noise reduction. Technical report, NASA/TM-1998-208661.

INTERACTION OF ACOUSTIC AND VORTICAL DISTURBANCES WITH AN ANNULAR CASCADE IN A SWIRLING FLOW

H. M. Atassi,* A. A. Ali,
University of Notre Dame, Notre Dame, IN 46556, USA

O. V. Atassi
Pratt & Whitney, East hartford, CT 06108, USA

Abstract A linearized Euler formulation is developed for the interaction and scattering of incident acoustic and vortical disturbances by an unloaded annular cascade in a swirling flow. Exact nonreflecting boundary conditions for the scattered sound are applied at the inlet/outlet of the computational domain. An explicit primitive variable scheme is implemented and validated by comparison with the uniform flow and narrow annulus limits. Acoustic and aerodynamic results are presented and show that the swirl changes the amplitude and radial phase of the incident disturbances and modifies the number and radial shape of the acoustic modes in the duct. These changes have significant effects on the aerodynamic and acoustic response of the cascade.

1. Introduction

For typical fan engines, the interaction of the rotor wakes with downstream guide vanes is a major source of noise and vibration. Downstream of the rotor the flow has a swirling motion produced by the work done on the flow by the rotor. The swirl strongly distorts the rotor wakes [Podboy et al., 2002] and produces centrifugal forces that deflects the fluid motion and couple the acoustic, entropic and vortical modes in the duct [Kerrobrock, 1977]. The present paper develops a model for the scattering of incident acoustic and vortical waves

*Corresponding Author: atassi@nd.edu

K.C. Hall et al. (eds.),
Unsteady Aerodynamics, Aeroacoustics and Aeroelasticity of Turbomachines, 247–259.

by an unloaded annular cascade and examines the effect of mean flow swirl, cascade geometry, and incident disturbances on the cascade acoustic and aerodynamic response.

The early model for the cascade scattering problem is the two-dimensional cascade which is obtained by unrolling the annular cascade into an infinite linear cascade. This approximation is valid in the limit where the annulus gap between the tip and hub radii is small compared to the average radius. For a flat plate linear cascade in a uniform flow, the unsteady velocity field can be split into purely convected incident vortical disturbances and scattered potential disturbances. These disturbances are only coupled by the impermeability condition along the blade surface. The linearized governing equations of the scattered field have constant coefficients and thus the problem can be formulated in terms of a singular integral equation [Kaji and Okazaki, 1970b, Goldstein, 1976, Atassi, 1994]. Numerical solutions have been obtained for the unsteady pressure distribution on the blades [Smith, 1971, Ventres, 1980], and the acoustic radiation upstream and downstream [Kaji and Okazaki, 1970a, Hamad and Atassi, 1981]. More recently, analytical formulations using the Wiener-Hopf method were developed for the linear cascade aerodynamic and acoustic fields [Peake and Kerschen, 1995, Glegg, 1999].

The three dimensional geometry of the annular duct was first considered by Schulten, 1982 and Namba, 1987 for a zero stagger cascade using a singularity method. Their model accounts correctly for the duct acoustic modes. However, such methods cannot be extended to staggered and/or loaded cascades since they cannot account for the effects of nonuniform mean flow.

A linearized Euler analysis was developed by Montgomery and Verdon, 1997. At the inlet, they assumed that the gust was convected by the mean flow, thus neglecting changes in amplitude and phase of the incoming disturbance caused by the mean flow. Golubev and Atassi, 2000b and Elhadidi et al., 2000 showed that these changes significantly modified the evolution of the unsteady incident vortical disturbances. More recently, Podboy et al., 2002 carried out measurements that show significant effect of the swirl on wake evolution. Golubev and Atassi, 2000a developed a model for the interaction of unsteady incident disturbances in a swirling mean motion with an annular cascade of unloaded blades. Numerical solutions were obtained only for the unsteady blade pressure. More recently, Atassi et al., 2004 developed a more complete analytical and numerical analysis of the cascade scattering problem in a swirling flow which gives the upstream and downstream scattered sound. They also examined the conditions that result in strong scattering.

In the present paper, the analytical and numerical analyses developed for the interaction of incident disturbances propagating in a mean swirling flow with an unloaded annular cascade are summarized, and aerodynamic and acoustic results are presented to examine the effect of cascade geometry and swirl dis-

tribution on the scattering of incident vortical and acoustic waves. The paper will also provide an accurate and efficient numerical scheme for the calculation of blade unsteady forces and the upstream and downstream radiated sound.

As a first step in the problem formulation, it is shown that the upstream disturbances cannot be specified arbitrarily. This is a result of the fact that the upstream flow is not uniform and for subsonic flows some information has to come from the solution inside the computational domain. The representation of upstream disturbances will be based on results from the normal mode analysis [Golubev and Atassi, 1998, Ali et al., 2000, Ali, 2001]. This analysis shows that mean swirl may significantly modify the acoustic and vortical spectral composition of the propagating modes in the duct. The analysis also shows that vortical nearly convected modes have very small pressure content. However, significant vorticity may be associated with the acoustic modes, if the mean flow is rotational.

Another important element in the formulation and implementation of the scattering problem is the derivation of nonreflecting boundary conditions. The authors [Ali et al., 2001] have previously derived nonreflecting boundary conditions for 'acoustic' and 'vortical' waves propagating in a duct with swirling flow. These boundary conditions have been implemented in an explicit scheme and tested by computing the propagation of 'acoustic' and 'vorticity' waves and comparing the solutions with the normal mode analysis. These solutions have also been validated in Atassi and Ali, 2002 for the scattering of vortical waves by an annular cascade in a uniform flow by comparison with the integral solutions of Namba and Schulten, 2000.

In § 2, the mathematical formulation is presented with the inflow/outflow boundary conditions. In § 3, numerical results are presented and show how swirl modifies the scattering phenomena and what conditions result in strong scattering of the incident field.

2. Mathematical Formulation

We consider a non-viscous, non-heat-conducting fluid and use the Euler Equations as the governing equations. The flow quantities are then expanded as follows

$$\mathbf{U}(\mathbf{x},t) = \mathbf{U}_0(\mathbf{x}) + \mathbf{u}(\mathbf{x},t), \tag{1}$$

$$p(\mathbf{x},t) = p_0(\mathbf{x}) + p'(\mathbf{x},t), \tag{2}$$

$$\rho(\mathbf{x},t) = \rho_0(\mathbf{x}) + \rho'(\mathbf{x},t), \tag{3}$$

where $\mathbf{x}$ stands for the position vector, t for time, and $\mathbf{U}_o$, p_o, ρ_o are the steady mean velocity, pressure, and density, respectively. The corresponding unsteady perturbation quantities, $\mathbf{u}$, p', ρ' are such that $|\mathbf{u}(\mathbf{x},t)| \ll |\mathbf{U}_0(\mathbf{x})|$, $|p'(\mathbf{x},t)| \ll p_0(\mathbf{x})$ and $|\rho'(\mathbf{x},t)| \ll \rho_0(\mathbf{x})$.

The mean flow is assumed axisymmetric and of the form,

$$\mathbf{U}(\mathbf{x}) = U_x(r)\mathbf{e}_x + U_\theta(r)\mathbf{e}_\theta, \tag{4}$$

where U_x and U_θ are the mean velocity components in the axial and circumferential directions, respectively. $\mathbf{e}_x$ and $\mathbf{e}_\theta$ represent unit vectors in the axial and circumferential directions, respectively.

We further assume the flow to be isentropic and nondimensionalize lengths with respect to the mean radius r_m, and define the reduced frequency as $\tilde{\omega} = \frac{\omega r_m}{c_{om}}$.

We assume time-harmonic disturbances of the form $e^{-i\omega t}$ and we use the linearized Euler equations. These equations are solved using the second order accurate Lax Wendroff scheme in the passage between two unloaded blades for an incoming upstream disturbance. The blades are placed in the middle third of the computational domain along the circumferential boundaries. The impermeability condition is imposed at the hub and tip radii and on the blades' surfaces.

Inflow/Outflow Representation

Without loss of generality, we can expand the velocity at the section $x = x_0$ in terms of a Fourier series,

$$\boldsymbol{u}^{(v)} = \sum_{m_g=-\infty}^{m_g=+\infty} \hat{\boldsymbol{u}}_{m_g}(x_0, r) e^{i(m_g\theta - \omega t)}. \tag{5}$$

Considering one Fourier component, dropping the subscript m_g, It was shown in [Atassi et al., 2004] that the vortical upstream disturbances must satisfy

$$i\alpha\hat{u}_x + \frac{im}{r}\hat{u}_\theta + (\frac{1}{r} + \frac{1}{\rho_0}\frac{d\rho_0}{dr} - \frac{1}{U_x}\frac{dU_x}{dr})\hat{u}_r + \frac{\partial \hat{u}_r}{\partial r} = 0, \tag{6}$$

where we have put,

$$\alpha = \frac{\omega}{U_x} - \frac{m_g U_\theta}{r U_x}. \tag{7}$$

To facilitate comparison with the two-dimensional theory, it is convenient to introduce the upwash velocity component normal to the streamlines in the $x - \theta$ plane

$$a_{(u)}(r) = \frac{-\hat{u}_x U_\theta + \hat{u}_\theta U_x}{U}, \tag{8}$$

where, $U = \sqrt{U_x^2 + U_\theta^2}$.

We can then express $\hat{u}_x$ and $\hat{u}_\theta$ in terms of $\hat{u}_r$ and $a_{(u)}(r)$. The radial velocity $\hat{u}_r(r)$ can be chosen arbitrarily but must satisfy the impermeability condition at the hub and the tip.

A quasi-periodic condition is applied in the θ direction,

$$\mathbf{Y}(x, \theta_e, r) = \mathbf{Y}(x, 0, r)e^{i\sigma}. \tag{9}$$

where $\sigma = m'\theta_e$, $\theta_e = \frac{2\pi}{V}$, and V is the number of blades (vanes) in the row. All variables upstream of the blades must satisfy this condition. This condition is equally applied to the density and the velocity component normal to the wakes downstream of the blades (vanes). Thus the propagating acoustic waves must satisfy the condition,

$$m\theta_e = m'\theta_e - 2q\pi, \tag{10}$$

where q is an integer. For a rotor/stator interaction, $m' = pB$ and hence we arrive at the Tyler and Sofrin Tyler and Sofrin, 1962 condition,

$$m = pB - qV. \tag{11}$$

Away from the blade row the farfield behavior of the scattered unsteady disturbances is governed by the eigenmode analysis. To satisfy the causality condition that energy from the source must propagate out of the computational domain, we use the group velocity to segregate the modes propagating downstream (upstream) and denote them with the superscript $+$ $(-)$. Thus we express the unsteady density in the farfield as follows,

$$\rho'^{\pm}(r, \theta, x) = \sum_{n=0}^{\infty} \sum_{m \in S_m^{\pm}} c_{mn}^{\pm} \mathcal{P}_{mn}^{\pm}(r) e^{i(k_{mn}^{\pm} x + m\theta)}, \tag{12}$$

where $k_{mn}^{\pm}$ are the axial wave numbers corresponding to the density eigenfunctions $\mathcal{P}_{mn}^{\pm}(r)$. $S_{mn}^{\pm}$ are the sets of all possible values of m.

For computational purpose this condition is truncated and cast in matrix form

$$\mathbf{P}_N = [C_N]\mathbf{c}, \tag{13}$$

where the elements of the vector $\mathbf{P}_N$ are the unsteady density of the different grid points at the exit plane at $x = x_N$. The elements of the vector $\mathbf{c}$ are the coefficients c_{mn}^{+}, and the elements of the matrix $[C_N]$ are the values of the normal modes $\mathcal{P}_{mn}^{+}(r_i)e^{i(k_{mn}^{+} x_N + m\theta_j)}$ at (i,j).

Similarly, we can write the solution at the previous axial cross-section located at $x = x_{N-1}$. This provides the following condition,

$$\mathbf{P}_N = [C_N][C_{N-1}]^{-1}\mathbf{P}_{N-1}. \tag{14}$$

Note that the number of modes used in the expansion may be smaller than the number of grid points of the computational domain.

3. Results

We examine the effects of the various parameters defining the cascade geometry and the characteristics of the incident disturbances. We present results for a swirling flow in a full annulus and study the effects of the cascade three-dimensional geometry, radial swirl distribution, reduced frequency, and incident disturbance characteristics on the unsteady aerodynamic forces and the radiated acoustics. These results are used to establish when the nonuniform swirling flow produces significant changes to the aeroacoustic response and to elicit the conditions which affect the magnitude and nature of the scattered field.

For simplicity, we model the mean swirl component as a combination of rigid body rotation and potential vortex swirl,

$$U_\theta = \Omega r + \frac{\Gamma}{r}. \tag{15}$$

This model is defined by the two constant parameters Ω and Γ. We further assume the flow to be isentropic with a uniform enthalpy from hub to tip. In this case, the axial component of velocity is given by

$$U_x^2 = U_m^2 - 2[\Omega^2(r^2 - r_m^2) + 2\Omega\Gamma \ln(\frac{r}{r_m})], \tag{16}$$

where U_m is the axial velocity at the mean radius of the duct r_m. It is convenient for presenting the numerical results to define the axial and swirl velocities in terms of the Mach numbers at the mean radius $M_m = U_m/c_{om}$, $M_{m(\Omega)} = (\Omega r_m)/c_{om}$ and $M_{m(\Gamma)} = \Gamma/(r_m c_{om})$.

We consider the scattering of both incident vortical and acoustic waves. For vortical waves, we take one Fourier component of (5),

$$\hat{\boldsymbol{u}}_{m_g} = \hat{u}_{xm_g}\boldsymbol{e}_x + \hat{u}_{rm_g}\boldsymbol{e}_r + \hat{u}_{\theta m_g}\boldsymbol{e}_\theta \tag{17}$$

As in [Atassi et al., 2004], we introduce the upwash velocity component normal to the streamlines in the $x-\theta$ plane

$$a_{m_g}^{(u)}(r) = \frac{-\hat{u}_{xm_g}U_\theta + \hat{u}_{\theta m_g}U_x}{U}, \tag{18}$$

where, $U = \sqrt{U_x^2 + U_\theta^2}$. This facilitates comparison with two-dimensional theory.

Incident acoustic waves are expanded in terms of the normal modes. The mn component of the incident pressure is of the form

$$p'_{mn} = c_{mn}^{(i)}\mathcal{P}_{mn}(r)e^{i(k_{mn}x + m\theta - \omega t)}, \tag{19}$$

and its velocity components are defined in terms of the pressure in [Atassi et al., 2004]. The upwash for the acoustic mode is defined as

$$a_{mn}^{(u)} = c_{mn}^{(i)} \frac{-u_{xmn} U_\theta + u_{\theta mn} U_x}{U}, \tag{20}$$

where u_{xmn} and $u_{\theta mn}$ are the axial and azimuthal acoustic velocity of the {mn} mode, respectively.

We define the sectional lift coefficient as,

$$c_L'(r) = \frac{L'}{\rho_o c a^{(u)} U}, \tag{21}$$

where L' is the force per unit span and c is the chord length and where we have dropped the subscript for $a^{(u)}$ so that it could represent either a gust (18) or an acoustic wave (20). The quantities ρ_o, c, $a^{(u)}$, and U are evaluated at the radial location of the considered section. The acoustic coefficients are calculated so that the maximum value of pressure eigenfunctions are equal to unity and the pressure is normalized by $(\rho_{om} c_{om} a_m^{(u)})$ where ρ_{om}, c_{om}, and $a_m^{(u)}$ are the values of the mean density, the mean speed of sound, and the upwash at the mean radius, respectively. The calculations are carried out with the x-axis centered at the mid-chord of the blade (vane) at the mean radius.

Effect of Hub-Tip Ratio

The effect of hub-tip ratio on the unsteady lift coefficient and acoustic coefficients is studied for hub-tip ratios of 0.6, 0.6667, 0.7391, 0.8182, and 0.9048. We consider rotor/stator interaction with $B = 16$ and $V = 24$ and a mean flow of $M_o = 0.3536$, $M_\Omega = 0.1$, $M_\Gamma = 0.1$. The c/r_m ratio at the mean radius is 0.3491, $\tilde{\omega} = 3\pi$, and a grid of $\{n_x \times n_\theta \times n_r\} = \{161 \times 21 \times 21\}$ is used.

Figure (1) compares the absolute value of the unsteady lift coefficient along the span for the different hub-tip ratios. The figure shows significant effect of the hub-tip ratio. For the largest two ratios, variations in the lift coefficient along the span is small. These variations become significant as the ratio decreases. For $r_h/r_t = 0.6$ and 0.6667, two propagating acoustic modes exist. For the other three values of r_h/r_t only one mode propagates. This explains the difference in the trend of the results between the two cases of $r_h/r_t = 0.6$ and 0.6667 and the other cases.

The magnitude of the upstream and downstream acoustic coefficients for the different hub-tip ratios are compared in Fig. (2). The downstream acoustic coefficient of the first radial mode ($n = 0$) increases as the hub-tip ratio decreases until the second mode cuts on where it starts to decrease. Both downstream and upstream coefficients of the second acoustic mode increase as the hub-tip ratio decreases. These results show that change in the number of cut-on modes has strong influence on the aerodynamic and acoustic coefficients.

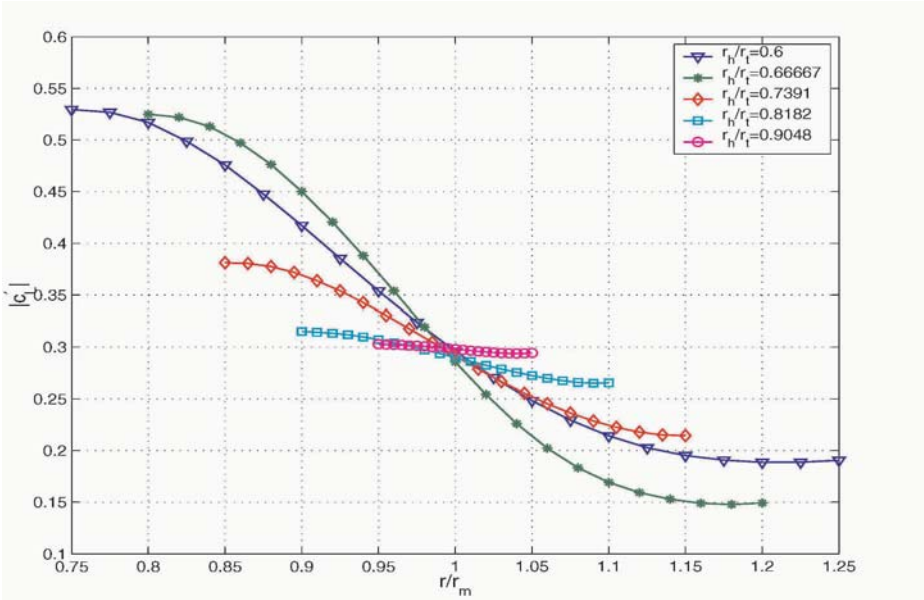

Figure 1. Comparison of the lift coefficient for different hub-tip ratios. $M_o = 0.3536$, $M_\Omega = 0.1$, $M_\Gamma = 0.1$ and $\tilde{\omega} = 3\pi$

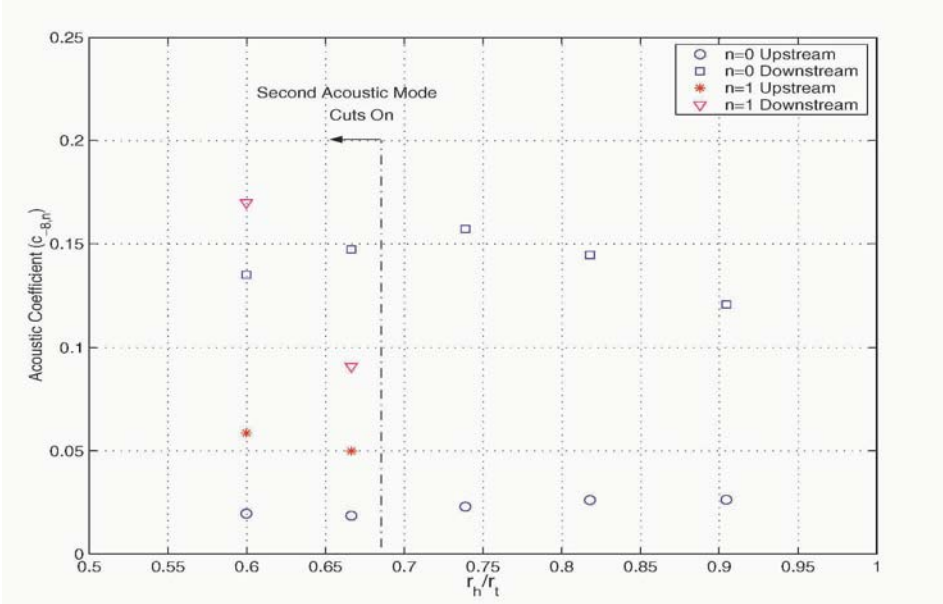

Figure 2. Comparison of the upstream and downstream acoustic coefficients for different hub-tip ratios. $M_o = 0.3536$, $M_\Omega = 0.1$, $M_\Gamma = 0.1$ and $\tilde{\omega} = 3\pi$

Effect of Mean Flow Variation on the Scattering

In a swirling mean flow various radial profiles can be obtained by considering different combinations of free vortex and rigid body swirl. To illustrate how the radial variation of the mean flow changes the aeroacoustic response, we consider four different mean flows with the same total Mach number of 0.4062 at the mean radius. The first mean flow is axial and uniform. The three swirling flows have the same axial and swirl Mach numbers of 0.3536 and 0.2, respectively, at the mean radius and consist of a free vortex swirl distribution with $M_\Gamma = 0.2$, a rigid body swirl with $M_\Omega = 0.2$ and a combination of free vortex and rigid body swirl, $M_\Gamma = 0.1$ and $M_\Omega = 0.1$. The c/r_m ratio at the mean radius is 0.3491, $\tilde{\omega} = 3\pi$, $m_g = B = 16$, $V = 24$, $r_h/r_t = 0.6$ and a grid of $\{n_x \times n_\theta \times n_r\} = \{161 \times 21 \times 21\}$ is used. The gust radial component $\hat{u}_r = 0$, and its upwash $a^{(u)} = 1$. For the uniform flow, only one propagating acoustic mode (-8, 0) exists, while two propagating modes [(-8, 0), (-8,1)] exist for the three swirling flows.

Figure (3) compares the absolute value of the unsteady lift coefficient along the span for the different mean flows. The figure shows significant difference in the value and variation trend between the uniform flow case and the swirling flow cases indicating that the swirl effect significantly modifies the unsteady lift. The differences in the lift coefficient of the three swirling flows are not significant. We now examine the magnitude of the upstream and downstream acoustic coefficients presented in Table (1). The table shows that the downstream acoustic coefficients are larger than those upstream for all mean flows. However, the difference between the downstream and upstream acoustics is much larger in the swirling flows than in the uniform flow.

Although the swirl radial distribution (blade twist) does not seem to have much effect on the magnitude of the unsteady lift coefficient, it has a significant effect on both upstream and downstream acoustic coefficients as shown in Table (1). The acoustic energy scattered by the incident gust is larger for the rigid body swirl distribution than that of the combined swirl which is larger than that of the free vortex. We also note that for the free vortex case most of the energy is scattered in the first mode whereas the second mode dominates for the rigid body swirl. In order to explain this result, we examine the incident gust radial phase variation. Since the gust is nearly convected and the distance travelled from the inlet to the leading edge in our computational domain is about a chord length $c << r_m$, the quantity α defined by equation(7) gives a good estimate of the gust phase. For a rigid body swirl, α increases by $\pi/2$ from hub to tip, whereas for the free vortex it increases by 3.28π. This affects the sectional lift phase but not its magnitude. However, the scattered acoustic energy which depends on the entire radial distribution of the gust is strongly affected.

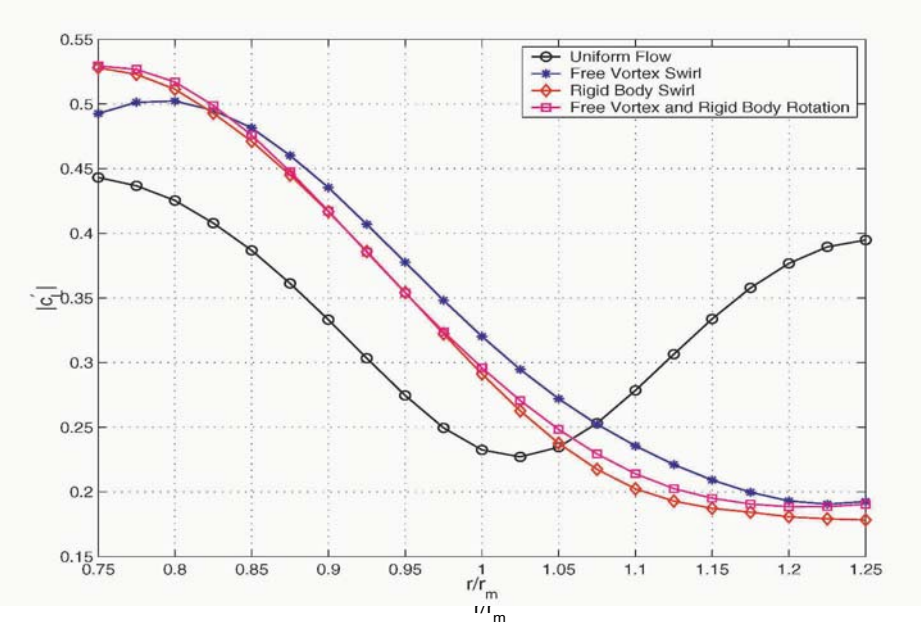

Figure 3. Comparison of the magnitude of the lift coefficient for different mean flows. $r_h/r_t = 0.6$ and $\tilde{\omega} = 3\pi$

	$M_o = 0.4062$ $M_\Omega = 0$ $M_\Gamma = 0$	$M_o = 0.3536$ $M_\Omega = 0$ $M_\Gamma = 0.2$	$M_o = 0.3536$ $M_\Omega = 0.2$ $M_\Gamma = 0$	$M_o = 0.3536$ $M_\Omega = 0.1$ $M_\Gamma = 0.1$
First Downstream Mode	0.2015	0.1610	0.1375	0.1349
Second Downstream Mode	Cut off	0.07869	0.2140	0.1698
First Upstream Mode	0.1363	0.0143	0.0313	0.0195
Second Upstream Mode	Cut off	0.0370	0.0763	0.0586

Table 1. Magnitude of the upstream and downstream acoustic coefficients c_{mn}. $r_h/r_t = 0.6$ and $\tilde{\omega} = 3\pi$

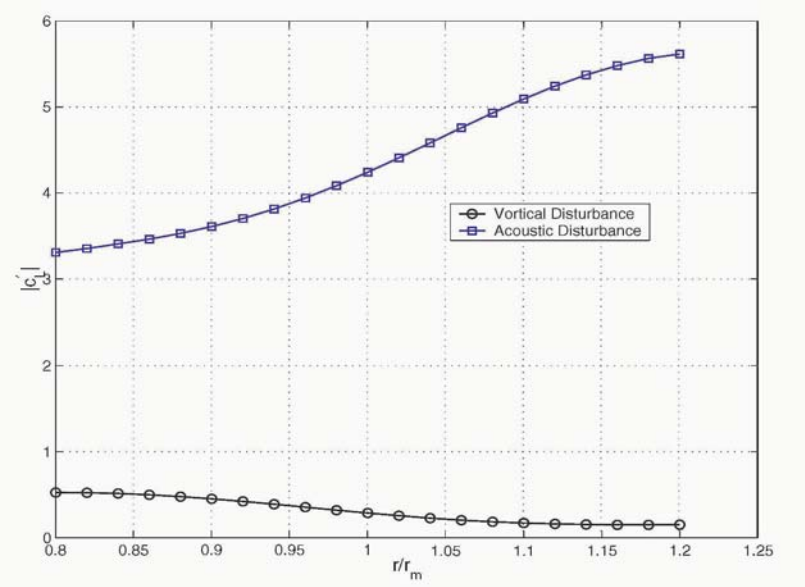

Figure 4. Comparison of the magnitude of the lift coefficient for acoustic and vortical incident disturbances. $M_o = 0.3536$, $M_\Omega = 0.1$, $M_\Gamma = 0.1$, $r_h/r_t = 0.6667$, and $\tilde{\omega} = 3\pi$

Sound Transmission Through a Cascade

We consider now the scattering of an incident acoustic mode of $m = -8$ and $n = 0$ and compare that to the scattering of a vortical disturbance. We take the upwash component to be the same at the mean radius and equal to unity for both disturbances. For the vortical disturbance the upwash is constant along the radius but for the acoustic mode it changes slightly (about 10%). This upwash corresponds to an acoustic mode with a coefficient $c_{-8,0} = 1.18$. In the two cases, $M_o = 0.3536$, $M_\Omega = 0.1$, $M_\Gamma = 0.1$, $r_h/r_t = 0.6667$, $c/r_m = 0.3491$ at the mean radius, $\tilde{\omega} = 3\pi$, and a grid of $\{n_x \times n_\theta \times n_r\} = \{161 \times 21 \times 21\}$ is used. The vortical disturbance has $\hat{u}_r = 0$.

Figure (4) compares the magnitude of the unsteady lift coefficient along the span for the two cases. The lift coefficient is much higher for the acoustic disturbance. This may be explained by the fact that the wavelength of the acoustic wave in the x-direction is much larger than that of the vortical wave. This causes phase cancellation along the blade in the case of the vortical disturbance thus reducing the lift coefficient compared to the case of upstream acoustic disturbance.

The magnitude of the upstream and downstream acoustic coefficients for the two cases are compared in Table (2). The acoustic coefficients are much higher in the case of the acoustic disturbance especially for the first acoustic mode.

Table 2. Magnitude of the upstream and downstream acoustic coefficients $c_{m\,n}$ for acoustic and vortical incident disturbances.

	Vortical Upstream Disturbance	Acoustic Upstream Disturbance
First Downstream Mode	0.1471	0.8608
Second Downstream Mode	0.0908	0.1458
First Upstream Mode	0.0185	0.0718
Second Upstream Mode	0.0498	0.0775

This is because the incident acoustic wave is the same as the first propagating duct mode and hence has identical radial profile.

Comparing the upstream and downstream coefficients in the case of acoustic disturbance, we see that most of the acoustic energy of the incident acoustic waves has been transmitted and propagated downstream and that the part which is reflected is relatively small.

4. Conclusions

Numerical results are presented to examine the effect of mean swirl on the aerodynamic and acoustic coefficients of an annular cascade. The results suggest that the swirl introduces additional nonuniformities which modify the physics of the scattering in three major ways: (i) it modifies the number of propagating acoustic modes in the duct, (ii) it changes their radial variation in the duct, and (iii) it causes significant amplitude and radial phase variation of the incident disturbances.

Acknowledgments

This research was supported by The Office of Naval Research grant No. N00014-00-1-0130 with Dr. Ki-Han Kim as program manager. H. M. Atassi would like to thank the Ohio Aerospace Institute Aeroacoustic Consortium for its support.

References

Ali, A. A. (2001). *Aeroacoustics and stability of Swirling Flow*. PhD thesis, University of Notre Dame.

Ali, A. A., Atassi, O. V., and Atassi, H. M. (2000). Acoustic eigenmodes in a coannular duct with a general swirling flow. AIAA 2000-1954, 6th AIAA/CEAS Aeroacoustics Conference at Maui, Hawaii.

Ali, A. A., Atassi, O. V., and Atassi, H. M. (2001). Derivation and implementation of inflow/outflow conditions for aeroacoustic problems with swirling flows. In *AIAA 2001-2173, 7th AIAA/CEAS Aeroacoustics Conference at Maastricht, The Netherlands*.

Atassi, H. M. (1994). *Unsteady Aerodynamics of Vortical flows: early and recent developments. In Aerodynamics and Aeroacoustics*, pages 121–172. ed. Fung, K.-Y., World Scientific.

Atassi, H. M., Ali, A. A., and Atassi, O. (2004). Scattering of incident disturbances by an annular cascade in a swirling flow. *Journal of Fluid Mechanics*, to appear.

Atassi, O. V. and Ali, A. A. (2002). Inflow/outflow conditions for time-harmonic internal aeroacoustic problems. *Journal of Computational Acoustics*, 10(2).

Elhadidi, B. M., Atassi, H. M., Envia, E., and Podboy, G. (2000). Evolution of rotor wake in swirling flow. AIAA 2000-1991, 6th AIAA/CEAS Aeroacoustics Conference at Maui, Hawaii.

Glegg, S. A. L. (1999). The response of a swept blade row to a three dimensional gust. *Journal of Sound and Vibration*, 227(1):29–64.

Goldstein, M. E. (1976). *Aeroacoustics*. Mcgraw-Hill International Book Company.

Golubev, V. V. and Atassi, H. M. (1998). Acoustic-vorticity waves in swirling flows. *Journal of Sound and Vibration*, 209(2):203–222.

Golubev, V. V. and Atassi, H. M. (2000a). Interaction of unsteady swirling flows with annular cascades. part II. aerodynamic blade response. *AIAA Journal*, 38:1150–1157.

Golubev, V. V. and Atassi, H. M. (2000b). Unsteady swirling flows in annular cascades. part I. evolution of incident disturbances. *AIAA Journal*, 38:1142–1149.

Hamad, G. and Atassi, H. M. (1981). Sound generation in a cascade by 3D disturbance convected in a subsonic flow. In *AIAA 81-2046, 7th Aeroacoustic Conference, Palo Alto, CA*.

Kaji, S. and Okazaki, T. (1970a). Generation of sound by rotor-stator interaction. *Journal of Sound and Vibration*, 13:281–307.

Kaji, S. and Okazaki, T. (1970b). Propagation of sound waves through a blade row. II. Analysis based on the acceleration potential method. *Journal of Sound and Vibration*, 11:355–375.

Kerrobrock, J. L. (1977). Small disturbances in turbomachine annuli with swirl. *AIAA Journal*, 15:794–803.

Montgomery, M. D. and Verdon, J. M. (1997). A three-dimensional linearized unsteady Euler analysis for turbomachinery blade rows. NASA CR-4770.

Namba, M. (1987). Three-dimensional flow. In Unsteady Turbomachinery Aerodynamics, AGARD-AG-298.

Namba, M. and Schulten, J. B. H. M. (2000). Category 4-fan stator with harmonic excitation by rotor wake. NASA/CP-2000-209790.

Peake, N. and Kerschen, E. J. (1995). A uniform asymptotic approximation for high-frequency unsteady cascade flow. *Proc. R. Soc. Lond.*, A 449:177–186.

Podboy, G. G., Krupar, M. J., Christopher, E. H., and Richard, P. W. (2002). Fan noise source diagnostic test-ldv measured flow field results. In *AIAA 2002-2431, 8th AIAA/CEAS Aeroacoustics Conference at Breckenridge, Colorado*.

Schulten, J. B. H. M. (1982). Sound generated by rotor wakes interacting with a leaned vane stator. *AIAA Journal*, 20:1352–1358.

Smith, S. N. (1971). Discrete frequency sound generation in axial flows of turbomachines. CUED/A-Turbo/TR29.

Tyler, J. M. and Sofrin, T. G. (1962). Axial flow compressor noise studies. *SAE Transactions*, 70:309–332.

Ventres, C. S. (1980). A computer program to calculate cascade 2D kernel. NASA Technical Memorandum.

INFLUENCE OF MUTUAL CIRCUMFERENTIAL SHIFT OF STATORS ON THE NOISE GENERATED BY SYSTEM OF ROWS STATOR-ROTOR-STATOR OF THE AXIAL COMPRESSOR

D. V. Kovalev, V. E. Saren and R. A. Shipov
The Central Institute of Aviation Motors
Aviamotornaya st. 2, Moscow, 111116, Russia *

Abstract As it was established in works [1-4], mutual circumferential shift of stators in a system of rows stator (IGV)-rotor (R)-stator (S) of the axial compressor significant change of pressure pulsations on the rotor blades and in a stream causes (clocking effect). It is possible to expect that similar change of pressure pulsations influences also on the noise, radiated by the specified system of rows. The given work is devoted to an experimental research of influence of stators clocking on the noise, radiated by rows upwards on a stream.

The basic idea of work consists in comparison of measurements of noise pressure in an entrance plenum of the experimental installation, containing in a working part system of rows IGV-R-S, with pressure pulsations on R blades and with intensity of periodic vortexes behind them at mutual circumferential shift of IGV and S. Such comparison allows not only to estimate scales of stator clocking influence on the radiated noise but also to establish the basic sources of observably effects. The received results result in a conclusion, that optimization of a mutual circumferential position of stators may be effective means of decrease of the noise, caused by a rotor-stator interaction in system of rows stator-rotor-stator. The main source of the effect is change of amplitude of pressure pulsations on R blades at stators clocking.

Keywords: Clocking effect, compressors noise

*Work is executed at financial support of International scientific and technical centre (ISTC), the grant number 672.2.

K.C. Hall et al.(eds.),
Unsteady Aerodynamics, Aeroacoustics and Aeroelasticity of Turbomachines, 261–273.

1. Noise in an entrance plenum

Experiments were carried out on the large-dimensional (external diameter 1,2m) low-speed (frequency of rotation of 2000rot/min) compressor, containing system of rows IGV-R-S and in detail described in [4-6]. Numbers of stators vanes are identical (Z_{IGV}=Z_S=36), and 2 variants of the investigated axial gaps were selected so that in one of them clocking effect were insignificant (assembly 1), and in other on the contrary clocking effect was clearly expressed (assembly 2). As shown in [4], to these conditions axial gaps Δ_{12} (between IGV and R) and Δ_{23} (between R and S) on the hub section are corresponded: assembly 1 – Δ_{12}=60mm, Δ_{23}=5mm; assembly 2 – Δ_{12}=15mm, Δ_{23}=15mm. Comparison of results of noise measurement at two specified assembly allows to allocate the effects, connected with IGV and S clocking.

The compressor flowing path with an entrance site and an entrance plenum is presented on Fig.1. The cascades of airfoils, appropriate to cylindrical section of a flowing path on mean radius, are presented on Fig.2.

Noise pressure in an entrance plenum was estimated on a reverberation chamber method. For certification of reverberation properties of a plenum the cycle of measurements of acoustic pressure was preliminary executed at radiation of broadband noise by an electromechanical standard source. Such measurements, executed in 78 points, have allowed to establish a point of a microphone position (the central point) in which vicinity rather uniform noise field is formed with the RMS deviation d within the limits of 0,75-2,5dB on the basic 1/3 octava frequencies exceeding 250Hz. It is necessary to notice that for the basic 1/3 octava frequencies f_0, near to frequencies, multiple to R blade passing frequency (1266,7Hz) the value d appeared within the limits of 0,75-1,25dB. It allows to accept that changes of noise pressure in the plenum, received in the central point and exceeding specified limits, are caused by change of acoustic properties of researched system of rows.

Other important acoustic characteristic of the plenum is time of reverberation τ, which was determined experimentally for everyone 1/3 octaves frequency in a range 500-10000Hz. The range of τ change has made 0,6-2,4 second. Comparison to the data for drown chambers (τ $\sim$0,2 sec.) allows to count reverberation properties of the plenum satisfactory for relative estimations of noise pressure change.

Measurements in the central point were carried out by a microphone of Firm Larson Davis (diameter 0,5 inches, type 2559). As a result of the received data processing levels of noise intensity in dB in 24 of 1/3 octaves frequency bands from 25Hz up to 20kHz with linear averaging during 30 sec. were determined.

All measurements were carried out at independent circumferential shifts of IGV and S to N positions in regular intervals distributed on one S vanes pitch

(all N^2 points of measurements). The matrix is formed from the received noise levels for the given 1/3 octava band

$$D=(Dlk);\ l,k=1,\ 2,\ \ldots,\ N,$$

where k-th column corresponds to shift of S relative IGV on value $\frac{k-1}{N}\cdot h_s$ (h_s is the IGV and S pitch) in a direction of R rotation, and the data in l-th line correspond to shift of IGV concerning its starting position on value $\frac{l-1}{N}\cdot h_s$ in the same direction.

According to the reverberation chamber theory elements of matrix D are connected to noise intensity L_{lk} by a ratio

$$D_{lk} = 10\lg\frac{L_{lk}}{L_0}, \tag{1}$$

where L_0 is some normalized level of the noise intensity ($\sim$10-13kgm/s.m.). According to (1) relative level of the noise intensity, received for various l and k, it was estimated by value size

$$\varepsilon_{lk} = \varepsilon(Y,\nu) = \frac{L_{lk}-\bar{L}}{\bar{L}}, \quad Y = \frac{l-1}{N} \quad , \quad \nu = \frac{k-1}{N}, \quad l,k = 1,2,...,N,$$

where $\bar{L} = \frac{1}{N^2}\sum\limits_{l=1}^{N}\sum\limits_{k=1}^{N}(10^{D_{lk}})^{1/10}$.

As have shown experiments noise level in a plenum for all 1/3 octava bands at given mutual circumferential position of the IGV and S (the parameter ν) essentially depends on coordinate Y, determining their common circumferential position. In the given researches circumferential position of the struts, located between IGV and an entrance aperture in a working part, did not change. Therefore it is possible to expect that influence of coordinate Y is connected to shift of pair rows IGV and S concerning struts, vortical wakes for which are intensive enough.

The received results are presented on Fig.3 (assembly 1) and Fig.4 (assembly 2). On the figures values $\varepsilon = \varepsilon(\nu)$ for 1/3 octava bands are given with the basic frequencies: 1000 Hz (Fig.3a, 4a), 1250Hz (Fig.3b, 4b), 2500Hz (Fig.3c, 4c) and 4000Hz (Fig.3d, 4d). Besides on Fig.3e and 4e the results, received for total noise in a range of frequencies 25-20000Hz are presented.

The choice of the specified 1/3 octava bands was determined by what in them dependences $\varepsilon = \varepsilon(Y,\nu)$ at fixed value Y were the most essential, whereas in other bands such dependences were absent. The data are represented as dependences

$$\varepsilon_{\min}(\nu) = \min_{0\le Y\le 1}\varepsilon(Y,\nu) \quad , \quad \varepsilon_{\max}(\nu) = \max_{0\le Y\le 1}\varepsilon(Y,\nu)$$

$$\varepsilon_0(\nu) = \frac{1}{N}\sum_{l=1}^{N}\varepsilon\left(\frac{l-1}{N},\nu\right)$$

It allows to estimate both an influence of the IGV and S shift relative each other (parameter ν), and total influence of their joint shift concerning struts. On each of Figs.3 and 4 the value is given

$$\overline{D} = \frac{1}{N^2}\sum_{l=1}^{N}\sum_{k=1}^{N} D_{lk},$$

determining average value of the noise, appropriate to the given band of frequencies.

Apparently from the presented results, the most essential dependence of radiated noise intensity from stator clocking is observed in 1/3-octava bands of the frequencies, containing the R blade passing frequency (1266,7 Hz) and multiple to it frequencies. It testifies that optimization of the stators mutual positioning allows to lower first of all tone noise, which basic source are pressure pulsations on the R blades. It is typical that in the specified bands of frequencies the most intensive noise is observed, and dependence from ν of total noise (Figs.3e and 4e) is similar to dependence for 1/3 octava band, containing the R blade passing frequency (Fig.3b and 4b).

As one would expect, all dependences $\varepsilon = \varepsilon(\nu)$ are more essential to assembly 2, where all clocking effects are stronger [6]. The attention appreciable enough (especially for assembly 2) dependence of relative intensity of a noise from stators clocking ν for 1/3 octava band with the basic frequency 1000Hz pays to itself. In this connection it is necessary to notice that, besides pulsations of pressure on the R blades, stators clocking in system of rows stator-rotor-stator essentially changes intensity of periodic, sweeped by a flow the vortexes descending with the R blades [5].

If to assume, that periodic vortexes, sweeped by a flow in a turbulent vortical wake, generate sound waves, that taking into account velocity of vortexes movement downwards on a flow concerning the motionless observer, Doppler frequency of generated sound waves appears equal:

$$f = \frac{1266,7}{1-\frac{v_x}{a}} \cong 1066Hz,$$

where v_x is axial flow velocity behind the R and a is a sound velocity. This frequency is in 1/3 octava band with the basic frequency 1000Hz.

Thus, results of measurements of noise intensity, radiated by system of rows IGV-R-S to an entrance plenum, shows that it depends on mutual circumferential position of the IGV and S. Thus influence of the stators clocking on intensity of radiated noise is caused by change of the tone noise, generated by

pressure pulsations on the R blades and periodic vortexes, descending with the R blades.

2. Flow pulsations on the rotor blades and intensity of free vortexes

Flow pulsations on the R blades were estimated by change in time of instant value of velocity circulation in peripheral sections of blades

$$\Gamma(t) = \sum_{k=-\infty}^{\infty} \Gamma_k e^{i2\pi k \frac{t}{T_0}} \quad , \quad i = \sqrt{-1} \quad , \quad T_0 = h_s/u, \tag{2}$$

where u is linear speed of moving of the given section; t is time.

Putting that γ=v$^+$−v$^-$ is difference of velocities on a pressure and suction blade surfaces, it is easily to receive the equation, connecting value γ with pressure difference ΔP on blade

$$\frac{1}{\rho}\Delta P(s,t) = \frac{\partial}{\partial t}\int_0^s \gamma(s,t)\,ds + v_0\gamma(s,t), \tag{3}$$

where ρ is density of gas, $v_0 = \frac{v^+ - v^-}{2}$ is a half-sum of velocities on a pressure and suction blade surfaces; s is length of airfoil camber line, counted from a leading edge. In assumptions of linearity (ρ=const, v_0=const) the decision of the equation (3) gives expression for factors Γ_k of decomposition (2)

$$\Gamma_k = \int_0^{S_0} \frac{1}{\rho v_0}\Delta P_k(s)\, e^{-i\frac{2\pi k}{T_0 v_0}(S_0 - s)} ds, \tag{4}$$

where S_0 is full length of airfoil camber line, pressure difference for n-th R blade is expressed by the formula

$$\Delta P(s,t) = \sum_{k=-\infty}^{\infty} \Delta P_k(s)\, e^{i2\pi k \frac{h_R}{h_s} n\cdot} \cdot e^{-2\pi k \frac{t}{T_0}}, \tag{5}$$

and h_R is a pitch of the R blades.

Thus, the formula (4) reduces calculation of a pulsation of velocity circulation on the R blade to definition of instant difference of static pressure in the system of coordinates connected with R.

The specified pressure difference was measured for assembly 2 of the compressor by six sensors of static pressure pulsations Ð, in regular intervals distributed along an axis of the compressor above R blade on the external R case. The data from each sensor were registered with frequency of discretization

19,2kHz during 1 second, then from the received time series it was allocated a periodic component with the basic frequency equal to the R blade passing frequency. Thus phase-locked for all sensors was provided by synchronous data recording with the R speed sensor.

After similar data processing for various values of coordinate Y, determining simultaneous circumferential shift of the IGV and S for each fixed value ν it is easy to receive experimental factors of the Fourier series of a kind

$$P(s,Y,\nu,t_0)=\sum_{k=-\infty}^{\infty}\sum_{l=-\infty}^{\infty}\Delta P_{kl}(s,\nu)\,e^{i2\pi kY}\cdot e^{i2\pi lY\,\frac{h_s}{h_R}}\cdot e^{i2\pi l\,\frac{t_0}{T}}, \quad (6)$$

where $T=\frac{h_R}{u}$ is the R blade passing period, $P(s,Y,\nu,t)$ is the instant static pressure, measured by the sensor to which arc coordinate s of airfoil camber corresponds.

For transition to the rotor (y, t) system of reference it is enough in decomposition (6) to make replacement of variables

$$Y=\tfrac{h_R}{h_s}y-\tfrac{t}{T_0},t_0=t.$$

Then the Fourier series of a kind turns out

$$P(s,y,\nu,t)=\sum_{k=-\infty}^{\infty}\sum_{l=-\infty}^{\infty}\Delta P_{kl}(s,\nu)\,e^{i2\pi ly}\cdot e^{i2\pi ky\frac{h_R}{h_s}}\cdot e^{i2\pi k\frac{t}{T}}, \quad (7)$$

determined for each coordinate y, counted along R blade to blade at the fixed time t. Instant difference of static pressure on the blade, determined as a difference of maximal (on a pressure surface) and minimal (on a suction surface) values P for the fixed time obviously gives the series (5) with known factors ΔP_k (s,ν).

At fixed number N=10 of various circumferential positions of the IGV and S the number of determined harmonics of series (7) obviously does not exceed 2 (k=0, ±1, ±2). Besides the integral (4) for six used sensors may be calculated only approximately. Using linear interpolation ΔP_k(s) between the next sensors for factor Γ_k the formula turns out

$$\Gamma_k(\nu)=\frac{1}{2\pi kqi}\sum_{m=1}^{6}\frac{\Delta P_k(s_m,\nu)}{\rho}A_{km}\quad,\quad k=1,2, \quad (8)$$

$$A_{km}=e^{-i2\pi kq(S_0-s_{m-1})}\left[e^{i2\pi kq\Delta s_{m-1}}\cdot\frac{e^{i2\pi kq\Delta s_m}-1}{i2\pi kq\Delta s_m}-\frac{e^{i2\pi kq\Delta s_{m-1}}-1}{i2\pi kq\Delta s_{m-1}}\right].$$

Here it is designated $\Delta s_m = \frac{s_{m+1}-s_m}{6}$, $m = 1, 2, ..., 6$, $\Delta s_0 = \Delta s_6 = 0$, $q = \frac{ub}{h_s v_0} = 1,18$ – Strouhal Number ; b=120mm – airfoil chord length; s_m – arc coordinate s, appropriate to position of the sensor with number m (s_1=0, s_6=S_0).

In table 1 values of Γ_1 and Γ_2, received under the formula (8) on a design operation mode of the compressor (u=2000rot/min, the air flow rate 30,8kg/s) at to assembly 2, are presented. From the table it is visible that the minimum level of periodic pulsations of velocity circulation is achieved at ν=0,3 and expressed first of all that the amplitude of 1-st harmonic $q = \frac{ub}{h_s v_0} = 1,18$ becomes much less amplitude of 2-nd harmonic. This circumstance is in full conformity with an explanation of clocking effects: decrease of flow pulsations on the R is caused by that synchronous disturbances from stators influence on the R blade in an antiphase. The maximum level of circulation pulsations is achieved for ν=0,8, at increase of amplitude of the first harmonic – disturbances from stators influence on the R blade in a phase.

On Fig.5 dependence from ν of values

$$\mu(\nu) = \frac{< \Gamma >_t - (< \Gamma >_t)_\nu}{(< \Gamma >_t)_\nu}$$

is presented, where $< \Gamma >_t$ and $((< \Gamma >_t)_\nu$ are, accordingly, RMS deviation of Γ from its time-average value and average value Γ_t on ν. For comparison on Fig. 5 values $\varepsilon_0 = \varepsilon_0(\nu)$ for 1/3 octava band with average frequency 1250Hz and total noise (see Fig.4b and 4e) are represented also. Comparison of dependences $\mu(\nu)$ and $\varepsilon_0(\nu)$ allows to see that area of mutual positioning of the IGV and S, appropriate to the increased and lowered acoustic disturbances in the plenum coincide with areas of the increased and lowered periodic pulsations on the R blades.

For an experimental estimation of intensity of sweeped by a flow the periodic vortexes descending with the R blades it was used laser anemometry of flow along a line LL parallel to exit front of the R on 8,75mm from it on mean radius of a flowing path [5]. The velocity pulsations was estimated by value

$$w_1(\nu) = << w(\nu, y, t) >_t >_y, w(\nu, y, t) = (W - W_0)_n,$$

where W and W_0, accordingly, are instant and time-averaged values of relative velocity in a point y of line LL, and $(W - W_0)_n$ is a projection of a difference $(W - W_0)$ on a direction of time-averaged and circle-averaged of relative velocity behind R.

On Fig.6 dependence

$$\mu(\nu) = \frac{w_1(\nu) - (w_1)_\nu}{(w_1)_\nu}$$

is presented for the measurements, executed on a line LL for assembly 2. The received dependence is compared to value $\varepsilon_0 = \varepsilon_0(\nu)$, received for 1/3 octava band of frequencies with the basic frequency 1000Hz (see Fig.4à). Apparently, dependences $\mu(\nu)$ and $\varepsilon_0(\nu)$ are correlated, that allows to assume, that change of intensity of radiated noise in the specified band of frequencies is connected to its generation by the periodic vortexes, descending with the R blades.

Comparing the data on Fig.5 and Fig.6, it is possible to notice that areas ν, providing lowered and increased noise radiation, are various for the noise, generated by flow pulsations on the R blades and periodic vortexes behind them. It is possible to explain this circumstance to that, according to Thomson theorem, intensity of free vortexes is proportional to value $\partial\Gamma/\partial t$, that as it is easy to see from elementary calculations, displaces values ν, appropriate to extreme values of intensity of free vortexes, including for 1-st harmonic.

3. Conclusion

3.1 Measurement of noise, radiated system of the blade rows IGV-R-S of the axial compressor and appreciated on a reverberation chamber method, at equal number of vanes IGV and S has shown the following:

–radiated noise essentially depends on mutual circumferential shift of stators;

– relative change of total intensity of radiated noise in a frequency range of 25–20000Hz for not optimum and optimum values of stators clocking achieves 80% ($\sim$3,7dB).

3.2 Comparison of results of measurement of noise and flow pulsations on the R blades and in vortical wakes behind R allows to assume that:

– specified in item 3.1 clocking effects are caused by change, at mutual circumferential shift of stators, the tone noise, generated by pressure pulsations on the R blades ($\sim$5dB) and vortical wakes behind R ($\sim$1,7dB);

– decrease of effect on total noise in a wide range of frequencies in comparison with effects of tone noise is caused by displacement of optimum mutual positioning of stators for various sources of tone noise.

The received results testify that optimization of a mutual circumferential position of stators in system of rows stator-rotor-stator an axial turbomachine may be used as effective practical means of decrease of the tone noise, caused by a rotor-stator interaction.

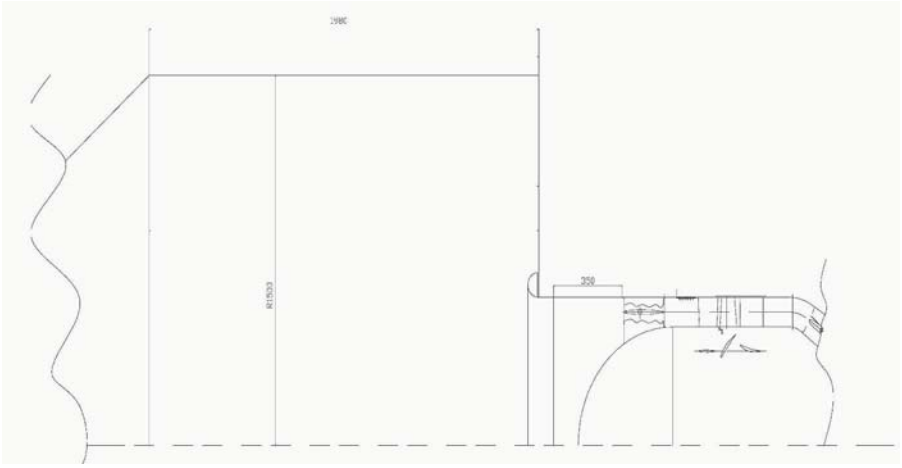

Figure 1. An entrance plenum and a working path of installation

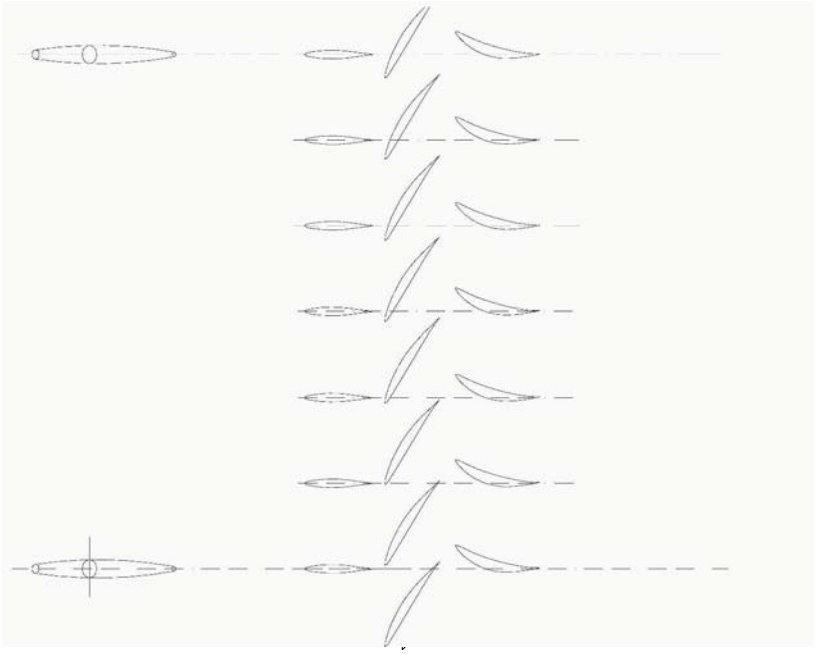

Figure 2. Cascsdes of airfoils on mean radius

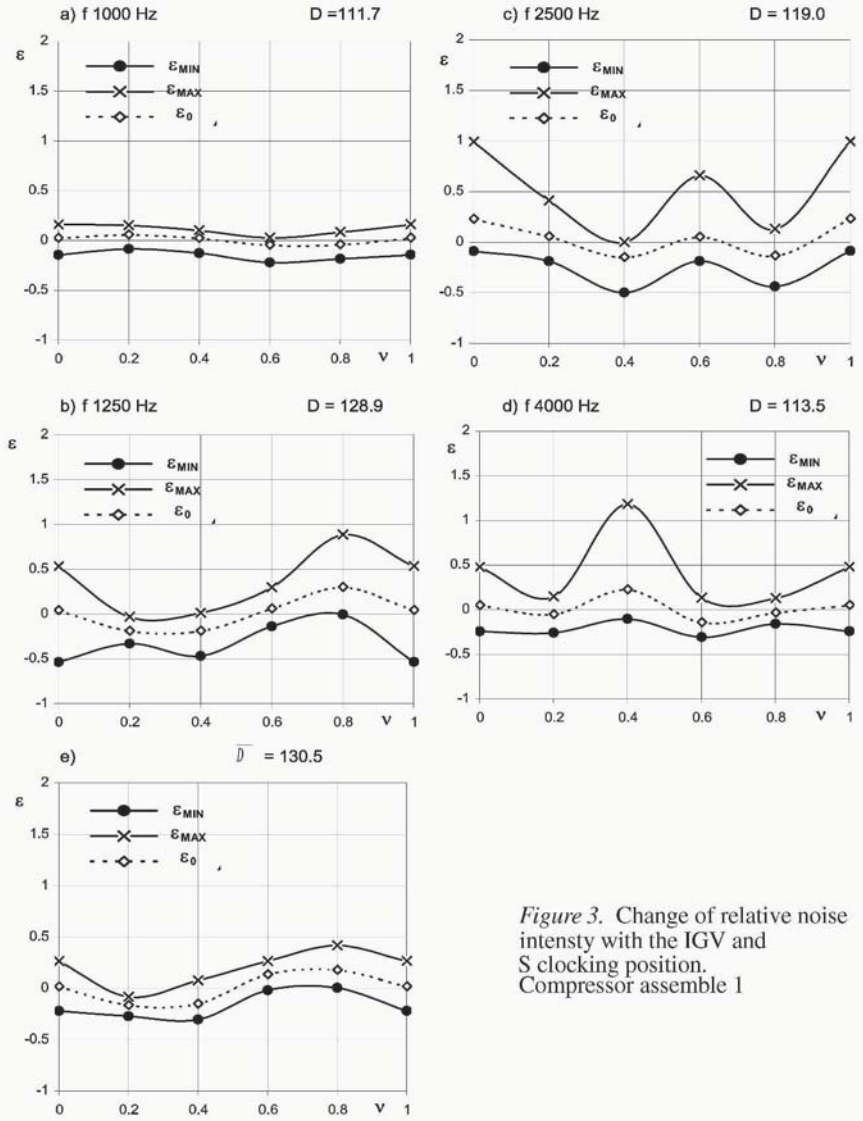

Figure 3. Change of relative noise intensty with the IGV and S clocking position. Compressor assemble 1

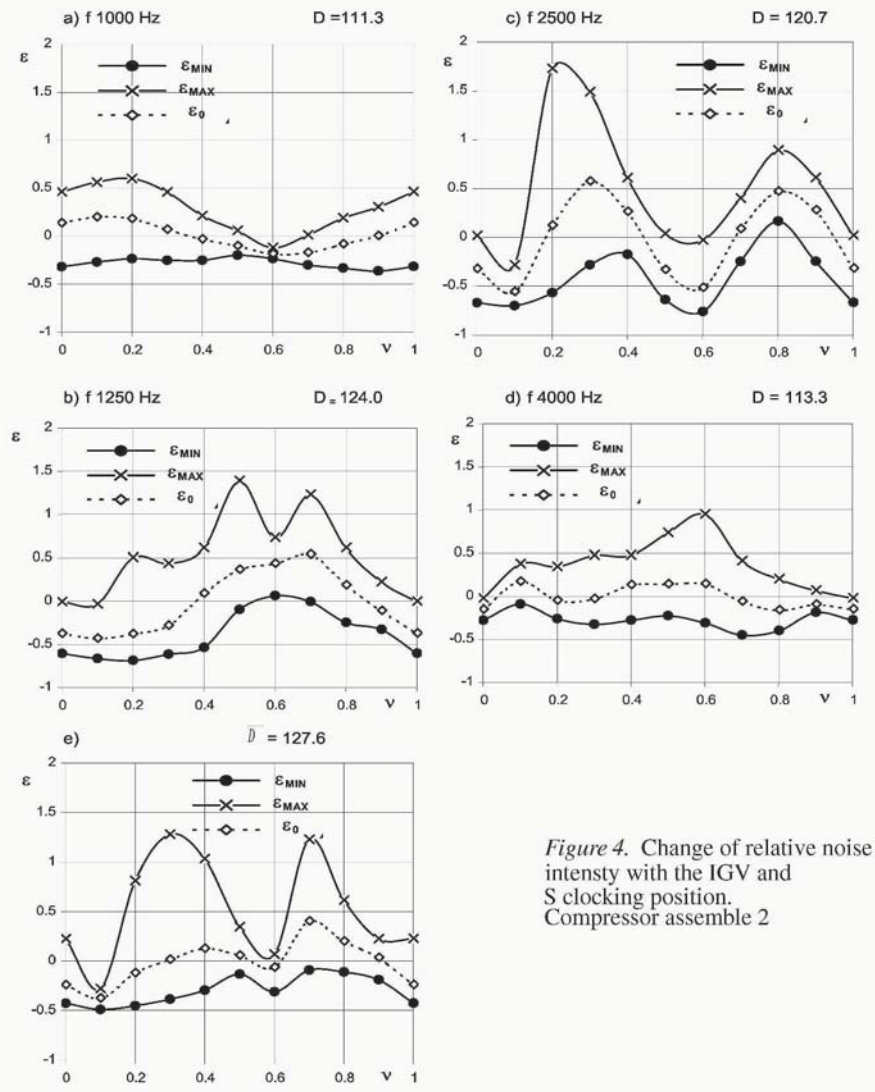

Figure 4. Change of relative noise intensty with the IGV and S clocking position. Compressor assemble 2

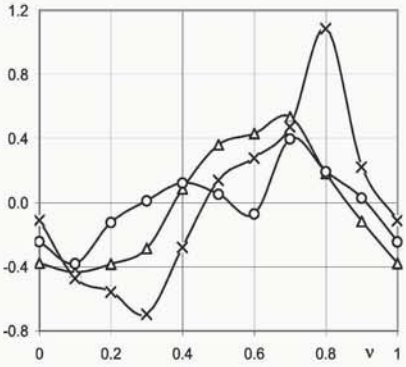

Fig.5. Change of relative values of RMS periodical velocity circulation μ on the R blades (x), noise intensity ε_0 in 1/3 octava freguency 1250 Hz (Δ) and intensity ε_0 of total noise (o) widh the IVG and S clocking posotion ν

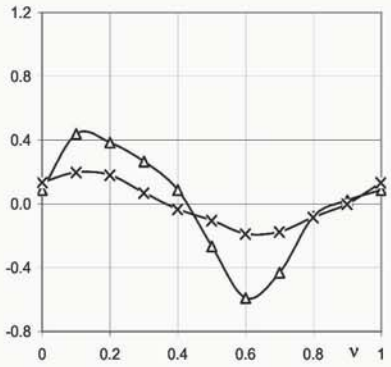

Fig.6. Change of relative values of velocity pulsations behind R μ (Δ) and noise intensity ε in 1/3 octava frequency 1000 Hz (x) with the IVG and S clocking position ν

Table 1

ν	Γ_1		Γ_2	
	Re	Im	Re	Im
0	0.153	0.149	0.027	0.054
0.1	0.18	0.128	0.074	0.005
0.2	0.08	0.13	0.091	0.075
0.3	0.005	0.008	0.063	0.029
0.4	0.06	0.134	0.13	0.033
0.5	0.093	0.154	0.066	0.074
0.6	0.089	0.205	0.0165	0.096
0.7	0.07	0.184	0.001	0.015
0.8	0.233	0.205	0.032	0.03
0.9	0.147	0.188	0.1	0.021

References

[1] Saren V.E. (1995) Relative Position of Two Rows of an Axial Turbomachine and Effects on the Aerodynamics in a Row Placed Between Them, *Unsteady Aerodynamics and Aeroelasticity of Turbomachines*, Elsevier, pp 421 – 425.

[2] Saren V.E., Savin N.M., Dorney D.J., Zacharias R.M. (1998) Experimental and Numerical Investigation of Unsteady Rotor-Stator Interaction on Axial Compressor Stage (with IGV) Performance, *Unsteady Aerodynamics and Aeroelasticity of Turbomachines*, 8 th Intern. Symp., Stockholm, 1997, Dordrecht et al.: Kluwer, P. 407-416.

[3] Savin N.M. and Saren V.E (2000) Hydrodynamic Interaction of the Blade Rows in the Stator-Rotor-Stator System of an Axial Turbomachine, *Fluid Dynamics*. Vol.35, ź3.

[4] Saren V.E., Savin N.M., Krupa V.G. (2000) Experimental and Computional Research of a Flow Structure in a Stator-Rotor-Stator System of an Axial Compressor, *The* 9^{th} *International Symposium on Unsteady Aerodynamics, Aeroacoustics and Aeroelasticity of Turbomachines (ISUAAAT)*, Lyon, France, September 4-8, pp 494-502.

[5] Saren V.E. and Smirnov S.A. (2003) Unsteady Vortical Wakes behind Mutually Moving Rows of Axial Turbomachine, *Thermophysics and Aerodynamics*, Vol.10, ź2.

[6] Savin N.M. and Saren V.E (2003) Stator Clocking Effect in a System of Rows Stator-Rotor-Stator of the Subsonic Axial Compressor, 10^{th} *Intern. Sump. on Unsteady Aerodynamics, Aeroacoustics and Aeroelasticity of Turbomachines (ISUAAAT)*, Durham, North Carolina, USA, Sept. 7-11.

A FREQUENCY-DOMAIN SOLVER FOR THE NON-LINEAR PROPAGATION AND RADIATION OF FAN NOISE

Cyrille Breard
Analytical Methods, Inc.
2133 152nd Avenue NE
Redmond WA 98052, USA
cyrille@amiwest.com

Abstract A numerical procedure for the numerical simulation of a fbw -impedance tube is presented and validated by the author [16]. This method is extended in the present paper to numerical simulation of noise radiation from lined ducts and to non-linear propgation of plane-wave in 2D and axisymetric lined duct.

K.C. Hall et al. (eds.),
Unsteady Aerodynamics, Aeroacoustics and Aeroelasticity of Turbomachines, 275–289.

Nomenclature

$p_o, u_o, v_o, w_o, \rho_o$	Mean flow quantites: pressure, velocities, density
p, u, v, w	Complex pressure, velocities perturbation quantities
$x, y/r$	Axial , transversal/radial coordinates
ξ, η	Computational coordinates
m	Circumferential coordinates
n	Radial mode number
SPL	Sound pressure level (dB) = $20log10(\frac{p}{p_{ref}})$, $p_{ref} = 10^{-5}$
S	Switch = 0 for 2D and =1 for axisymetric
i	$I^2 = -1$
c_o	Local speed of sound = $\sqrt{(\frac{\gamma p_o}{\rho_o})}$
ω	Pulsation = $2\pi f$
k	Wave number = $\frac{\omega}{c_o}$
k_r	Radial wave number
k_x	Axial wave number
$p^o_{(m,n)}$	Amplitude of the (m,n) mode
J_m , Y_m	m^{th} order Bessel functions of the first and second kind
R	Radius of the nacelle
R_c	Radius of the wall curvature
M^o_x	Axial mean Mach number = $\frac{u_o}{c_o}$
vt_o	Tangent component of the mean velocity at the wall
vt	Tangent component of the perturbation velocity at the wall
PPW	Points per wavelength
Z	Impedance of the liner
vn	Normal component of the perturbation velocity at the wal

1. Introduction

The requirement of accurate and fast prediction of propagation and radiation of fan noise is now part of the design of aeroengine and nacelle. Acoustic lining material is the most effective way of suppressing indesirable noise radiated from the nacelle. Computational aero-acoustics (CAA) have already demonstrated the great potential in modelling accurately complex aero-acoustics problems. However, CAA will serve as a tool for design purpose in the industrial environment only if the computational cost is reduced dramatically. Very interesting research work from Stanescu & al [6] has been presented recently, showing scattering of fan noise radiation due to fuselage, wing and pylon presences in the time domain. However, Ozyoruk & al. [5], Astley & al. [8] recently presented a frequency-domain solver for propagation, scattering and radiation, and showed that such methods become attractive for industrial application due to their shorter computational time compared to the time domain method. Aircraft, nacelle and aero-engine manufacturers have been using liners to attenuate forward-arc fan noise for many years. And keeping in mind that the impedance (property of liner) is defined in the frequency domain, it is very suitable and accurate to consider radiation problem with acoustic liner in the

frequency domain. Moreover, a frequency domain solver is in general faster to compute than time-domain solver as acceleration technique can be used. Furthermore, solution of the prediction can be immediately used for more analysis without post-processing of the prediction, a feature in industry environment makes frequency-domain solver more appropriate. A numerical procedure for the numerical simulation of a flow -impedance tube is presented and validated by the author [16]. This method is extended in the present paper to numerical simulation of noise radiation from lined ducts and to non-linear propgation of plane-wave in 2D and axisymetric lined duct.

2. Methodology of the linear solver

Governing equations

In cylindrical coordinates and by assuming harmonic variation of the form exp(i ω t) and exp(im) in time and in the azimuthal direction, respectively, the linearized Euler equations for 2D or axisymmetric configuration can be described by:

$$\begin{aligned} i\omega p + u_o\frac{\partial p}{\partial x} + v_o\frac{\partial p}{\partial r} + \gamma p_o(\frac{\partial u}{\partial x} + \frac{\partial v}{\partial r}) + \gamma p_(\frac{\partial u_o}{\partial x} + \frac{\partial v_o}{\partial r}) \\ + u\frac{\partial p_o}{\partial x} + v\frac{\partial p_o}{\partial r} + S(\gamma p_o(\frac{im}{r}w + \frac{v}{r}) + \gamma p\frac{vo}{r}) = 0 \end{aligned} \quad (1)$$

$$i\omega u + u_o\frac{\partial u}{\partial x} + v_o\frac{\partial u}{\partial r} + \frac{1}{\rho_o}\frac{\partial p}{\partial x} + u\frac{\partial u_o}{\partial x} + v\frac{\partial u_o}{\partial r} - \frac{p}{\rho_o\gamma p_o}\frac{\partial p_o}{\partial x} = 0 \quad (2)$$

$$i\omega v + u_o\frac{\partial v}{\partial x} + v_o\frac{\partial v}{\partial r} + \frac{1}{\rho_o}\frac{\partial p}{\partial r} + u\frac{\partial v_o}{\partial x} + v\frac{\partial v_o}{\partial r} - \frac{p}{\rho_o\gamma p_o}\frac{\partial p_o}{\partial r} = 0 \quad (3)$$

$$i\omega w + u_o\frac{\partial w}{\partial x} + v_o\frac{\partial w}{\partial r} + \frac{im}{\rho_o\gamma}p + \frac{v_o w}{r} = 0 \quad (4)$$

Equations 1, 2, 3 and 4 are solved on the curvilinear mesh using uniform computational coordinates (ξ, η). Metrics terms and spatial derivatives are computed using the optimised 4th order DRP scheme from Tam & al. [Tam and Webb, 1993]. The numerical scheme is stabilized for the spurious wave by adding a selective damping term for cartesian grid or by filtering the solution [11] for curvilinear grid. To solve equations 1, 2, 3 and 4, a pseudo-time derivative is introduced so that the equations may be marched to a steady state condition using conventional computational fluid dynamic scheme. In

the present investigation, the pseudo-time technique is discretized using a simple forward-Euler scheme. At each iteration, the selective damping and/or the filter (8th order) are applied as well as the boundary condition.

Boundary conditions

Fan face boundary conditions. At the fan face, outflow boundary condition is applied by imposing an incoming spinning mode (m,n):

$$\frac{\partial \begin{bmatrix} u \\ v \\ w \end{bmatrix}}{\partial t} + u_o \frac{\partial \begin{bmatrix} u \\ v \\ w \end{bmatrix}}{\partial x} + \frac{1}{\rho_o}\frac{\partial p}{\partial x} = \frac{\partial \begin{bmatrix} u_{fan} \\ v_{fan} \\ w_{fan} \end{bmatrix}}{\partial t} + u_o \frac{\partial \begin{bmatrix} u_{fan} \\ v_{fan} \\ w_{fan} \end{bmatrix}}{\partial x} + \frac{1}{\rho_o}\frac{\partial p_{fan}}{\partial x} \tag{5}$$

$$\frac{\partial p}{\partial t} + V\frac{\partial p}{\partial x} = \frac{\partial p_{fan}}{\partial t} + V\frac{\partial p_{fan}}{\partial x} \tag{6}$$

with $V = u_o + sqrtc_o^2 - u_o^2$.

$$p_{fan} = p^o_{(m,n)}(AJ_m(k_r R) + BY_m(k_r R))$$

$$u_{fan} = \frac{-ik_x p^o_{(m,n)}(AJ_m(k_r R)+BY_m(k_r R))}{-i\rho_o c_o(k-M_x^o k_x)}$$

$$v_{fan} = \frac{k_r p^o_{(m,n)}(AJ'_m(k_r R)+BY'_m(k_r R))}{-i\rho_o c_o(k-M_x^o k_x)}$$

$$w_{fan} = \frac{imp^o_{(m,n)}(AJ'_m(k_r R)+BY'_m(k_r R))}{r(-i\rho_o c_o(k-M_x^o k_x))}$$

At the far-field boundary, radiation or outflow boundary condition of Tam is applied. For 2D problems, radiation boundary conditions can be applied also, but non-reflective boundary conditions from Giles [12] are more suitable.

Hard and soft walls. Non-penetration boundary condition on the hard wall is expressed as:

$$\boldsymbol{u}.\boldsymbol{n} = 0$$

Setting the pressure at the ghost point enforces the normal velocity to be zero :

$$\frac{\partial p}{\partial \eta} = \frac{2\rho_o vt_o vt - \frac{\rho_o p vt_o^2}{\gamma p_o}}{\sqrt{(\eta_x^2 + \eta_y^2)}R_c} \tag{9}$$

In the previous expression, the grid lines are assumed to be orthogonal to the wall,

Following Myers impedance condition defined in the frequncy domain, acoustic impedance boundary condition is applied on the soft wall boundary using the following relation:

$$i\omega p + u_o \frac{\partial p}{\partial x} + v_o \frac{\partial p}{\partial r} = -i\omega Z v n \tag{10}$$

Extension to non-linear propagation

The non-linear solver is based on the linear solver, each harmonics considered in the computational domain is calculated seperately as described above. The non-linear term of the Euler equations are added to the linearized Euler equations 1, 2, 3 and 4 after the solution and spatial derivatives are transformed in the time domain via Fourier transform. Residuals of the Euler equations are calculated and are transformed back to the frequency domain. The boundary conditions at the far-field, fan face and hard wall are imposed for each harmonic in the same manner, as well as for the soft wall boundary condition. Thanks to the frequency domain approach, the impedance boundary condition for each harmonic is satisfied with the frequency dependency.

3. Results

NASA flow impedance tube case

The present solver is validated with experimental data from NASA Langley Grazing flow impedance tube. It is used for evaluation of liner in control flow and acoustic environment. The test section is described in [7] and it has been used intensively for validation of acoustic liner model in frequency domain as well as in time domain [3]. The grid size is 60x11, and cases for Mach number of 0.3 at frequencies of 500 and 3000 Hz and for Mach number of 0.5 at frequeny of 2500 Hz are reported here. The mean flow is a very important factor in the accurate representation of the experimental set-up. As reported by Ozyoruk & al. [5] and Ju & al. [14], the refraction effect is taken into account and improved results are obtained. Thus, two mean flows are considered in this study: uniform flow and sheared flow characterized by a fully developed laminar channel flow as follow:

$$u_o = \frac{M_o c_o}{4}(1 - \frac{y}{h})\frac{y}{h} \tag{11}$$

The impedances used for the calculation are (0.41,-1.56), (1.224,-1.145) and (0.69 ,-0.24) for 500, 2500 and 3000 Hz, respectively.

The results of the computation with uniform flow and shear flow and frequency $f = 500$ Hz confirm the importance in the mean flow in the propagation of acoustic wave in rectangular lined duct. The SPL along the duct is

shown in Figure 1. The improvement is very clear in Figure 2 showing the phase distribution.

The next case considered is the same as the previous one but the frequency is increaesed to 3000 Hz. For this case, the number of points per wavelenght is about 11 for the downstream wave. The acoustic field is computed with the uniform and the shear flow. Very good agreement is obtained with the mean shear flow (Figure 3). The comparison between experimental and computational phase (Figure 4) confirms that the present method predicts correctly the propagation and absorption of noise in a rectangular lined duct.

The last case corresponds to M=0.5 and f=2500 Hz. Again, the SPL computed with the shear mean flow is in good agreement (Figure 5). Small difference around the trailing edge of the liner is present. The discrepancy is probably due to the small number of point per wavelength. The downstream wave is well resolved with about 15 PPW but the reflected wave (upstream) is represented with only 5 PPW.

The agreements between computational and experimental results are excellent when the mean flow is treated as sheared flow. For each case, the CPU time is extremely low, as only 1 min is required on Linux PC Pentium 4 (1.7GHz) with 6000 iterations. Due to the low CPU time, the code may be used for optimization or for the eduction of liner properties. In [16], the author presents an example of eduction of the liner where the present solver is coupled with a commercial optimizer Pointer ([18]).

Non-linear propagation of plane wave in a 2D duct

The non-linear implementation is validated against the analytical solution, exact for the first and second order terms given by C. Campos-Pozuelo & J.A. Gallego-Juarez [2]. The test case is a plane wave with high amplitude propagating in a 2D duct. According to the theory, the second harmonic will grow proportionally to the distance of the source location. The frequency of the plane wave is 100 Hz, the duct length is 10 m, the mesh size is 201x11 and it is a zero flow case. Only two harmonics are considered in the computation. The real part of the pressure for the 1st and the 2nd harmonics versus distance from the source plane are plotted in Figure 16. The comparison between analytical and computational amplitude of the 2nd harmonic along the duct is shown in Figure 17. Excellent agreement is achieved, although some reflection at the outflow boundary is present. The present method is therefore suitable for the propagation of N-wave. An example of such computation with 4 harmonics is shown in Figure 18 and Fig ure 19. The N-wave characteristics are conserved during the propagation, showing that the current modeling might be suitable for the modeling of the spinning mode with high sound pressure level or N-wave type.

Radiation of duct mode with acoustic liner

In [15], the present solver is validated with experimental data with wall case. The same type of computation is reported here with the filght inlet from the experimental set-up reported by Silcox [17]. Figure 6 illustrates the resultant acoustic wave patterns for the mode (2,2) ka=11.67 corresponding the Figure 12 of [17]. The corresponding far-field SPL is displayed in Figure 7. The three lobes pattern in SPL are particular to the 2nd radial mode. The computed far-field SPL reproduces well the directivity as well as the magnitude. The second lobe is underestimated by about 2-4 dB.

Now, the ability of the code is demonstrated with acoustic liner. The case from [15] is repeated with the acoustic liner set-up with the following parameters: Z=(2.21,-1.54),2 different frequencies (853 Hz and 1853 Hz) and mode (4,0). Figure 7 and 9 illustrates the acoustic pressure contours (real part). It is clear from the acoustic pressure contours that the liner caused absorption of sound, and that the scattering of higher radial modes is present for higher cut-on mode (1853Hz). At the fan face, only the first radial mode was imposed, but the SPL in far-field will exhibits a strong three lobes pattern from the 2nd radial mode. The first radial mode is also present but not clear due to its lower amplitude.

Non-linear propagation of plane-wave mode in an axisymteric lined duct

We now consider the non-linear propagation of a plane-wave (ka=7.39, R=1) with 2 harmonics. The impedances for the first and second harmonic are (3,-0.1) and (2,-0.1). The mesh size is 201x11. At the fan face, only the first harmonic is imposed with a high amplitude of 4000 Pa corresponding to 172 dB SPL. The liner is positionned between x=2.5 and x=7.5. The real part of the acoustic pressure is displayed in Figure 12. It is clear that the second harmonic grows fairly rapidly due to the non-linear effect and reachs more than 160 dB at the liner leading edge. Next both amplitudes decreased due to the presence of the liner. It is noted that the amplitude of the second harmonic grows again in the hard wall section. The SPL at the tip section is shown in Figure 13 for both harmonic. It is noted that the mesh size is sufficient for the highest harmonic with about 8.5 PPW.

4. Summary

A numerical method for studying the linear and non-linear, 2D and axisymetric propagation of acoustic waves has been presented. The numerical results confirm its accuracy and efficiency. Excellent results were obtained for the NASA Flow impedance tube. The propagation and radiation of spinning

mode in a lined duct are presented. Good agreements are obtained for non-linear propagation in a 2D duct. The propagation of high SPL fan tone noise is presented with the lined duct. Further work will be focused on the non-linear propagation and radiation of spinning mode with acoustic liner as well as validations.

References

[1] C.K.W. Tam & J.C. Webb, Dispersion-Relation-Preserving Finite Difference Schemes for Computational Acoustics, J. Compute. Phys. 107, 262-282, 1993

[2] C. Campos-Pozuelo, B. Dubus & J.A. Galego-Juarez, Finite-Element analysis of the non-linear propagation of high-intensity acoustic waves, J. Acoust. Soc. Am. 106 (1) 91-101, July 1999.

[3] Ozyoruk, Y., Long, L. N. & Jones, M. G., Time-domain numerical simulation of a flow-impedance tube, Journal of Computational Physics, 146, 29-57,1998.

[4] Tester, B. J., The propagation and attenuation of sound in lined ducts containing plug flow, Journal of Sound and Vibration, 28,151-203,1973.

[5] Ozyoruk, Y., E. Alpman, V. Ahuja & Long, L. N. A frequency-domain numerical method for noise radiation from ducted fans AIAA-2002-2587

[6] D. Stanescu, M.Y. Hussaini & F. Farassat, Aircraft engine noise scattering A discontinuous spectral element approach

[7] T.L. Parott, W.R. Watson, & M.G. Jones Experimental validation of a two-dimensional shear flow model for determining acoustic impedance NASA TP-2679, 1987.

[8] R.J, Astley, G.J. Macaulay, J.P. Coyette & L. Cremers Three-dimensional wave-envelope elements of variable order for acoustic radiation and scattering. Part I. Formulation in the frequency domain J. Acoust. Soc. Am. 103 (1) Jan. 1998

[9] M. McMullen A. Jameson & J. J. Alonso, Application of a non-linear frequency domain to the Euler and Navier-Stokes equations AIAA-2002-0120, 40th AIAA ASME, Reno, NV, 2002

[10] K.C. Hall, J.P. Thomas & W.S. Clark, Computation of unsteady non-linear flows in cascade using harmonic balance technique, Proceedings of the 9th International Symposium on Unsteady Aerodynamics, Aeroacoustics and Aeroelasticity of Turbomachines, Lyon, France September 2000, p.409-426

[11] D.V. Gaitonde & M.R. Visbal, Further development of Navier-Sokes solution procedure based on higher-order formulas. AIAA99-0557, 37th AIAA AIAA ASME, Reno, NV, 1999

[12] M.B. Giles Nonreflecting boundary condition for Euler equation calculations AIAA Journal 28 (12) 2050 1990.

[13] Y. Ozyoruk & L.N. Long Time-domain calculation of sound propagation in lined ducts with sheared flows 5th AIAA-CEAS AIAA-99-1817

[14] H. Ju & K.Y. Fung, Time-domain impedance boundary conditions with mean flow effects AIAA Journal Vol.39, No 9, 2001, pp.1683-1690

[15] J. H. Lan, Y. Guo & C. Breard, Validation and application of two frequency domain acoustic propagation codes AIAA-2003-3244 9th AIAA/CEAS Aeroacoustics Conference and Exhibit

[16] C. Brŕeard, Acoustic propagation and radiation modeling of lined duct with linear and non-linear freequency-domain solver AIAA-2003-3265 9th AIAA/CEAS Aeroacoustics Conference and Exhibit

[17] R.J. Silcox, Experimental investigation of geometry and flow effects on acoustic radiation from duct inlets. AIAA-83-0713, 8th Aeroacoustics Conference, Atlanta, 1983

[18] www.synaps.com

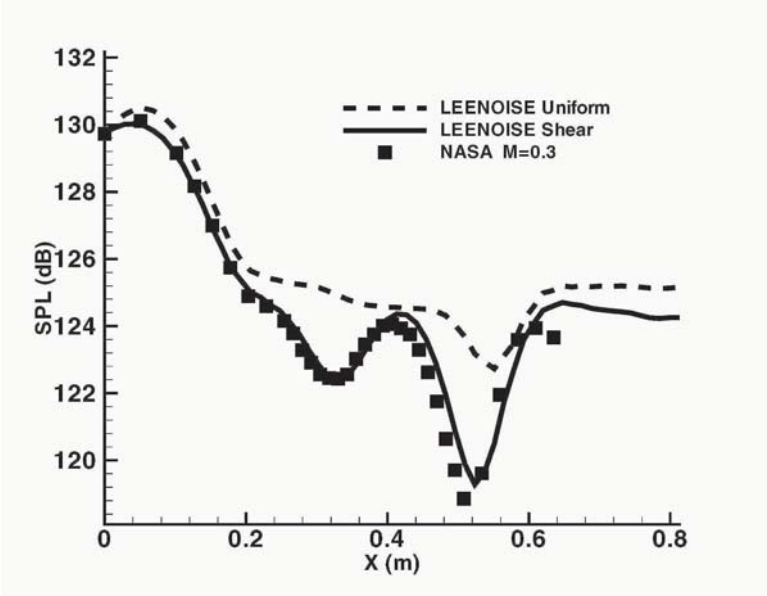

Figure 1. NASA Flow Impedance Tube: SPL for M = 0.3 and f = 500 Hz

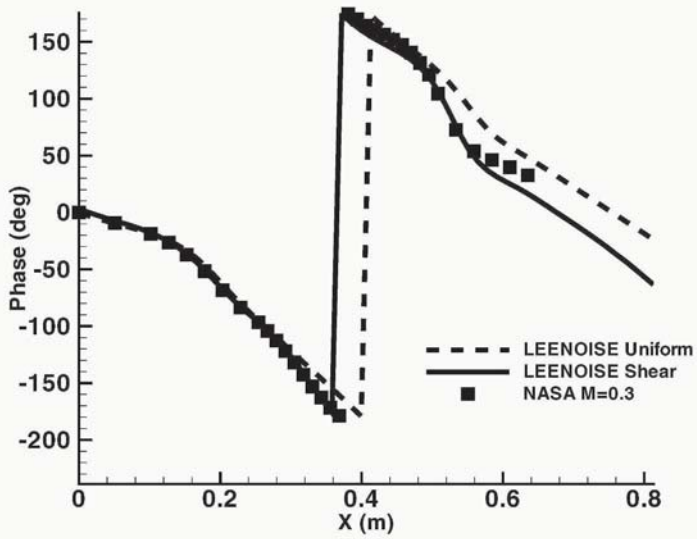

Figure 2. NASA Flow Impedance Tube: Phase for M = 0.3 and f = 500 Hz

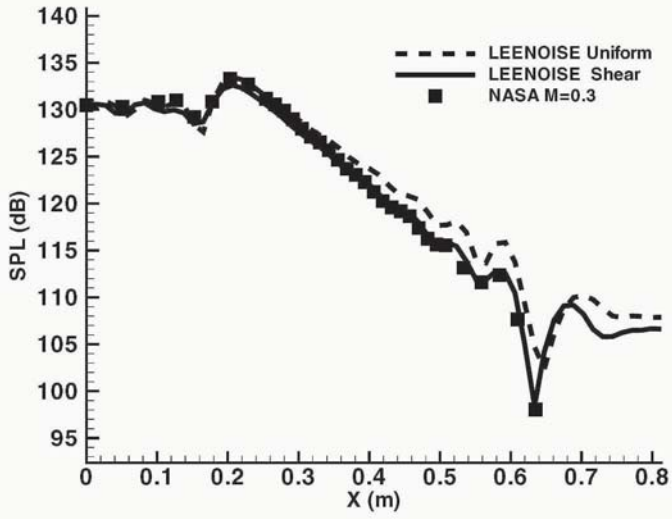

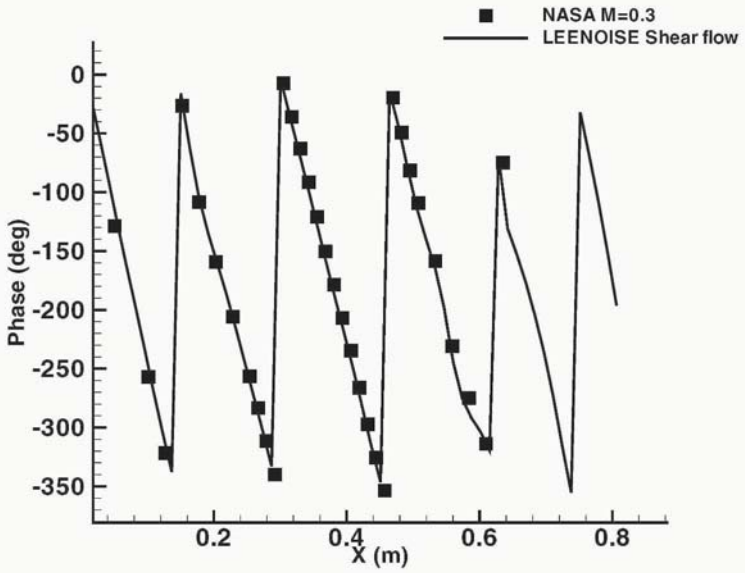

Figure 4. NASA Flow Impedance Tube: Phase for M = 0.3 and f = 3000 Hz

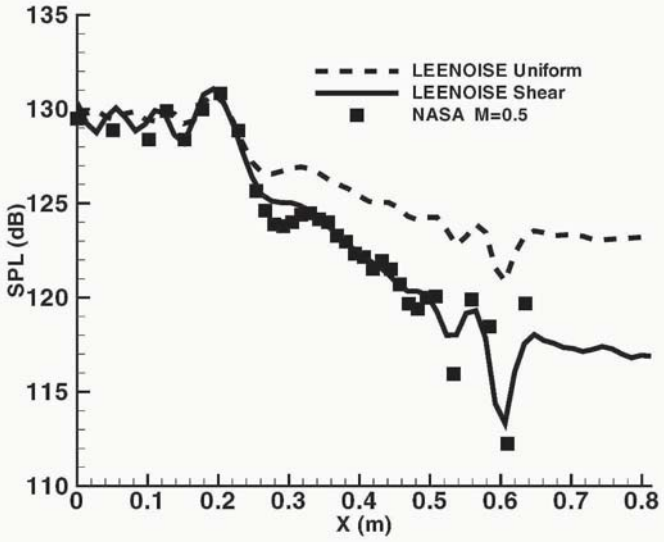

Figure 5. NASA Flow Impedance Tube: SPL for M = 0.5 and f = 2500 Hz

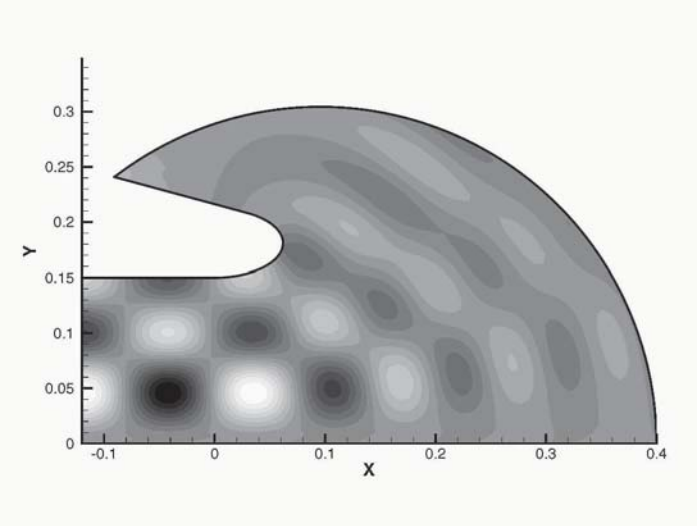

Figure 6. Acoustic field with the flight inlet

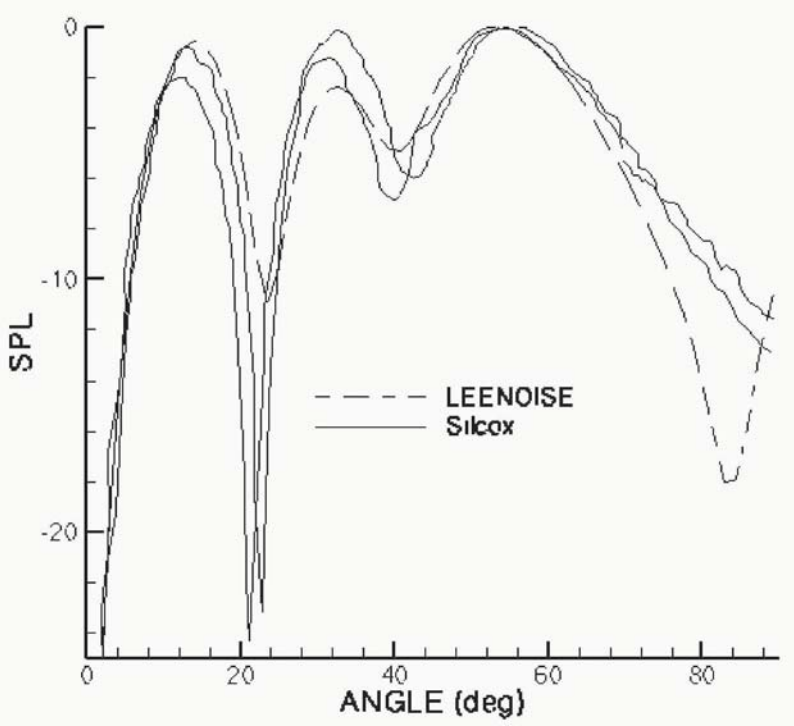

Figure 7. Far-field sound pressure level for the (2,2) mode with ka = 11.67

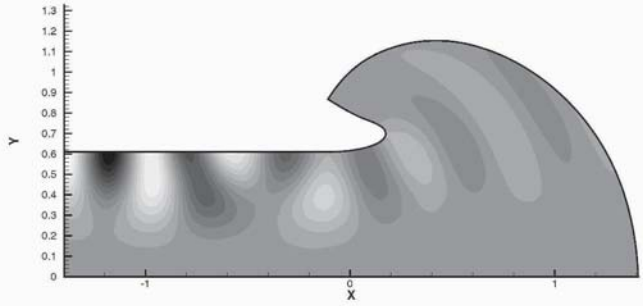

Figure 8. Acoustic field for the NASA Glenn fan with f = 853Hz

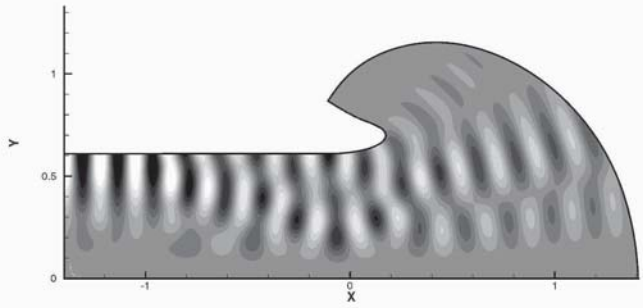

Figure 9. Acoustic field for the NASA Glenn fan with f=1853Hz

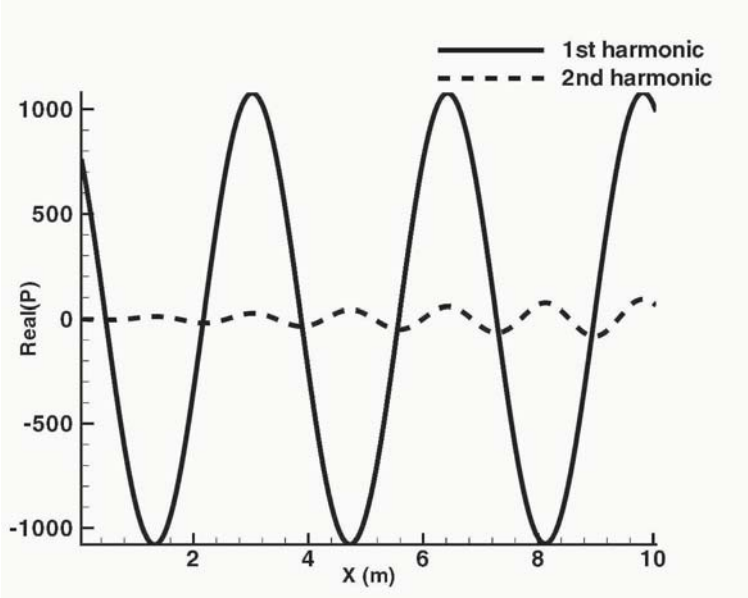

Figure 10. Pressure distribution of the first and second harmonics

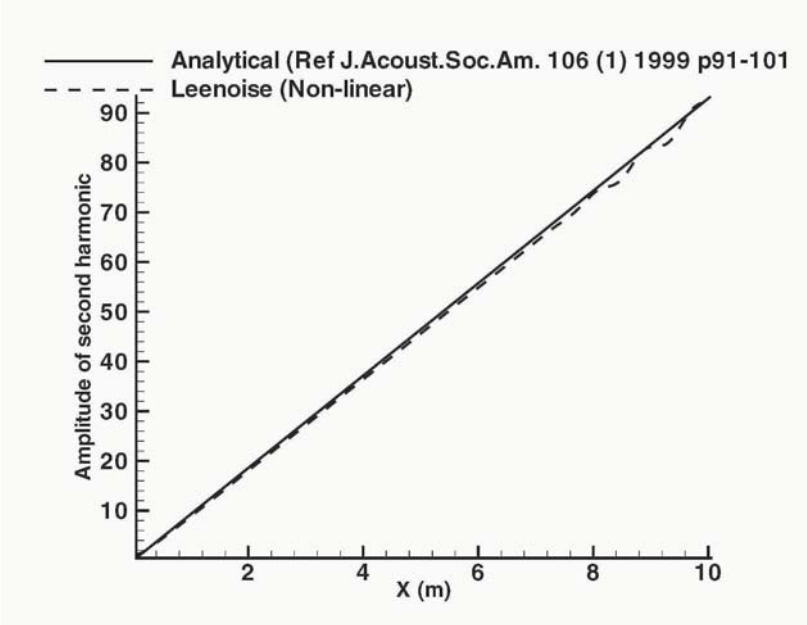

Figure 11. Amplitude of the second harmonics

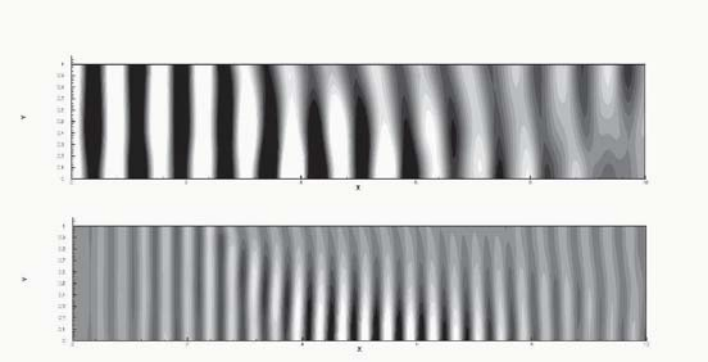

Figure 12. Acoustic field of the first and second harmonics for a plane wave propagation in a axisymetric lined duct. Top: 1st harmonic - Bottom: 2nd harmonic

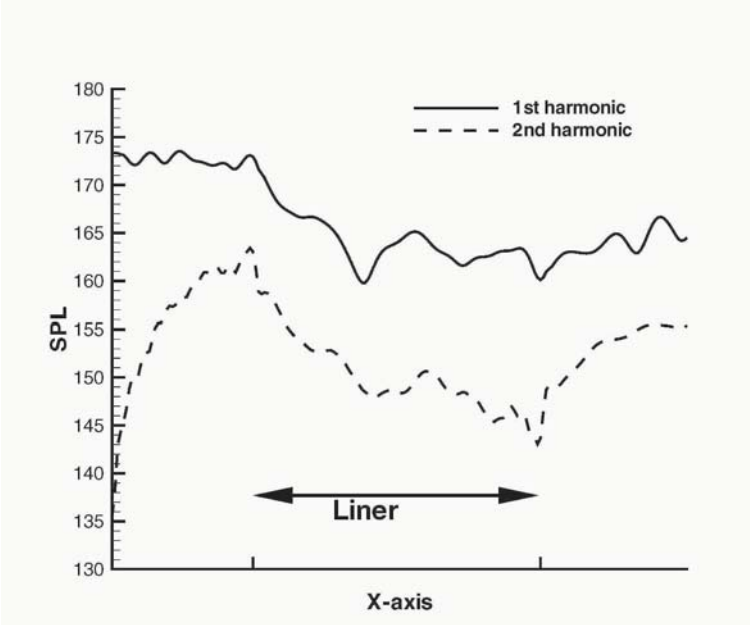

Figure 13. SPL (tip) of the first and second harmonics for a plane wave propagation in a axisymetric lined duct Z1 = (3,-0.1),Z2 = (2,-0.1)

V

FLOW INSTABILITIES

ANALYSIS OF UNSTEADY CASING PRESSURE MEASUREMENTS DURING SURGE AND ROTATING STALL

S. J. Anderson (CEng)
QinetiQ
SJANDERSON@qinetiq.com

Dr. N. H. S. Smith (CEng)
Rolls Royce PLC
nigel.h.s.smith@rolls-royce.com

Abstract This paper presents a unique set of unsteady pressure measurements during a surge and rotating stall event in a modern transonic high speed single stage axial flow fan rig. The unsteady pressure data were acquired using an array of 22 high frequency response Kulite transducers positioned over the rotor tip to show detail of the in-passage flow behaviour during stall and surge. In addition, Kulites were also positioned upstream, downstream and in the bypass duct of the rig to give a more general overview of the fan operation during the rotating stall and surge events.

1. Introduction

The modern large turbofan engine will experience unsteady flow phenomena when there is an excursion of the fan from its nominal operating line. An example of such behaviour is given in Ref. 1 (ASME 99-GT-344 Freeman & Rowe). To further understand typical unsteady flow phenomena – such as rotating stall and surge – detailed in-passage casing measurements of the unsteady pressures have been acquired from an experimental high speed single stage axial flow transonic fan rig using an array of 22 high frequency response pressure transducers. The transducer array was positioned in the rotor tip casing to allow the in-passage pressure distribution and shock structure for each blade passing to be visualised with coverage extending upstream and down-

K.C. Hall et al. (eds.),
Unsteady Aerodynamics, Aeroacoustics and Aeroelasticity of Turbomachines, 293–312.

stream of the rotor leading and trailing edges. The array data were recorded on a digital data acquisition system which incorporated a signal conditioning unit to give approximately 100 samples per blade passage on each transducer.

In addition to the in-passage array, additional rings of pressure transducers were positioned upstream and downstream of the rotor and in the bypass duct to give a more general overview of the behaviour of the fan during the rotating stall and surge events. This set of data was sampled at a much reduced sample rate, and as a result only the rotating stall cells and the harmonics were detected.

The on-set of the rotating stall or surge event was achieved by throttling the bypass duct at constant speed, resulting in the fan operating further up its characteristic, the throttle was continually closed until the fan dropped into rotating stall or a surge cycle, once data had been captured the fan was recovered by rapidly opening the bypass valve.

This paper presents an example of rotating stall at part speed and a high speed surge event. The data for each event are firstly shown on the upstream and downstream rings of transducers to present an overview of each event and then the detailed in-passage data are shown.

2. Experimental Procedure

The Test Facility

The tests were performed in the Rolls-Royce compressor test facility in Derby on a 34-inch diameter fan rig with an engine representative bypass ratio. The fan blade tested was a typical wide chord fan blade at 26-off with a design blade tip Mach no. of 1.4. The rotor path incorporated an array of 22 high-response, temperature compensated transducers for measuring the unsteady static pressure between leading edge and trailing edge. In addition, absolute pressure levels were measured for comparison using pneumatic pressure tappings fitted at the same axial locations, but offset circumferentially. The arrangement of the transducers and the pneumatic tappings is illustrated in Fig. 1. To obtain the density of measurement points required, the transducers were mounted in two parallel rows approximately aligned with the blade tip. The comparison between the Kulites and the pneumatic tappings was shown to give good agreement. One transducer close to the leading edge failed during testing, the results presented here are based on the remaining 21 transducers.

Data Acquisition

During operation of the facility, constant speed characteristics were mapped out by throttling the bypass, to the stability boundary. Overtip unsteady data were acquired during two stability events: a complete surge cycle at 105%

speed and the recovery from rotating stall at 60% speed. The 105% speed data covered 0.18 seconds taken during a multiple surge cycle which lasted approximately 1.5 seconds. For the 60% speed the data acquisition system was set up to measure rotating stall for 1.5 seconds of an event which lasted 3.6 seconds. In both cases the unsteady pressure signals from the Kulites were recorded on a high speed digital data acquisition system at 500 kHz. The data acquisition system contained a signal conditioning unit which amplified the signal and provided anti-aliasing filters.

Data from three further rings of Kulites at varying axial locations were also acquired to give the overall performance of the rig during stall and surge cycles. The transducers were located approximately $^1/_2$ an axial chord upstream and downstream of the fan leading and trailing edge, and in the bypass duct downstream of the outlet guide vane. These data were sampled at a frequency of 2.5 kHz, therefore the bulk fluctuations produced by the stall and surge can be seen, but not those produced by the individual blade passing.

3. Results

Greitzer (Ref. 2) has previously defined the **B** parameter that defines whether a fan will operate in rotating stall or surge at the stability point. The **B** parameter is equivalent to the ratio of the compressor pressure rise capability to the pressure rise required to induce mass flow oscillations. Where,

$$\mathbf{B} = \frac{\left(\rho u^2/2\right) A}{\rho A L u \omega_{\mathsf{HELM}}}$$

ρAL represents the mass of gas (density x duct area x duct length), u is the blade speed and ω_{HELM} is the frequency of natural oscillations.

If **B** is low then a compressor does not have much pressure rise capability compared to that required to begin a surge. If **B**< Bcrit, then stall occurs, If **B**> Bcrit then surge occurs, where Bcrit is the boundary between stall and surge (where typically Bcrit =0.8).

The above equation shows that if only blade speed is changed then the fan is more likely to surge as speed is increased. The test experience for the fan discussed here shows rotating stall occurs between low speed and 100% with surge at 105% speed. The following sections present data for the overtip and rings of Kulites for a stall event and a surge event to show the nature of the two types of instability.

Rotating Stall Event at 60% Speed

The complete rotating stall event at 60% speed lasts for 3.6 seconds from initiation to fan recovery. The time histories from the ring of Kulites positioned half an axial chord upstream of the fan against circumferential position show

a distinct change in the fluctuations caused by the rotating stall transitioning from one stall cell to two at approximately 1.1 seconds after initiation (Fig. 2). Figure 3 shows the Fourier analysis for one of the upstream Kulites with a distinct transition in frequency from one to two cells, the figure also shows the harmonics of the cells. This transition is unusual with previous fans typically only showing a one cell pattern rotating at 0.6EO: the reason for this dividing of the stall cell is unknown. However, data reported by Pampreen (Ref. 3) show single and double stall cells in a single stage system rotating at approximately 60% of the rotational speed. Figure 4 shows a zoom of the time histories with a 'spike' initiation of the stall event being picked up first at 305 degrees. The stall cell development is a rapid process occurring over two revs with the cell rotating at 0.60 EO after 10 revs. After the transition to two cells the rotational cell speed increases slightly to 0.63EO. Kulites positioned at the same circumferential position ahead of and behind the fan and downstream of the OGV, see the same phase, suggesting the stall cell is axial aligned and not spiraling; this is analogous to a cut-off pressure wave as defined by Tyler & Sofrin (Ref. 4).

The over tip high frequency data were acquired after the transition, approximately 0.6 seconds prior to the recovery point. The data show the stall cell passing at both the leading edge and mid chord as an increase in pressure and a fall in pressure at the trailing edge. This is consistent with a flow reduction at inlet in the stall cell and an increase in blockage at the fan trailing edge, which effectively increases the exit Mach number.

To resolve the frequency components of the over-tip data a power spectral density analysis has been performed, both in rotating stall and post stall. The results for the leading edge Kulites are shown in Fig. 5. For post stall only, the blade passing frequency and first harmonic are clearly defined. During rotating stall the stall frequency and the first two harmonics are clearly visible. Additional frequencies around the blade passing frequency can be seen. These are offset from blade passing by the rotating stall frequency and its harmonics, showing the strong interaction between the stall cell and the blading. These 'sum and difference' tones are expected and are explained further in Refs. 5 and 6. A similar pattern is seen around the first harmonic of blade passing. Although not presented, the power spectra for all gauges were inspected and it was found that similar trends could be seen throughout the passage.

The overtip data suggest that the size and structure of both stall cells were very similar, with the cells occupying approximately four blade passages. The data presented in animation format shows that, even during the 'stable' portion of the flow between stall cells, there are significant blade to blade fluctuations in the rotor flow field.

Recovery

The fan was recovered by rapidly opening the bypass throttle to max flow. The point at which drop-out occurs is of interest as it helps define a suitable operating or working line for the fan to ensure recovery from rotating stall. Once the fan is operating in rotating stall, a much larger throttle opening is required to unstall the blade than was in use at the time when stall first occurred; this effect is called hysteresis. Much work has been performed on low speed compressors to define the degree of this (Day & Cumpsty - Ref. 7), but for a supersonic fan it is not clear what determines the extent of the hysteresis.

To determine the point of recovery for the transonic fan the time-averaged casing pressures at instances within the rotating stall data set have been compared with the pneumatic casing pressure rise measured during the mapping of the unstalled characteristic. This comparison can be seen in Fig. 6. Due to the relatively long time the bypass valves take to open (seconds), when compared to the rotational speed (100 revolutions per second), discrete periods of time can be defined and are presented from the rotating stall data set. In rotating stall (top solid line on Fig. 6), a raised pressure at the leading edge is found compared to the steady operating points shown due to compressed air coming forward as the stall cell passes. The reduction in the overall pressure rise can also be seen relative to the peak trailing edge pressure at the near surge condition. The stall recovery point (second solid line on Fig. 6), represents data from the first 2 revolutions after the last evidence of rotating stall. They show a similar profile of pressure rise as seen with the fourth steady state point from max pressure rise, suggesting that the performance demanded from the fan must be reduced to this point or below for the fan to recover. The pressure distribution for the very end of the data set, one second after recovery is presented (bottom solid line on Fig. 6). This shows the continued recovery from rotating stall and the operating point has dropped to below the working line.

The time histories of three of the gauges as the fan recovers from the stalled state are shown in Fig 7. These suggest that one stall cell drops out before the other: it has reduced strength at 0.54 seconds and is then missing at 0.56 seconds as illustrated on the upstream gauge.

McKenzie (Ref. 8) previously observed that during rotating stall the non-dimensional inlet stagnation to outlet static pressure rise is independent of the compressor blading and the unstalled pressure rise and operates at two fixed levels. For incompressible flow $\psi_{TS} = (p_{exit} - P_{o_{inlet}})/\rho U^2 \approx 0.11N$ for full span rotating stall and $\psi_{TS} = 0.17N$ for part span stall where N is the number of stages.

For a supersonic fan the loading parameter ψ_{TS} is effectively a loading parameter or equivalent to $\Delta h/U^2$ for compressible flow, and represents the actual work input by the compressor relative to the potential work available. Starting

from the thermodynamic relationship:

$$\mathrm{d}h = \frac{\mathrm{d}p}{\rho} + t\mathrm{d}s$$

$$\frac{dh}{U^2} = \frac{1}{U^2}\int_{01}^{2} \frac{dp}{\rho},$$

where $P/\rho^{\gamma} = C$. If we assume the process is isentropic (reversible adiabatic) then

$$\frac{\mathrm{d}h}{U^2} = \gamma R T_o \frac{(p/P_o)^{(\gamma-1)/\gamma} - 1}{(\gamma-1)U^2} + \mathsf{losses} \tag{1}$$

where p is the mean Kulite static pressure, P_o is the inlet (freestream) total pressure, T_o is the inlet total temperature, and U is the inlet blade speed.

Ignoring losses in Eq. 1 and assuming the inlet total temperature and average total pressure are constant during rotating stall, dh/U^2 at 60, 95 & 100% speed can be plotted against non-dimensional flow (Fig. 8). The static pressure is taken from the ring of Kulites between the fan and OGV and the inlet flow is calculated from the ring of Kulites ahead of the fan. After the fan drops into rotating stall it operates at an approximately constant value of 0.11 for 95 & 100% speeds and at 0.09 for the 60% speed. Day et al. (Ref. 9) have previously shown full span and part span rotating stall operates at different levels of blockage λ where the effective blockage created by the stall cell can be calculated as defined by, $\phi_{average} = \phi_{unstall}(1-\lambda)$ where λ is the blockage 0-1. When $\lambda > 0.3$ full span rotating stall results and part span dominates for $\lambda < 0.3$. For 60% speed $\lambda = 0.44$, 95% $\lambda = 0.18$, and for 100% $\lambda = 0.13$. The two observations of increased blockage and a lower dh/U^2 for the 60% speed case both suggest the stall cell occupies a greater span of the fan at lower speeds than at high speed. Unfortunately inlet total pressure is not measured dynamically on the rig. However, inlet total pressure measured dynamically with a close-coupled Kulite on an engine test has shown that the fan operates in rotating stall with constant mean inlet total pressure. Based on this, Fig. 8 uses the rig value of free stream unstalled total pressure as a reference pressure as well as the measured blade speed U and the dynamic Kulite static pressure; T_o is assumed to be a constant and is a steady state measurement. In addition, steady state data have also been plotted to show the position of the primary characteristic. The calculated dynamic flow agrees reasonably well with the steady state measurements. Based on the dynamic measurements of the upstream and downstream rings of Kulites the stalled fan at 60% speed drops out at the 4^{th} steady state point from the max pressure rise point.

Agreement between the drop-out point inferred from the over tip unsteady data and the rings of upstream and downstream Kulites is very good, but both methods rely on the steady state data for reference.

Surge cycle at 105% Speed

Data showing the full time history of the surge event from breakdown to recovery, from the Kulites mounted upstream and downstream of the fan and in the bypass duct, are presented in Fig 9. As mentioned earlier, these data have been sampled to remove the blade passing frequency and therefore only the large scale fluctuations are seen. The figure shows eleven bursts of activity before the fan is recovered. The data show that the initial flow breakdown has a different signature to the subsequent cycles (Figs. 10a and 10b), with the first burst of activity showing the flow break down initiated by an upstream 'spike' feature at 90 degrees circumferentially (Fig 10a). Figure 11 (Ref. 10) shows a schematic of an axisymmetric surge cycle where the surge is initiated at A, the fan jumps to operation with reverse flow at B. A large pressure rise is required to sustain the reverse flow, which is not available, forcing positive flow again to C where the flow cleans up and returns to the primary characteristic at D with pressure recovery, once peak pressure rise is reached at point A the cycle begins again. These features can be seen on the downstream Kulites as the back pressure dropping until the fan recovers allowing peak pressure rise to be achieved before the cycle starts over. The data show the frequency of the surge cycle to be 7.5 Hz, which corresponds to the multiple collapse, and recovery cycles for the average annulus pressure, but superimposed are higher frequencies of the local flow around the annulus. The breakdown from surge into a deep, full span rotating stall has been observed in other tests reported by Pampreen (Ref. 3). As each surge occurs it is noticeable that the initiation becomes more axisymmetric with a non-axisymmetric behaviour once the back pressure falls, Fig. 12.

The 0.18 seconds of the overtip data during the surge cycle are shown in Fig. 13. Three Kulites are shown, the furthest upstream, mid chord and the furthest downstream. The data cover one surge cycle and correspond to one of the intermediate surge cycles. The cycle can be divided into three phases, as indicated on the figure: Phase A is the main flow breakdown when surge occurs. Phase B appears to be a non-axisymmetric behaviour akin to rotating stall that develops between surge and recovery. Phase C is a region during which the downstream pressure steadily increases before the flow breaks down again. The time taken for the complete cycle is 0.134 seconds suggesting a frequency of 7.4Hz.

The flow structure can be seen more easily when these data are built into an area distribution. This is achieved by plotting the axial location on one axis and distance travelled by the rotor on the other. Due to the large quantity of data a number of time 'snapshots' are presented showing the pressure distribution during the surge cycle. These are presented in Fig. 14 (a, b, c). Additionally these figures include the time history of the leading edge gauge with a line

indicating the time of that snap shot. Pressure distributions A and B show a fairly clean flow structure, as was seen when taking data to define the tip flow structure over the normal (stable) operating range. Pressure distribution C however shows the flow breakdown during the surge event. Analysis of the overtip data shows the recovery point is close to the 9^{th} steady state point from peak pressure rise shown on figure 8.

4. Conclusions

For the first time unsteady pressure measurements have been obtained and reported from an overtip Kulite array and Kulites at different axial locations for a transonic wide chord fan during surge and rotating stall. The data provide a clear indication of the operation of the rotor tip during surge at 105% speed and in rotating stall at 60%.

At 60% speed, the overtip measurements show the variation in casing pressure distribution through the stall cell and the extent to which the flow field varies during the 'stable' portion of the rotating stall. The overtip data show two stall cells present, rotating at 63% of the rotor speed. When the throttle was opened, one stall cell dropped out just before the other. Due to the relatively long period of time that the bypass valves take to open it was possible to define the stall recovery point, this cannot be done using steady state measurements.

The surge event lasted 1.4 seconds with overtip data covering a period of 0.18 seconds, or about 25 rotor revolutions. This period included one complete surge event, lasting 0.134 seconds, a frequency of 7.4 Hz. Three distinct phases of flow could be distinguished; breakdown, rotating stall and recovery. The initial recovery point is just below the normal working line, but the back pressure then rises until the surge point is reached and the surge cycle starts again.

This highly detailed data set is still being evaluated to increase the understanding of the flow in a transonic fan during rotating stall and surge and how to use these data to improve the fan design.

Acknowledgement

The authors would like to acknowledge the financial support of this programme of work by the DTI (UK).

References

[1] [1] C Freeman AL Rowe, 1999, Intake engine interactions of a modern large turbofan engine ASME 99-GT-344

[2] [2] EM Greitzer EM 1976 Surge and rotating stall in axial flow compressors Part I & II Trans ASME Journal of Engineering for Power 98 190-217

[3] [3] RC Pampreen, Compressor Surge and stall, 1993 ISBN 0-933283-05-9

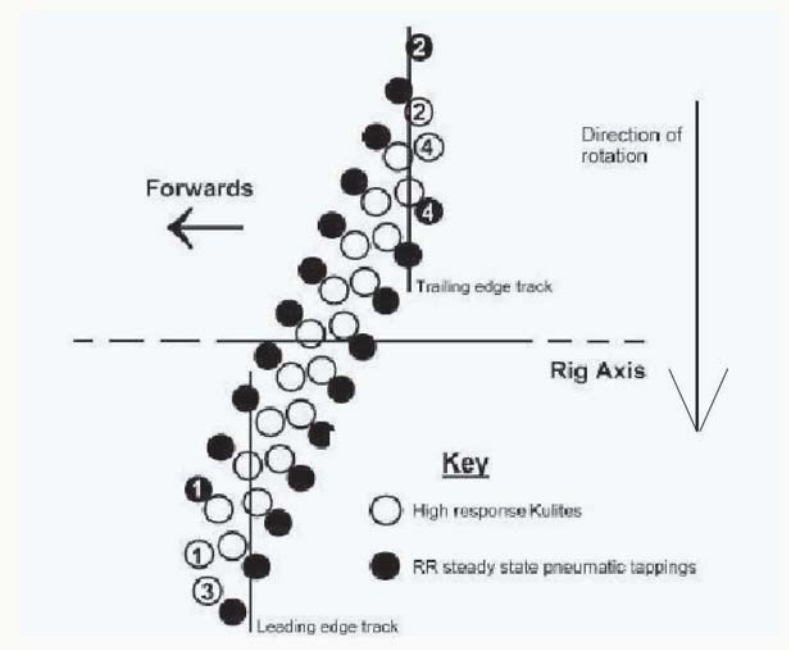

Figure 1. Overtip Kulite arrangement

[4] [4] Tyler JM & Sofrin TG 1962 Axial compressor noise studies Trans SAE 70:309-322

[5] [5] Smith MJT Aircraft noise ISBN 0-521-33186-2

[6] [6] Oppenheim AV & Willsky AS, Signals & Systems ISBN 0-13-809731-3, 1983

[7] [7] I.J. Day NA Cumpsty, The measurement and interpretation of fbw within rotating stall cells in axial compressors, Journal Mechanical Engineering Science vol. 20 No2 1978

[8] [8] AB McKenzie, Axial fbw fans and compressors

[9] [9] I.J. Day EM Greitzer NA Cumpsty, Prediction of Compressor Performance in Rotating stall, Journal of Engineering for Power, Jan 1978 vol. 100 No.1

[10] [10] AG Wilson, Stall and Surge in axial fbw compressors, PHD thesis 1996 Cranfield

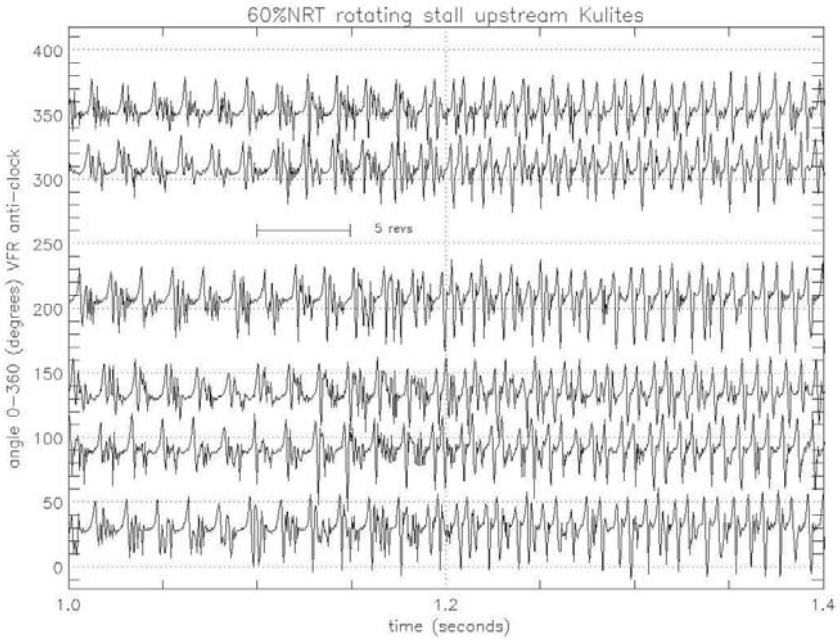

Figure 2. Time histories of upstream Kulite during transition from one to two stall cells

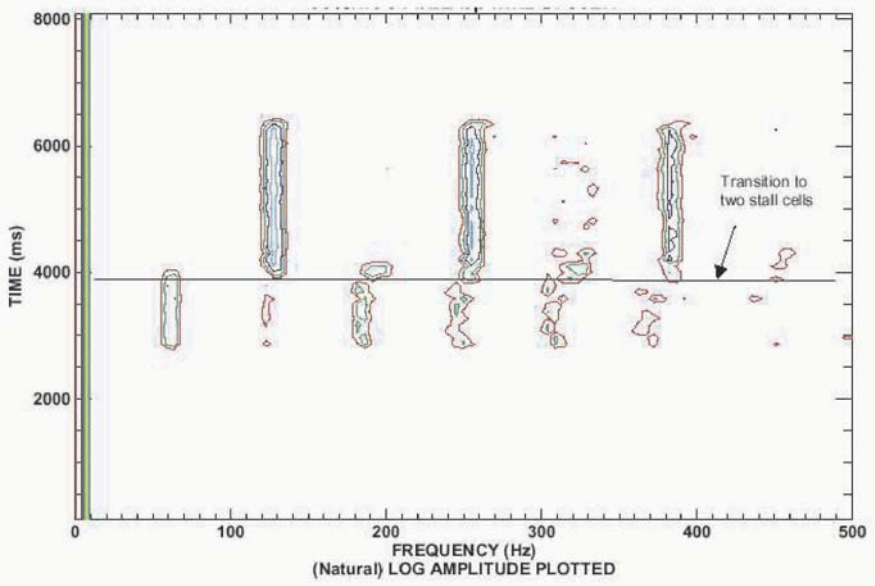

Figure 3. Variation of frequency components with time for 60% speed rotating stall

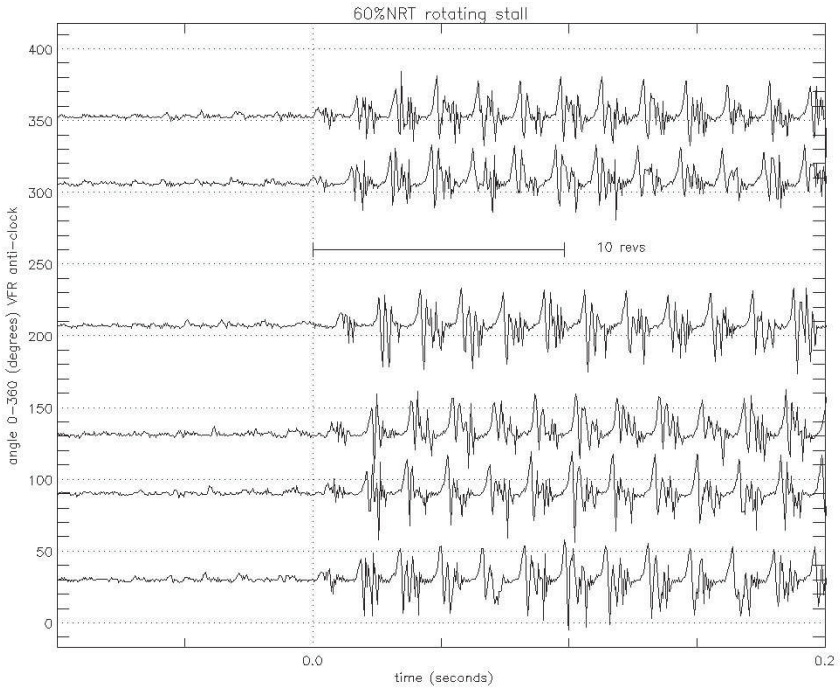

Figure 4. 60% speed time history of stall initiation

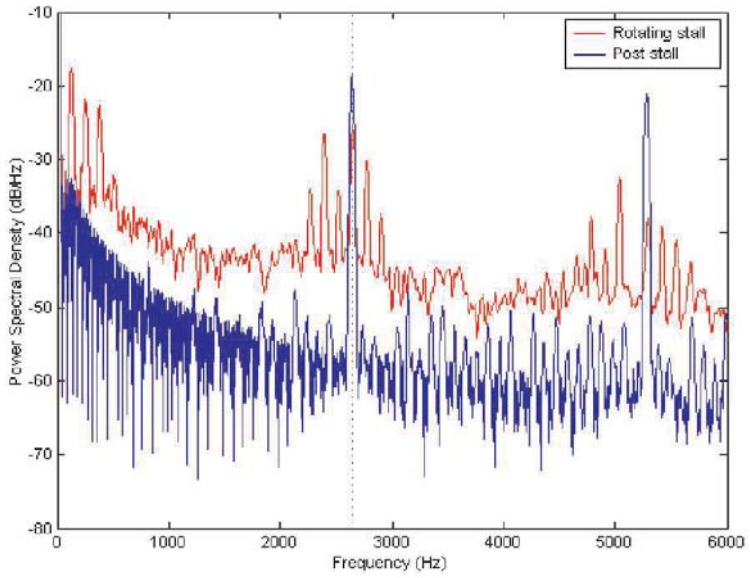

Figure 5. Power spectral density for both rotating stall and post stall data for leading edge Kulite

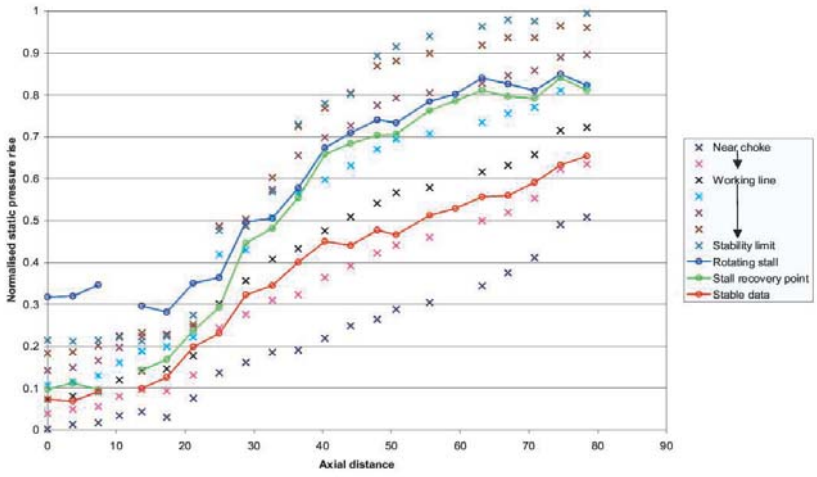

Figure 6. 60% speed stall recovery – symbols steady state, solid lines unsteady data

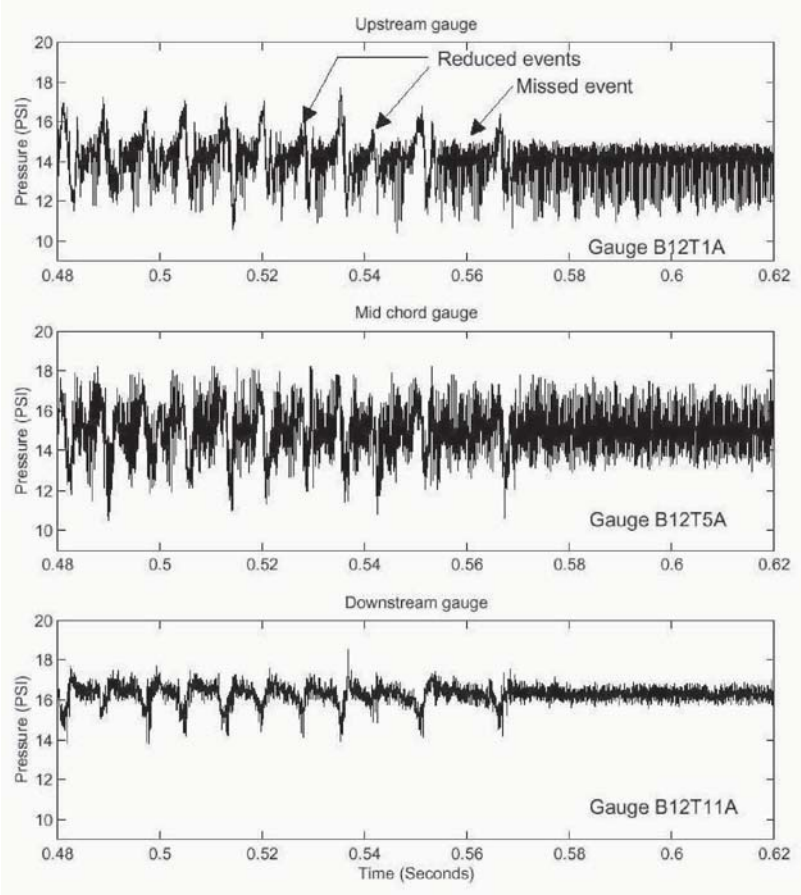

Figure 7. In-passage time histories at three axial positions during 60% stall recovery

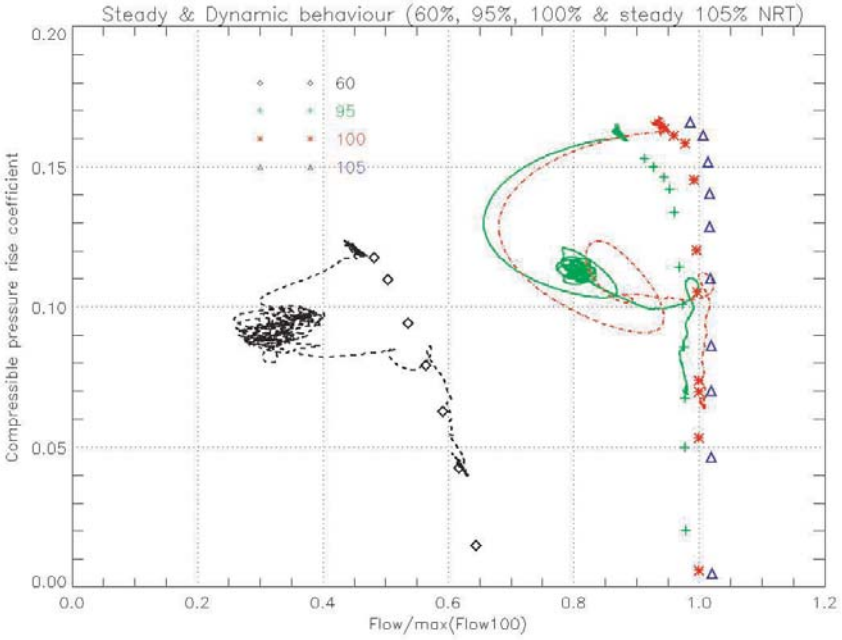

Figure 8. $\Delta H/U^2$ against non-dimensional flow for steady and dynamic behaviour

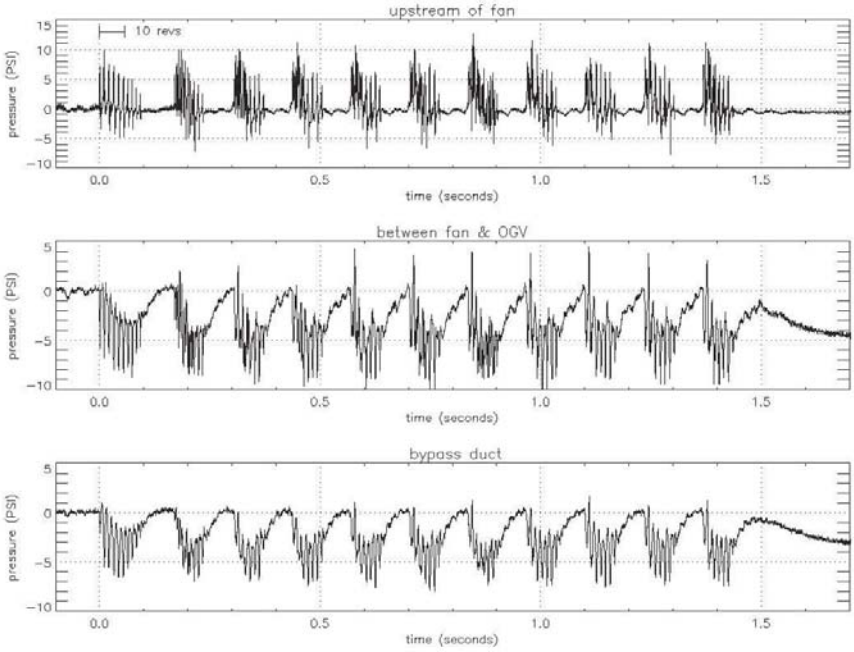

Figure 9. 105% surge event Kulite trace upstream and downstream of fan and in bypass duct

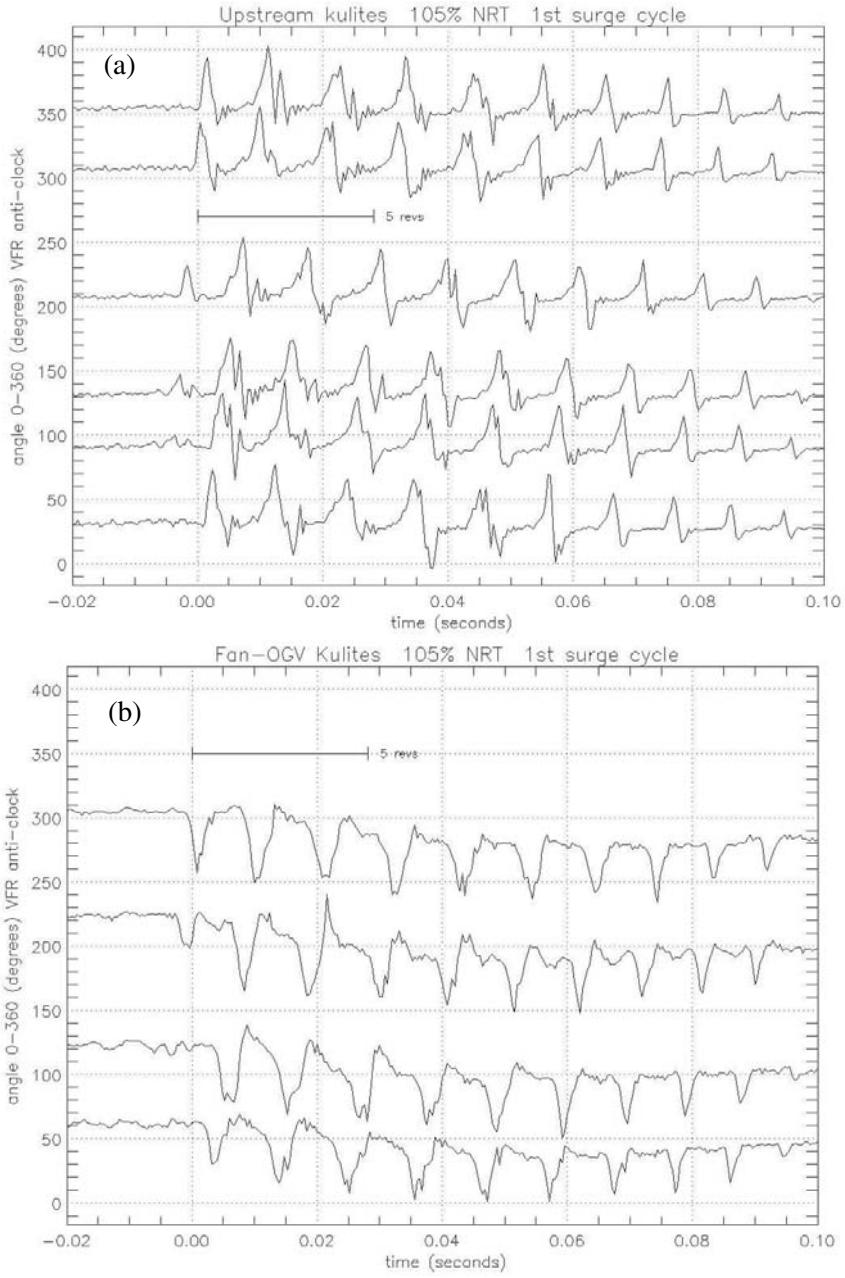

Figure 10. Time trace of first surge cycle - (a) upstream Kulite, (b) downstream of fan Kulites

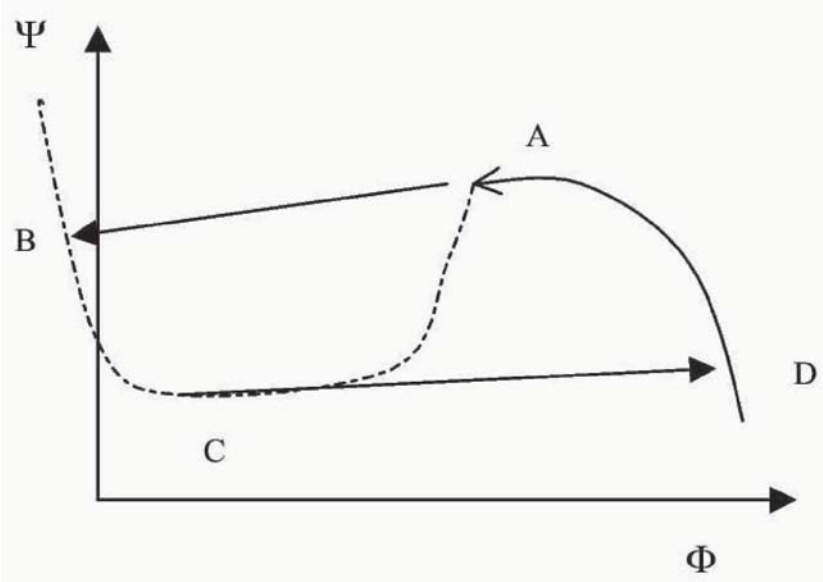

Figure 11. Schematic of the pressure rise characteristic during surge

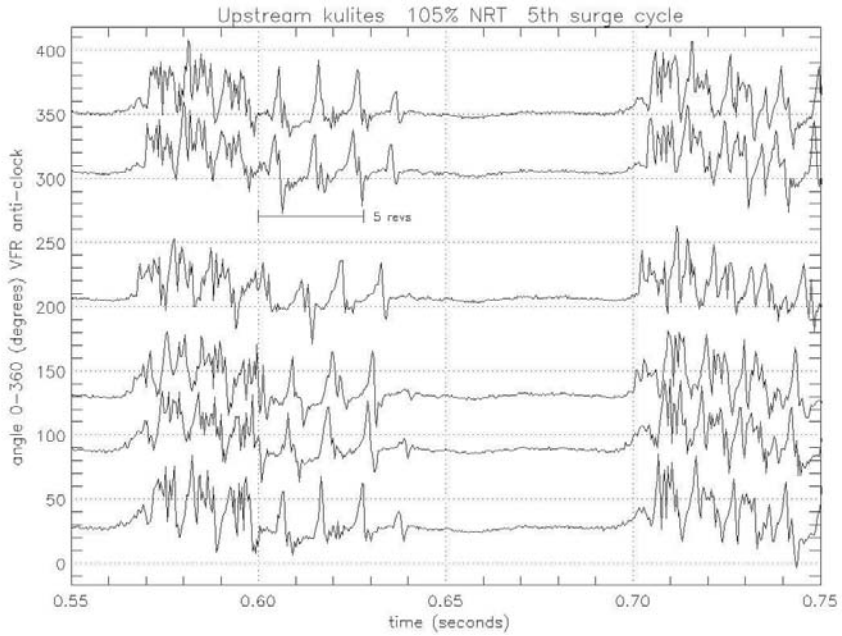

Figure 12. 5^{th} and 6^{th} surge cycle upstream Kulite showing axisymmetric initiation

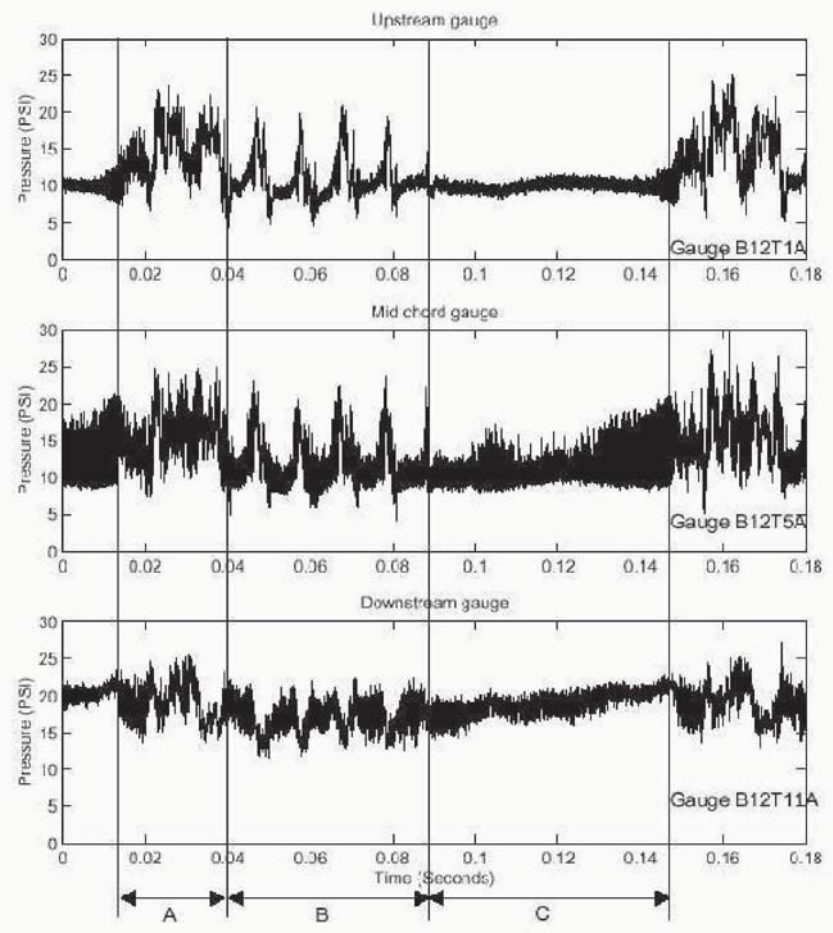

Figure 13. Zoom of surge cycle from in-passage Kulites

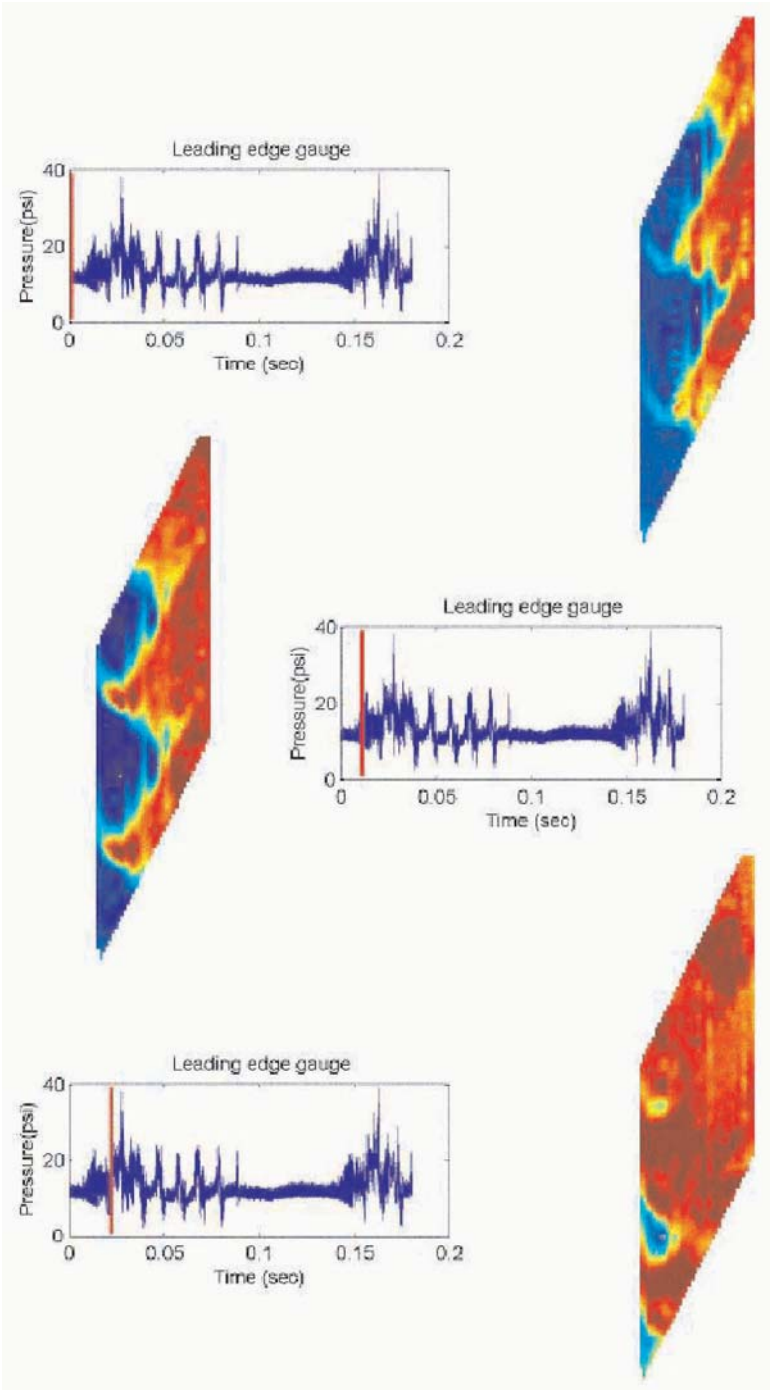

Figure 14. Snap shots of casing pressure distribution during surge event

CORE-COMPRESSOR ROTATING STALL SIMULATION WITH A MULTI-BLADEROW MODEL

M. Vahdati, A I Sayma, M Imregun
Imperial College London,
Vibration UTC, MED, London, SW7 2BX, UK
m.vahdati@imperial.ac.uk, a.sayma@imperial.ac.uk, m.imregun@imperial.ac.uk

G. Simpson
Rolls-Royce plc,
Compressor Engineering, Derby DE24 8BJ, UK
George-Simpson@rolls-royce.com

Abstract The paper will focus on one specific core-compressor instability, rotating stall, because of the pressing industrial need to improve current design methods. The long-term aim is to minimize the forced response due to rotating stall excitation by avoiding potential matches between the vibration modes and the rotating stall pattern characteristics. Using a 3D viscous time-accurate flow representation, the front bladerows of a core-compressor were modeled in a whole-annulus fashion. The engine core flow boundary conditions were obtained from a mixing-plane steady-state calculation for which the low pressure compression domain was also modeled. A variable-area nozzle, placed after the last compressor bladerow in the model, was used to impose ambient boundary conditions downstream. The rotating stall behavior at two different compressor operating points was studied by considering two different variable-vane scheduling conditions for which experimental data were available. In all cases, the rotating stall was initiated by introducing a small amount of geometric mistuning to the rotor blades. Using 3- and 6-bladerow models, the unsteady flow calculations were conducted on 32-CPUs of a parallel cluster, typical run times being around 3-4 weeks for a grid with about 30 million points. The simulations were conducted over several engine rotations. As observed on the actual development engine, 6 rotating stall cells were obtained for the first scheduling condition while mal-scheduling of the stator vanes increased the number of rotating stall cells to 13. Although there was some discrepancy between predicted and measured speed of the rotating stall pattern, it was concluded that the large-scale modeling methodology could simulate both the onset of rotating stall and its development as a function of vane scheduling.

Keywords: Rotating stall, core compressor forced response, compressor mal-scheduling

K.C. Hall et al.(eds.),
Unsteady Aerodynamics, Aeroacoustics and Aeroelasticity of Turbomachines, 313–329.

1. Introduction

Unsteady turbulent high-speed compressible flows often give rise to complex aeroelasticity phenomena by influencing the dynamic behavior of structures on which they act. Under certain conditions, the energy transfer from the fluid to the structure can cause excessive vibration levels and structural integrity may be compromised. The problem is particularly severe for gas turbines where virtually all bladerows are susceptible to aeroelasticity effects either by inherent self-induced motion (flutter) or by response to aerodynamic flow distortions and blade wakes (forced response). Different aeroelasticity phenomena are associated with different components. For instance, fan and core-compressor blades are known to suffer from flutter and rotating stall. Turbine blades are subjected to aerodynamic excitation containing both high and low harmonics, the former due to wakes from upstream blades and the latter due to the general unsteadiness of the flow, usually caused by a loss of symmetry. The most complex and the least understood aeroelasticity phenomena occur in multi-stage core compressors, the subject of this paper, because of their wide operating envelope. During engine development programs, costly structural failures are known to occur because of a mixture of aeroelastic instabilities such as acoustic resonance, flutter, forced response, buffeting, vortex shedding, etc. Most such phenomena are believed to be caused by at least one bladerow undergoing severe stall, but the overall compressor still managing to function because of the overall pressure ratio. The numerical modeling of such a situation is a formidable challenge as the analysis must be able to represent accurately not only the aerodynamic and structural properties of a large number of bladerows but also the interactions through these.

Since the avoidance of stall and surge is a major design consideration, a considerable amount of research effort has been devoted to the understanding of the physical mechanisms that give rise to such instabilities. After the initial inception stage, it is not clear which conditions will cause surge or rotating stall, though a simplified non-dimensional parameter, based on basic geometry, the mean flow speed and the speed of sound, has been proposed by Greitzner (1978) who provided a means of assessing how design changes were likely to affect the stall/surge behavior of a particular compressor. However, in the general case, there are no rules to determine the speed of rotating stall, its circumferential and radial extent as well as the number of rotating cells. So far, due to modeling difficulties, much of the stall and surge research has been experimental (Longley et al. 1990, Weigl et al. 1998), or based on simplified models (Moor et al. 1986, Paduano et al 1994), though numerical simulations with simplified or partial geometries are beginning to emerge (Niazi 2000, He 1997).

Unlike other instabilities of aeroelastic origin, core-compressor rotating stall behavior needs to be simulated not only at the onset, but also during the event itself. Such a requirement arises from the need to avoid a match between the number and speed of rotating stall cells and the assembly resonances. From an industrial perspective, it is important to understand the factors which influence changes in stall characteristics as it may result in moving from a safe operating regime to one which causes rotor blade failure. These effects are normally assessed by engine strain gauge tests which are used to map out rotating stall boundaries. However, due to the high cost of these tests and the limited scope for varying engine configuration and operation, the objective of this work is to develop a predictive capability which will minimize rig and engine testing by means of advanced simulations that will cover the flight envelope in an efficient manner.

2. Overview of the forced response methodology

Flow model

The unsteady, compressible Reynolds-averaged Navier-Stokes equations for a 3D bladerow can be cast in terms of absolute velocity $\boldsymbol{u}$ but solved in a relative reference frame rotating with angular velocity ω. This system of equations, written in an arbitrary Eulerian-Lagrangian conservative form for a control volume Ω with boundary Γ, take the form:

$$\frac{d}{dt}\int_{\Omega}\mathbf{U}\,d\Omega+\oint_{\partial\Omega}\left(\mathbf{F}-\frac{1}{Re}\mathbf{G}\right)\cdot\boldsymbol{n}\,d\Gamma=\int_{\Omega}\mathbf{S}\,d\Omega \tag{1}$$

where $\boldsymbol{n}$ represents the outward unit vector of the control volume boundary . The viscous term $\mathbf{G}$ on the left hand side of (1) has been scaled by the reference Reynolds number for non-dimensionalization purposes. The solution vector $\mathbf{U}$ of conservative variables is given by:

$$\mathbf{U}=\begin{bmatrix}\rho\\ \rho\boldsymbol{u}\\ \rho e\end{bmatrix} \tag{2}$$

The inviscid flux vector $\mathbf{F}$ can be written as:

$$\mathbf{F}=\mathbf{U}\boldsymbol{v}+\begin{bmatrix}0\\ p\delta_{ij}\\ u_j p\end{bmatrix} \tag{3}$$

where δ_{ij} represents the Kronecker delta function and $\boldsymbol{v}$ is the velocity in the relative frame of reference. The pressure p and the total enthalpy h are related to density ρ, absolute velocity $\boldsymbol{u}$ and internal energy e by two perfect gas

equations:

$$p = (\gamma - 1)\,\rho \left[e - \frac{|\boldsymbol{u}|^2}{2} \right], \quad h = e + \frac{p}{\rho} \tag{4}$$

where γ is the constant specific heat ratio. The viscous flux vector $\mathbf{G}$ has the following components

$$\mathbf{G} = \begin{bmatrix} 0 \\ \sigma_{ij} \\ u_k \sigma_{ik} + \dfrac{\gamma}{\gamma - 1} \left(\dfrac{\mu_l}{Pr_l} + \dfrac{\mu_t}{Pr_t} \right) \dfrac{\partial T}{\partial x_i} \end{bmatrix} \tag{5}$$

Where μ_l represents the molecular viscosity given by the Sutherland's formula, μ_t denotes the turbulent eddy viscosity, which must be determined by a suitable turbulence model. Therefore, $\mu = \mu_l + \mu_t$ is the total viscosity of the fluid. The value of λ is given by the Stokes relation $\lambda = -\frac{2}{3}\mu$ while the laminar Prandtl number, Pr_l, is taken as 0.7 for air. The turbulent Prandtl number, Pr_t, is taken as 0.9.

The term $\mathbf{S}$ in (1) is given by:

$$\mathbf{S} = \begin{bmatrix} 0 & 0 & \rho\omega u_2 & \rho\omega u_3 & 0 \end{bmatrix}^T \tag{6}$$

Equation (1) is discretised on unstructured mixed-element grids via a finite volume method, the details of which are given by Sayma et al. (2000a) . As described by Sbardella et al. (2000), the blades are discretized using a semi-structured mesh which consists of brick elements in the boundary layer and triangular prisms further away in the blade passage. To achieve further computational efficiency, the mesh is characterized via an edge-based data structure, i.e. the grid is presented to the solver as a set of node pairs connected by edges, a feature that allows the solver to have a unified data structure. Furthermore, the edge-based formulation has the advantage of computing and storing the edge weights prior to the main unsteady flow calculation, hence reducing the CPU effort. The central differencing scheme is stabilized using a mixture of second- and fourth-order matrix artificial dissipation. In addition, a pressure switch, which guarantees that the scheme is total variation diminishing (TVD) and reverts to a first-order Roe scheme in the vicinity of discontinuities, is used for numerical robustness. The resulting semi-discrete system of equations is advanced in time using a point-implicit scheme with Jacobi iterations and dual time stepping. Such an approach allows relatively large time steps for the external Newton iteration. For steady-state calculations, solution acceleration techniques, such as residual smoothing and local time stepping are employed. For unsteady computations, an outer Newton iteration procedure is used where the time steps are dictated by the physical restraints and fixed

through the solution domain. Within the Newton iteration, the solution is advanced to convergence using the traditional acceleration techniques described previously.

For the sliding planes that occur at bladerow boundaries, the solution is updated at the interface by interpolating the variables in the stator computational domain to obtain rotor fluxes, and in the rotor computational domain to obtain the stator fluxes (Rai 1986, Sayma et al. 2000b). The fluxes are computed using a characteristic technique, which allows the correct propagation of the information. In other words, flow data are exchanged between the two grids via specially formulated boundary conditions at the interface.

Structural model and calculation of the aeroelastic response

It is implicitly assumed that the vibration amplitude remains within the bounds of linear behavior. The global aeroelasticity equations of a structural motion can be written as:

$$[\mathbf{M}]\{\ddot{\boldsymbol{x}}\} + [\mathbf{C}]\{\dot{\boldsymbol{x}}\} + [\mathbf{K}]\{\boldsymbol{x}\} = \{\mathbf{p}(t)\, A\boldsymbol{n}\} \tag{7}$$

where $\mathbf{M}, \mathbf{C}, \mathbf{K}$ are the mass, stiffness and damping matrices, $\boldsymbol{x}$ is the displacement vector, $\mathbf{p}(t)$ is a vector of pressures, A being the application area and $\boldsymbol{n}$ is the normal unit vector of the blade's surface. A standard structural finite element formulation is used to obtain the left-hand side while the flow model above is used to obtain the unsteady forcing of the right-hand side. The free vibration problem can be solved to yield the natural frequencies ω_r and mode shapes $[\mathbf{\Phi}_r]$ of the bladed disk assembly in vacuum, r being the mode index.

The aeroelasticity analysis can be conducted in two different ways, the so-called fully-coupled and the uncoupled approaches. In the fully-coupled method, the structural mode shapes are interpolated onto the aerodynamic mesh as the two discretization levels between structural and aerodynamic meshes are unlikely to be wholly coincident. To accommodate the structural motion, the fluid mesh is moved at each time step using a network of springs whose compression/extension is prescribed by the mode shape at the blade surface and becomes zero at the far field. The frequency of the motion is dictated by the natural frequency of the corresponding mode. An exchange of boundary conditions takes place at the fluid-structure interface at each time step. The main advantage of the fully-coupled method is the automatic inclusion of the aerodynamic damping while the main drawback is the computational overhead arising from the mesh movement. However, unless the change in aerodynamic damping is likely to be important, say in the case of a large blade vibrating at resonance, the forced response analysis can be simplified by considering the unsteady flow and the blade motion separately. Such an uncoupled

analysis consists of computing the blade unsteady pressures without any blade movement. The aerodynamic damping may still be obtained from a transient aeroelasticity, or flutter, analysis, and such damping values can be used when calculating the blade's response. A case study comparing the relative accuracy of both approaches is reported by Vahdati et al. (2003a).

A convenient indicator of the blade response is the modal force, which is a measure of the correlation between the structural mode shape and the unsteady pressure fluctuation, the other two key parameters being the amplitude and frequency of the fluctuation. The modal force represents the strength of the unsteady forcing in a particular mode of vibration. In simple terms, the modal force can be thought as the product of the unsteady pressure and the structural mode shape. It can best be visualized by considering a rigid body motion where the blade is plunging only. In this case, the modal force is equivalent to the unsteady lift on the blade.

3. Case study

As stated earlier, the objective of the work is to develop a methodology to predict the effects of multi-lobe rotating stall on blade vibration levels. Of particular importance is to link the variable vane scheduling to the number, size, distribution and speed of rotating stall cells so that the critical modes of vibration can be identified and avoided. Two vane settings, namely nominal and mal-scheduled, were used in the computations because of the availability of experimental data for these two conditions. The work was undertaken in two stages, first with a 3-bladerow model and then with a 6-bladerow model.

3-bladerow studies

As shown in Fig. 5, the case study was initially conducted for the first 3 bladerows of an aero-engine core compressor at some part-speed. The first bladerow consists of variable inlet guide vanes (VIGVs), while the next one is the first rotor bladerow (R1) and the last one is the first stator bladerow (S1). The nominal vane setting was used for all calculations reported in this section.

For this particular study, where the part-speed behavior is of primary interest, the compressor inlet boundary conditions were not available because of the very low fan speed. Therefore, it was decided to include the low pressure compression (LPC) domain in the model and to derive the required boundary conditions from a steady-state flow solution over the computational domain shown in Fig 5. A novel feature of the computational domain are two variable area nozzles (VANs), one upstream of the fan, labelled VANF in Fig. 5 , and one downstream of the compressor, labelled VANC in Fig. 5 . The VANF was used to control the by-pass mass flow and it was tuned until an appropriate working line point on the part-speed fan characteristic was obtained. The

nozzle area was then kept constant for all remaining calculations. Therefore, it was implicitly assumed that the fan operating point would remain the same for the two compressor operating points that were being considered.

Once a steady-state solution was obtained, the computational domain was reduced by removing the LPC domain and the VANF. The reduced domain still included VANC which was used to control the core-compressor mass flow as an alternative to prescribing a static pressure distribution at the compressor exit. The need for such an approach, described by Vahdati et al. (2003b), arises from the difficulties of defining accurate boundary conditions at the outlet compressor exit. Indeed, upstream downstream boundary conditions for most multi-bladerow computations use are derived from a 1D throughflow analysis calibrated by available experimental data. Such an approach is not suitable for stall and surge studies where the flow through the downstream bladerows undergoes significant temporal and spatial variations. When fixed conditions are imposed at the boundaries, the flow solution is stable at lower working lines but, higher working lines, which are of more interest here, are known to exhibit modeling difficulties because of potential inconsistencies between the actual solution and the imposed boundary conditions. Rigid boundary conditions, based on imposing given exit pressure distributions, are not suitable for numerical studies because the bladerow exit pressure profiles are neither known nor fixed. Furthermore, at high working lines, the flow becomes genuinely unsteady near the stall boundary, and the imposition of a fixed exit static pressure results in numerical instabilities, the so-called "numerical stall". Therefore, the use of a downstream VAN alleviates some of the difficulties above by allowing the flow to develop naturally by providing a volume after the last bladerow included in the model. The ideal situation would be to include as many compressor bladerows as possible and to keep the LPC domain in the model so that atmospheric conditions can be used at either end. However, as will be discussed later, the rotating stall computations were conducted with the reduced-size model and keeping the VANC only because of computational considerations.

The rotating stall calculations were conducted in a time-accurate fashion using a viscous flow representation and by adjusting the VANC to obtain the required compressor operating point on the part-speed characteristic. A well-known difficulty is the initiation of rotating stall when using a numerical model since an initial perturbation is needed. Even if the flow structure is near instability, a perturbation may still be needed for stall initiation. After some deliberation, it was decided to introduce a small amount of aerodynamic mistuning to Rotor 1 where each blade was given a random small geometric change in stagger (Fig. 5). Two different vane settings, listed in Table 1, were considered for two operating points, corresponding to two different VANC configurations, la-

belled VANC1 and VANC2 in Fig. 5. Therefore four rotating stall simulations were undertaken using the 3-bladerow model (Table 2).

Table 1. Vane settings

Vane setting	VIGV Angle	S1 Angle	S2 angle
Nominal	0^o	0^o	0^o
Mal-scheduled	-5^o	5^o	-5^o

Stall behavior was examined by monitoring the mass flow at Rotor 1 exit for the VANC1 and VANC2 configurations for the nominal vane configuration. VANC1 corresponds to an operating point near stall and hence the sudden drop in the mass flow rate persists, indicating that that there is no recovery from stall. On the other hand, VANC2 is on a lower working line and hence the compressor recovers from rotating stall after a short while. The effect of temperature was also investigated by lowering the inlet temperature by 15 degrees for the VANC1 configuration. No appreciable difference was noted.

It is best to visualize the rotating stall phenomenon by inspecting an animation of the static pressure at Rotor 1 inlet, or negative mass flow at Rotor 1 exit. As discussed earlier, Configuration VANC1 yields persistent rotating stall, but the compressor recovers for Configuration VANC2. A typical snapshot for VANC1 is given in Fig. 5 where about 13 rotating stall cells can be seen along the circumference. From a structural viewpoint, a 13-cell pattern is likely to excite a 13 nodal diameter/first flap assembly mode provided there is also a frequency match between the natural frequency of the mode and the speed of the rotating stall pattern. The modal force for this particular mode is shown in Fig. 5. A Fourier transform of the modal force indicates an excitation frequency of about 910 Hz, suggesting that the stall pattern's rotation occurs at about 910/13=70 Hz, the assembly speed being about 120 Hz. Therefore, it may be concluded that the speed of the rotating stall cells is 50Hz, a value that is consistent with previous experience of about half the rotational speed.

Experimental evidence suggested that the actual number of rotating stall cells was about 6, and not 13 as predicted here, for the nominal vane set-

Table 2. Summary of 3-bladerow rotating stall calculations

	VANC1 (High working line)	VANC2 (Low working line)
Nominal	13 R/S Cells	No R/S
Mal-scheduled	No convergence	13 R/S Cells but recovers

ting. The calculations were repeated for the mal-scheduled vane setting but it was not possible to obtain a converged solution for this condition. It was thought that the inclusion of further downstream bladerows would improve the modeling accuracy by allowing the flow to develop more naturally. As will be described in the next section, the stall calculations were repeated with a 6-bladerow model.

6-bladerow studies

As shown in Fig. 5, the computational domain was extended by three bladerows, namely Rotor 2 (R2), Stator 2 (S2) and Rotor 3 (R3). The VANC was placed after the R3 bladerow. As before, a single-passage mixed-plane steady state-solution was obtained (Fig. 5). The two different vane settings, listed in 1, were considered. The computations were performed for an operating point near stall, corresponding to VNAC1 configuration.

A comparison of the overall compressor characteristic is shown in Fig. 5 for the two vane settings while the corresponding individual rotor characteristics are given in Fig 5. As expected, there is a performance degradation with the mal-scheduled case. Of some interest is the individual rotor characteristic for the datum case when using steady-state and averaged unsteady flow results. It is seen that there are significant differences, indicating that there is significant unsteadiness, a result that can also be seen from the separation zones of Fig. 5.

The instantaneous rotating stall patterns are shown in Fig. 5 for the nominal and mal-scheduled vane settings by plotting the static pressure at R1 inlet. In agreement with measured data, there are 5-6 stall cells for the nominal setting while the number of cells switches to 11 for the mal-scheduled setting. A summary of all rotating stall calculations is given in 3. The modal force time histories are plotted in Fig. 5 for the same two configurations where 5, 6, 7, 10 & 12 nodal diameter modes have been included for the nominal vane setting, and the 11 nodal diameter mode for the mal-scheduled setting. As can be from the Fourier transforms, the main excitation is at about 430 Hz for the former and 770 Hz for the latter, corresponding to stall pattern rotation speeds of 34 Hz and 50 Hz respectively. Although there is good agreement with the number of stall cells in both cases, the measured rotating stall speed is about 60% higher for both settings. However, as can be seen from the static pressure plots of Fig. 5, the distribution of the rotating stall cells along the circumference is not uniform and hence several harmonics with different frequencies can be assumed to be present in the measured signal. Therefore, it is difficult to compare the measured and predicted peak excitation frequencies. Indeed, it is possible that the number of rotating stall cells might change by one or two between successive rotations. Furthermore, it is likely that the detail of the rotating stall pattern may be influenced by the downstream bladerows which

are not included in the model. Finally, the rotation stall excitation may interact with the dynamic characteristics of a bladerow and even lock into a mode of vibration.

Table 3. summary of rotating stall calculations

Vane setting	VANC setting	No of cells in test	No of cells predicted by 3-bladerow calculations	No of cells predicted by 6-bladerow calculations
Nominal	High working line	6	13	5-6
Mal-scheduled	High working line	13	No convergence	11

4. Concluding Remarks

- The most important conclusion is the feasibility of simulating rotating stall with a large scale numerical model. Although the computational effort is significant, parallel processing on inexpensive PC clusters allows the runs to be undertaken in "advanced design" timescales. For instance, the 6-bladerow model has about 30 million grid points and a typical run taking about 3 weeks on a 32-CPU cluster, each node consisting of a 2 GHz Intel Xeon CPU. Given Moore's law for single-CPU speed increases, which is acceptable in industrial environments.
- From a numerical viewpoint, numerical stall initiation can be achieved by aerodynamically mistuning the rotor blade. Ideally, a systematic study needs to be undertaken to see if the obtained stall pattern and speed are independent of the initial stagger angle perturbation. Also, stall initiation is still relatively slow, requiring the simulation of 5-6 full engine revolutions. Further work is needed to see if white noise excitation can be used to represent flow randomness as an alternative to rotor blade mistuning.
- It has been confirmed that the most important parameter for rotating stall pattern and speed is the stator vane setting. Inlet temperature effects were seen to be of secondary importance.
- It appears that the inclusion of further bladerows downstream improves modeling accuracy in the sense that the correct number of rotating stall cells was obtained with the 6-bladerow model only. Furthermore, it was not possible to obtain a solution for the mal-scheduled vane setting using the 3-bladerow model.

- From a design viewpoint, both the exact pattern and the speed of the rotating stall cells must be determined so that the critical vibration modes can be identified and avoided. However, such a requirement may not only be beyond the available modeling accuracy but it also relies on both the pattern and speed to remain constant between successive rotations. The latter issue needs to be studied by undertaking long rotating stall simulations, say over 100 engine rotations, with representative inlet perturbations to see the stability or otherwise of the rotating stall structure.

Acknowledgments

The authors thank Rolls-Royce plc for both sponsoring the work and allowing its publication.

References

Greitzner, E. M. (1978) "Surge and rotating stall in axial flow compressors. Parts 1 & 2" *ASME J. of Engineering for Power* **98**, 190–217.

Longley, J. and Hynes, T. P. (1990) "Stability of flow through multi-stage axial compressors", *ASME J of Turbomachinery* **112**, 126–132.

Weigl, H. J., Paduano, J. D., Frechette, L. G., Epstein, A. H., Greitzer, E. M., Bright, M. M. and Strazisar, A. J. (1998) "Active Stabilization of Rotating Stall and Surge in a Transonic Single-Stage Compressor" *Journal of Turbomachinery* **120**, 625–636.

Moore, F. and Greitzer, E. M. (1986) "A theory of post-stall transients in axial compressors". *ASME J. of Eng for Gas Turbines & Power* **108**, 371–379.

Paduano, J., Epstein, A. H., Greitzner, E. M. and Guenette, G. (1994) "Modelling for control of rotating stall" *Automatica* **30**, 1357–1373.

Niazi, S. (2000) *Numerical simulation of rotating stall and surge alleviation in axial compressors*. PhD thesis, Georgia Institute of Technology, Dept of Aerospace Engineering, Atlanta, USA

He, L., (1997) "Computational study of rotating stall inception in axial compressors", *AIAA Journal of Power and Propulsion* **13(1)**, 31–38.

Sayma, A. I, Vahdati, M., Sbardella, L. and Imregun, M. (2000) "Modelling of 3D viscous compressible turbomachinery flows using unstructured hybrid grids". *AIAA Journal*, **38(6)**, 945–954.

Sbardella, L. Sayma, A. and Imregun, M. (2000) "Semi-structured meshes for axial turbomachinery blades". *International Journal for Numerical Methods in Fluids* **32(5)**, 569–584.

Rai, M. M. (1986) "Implicit conservative zonal boundary scheme for Euler equation calculations" *Computers & Fluids* **14**, 295–319.

Sayma, A. I., Vahdati, M. and Imregun, M. (2000) "Multi-bladerow fan forced response predictions using an integrated 3D time-domain aeroelasticity model" *J of Mechanical Engineering Science, Part C*, **214(12)**, 1467–1483.

Vahdati, M., Breard, C., Sayma, A. and Imregun, M. (2003) "An integrated time-domain aeroelasticity model for the prediction of fan forced response due to inlet distortiona" *ASME Journal of Engineering for Gas Turbines & Power* **124(1)**, 196–208.

Vahdati, M., Sayma, A., Freeman, C. and Imregun, M. (2003) "On the use of atmospheric boundary conditions for axial-flow compressor stall simulations". Submitted to the ASME J of Turbomachinery

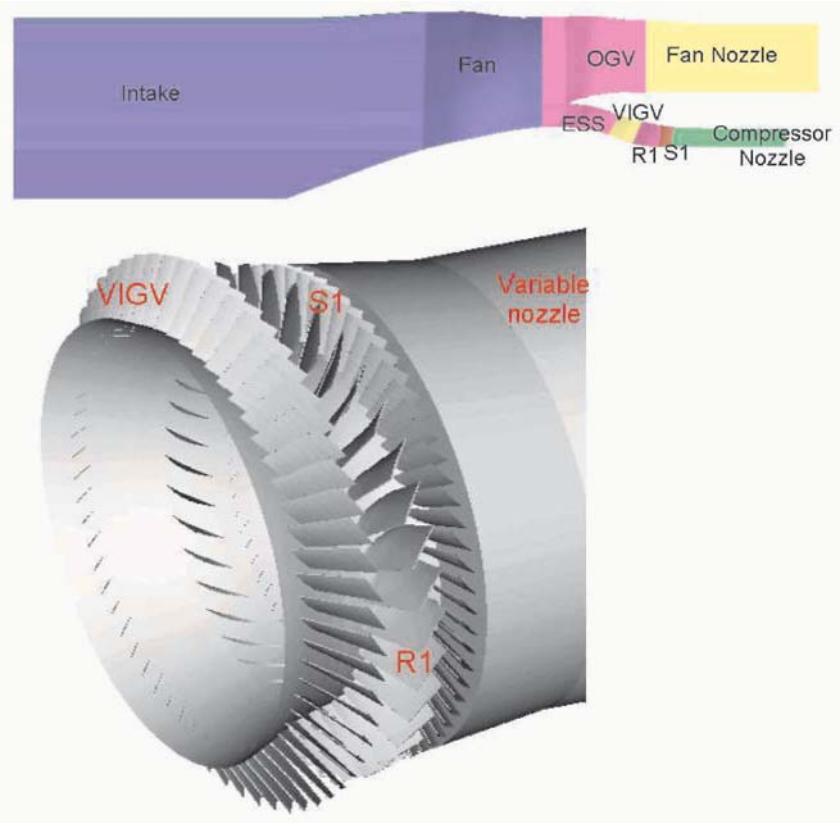

Figure 1. omputational domain for steady-state computations (top) 3-bladerow model (bottom)

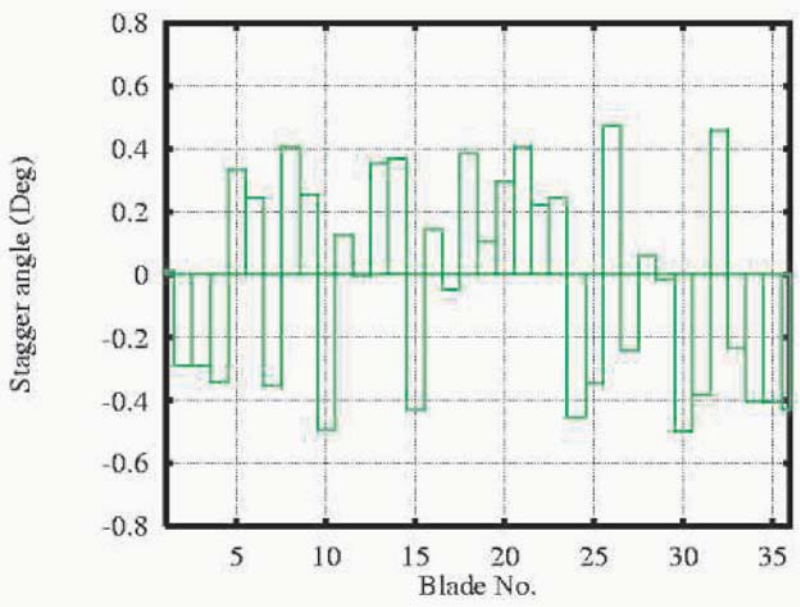

Figure 2. Mistuning of Rotor 1

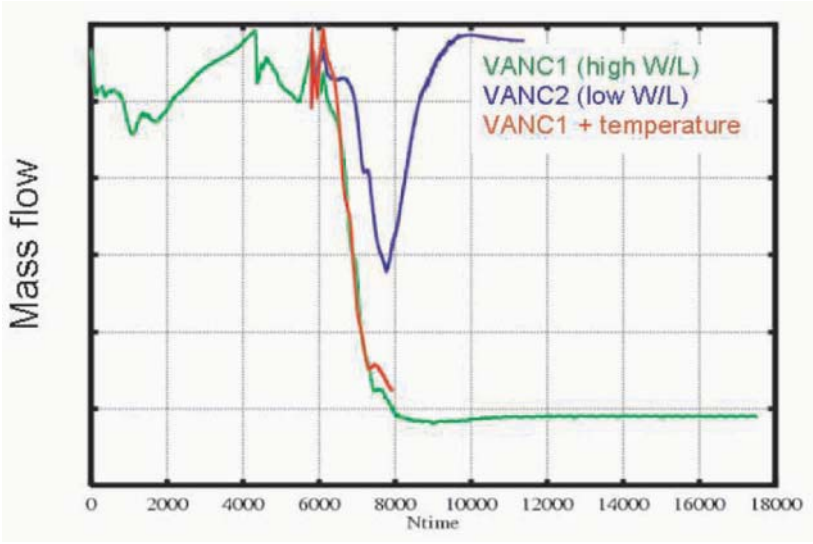

Figure 3. Mass flow at Rotor 1 exit

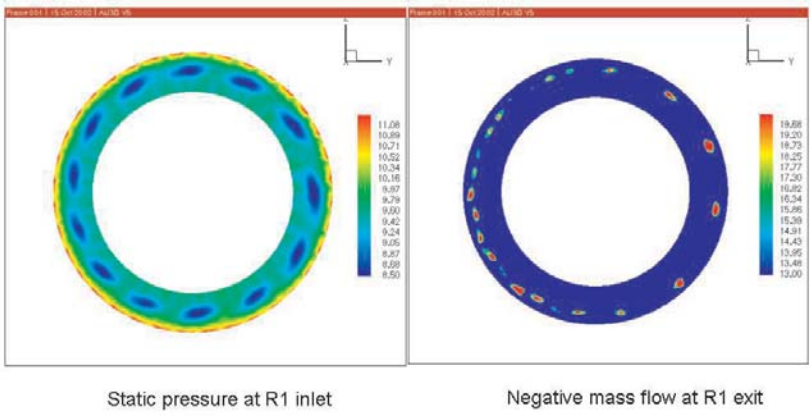

Figure 4. Instantaneous static pressure and negative mass flow VANC1

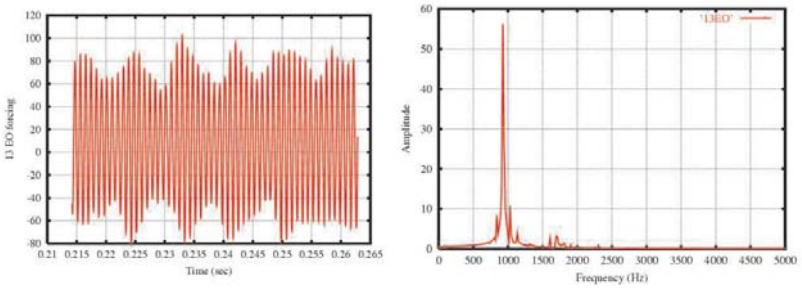

Figure 5. 13ND/1F modal force and its Fourier transform

Figure 6. 6-bladerow model

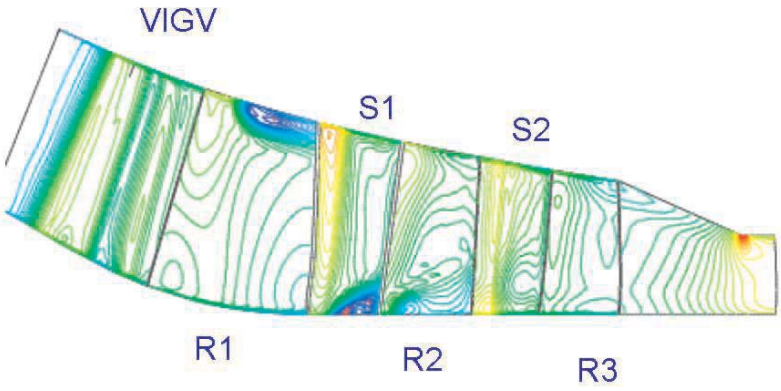

Figure 7. Steady-state solution for 6-bladerow model

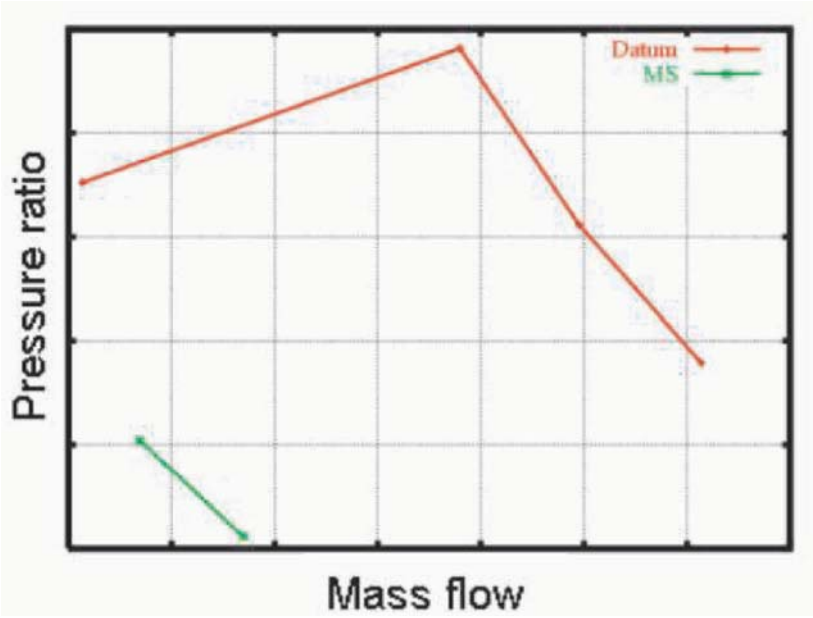

Figure 8. Comparison of the overall characteristic

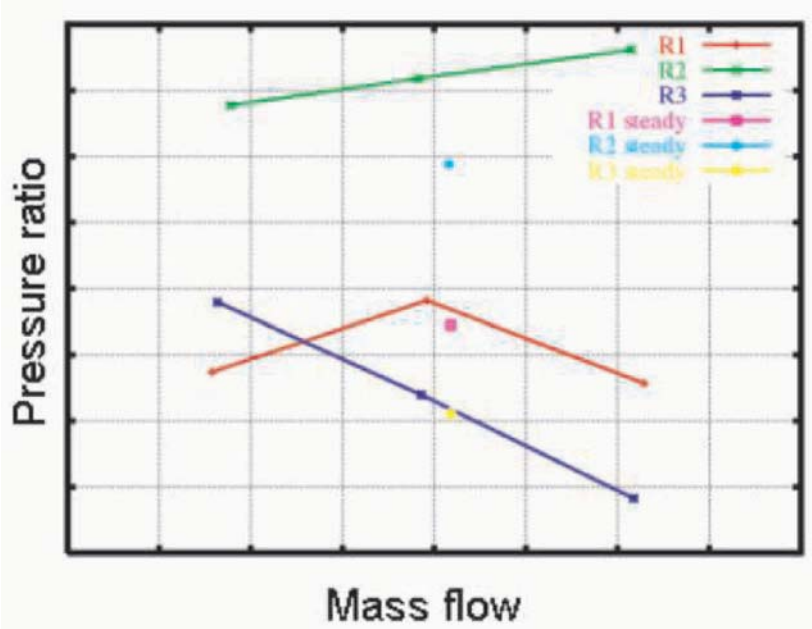

Figure 9. Individual rotor characteristics for datum scheduling

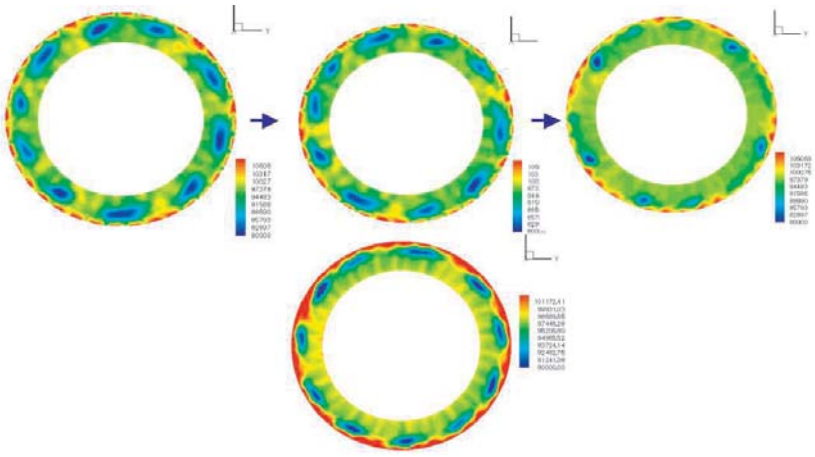

Figure 10. Instantaneous stall bands for high W/L. Nominal (upper) vs mal-scheduling (lower) cases

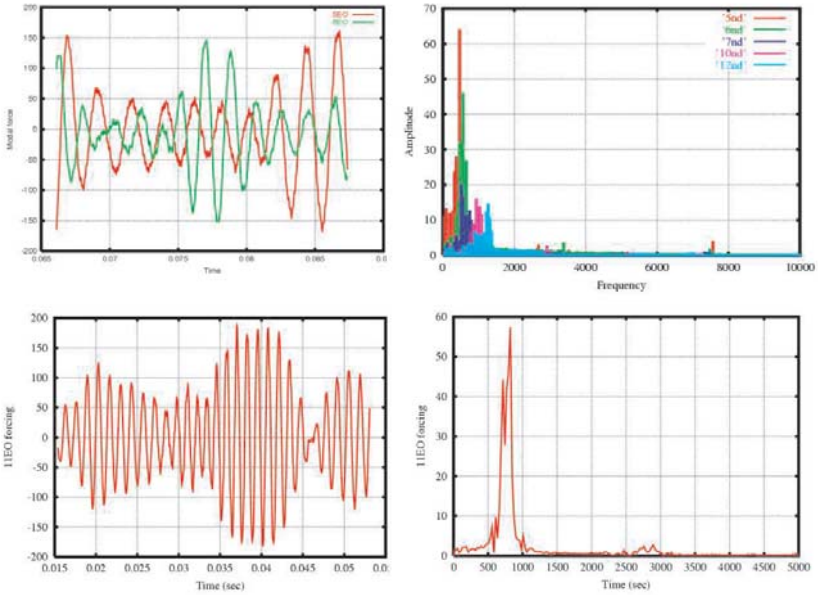

Figure 11. Instantaneous stall bands. Nominal condition (top) and mal-scheduled condition (bottom)

PARAMETRIC STUDY OF SURFACE ROUGHNESS AND WAKE UNSTEADINESS ON A FLAT PLATE WITH LARGE PRESSURE GRADIENT

X. F. Zhang, H. P. Hodson
Whittle Laboratory
University of Cambridge, UK

Abstract The combined effects of surface roughness and upstream unsteady wakes were investigated on a flat plate subjected to the same pressure distribution as that on the suction surface of an ultra high lift low-pressure (LP) turbine blade. The parametric study included the effects of roughness size, type and location under steady and unsteady flow conditions. The roughness elements included straight wires, straight square steps, wavy steps and wavy wires. The experimental results show that the combined effects of surface roughness and upstream unsteady wake can further reduce the profile losses of the ultra highly loaded LP turbine blades. For each flow condition, there is a height of roughness element, which results in the lowest loss. The step-type roughness elements are more effective at inducing boundary layer transition than the wire-type roughness due to the higher disturbance level generated after the sharp edges. The wavy roughness elements are more effective at inducing transition and further reduce the profile losses under steady flow conditions. However, the strong stream-wise vortexes generated by the wavy elements will increase the loss in unsteady conditions. The optimum location of the roughness element is between the blade suction peak and the separation onset location.

Keywords: high lift, LP turbine, boundary layers, separation bubble, unsteady flow, wakes, surface roughness, loss

1. Introduction

The recent studies of wake-separated boundary layer interaction have made the development of the high lift low-pressure (LP) turbine blades possible. The wakes from the previous blade row impinge on the blade surfaces and induce transition around the separation onset location on the suction surface. The wake-induced turbulent region as well as the calmed region that follows it will suppress the separation bubble. The calmed region, which is laminar-like in nature and attached, will reduce the production of loss (Schulte and Hodson, 1998). The understanding of the unsteady flow behaviour has been

K.C. Hall et al.(eds.),
Unsteady Aerodynamics, Aeroacoustics and Aeroelasticity of Turbomachines, 331–344.

successfully incorporated into the design of new high lift LP turbine profiles (Howell et al., 2002).

Further increases in the blade loading will result in a higher adverse pressure gradient and a larger separation bubble on the blade suction surface. Howell et al. (2002) showed that the wake unsteadiness still worked well on the ultra high lift blades ($Z_w = 1.2$) at Reynolds numbers of about 200000. However, in the case of lower Reynolds numbers, the incoming wakes may not be strong enough to suppress the large separation and the separation bubble will have more time to re-establish due to the lower wake passing frequency. There will be a larger separation bubble between the wake pass resulting in a larger profile loss. Therefore, another loss reduction mechanism is required.

The current study, funded by the European Commission, is concerned with the combined effects of wake unsteadiness and surface roughness on the boundary layer development on an ultra high lift LP turbine blade - T106C. The object is to determine if these disturbances and their effects enable further increases in blade loading and if so, to further understand the physical mechanisms involved. The T106C LP turbine cascade has a pitch that is 20 percent larger than the well-studied T106A cascade, (Stieger, 2002 and Brandt et al., 2000), resulting in a Zweifel coefficient of 1.19. The first part of the study concerned this parametric study of the effect of roughness elements under steady and unsteady flow conditions. The experiments were conducted on a flat plate, which is subjected to the same pressure distribution as that on the suction surface of T106C profile.

2. Experimental Methods

Experimental Facilities

The current study was conducted on a flat plate test rig with a moving bar system, as shown in Figure 1. The test section was fitted to the exit of an open-return wind tunnel. The test rig consists of an aluminum plate that is 738 mm long by 458 mm wide and 12.8 mm thick. The flat plate has a 6:1 elliptical leading edge to avoid the separation of flow at the leading edge. In the present study, only the front 500 mm of the plate was used to achieve the test Reynolds number range and a reasonable measurement resolution.

A pair of contoured walls was used to impose the pressure distribution on the flat plate. The shape of the contoured walls was designed by ITP, a partner in the project, to match the same pressure distribution as that on the suction side of T106C LP turbine blade. Bleed slots and two overlapping perforated sheets at the outlet were used to avoid the flow separation from the contoured walls due to the large diffusion after the throat. A bi-planar cylindrical rod type turbulence grid can be placed upstream to increase the free stream turbulence intensity up to 3.5% to create a more realistic test environment.

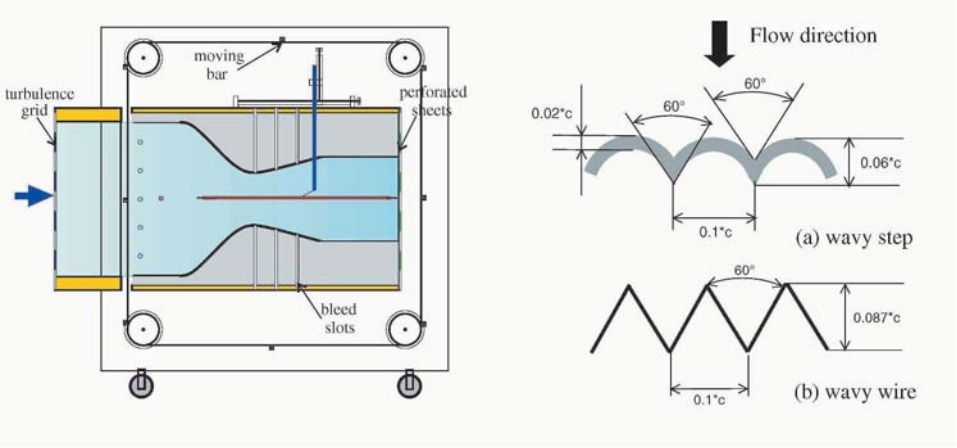

Figure 1. Flat plate test rig with moving bars

Figure 2. Wavy type roughness element geometry

To simulate the rotor-stator interaction, moving bars were used to generate the incoming wakes. Carbon fibre bars of 7.8 mm diameter were attached to a pair of reinforced nylon belts. The axial distance between the bar moving plane and the plate leading edge is 465 mm. As the bars pass across the inlet of the test section, they shed wakes, which convect over the flat plate and simulate the wake passing conditions in a turbomachine. In the flat plate test, the flow coefficient (ϕ) was defined as the ratio of the exit velocity (V_{2is}) to the bar speed (U_b), i.e. $\phi = V_{2is}/U_b$ (Stieger, 2000) and $\phi = 0.83$ was chosen to be representative of a repeating stage of the T106C profile. The reduced frequency, defined as $f_r = f_{bar} \cdot \mathcal{C}/V_{2is}$, was set at 0.84. The Reynolds numbers based on the plate surface length (S_0) and exit velocity (V_2) covered a range between 134000 and 285000.

The roughness elements used in the current study include straight wires, straight steps, wavy steps and wavy wires. The roughness elements were mounted on the plate surface using double-sided tape, which has a thickness of 0.1 mm. Table 1 summaries the parameters of the roughness elements. The relative roughness height k/δ^* is calculated from the displacement thickness at $50\%S_0$ with Re=174000 and $Tu = 0.5\%$ on smooth surface in steady flow condition. Re_k is based on the height of the roughness element and the local freestream flow velocity at Re=174000. The wavy roughness elements were proposed by MTU, a partner in the present program, having previously been described in a lapsed patent. The geometry is shown in Figure 2. The thickness or diameter of the element was changed but the other dimensions were kept the same as those shown in the figures.

Table 1. Surface roughness element parameters

Roughness	Height (k)	Width	$k/S_0(\%)$	k/δ^*	Re_k	Ref. Code
straight wire	1.20 mm	n/a	0.24	1.01	442	W-1
straight wire	0.81 mm	n/a	0.16	0.68	286	W-2
straight wire	0.74 mm	n/a	0.15	0.62	257	W-3
straight wire	0.61 mm	n/a	0.12	0.51	205	W-4
straight wire	0.68 mm	n/a	0.14	0.57	233	W-7
straight step	0.68 mm	10 mm	0.14	0.57	233	S-2
wavy step	0.68 mm	10 mm	0.14	0.57	233	S-3
wavy wire	0.68 mm	n/a	0.14	0.57	233	W-9

Measurement Techniques and Data Presentation

Surface static pressure distributions on the flat plate were measured by using a Scanivalve system. The isentropic static pressure coefficient is defined as:

$$C_p = (P_{01} - P_s)/(P_{01} - P_{97\%,s}) \tag{1}$$

where P_s is the measured surface static pressure, $P_{97\%,s}$ is the static pressure at $97\%S_0$ on the flat plate surface and P_{01} is the inlet total pressure after the moving bars.

A constant temperature anemometry system was used for hot-wire measurements with an overheat ratio of 1.8 . For each measurement, 128 ensembles of AC data and 32 ensembles of DC data were taken. Each ensemble consists 4096 samples covering at least three wake passing periods.

A Dantec single-wire 55P15 boundary layer probe was used to make the boundary layer traverses. The hot-wire was calibrated in a suction calibration facility in accordance with a modified form of King's Law. The effects of the ambient temperature drift were taken into account using the correction of Bearman (1971).

Hot-wire traverses were performed normal to the plate surface. Typically, 34 positions were used through the boundary layer with the distance between positions increasing exponentially as the probe left the plate surface. In order to account for the influence of the plate surface proximity on the cooling of the heated wire, the Cox correction was applied to the measured data.

The suction surface profile loss coefficient can be determined according to the approximal expression given by Denton (1993)as:

$$\xi = 2\theta/(\underline{p} * cos(\alpha_2)) \tag{2}$$

where θ is the trailing edge momentum thickness calculated from the hot-wire traverses at $97\%S_0$, $\underline{p}$ is the equivalent pitch of the pressure distribution under investigated calculated from the T106C linear cascade pitch and surface length ratio and α_2 is taken the value of T106C linear cascade exit flow angle.

3. Measurement Results on Smooth Surface

The baseline of the parametric study of the surface roughness elements on flat plate was provided by an investigation of the flow properties on the smooth surface. The measured surface static pressure distributions at Re=174000, as well as the numerical simulation results from ITP, are presented in Figure 3. The peak velocity occurs around $45\%S_0$ and the diffusion factor $(D_v = (V_{max} - V_{97\%S})/V_{max})$ is about 0.27. The boundary layer separated at about $55\%S_0$. At $Tu = 0.5\%$, the flow reattaches at about $80\%S_0$. At $Tu = 3.5\%$, the high level of disturbance in the freestream flow helps to reattach the separated flow earlier and results in a smaller bubble.

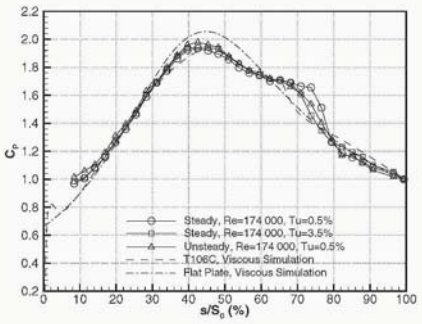

Figure 3. Surface static pressure distribution

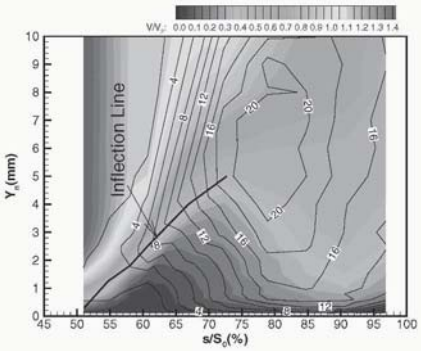

Figure 4. Steady boundary layer measurements on smooth surface

The surface static pressure distributions under unsteady flow conditions were also measured by using the same technique as that in the steady flow. Due to the low frequency response of the Scanivalve system, only time-averaged information can be provided. The measurement results at $\phi = 0.83$ and $f_r = 0.84$ for Re=174000 with Tu=0.5% is also presented in Figure 3. The incoming wakes periodically reduce the separation bubble size. This can be identified by the large change in C_p distribution near $70\%S_0$, where the maximum height of separation bubble is located under the steady condition.

To further study the flow patterns, the boundary layer development on the flat plate with a smooth surface was surveyed using hot-wire traverses at 11 different stream-wise locations between $51\%S_0$ and $97\%S_0$ under both steady and unsteady flow conditions. Figure 4 presents the measured velocity contours normalized by the exit velocity for Re=174000 with Tu=0.5% under steady flow condition. The velocity contour plot suggests that the boundary layer separates at $55\%S_0$ and reattaches around $83\%S_0$. The contour lines of turbulence intensity normalized by the exit velocity and the inflection line are

also plotted in the figure. It can be clearly see that the instabilities originate at the inflection point.

The selected boundary layer integral parameters for the unsteady condition with $\phi = 0.83$ and $f_r = 0.84$ at Re= 174000 and Tu=0.5% are presented in Figure 5 as S-T diagrams. Four velocity trajectories are also plotted in the figures. The wakes travel at the free stream velocity (V_∞). The leading edge of the wake-induced transitional/turbulent region travels at about $0.9V_\infty$. The trailing edge of the wake-induced transitional/turbulent flow or the leading edge of the calmed region travels at about $0.5V_\infty$ and the trailing edge of the calmed region travels at about $0.3V_\infty$.

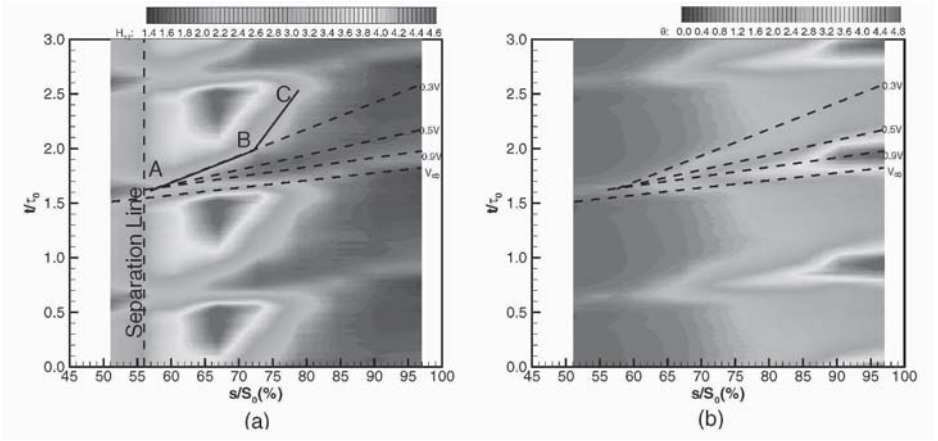

Figure 5. Unsteady boundary layer integral parameters on smooth surface

The shape factor, H_{12}, presented in Figure 5(a) clearly shows the periodic interaction between the coming wakes and separation bubble. The boundary layer separates at almost the same location as that in the steady flow conditions, marked as a dashed line in the figure. The separation bubble is prevented from reestablishing by the wake-induced turbulent region and the calmed region until the trailing edge of the calmed region, along the line A-B marked in the figure. Then the separation bubble between the wakes starts to reestablish. The steep slope of the separation reattachment line (marked B-C in the figure) suggests that the bubble recovery rate between wakes is very slow. The momentum thickness θ, shown in Figure 5(b), also clearly shows the periodic effects of wake passing. In the wake-induced turbulent region, there is higher momentum thickness. In the calmed region, the θ value is lower, which is one of the important features of the calmed region as it corresponds to the loss reduction. The effect of the calmed region almost persists to the trailing edge.

Between the wakes, the momentum thickness increases as the separation bubble reestablishes.

The boundary layer development strongly affects the profile loss. The loss coefficients, calculated based on Equation 2, at different flow conditions on smooth surface are presented in Figure 6. The loss coefficients under steady conditions with Tu=0.5% decrease as the Reynolds number increases. Due to the existence of the large separation bubble in the steady conditions, the loss level is high, especially at low Reynolds numbers. Increasing the free stream turbulence intensity (Tu=3.5%) causes the boundary layer to transition earlier and reduces the bubble size. Thus the loss is reduced. However, at lower Reynolds numbers the reduction in losses is not as large as that at higher Reynolds number due to the larger separation bubble and the later transition that occurs at lower Reynolds numbers.

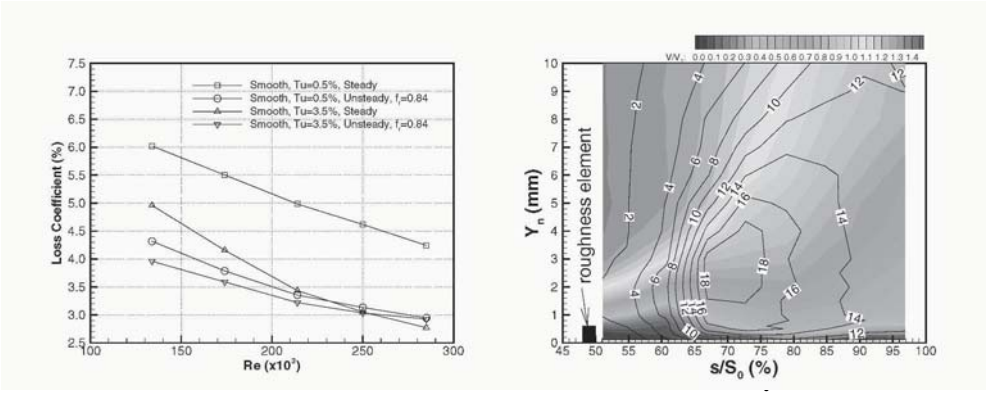

Figure 6. Loss coefficients on the smooth surface

Figure 7. Steady velocity distribution with S-2

In the unsteady flow condition, with $f_r = 0.84$ and Tu=0.5%, the periodic suppression of the separation bubble due to the wake passing and the calmed region following it significantly reduce the losses. At Tu=3.5%, the losses are further reduced at the lower Reynolds numbers. However, at the highest Reynolds number, the loss does not change much. This is because the loss variation is a balance between the positive effect of the bubble reduction and the negative effect of the increase in the turbulent wetted area. At high Reynolds numbers, with high free stream turbulence intensity, the separation bubble is already small under steady conditions. In this case, the negative effect caused by the wake passing is larger than the benefit that arises due to the reduction in the size of the bubble and the calmed region.

4. Measurement Results with Roughness

Even under unsteady flow conditions, the losses on the smooth flat plate are still high, especially at low Reynolds numbers. This is because that the profile is not an optimal design and there is a large separation bubble between the passing wakes. Ramesh et al. (2001) and Roman et al. (2003) showed that the profile loss of the ultra high lift aerofoil can be further reduced by the combined effects of surface roughness and wake unsteadiness. The current study is aimed at optimizing the roughness parameters, including the roughness size, type and location, so as to reduce the loss of ultra high lift LP turbine blades.

Boundary Layer Behavior with Roughness

The steady velocity contour plots from hot-wire measurements at Re=174000 and Tu=0.5% with the straight step S-2 ($k/\delta^* = 0.57$) placed at $50\%S_0$ are presented in Figure 7. Due to the high disturbance level after the roughness element, the separation bubble is much smaller than that on the smooth surface in both length and height. The turbulence intensity contour lines indicate that the roughness element does not induce transition immediately but that it hastens the transition process in the separated shear flow.

The measured unsteady boundary layer integral parameters are presented in Figure 8. The shape factor, H_{12}, is shown in Figure 8(a). Due to its small size, the recovery of the separation bubble after the wake passing is very quick, which is indicated by the short reattachment line A-B being followed by the almost vertical reattachment line B-C in . Figure 8(b) shows the momentum thickness, θ, at this flow condition. Under the wake, at the beginning the momentum thickness is larger than that on the smooth surface due to the effect of the roughness element. However, its growth rate is lower, so that the highest value at the trailing edge is lower. This is the main contribution to the loss reduction. The momentum thickness associated with the calmed region is similar to that on the smooth surface at first but becomes higher close to the trailing edge. Between the wakes, the momentum thickness after the roughness element is slightly higher due to the high disturbance after the roughness. However, near the trailing edge, it is almost at the same level as that on the smooth surface.

Effect of Roughness Height

The height of the roughness element directly affects the boundary layer development. To study the effect of the roughness height on the profile loss, straight wires with different diameters were tested in both steady and unsteady flow conditions.

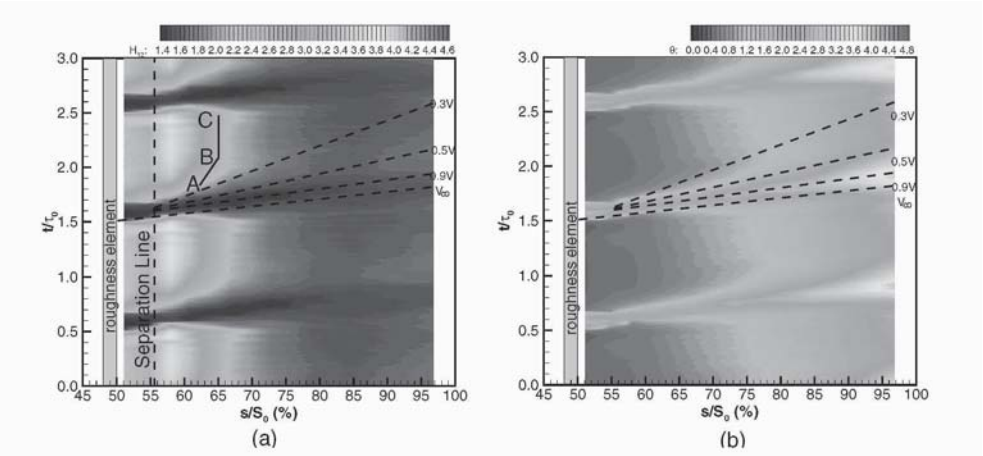

Figure 8. Unsteady boundary layer integral parameters with S-2.

Figure 9 shows the effect of the diameter of the straight wires placed at $50\%S_0$ on the loss coefficient under unsteady flow conditions with $\phi = 0.83$ and $f_r = 0.84$. Initially, as the wire diameter is reduced, the loss coefficient decreases. However, as the wire diameter further reduces, the loss increases again at low Reynolds numbers. This is because the loss results from a compromise between the beneficial effect of the bubble size reduction and the calmed region and the negative effect from the earlier formed turbulent flow caused by the wakes. The largest diameter wire induces transition too early and results in a large amount of turbulent flow. The smallest diameter wire does not induce transition effectively at low Reynolds numbers. Thus, there is an optimum diameter for each flow condition.

In the current study we are mainly interested in the flow behaviour at low Reynolds numbers. Figure 10 shows the loss coefficients varying with the diameter of the straight wires at Re=174000 in steady and unsteady flow conditions. In the steady flow conditions, the loss coefficient with roughness was reduced significantly compared with that on the smooth surface. The loss continues to decrease as roughness height increases, even for the largest tested wire. However, under the unsteady flow conditions, there exits an optimum height. In the current test condition, W-3, which has a relative height of $k/S_0 = 0.15\%$ or $k/\delta^* = 0.62$, produces the lowest loss. W-4 ($k/S_0 = 0.12\%$, or $k/\delta^* = 0.51$) was found to produce the lowest loss for Tu=3.5%. Another feature that needs to be noted is that the loss coefficient under unsteady conditions is lower than that in the steady condition if the roughness element is not too high. In this case, the benefit can come from both surface roughness and wake unsteadiness.

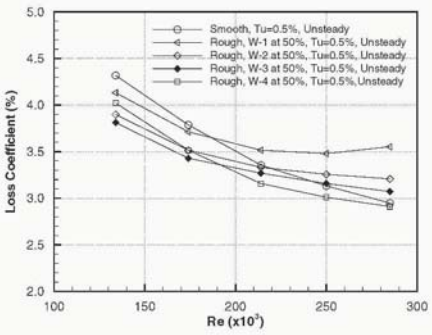

Figure 9. Effects of roughness height on loss in unsteady conditions

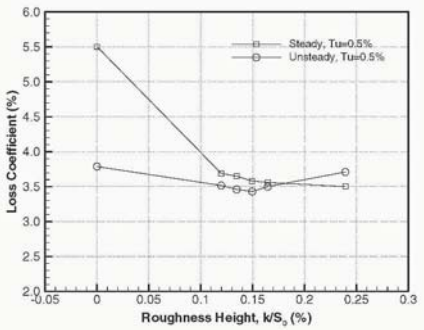

Figure 10. Loss coefficients vs. roughness height at Re=174000

Effect of Roughness Type

The shape of the roughness elements also has effect on the transition process. To investigate the influence of the roughness shape on the loss reduction, different types of roughness elements were tested under steady and unsteady conditions with Tu=0.5%. The tested roughness elements included straight steps, wavy steps and wavy wires.

The measured loss coefficients for the straight step S-2 ($k/\delta^* = 0.57$) are presented in Figure 11. The loss coefficient for W-7, which has the same diameter as the height of S-2, is also plotted in the figure. Under steady conditions, the step is more effective at reducing the loss than the wire with the same dimensions. This observation is the same as that of Pinson and Wang (2000). This is because that the disturbances generated by the sharp edge of the step are stronger than these after the wire, as shown in Figure 12. This figure shows the RMS profiles measured just after the roughness elements at $51\%S_0$. However, under the unsteady flow conditions, the difference in the loss coefficients for these two roughness elements is not much. This is again because that the loss coefficient is due to the combined effects of the bubble size reduction and larger turbulent wetted area.

Another two types of roughness elements, a wavy step and a wavy wire as shown in Figure 2, were also tested. Figure 13 presents the measured loss coefficients with the wavy step S-3. Under steady flow conditions, the wavy step is more effective than the straight step S-2 in loss reduction although they have the same heights. To find the reason for this difference, the disturbance levels after S-3 were measured at two different span-wise locations: after the tail and between the tails of the roughness element(see Figure 2). As shown in Figure 14, between the tails the RMS level is similar as that after S-2. However,

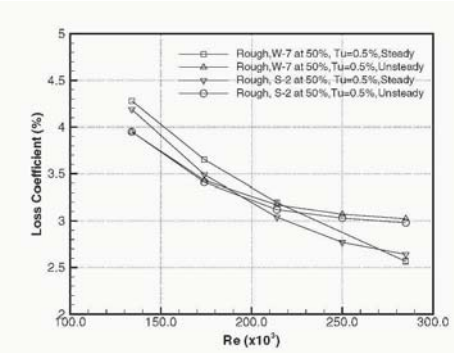

Figure 11. Loss coefficients with straight wire and straight step

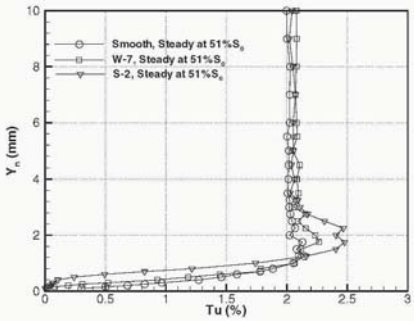

Figure 12. Measured RMS after roughness elements

there is very high level of turbulence after the tail. There are strong streamwise vortices generated in the region of the tails. These help to trigger early transition and further reduces the losses. However, under unsteady flow condition, the stronger streamwise vortices cause more turbulent mixing and weaken the calmed region resulting in a higher loss. The wavy wire, which has a diameter equal to the height of S-3, gave the similar results as that of the wavy step S-3.

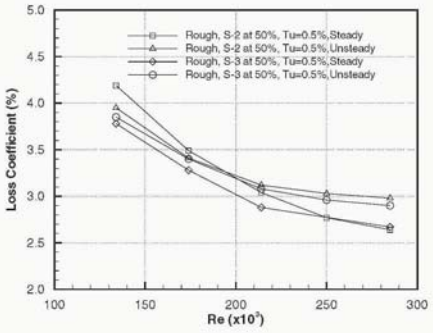

Figure 13. Loss coefficients with wavy elements

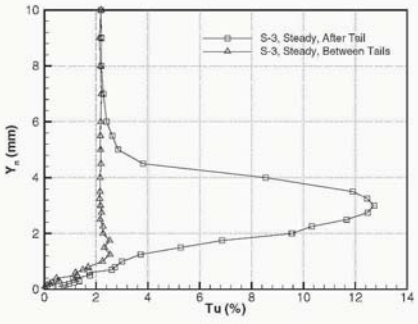

Figure 14. Measured RMS after wavy step in steady conditions

Effect of Roughness Location

To study the effect of the location of the roughness elements on the loss reduction, the straight step S-2 was placed at three different streamwise locations between the velocity peak and the separation onset location, i.e. at

$46\%S_0, 50\%S_0$ and $54\%S_0$. The measured loss coefficients under steady and unsteady flow conditions are presented in Figure 15(a) and 15(b), respectively.

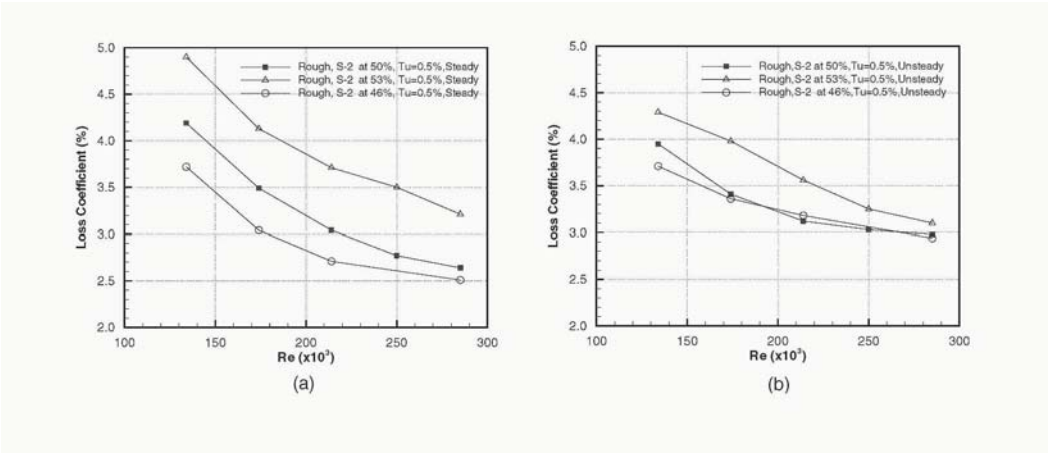

Figure 15. Loss coefficients with s-2 at different streamwise locations

As the roughness elements were moved upstream to $46\%S_0$, just after the velocity peak, the roughness elements induce transition earlier due to the higher local velocity and result in smaller separation bubbles. In the case of the steady flow conditions, the loss is reduced at all the Reynolds numbers. In unsteady flow conditions the losses are further reduced at lowest Reynolds numbers. However, at high Reynolds numbers, the earlier induced transition results a larger area covered by the turbulent flow. This results in a higher loss than that when the roughness was place at $50\%S_0$. When the roughness element S-2 was moved downstream to $53\%S_0$, the loss coefficients increase significantly under steady and unsteady conditions. This is not only because the roughness element induces transition a little later and thus results in a larger separation bubble but also because that the separation after the roughness element merges with the separation bubble due to the pressure gradient. The combined bubble gets larger, especially in height. Once the roughness element is placed inside of the separation bubble, there will be little effect from roughness on the boundary layer transition. Roman et al. (2002) made the same observation. Therefore, the optimum location of the surface roughness is at the halfway between the velocity peak and the separation onset location.

5. Conclusions

The parametric study of roughness elements including roughness size, type and location under steady and unsteady flow conditions was performed on a flat plate. The boundary layer was subjected to the pressure distribution representative of that on the suction surface of an ultra high lift LP turbine blade.

The combined effects of surface roughness and unsteady wakes can further reduce the profile losses of ultra highly loaded LP turbine blades, for which the separation bubble is large due to the high adverse pressure gradient and low wake passing frequency. The loss reduction due to unsteady flow and surface roughness is a compromise between the positive effects from the separation bubble reduction due to the surface roughness and the calmed region and the negative effects from the larger turbulent wetted area, the latter two being a direct consequence of the wake-induced transition.

There is an optimum height of roughness element for each flow condition. The optimum roughness height is only 0.15% of the surface length or about 62% of the local displacement thickness. The roughness element does not induce transition immediately after itself but only hastens the transition in the separated shear layer.

The step-type roughness elements are more effective at inducing boundary layer transition than the wire-type roughness due to the higher disturbance level generated after the sharp edges. The wavy roughness elements are more effective at inducing transition and further reduce the profile losses under steady flow conditions due to the strong vortices generated by the tails. However, the strong vortices may weaken the effects of the calmed region and result in a negative effect in the loss reduction in unsteady conditions.

The optimum location of the roughness element is at the halfway between the velocity peak and the separation onset location.

Acknowledgments

The work reported in this paper was conduced as a part of the research project UTAT - "Unsteady Transitional Flows in Axial Turbomachineries", funded by the European Commission under contract number G4RD-CT-2001-00628. The authors wish to thank ITP for the design work of the contour walls. The help provided by Mr. Maciek Opoka is also gratefully acknowledged.

References

[1] Bearman, P.W., 1971, "Correction for the effect of ambient temperature drift on hotwire measurements in incompressible flow", DISA Information, No. 11, pp. 25-30.

[2] Brandt, H., Ganzert, W.and Fottner, L., 2000, "A Presentation of Detailed Experimental Data of a Suction Side Film Cooled Turbine cascade", ASME paper, 2000-GT-296.

[3] Denton, J.D., 1993, "Loss mechanisms in turbomachines", ASME Journal of Turbomachinery, Vol. 115, No. 4, pp 621-656.

[4] Howell, R. J., Hodson, H. P., Schulte, V., Schiffer, H. P., Haselbach, F., and Harvey, N. W., 2002, "Boundary Layer Development in the BR710 and BR715 LP Turbines - The Implementation of High Lift and Ultra High Lift Concepts", ASME Journal of Turbomachinery, Vol. 123, pp 385-392.

[5] Pinson, M. W., and Wang, T., 2000, "Effect of Two-Scale Roughness on Boundary Layer Transition Over a Heated Flat Plate: Part 1 - Surface Heat Transfer," ASME Journal of Turbomachinery, Vol. 122, pp301-307.

[6] Pinson, M. W., and Wang, T., 2000, "Effect of Two-Scale Roughness on Boundary Layer Transition Over a Heated Flat Plate: Part 2 - Boundary Layer Structure," Transactions of the ASME, Vol. 122, pp308-316.

[7] Ramesh, O. N., Hodson, H. P., and Harvey, N. W., 2001, "Separation control in ultra-high lift aerofoils by unsteadiness and surface roughness," ISABE

[8] Roman, KM., "The Effect of Roughness and Wake Unsteadiness on Low-Pressure Turbine Performance," Master Thesis, Cambridge University, UK.

[9] Schulte, V, and Hodson, HP, 1998, "Unsteady wake-induced boundary layer transition in high lift LP turbines", ASME Journal of Turbomachinery, Vol 120.

[10] Stieger, R.D., 2002, "The effects of wakes on separating boundary layer in low pressure turbines," PhD Thesis, Cambridge University, UK.

BYPASS FLOW PATTERN CHANGES AT TURBO-RAM TRANSIENT OPERATION OF A COMBINED CYCLE ENGINE

Shinichi Takata
Researcher, Kakuda Space Center, NASDA

Toshio Nagashima
Professor, Department of Aeronautics and Astronautics, Univ. Tokyo

Susumu Teramoto
Lecturer, Department of Aeronautics and Astronautics, Univ. Tokyo

Hidekazu Kodama
Assistant General Manager, Advanced Technology Department, IHI Co, Ltd

Abstract Turbo-Ramjet Combined Cycle Engine is composed of a turbofan engine and a ramjet engine that is expected to be a candidate of future hypersonic propulsion systems. It can operate as turbofan mode for low speed range (Mach number 0∼3), then changes into ramjet mode for the higher speed range(Mach number 2.5∼5). In order to achieve smooth mode transition, it inevitably employs variable geometry components, so that the latter control sequence has to be carefully scheduled to maintain air flow rate and thrust at cruise condition during the mode transition. The present study therefore examines the flow pattern changes due to ram air mixing with fan bypass air, that are not available from the transient engine thermo-cycle simulation. CFD calculation showed that such flow patterns be feasible, yielding rather good agreement between the thermo-cycle and flow simulations with respect to total engine air flow rate and thrust.

1. Introduction

Turbo-Ramjet Combined Cycle Engines (CCE) are expected to be a promising choice for the next generation hypersonic flight propulsion system, which was successfully demonstrated a couple of years ago by Japanese HYPR project with US and EU international collaboration. (Miyagi et al., 1995a, Miyagi

K.C. Hall et al.(eds.),
Unsteady Aerodynamics, Aeroacoustics and Aeroelasticity of Turbomachines, 345–356.

et al., 1995b, Takeo et al., 1999) A key issue in the project was concerning the transition in the engine operation from turbofan mode (Mach number 0∼3) to ramjet mode (Mach number 3∼5) that takes place at Mach 2.5 through 3.0 climb around the altitude of 20 km. The engine thrust and air flow rate need to be maintained for smooth and stable acceleration to the hypersonic cruise, so that a sequence of controls for variable geometry mechanism was adopted. HYPR engine employed a tandem arrangement of the turbo core engine and the ram combustor, attaching 2D variable area nozzle at the exhaust end. The ram air is introduced through Mode Selector Valve (MSV) at the entrance of the ram inlet duct which wraps around the core fan engine and mixes in the bypass duct with the bypass fan air through forward-Variable Area Bypass Injector (FVABI). Upon opening MSV to start the ramjet mode and depending upon the rear pressure level, a flow reversal or recirculation of the bypass fan air jet through mixing in the ram inlet duct is alarmed to cause unstable flows, which may lead to the ram combustion instability.

The primary objective of this paper is therefore to investigate whether the conjectured control sequences suit to yield safe and smooth transition or not, by means of flow pattern visualization in accordance with CFD simulation.

In the following, a series of flow patterns in the ram inlet/bypass duct and the rear mixing zone, representing important stages as the engine shifts from turbofan to ramjet, will be shown, which may not be adequately consistent in the sense that the domain interface conditions should be also available as a part of the solution in a fully coupled dynamic analysis of the fan and core engine flow fields. The latter treatment requires quite a heavy CPU burden, so that a transient thermo-cycle model was presently adopted to yield the proper temporal values of the thermo dynamic parameters at the interfaces. Since the turbo-ram mode transition is scheduled during a time interval of several tens of seconds, long enough for each control sequence to be well settled down, the present predictions are expected to be satisfactory for such engine operation.

2. Turbo-Ram Mode Transition

Variable Engine Geometry

The general engine layout is shown in Figure 1, wherein 6 variable geometry positions are indicated. MSV is the key valve designed to close at turbo mode, opening gradually to allow the air into the ram inlet duct. The exhaust nozzle needs to be adjusted for supersonic capability of convergent divergent geometry. (Hyper engine introduced two dimensional configuration with mixer-ejector noise reduction device.) RVABI are used to control the fan bypass air and pressure ratio for optimizing the balance of total pressure between bypass stream and core stream at the rear mixing zone, whilst FVABI is used for adjusting the static pressure balance between the ram air and fan bypass air when

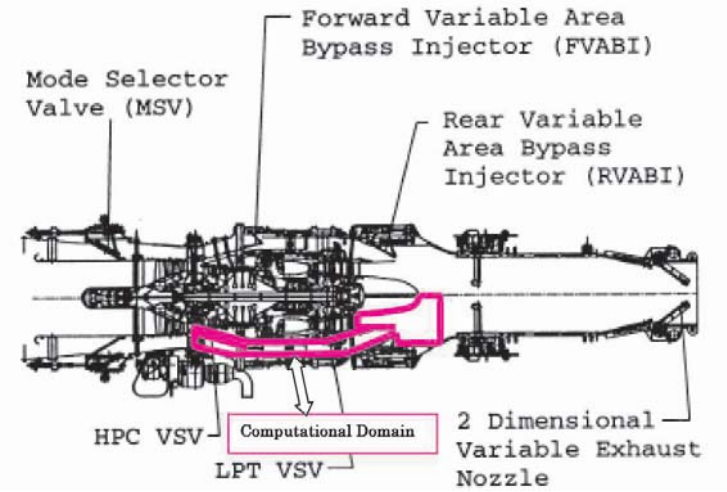

Figure 1. HYPR Combined Cycle Engine

MSV is being opened. LPT and HPC VSVs are for work split between HP and LP turbine rotor, and for surge margin of HP compressor stage, respectively.

Transient Engine Thermo-cycle Simulation

In the present transient simulation, there are two dynamic factors incorporated into the conventional fan engine cycle analysis, that are, 1) volumes placed at the end of each engine component (See Fig. 2), and 2) the inertia of the rotor elements, wherein the power balance between turbine and compressor yields the following rotor dynamic response relation:

$$W_T \times H_T = W_C \times H_C + I_P \times \Omega \frac{d\Omega}{dt}$$

where, W_T and W_C are mass flow rates through turbine and compressor, H_T and H_C are total enthalpy changes in turbine and compressor, I_P is the moment of the rotor inertia and Ω is the angular acceleration. A thorough investigation with experimentally proven data was carried out to obtain detailed off-design performance for the turbo components, such like fan, HPC, HPT and LPT, including the effects of LPT VSV and RVABI operation, which altogether confirmed the capability to simulate total engine system thermo-cycle parameters during the transition from turbo to ram mode operation at the corresponding flight Mach condition.

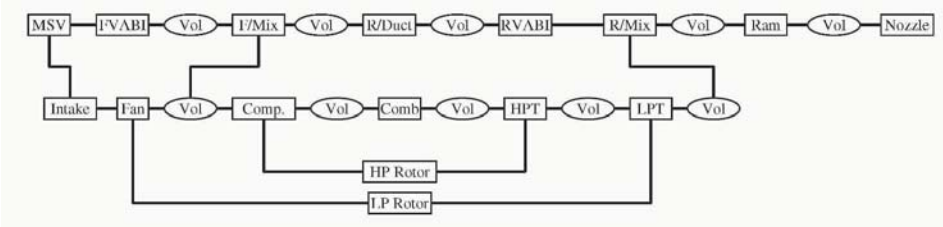

Figure 2. Block Chart for Transient CCE Engine Simulation Model

Control Sequences

In order to achieve smooth mode transition, the following measures were employed:

1 Turbo mode at Mach 3.

2 Exhaust nozzle pre-opened to prevent fan stall due to ignition spike of ram combustor.

3 Ram combustor set burning.

4 FVABI narrowed to accelerate fan bypass air jet to reduce the exit static pressure.

5 MSV opened to match FVABI control, allowing air flow into the ram inlet duct.

6 Increase ram rating and decrease turbo rating down to idle, maintaining constant engine thrust and air flow rate.

The corresponding control sequences are described in Figure 3, in which variable geometry parts are schematically illustrated to be operable, as well as the scheduled development of control parameters is marked by vertical lines with respect to time, such as turbo and ram fuels and relative openings of exhaust nozzle, MSV, FVABI and RVABI. Cases 1-5 indicate five representative instances at which CFD simulation is presently carried out to investigate the flow pattern changes according to this control sequence. (CASE1: Turbo mode, CASE2: Ram combustion chamber ignition, CASE3: FVABI narrowed, CASE4: MSV open, CASE5: Shift to ram mode) The corresponding opening area settings for MSV, FVABI and RVABI are detailed in Table 1.

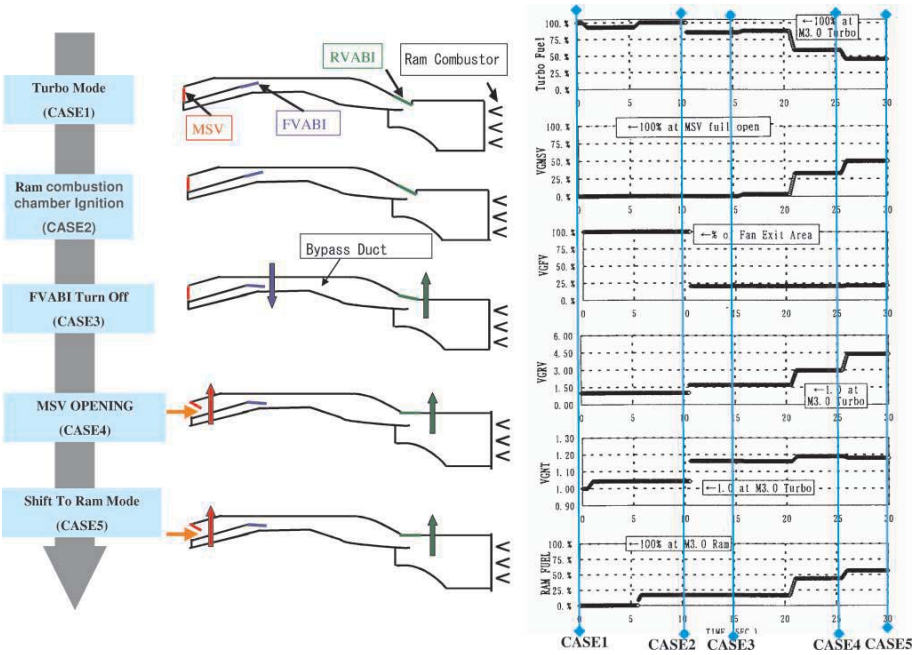

Figure 3. Mode Transition and Move of Variable valve

Table 1. Opening Area Settings of MSV and F/RVABIs

	MSV	FVABI	RVABI
CASE 1	0	0.3211	0.0913
CASE 2	0	0.3211	0.0913
CASE 3	0	0.0908	0.174
CASE 4	0.1125	0.0908	0.263
CASE 5	0.1807	0.0908	0.3979

3. Flow Pattern Simulation

Computational Model

Figure 4 shows schematically the computational region involving the variable geometry parts of the ram inlet/bypass duct and the rear mixing region leading to the ram combustor. The corresponding grids are also illustrated, in which the axisymmetric cylindrical coordinate system was employed.

The numerical scheme is based on LU-ADI approximate factorization TVD finite difference formulation of 2D axisymmetric Navier-Stokes equations for compressible fluids. No turbulence model was presently incorporated.

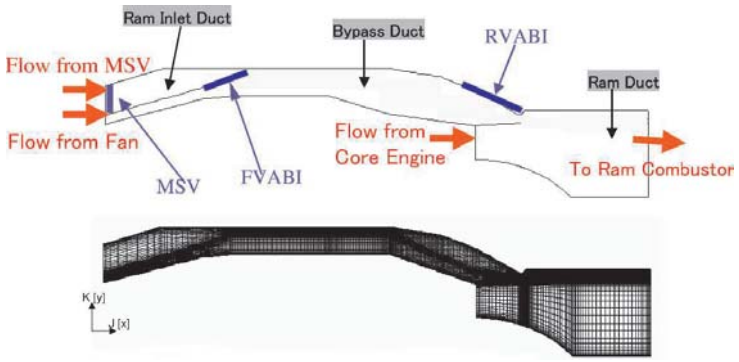

Figure 4. Computational Region and Grids (CASE 1)

Boundary Conditions

As shown in Figure 4, the inlet boundary consists of several interface planes representing MSV exit, the fan outlet towards FVABI and the core engine exhaust, respectively, whilst the outlet boundary is the plane facing to the ram combustor downstream. The rest is solid and viscous sidewall surfaces of the ram inlet/bypass duct and the rear mixing region. The total pressure and temperature at each of the inlet planes, as well as the static pressure at the outlet boundary were determined from the transient engine thermo-cycle simulation results. Table 2 gives a list of those parameter values corresponding to CASEs 1-5 for the present flow pattern visualization.

Results

Figure 5 is a summary result of the flow pattern simulation, which shows the iso-contours of Mach number (left) and static pressure (right) in the computational domain.

Table 2. Thermo-cycle Parameters at Inlet and Outlet Boundary

	Core Exhaust	Fan Exit	MSV Exit	Outlet
Inlet flow angle for all cases	0	15	15	

	Core Exhaust		Fan Exit		MSV Exit		Outlet
	T_{total}	P_{total}	T_{total}	P_{total}	T_{total}	P_{total}	P_{static}
Case 1 (Turbo Mode)	1270.4	149.4	668.0	192.7	603.8	147.4	151.9
Case 2 (Ram burner set)	1311.4	157.3	669.6	194.9	603.8	147.4	158.6
Case 3 (FVABI narrowed)	1228.6	142.5	667.5	195.9	603.8	147.4	139.3
Case 4 (Dual mode $\alpha = 0.717$)	1237.6	141.0	636.5	170.2	603.8	147.4	138.5
Case 5 (Dual mode $\alpha = 0.570$)	1266.4	141.5	621.9	159.0	603.8	147.4	138.9

CASE1: During the turbo mode, MSV is firmly closed, and CCE is working just as a turbo fan engine. In this status the opening area of FVABI is large and the cross-sectional stream area of fan exit flow is continued to increase in the bypass duct following FVABI, with the result of static pressure rise due to flow diffusion. It becomes necessary, therefore, that the opening area of RVABI be kept small to accelerate the bypass duct flow to reduce its static pressure for a balance with that of the core flow meeting at the rear mixing region. It causes a particularly large velocity gradient in the radial direction, leading to non-uniformity at the ram combustor interface.

CASE2: When the ram combustor is ignited, it is predicted by the engine thermo-cycle performance analysis that the static pressure in the ram combustor becomes raised a little bit, wherefrom transmitted to the upstream steadily. Presently, no such instantaneous pressure sign can be expected traceable, but the pressure level in the bypass duct showed slight elevation. It must be rather pointed out that there is very little difference in the flow patterns between CASE1 and CASE2, which indicates continued flow pattern stability against the ram combustor ignition without giving a fatal damage to the engine operation.

CASE3: To open MSV for transition into the ram combustion mode, the static pressure in the bypass duct should be decreased in order to prevent the recirculation phenomenon. The latter is explained that the fan exit flow through FVABI be reversed upstream as MSV is opened. To avoid such a dangerous phenomenon, a precaution is taken to reduce the opening area of FVABI and to increase that of RVABI. The latter operation is necessary for the pressure balance between the bypass duct and the core engine exhaust. The static pressure at FVABI exit becomes lower enough than the total pressure in front of MSV inlet, now ready to open MSV. It is thus important that the static pressure balance in the ram inlet duct be carefully checked at any time during the mode transition. CFD results yielded rather unsatisfactory flow pattern in the bypass

duct that the main stream is seen to separate from the hub wall in the region near RVABI inlet to form a backflow in the bypass duct. As a result, two big vortexes are observed to indicate large flow inefficiency. Several reasons for the latter might be explained, for instance, that the back pressure of the RVABI is fixed according to the flight altitude, nozzle area ratio and ram combustion status, and that the downstream of the FVABI tends to be little diffused in the bypass duct just because of the narrowed opening area of FVABI. It is apparent that the predicted fan exit flow area be much less than the actual one, so it has to be rapidly diffused into the whole duct in conformity with the higher back pressure at RVABI, leading to a back flow in the rear part. There seemed to be another reason that the slope of the hub wall near RVABI is steep, which can cause the flow separation. Since no turbulence model was introduced in the present CFD calculation, no further discussions may be available, but it became clear that there is unfavorable tendency of flow separation in the bypass duct due to a lack of flow diffusion.

CASEs4-5: MSV is gradually opened, so air is introduced into the ram inlet duct. In CASE4 (MSV opening area is small), there appears also a separation like in CASE3, however, in CASE5 (MSV opening area is large), there is no disturbance near RVABI and the flow becomes very smooth. That means the introduction of a flow in the shroud wall region yields favourable flow diffusion in the whole bypass duct, whence it may be concluded that the flow instability in the bypass duct is influenced much due to the degree of flow diffusion.

To sum up, all the five cases representing control sequences during mode transition showed no sign of recirculation or flow reversal towards MSV in the ram inlet duct, indicating a possible stable transition assignment according to the present variable geometry control procedure. The bypass air jet is seen to be more diffused in the ram air duct as MSV becomes open wider, yielding better and clean flow pattern downstream. In this way, the present CFD simulation method will provide a very helpful tool to predict the effects of variable geometry control upon CCE flow patterns.

4. Recirculation Margin and Engine Performance

Inlet Recirculation

In order to prevent recirculation, it was shown that FVABI control is necessary to accelerate the fan flow to reduce the static pressure, thereupon, there was no sign of flow reversal towards MSV, as it is gradually opened. To estimate how the opening area of the F/R-VABI affects the flow pattern, especially recirculation, CFD calculation was employed to simulate such a condition that the opening areas of F/R-VABI are the same as those in CASE1, whilst the inlet and outlet thermo-cycle parameters are the same as those in CASE5. The

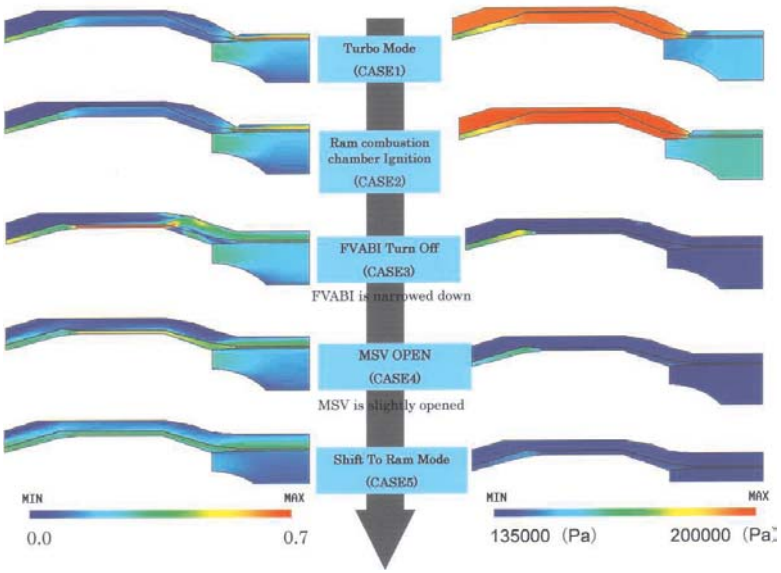

Figure 5. Mach number (Left) and static pressure (Right) contours

flow pattern thus obtained is shown in the upper part of Figure 6. It is apparent that the recirculation does occur unless FBAVI is narrowed. The fan bypass air pressure becomes much higher than the total pressure of the air at MSV inlet. If the static pressure in the bypass duct be not reduced to yield negative gradient along the ram inlet duct, there occurs a back flow towards MSV as it opens gradually, therefore, the present control sequence is necessary.

Rear Flow Separation

CFD calculation also showed a tendency that the largest flow disturbance occurs in the procedure associated with slight opening of MSV, in which the fan bypass jet remains not much diffused till rapidly matching the rear pressure near RBAVI. The flow separation at the hub wall must be also influenced by the wall shape, in particular, its slope towards downstream. Figure 7 compares the flow patterns corresponding to CASE3 when the hub wall slope was modified to become flattened. There is still a vortex structure in the center part, but the separation at the hub wall disappeared remarkably. Examining various cases for the static pressure distributions along the bypass duct axis, it was revealed that rather smooth tendency is obtainable for most of the cases, except CASE3 with the original hub wall slope. It seems CASE3 (FVABI narrowed) is rather

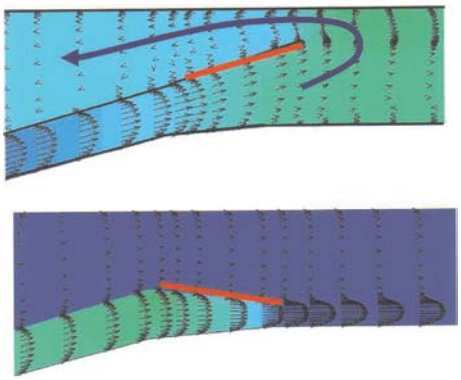

Figure 6. Velocity contours at CASE3 (upper: FVABI kept wide, lower: FVABI narrowed.)

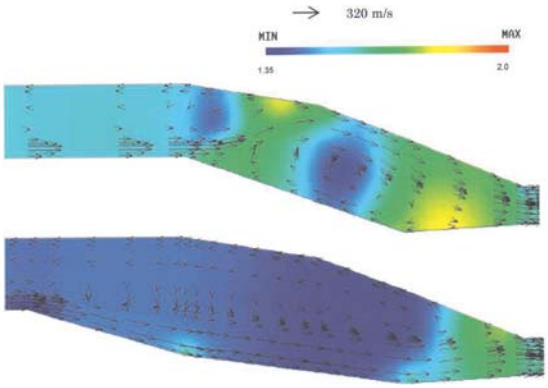

Figure 7. Flow pattern at CASE3. (upper: Original Hub, lower: Modified)

peculiar, that all the influencing factors bring about a coupled effect upon the resulting flow pattern, so that more careful study is required.

Mass Flow Rate and Net Thrust

To achieve smooth mode transition, it is vital for CCE system to maintain the cruise conditions of air flow rate and propulsive thrust. The aforementioned control sequence has been so far discussed from the point of view of flow patterns relating to variable geometry manipulation, whereas it is also necessary to check the latter consequence against the thermo-cycle estimation with respect to total air flow rate and thrust. Concerning the air flow rate, it is obvious

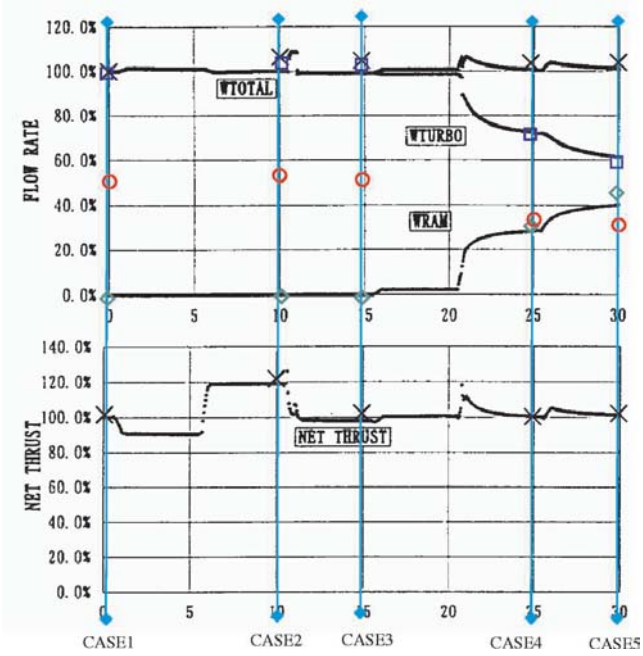

Figure 8. Mass Flow Rates and Net Thrust during Mode Transition

that, as MSV opening area becomes larger, the core engine air flow rate should be reduced to keep the constant total air flow rate. In order to evaluate the net thrust, however, further assumptions are needed to handle the flow conditions in ram combustor and exhaust nozzle. A simplest 1D flow analysis was presently adopted, wherein the ram fuel control sequence was referred to the thermo-cycle simulation and the nozzle was assumed to behave just like an ideal one, with fully matched expansion of the perfectly burned fuel and air mixture.

The results of calculation for CASEs 1-5 are thus plotted in Figure 8, in which the corresponding curves from the thermo-cycle simulation are shown altogether. The upper part of Figure 8 shows the air flow rates (total $-\times-$, turbo(fan) $-\square-$, core $-\circ-$, and ram$-\diamond-$, respectively). As ram rating is increased, turbo and core flow rates decrease accordingly, so that the total air flow rate is almost kept constant. The lower part of Figure 8 shows the net thrust, in which slightly larger values, due to idealized 1-D nozzle flow modeling, were plotted against the thermo-cycle prediction curve. CFD calculation results were thus found to give surprisingly good agreement with the thermo-cycle simulation results.

5. Conclusions

Turbo-ram combined cycle engine employs several variable geometries to ensure smooth transition from turbo to ram or reverse mode operation. A control sequence for those variable parameters was established based upon transient engine thermo-cycle simulation, so that the corresponding flow patterns were examined by CFD visualization within the fan bypass and ram inlet duct, and the rear mixing region.

According to the present control sequence, a smooth mode transition seems feasible, since there appeared neither recirculation nor disruptive difficulty in the flow pattern changes from the aerodynamic point of view. Nevertheless, careful investigation is further needed for fan bypass jet mixing at a particular instance when the ram air starts to be introduced. It may be also mentioned that there appears strong shear in the radial direction due to presence of the core engine and bypass duct flows, which must be negotiated in the ram combustor.

The total air flow rate and net thrust of the engine showed a surprisingly good agreement between the engine thermo-cycle simulation and CFD model calculation. Since it is very much difficult to perform experiments of CCE as a complete engine system, the present approach of integrating CFD numerical simulation may be advantageously used to figure out the system feasibility during the mode transition. Further improvement to achieve fully unsteady treatment at several component interfaces is definitely needed in future.

References

Miyagi, H., Miyagawa, H. et al (1995a). Combined cycle engine reserch in japanese hypr project. AIAA Paper 95-2751.

Miyagi, H., Miyagawa, H. et al (1995b). Research and development status of combined cycle engine demonstrator. In *Proceedings of Second International Symposium on Japanese National Project for Super-Hypersonic Transport Propulsion System*, pages 237–244.

Takeo, M., Yasushi, N. et al (1999). Research and development of combined cycle engine demonstrator. In *Proceedings of Third International Symposium on Japanese National Project for Super-Hypersonic Transport Propulsion System*, pages 229–236.

EXPERIMENTAL INVESTIGATION OF WAKE-INDUCED TRANSITION IN A HIGHLY LOADED LINEAR COMPRESSOR CASCADE

Lothar Hilgenfeld and Michael Pfitzner
Institut fuer Strahlantriebe, Universitaet der Bundeswehr Muenchen
Werner-Heisenberg-Weg 39, 85579 Neubiberg, Germany
Lothar.Hilgenfeld@unibw-muenchen.de

Abstract The effects of wake passing on boundary layer transition in a highly loaded linear compressor cascade were investigated using different measurement techniques, such as fast-response Kulite sensors, hot-film array and hot-wire measurements. The experiments were performed in a high speed cascade wind tunnel with an inlet Mach number of 0.67 and Reynolds number 450000. Cylindrical bars moving parallel to the cascade inlet plane simulate the wakes of an upstream blade row. These basic investigations of unsteady transition also contribute to a database for numerical code validation at Mach and Reynolds numbers representative for real turbomachinery conditions.

Keywords: unsteady compressor flow, wake passing, boundary layer transition

1. Introduction

The periodic disturbances caused by wake shedding of upstream blade rows and their downstream migration are a major source of unsteadiness in turbomachines. This inherently unsteady flow plays a significant role in the loss generation process of axial turbomachinery blades. The boundary layer transition on the profile from laminar to turbulent is the main source of loss generation and significantly affected by the unsteady behavior of the flow.

An overview of the fundamental transition modes relevant in turbomachines was given by Mayle (1991), who pointed out that the free stream turbulence, the pressure gradient and the strength of the wake are the major parameters in the multimode transition process dominated by wake-passing effects. An increase in wake passing frequency results in a higher freestream turbulence level (Schobeiri et al. 1995). Over the past years many experimental investigations of the boundary layer in turbomachines were performed. Detailed basic

K.C. Hall et al. (eds.),
Unsteady Aerodynamics, Aeroacoustics and Aeroelasticity of Turbomachines, 357–368.

research work on the boundary layer development on compressor blades were carried out by Halstead et al. (1997) and Walker et al. (1999). They reveal the fundamental effects regarding to wake passing like early onset of transition in the wake-induced path, suppression of a laminar separation bubble and the existence of a calmed region. The calmed region partially suppress laminar separation due to its higher shear stress level and delays the onset of transition in regions where under steady inflow conditions the flow is fully turbulent.

Most of the boundary layer investigations were conducted in low speed wind tunnel flows or low speed research compressors (e.g. Mailach and Vogeler 2003). Only few investigations are available for compressible, high-speed compressor flow, see for example Teusch et al. (2000).

Considering these unsteady effects in current aerodynamic design methods, reliable transition and turbulence models in unsteady CFD codes are necessary, which consider the effects of wake passing. Nevertheless numerical code validation has still to be performed based on experimental test cases. Hence, one objective of the present investigation is to provide a detailed unsteady database for numerical code validation. The present work contributes to this objective as part of a joint research effort on unsteady flows in turbomachines. An overview of the complete project and its scope is given by Hourmouziadis (2000). For this reason experimental investigations focusing on wake-induced transition have been performed in a highly loaded linear compressor cascade at Mach and Reynolds numbers representative for real turbomachinery conditions.

2. Experimental setup

2.1 Compressor cascade

The measurements were performed on a large-scale compressor cascade called V103-220 consisting of three NACA 65 blades, which represent the mid-span of the hub section of a stator blade in a highly loaded axial compressor. Only the center blade is used for the measurements. To achieve a higher resolution of the boundary layer effects, a blade chord length of l = 220 mm was chosen. The design conditions with an inlet Mach number of $Ma_1 = 0.67$, a Reynolds number based on the blade chord length of $Re_1 = 450000$ and an inlet flow angle of $\beta_1 = 132^\circ$ lead to a fully subsonic cascade flow. The geometrical data of the cascade as well as the definitions of distances are displayed in Fig 1.

2.2 The wake generator

The periodically unsteady flow caused by the relative motion of rotor and stator rows and its influence on the compressor cascade is simulated by a moving bar type wake generator with a bar diameter of $d_{bar} = 2$ mm. This so-called

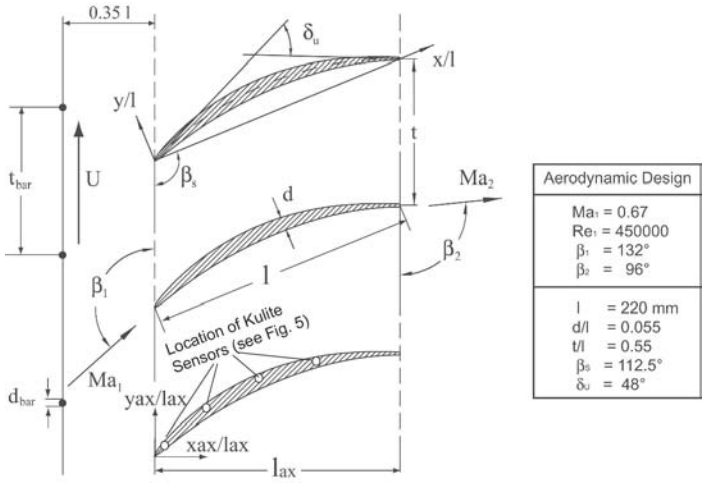

Figure 1. Compressor Cascade V103-220

EIZ (Erzeuger Instationaerer Zustroemung, see Fig. 2) and its constructional principles are explained by Acton and Fottner (1996) in more detail. The cylindrical steel bars create a far wake very similar to the one produced by an actual airfoil (Pfeil and Eifler 1976). Preliminary tests showed that the wakes shed by bars of 2 mm diameter are representative for the wakes of the V103 profile geometry regarding the wake width. The distance ratio between the bars and the cascade inlet plane is about x/l = 0.35 (see Fig. 1). Two different bar pitches of 40 mm and 120 mm were used. The belt mechanism drives the bars with speeds of up to 40 m/s. However, the maximum bar speed for the present investigation is 20 m/s, thus generating Strouhal numbers between 0.22 and 0.66 for the investigated test cases.

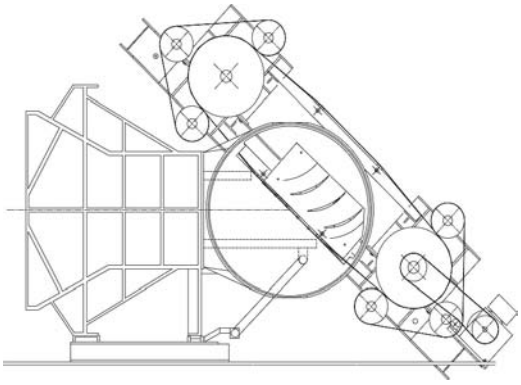

Figure 2. Wake generator (EIZ) with installed compressor cascade

It should be noted that the maximum bar speed together with the axial velocities is still too slow to produce a Strouhal number and inlet velocity triangle representative for modern compressors. The wakes enters the cascade passage almost parallel to the blades. Therefore the data acquired with this setup cannot be transferred directly to real turbomachines. The measurements should be considered as basic investigations of the unsteady multimode transition process. As the main purpose of the present experimental investigations is to obtain a deeper unterstanding of the flow phenomena and to provide a sound database for the validation of unsteady numerical flow solvers and particular transition models, the angle of the incoming wake is of minor importance.

2.3 Test facility

The experiments were carried out in the High Speed Cascade Wind Tunnel of the University of the Federal Armed Forces Munich, which is an open-loop test facility located inside an evacuable pressure tank (Fig. 3). Mach and Reynolds number in the test section can be varied independently by lowering the pressure level inside the tank and keeping the total temperature constant by means of an extensive cooling set-up, therefore allowing to simulate real turbomachinery conditions (Sturm & Fottner 1985). All test were performed with a constant total temperature of 303 K. The turbulence intensity of the inlet flow is adjusted by fitting a turbulence grid upstream of the nozzle.

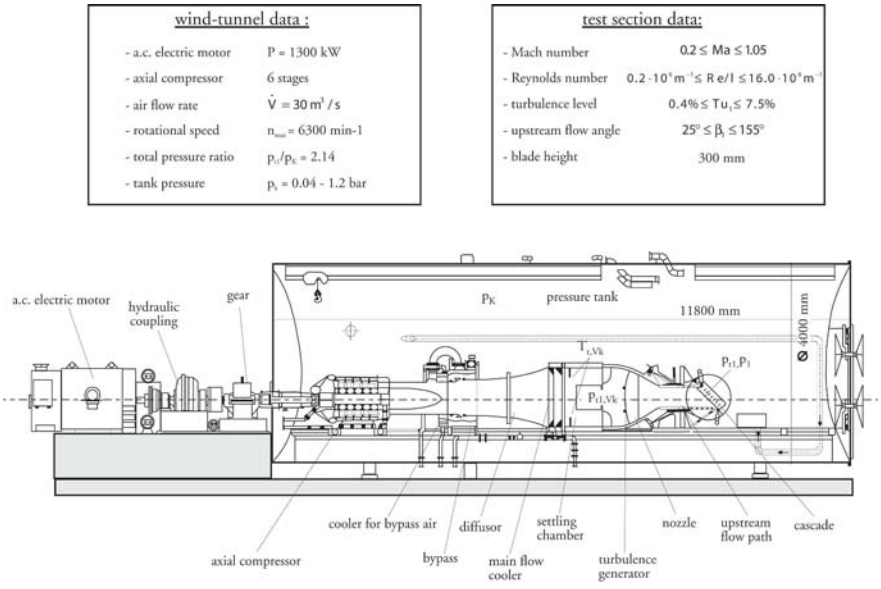

Figure 3. High Speed Cascade Wind Tunnel

2.4 Measuring techniques

The experimental data acquired provides time-averaged as well as time-resolved information regarding the boundary layer development on the suction side of a compressor blade. The time-averaged loading of the compressor cascade was measured by means of conventional static pressure tappings on both the suction and the pressure side at mid-span connected to a Scanivalve system. These pneumatic data were recorded via computer control and represent mean values. The time-resolved compressor profile loading was determined using 10 Kulite fast-response absolute pressure sensors embedded into the suction side of the center blade. For each Kulite sensor a static calibration in the range of 50 to 350 hPa has been performed inside the pressure tank prior to the measurements.

To document the unsteady inflbw conditions, 3D hot-wire measurements were performed in the cascade inlet plane. The probe employed in the present investigation consists of three sensing tungsten wires of 5 μm diameter with a measuring volume of approximately 1 mm in diameter. The relative error of the hot-wire velocity is estimated to be less than 5%; the absolute angle deviation is less than 1°. To measure the qualitative distribution of unsteadiness and the quasi wall shear stress on the suction side, surface mounted hot-film sensors are used. The entire length of the suction surface is covered with an array of 36 gauges at midspan with their spacing varying between 2.5 and 5 mm. The sensors consist of a 0.4 mm thin nickel film applied by vapor deposition process onto a polyamide substrate. They were operated by a constant-temperature anemometer system in sets of 12 sensors and logged simultaneously at a sampling frequency of 50 kHz.

As shown e.g. by Hodson (1994), the boundary layer characteristics can be derived directly from the anemometer output and do not necessarily require an extensive calibration procedure. The quasi-wall shear stress QWSS is determined by the output voltage E and the output voltage under zero flbw conditions E_0, which is measured subsequent to the unsteady measurements, according to Eq. (1)

$$\text{QWSS} = \text{constant} \cdot \tau_w{}^{\frac{1}{3}} = \frac{E^2 - E_0^2}{E_0^2} \tag{1}$$

The wake passing effects were studied for 5 wakes produced by 5 identical bars, which could be ensured due to a once-per-revolution trigger mechanism. Processing of the raw hot-wire and hot-film measurement data for the unsteady case was done using the PLEAT technique (**P**hase **L**ocked **E**nsemble **A**veraging **T**echnique, Lakshminarayana et al., 1974) in order to separate random and periodic signals. The time-dependent signal b is composed of a periodic component $\tilde{b}$ and the turbulent component b' according to Eq. (2)

$$b = \tilde{b} + b'$$
$$\tilde{b}(t) = \frac{1}{N} \cdot \sum_{i=1}^{N} b_i(t) \tag{2}$$

In case of the hot-film sensor measurements, a total of N = 300 ensembles was logged and evaluated for quasi-wall shear stress (see Eq. 1), random unsteadiness RMS (Eq. 3) and skewness (Eq. 4), where the variable b(t) represents the anemometer output voltage. To be able to compare the hot film sensors, the resulting values were normalized with the anemometer voltage at zero flow, thereby eliminating the influence of manufacturing differences between the gauges.

$$\text{RMS}(t) = \sqrt{\frac{1}{N} \sum_{i=1}^{N} \left(b_i(t) - \tilde{b}(t) \right)^2} \tag{3}$$

$$\text{Skewness}(t) = \frac{\frac{1}{N} \sum_{i=1}^{N} \left(b_i(t) - \tilde{b}(t) \right)^3}{\left(\frac{1}{N} \sum_{i=1}^{N} \left(b_i(t) - \tilde{b}(t) \right)^2 \right)^{3/2}} \tag{4}$$

3. Results

All measurements in the present investigation were performed at the design conditions with an inlet Mach number of Ma_1 = 0.67 and an inlet Reynolds number of Re_1 = 450.000. To get an impression of the cascade flow, the mean blade loading in terms of the isentropic profile Mach number distribution is plotted in Fig. 4. Both steady and unsteady inflow conditions, measured with conventional static pressure tappings technique and fast-response Kulite sensors, are shown. The unsteady runs are performed at a bar pitch of t_{bar} = 40 mm and t_{bar} = 120 mm at bar speeds of u_{bar} = 20 m/s, resulting in Strouhal numbers of Sr_1 = 0.66 and Sr_1 = 0.22 based on axial inlet velocity.

The differences compared to the steady inflow case are due to a reduced time-mean inflow velocity. The velocity deficit in the wake lowers the mean value resulting in lower velocities on the blade surface. This is more obvious for the small bar pitch of t_{bar} = 40 mm, where additionally a further change in inlet flow angle compared to the steady case occurs. The mean Kulite data (filled symbols) show an excellent agreement with the values obtained from the static pressure tappings.

At unsteady inlet flow conditions, the separation bubble on the suction side starting at about x_{ax}/l_{ax} = 0.40, is somewhat reduced compared to the steady case, but still existent.

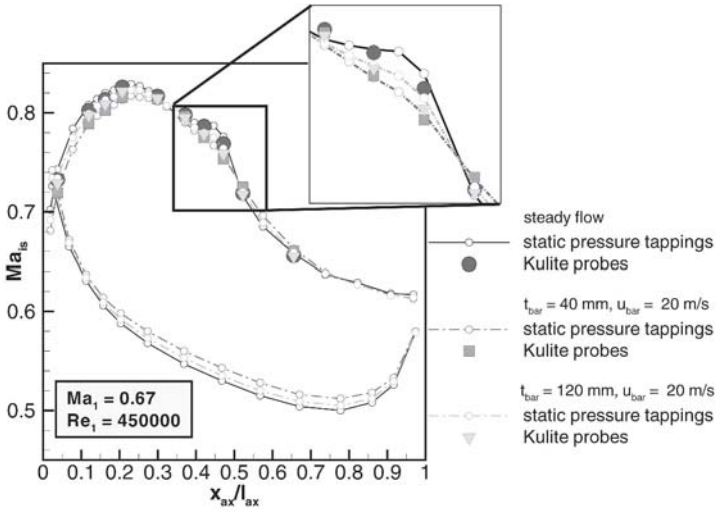

Figure 4. Isentropic profile Mach number distribution

The ensemble-averaged time traces of the unsteady pressure fluctuations are displayed in Fig. 5. For clarity reasons, only four axial chord positions on the suction side are shown for each bar pitch. The loactions of these four Kulite-Sensors are shown in Fig. 1.

In case of the bar pitch 40 mm, the first sensors located in the acceleration part of the suction side register only small pressure peaks due to incoming wakes, while with increasing streamwise distance, the amplitude of the wave-like fluctuations raises. There is also a slight phase shift in the Kulite signals detectable. The ensemble-averaged pressure fluctuations for the high bar pitch 120 mm indeed show strong variations in time and amplitude starting right from the start. Therefore the wake passing leads to a periodically change of the blade loading. Sensor seven, which is located at the beginning of the separation bubble, displays a distinct maximum in pressure fluctuations and a saw tooth distribution. The pressure signals of the last Kulite sensor, located at x_{ax}/l_{ax} = 65.5% in the turbulent part of the boundary layer, show several peaks during one wake passing period.

To provide a comprehensive unsteady data set for numerical modeling of wake passing, the inflow conditions for the cascade have to be investigated in detail. Triple hot wire measurements were taken up-stream of the cascade inlet at about x_{ax}/l_{ax} = -0.16. Results for both bar pitches are shown in Fig. 6, where the normalized inflow velocity, the turbulence level Tu and the inflow angle β_1 are plotted for four bar passing periods t/T. The velocity deficit in the wake reaches about 12% of the inflow velocity. In case of the low bar pitch,

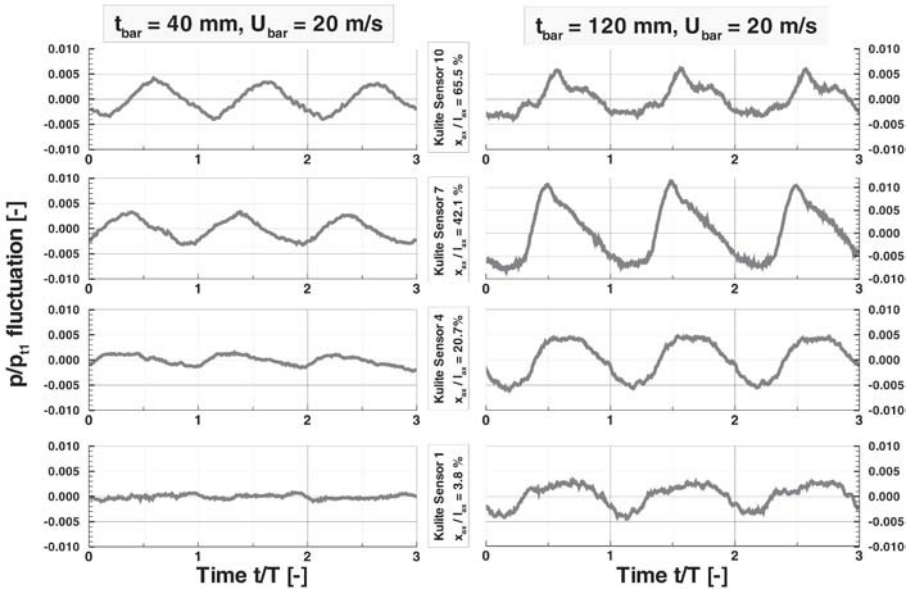

Figure 5. Ensemble-averaged time traces of pressure fluctuations

the turbulence level rises from about 6% background level to 9.5 % in the bar wake. The distribution correlates with the velocity during the wake passing period. Compared to steady inflow conditions with a freestream turbulence intensity of 3.5%, the overall turbulence intensity in the unsteady case (bar pitch = 40 mm) is substantially larger. The turbulence level in case of the high bar pitch of 120 mm rises from about 4% to 9.5% in the bar wake, but in contrast to the case with low bar pitch, the turbulence intensity decreases very slowly to a value comparable with steady inflow conditions. As the flow velocity is nearly constant during most part of the wake passing period, the turbulence level decrease must be caused by the decay of turbulence. Due to the high bar pitch, the absolute time between two bar wakes is large enough for a decay process until the next wake arrives. This could also explain the high background level in case of the lower bar pitch 40 mm, because the following wake arrives before the turbulence is completely decayed. The reduction in flow velocity also affects the velocity triangle and results in a periodic increase of the inflow angle of about $\Delta\beta = 2^{\circ}$ during every wake passing. The wake width can be easily extracted from the figures.

The results of the hot-film measurements in terms of space-time diagrams of ensemble averaged normalized RMS values and ensemble averaged quasi wall shear stress (QWSS) are shown in Figure 7 a-d. The data is mapped only qualitatively, where dark regions indicate maximum and light areas minimum

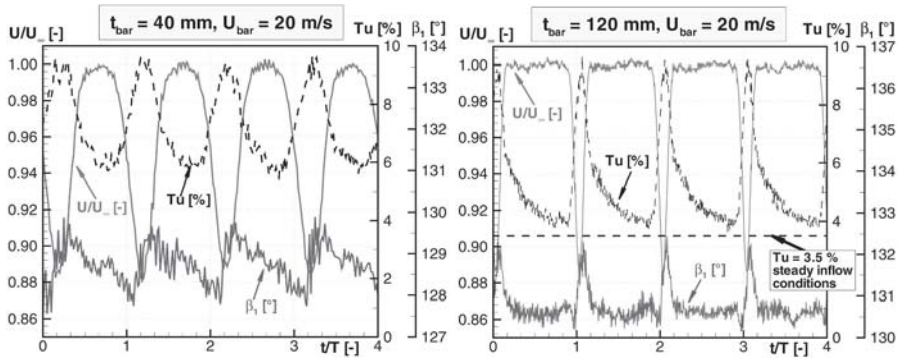

Figure 6. Unsteady inflow conditions (ensemble averaged)

values. To identify the movement of the transition point, the dash-dotted white lines in the RMS diagrams, representing zero skewness, are used. The transition point under steady inflow conditions is shown as a dotted vertical line. To illustrate the wake-induced transition process, different regions representative for various boundary layer states are marked in the figures similar to Halstead et al. (1997).

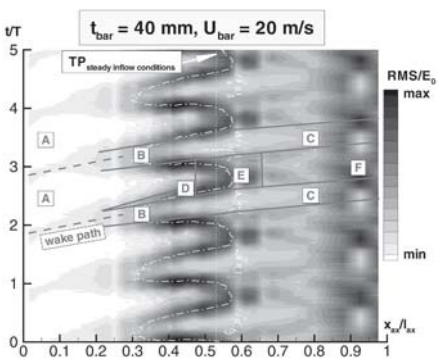

Figure 7a. Ensemble averaged RMS voltage, t_{bar} = 40 mm

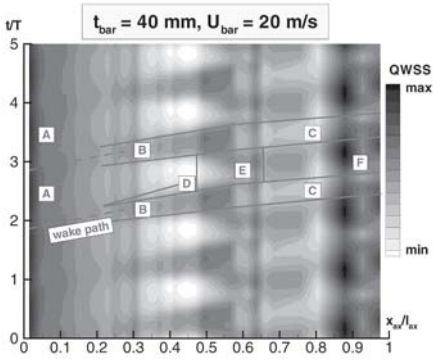

Figure 7b. Quasi wall shear stress, t_{bar} = 40 mm

The flow development takes place along a wake-induced path and a path between two wakes. Following the wake path, a wake-induced transitional flow regime (B) emerges, where early transition is forced as can be seen in the RMS values and the white zero skewness line (Fig. 7 a, b). The migration of the transition point covers about 25% of the surface length. The path between two wakes remains still laminar (A). The transitional region (B) is followed in

time by a stable calmed region (D) with decreasing RMS values. The calmed region is able to delay the onset of transition in the path between two wakes (E). The transition point moves periodically downstream in the region influenced by calming effects (D) as compared with steady inflow conditions. The regions (C) and (F) are turbulent up to the trailing edge, but the boundary layer properties significantly in time.

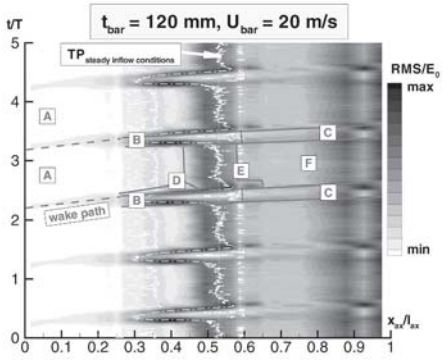

Figure 7c. Ensemble averaged RMS voltage, t_{bar} = 120 mm

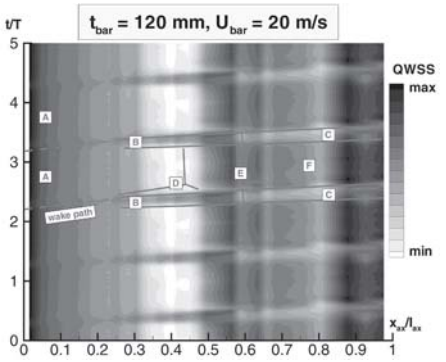

Figure 7d. Quasi wall shear stress, t_{bar} = 120 mm

The RMS plots reveal, that the wake-induced transitional region (B) exhibits a double peak of high RMS values, which might be caused by shedded vortices in the wake. The wake vortices seem to be not mixed out as they enter the cascade inlet plane, although the inlet turbulence distribution in the wake region (Fig. 6) does not clearly show any double peaks indicating vortex shedding. However, the wake width in the RMS diagrams corresponds to the results of the triple hot wire measurements displayed in Fig. 6. In the investigations of Teusch et al. (1999) one can also find double peaks in the RMS distribution for the high Reynolds number test case. The space-time diagram of quasi wall shear stress on the suction side surface allows identifying the location and extent of the laminar separation bubble characterized by minimum values in the QWSS distribution. Every wake passing, the transitional flow regime (B) prevents the formation of a separation bubble and transition takes place via bypass mode. The laminar separation is also suppressed by the calmed region (D). In case of the high bar pitch 120 mm, a region of undisturbed transition via laminar separation bubble exists between two wakes. As the bar pitch is reduced to 40 mm, this undisturbed region almost disappears. The separation bubble is getting smaller and still exists. The location of the transition point is shifted somewhat downstream in case of the low bar pitch.

4. Conclusions

Detailed experimental investigations focusing on wake-induced transition were performed in a highly loaded linear compressor cascade using different measurement techniques. Cylindrical bars moving parallel to the cascade inlet plane simulate the periodically unsteady flow caused by the relative motion of rotor and stator rows. The experiments were carried out at the design conditions of the compressor cascade using two different bar pitches of the wake generator.

In case of the high bar pitch of 120 mm, the passing wakes lead to a periodically change of the blade loading, which is accompanied by large pressure fluctuations with high amplitudes. The reduction in flow velocity also affects the velocity triangle and results in a periodic increase of the inflow angle of about $\Delta\beta = 2^{\circ}$ during every wake passing. The background turbulence level in case of the low bar pitch is significant larger compared to the higher bar pitch case, but the maximum turbulence value is uneffected by variation of the bar pitch.

For both bar pitches, the separation bubble is periodically reduced, but still existent. The migration of the transition point covers about 25% of the surface length. The RMS values in the wake-induced transitional region exhibit a double peak. This might be caused by shedded vortices in the wake, which are not mixed out as they enter the blade passage.

The measurements are intended as a contribution to the validation process of unsteady codes.

Acknowledgments

The authors wish to acknowledge the support of the Deutsche Forschungs Gemeinschaft (DFG) for the research program partly reported in this paper.

References

Acton, P. and Fottner, L. (1996). *The generation of instationary flow conditions in the high-speed cascade wind tunnel*. 13th Symposium on Measuring Techniques in Transonic and Supersonic Flow in Cascades and Turbomachines.

Halstead, D.E., Wisler, D.C., Okiishi, T.H., Walker, G.J., Hodson, H.P., Shin, H.W. (1997). *Boundary layer development in axial compressors and turbines: Part 1-4*. ASME Journal of Turbomachinery, Vol. 119, Part 1, pp. 114-127, Part 2, pp. 426-444, Part 3, pp. 225-237, Part 4, pp. 128-139.

Hodson, H.P., Huntsman, I., Steele, A.B. (1994). *An Investigation of Boundary Layer Development in a Multistage LP Turbine*. Journal of Turbomachinery, Vol. 116, pp. 375-383

Hourmouziadis, J. (2000).*Das DFG-Verbundvorhaben Periodisch Instationaere Stroemungen in Turbomaschinen.* DGLR Paper JT2000-030

Lakshminarayana, B., Poncet, A. (1974).*A method of measuring three-dimensional rotating wakes behind turbomachines.* J. of Fluids Engineering, Vol. 96, No. 2

Mailach, R., Vogeler, K. (2003).*Aerodynamic Blade Row Interaction in an Axial Compressor, Part I: Unsteady Boundary Layer Developmen.* ASME-GT2003-38765

Mayle, R.E. (1991). *The role of laminar-turbulent transition in gas turbine engines*. ASME Journal of Turbomachinery, Vol. 113, pp. 509-537

Pfeil, H., Eifler, J. (1976).*Turbulenzverhaeltnisse hinter rotierenden Zylindergittern.* Forschung im Ingenieurwesen, Vol. 42, pp. 27-32

Schobeiri, M.T., Read, K., Lewalle, J. (1995). *Effect of unsteady wake passing frequency on boundary layer transition: experimental investigation and wavelet analysis.* ASME Paper 95-GT-437

Sturm, W., Fottner, L. (1985). *The High-Speed Cascade Wind Tunnel of the German Armed Forces University Munich.* 8th Symp. on Meas. Techn. for Transonic and Supersonic Flows in Cascades and Turbomachines, Genoa

Teusch, R., Brunner, S., Fottner, L. (2000). *The Influence of Multimode Transition Initiated by Periodic Wakes on the Profile Loss of a Linear Compressor Cascade.* ASME Paper No. 2000-GT-271

Teusch, R., Swoboda, M., Fottner, L. (1999). *Experimental Investigation of Wake-Induced Transition in a Linear Compressor Cascade with Controlled Diffusion Blading.* ISOABE-Paper IS-7057

Walker, G.J., Hughes, J.D., Solomon, W.J. (1999). *Periodic Transition on an Axial Compressor Stator: Incidence and Clocking Effects: Part I – Experimental Data.* ASME Journal of Turbomachinery, Vol. 121, pp. 398-407.

EXPERIMENTAL OFF-DESIGN INVESTIGATION OF UNSTEADY SECONDARY FLOW PHENOMENA IN A THREE-STAGE AXIAL COMPRESSOR AT 100% NOMINAL SPEED

Andreas Bohne
andreas.bohne@web.de

Reinhard Niehuis
Institute of Jet Propulsion and Turbomachinery
RWTH Aachen University
D-52056 Aachen, Germany
niehuis@ist.rwth-aachen.de

Abstract This paper deals with unsteady measurements in a high-speed three-stage axial compressor with inlet guide vanes (IGV) and controlled diffusion airfoils (CDA) at off-design conditions. The compressor under consideration exhibits design features of real industrial compressors. The main emphasis is put on the experimental investigation of two operating points at 100% nominal speed. The first one represents design conditions whereas the second one is the last stable operating point near the surge margin. Probe traverses, with a high resolution both in space and time, show the significant potential upstream influence of the blades dependent on varying operating conditions. Besides that, the structure of the rotor tip clearance flow changes with further throttling of the compressor. Dynamic pressure transducers on the casing show the appearance of both spiral-type- and bubble-type-vortices as these are described by Furukawa et al. (2000). The convected wakes of the airfoils strongly influence the flow field downstream, and the varying incidence even causes fluctuating flow separations in the blade rows downstream.

Keywords: Axial Compressor, Multistage, Unsteady Flow, Off-Design, Experimental Investigation

K.C. Hall et al. (eds.),
Unsteady Aerodynamics, Aeroacoustics and Aeroelasticity of Turbomachines, 369–380.

Glossary

EA Ensemble Average
IGV Inlet Guide Vane
R1 Rotor of the first stage
R2 Rotor of the center stage
R3 Rotor of the last stage
RMS Root Mean Square
S1 Stator of the first stage
S2 Stator of the center stage
S3 Stator of the last stage
p Static pressure
$\mathrm{p_t}$ Total pressure
$_{\mathrm{m}}$ Averaged in space and time

1. Introduction

In the field of multistage compressor development, remarkable effort is spent to achieve higher efficiencies and wider operating ranges. In order to consider all relevant aspects of the highly complex three-dimensional flow within the design process, especially viscous and unsteady flow phenomena, highly-sophisticated and well-calibrated design tools are essential. The development of reliable design tools, however, requires detailed experimental data of all relevant flow phenomena in adequate multistage components. The highly three-dimensional flow in turbomachines features complex unsteady flow phenomena due to the existence of stationary and rotating blade rows. These effects vary depending on different aerodynamic loading and different throttling of the compressor respectively. With a higher loading, the boundary layers enlarge, resulting in wider wakes, which do strongly influence the blade rows downstream. Due to varying incidence, the intensity and structure of the tip clearance flow changes. Besides that, the potential upstream influence of both rotor and stator blades increases with higher aerodynamic loading. In a multistage environment, these phenomena do not only influence the generating blade row, but the entire flow field of the compressor, known as stage interaction.

1.1 Test Facility

In the past years, a high-speed, three-stage axial compressor with IGV was built up at the Institute of Jet Propulsion and Turbomachinery at RWTH Aachen University (Hoynacki, 1999). Retaining the front stage, the rig is based on a compressor built up by Schulte (1994). All blade rows of the three-stage axial compressor were inversely designed by a two-dimensional method on five rotational symmetric stream surfaces (Grein and Schmidt, 1994). In Fig. 1, the cross-sectional view of the compressor is shown. The IGV and the stator blades are mounted in inner shroud rings with negligible small radial clearances both at the hub and the casing. The rotor tip clearances are less than 0.3 mm during operation yielding a relative clearance of 0.35% for the first rotor row, and 0.49%, and 0.64%, for the subsequent rotor rows. Fundamental parameters of

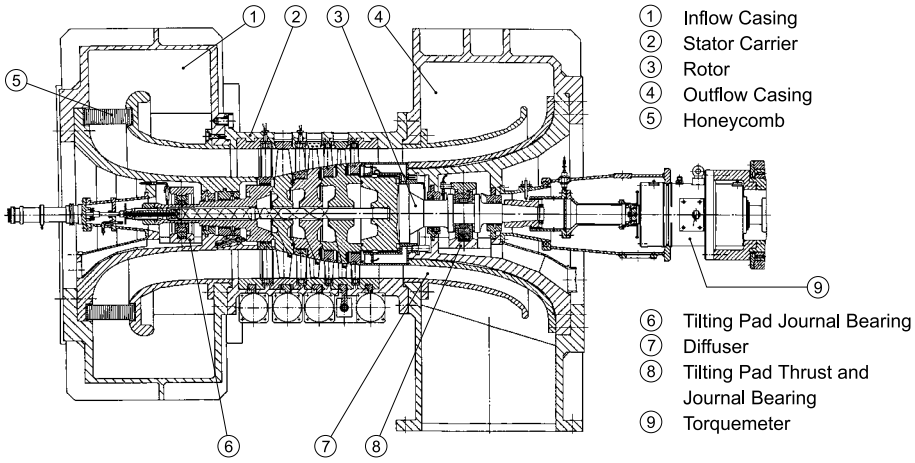

Figure 1. Cross section of the three-stage axial compressor

Table 1. Characteristic parameters of the three-stage axial compressor

Operating point	*Design*	*OP1*	*OP3*
Corrected rotor speed $[min^{-1}]$	17 000	17 000	17 000
Overall total pressure ratio [-]	2.03	2.03	2.29
Total pressure ratio 1st stage [-]	1.30	1.31	1.35
Total pressure ratio 2st stage [-]	1.28	1.26	1.32
Total pressure ratio 3st stage[-]	1.22	1.23	1.28
Corrected mass flow [kg/s]	13.40	13.66	13.35
Corrected power input [kW]	920.00	996.14	1155.68

the compressor are summarized in Table 1. The compressor has a nominal total pressure ratio of 2.03, and a mass flow of $13.4\,\mathrm{kg/s}$ at a rotational speed of $17000\,\mathrm{RPM}$. With a circumferential tip speed of 345 m/s, the maximum relative Mach number is 0.89 at the tip of the first rotor. Although the compressor was up to now investigated in much detail for five different operating points on three different speedlines, this paper will focus on two operating points on the 100% speedline. As can be seen, operating point OP1 is close to design conditions. OP3 is the last stable operating point close to surge.

1.2 Instrumentation

Fundamental measurements were performed with both 2D and 3D pneumatic probes in the axial gaps between the blade rows, and with surface pressure tappings at the casing and on the vanes. In addition to that, a comprehen-

Figure 2. Single sensor dynamic pressure probe (left), dynamic pressure transducer at the casing (center and right)

sive analysis of the unsteady flow field was carried out. Field traverses with high resolution both in space and time were performed using single sensor dynamic pressure probes. The probe shown in Fig. 2 (left hand side) was developed and manufactured at the Institute of Jet Propulsion and Turbomachinery. The head diameter is 2 mm, and the probe is equipped with an Entran EPIH-112 fast response semiconductor pressure transducer. It is supplied by constant current and calibrated by an independent variation of pressure and temperature. The approximation of the characteristics is realized by two-dimensional polynoms (Maass, 1995). Additional investigations with flush mounted dynamic pressure transducers at the casing above the rotors show the effects on the tip clearance flow. One Kulite XCP-062-25D fast response semiconductor pressure transducer (Fig. 2 right hand side) is mounted at different axial positions of the casing element shown in Fig. 2 (center). The circumferential traverse of the element enables field measurements with a resolution of 550 (R3) to 600 (R1) measuring points.

2. Experimental Results

As the performance and the stage characteristics of the compressor under consideration have already been published by Niehuis et al. (2003), only a brief description will be given below. At operating point OP1, the aerodynamic loading is highest for the last stator, which was the design intent in order to study the effect of high loading. Consequently, further throttling (OP3) increases the loading significantly on all blades except for the last stator, which exhibits only a slight increase. It is assumed that surge of this particular compressor is triggered by the last stator. Concerning the overall unsteady behavior, Niehuis et al. (2003) also presented a detailed analysis and proposed a characteristic parameter based on the calculation of the total energy of the periodic pressure fluctuations generated by the rotor blades. Doing this for each measuring plane, the influence of the pressure fluctuations of each blade row can be recognized in terms of their upstream and downstream influence. It was concluded that

- the influence of the rotor blades on the unsteady flow field depends on the aerodynamic loading of the blade rows
- higher loading causes an increasing potential upstream influence as well as the downstream stability of the wakes decreases

In this paper, the detailed analysis of the flow field is focused on the front and the last stage of the compressor. The front stage operates at the overall highest Mach number level, and it enables the separation of different secondary flow phenomena, as there is a comparatively low level of unsteadiness. Besides that, the differences in aerodynamic loading increase in the last stage of the compressor. The effect on the development of secondary flow phenomena becomes more clear.

2.1 Front Stage, Analysis in Detail

This section deals with the analysis of the unsteady flow field of the IGV, as well as the first rotor blades. Due to the fact, that upstream of the first rotor no other periodic disturbances of the flow field occur, its potential upstream influence can be isolated. With the dynamic pressure measurements above the first rotor, a change in structure and intensity of the tip clearance flow is detected due to the different operating conditions at OP1 and OP3.

Inlet Guide Vane. At the outlet of the IGV, a remarkable potential upstream influence of the first rotor is obtained. Figure 3 shows snapshots of field traverses with total pressure probes downstream the IGV. The results are ensemble averaged and related to the total pressure averaged in space and time over the entire measuring field. In addition to the experimental results, the theoretical position of the trailing edge of the IGV is depicted. The upstream influence of the first rotor is indicated by low values of the ensemble averaged total pressure. Neglecting the losses in the stagnation area of the leading edge, the total pressure is assumed to be constant over the entire pitch. Besides that, the stochastic fluctuations increase in the stagnation area, and lower values of the ensemble averaged total pressure occur. Throttling the compressor from OP1 to OP3 the aerodynamic load of the first rotor changes significantly. Regarding the higher load at OP3 the affected area expands in circumferential and midspan direction. The potential field of the first rotor significantly influences the boundary layer development on the IGV, as has been illustrated by Niehuis et al. (2003).

First Blade. Regarding the flow field downstream the first rotor (Fig. 4), at OP1, the tip clearance vortex, indicated by transient maximum RMS values, interacts with the convected wake of the IGV. Passing the wake, the RMS values, as well as the spatial extent of the affected area, decrease. This effect is due to the lower meridional velocity, and therefore less intensive secondary flow in

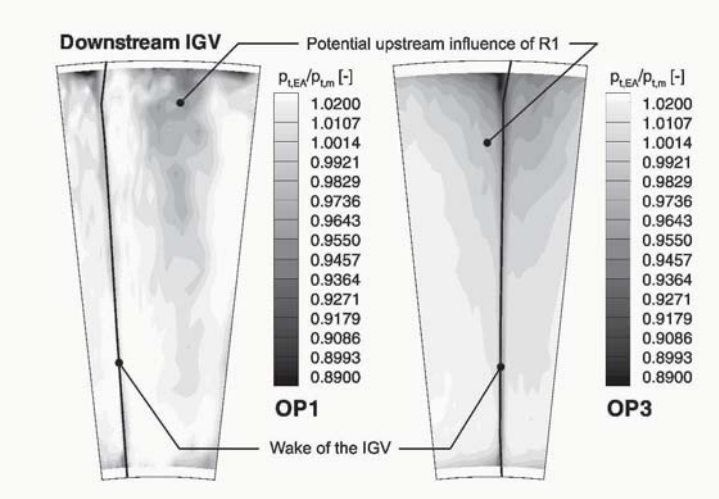

Figure 3. Snapshot of the dynamic total pressure distribution downstream the IGV, ensemble average, 100% speedline

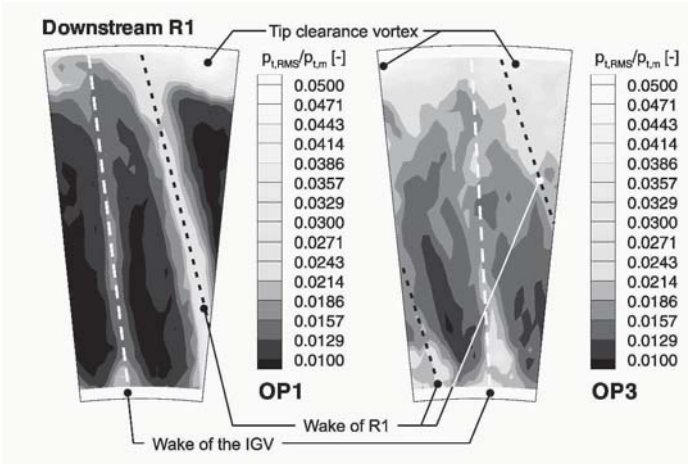

Figure 4. Snapshot of the dynamic total pressure distribution downstream R1, RMS, 100% speedline

the wake area. At OP3, a similar phenomenon is detected, but the tip clearance flow leaves the blade duct closer to the casing, and comparatively high RMS values are obtained over the entire pitch. In contrast to OP1, a sharply defined wake of the rotor is only detected on the left and the right side of the measuring field where no disturbance of the rotor inflow by the wake of the IGV is present. Similar results are presented by Suder and Celestina (1994) investigating a comparable rig. A further analysis of the tip clearance flow is enabled considering the measurements with flush mounted dynamic pressure transducers at the casing above the blades. Figure 5 shows a snapshot of the ensemble

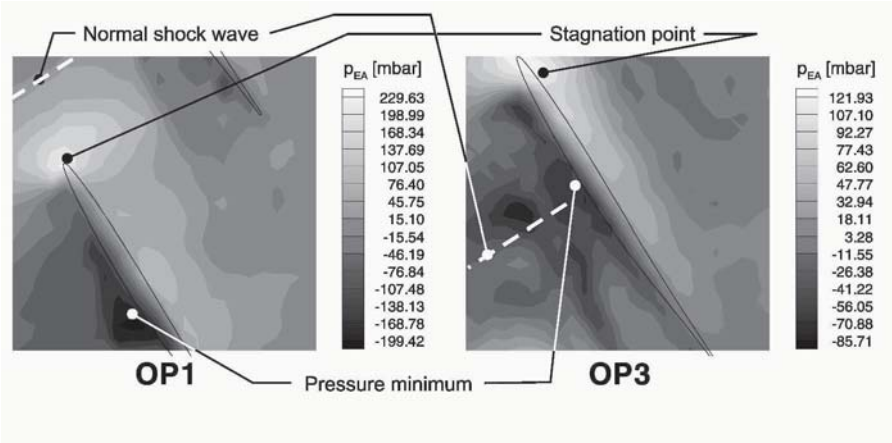

Figure 5. Snapshot of the dynamic wall pressure distribution, first rotor, ensemble average, 100% speedline

averaged data as well as the position of the moving rotor tip. While at OP1, the stagnation point can be found close to the leading edge, it moves to the pressure side with the increased incidence at OP3. Besides that, the axial position of the separated pressure minimum moves upstream from 48% chord (OP1) to 38% chord (OP3). Since the inlet Mach number at the tip section is almost identical at both operating points, a normal shock wave is generated downstream of the pressure minimum in both cases. The time resolved ensemble averaged pressure distribution captures the trajectory of the tip clearance vortex. At OP3 the trajectory close to the suction side of the blade is more inclined in the direction of the circumferential velocity. A similar result was found by Mailach et al. (2001) in a low-speed compressor without any shock wave present. They explain this effect with the different momentum of tip-clearance flow and core flow. With a higher aerodynamic loading, the momentum of the tip clearance flow increases due to the enlarged pressure gradient between the pressure and suction side. Simultaneously, the momentum of the core flow decreases due to the reduced mass flow. The resulting force on the tip leakage fluid turns in the direction of the circumferential velocity. Interacting with the perpendicular shock at OP3, the trajectory bends in meridional direction. The same effect was again detected by Suder and Celestina (1994). The shock causes a loss of momentum of the leakage fluid, and the resulting force on the fluid turns. Contrary to the measurements downstream of the rotor (see Fig. 4), an indexing of the tip clearance flow by the wake of the IGV can not be detected at the casing above the rotor tip. A further analysis of the leakage flow would be enabled regarding the RMS distribution. As the flow field is widely similar to the one of the last rotor, the phenomena will be discussed below in more detail.

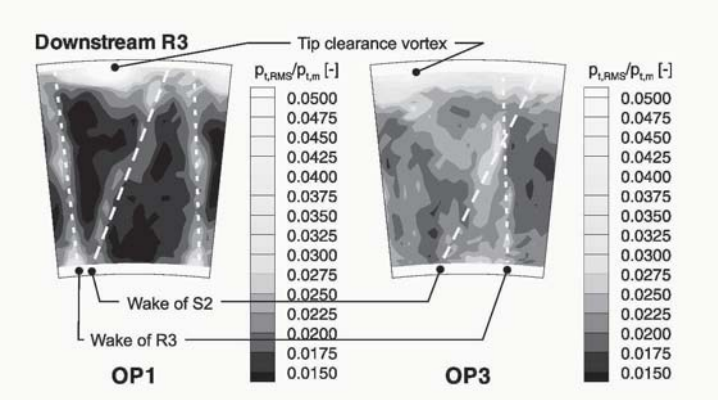

Figure 6. Snapshot of the dynamic total pressure distribution downstream the last rotor, RMS, 100% speedline

2.2 Last Stage, Analysis in Detail

Regarding the last stage of the compressor, the downstream stability of rotor and stator wakes along the machine axis can be illustrated. The shape of the rotor tip clearance flow depends strongly on varying operating conditions. Last but not least, a flow separation in the last stator, resulting in a hub corner stall, occurs already at design conditions and is influenced by the wakes of the rotor upstream. Further throttling leads to a significantly growing separation, and it is assumed that the last stator triggers surge at the 100% speedline.

Last Blade. The flow field downstream the last blade (Fig. 6) is dominated by the wakes of the second vane, which are tilted in the direction of the circumferential velocity. Basically, two differences exist between the operating points OP1 and OP3. In the wake area of the second vane close to the hub, high RMS values occur at OP3. At this position, the decreased meridional velocity in the wake of the vane causes an increasing incidence on the pressure side in the inlet plane of the last blade. Due to the incidence, the stochastic fluctuations increase periodically and a fluctuating separation on the suction side is likely to occur in the hub region of the blade. At OP1, the region influenced by the tip clearance vortex can be identified by maximum gradients of the RMS values. Though similar regions can be detected at OP3 as well, the gradients are smaller, and there is an additional region above 83% span with high RMS values over the entire pitch. The mechanism of the tip clearance flow and its variation due to different aerodynamic loading can be analyzed in more detail using the dynamic pressure field at the casing above the rotor tip (Fig. 7). Except for the shock wave, the flow field corresponds widely to the one of the first rotor. The increased aerodynamic loading at OP3 results in a pressure minimum moving upstream from 47% chord at OP1 to 35% chord at OP3. At

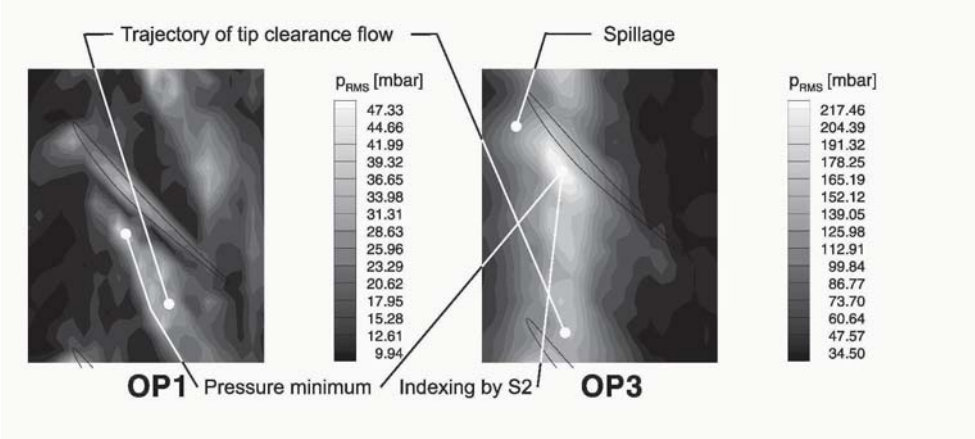

Figure 7. Snapshot of the dynamic wall pressure distribution, last rotor, RMS, 100% speedline

both operating points, it is apart from the suction side of the blade. At OP1, the trajectory of the tip clearance flow is detected which originates close to the leading edge and leaves the blade duct close to the pressure side of the adjacent blade. At OP3, a trajectory of this shape is not detected. A corresponding area extends over the entire pitch from the leading edge to 71% chord. Furukawa et al. (2000) report on similar effects investigating an one-stage axial compressor with a NACA 65 blading. At design conditions, the leakage flow originates at the leading edge up to 30% chord downstream. In the region of the pressure minimum, the flow changes into a coil-shaped structure. Downstream of the pressure minimum, the resulting vortex grows and moves to the pressure side of the adjacent blade. Furukawa et al. (2000) called this structure a spiral-type vortex. Approaching the surge margin, the leakage flow is coiled very close to the tip clearance. Downstream of the pressure minimum, a breakdown of the resulting vortex occurs, and it drifts to the pressure side of the adjacent blade. This effect is accompanied by a deceleration and the appearance of reversed flow regions covering the entire pitch. Consequently the leakage flow can not be detected anymore at the casing in the vicinity of the trailing edge. Nevertheless, the flow appears downstream the blade row in the upper 20% of span (see Fig. 6). It can be concluded, that the vortex dives into mid-duct direction. Furukawa et al. (2000) call this structure a bubble-type vortex. Besides that, a remarkable spillage upstream the leading edge is obtained. As Suder and Celestina (1994) already mentioned, this spillage is caused by a significant positive incidence and reversed flow due to the axial pressure gradient at this particular spanwise position. Unlike the front stage, the flow interacts periodically with the wake of the vane upstream. Using animated temporal plots, this indexing can clearly be seen in the fluctuating maxima of the RMS distribution

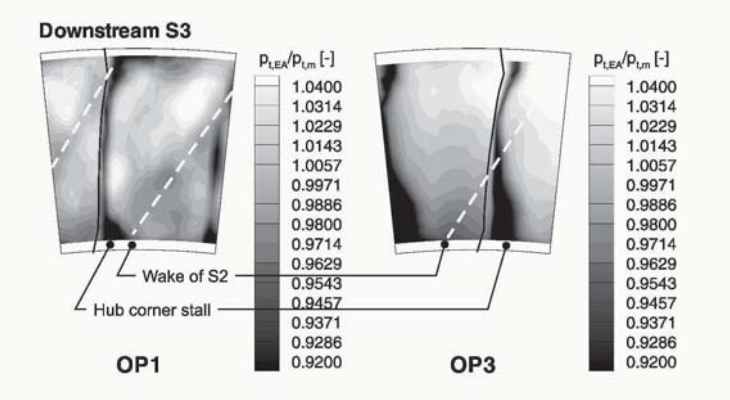

Figure 8. Snapshot of the dynamic total pressure distribution downstream the last stator, ensemble average, 100% speedline

both in intensity and axial position, and is more distinctive at OP3. The region of the maximum RMS values in time can be assigned to the wake of the second vane upstream. The boundary layer of the vane upstream grows at the surge line (OP3) resulting in a wider wake. This effect causes increasing fluctuations of the incidence angle upstream of the last blade, and a time dependent variation of its flow field, especially of the tip leakage flow.

Last Vane. By design intent, the third stator exhibits the highest aerodynamic loading of all airfoils in this particular compressor resulting in a hub corner stall which is already present at design conditions. Further information about the mechanism of the hub corner stall in general can be found in Hah and Loellbach (1997). The extent of the stall in the circumferential as well as radial direction becomes very clear in the ensemble averaged distribution of the total pressure downstream the last vane (Fig. 8). Besides that, the separation grows at OP1 when the wake of the last rotor is passing the last vane. The fluctuating incidence due to the transient wake is forcing a periodic flow separation. At OP3, the flow is separated all the time, damping the periodic fluctuations. The differences concerning the tip clearance flow which were obtained by the dynamic wall pressure distribution can still be found at the exit of the last vane. Whereas at OP1 the influence of the leakage flow is still visible, at OP3 no corresponding phenomenon is detected. With the lower aerodynamic loading at OP1, the mechanisms of mixing and vortex breakdown are less intensive and take up an increased axial distance. At the exit of the last stator, the wakes of the second stator are still visible. The wakes and the hub corner stall of the last stator strongly influence the flow in the outlet diffuser as well. Measurements 144% chord downstream of the last vane show a remarkable inhomogeneous flow field in radial and circumferential direction. The downstream stability of

viscous flow phenomena is confirmed, which has already been seen in the front stage.

3. Summary

This paper presents measurements with high resolution both in space and time in an industry-like three-stage axial compressor with inlet guide vanes. Besides a brief description of the experimental facility and its overall behavior, the detailed analysis of the flow field is focused on the front stage and the last stage of the compressor. The front stage operates at the overall highest Mach number level which results in transonic flow conditions at the tip of the first rotor. Due to the fact that upstream of the first rotor, no other periodic disturbances of the flow field occur, the potential upstream influence can be isolated. Regarding the first rotor, the structure and the intensity of the tip clearance flow change due to different throttlings of the compressor. At design conditions, the tip leakage flow can be identified as a spiral-type vortex. With the approach towards the surge line, a bubble-type vortex occurs. Though the wakes of the blade rows become wider with higher aerodynamic loading, they are less stable along the machine axis. Concerning the aerodynamic loading, the differences between the investigated operating points are more significant in the last stage of the compressor. The effect on the development of secondary flow phenomena becomes more clear. Firstly, the downstream stability of stator wakes along the machine axis is confirmed. The wake of the second stator causes slight periodic flow separations in the adjacent rotor blade and is still visible downstream of the last stator. As well as the first one, the last rotor shows a varying shape of its tip clearance flow dependent on aerodynamic loading. Because of a high aerodynamic loading of the last vane, a flow separation occurs already at design conditions resulting in a corner stall. It is influenced by the wakes of the rotor upstream. Further throttling leads to a significantly growing separation and it is assumed that the last stator triggers surge at the 100% speedline.

Acknowledgments

This work was supported by the Forschungsvereinigung Verbrennungskraftmaschinen e.V. (FVV) and the Arbeitsgemeinschaft Industrieller Forschungsvereinigungen e.V. (AIF), which is gratefully acknowledged.

References

Furukawa, M., Kazuhisa, S., Kazutoyo, Y., Inoue, M. (2000). Unsteady Flow Behaviour due to Breakdown of Tip Clearance Vortex in an Axial Compressor Rotor at Near-Stall Condition. ASME Paper No. 2000-GT-666.

Grein, H.-D., Schmidt, E. (1994). Verlustarme Verdichterauslegung (Theorie II). Forschungsbericht FVV, Heft 566.

Hah, C., Loellbach, J. (1997). Development of Hub Corner Stall and its Influence on the Performance of Axial Compressor Blade Rows. ASME Paper No. 97-GT-42.

Hoynacki, A. (1999). Experimentelle Untersuchung instationaerer Stroemungsvorgaenge in einem dreistufigen Axialverdichter mit CDA-Beschaufelung. Dissertation, RWTH Aachen University, Germany.

Maass, M. (1995). Kalibrierung von Halbleiter-Drucksonden. DLR-Mitteilung 95-03, Deutsche Forschungsanstalt fuer Luft- und Raumfahrt e.V. Koeln.

Mailach, R., Sauer, H., Vogeler, K. (2001). The Periodical Interaction of the Tip Clearance Flow in the Blade Rows of Axial Compressors. ASME Paper No. 2001-GT-0299.

Niehuis, R., Bohne, A., Hoynacki, A. (2003). Experimental Investigation of Unsteady Flow Phenomena in a Three Stage Axial Compressor. Proceedings of the 5th European Conference in Turbomachinery, Prag, March 17 - 22, 2003, pp. 209 - 219

Schulte, J.H.G. (1994). Experimentelle Untersuchung der stationaeren dreidimensionalen Stroemung an einem invers ausgelegten Axialverdichter mit Vorleitrad. Dissertation, RWTH Aachen University, Germany.

Suder, K.L., Celestina, M. L. (1994). Experimental and Computational Investigation of the Tip Clearance Flow in a Transonic Axial Compressor Rotor. ASME Paper No 94-GT-365.

ANALYSES OF URANS AND LES CAPABILITIES TO PREDICT VORTEX SHEDDING FOR RODS AND TURBINES

P. Ferrand, J. Boudet, J. Caro
Ecole Centrale de Lyon - LMFA - UMR 5509
36, avenue Guy de Collongues
69134 Ecully (France)
pascal.ferrand@ec-lyon.fr

S. Aubert, C. Rambeau
Fluorem, Ecully (France)

Abstract The objective of this study is to evaluate the capability of codes to simulate vortex shedding that occurs at the trailing edge of turbine blades. Firstly, unsteady RANS simulations (various $k-\omega$ models) are presented on the VKI turbine, and the results are compared to experiments. Next, results are interpreted for an academic test-case of flow past a rod. This latter configuration allows a deeper analysis and provides an outlook by the use of large-eddy simulation (LES). It appears that URANS provides qualitative results, and LES is an interesting way to get accurate predictions.

1. Introduction

Large unsteady coherent structures appear downstream turbine blade with thick trailing edge. These "von Karman" vortex structures are similar to vortex shedding in wake of a rod. The phenomenon has been investigated experimentally by many authors at low (Han and Cox, 1983, Cicatelli and Sieverding, 1997) and high speed (Sieverding et al., 2003). The experimental results present quantitative information on unsteady pressure, velocity, and temperature. Sieverding's results are a precious source of analysis and validation of numerical simulations. The presented results try to evaluate the capabilities of URANS and LES to predict these phenomena. In fact, through these different models, the question is to know if the turbulent scales interact or not with

K.C. Hall et al. (eds.),
Unsteady Aerodynamics, Aeroacoustics and Aeroelasticity of Turbomachines, 381–393.

macroscopic vortices. If yes, LES must be performed to simulate vortex shedding process, if no, URANS can be enough. Experimental results (Sieverding et al., 2003) on turbine blade, and presented results, are based on European Research Projects "Turbulence modeling for unsteady flows in axial turbines".

2. Flow solver: Proust / TurbFlow

The equations solved are the 3D, unsteady, compressible, Reynolds averaged (RANS) or spatially filtered (LES), Navier-Stokes equations cast in the absolute frame where the laminar viscosity is assumed constant or calculated by the Sutherland's law.

2.0.1 Spatial discretization. The space discretization is based on a MUSCL finite volume formulation with moving structured meshes, which utilizes vertex variable storage. The convective fluxes are evaluated using a 3rd order upwind scheme (Van Leer's Flux Vector Splitting with the Hanel correction, Roe's Approximate Riemann Solver, or Liou's Advection Upwind Splitting Method), or 4th order centered scheme (for LES). An hybrid method combining the advantages of the central scheme in subsonic regions with the properties of the upwind scheme through discontinuities has been introduced to reduce the numerical losses in very low Mach number regions. The viscous terms are computed by a second order centered scheme. The resulting semi-discrete scheme is integrated in time using an explicit five steps Runge-Kutta time marching algorithm.

2.0.2 Boundary conditions. Compatibility relations are used to take into account physical boundary conditions. The outgoing characteristics are retained, since these provide information from inside the domain. The incoming characteristics, on the other hand, are replaced by physical boundary conditions, i.e. total pressure, total temperature and flow angles for a subsonic inlet, static pressure for a subsonic outlet, zero normal velocity component for a slip wall and zero velocity and heat flux for an adiabatic wall. Ghost cells for which the equations are not solved are built around the domain to simulate geometrical boundary conditions, like periodicity and symmetry. Non reflective boundary conditions are implemented by retaining the equations associated to the incoming characteristics, in which the wave velocity is fixed to zero to prohibit propagation directed into the computational domain.

2.0.3 Turbulence Models. For the RANS approach, turbulence is taken into account by a $k-\omega$ model. Two transport equations are implemented, governing the turbulent energy k and the dissipation ω. The evaluation of the Reynolds tensor and of the turbulent viscosity are carried out by different turbulence models: the linear model of Wilcox, 1993b, the low-Reynolds model

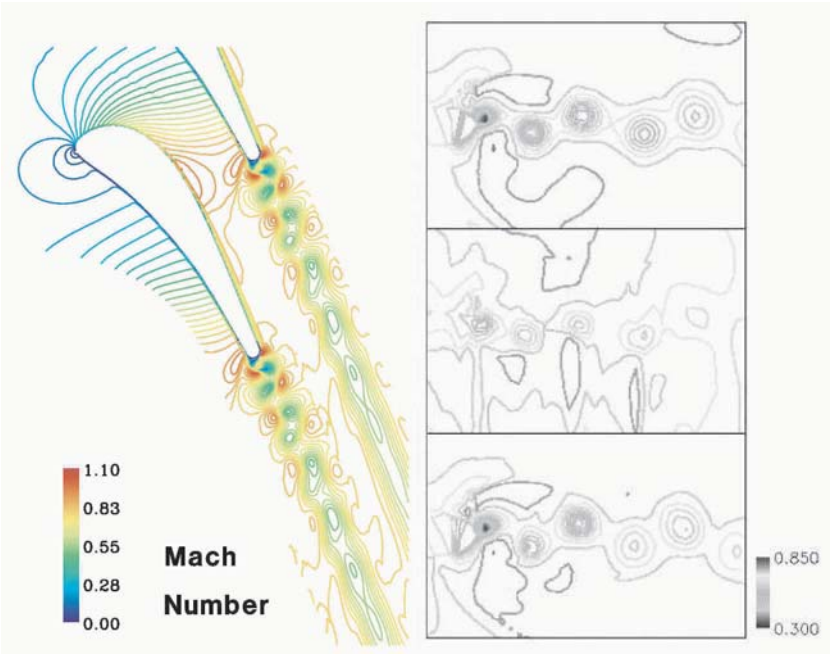

Figure 1. VKI turbine. Left: Mach numbers contours. Right: Comparison of density iso-contours [Upper : linear k-ω model; Middle : experimental data (ONERA); Lower : non-linear k-ω model]

of Wilcox, 1993a, the non-linear model of Shih et al., 1995 and the non-linear model of Craft et al., 1996.
For the LES, the subgrid scales are represented by a viscosity, computed using the auto-adaptive model of Casalino et al., 2003. This formulation enables an effective evaluation of the subgrid-scale viscosity, even for complex geometries.

3. VKI Turbine

Unsteady RANS simulations have been achieved for the VKI turbine case. A coarse grid (18 000 nodes, referenced as stp2) was firstly used, but in order to resolve the shocks appropriately, a finer grid has been also designed (72 000 nodes, referenced as stp1). The sonic region and the Von Karman street can be seen on the instantaneous map of the computed Mach number contours on Fig. 1-left.

The time averaged isentropic Mach number distributions along the pressure and the suction sides are shown on Fig. 2. The computational results (linear model of Wilcox, 1993b, and non linear model of Craft et al., 1996) are

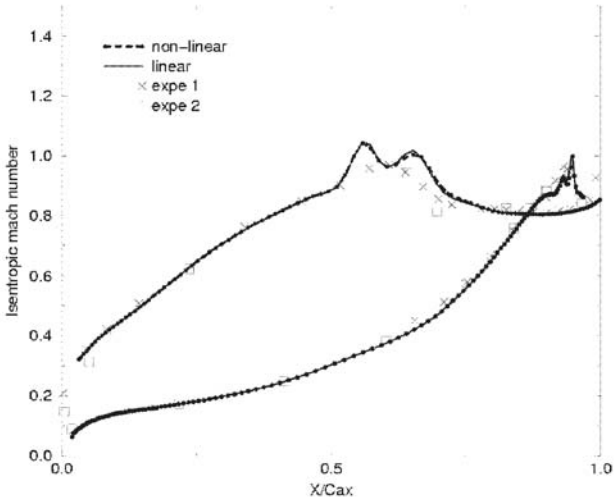

Figure 2. VKI turbine. Time averaged isentropic Mach number distribution on the blade

very close to the experimental results. The prediction is very good on the pressure side, and a good agreement is noticeable on the suction side where the numerical distribution is above the experimental points, probably a time-integration effect of the experimental data. The unsteadiness due to the vortex shedding modify mainly the area located downstream of the nearly sonic area ($x/c \geq 0.5$), on the suction side.

The stabilization on one specific frequency is difficult to obtain with the non-linear $k - \omega$ model. It seems that unsteady shock boundary layer interactions was not completely stabilized. All simulated Strouhal numbers are quite close to the experimental value of 0.219, as shown in Table 1.

Table 1. VKI turbine. Strouhal number

	RANS lin.	**RANS non-lin.**
Fine grid (stp1)	0.253	0.225
Coarse grid (stp2)	0.231	

.

Results are better on the coarse grid than on the fine grid. Consequently, one needs to be careful when analyzing the numerical results. $k - \omega$ models give a frequency a little too high, which suggests a too small value of the turbulent kinetic energy.

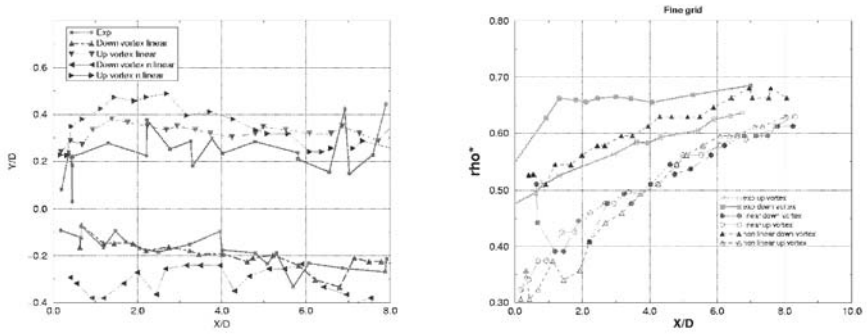

Figure 3. VKI turbine. Left: Comparison of vortex location. Right: Comparison of vortex density evolution at the center of vortex (fine grid).

Figure 1-right shows the density iso-contours for the experiment and for the linear and non-linear $k-\omega$ models. The vortex locations and the shock wave structures are close, but the intensity of the numerical results seems higher than the experimental results. The vortex location obtained by experiment is well compared to linear and non-linear $k-\omega$ model (Fig. 3-left). For the numerical results, the distance between the lower and upper vortex is a little too wide suggesting that the amplitude of the fluctuations is too strong near the trailing edge.

The density at the vortex center is compared to the extrema of VKI experimental data for linear and non-linear $k-\omega$ model (Fig. 3-right). The experimental results show a symmetric vortex shedding. The linear and non-linear $k-\omega$ models increase the deficit of density which shows that the fluctuation level is over-predicted as was suggested on Fig. 1-right. For the linear model, the modification is non-symmetric and affects mainly the pressure side of the trailing edge. As for the non-linear $k-\omega$ model, it predicts correctly the lower vortex intensity, but over-estimates the upper vortex intensity.

Time averaged static pressure at different angular locations around the trailing edge is presented in Fig. 4-left. With the linear model, the agreement is reasonable on the pressure side, whereas more discrepancies are visible on the suction side. Otherwise, the non-linear model gives better results on the suction side except at 80 degrees where the shock wave appears. It seems that the computation is not completely stabilized (locally). It will be noticed that the experimental values are almost symmetric, the numerical solution appearing more influenced by the small supersonic regions upstream of the trailing edge. More investigation will be necessary on spatial schemes and limiters. An interesting point is to observe the comparison between the time averaged value

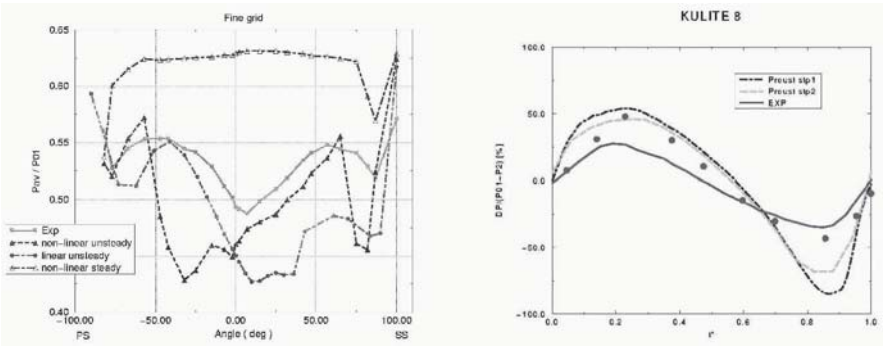

Figure 4. VKI turbine. Left: Comparison of the trailing edge static pressure distribution from pressure side (left hand) to suction side (right hand) (fine grid). Right: Comparison of unsteady static pressure fluctuation between numerical results and phase-locked Fourier analysis (solid line) or wavelet experimental analysis (dots).

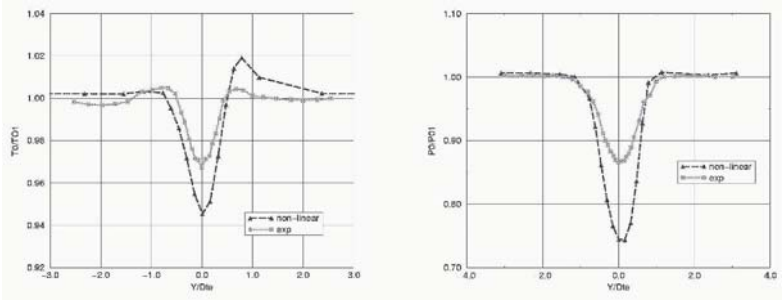

Figure 5. VKI turbine. Time averaged stagnation temperature (left) and stagnation pressure (right) at X/D=2.5.

and the steady value. The higher level on steady static pressure confirms that the vortex shedding increases the losses.

The excessive amplitude of the deficit given by the linear $k-\omega$ model is also visible looking the instantaneous static pressure fluctuations due to vortex shedding in Fig. 4-right. The curve shapes are similar, but the amplitude is higher for the finer grid, particularly on the suction side where the increase of fluctuations represents 40% of the total fluctuation amplitude. This is consistent with a sharper description of local gradients. Two decompositions of raw experimental data were done at VKI using phase-locked Fourier analysis (solid line) or wavelet analysis (dots). The amplitude measured using wavelet analysis is in better agreement with the numerical results. This could be ex-

plained by a slight random frequency variation during the experimental vortex shedding to which the Fourier analysis is more sensitive.

Total temperature and total pressure fluctuations were recorded 2.5 diameters downstream the trailing edge (Fig. 5). Once again, the curve shapes are similar, particularly on the pressure side, the amplitude being slightly over predicted.

4. Rod test-case

The flow past a circular rod is an interesting academic study about vortex shedding. It will be used to pursue a deeper analysis, taking advantage of the extensive experimental database. Three URANS $k-\omega$ turbulence models will be compared, in order to estimate the influence of this parameter. Also, a large-eddy simulation (LES) has been carried-out. It enables an interesting comparison and creates an outlook.

4.0.4 Description of the configuration. In the present study, the flow past the rod is characterized by a Reynolds number of $Re_d = 48,000$ [the inflow velocity is $U_\infty = 72$ m/s and the rod diameter: $d = 0.01$ m]. According to the experiments, the vortex shedding occurs at the Strouhal number: $St = fd/U_\infty \sim 0.2$, and the transition to turbulence takes place in the shear layer, just after the separation (sub-critical regime). As a consequence, the wake is fully turbulent, though dominated by the von Karman vortices. This flow topology is sufficiently complex to be compared to practical applications.

The results analyzed in this paper are extracted from a larger configuration previously used to study the emission of broadband noise. This configuration involves a symmetric airfoil (chord length: $c = 10\,d$) located in the wake of a rod, one chord length downstream. We are here concerned with the vortex shedding, so only the flow past the rod will be analyzed. The studies have shown that the airfoil has nearly no influence on the rod because of the distance between the two bodies. Information about the study on the whole rod-airfoil configuration can be found in references Jacob et al., 2002 and Boudet, 2003.

4.0.5 Numerical characteristics. Figure 6 presents the overall rod-airfoil computational domain and a view of the mesh near the rod. The URANS mesh is 2D and involves 197 points around the circumference, with the first grid line located at $y^+ < 8$ from the wall. A 3D mesh is not necessary because URANS only features the mean components of the flow, which are bi-dimensional in this case.

The LES mesh is the same, but duplicated along span to cover 3 diameters (31 points), in order to simulate the tri-dimensionality induced by the turbulence. In the turbulent region, the resolution is characterized by $y^+ < 3$ per-

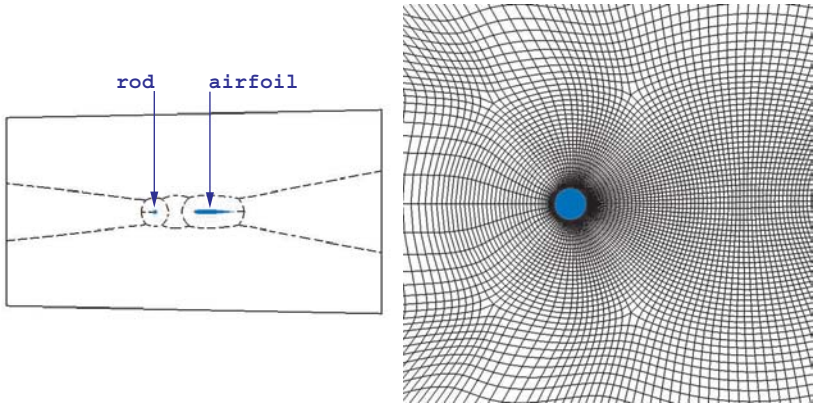

Figure 6. Rod test-case. Left: Rod-airfoil computational domain (7 blocks). Right: mesh near the rod (1pt/2).

pendicularly to the wall, $x^+ < 50$ tangentially to the curvature of the wall, and $z^+ < 200$ along the span.

Three URANS computations were carried-out, using respectively three $k - \omega$ models: the linear model of Wilcox, 1993b, the low-Reynolds number model of Wilcox, 1993a, and the non-linear model of Shih et al., 1995. A no-slip condition is imposed at the walls, and a non-reflecting condition reduces the spurious confinement at the outer boundaries. The computation was led to convergence for 10 aerodynamic cycles, then it was saved 100 times per cycle for 18 cycles.

The LES computation used the auto-adaptive model of Casalino et al., 2003, to estimate the subgrid scale viscosity. As for URANS, no-slip and non-reflecting conditions are imposed at the relevant boundaries, and a slip condition is applied to the limiting plane in the spanwise direction. The computation was led to convergence for 6 aerodynamic cycles (initial field: URANS), then it was recorded 100 times per cycle for 18 cycles.

4.0.6 Results. The vortex shedding occurs naturally for all the computations. However, as mentioned in table 2, URANS overestimates the frequency: the Strouhal number is $St = 0.24$ for the three $k - \omega$ models, whereas the experimental value is $St = 0.20$. LES performs better, it predicts the experimental value.

Table 2 also presents the integral forces on the rod: the mean drag ($< C_D >$), the fluctuating drag (C'_D), and the fluctuating lift (C'_L). The linear URANS model underestimates these forces. As a comparison, the low-Reynolds number model performs slightly better. The non-linear model is fi-

Table 2. Rod test-case. Vortex shedding Strouhal number and aerodynamic forces on the rod - (measurements: Gerrard, 1961, Achenbach, 1968, Cantwell and Coles, 1983, Szepessy and Bearman, 1992).

	RANS lin.	**RANS low-Re**	**RANS non-lin.**	**LES**	**Measurements**
$\mathbf{St}$	0.24	0.24	0.24	0.19	~ 0.20
$< \mathbf{C_D} >$	0.79	0.86	1.03	1.17	$[1.0, 1.35]$
$\mathbf{C'_D}$	0.012	0.021	0.079	0.12	$[0.08, 0.16]$
$\mathbf{C'_L}$	0.34	0.48	0.76	0.57	$[0.4, 0.8]$

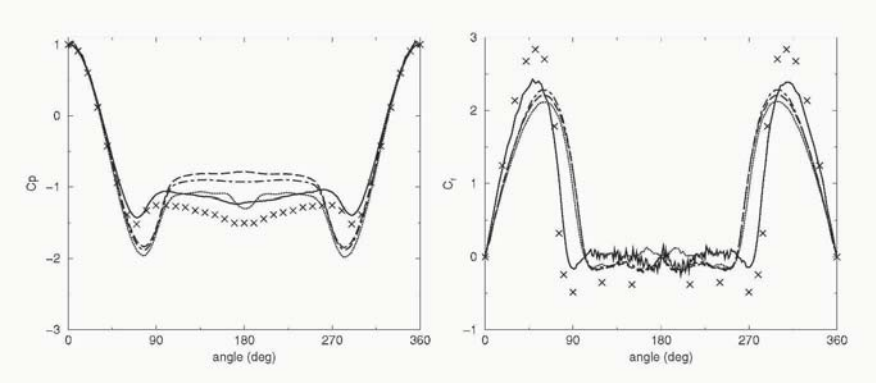

Figure 7. Rod test-case. Left: Mean pressure on the wall. Right: Mean friction on the wall. [$\times$ $\times$: measurements (Szepessy and Bearman, 1992, Achenbach, 1968), – – –: RANS lin., — · —: RANS low-Re, · · · · ·: RANS non-lin., ———: LES]. $Angle = 0$ deg is the forward stagnation point.

nally better than the two other URANS computations. It performs as well as LES, they both exhibit results in agreement with the experimental ranges.

Next, Fig. 7 presents the mean pressure and the mean friction on the wall. Concerning the mean pressure, we first notice a discrepancy in the recirculation region, represented by the plateau near the angle 180 deg. This turbulent recirculating region is the most sensitive. However, the non-linear URANS and the LES exhibit better results. The region near the separation is more interesting. There, all the URANS computations fail, exhibiting similar curves. They emphasize the minimum, and this can be related to a delaying of the separation. As a comparison, LES achieves to predict the experimental curve.

The mean friction confirms the preceding comments. The separation, located by $Cf = 0$, is delayed by the URANS computations, whereas the LES features the experimental location.

The overestimate of the Strouhal number by the URANS can be related to the delaying of the separation. The mean recirculation bubble is thiner than

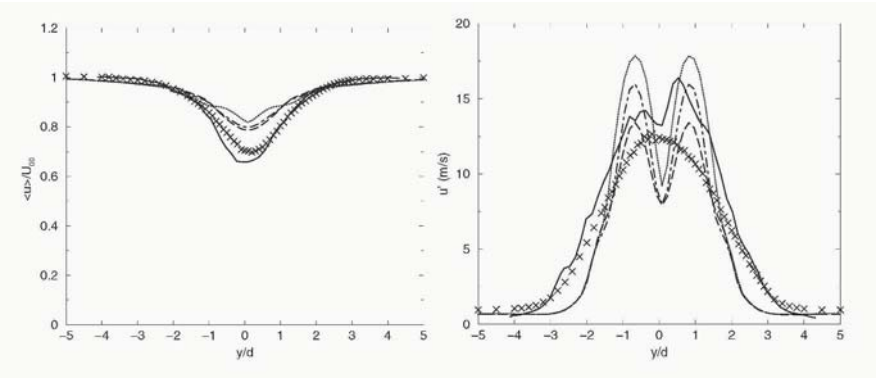

Figure 8. Rod test-case. Left: Mean velocity. Right: Fluctuating velocity. $x/d = 7.5$. [$\times$ $\times$: measurements (Jacob et al., 2002), − − −: RANS lin., — · —: RANS low-Re, · · · · ·: RANS non-lin., ———: LES].

in the experiments, and the vortex shedding frequency is consequently higher. Also, the good estimate of the shedding frequency by LES is consistent with the simulation of the separation, located in agreement with the measurements.

Figure 8 presents the mean and fluctuating velocities in a section perpendicular to the wake, at $x/d = 7.5$ downstream of the rod axis. This location is influenced by the airfoil, but computations and experiments are consistent, carried-out for the same configuration (rod + airfoil). We notice similar results for the three URANS computations, but level differences appear. The URANS wake is thiner than in the experiment, in agreement with the delaying of the separation. Also, the two peaks on each side of the axis show that the von Karman vortices are convected along the same path from one cycle to another. This is not true for the experiment and the LES, because they take the turbulent dispersion of the trajectories into account.

Finally, Fig. 9 shows views of the instantaneous vortex identification function, Γ_2, designed by Graftieaux et al., 2001. The experiment (PIV), the linear URANS and the LES are presented. We notice a good agreement between LES and PIV, many small vortical scales agglomerates to shape the major eddies. On the contrary, URANS only exhibits large von Karman vortices, with a small inter-vortices distance due to the higher frequency.

Figure 10 presents the same quantity, but reconstructed using only the mean field and the two major POD modes (POD: Proper Orthogonal Decomposition). The agreement is good between the three images. It shows that URANS is able to feature the major modes, in agreement with PIV and LES.

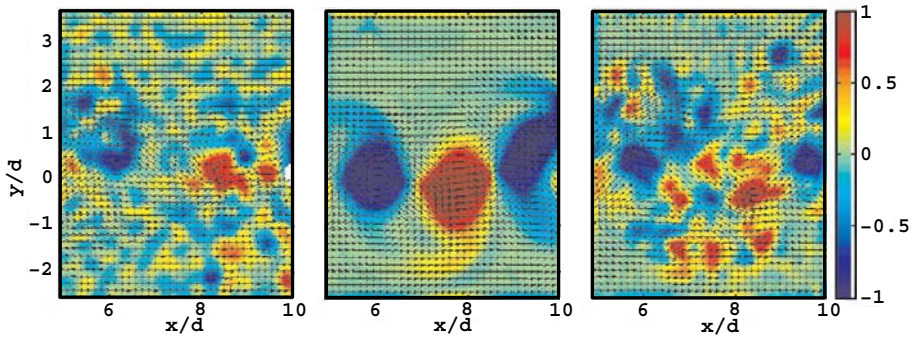

Figure 9. Rod test-case. Instantaneous Γ_2. Left: PIV (Michard et al., 2002, Jacob et al., 2002), Middle: RANS linear, Right: LES.

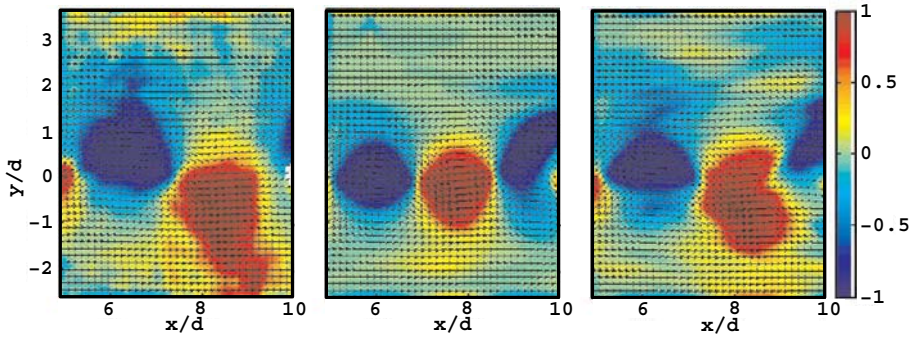

Figure 10. Rod test-case. Instantaneous Γ_2 reconstructed using the mean field and the two major POD modes. Left: PIV (Michard et al., 2002, Jacob et al., 2002), Middle: RANS linear, Right: LES.

5. Conclusion

The present studies focused on the abilities of the numerical approaches to predict vortex shedding. Firstly, various U-RANS results has been presented on the VKI test-case. Then, an academic study was pursued on an isolated rod undergoing a sub-critical vortex street. One observes that RANS is able to predict the main features of the flow, qualitatively. However, differences are noticeable between the various turbulence models used. As an outlook, LES performs better because of its direct description of the flow, including the diversity of the scales. For example, boundary layer separation has an important influence on the vortex shedding, and it is accurately featured by LES.

Acknowledgments

This study was carried out with the support of the European Community in the projects Turmunsflat and TurboNoiseCFD. The CINES (centre informatique de l'enseignement supérieur) provided the parallel computing facilities.

References

Achenbach, E. (1968). Distribution of local pressure and skin friction around a circular cylinder in cross-flow up to $re = 5.10^{6}$. *J. Fluid Mech.*, 34:625–639.

Boudet, J. (2003). *Approches numériques pour la simulation du bruit à large bande en vue de l'application aux turbomachines*, PhD thesis, Ecole Centrale de Lyon, Ecully.

Cantwell, B. and Coles, D. (1983). An experimental study of entrainment and transport in the turbulent near wake of a circular cylinder. *J. Fluid Mech.*, 136:321–374.

Casalino, D., Boudet, J., and Jacob, M. C. (2003). A shear flow subgrid-scale model for large-eddy simulation. submitted to *Theo. Comp. Fluid Dyn.*

Cicatelli, G. and Sieverding, C. H. (1997). The effect of vortex shedding on the unsteady pressure distribution around the trailing edge of a turbine blade. *J. of Turbomachinery*, 119:810–819.

Craft, T. J., Launder, B. E., and Suga, K. (1996). Development and application of a cubic eddy-viscosity model of turbulence. *Int. J. Heat and Fluid Flow*, 17:108–115.

Gerrard, J. H. (1961). An experimental investigation of the oscillating lift and drag of a circular cylinder shedding turbulent vortices. *J. Fluid Mech.*, 11:244–256.

Graftieaux, L., Michard, M., and Grosjean, N. (2001). Combining piv, pod and vortex identification algorithms for the study of unsteady turbulent swirling flows. *Meas. Sci. Technol.*, 12:1422–1429.

Han, L. S. and Cox, W. R. (1983). A visual study of turbine blade pressure side boundary layer. *J. of Eng. for Power*, 15(105):47–52.

Jacob, M. C., Boudet, J., Casalino, D., and Michard, M. (2002). A rod-airfoil experiment as benchmark for broadband noise modelling. In Proc. of the 3rd SWING Aeroacoustics Workshop, Stuttgart. submitted to *J. Theo. Comp. Fluid Dyn.*

Michard, M., Jacob, M. C., and Grosjean, N. (2002). An experimental characterization of the flow past an airfoil in the wake of a circular rod. In ASME Fluids Engineering Division Summer Meeting, FEDSM2002-31344, Montréal.

Shih, T. H., Zhu, J., and Lumley, J. L. (1995). A new reynolds stress algebraic equation model. *Comput. Methods Appl. Mech. Engrg.*, 125:287–302.

Sieverding, C. H., Ottolia, D., Bagnera, C., Cimadoro, A., and Desse, J. M. (2003). Unsteady turbine blade wake characteristics. In ASME IGTI conference, GT 2003-38934.

Szepessy, S. and Bearman, P. W. (1992). Aspect ratio and end plate effects on vortex shedding from a circular cylinder. *J. Fluid Mech.*, 234:191–217.

Wilcox, D. C. (1993a). Comparison of two-equation turbulence models for boundary layers with pressure gradient. *AIAA Journal*, 31(8):1414–1421.

Wilcox, D. C. (1993b). *Turbulence modeling for CFD*. DCW Industries, Inc., La cañada, CA.

VI

COMPUTATIONAL TECHNIQUES

FREQUENCY AND TIME DOMAIN FLUID-STRUCTURE COUPLING METHODS FOR TURBOMACHINERIES

Duc-Minh Tran and Cédric Liauzun
Structural Dynamics and Coupled Systems Department
Office National d'Études et de Recherches Aérospatiales
B. P. 72, 29 avenue de la Division Leclerc, 92322 Châtillon Cedex, France
minh.tran_duc@onera.fr, cedric.liauzun@onera.fr

Abstract Two methods of fluid-structure coupling for turbomachinery are presented, the first one in the frequency domain and the second in both frequency and time domains, with the assumptions of linearized aerodynamics and cyclic symmetry.

Keywords: fluid-structure coupling, aeroelasticity, turbomachinery

1. Introduction

This paper is concerned with the coupled fluid-structure dynamic analysis of turbomachinery. The structure consists of a rotating bladed disk submitted to the unsteady aerodynamic forces exerted by the fluid, which are themselves generated by the structural motion. The structure and the fluid are assumed to have a perfect circumferential cyclic symmetry, so that the classical reduction of the analysis to only one reference sector can be applied. The study of the structure comes down to that of the reference sector by applying the appropriate boundary conditions for each phase number. The displacements of the reference sector in the travelling wave coordinates are expressed as a linear combination of the complex modes or Craig and Bampton's basis and the motion equations are projected on these bases to obtain a reduced system.

In the coupling methods proposed here Tran et al., 2003, the unsteady aerodynamic forces are assumed to depend linearly on the structural displacements and velocities and they are expressed in terms of those induced by the modes. The mode-induced aerodynamic forces are computed only once at the beginning of the simulation by using an aerodynamic code (solving the Euler equations) with the assumption of harmonic motion of the modes, for an inter-blade phase angle and a number of reduced oscillation frequencies.

K.C. Hall et al. (eds.),
Unsteady Aerodynamics, Aeroacoustics and Aeroelasticity of Turbomachines, 397–408.

In the frequency domain, the projection of the mode-induced aerodynamic forces on the modes provides a complex matrix of aerodynamic coefficients whose product with the modal coordinates gives the generalized aerodynamic forces, leading to a nonlinear eigenvalue system. This flutter equation is solved by using two well-known iterative techniques already used for aircrafts, which are the double scanning method Dat and Meurzec, 1969 (also called $p-k$ method) and Karpel's minimum state smoothing method Karpel, 1982.

In the time domain, Karpel's minimum state smoothing of the aerodynamic coefficient matrix is used to obtain a time-domain approximation of the generalized aerodynamic forces by means of auxiliary state variables. Structural nonlinearities such as friction or free-play are taken into account. This numerical strategy is applied to a compressor blade for different configurations (phase numbers, rotation speeds). The results are compared between the proposed methods and to those of the direct coupling method Sayma et al., 2000 where the structural and the fluid equations are solved alternately at each time step and the assumptions of linearity and harmonic motion are not necessary.

2. Reduced coupled system

A structure with cyclic symmetry is composed of N identical sectors S_0, $S_1, \ldots, S_{N-1}$ which close up on themselves to form a circular system. The whole structure is obtained by $N-1$ repeated rotations of a reference sector S_0 through the angle $\beta = 2\,\pi/N$. Each sector is limited by a left and a right frontier L_l and L_r with the adjacent sectors. The fluid surrounding the structure is also assumed to have the same cyclic symmetry while the applied external forces can vary arbitrarily from one sector to another sector.

Using the cyclic symmetry properties, the motion equation of the structure comes down to N motion equations of the reference sector S_0, in terms of the travelling wave coordinates and with the appropriate second members and boundary conditions. Only sector S_0 has then to be modelized and, after a finite element discretization, the following reduced matrix systems will be solved to obtain the vector of the travelling wave coordinates $\mathbf{u}_n = \mathbf{u}_n(S_0, t)$ of sector S_0, for each phase number $n = 0, \ldots, N-1$ and with $\sigma_n = n\,\beta$:

$$\mathbf{K}\,\mathbf{u}_n \;+\; \mathbf{C}\,\dot{\mathbf{u}}_n \;+\; \mathbf{M}\,\ddot{\mathbf{u}}_n = \mathbf{f}_{an}(\mathbf{u}_n, \dot{\mathbf{u}}_n) \;+\; \mathbf{f}_n \;+\; \mathbf{r}_n, \tag{1}$$

$$\mathbf{f}_{an} = \frac{1}{N}\sum_{k=0}^{N-1} \mathbf{f}_a(S_k)\,\mathrm{e}^{-\mathrm{i}\,k\,\sigma_n} \quad \text{and} \quad \mathbf{f}_n = \frac{1}{N}\sum_{k=0}^{N-1} \mathbf{f}(S_k)\,\mathrm{e}^{-\mathrm{i}\,k\,\sigma_n}, \tag{2}$$

$$\mathbf{u}_{n|L_l} = \mathbf{u}_{n|L_r}\;\mathrm{e}^{\mathrm{i}\,\sigma_n}. \tag{3}$$

$\mathbf{K}$ is the stiffness matrix of sector S_0, including the centrifugal stress stiffening and the spin softening effects, $\mathbf{C}$ is the damping and gyroscopic effect matrix and $\mathbf{M}$ is the mass matrix. $\mathbf{f}_a(S_k)$ is the vector of the aerodynamic forces

applied to sector S_k and which depends on the displacements and the velocities of sector S_k. $\mathbf{f}(S_k)$ is the vector of the other external forces applied to sector S_k, including the centrifugal forces. $\mathbf{r}_n$ is the vector of the interface reactions applied to the frontiers of S_0 with the adjacent sectors, it does not intervene in the solutions of Eqs. (1-3) and it is only present due to the contraints Eq. (3). The cyclic symmetry boundary conditions Eq. (3) are expressed in the cylindrical coordinate system. It is remarked that, the aerodynamic forces $\mathbf{f}_{an}$ applied to the coordinates $\mathbf{u}_n$ in Eq. (1) depend only on $\mathbf{u}_n$ and not on the other travelling wave coordinates $\mathbf{u}_m$ for $m \neq n$, and they are equal to the physical aerodynamic forces $\mathbf{f}_a(S_0, \mathbf{u}_n, \dot{\mathbf{u}}_n)$ induced by $\mathbf{u}_n$ on sector S_0.

For each phase number n, the travelling wave coordinates are expressed as a linear combination of the first m_n complex modes $\mathbf{\Phi}_n$ of the undamped, rotating structure in vacuum (solutions of Eqs. (1-3) without $\mathbf{C}$, $\mathbf{f}_n$ and $\mathbf{f}_{an}$) :

$$\mathbf{u}_n = \mathbf{\Phi}_n \, \mathbf{q}_n . \tag{4}$$

Introducing Eq. (4) in Eq. (1) and premultiplying by ${}^{\mathrm{t}}\overline{\mathbf{\Phi}_n}$, we obtain the reduced coupled system in the m_n complex modal coordinates $\mathbf{q}_n(t)$:

$$\mathbf{K}_{gn} \, \mathbf{q}_n \; + \; \mathbf{C}_{gn} \, \dot{\mathbf{q}}_n \; + \; \mathbf{M}_{gn} \, \ddot{\mathbf{q}}_n = \mathbf{f}_{agn}(\mathbf{\Phi}_n \, \mathbf{q}_n, \mathbf{\Phi}_n \, \dot{\mathbf{q}}_n) \; + \; \mathbf{f}_{gn}, \tag{5}$$

with $\mathbf{K}_{gn} = {}^{\mathrm{t}}\overline{\mathbf{\Phi}_n} \, \mathbf{K} \, \mathbf{\Phi}_n$, $\mathbf{C}_{gn} = {}^{\mathrm{t}}\overline{\mathbf{\Phi}_n} \, \mathbf{C} \, \mathbf{\Phi}_n$, $\mathbf{M}_{gn} = {}^{\mathrm{t}}\overline{\mathbf{\Phi}_n} \, \mathbf{M} \, \mathbf{\Phi}_n$, $\mathbf{f}_{agn} = {}^{\mathrm{t}}\overline{\mathbf{\Phi}_n} \, \mathbf{f}_{an}$ and $\mathbf{f}_{gn} = {}^{\mathrm{t}}\overline{\mathbf{\Phi}_n} \, \mathbf{f}_n$; $\mathbf{K}_{gn}$ and $\mathbf{M}_{gn}$ are the diagonal, real generalized stiffness and mass matrices, $\mathbf{C}_{gn}$ is the complex generalized damping and gyroscopic effect matrix, $\mathbf{f}_{agn}$ and $\mathbf{f}_{gn}$ are the complex generalized aerodynamic and external forces. As the modes $\mathbf{\Phi}_n$ have already satisfied the cyclic symmetry boundary conditions Eq. (3), the latter are already taken into account and by consequent the interface reactions disappear from Eq. (5).

For the aeroelastic stability analysis, all the external forces are null except the aerodynamic forces. The solutions are looked up under the form:

$$\mathbf{u}_n(t) = \tilde{\mathbf{u}}_n \, \mathrm{e}^{p\,t} \quad \text{and} \quad \mathbf{q}_n(t) = \tilde{\mathbf{q}}_n \, \mathrm{e}^{p\,t} \quad \text{with} \quad p = \mathrm{i}\,\omega\,(1 + \mathrm{i}\,\alpha), \tag{6}$$

where ω is the unknown aeroelastic eigenfrequency ($\omega > 0$) and α is the unknown aeroelastic damping factor ($\alpha \in$). Using the hypothesis of linearity, the generalized aerodynamic forces are written as :

$$\mathbf{f}_{agn}(\mathbf{\Phi}_n \, \mathbf{q}_n, \mathbf{\Phi}_n \, \dot{\mathbf{q}}_n) = \tilde{\mathbf{F}}_{agn}(\mathbf{\Phi}_n, p) \, \tilde{\mathbf{q}}_n \, \mathrm{e}^{p\,t}. \tag{7}$$

Substituting Eqs. (6) and (7) in Eq. (5), we obtain the flutter equation :

$$[\; \mathbf{K}_{gn} \; + \; p \, \mathbf{C}_{gn} \; + \; p^2 \, \mathbf{M}_{gn} \; - \; \tilde{\mathbf{F}}_{agn}(\mathbf{\Phi}_n, p) \;] \; \tilde{\mathbf{q}}_n = \mathbf{0}, \tag{8}$$

which is a complex, nonlinear eigenvalue system in which the aerodynamic coefficient matrix $\tilde{\mathbf{F}}_{agn}(\mathbf{\Phi}_n, p)$ depends on the complex modes $\mathbf{\Phi}_n$ and the unknown complex eigenvalue p.

When structural nonlinearities such as friction or free-play are to be introduced in the reduced coupled system Eq. (5), we need to keep some physical coordinates among the generalized coordinates $\mathbf{q}_n$. These "nonlinear" coordinates $\mathbf{u}_{n|NL}$ can be for example the displacements of the reference sector nodes located at the junction between the blade and the disk, where friction dampers are introduced. For this aim, the Craig and Bampton Craig and Bampton, 1968 projection basis $\mathbf{Q}_n = [\mathbf{\Phi}_n,\ \mathbf{\Psi}_{cn}]$ is used instead of the eigenmodes :

$$\mathbf{u}_n = \mathbf{\Phi}_n\ {}_n + \mathbf{\Psi}_{cn}\ \mathbf{u}_{n|NL} = \mathbf{Q}_n\ \mathbf{q}_n. \tag{9}$$

$\mathbf{\Phi}_n$ are the first m_n complex normal modes of S_0 with the cyclic symmetry conditions and with $\mathbf{u}_{n|NL}$ fixed; $\mathbf{\Psi}_{cn}$ are the complex static constraint modes of S_0 with the cyclic symmetry conditions and a unit displacement on one coordinate of $\mathbf{u}_{n|NL}$, while the remaining coordinates of $\mathbf{u}_{n|NL}$ are fixed; and ${}_n$ is the vector of the modal generalized coordinates. By projecting Eq. (1) on $\mathbf{Q}_n$, we obtain a complex reduced coupled system similar to Eq. (5) whose size is the number of eigenmodes m_n plus the number of the nonlinear coordinates.

3. Computation of the generalized aerodynamic forces

The unsteady aerodynamic forces are computed from a basis of m_n real mode shapes $\mathbf{\Psi}$ of the reference sector, for an oscillation frequency ω and an inter-blade phase angle σ_n. By expressing the displacements of the reference sector as a linear combination of the modes $\mathbf{\Psi}$ and by assuming that the structural motion is harmonic and that all the sectors have the same motion with a constant phase angle σ_n between two adjacent sectors, the generalized aerodynamic forces generated by the displacement $\mathbf{u}_n(t)$ are written, by linearity :

$$\mathbf{f}_{agn}(\mathbf{u}_n(t), \dot{\mathbf{u}}_n(t)) = \mathbf{F}_{agn}(\mathbf{\Psi}, \mathrm{i}\,\omega, t)\,\tilde{\mathbf{q}}_n.$$

$\mathbf{F}_{agn}(\mathbf{\Psi}, \mathrm{i}\,\omega, t)$ is the time-dependant aerodynamic coefficient matrix whose (i, j)-term is obtained by projecting the unsteady aerodynamic force generated by the harmonic motion of the j-th mode on the i-th mode :

$$\mathbf{F}_{agn,ij}(\mathbf{\Psi}, \mathrm{i}\,\omega, t) = -\int_{M\in\Sigma} [P_n(M, \mathbf{\Psi}_j, \mathrm{i}\,\omega, t) - P_s(M)]\,\overrightarrow{n}(M)\cdot\overrightarrow{\Psi}_i(M)\,\mathrm{d}\Sigma \tag{11}$$

where P_n is the unsteady pressure generated by the j-th mode $\mathbf{\Psi}_j$, P_s the steady pressure, $\overrightarrow{\Psi}_i$ is the displacement vector of the i-th mode, $\overrightarrow{n}$ is the unit external normal vector to the surface Σ and $\mathrm{d}\Sigma$ is an elementary surface of Σ. Let's introduce the aerodynamic coefficient matrix $\mathbf{A}_n(\mathbf{\Psi}, \mathrm{i}\,\omega, t)$ obtained from the integral in Eq. (10) with P_n and P_s replaced by the associated pressure coefficient $C_P = (P - P_\infty)/(\frac{1}{2}\,\rho_\infty\,V_\infty^2)$, where P_∞, ρ_∞ and V_∞ are the pressure, the density and the velocity of the upstream unperturbed fluid.

By performing a Fourier analysis of $\mathbf{F}_{agn}(\mathbf{\Psi}, \mathrm{i}\,\omega, t)$ and by keeping only the first harmonic term, we have :

$$\mathbf{F}_{agn}(\mathbf{\Psi}, \mathrm{i}\,\omega, t) \simeq \tilde{\mathbf{F}}_{agn}(\mathbf{\Psi}, \mathrm{i}\,\omega)\,\mathrm{e}^{\mathrm{i}\,\omega\,t} = -\tfrac{1}{2}\,\rho_\infty\,V_\infty^2\,\tilde{\mathbf{A}}_n(\mathbf{\Psi}, \mathrm{i}\,\omega)\,\mathrm{e}^{\mathrm{i}\,\omega\,t}.$$

The generalized aerodynamic forces generated by $\mathbf{u}_n(t)$ become :

$$\mathbf{f}_{agn}(\mathbf{u}_n(t), \dot{\mathbf{u}}_n(t)) \simeq \tilde{\mathbf{F}}_{agn}(\mathbf{\Psi}, \mathrm{i}\,\omega)\,\tilde{\mathbf{q}}_n\,\mathrm{e}^{\mathrm{i}\,\omega\,t} = -\tfrac{1}{2}\,\rho_\infty\,V_\infty^2\,\tilde{\mathbf{A}}_n(\mathbf{\Psi}, \mathrm{i}\,\omega)\,\tilde{\mathbf{q}}_n\,\mathrm{e}^{\mathrm{i}\,\omega\,t}. \tag{13}$$

$\tilde{\mathbf{F}}_{agn}(\mathbf{\Psi}, \mathrm{i}\,\omega)$ and $\tilde{\mathbf{A}}_n(\mathbf{\Psi}, \mathrm{i}\,\omega)$ are complex, asymmetric square matrices of dimension m_n. They are computed for n_ω oscillation frequencies $\omega_1, \ldots, \omega_{n_\omega}$.

In the flutter equation (8), the aerodynamic coefficient matrix should be determined from the m_n complex modes $\mathbf{\Phi}_n$. Using the linearity hypothesis, the aerodynamic coefficient matrix $\tilde{\mathbf{F}}_{agn}(\mathbf{\Phi}_n, \mathrm{i}\,\omega)$ generated by $\mathbf{\Phi}_n$ can be extracted from the aerodynamic coefficient matrix computed from the basis of the $2\,m_n$ real vectors formed by the real and imaginary parts of $\mathbf{\Phi}_n$.

The unsteady aerodynamic forces are obtained solving the Euler equations for an ideal gas using an aerodynamic code called CANARI and developed for years at ONERA Dugeai et al., 2000. Because of the cyclic symmetry of the flow, a chorochronic boundary condition is applied to the simulated channel :

$$F(r, \theta + k\,\beta, z, t) = F(r, \theta, z, t + \tfrac{k\,\sigma_n}{\omega}) \quad \text{for } n = 0, \ldots, N-1 \text{ and } \forall k \in .$$

F is any flowfield variable, r is the rotation radius, and θ the azimuthal angle. In a first step, a steady state is computed depending on the rotation speed, on the pressure ratio and on the far-field total temperature, total pressure, and velocity. In a second step, unsteady simulations are performed by forcing an oscillating blade motion at different frequencies. These simulations depend on the steady flowfield previously computed and used as initial conditions, on the inter-blade phase angle, and on the forced motion shape and frequency. A blowing condition is then used to simulate the blade motion. Once a pseudo-steady oscillating state has been reached (no transient effect), a Fourier transform is performed over the pressure to get the unsteady aerodynamic forces.

4. Solution of the coupled system

4.1 Double scanning method

For motions defined by Eq. (6) in the frequency domain, the aerodynamic coefficient matrix $\tilde{\mathbf{A}}_n(\mathbf{\Phi}_n, p)$ defined in Eq. (11) depends only on the quotient $p\,c/V_\infty$ and can be written as $\tilde{\mathbf{A}}_n(\mathbf{\Phi}_n, p\,c/V_\infty)$ where c is a reference length, for exemple the blade chord. Let's define the reduced frequency $\kappa = \omega\,c/V_\infty$.

Using Eq. (11) and denoting $\tilde{\mathbf{A}}'_n(\mathbf{\Phi}_n, pc/V_\infty)$ and $\tilde{\mathbf{A}}''_n(\mathbf{\Phi}_n, pc/V_\infty)$ the real and imaginary parts of $\tilde{\mathbf{A}}_n(\mathbf{\Phi}_n, p\,c/V_\infty)$, the flutter equation (8) can be written

under the form of a non-linear eigenvalue system of dimension $2\,m_n$:

$$\begin{bmatrix} \mathbf{0} & \mathbf{I} \\ -\mathbf{M}_{gn}^{-1}\,\mathbf{K}_{gn}^{*}(p\,c/V_\infty) & -\mathbf{M}_{gn}^{-1}\,\mathbf{C}_{gn}^{*}(p\,c/V_\infty) \end{bmatrix} \begin{Bmatrix} \tilde{\mathbf{q}}_n \\ p\,\tilde{\mathbf{q}}_n \end{Bmatrix} = p \begin{Bmatrix} \tilde{\mathbf{q}}_n \\ p\,\tilde{\mathbf{q}}_n \end{Bmatrix} \quad (15)$$

or $\mathbf{H}(p\,c/V_\infty)\,\mathbf{x} = p\,\mathbf{x}$, with $\mathbf{K}_{gn}^{*}(p\,c/V_\infty) = \mathbf{K}_{gn} + \frac{1}{2}\rho_\infty V_\infty^2 \tilde{\mathbf{A}}'_n(\mathbf{\Phi}_n, p\,c/V_\infty)$ and $\mathbf{C}_{gn}^{*}(p\,c/V_\infty) = \mathbf{C}_{gn} + \mathrm{i}\frac{1}{2}c\rho_\infty V_\infty \tilde{\mathbf{A}}''_n(\mathbf{\Phi}_n, p\,c/V_\infty)/(p\,c/V_\infty)$.

If the damping factor is small ($|\alpha| \ll 1$), we have $p\,c/V_\infty \simeq \mathrm{i}\,\kappa$ and the matrices $\tilde{\mathbf{A}}'_n(\mathbf{\Phi}_n, p\,c/V_\infty)$, $\tilde{\mathbf{A}}''_n(\mathbf{\Phi}_n, p\,c/V_\infty)$ and $\mathbf{H}(p\,c/V_\infty)$ can be approximated by $\tilde{\mathbf{A}}'_n(\mathbf{\Phi}_n, \mathrm{i}\,\kappa)$, $\tilde{\mathbf{A}}''_n(\mathbf{\Phi}_n, \mathrm{i}\,\kappa)$ and $\mathbf{H}(\mathrm{i}\,\kappa)$. Eq. (12) becomes :

$$\begin{bmatrix} \mathbf{0} & \mathbf{I} \\ -\mathbf{M}_{gn}^{-1}\,\mathbf{K}_{gn}^{*}(\mathrm{i}\,\kappa) & -\mathbf{M}_{gn}^{-1}\,\mathbf{C}_{gn}^{*}(\mathrm{i}\,\kappa) \end{bmatrix} \begin{Bmatrix} \tilde{\mathbf{q}}_n \\ p\,\tilde{\mathbf{q}}_n \end{Bmatrix} = p \begin{Bmatrix} \tilde{\mathbf{q}}_n \\ p\,\tilde{\mathbf{q}}_n \end{Bmatrix} \quad (16)$$

or $\mathbf{H}(\mathrm{i}\,\kappa)\,\mathbf{x} = p\,\mathbf{x}$, with $\mathbf{K}_{gn}^{*}(\mathrm{i}\,\kappa) = \mathbf{K}_{gn} + \frac{1}{2}\,\rho_\infty\,V_\infty^2\,\tilde{\mathbf{A}}'_n(\mathbf{\Phi}_n, \mathrm{i}\,\kappa)$, $\mathbf{C}_{gn}^{*}(\mathrm{i}\,\kappa) = \mathbf{C}_{gn} + \frac{1}{2}\,c\,\rho_\infty\,V_\infty\,\tilde{\mathbf{A}}''_n(\mathbf{\Phi}_n, \mathrm{i}\,\kappa)/\kappa$ and $\kappa = \Im\mathrm{m}(p)\,c/V_\infty$. $\mathbf{H}(\mathrm{i}\,\kappa)$ is a real matrix which depends on $\tilde{\mathbf{A}}'_n(\mathbf{\Phi}_n, \mathrm{i}\,\kappa)$, $\tilde{\mathbf{A}}''_n(\mathbf{\Phi}_n, \mathrm{i}\,\kappa)$ and V_∞. The solutions of the approximated eigensystem (13) should be determined for n_V increasing velocities $V_\infty^1, \ldots, V_\infty^{n_V}$ and the frequencies should satisfy $\omega = \Im\mathrm{m}(p) = \kappa\,V_\infty/c$. For each velocity V_∞^k, the following eigensytems are solved for $i = 1, \ldots, 2\,m_n$ and $j = 0, 1, 2, \ldots$, until the convergence on κ is obtained :

$$\mathbf{H}(\mathrm{i}\,\kappa_{i,j})\;\mathbf{x}_{i,j+1} = p_{i,j+1}\,\mathbf{x}_{i,j+1}, \quad \kappa_{i,j} = \omega_{i,j}\,c/V_\infty^k = \Im\mathrm{m}(p_{i,j})\,c/V_\infty^k,$$

where $(p_{i,j}, \mathbf{x}_{i,j})$ are the i-th complex eigenvalue and eigenvector obtained at the j-th iteration. The matrix $\mathbf{H}(\mathrm{i}\,\kappa_{i,j})$ is computed by interpolating $\tilde{\mathbf{A}}'_n(\mathbf{\Phi}_n, \mathrm{i}\,\kappa)$ and $\tilde{\mathbf{A}}''_n(\mathbf{\Phi}_n, \mathrm{i}\,\kappa)/\kappa$ from the tabulated values. It is remarked that the double scanning method is not valid for small velocities since the latter lead to very large reduced frequencies and the extrapolation of $\mathbf{H}(\mathrm{i}\,\kappa_{i,j})$ will be incorrect.

4.2 Minimum state smoothing method

The matrix $\tilde{\mathbf{A}}_n(\mathbf{\Phi}_n, \mathrm{i}\,\omega)$ has been computed for n_κ reduced frequencies $\kappa_1, \ldots, \kappa_{n_\kappa}$ with the assumption of harmonic motion. For arbitrary motions like those defined by Eq. (6), it is necessary to extend the values of the aerodynamic coefficient matrix to an area of the complex plane containing the imaginary axis, i.e. to determine $\tilde{\mathbf{A}}_n(\mathbf{\Phi}_n, p)$ for $p = \mathrm{i}\,\omega(1 + \mathrm{i}\alpha)$ with $\alpha \neq 0$.

The minimum state smoothing method Karpel, 1982 consists in modelling the generalized aerodynamic forces by using a rational approximation and auxiliary state variables :

$$\tilde{\mathbf{A}}_n(\mathbf{\Phi}_n, p) \simeq \mathbf{A}_{n0} + \frac{p\,c}{V_\infty}\,\mathbf{A}_{n1} + \frac{p^2\,c^2}{V_\infty^2}\,\mathbf{A}_{n2} + \frac{p\,c}{V_\infty}\,\mathbf{D}_n \left[\frac{p\,c}{V_\infty}\,\mathbf{I} - \mathbf{R}_n\right]^{-1} \mathbf{E}_n. \quad (18)$$

$\mathbf{A}_{n0}$, $\mathbf{A}_{n1}$, $\mathbf{A}_{n2}$, $\mathbf{D}_n$ and $\mathbf{E}_n$ are matrices with dimensions $(m_n \times m_n)$ for $\mathbf{A}_{n0}$, $\mathbf{A}_{n1}$ and $\mathbf{A}_{n2}$, $(m_n \times n_p)$ for $\mathbf{D}_n$ and $(n_p \times m_n)$ for $\mathbf{E}_n$. $\mathbf{R}_n = \mathrm{diag}(r_1, \ldots, r_{n_p})$ is a diagonal matrix where n_p is the degree of the denominator of the rational function or the number of poles and $r_i < 0$ are the poles. These matrices are computed by using a method of least squares minimization Poirion, 1995.

Using Eq. (14), the flutter equation (8) can be written under the form of a non-linear eigenvalue system of dimension $2\,m_n$:

$$\begin{bmatrix} \mathbf{0} & \mathbf{I} \\ -\mathbf{M}_{gn}^{*-1}\,[\mathbf{K}_{gn}^{*} + \mathbf{G}_n(p)] & -\mathbf{M}_{gn}^{*-1}\,\mathbf{C}_{gn}^{*} \end{bmatrix} \begin{Bmatrix} \tilde{\mathbf{q}}_n \\ p\,\tilde{\mathbf{q}}_n \end{Bmatrix} = p \begin{Bmatrix} \tilde{\mathbf{q}}_n \\ p\,\tilde{\mathbf{q}}_n \end{Bmatrix} \tag{19}$$

or $\mathbf{H}(p)\,\mathbf{x} = p\,\mathbf{x}$, with $\mathbf{K}_{gn}^{*} = \mathbf{K}_{gn} + \frac{1}{2}\rho_\infty\,V_\infty^2\,\mathbf{A}_{n0}$, $\mathbf{C}_{gn}^{*} = \mathbf{C}_{gn} + \frac{1}{2}\rho_\infty\,c\,V_\infty\,\mathbf{A}_{n1}$, $\mathbf{M}_{gn}^{*} = \mathbf{M}_{gn} + \frac{1}{2}\rho_\infty\,c^2\,\mathbf{A}_{n2}$ and $\mathbf{G}_n(p) = \frac{1}{2}\rho_\infty\,V_\infty^2\,(p\,c/V_\infty)\,\mathbf{D}_n\,[(p\,c/V_\infty)\,\mathbf{I} - \mathbf{R}_n]^{-1}\mathbf{E}_n$. The matrices $\mathbf{G}_n(p)$ and $\mathbf{H}(p)$ are complex and depend on V_∞. The nonlinear eigenvalue problem Eq. (15) is solved for n_V increasing velocities $V_\infty^1, \ldots, V_\infty^{n_V}$ by using an iterative process based on the method of successive approximations for finding a fixed point of a function Tran et al., 2003.

In Eq. (14), a vector of n_p auxiliary state variables $\tilde{\mathbf{z}}_n$ have been defined. They satisfy a system of first-order differential equations in the time domain :

$$\dot{\mathbf{z}}_n(t) = (V_\infty/c)\,\mathbf{R}_n\,\mathbf{z}_n(t) + \mathbf{E}_n\,\dot{\mathbf{q}}_n(t). \tag{20}$$

The generalized aerodynamic forces are then written in the time domain as

$$\mathbf{f}_{agn}(\mathbf{\Phi}_n\mathbf{q}_n, \mathbf{\Phi}_n\dot{\mathbf{q}}_n) = -\frac{1}{2}\rho_\infty V_\infty^2 \left(\mathbf{A}_{n0}\mathbf{q}_n + \frac{c}{V_\infty}\mathbf{A}_{n1}\dot{\mathbf{q}}_n + \frac{c^2}{V_\infty^2}\mathbf{A}_{n2}\ddot{\mathbf{q}}_n + \mathbf{D}_n\mathbf{z}_n\right). \tag{21}$$

Combining the reduced coupled system (5) with Eqs. (16) and (17), we obtain a linear system of second-order differential equations of dimension $m_n + n_p$:

$$\begin{bmatrix} \mathbf{K}_{gn}^{*} & \frac{1}{2}\rho_\infty V_\infty^2\,\mathbf{D}_n \\ \mathbf{0} & (V_\infty/c)\mathbf{R}_n \end{bmatrix} \begin{Bmatrix} \mathbf{q}_n \\ \mathbf{z}_n \end{Bmatrix} + \begin{bmatrix} \mathbf{C}_{gn}^{*} & \mathbf{0} \\ \mathbf{E}_n & -\mathbf{I} \end{bmatrix} \begin{Bmatrix} \dot{\mathbf{q}}_n \\ \dot{\mathbf{z}}_n \end{Bmatrix} + \begin{bmatrix} \mathbf{M}_{gn}^{*} & \mathbf{0} \\ \mathbf{0} & \mathbf{0} \end{bmatrix} \begin{Bmatrix} \ddot{\mathbf{q}}_n \\ \ddot{\mathbf{z}}_n \end{Bmatrix} = \begin{Bmatrix} \mathbf{f}_{gn} \\ \mathbf{0} \end{Bmatrix}$$

where $\mathbf{K}_{gn}^{*}$, $\mathbf{C}_{gn}^{*}$ and $\mathbf{M}_{gn}^{*}$ are the same matrices as in Eq. (15). This second-order system is solved using the Newmark numerical integration scheme.

5. Numerical applications

The previously described coupling methods have been applied to a numerical model of a compressor disk composed of 22 large chord blades, for different rotation speeds and phase angles. The structural finite element model of a reference sector with one blade has 19 539 degrees of freedom. The eigenfrequencies and modes in vacuum are computed by using the cyclic symmetry and

by taking into account the stiffening and softening rotational effects. The aerodynamic computations were performed on a two-block structured grid, each block having $61\times18\times30$ points with 60 points on the profile. Figure 1 shows the mesh of one channel of the embedding fluid. For the coupling calculation, the blade is assumed not to have any structural damping. In addition to the indirect coupling methods described in this paper, and for comparison, we also use the direct coupling method in the time domain (Case 1).

5.1 Case 1 : $\Omega = 4066.4$ rpm

The simulations were performed for the following aerodynamic conditions: rotation speed $\Omega = 4066.4$ rpm, upstream total temperature $T_{i1} = 288$ K, upstream total pressure $P_{i1} = 101325$ Pa, pressure ratio $P_2/P_{i1} = 1.05$, phase angle $\sigma_0 = 0\,^\circ$. The steady aerodynamic simulation gives for the inflow a Mach number of 0.5, a velocity of 166 m/s and a mass flow of 462.92 kg/s. Figure 2 shows a shock whose position depends on the applied pressure ratio. The coupled simulations are then performed under transonic conditions.

For the coupling computation, only the first two bending modes of the blade whose frequencies are 97.4 Hz (1F) and 204.3 Hz (2F) are retained to form the projection basis. Unsteady aerodynamic simulations are performed using the mode shapes as oscillating motion shape for the frequencies given in Table 1.

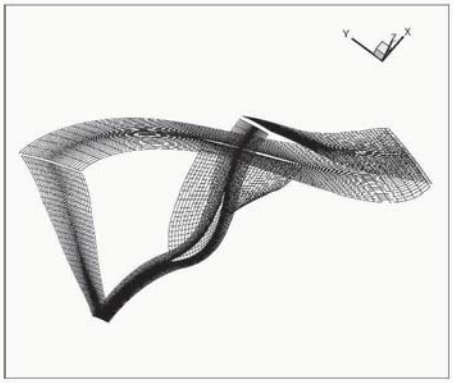

Figure 1 Fluid mesh

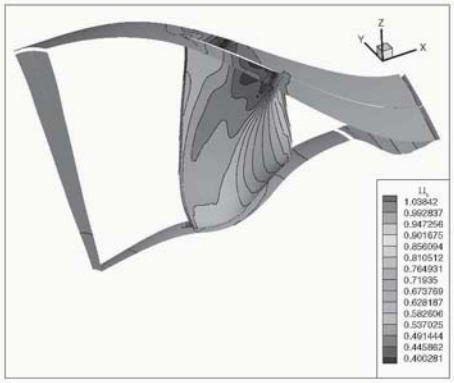

Figure 2 Case 1 – Steady pressure

Table 1 Case 1 – Excitation frequencies

Frequencies f (Hz)	5.28	79.25	97.4	105.7	184.9	204	211.3
Reduced frequencies $\kappa = 2\pi f/V_\infty$	0.2	3.0	3.69	4.0	7.0	7.72	8.0

In order to perform a time simulation, a minimum state smoothing of the generalized aerodynamic forces is performed with a relative error of 0.197%. The time increment is determined to have 60 time steps per period (second mode). An initial velocity is applied to all generalized coordinates. Figure 3 shows the time evolution of both generalized coordinates computed using three

methods : the first method is the indirect coupling in the time domain (smoothing method), the second one is a direct coupling numerical simulation using a grid deformation technique, and the last one is a direct coupling numerical simulation using a blowing condition. The results from the three methods are similar, although the aeroelastic damping computed with the direct simulation using the grid deformation technique is quite a lot smaller than those computed with the other methods. The good agreement between the results of the smoothing method and those of the direct coupling method with a blowing condition can be explained by the fact that a blowing condition was also used in the smoothing method. Table 2 gives the frequencies and the damping factors computed using the three methods. Moreover, the results from the smoothing method in the time domain is similar to the one from the double scanning method in the frequency domain. The time simulation has been performed for an upstream infinite velocity $V_\infty = 166$ m/s.

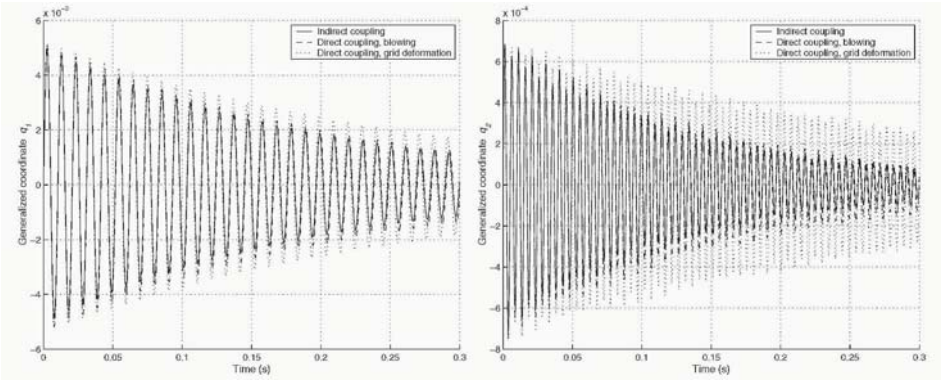

Figure 3 Case 1 – Time evolution of q_1 and q_2

Table 2 Case 1 – Frequencies (Hz) and damping factors of q_1 and q_2 ($V_\infty = 166$ m/s)

	Time domain						Frequency domain	
	Smoothing		Direct (grid deform.)		Direct (blowing)		Double scanning	
	Freq.	Damping	Freq.	Damping	Freq.	Damping	Frequency	Damping
q_1	96.70	0.0082	96.94	0.0061	96.54	0.0077	96.69	0.0085
q_2	203.21	0.0056	203.47	0.0025	203.54	0.0048	203.13	0.0057

5.2 Case 2 : $\Omega = 4516.8$ rpm

A coupling calculation is performed on the same blade at a higher rotation speed for two inter-blade phase angles, $\sigma_0 = 0°$ and $\sigma_1 = 360°/22$. The only changes in the aerodynamic conditions are: rotation speed $\Omega = 4516.8$ rpm, pressure ratio $P_2/P_{i1} = 1.12$. For the inlet flow, the Mach number is 0.5, the velocity is 166 m/s and the mass flow is 487.95 kg/s. Like in the previous case, the coupled simulations are performed under transonic conditions.

A first coupling calculation is performed for an inter-blade phase angle $\sigma_0 = 0°$. The projection basis is formed by the first two bending modes and the

first torsion modes whose frequencies are respectively 101.7 Hz (1F), 212.8 Hz (2F) and 448.9 Hz (1T). The generalized unsteady aerodynamic forces are computed at the frequencies given in Table 3.

Figure 4 shows the flutter diagrams obtained with the double scanning and the smoothing methods. Both methods give similar results : the blade is stable in the upstream infinite velocity range from 100 m/s to 250 m/s.

A time simulation is performed for an upstream infinite velocity $V_\infty = 166$ m/s with the minimum state smoothing method. The aerodynamic forces are approximated using 6 poles with a relative error of 1.13% . The time increment is determined to have 60 time steps per period (third mode). Figure 5 shows the time evolution of the three generalized coordinates q_1, q_2 and q_3. Table 4 shows a Fourier analysis of those signals. The resulting frequencies and damping factors are similar to those obtained from the computation in the frequency domain (double scanning method).

Table 3 Case 2 – Excitation frequencies

Phase angle $\sigma_0 = 0^\circ$								
Frequencies f (Hz)	0	5.0	70.0	101.7	230.1	448.9	600.0	
Reduced frequencies $\kappa = 2\pi f / V_\infty$	0	0.185	2.59	3.755	8.5	16.58	22.16	
Phase angle $\sigma_1 = 360^\circ/22$								
Frequencies f (Hz)	10.0	20.0	50.0	105.3	139	191.8	278.3	350.0
Reduced frequencies $\kappa = 2\pi f / V_\infty$	0.37	0.74	1.85	3.89	5.26	7.08	10.28	12.93

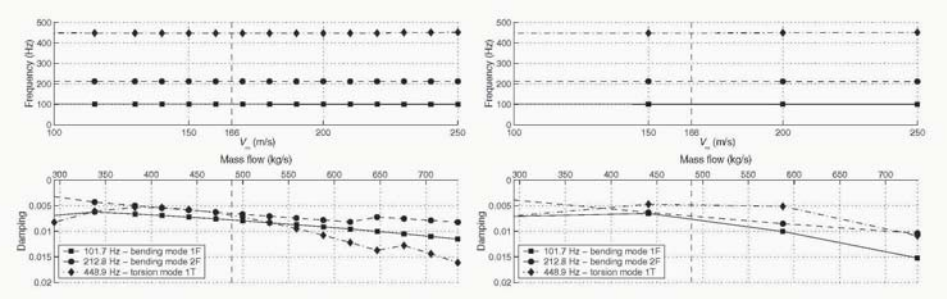

Figure 4 Case 2, σ_0 – Flutter diagrams, double scanning and smoothing

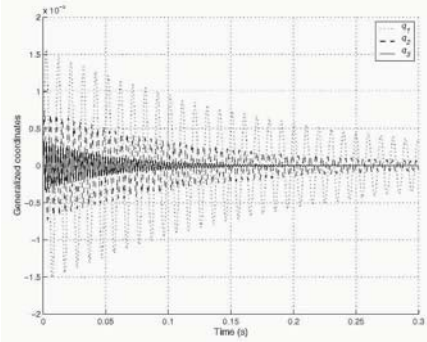

Figure 5 Case 2, σ_0 – Time evolution of q_i

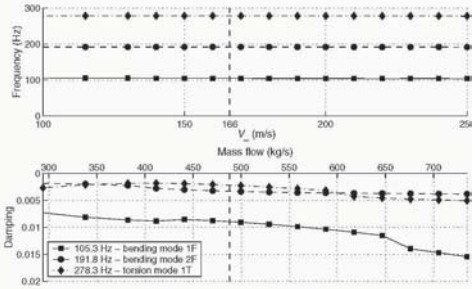

Figure 6 Case 2, σ_1 – Flutter diagram (double scanning)

Table 4 Case 2, σ_0 - Frequencies (Hz) and damping factors ($V_\infty = 166$ m/s)

	Smoothing (time)		Double scanning	
	Freq.	Damp.	Freq.	Damp.
q_1	101.02	0.0080	100.96	0.0080
q_2	212.18	0.0062	211.86	0.0063
q_3	447.00	0.0069	447.21	0.0073

Table 5 Case 2, σ_1 - Frequencies (Hz) and damping factors ($V_\infty = 166$ m/s)

	Smoothing (time)		Double scanning	
	Freq.	Damp.	Freq.	Damp.
q_1	104.92	0.0092	104.14	0.0091
q_2	191.34	0.0031	191.42	0.0034
q_3	277.40	0.0022	277.73	0.0023

A coupling calculation is now performed for an inter-blade phase angle $\sigma_1 = 1 \times 360^\circ/22$. The method is then tested for a non-zero phase angle and for a complex projection basis. The latter is formed by the first two bending modes and the first torsion mode whose frequencies are respectively 105 Hz (1F), 191.8 Hz (2F) and 278.3 Hz (1T). The generalized unsteady aerodynamic forces are computed for the frequencies given in Table 3.

Figure 6 shows the flutter diagram resulting from a computation using the double scanning method. As in the zero phase angle case, the blade is stable in the upstream infinite frequency range from 100 m/s to 250 m/s.

A time calculation is performed for an upstream infinite velocity $V_\infty = 166$ m/s. The time increment is determined to have 60 time steps per period (third mode). The smoothing method uses 8 poles and gives a relative error of 1.18%. As for a zero phase angle, the frequencies and the damping factors resulting from the computations in the time domain (smoothing method) and in the frequency domain (double scanning method) are similar (Table 5).

A non-linear friction force (model of Coulomb) is applied on the blade for the phase angle σ_0. The coupled simulation is performed by projecting the motion equation of the structure on a Craig and Bampton basis which is composed of six normal modes and one static constraint modes, and by using the minimum state smoothing of the generalized aerodynamics forces in the time domain. Figure 7 shows the time evolution of the generalized coordinates q_1 (first normal mode) and q_7 (static mode, on which the friction force is applied) for different intensities of the friction force : 0 N (linear case), 50 N and 500 N. We can see the influence of the intensity of the friction force on the response.

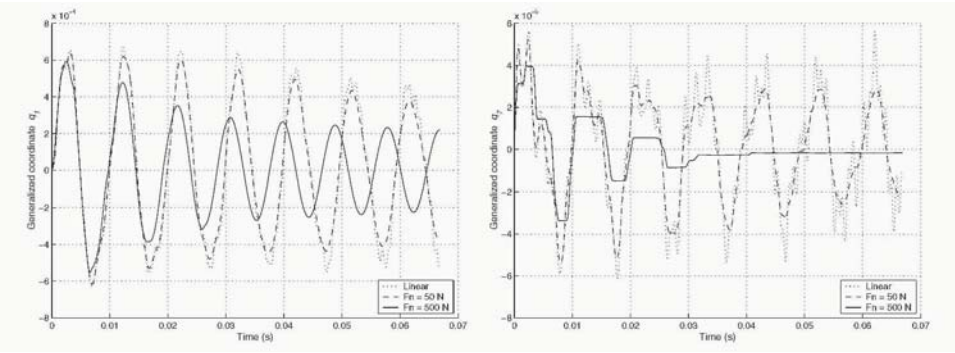

Figure 7 Case 2, σ_0 – Time evolution of q_1 (first normal mode) and q_7 (static mode)

6. Conclusion

Two fluid-structure coupling methods for a rotating bladed disk system based on the cyclic symmetry properties and the projection on the complex modes are presented. The double scanning method is more robust but it is only applicable for solving the flutter equation in the frequency domain. The minimum state smoothing method can be used for both frequency and time domain simulations but its implementation is more complex and it requires more attention and know-how from the user. The main advantage of the proposed indirect coupling method in the time domain is that it is generally less time consuming than the direct coupling method since the aerodynamic calculations are performed only once at the beginning of the simulation and not at each time step. Therefore, the aerodynamic forces do not need to be computed again if the modes that generate them are unchanged and they can be re-used for other computations, for example when the applied external forces change or when we want to study the influence of a friction damper on the stability of the bladed-disk. However, the proposed indirect coupling method is more restrictive and less accurate since it is based on the assumptions of linearized aerodynamics and harmonic motion, which is not the case of the direct coupling method.

The good agreement between the results of the different methods shows that the extension of the proposed coupling methods from aircraft applications to turbomachinary is feasible. However, further validation tests should be carried out under various conditions such as other rotation speeds, phase angles, pressure ratios, viscous fluid etc. The future work consists in numerical simulations of an unstable configuration and the introduction of the blade mistuning.

References

Craig, Jr., R. R. and Bampton, M. C. C. (1968). Coupling of substructures for dynamic analysis. *AIAA Journal*, 6(7):1313–1319.

Dat, R. and Meurzec, J.-L. (1969). Sur les calculs de flottement par la méthode dite du "balayage en fréquence réduite". *La Recherche Aérospatiale*, (133):41–43.

Dugeai, A., Madec, A., and Sens, A. S. (2000). Numerical unsteady aerodynamics for turbomachinery aeroelasticity. In *Proceedings of the 9th International Symposium on Unsteady Aerodynamics, Aeroacoustics and Aeroelasticity of Turbomachines*, Lyon, pages 830–840.

Karpel, M. (1982). Design for active flutter suppression and gust alleviation using state-space aeroelastic modeling. *AIAA Journal of Aircraft*, 19(3):221–227.

Poirion, F. (1995). Modélisation temporelle des systèmes aéroservoélastiques. Application à l'étude des effets des retards. *La Recherche Aérospatiale*, (2):103–114.

Sayma, A. I., Vahdati, M., and Imregun, M. (2000). An integrated nonlinear approach for turbomachinery forced response prediction. Part I: Formulation. *Journal of Fluids and Structures*, 14:87–101.

Tran, D.-M., Labaste, C., and Liauzun, C. (2003). Methods of fluid-structure coupling in frequency and time domain using linearized aerodynamics for turbomachinery. *Journal of Fluids and Structures*, 17(8):1161-1180.

STUDY OF SHOCK MOVEMENT AND UNSTEADY PRESSURE ON 2D GENERIC MODEL

Davy Allegret-Bourdon
Chair of Heat and Power Technology
Royal Institute of Technology, Stockholm, Sweden
davy@energy.kth.se

Torsten H. Fransson
Chair of Heat and Power Technology
Royal Institute of Technology, Stockholm, Sweden
fransson@energy.kth.se

Abstract A flexible generic model has been developed at the Chair of Heat and Power Technology in order to perform flutter experiments in a more fundamental fashion. It is made of engineered flexible material and oscillate in a controlled way at non-uniform amplitude and variable frequencies. Time-resolved measurements of the unsteady surface pressures, the instantaneous model geometry as well as unsteady Schlieren visualizations are performed in order to study the shock wave motion and the aerodynamic load acting over this flexible generic bump. The model oscillates at reduced frequencies from 0.015 to 0.294 at transonic flow condition. The mode shapes of such a flexible bump strongly depends on the excitation frequency of the generic model. Schlieren pictures are obtained for an operating point characterized by an inlet Mach number of 0.63. Moreover, the presented results demonstrate that the phase of shock wave movement towards bump local motion shows a decreasing trend for the third bending mode shapes at reduced frequency higher than k=0.074. At the pressure taps located after the shock wave formation, the phase of pressure fluctuations towards bump local motion presents the same decreasing trend.

Keywords: Fluid-structure interaction, Schlieren, Long line probe, shock wave movement, Unsteady static pressure, first bending mode shape, Flexible generic model

K.C. Hall et al.(eds.),
Unsteady Aerodynamics, Aeroacoustics and Aeroelasticity of Turbomachines, 409–421.

Nomenclature

c_{ax}	[mm]	Axial chord of the generic model
$\widetilde{C}_p$	[-]	Unsteady pressure coefficient, $\widetilde{C}_p = \frac{\Delta P_s}{P_t - P_{s1}} \cdot \frac{1}{h'_{bump}}$
D	[mm]	Test section width
E	[MPa]	Young modulus
f	[Hz]	Excitation frequency
H	[mm]	Test section channel height
y	[mm]	Local generic bump height
y_{max}	[mm]	Maximum generic bump height
h'_{bump}	[-]	Bump bending amplitude, dimensionless with channel heigth
h'_{shock}	[-]	Shock wave amplitude, dimensionless with bump amplitude
k	[-]	Inlet reduced frequency based on the half chord, $k = \pi.f.c_{ax}/v_{ax}$
M_{iso1}	[-]	Inlet isentropic Mach number, $M_{iso1} = \left(\frac{1}{2}(\frac{P_{s1}}{P_t})^{\frac{1}{\gamma}}\right)^{1/2}$
M_{iso2}	[-]	Outlet isentropic Mach number, $M_{iso2} = \left(\frac{1}{2}(\frac{P_{s2}}{P_t})^{\frac{1}{\gamma}}\right)^{1/2}$
P_s	[kPa]	Local static pressure on the bump surface
P_{s1}	[kPa]	Upstream static pressure
P_{s2}	[kPa]	Downstream static pressure
P_t	[kPa]	Upstream stagnation pressure
Q	[kg/s]	Mass flow
Re	[-]	Reynolds number
t	[s]	Instantaneous time
t'	[-]	Time dimensionless with the excitation period, $t' = \frac{t}{T}$
T	[s]	Period of excitation
T_t	[K]	Stagnation temperature
v_{ax}	[m/s]	Axial flow velocity
x	[m]	Bump chord wise location
$\Delta\phi_{bump}$	[Deg.]	Largest phase difference of bump motion for one mode shape
ϕ_{shock}	[Deg.]	Phase lead of shock wave movement towards bump motion
ϕ_p	[Deg.]	Phase lead of pressure fluctuation towards bump motion

1. Introduction

Structure oscillating phenomena occur in many industrial applications in the field of energy technology. Under certain conditions a curved shape located in an uniform flow, such as a blade, an airfoil or the surface of a nozzle, can enter into a self-excited vibration known as flutter. Under flutter condition, aerodynamic loads can rapidly increase the amplitude of vibration of a structure until its failure.

Experiments on controlled vibrating models have been performed by several researchers to investigate such aerodynamic loads and observe the shock wave motion related to it. Kobayashi et al. [1994] studied this relationship on an annular blade row oscillating in torsional mode with interblade phase angle. They drew the conclusion that at an inlet Mach number of 1.19 the shock wave movement significantly changed between the reduced frequencies

of 0.102 and 0.136, and that after this range of reduced frequencies the unsteady force damps the blade oscillation. Fujimoto et al. [1997] studied this unsteady fluid structure interaction on a transonic compressor cascade oscillating in a controlled pitching angle vibration. They noticed that although the amplitude of the shock wave displacement did not change much within the range of this experiment, the phase lag relative to the blade oscillation increases up to almost 90ř as the blade oscillation reduced frequency increases to 0.284. Later, Hirano et al. [2000] performed other experimental campaigns on this transonic compressor cascade oscillating in a controlled pitching angle vibration. They conclude that the shock wave movement has a large effect on the amplitude and the phase angle of unsteady pressures on the blade surfaces; the amplitude of unsteady pressure becomes large upstream of the shock wave but decreases rapidly downstream; the phase angle across the shock wave changes largely for the surfaces facing the flow passages adjacent to the oscillating blade, the amplitude of shock wave movement increases following the increase of the reduced frequency, and the phase angle relative to the blade displacement lags almost linearly as the reduced frequency increases.

In such kind of experiments, a driving system is creating an artificial oscillation of the rigid structure, whose amplitude and frequency can be controlled. The compressor blade of Lehr and Bölcs [2000], for example, is made oscillating in a controlled plunging mode by a hydraulic excitation system. The high-speed pitching vibrator of Hirano et al. [2000] is able to reach a 500Hz frequency of a 2D mode shape controlled oscillation in a linear cascade. In most of the cases, the vibrating structures are designed in metal to be close to real applications. Thus, large amplitudes of vibration at high oscillation frequencies prompt the failure of the structures. Moreover, recent research has presented a 2D blade harmonically driven in a 3D mode shape controlled vibration such as in Queune et al. [2000].

To date, this kind of flutter experimental investigations have been limited to stiff models made of metal, which oscillate in a pitching mode. Rather than studying the complex geometry of a turbomachine and specific industrial applications, the here presented generic experiments are voluntarily not taking into account inertial effects, radial geometry, numerous blades or 3D aspect of the flow occurring in industrial applications. Thus a generic oscillating flexible model is studied in order to reach a better understanding of the physics of the flutter phenomenon under transonic operating conditions.

2. Objectives

The objective is to show the variations of amplitudes and phase lead towards bump motion of both the shock wave movement and the unsteady static

pressure relatively to the reduced frequencies characterizing this experimental study.

3. Description of the experimental set-up

The test facility features a straight rectangular cross section. The oscillating model used in the here presented study is of 2D prismatic shape and has been investigated as non-vibrating in previous studies (Bron et al. [2001] ,Bron et al. [2003]), from where extensive baseline data are available. In order to introduce capabilities for the planned fluid-structure tests, a flexible version of the model was built. Figure 1 shows the way the generic model oscillates in the test section and presents the optical access offered by this test facility. The flow

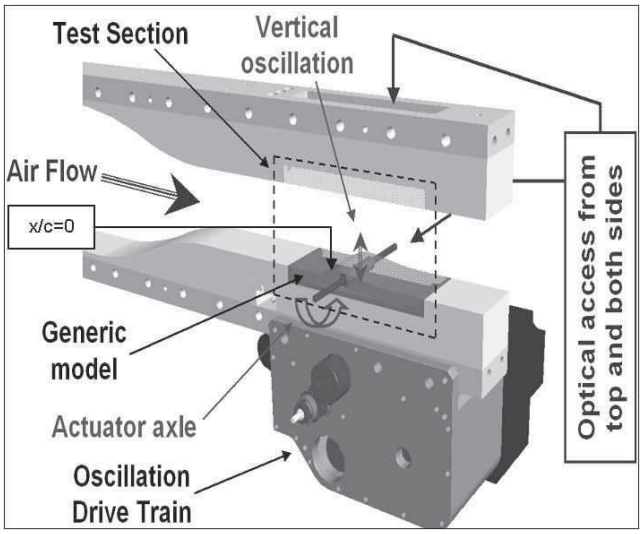

Figure 1. Test facility composition and optical access

entering the test section can be set to different operating conditions characterized by different inlet Mach number, Reynolds number and reduced frequency (Table 1). The generic model is molded of polyurethane, at defined elasticity (E=36.10^6MPa) and hardness (80 shore), by vulcanization over a steel metal bed. As shown in Figure 2, it includes a fully integrated mechanical actuator allowing smooth surface deformations. This oscillating mechanism actuates the flexible model (bump) in a first bending controlled mode shape. While the highest point located at 57% of the chord vibrates in a sinusoidal motion of 0.5mm amplitude, the two edges of the chord stay fixed. A 1D laser sensor measures the model movement through the optical glass top window in one direction with a bandwidth of 20kHz and a resolution of +/-0.01mm. Time-

Table 1. Operating fbw parameters

Mass fbw (4bar, 303K)	Q=4.7kg/s
Stagnation temperature	$303K \leq T_t \leq 353K$
Test section height	H=120mm
Test section width	D=100mm
Generic model axial chord	$c_{ax} = 120mm$
Oscillating frequency range	$10Hz \leq$f$\leq 500Hz$
Isentropic Mach number at the inlet of the test section	$0.6 \leq M_{iso1} \leq 0.67$ (subsonic) (transonic)
Reynolds number for a characteristic length of 650mm	$43.10^3 \leq$Re$\leq 27.10^6$
Reduced frequency based on the half chord for $M_{iso1} = 0.63$	$0.01 \leq$k≤ 0.66

Table 2. Long line probe measurements performed

Encoder accuracy on the position of the camshaft	$\pm$10.8Deg.
Inner diameter of the 15 Tefbn tubes	$0.9mm$
Length of the 15 Tefbn tubes	$0.5m$
Number of Kulite fast response transducers	15
Inner diameter of the 15 long lines	1.3mm
Length of the 15 long lines	5m
Amplitude of the first bending mode shape	$\pm$0.5mm
Average maximum height of the generic model	$h_{max} = 10mm$
Tested excitation frequencies range	10Hz$\leq$f$\leq$200Hz
Tested reduced frequency based on the half chord for $M_{iso1} = 0.63$	$0.015 \leq$k≤ 0.294

resolved pressure measurements are performed on the oscillating surface using pressure taps and Kulite fast response transducers. To achieve this, Tefbn tubes are directly moulded in the 2D flexible generic model and plugged to the Kulite transducers mounted with the long line probe technique far from the oscillating measured surface (Schäffer and Miatt [1985], see Table 2). These fast response transducers deliver signals with delays and large damping but exempt of resonance effect. The delays, damping, tubes vibrations and tubes elongations have been carefully calibrated. All components of this test facility are fully described in Allegret-Bourdon et al. [2002]. The test section offers optical access from three sides (Figure 1). While the instantaneous model shape is scanned using the geometry measurement system through the top window, Schlieren measurement can be performed using the access through two sides windows. A high-speed video camera produces the Schlieren videos with a sampling frequency of 8kHz.

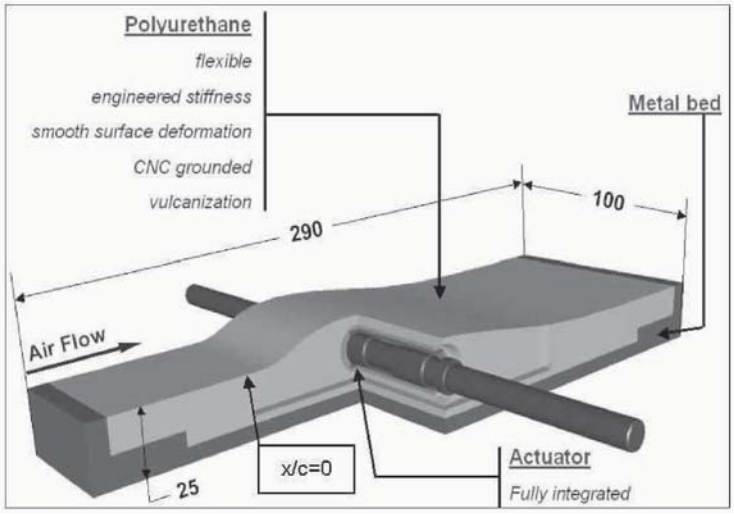

Figure 2. Cut view of the generic model (bump)

4. Experimental results

4.1 Description of the operating condition

In these experiments, inlet and outlet time averaged isentropic Mach numbers are set and a time averaged "lambda" shock wave is generated over the generic model surface at 67% (+/-1%) of the bump chord. Figure 3 shows a typical shape of the shock wave created during those experiments. To define this operating condition, the stagnation pressure and the stagnation temperature of the flow are measured ($P_t = 159kPa$ at $T_t = 305K$) at ten chords upstream and the corresponding isentropic inlet Mach number is calculated ($M_{iso1} = 0.63$). The downstream static pressure is measured on the ground wall and allows calculation of a downstream isentropic Mach number $M_{iso2} = 0.61$ at two chords after the generic model. Figure 4 shows the chord wise distribution of local static pressures for the same operating condition. The generic model acts as a contraction of the channel. M_{iso2} decreases until 10% of the chord and then increases until 50% of the chord where the flow speed is maximal. Then M_{iso2} decreases through the shock wave formation. Because of the manufacturing method, the pressure taps are not exactly perpendicular to the surface and thus do not measure the exact static pressure profile as well as the unsteady pressure fluctuations.

Figure 4 describes the way the generic model is oscillating. A regular repartition of the amplitudes along the bump half chords shows a maximal deformation at $x/c_{ax} = 0.47$. Due to its flexible nature, a first bending mode shape

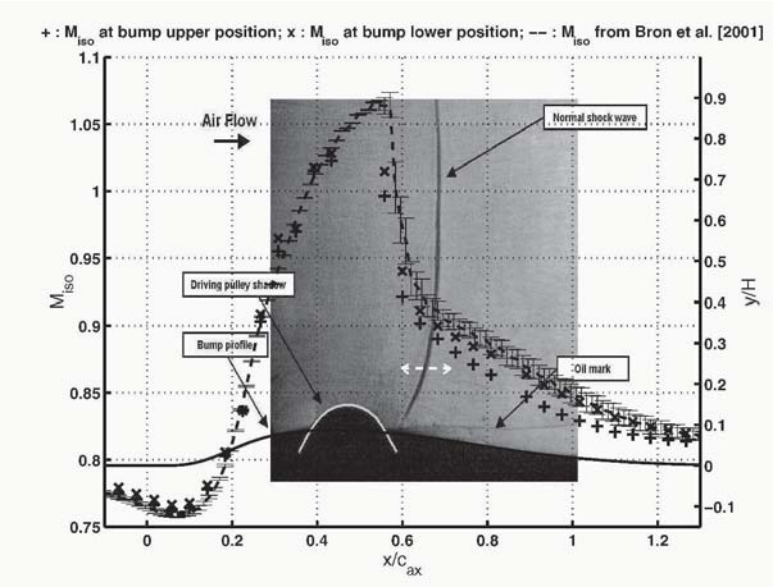

Figure 3. Schlieren picture of the shock wave created in the test section ($M_{iso1} = 0.63$, $M_{iso2} = 0.61$) and isentropic Mach number profile at upper and lower bump positions

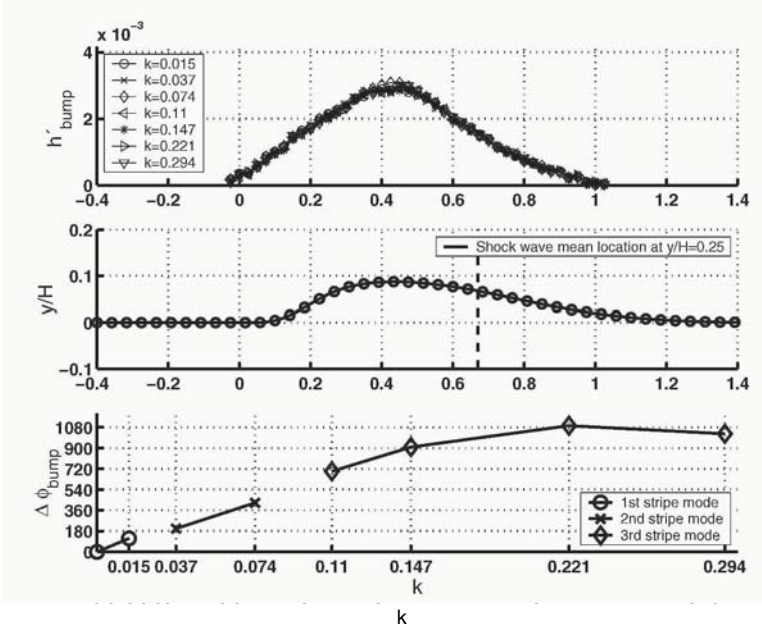

Figure 4. Description of the bump oscillations for all operating flow conditions

at k=0.015 changes in a second bending mode shape at k=0.074, and reaches a third bending mode shape at higher reduced frequencies. At the mean shock wave location $x/c_{ax} = 0.67$, the local geometry presents a phase towards bump top motion. This phase is 20Deg. at k=0.015, 45Deg. at k=0.037, 120Deg. at k=0.074, -180Deg. from k=0.11 to k=0.147, -45Deg. at k=0.221 and -90Deg. at k=0.294.

4.2 Schlieren pictures over one period of shock wave oscillation

At this operating condition, the generic bump is controlled-oscillated in bending mode shapes at frequency between 10 and 200Hz. For each oscillating frequency, the synchronized data of the bump motion, shock wave movement and static pressure fluctuations are acquired. The shock wave motion is measured at one vertical location corresponding to 15mm ($y/H = 0.25$) over the top of the bump neutral position (it is symbolized by the white dashed arrows in Figure 3). Figure 5b shows successive pictures of this shock wave oscillating at 10Hz oscillation frequency. A reference line indicates the mean location of the shock wave (67% of the bump chord). From t'=0 to t'=0.250, the shock wave moves through its mean position in an upstream direction. From t'=0.500 to t'=0.750, the shock wave moves again through its mean position in a downstream direction. Due to the sinusoidal oscillation of the bump, the shock wave

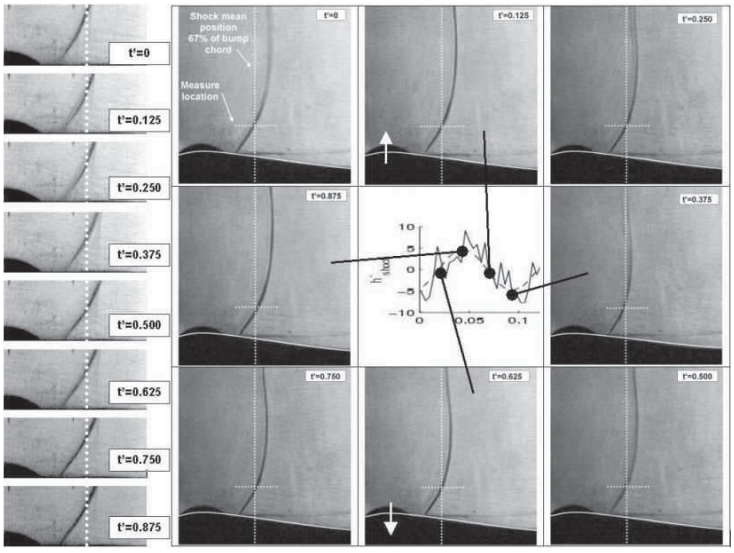

Figure 5. Schlieren pictures of the shock wave oscillation cycle at a) f=200Hz and b) f=10Hz perturbation frequencies

stays a longer time in the two extreme positions (upstream and downstream) and crosses quickly its mean position during one period at 10Hz bump oscillatory frequency. Figure 5a shows in the same way one oscillation of the vertical part of the shock wave at 200Hz excitation frequency. These pictures demonstrate a movement close to be sinusoidal.

4.3 Power spectra of pressure fluctuation, bump motion and shock wave movement

Time-variant signals and corresponding power spectra of pressure fluctuations, bump top motions and shock wave movements are shown in Figure 6 for three bump oscillatory frequencies (10Hz, 75Hz and 200Hz). Both pressure fluctuation and shock wave motion signals seem to follow the shape of the sinusoidal signal generated by the bump displacement at the oscillatory frequencies of 10Hz, 75Hz and 200Hz. At these three excitation frequencies, the pressure fluctuation and shock wave motion power spectra show the same clear fundamental harmonic. The bump top location movement power spectra contains one supplementary higher harmonic component that is not shown here. It does not exist in the power spectra of the pressure fluctuation and shock wave motion signals. It is interpreted as being linked to external mechanical vibrations coming from the oscillation drive train and the wind tunnel. All three oscillations seem to be of a sinusoidal type after ensemble averaging posttreatment.

4.4 Schlieren visualization results

Figure 7 characterized the measured oscillations of the shock wave up to k=0.294. The mean location of the shock stays the same for all excitation frequencies. Moreover one can notice that the amplitude of the shock wave oscillations increases slightly from 0.015 to 0.294. The first bending mode shape at k=0.015 is characterized by a phase lag towards bump motion close to 315Deg., and the phases range between 30Deg. and 90Deg. for the second bending mode shape from k=0.03 to k=0.074. The phase decreases significantly from 270Deg. to almost 0Deg. at reduced frequencies higher than k=0.089 for what has been considered as a third bending mode shape.

4.5 Unsteady pressure results

The unsteady pressure fluctuations are measured along the bump and the corresponding unsteady pressure coefficient and phase leads towards bump motion are deduced for five chosen pressure taps. The amplitudes of the unsteady pressures fluctuations shift significantly at the reduced frequency k=0.221 for the pressure taps located 20% upstream and downstream of the

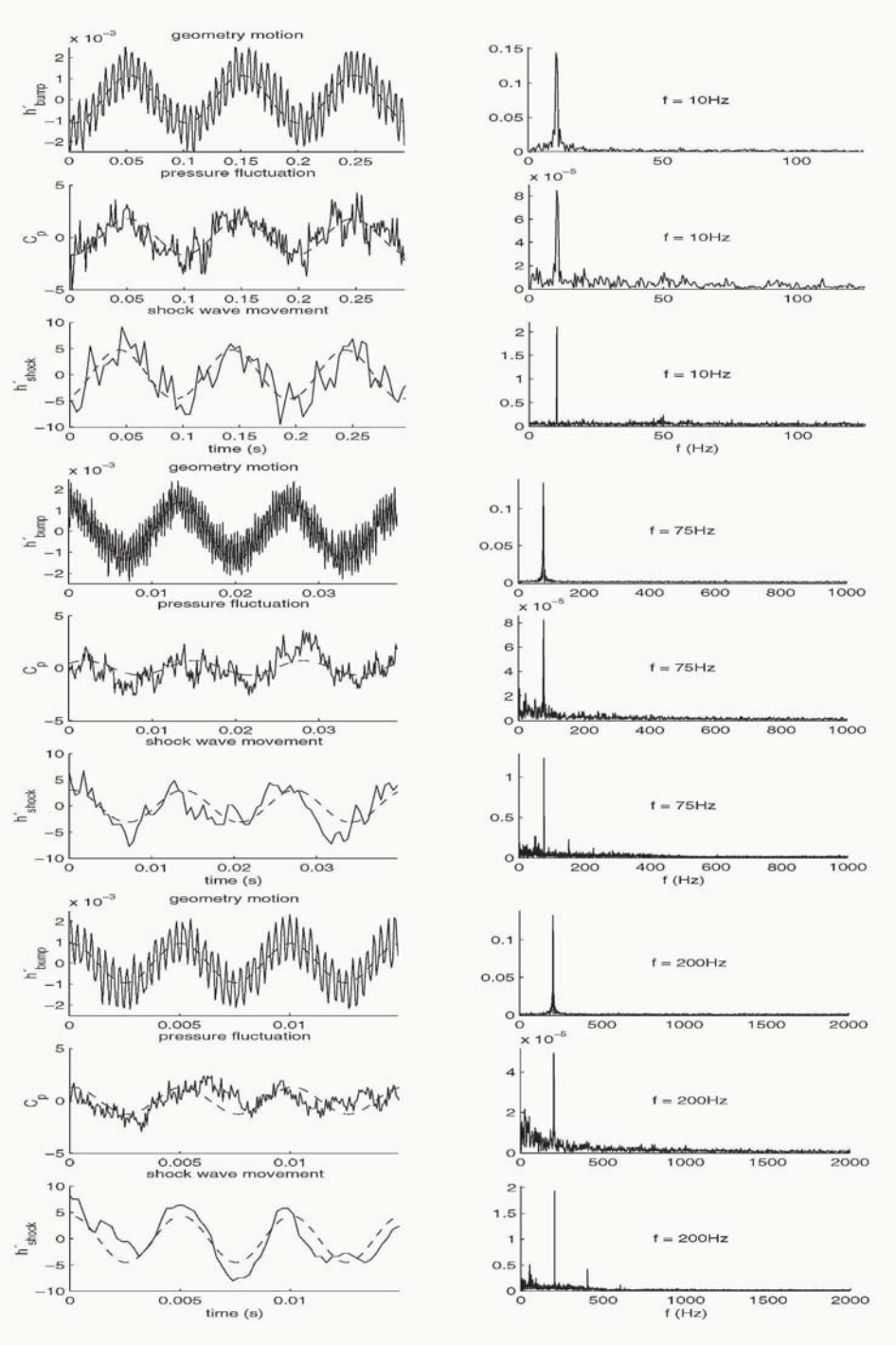

Figure 6. Time-variant and power spectra of static pressure, shock wave movement and bump top motion at 10Hz, 75Hz and 200Hz perturbation frequencies

bump axial chord as shown in Figure 8. Moreover the unsteady pressure coefficients remain stable and range between 2 and 4 for the three pressure taps located within 40% to 80% of the bump axial chord. The phase lead towards bump motion of the static pressure fluctuations range between 90Deg. and 180Deg. for the pressure taps located before the bump max height, and between -180Deg. and 90Deg. for the pressure taps located after the max bump height. At the pressure tap located close to the shock wave mean location (67% of the bump chord) and at y/H=0.25, the phase leads towards bump motion follow the same decreasing trend. In comparison with the shock wave motion phase variation, a global decrease in phase close to 270Deg. is observed for the pressure taps located after the shock wave.

5. Conclusion

Phase relations among oscillatory bump motion, shock wave movement and unsteady pressure fluctuations are investigated in the case of a flexible generic model controlled-oscillated in bending mode shapes at an inlet Mach number of 0.63, over a range of reduced frequencies from 0.015 to 0.294. The following conclusions are drawn:

- The mode shapes of such a flexible bump strongly depends on the excitation frequency of the generic model.

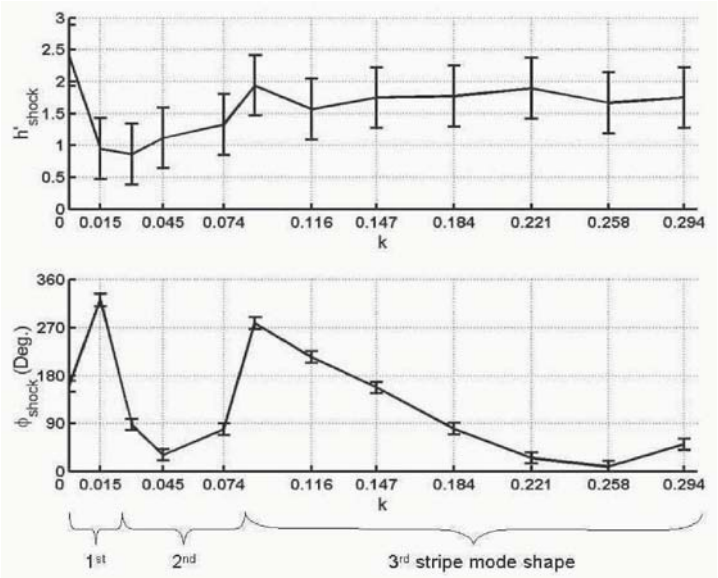

Figure 7. Variation of shock wave movement towards bump motion against the inlet reduced frequency

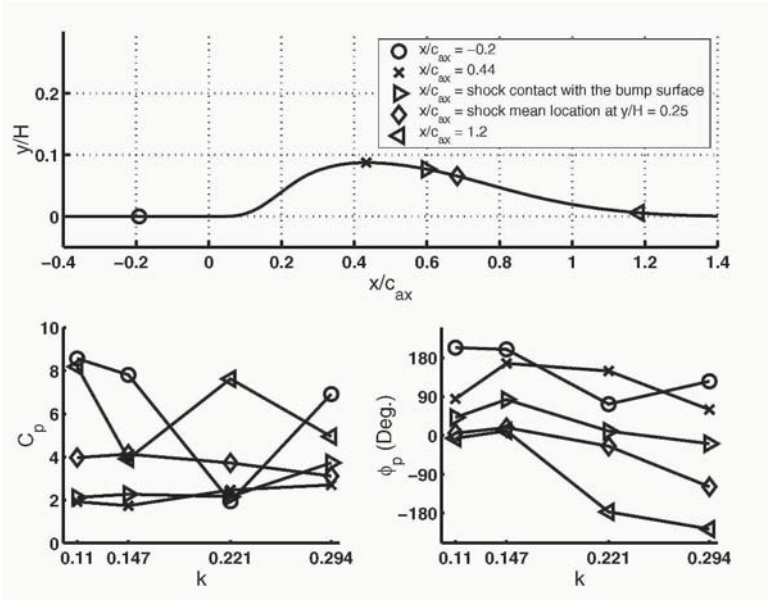

Figure 8. Chord wise static pressure fluctuations at reduced frequencies from k=0 to k=0.294 at $M_{iso1} = 0.63$

- The phase of shock wave movement towards bump local motion shows a decreasing trend for the third bending mode shapes at reduced frequency higher than k=0.074.
- At the pressure tap located after the shock wave formation (67% of the bump chord), the phase of pressure fluctuations towards bump local motion presents the same decreasing trend as for the shock wave movement analysis.
- For those same pressure taps, lower and stable pressure coefficients are also observed.

Acknowledgements

The present research was accomplished with the financial support of the Swedish Energy Agency research program entitled "Generic Studies on Energy-Related Fluid-Structure Interaction" with Dr. J. Held as technical monitor. This support is gratefully acknowledged. The authors would also like to thank O. Bron and D. Vogt of the Chair of Heat and Power Technology in KTH for their advices related to this project.

References

Allegret-Bourdon, D., Vogt, D. M., Fransson, T. H. [2002] *A New Test Facility for Investigating Fluid-Structure Interactions Using a Generic Model,* Proceedings of the 16th Symposium on Measuring Techniques in Transonic and Supersonic Flow in Cascades and Turbomachines, Cambridge, UK.

Bron, O., Ferrand P., Fransson T. H., Atassi H. M., [2001] *Non linear Interaction of Acoustic waves with Transonic Flows in Nozzle,* 7th AIAA/CEAS Aeroacoustics Conference Maastricht, 28-30 May, 2001. AIAA-2001-2247.

Bron, O.; Ferrand P.; Fransson T. H.; [2003] *Experimental and numerical study of Non-linear Interactions in 2D transonic nozzle Flows,* Proceedings of the 10th International Symposium of Unsteady Aeroacoustics, Aerodynamics and Aeroelasticity of Turbomachines, Durham, USA.

Fujimoto, I., Hirano, T., Tanaka, H., [1997] *Experimental Investigation of Unsteady Aerodynamic Characteristics of Transonic Compressor Cascades,* Proceedings of the 8th International Symposium of Unsteady Aeroacoustics, Aerodynamics and Aeroelasticity of Turbomachines, Stockholm, Sweden.

Hirano, T., Tanaka, H., Fujimoto, I., [2000] *Relation between Unsteady Aerodynamic Characteristic and Shock Wave Motion of Transonic Compressor Cascades in Pitching Oscillation Mode,* Proceedings of the 9th International Symposium of Unsteady Aeroacoustics, Aerodynamics and Aeroelasticity of Turbomachines, Lyon, France.

Kobayashi, H., Oinuma, H., Araki, T., [1994] *Shock Wave Behaviour of Annular Blade Row Oscillating in Torsional Mode with Interblade Phase Angle,* Proceedings of the 7th International Symposium on Unsteady Aerodynamics and Aeroelasticity of Turbomachines, Fukuoka, Japan.

Lehr, A., Bölcs, A., [2000] *Investigation of Unsteady Transonic Flows in Turbomachinery,* Proceedings of the 8th International Symposium of Unsteady Aeroacoustics, Aerodynamics and Aeroelasticity of Turbomachines, Lyon, France.

Queune, O. J. R., Ince, N., Bell, D., He, L., [2000] *Three Dimensional Unsteady Pressure Measurements for an Oscillating Blade with Part-Span Separation,* Proceedings of the 8th International Symposium of Unsteady Aeroacoustics, Aerodynamics and Aeroelasticity of Turbomachines, Lyon, France.

Schäffer, A., Miatt, D. C., [1985] *Experimental evaluation of heavy fan high-pressure compressor interaction in three-shaft engine; Part1 - experimental set-up and results,* Journal Eng for Gas Turbines and Power 107: 828-833.

NUMERICAL UNSTEADY AERODYNAMICS FOR TURBOMACHINERY AEROELASTICITY

Anne-Sophie Rougeault-Sens and Alain Dugeai
Structural Dynamics and Coupled Systems Department
Office National d'Études et de Recherches Aérospatiales
B. P. 72, 29 avenue de la Division Leclerc, 92322 Châtillon Cedex, France
Anne-Sophie.Sens_Rougeault@onera.fr, Alain.Dugeai@onera.fr

Abstract This paper presents ONERA's recent advances in the experimental and numerical understandings about the aeroelastic stability of aeronautical turbomachineries. Numerical features of a quasi-3D and a 3D Navier-Stokes unsteady aeroelastic solver are discussed: turbulence models, grid deformation techniques, specific boundary conditions, dual time stepping. A dynamically coupled fluid-structure numerical scheme is presented. Isolated profile, rectilinear cascades computational results are compared to experimental data. Results of aeroelastic Navier-Stokes computations for 3D fans are shown.

Keywords: fluid-structure coupling, aeroelasticity, turbomachinery

1. Introduction

For several years, ONERA has been interested in aeronautical turbomachinery aeroelasticity studies. The goal of this research has been to improve the experimental and numerical knowledge about the aeroelastic stability and forced response of aeronautical turbomachineries.

One of the main challenges in this matter concerns the prediction of the aeroelastic stability of fans, especially in the case of the transonic regime. In this case, the dynamic behavior of the boundary layer needs to be accurately predicted using RANS numerical modeling with transport equations turbulence models. Numerical simulations have to be performed in a deforming grid framework using an Arbitrary Lagrangian Eulerian formulation.

In order to perform validations of the developed numerical tools, several unsteady data bases were built first for an isolated profile, and then for a rectilinear cascade. Theses databases have been extensively used to conduct numerical unsteady Navier-Stokes aeroelastic validations.

Another point concerns computational time reduction. Unsteady aeroelastic Navier-Stokes computations are extremely time-consuming due to the small

K.C. Hall et al. (eds.),
Unsteady Aerodynamics, Aeroacoustics and Aeroelasticity of Turbomachines, 423–436.

time-step needed to keep the numerical scheme stable in the small boundary-layer cells. This is the reason why the numerical technique of dual time-stepping has been implemented in the various unsteady Navier-Stokes codes used at ONERA. This technique allows one to reduce the time of aeroelastic Navier-Stokes computations in such a way that simulations that would have been unaffordable using global time stepping are now possible.

The last purpose of this paper is to show some results for direct fluid-structure coupling simulations. A coupled scheme using Newmark's time discretization has been developed and implemented in our aeroelastic Navier-Stokes codes (Girodroux et al.,2003). Coupled time domain simulations have been performed in the case of a compressor fan blade.

This paper presents some of the unsteady aerodynamic numerical developments and results of the experimental campaigns. Some results of the validation processes of the 2.5D and 3D aeroelastic Navier-Stokes codes will be detailed. An example of a dynamically coupled 3D Navier-Stokes fluid-structure computation will be given.

2. 3D Unsteady aerodynamics solver features

In this section, we present the numerical features of the ALE Navier-Stokes code Canari (Vuillot et al., 1993). This 3D code solves Euler and Reynolds-averaged Navier-stokes equations in multi-block structured grids.

2.1 Space and time ALE discretization for the mean flow

Unsteady Navier-Stokes computations have to be performed in a moving grid framework. An ALE (Arbitrary-Lagrangian-Eulerian) numerical scheme has therefore been developed. The spatial discretization is based on a centered finite volume approach. The fluid motion equations are written in a frame, which rotates at circular frequency Ω. In this frame, the grid is moving at velocity V_g :

$$\frac{d}{dt}\int_{V(t)} QdV + \int_{\partial V(t)} \Big[[F_c[Q,V_g] + F_d[Q,gradQ]\Big] d\Sigma = \int_{V(t)} T[Q]dV$$

where $Q = (\rho, \rho W, \rho E)^t$ is the unknown field vector, $F_c[Q,V_g]$ the convective flux, $F_d[Q,gradQ]$ the diffusive flux and $T[Q]$ the source term. W is the relative velocity of the fluid and E the relative total energy in the rotating frame.

The time integration (Jameson et al.,1981) is performed using a Jameson-like four stage Runge-Kutta scheme. Second and fourth order artificial viscosity terms are added to the original scheme in order to obtain suitable dissipative

properties. The implicit spectral radius method of Lerat (Lerat et al., 1982) is used to increase the stability domain.

2.2 Mesh deformation techniques

Numerical techniques have been developed at ONERA for 2D and 3D mesh deformation (Dugeai et al., 2000). They are based on a linear structural analogy, with discrete spring networks or continuous elastic analogy. A finite element formulation is used, and special features allow the reduction of the size of the problem, especially in the Navier-Stokes case.

In the case of the spring analogy, two different techniques have been developed. The first one is the method proposed by Batina (Batina, 1989), and the second one is an extension in which the 3 components of the displacement vector are coupled.

In the case of the continuous elastic analogy, 8-node hexahedral finite elements are used to discretize the problem of the deformation of a linear elastic medium. The local stiffness matrix is computed using a numerical Gauss integration procedure with a cheap but not exact one Gauss point integration, which leads to Hour-Glass modes terms. A special procedure is used to remove the singularity of the stiffness matrix, giving satisfactory enough results for the grid deformation purpose.

For both approaches, spring network or elastic material analogy, the static equilibrium of the discretized system leads to the following linear system:

$$K_{ii}\, q_i \;=\; -K_{if}\, q_f$$

where q_i and q_f are respectively the induced and prescribed displacement vectors. As the stiffness matrix is positive definite, the system is solved using a pre-conditioned conjugated gradient method. The technique has been implemented in the case of multi-block structured grids. The full mesh deformation is defined as a sequence of individual block deformations. Additional conditions are set on the boundaries to impose zero or prescribed displacement values, and to get a continuity of the deformations at block interfaces.

A macro-mesh technique is used for large grid sizes, which is often the case in 3D Navier-Stokes computations. The macro-mesh is defined from the original one by packing several cells, typically 2, 3, or 5 cells, in each direction. In the case of Navier-Stokes meshes, the whole boundary layer region is packed, in normal direction, in a single macro-cell. The coarse macro-mesh is then deformed using the structural analogy techniques, and the inner node displacements are finally interpolated in each macro-cell.

2.3 Specific chorochronic boundary condition

In order to reduce the size of the unsteady harmonic response computations, a specific time-space periodicity boundary condition is used for the turbomachinery numerical simulations. The cascade is supposed to be made of N geometrically and structurally identical blades. Therefore, using this boundary condition, only a single channel needs to be meshed and computed for various inter-blade phase angles, in order to obtain the values of the unsteady aerodynamic forces for the complete cascade.

The chorochronic boundary condition is applied between the upper and lower boundaries of the channel. This condition reads:

$$F(x, R, \theta, t) = F(x, R, \theta + j\frac{2\pi}{N}, t + j\sigma)$$

where F is any function, θ the azimuthal angle and σ the inter-blade phase angle. σ is defined by $\sigma = 2\pi\frac{n}{N}$ where $0 < n < N - 1$

In order to reduce the storage, the flow field at the chorochronic boundaries is simply stored at a reduced number of time steps during the cycle. The field at inner time steps is then rebuilt using a specific time interpolation technique.

2.4 Turbulence models

Several turbulence models are available. The first one is the mixing length turbulence model of Michel. It gives an expression of the turbulent viscosity as a function of a mixing length depending on the local distance from the wall and on the boundary layer thickness.

The second one is the one-equation model of Spalart-Allmaras (Spalart et al., 1992). In this case, one transport equation for the kinematic turbulent viscosity ν_t is added to the set of mean flow equations. Several algorithms may be used, with either strong or weak coupling between mean flow and turbulent equations at each time step.

The third model is the Launder-Sharma $k\epsilon$ two-equation model. Using this model, the mean flow equations are closed by two additional equations for the turbulence kinetic energy and for its dissipation rate. Low-Reynolds number corrective terms are used.

The time-step is adapted to ensure the stability of the conservative turbulent equations. Numerical 2nd and 4th order viscosity terms are added as well as limiting functions for the turbulent variables.

In the following numerical validations, only the Spalart-Allmaras model will be considered.

2.5 Dual time stepping implementation

2.5.1 Dual time stepping interest. Aeroelasticity and fluid-structure coupling computations are usually performed using a very small global time step value. This is especially true when studying low frequency phenomena. Therefore a very large number of iterations is required, and this leads to very expensive computations. In the viscous case, large and very refined meshes are used, and the time step requirements for numerical stability are even more critical. Moreover, moving meshes computations are required, which increases CPU costs.

This is the reason why the use of dual time stepping for Navier-Stokes aeroelastic computations becomes very interesting. The physical time step used to describe the unsteady phenomenon is no longer constrained by stability time step values in the smallest cells. At each physical time step, a modified steady problem is solved in a dual pseudo time. Usual convergence acceleration techniques such as local time stepping or multi-grid scheme may be used. Dual local time steps are bounded by specific stability requirements.

As far as moving meshes computations are concerned, the dual time step technique helps to reduce the number of remeshing computations. Dual time iterations are performed at a fixed physical time step, that is to say in a fixed mesh. This is much more important in the case of coupled fluid structure computations, where the position and velocity of the grid is not prescribed, but derives from the resolution of the coupled equations.

2.5.2 Dual time stepping scheme for moving meshes. Let us consider equation $(E) : \dfrac{du}{dt} + f(u) = 0$, where u is a numerical function of time . Writing 2nd order Taylor's expansions for $u(t_n)$ and $u(t_{n-1})$ at time t_{n+1} allows us to write equation (E) at time t_{n+1} as follows :

$$\frac{u(t_{n-1}) - 4u(t_n) + 3u(t_{n+1})}{2\Delta t} + f(u(t_{n+1})) + o(\Delta t) = 0$$

$u(t_{n+1})$ is then obtained as the solution at steady state of a differential equation for the variable u^*, function of the pseudo-time t^*:

$$\frac{du^*}{dt^*} + \frac{u(t_{n-1}) - 4u(t_n) + 3u^*}{2\Delta t} + f(u^*) + o(\Delta t) = 0$$

Pseudo-time t^* is called dual time. The resolution of the unsteady problem is now performed within a system of two time loops. The external one is the physical time loop. The inner one is the dual time loop. The dual time loop is carried out using local time stepping, because it solves a steady state problem. The usual four step Runge-Kutta scheme is used to perform the dual loop res-

olution. Within this loop, the grid is fixed at physical time t_{n+1}. Applying this approach to the conservative fluid equations in moving grid, we obtain:

$$Q^{*(k)} = Q^{*(0)} - \alpha_k \frac{\Delta t*}{V^{n+1}} \left[R_V^{*(k-1)} + \frac{V^{n-1}Q_{n-1} - 4V^nQ_n + 3V^{n+1}Q^{*(k-1)}}{2\Delta t} \right]$$

with $Q^{*(0)} = Q^n$, $Q^{*(n+1)} = Q^{*(4)}$, $\alpha_{k,k=1,4} = (\frac{1}{4}, \frac{1}{3}, \frac{1}{2}, 1)$ and

$$R_V^{(q-1)} = \sum_{i=1}^{6} F^{(q-1)} N_{\Sigma i} - VT_V^{(0)} \quad \text{and} \quad F^{(q-1)} = F_c^{(q-1)} + F_d^{(q-1)} + D^{(0)}$$

In these formulae, Δt and Δt^* denote the physical and dual time steps, respectively . At steady state of the dual loop, the conservative variables vector Q is obtained at time $t^{(n+1)}$. The stability condition for the dual time scheme depends on the value of the physical time step as follows:

$$\Delta t^* < CFL \times \frac{4}{3} \Delta t$$

This condition is added to the those given by the properties of the Jacobian matrices of the convective and viscous fluxes.

3. Direct dynamic coupling using dual time stepping for moving meshes

Direct dynamic coupling methodology for moving meshes depends on the structural model. In the case of a linear or weakly non-linear model, the deformation of the structure may be described using a modal basis. The grid deformation and velocity are then given by a linear combination of modal grid deformations and velocities at any time. The grid motion is interpolated. In the strongly non-linear case, structural deformations and velocities have to be computed at each time step of the coupled system from a finite element model. The grid's motion has to be fully computed at each time step as well.

Assuming now that we use a linear structural model, the dynamic behavior of the structure is properly given by a linear combination of modal deformations. We may write at any time t the vector $\overrightarrow{u}$ of the displacement at node M as:

$$\overrightarrow{u}(M,t) = \sum_i q_i(t)\, h_i(M)$$

where $q_i(t)$ stands for the instantaneous generalized coordinates. Writing the mechanical principle in the modal basis gives :

$$M\ddot{q}(t) + D\dot{q}(t) + Kq(t) = F_A(q, \dot{q}, t)$$

where M, D, K and F_A respectively stand for the mass, damping and stiffness matrices and the instantaneous aerodynamic forces.

3.1 Newmark scheme

Using the variable $Q = (q, \dot{q})^t$ gives a first order in time differential equation:

$$A\dot{Q} + BQ = F \quad \text{with} \quad A = \begin{pmatrix} 1 & 0 \\ 0 & M \end{pmatrix} \quad B = \begin{pmatrix} 0 & -1 \\ K & D \end{pmatrix} \quad F = \begin{pmatrix} 0 \\ F_A \end{pmatrix}$$

At time $t^{n+\frac{1}{2}}$, a second order in time discretization is obtained using Newmark's scheme.

$$A\frac{Q^{n+1} - Q^n}{\Delta t} + B\frac{Q^{n+1} + Q^n}{2} = F(Q^{n+1/2}, t^{n+1/2})$$

With aerodynamic forces being calculated at time $t^{n+\frac{1}{2}}$, a mechanical coupling iteration has to be performed in order to equilibrate generalized coordinate at time t^{n+1}. The following numerical scheme is implemented:

· Modal mesh deformations computation
TIMELOOP: *Physical time loop*
· Generalized coordinates estimate at t^{n+1}
MECALOOP: *Coupled fluid-structure equilibrium loop*
· Grid velocity computation
DUALLOOP: *Dual time loop*
RKLOOP : *Runge-Kutta loop*
· Unsteady Aerodynamic dual step
END RKLOOP
END DUALLOOP
· Generalized coordinates and metric updating at t^{n+1}
END MECALOOP *if convergence criterium is reached*
END TIMELOOP

4. Experimental test

The first test campaign concerned the isolated PFSU profile for which a large amount of well-documented data has been obtained during the experiments located at Onera Modane in the S3 transonic wind tunnel. Steady and unsteady measurements have been performed for inlet Mach numbers of 0.5 to 0.75, with various static incidence angles (0 to 5 degrees) and pitching movements of the profile at a frequency of 40 Hertz. Beside this, the LDV (Laser Doppler Velocimetry) technique was used to assess the velocity profile in the vicinity of the profile, in order to get a proper description of the separated zone, which occurs at the leading edge.

The second test campaign aimed at improving the knowledge of the aerodynamic flow field around the central blade of a straight blade cascade (Leconte et al., 2001). This test took place in ONERA R4 blow-down wind-tunnel for both steady and unsteady configurations. Conventional measurement techniques such as steady and unsteady pressure recording on the surfaces of the blades were used. To acquire a knowledge of the flow velocity field in the channels contiguous to the central blade of the cascade, PIV (Particle Image Velocimetry) technique was used. The test matrix featured various Mach numbers (subsonic,transonic and supersonic), cascade angle-of-attack, plunging and pitching movements of the central blade.

5. Numerical validations

We present first some unsteady Navier-Stokes results obtained with the 2.5D solver for an isolated profile and the rectilinear cascade.

5.1 Isolated PFSU profile

The aerodynamic conditions for this 2D computation are an upstream Mach number value of 0.75, a total pressure of 1108121 Pa, and a total temperature of 299.8 Kelvin. The steady angle-of-attack of the flow is 3 degrees. The chord of the profile is 0.3 meter. The profile is moving in pitch at a frequency of 40Hz, with an amplitude of 0.25 degree. Navier-Stokes steady and unsteady computations were run using the turbulence model of Michel and that of Spalart-Allmaras. We used a 300x100 C-like mesh.

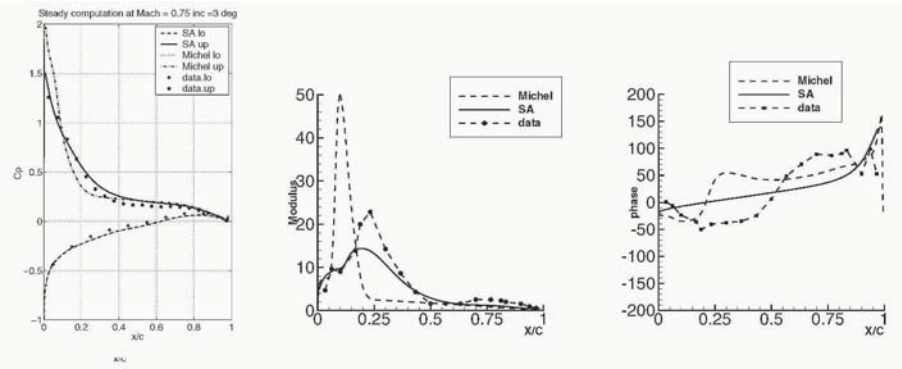

Figure 1 Steady and Harmonic analysis of the pressure coefficient

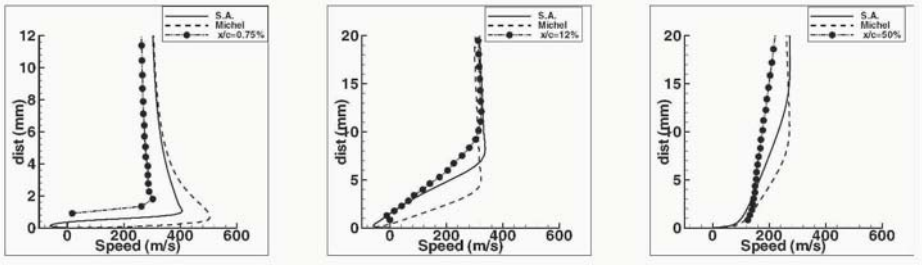

Figure 2 Steady Velocity profiles for the PFSU profiles

The unsteady run needed the computation of 4 periods of about 50000 iterations using a uniform time step at a maximum CFL value of 10. The previous sketch shows the mean and unsteady pressure coefficients on the profile (Fig. 1) and a comparison of steady velocity profiles for three axial positions (Fig. 2). Spalart-Allmaras results and available experimental data compare fairly well. Algebraic turbulent model seems to be insufficient to get a good description of the leading edge separated zone.

5.2 PGRC Cascade

We next present Navier-Stokes computations dealing with a high subsonic unsteady flow over a PGRC profile cascade. The upstream Mach number is 0.9. The flow angle of attack is 12 degrees. The computation was performed for a total pressure of 159881 Pa and a total temperature of 285.16 K. For this computation, a 3 domain HCH grid was designed for a single channel using a total of 16433 nodes. Continuity boundary conditions were used in the steady case at channel interfaces. We present in Fig. 3 the steady isomach lines map obtained by PIV technique and by the computation, over 2 channels.

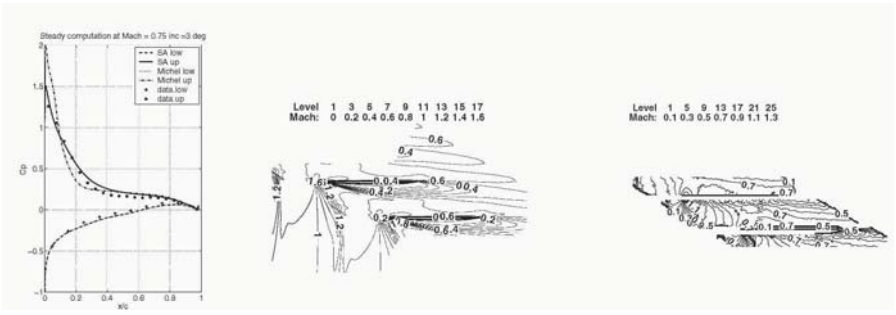

Figure 3 Steady iso-Mach lines and Pressure distribution.

The unsteady computations have been performed for 5 inter-blade phase angles. The dual timestep technique has been used with a CFL number of 4.

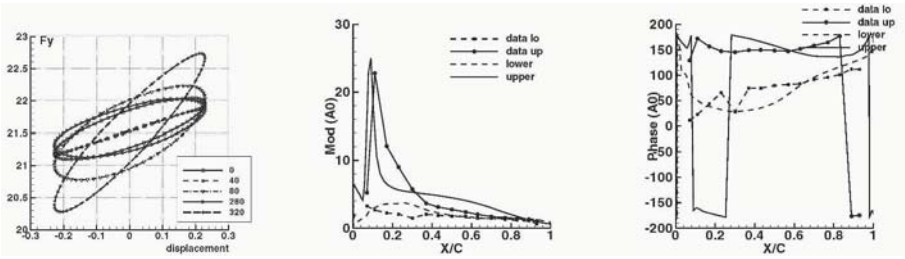

Figure 4 Harmonic analysis of the pressure coefficient

At each physical timestep, the first component of the flow field must decrease of two order. To describe a cycle we need 64 time-steps. When the inter-blade phase angle is different from zero, we need to run about 20 periods (6 periods are enough for the zero inter-blade phase angle).We present the unsteady results, for a pitching motion of the central blade at a frequency of about 300 Hz, compared to experimental data. A rather good agreement with the experimental distribution can be noticed.

5.3 3D Navier-Stokes fan blade computations

5.3.1 Unsteady Navier-Stokes response to harmonic motion. Prescribed harmonic motion Navier-Stokes simulations have been performed for a 3D wide chord fan. This fan is made up with 22 swept blades. The maximum radius of the fan is about 0.9 m. A Navier-Stokes grid of moderate size has been built in order to run Spalart steady and unsteady computations. It is made up with 6 blocks, and its total number of nodes is 397044. The first grid layer thickness at the wall is about 5.e-06 m. A view of the grid and of its multi-block topology is given in the next figure.

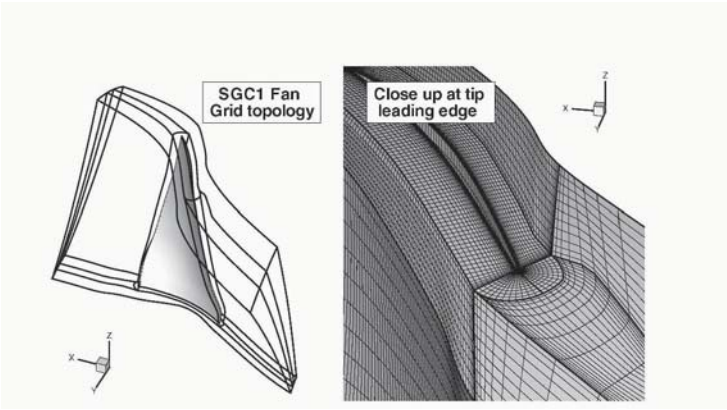

A steady computation is initially performed for an upstream absolute Mach number of 0.5. The rotating speed of the compressor for this computation is 4066.4 RPM. 4000 iterations were run using the Spalart-Allmaras model at a CFL value of 5. The computation time was about 12 hours on a single Itanium2 900MHz processor. Here is shown the quadratic residual convergence history of the conservative variables for one block.

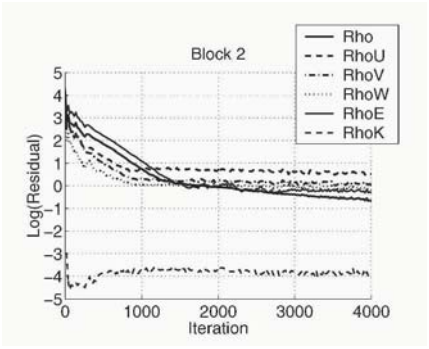

Figure 6 Convergence history

The outlet boundary condition prescribes the value of the output pressure on the hub. For this computation, the mass flow of the compressor is about 458 kg/s. A shock occurs near the tip, either on the suction side or on the pressure side. The maximum Mach number is about 1.5. Figure 7 shows the Mach contours on the suction and pressure sides.

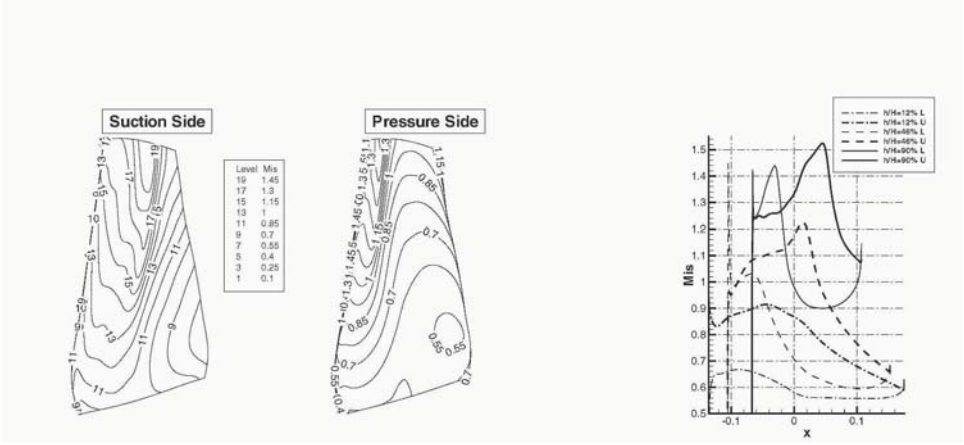

Figure 7 Isentropic Mach contours

An unsteady Navier-Stokes numerical simulation of the aeroelastic harmonic response to the 2nd bending mode at 206Hz has then been performed, with a maximal amplitude of 1 mm. The dual time stepping scheme with unsteady mesh deformation described in the previous sections has been used to reduced CPU time. Five periods of 64 physical time steps have been computed. A convergence criterium of 0.02 and a maximum iteration number of 150 have been chosen for the inner dual time loop. An overall computation time of 150 hours has been necessary on the same Itanium2 processor to perform this simulation. The first harmonic unsteady pressure analysis at three positions on the blade (hub, middle and casing) is drawn on Fig. 8. Figure 9 gives a view of the pressure and turbulent viscosity Lissajous curves at 4 blade nodes during the last cycle.

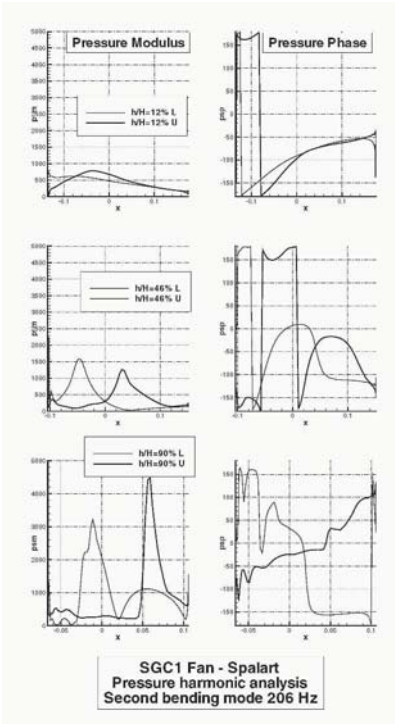

Figure 8 Harmonic pressure analysis

These curves show the periodicity of the phenomena, but also the strong variation of the turbulent viscosity during the unsteady cycle, and the existence of higher rank harmonics in the response.

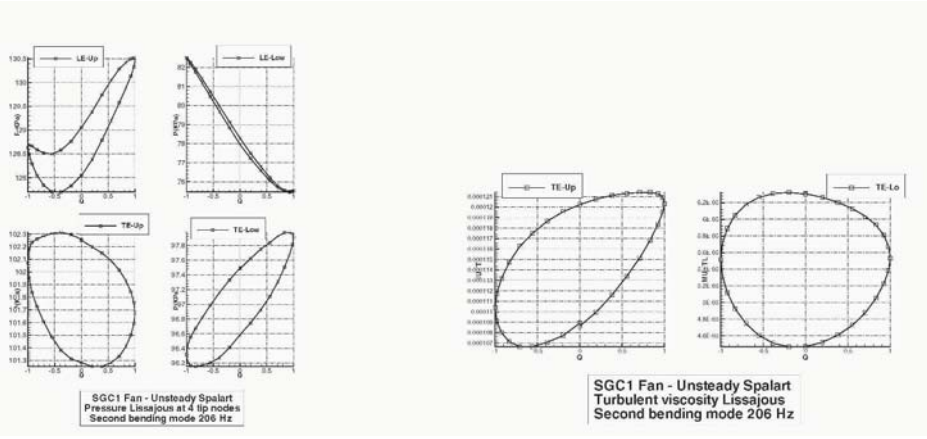

Figure 9 Pressure and turbulent viscosity Lissajous

5.3.2 Dynamic Navier-Stokes fluid-structure coupling. Navier-Stokes dynamic fluid-structure coupling computations have been performed for an advanced wide-chord swept blade fan. The linear structural model was made of 10 modes. The numerical coupled scheme as described in a previous section has been used. The computation was performed on a 6 block grid gathering 372036 nodes. 320 physical iterations have been performed for a total simulated time of about 0.1 s. 100 dual time steps have been run at each physical time step, leading to a total computation CPU time of about 150 hours on Itanium2. We present in Figs. 10 and 11 the time history of the generalized coordinates and that of the mechanical energy of the blade, for specific operating point and initial conditions.

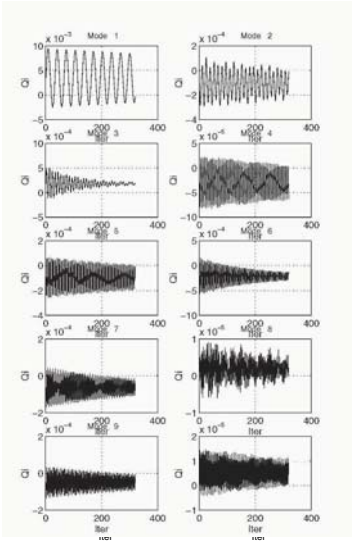

Figure 10 Generalized coordinates time history

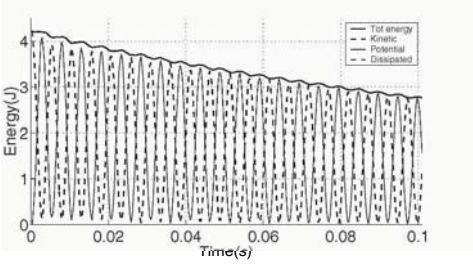

Figure 11 Energy time history

The blade is clearly aeroelastically stable, which can be more precisely characterized through the processing of the generalized coordinates time histories, in order to extract frequencies and damping for this operating point.

6. Conclusion

A Navier-Stokes numerical tool has been developed for the computation of unsteady turbomachinery applications. An Arbitrary Lagrangian Eulerian formulation has been developed, and the dual time stepping acceleration technique has been implemented in the 3D code. The basic scheme has also been modified in order to allow moving meshes computations. Static and dynamic fluid-structure coupling schemes have also been developed in the case of a modal structural model. Some results of the validation processes of the 2.5D

and 3D aeroelastic Navier-Stokes codes have been presented. An example of a dynamically coupled 3D Navier-Stokes fluid-structure computation has been given. We intend to go on with 3D developments in order to be able to perform fully 3D Navier-Stokes unsteady turbomachinery computations for more complex configurations.

References

Batina, J.T. (1989). Unsteady Euler airfoil solutions using unstructured dynamics meshes. *27th Aerospace sciences meeting*, AIAA Paper 89-0115.

Dugeai, A., Madec, A., and Sens, A. S. (2000). Numerical unsteady aerodynamics for turbomachinery aeroelasticity. In P., Ferrand and Aubert, S., editors, *Proceedings of the 9th International Symposium on Unsteady Aerodynamics, Aeroacoustics and Aeroelasticity of Turbomachines*, pages 830–840. Lyon, PUG.

Girodroux-Lavigne, P., and Dugeai, A. (2003) Transonic aeroelastic computations using Navier-Stokes equations. *International Forum on Aeroelasticity and Structural Dynamics*, Amsterdam, June 4-6.

Jameson, A., Schmidt,W. , and Turkel, S. (1981). Numerical Solution of the Euler Equation by Finite Volume Methods using Runge-Kutta Time Stepping schemes. *14th Fluid and Plasma Dynamics Conference*, Palo Alto (CA), USA, AIAA Paper 81-1259.

Leconte, P., David, F., Monnier, J.-C., Gilliot, A. (2001). Various measurement techniques in a blown-down wind-tunnel to assess the unsteady aeroelastic behavior of compressor blades *2001 IFASD*, June 05-07.

Lerat, A., Sidès, J. and Daru, V. (1982) An Implicit Finite Volume Method for Solving the Euler Equations *Lectures notes in Physics*, vol 170, pp 343-349.

Spalart P., and Allmaras, S. (1992). One Equation Turbulence Model for Separated Turbulent Flows *30th Aerospace Science Meeting*, AIAA Paper 92-0439, Reno (NV).

Vuillot, A.-M., Couailler, V., and Liamis N. (1993). 3D Turbomachinery Euler and Navier-Stokes Calculation with Multidomain Cell-Centerd Approach. *AIAA/SAE/ASME/ASEE 29th Joint propulsion conference and exhibit*, Monterey (CA), USA, AIAA Paper 93-2573.

DEVELOPMENT OF AN EFFICIENT AND ROBUST LINEARISED NAVIER-STOKES FLOW SOLVER

Paul Petrie-Repar
Institute of Aeroelasticity, German Aerospace Center
Bunsenstrasse 10, 37073 Göttingen, Germany.
Email: Paul.Petrie-Repar@dlr.de

Abstract A time-linearised Navier-Stokes flow solver is presented. The turbulence model of Spalart & Allmaras has been included in the flow model. The main feature of the current method is that GMRES with preconditioning is used to solve the linearised equations in a robust and efficient manner. The method is verified by the presentation of solutions of test cases from Standard Configuration 10 and 11. The use of various upwind schemes is also examined.

Keywords: linearised Navier-Stokes, Spalart and Allmaras turbulence model, GMRES, preconditioning

1. Introduction

Blade flutter in turbomachinery is highly undesirable as it can lead to dramatic blade failure. In order to design blading that will be free of flutter, the design engineer requires a tool that is capable of accurately predicting blade flutter. Unsteady flow simulation is an essential component of flutter analysis. For transonic flow or separated flow, it is necessary to consider viscous effects. Time-marching of the Navier-Stokes equations [1] is one method of simulating the unsteady flow, however this is computationally expensive and hence has a limited use in real design. An alternative to the time-marching method is the so called time-linearised method [2]. Here the unsteady flow is assumed to be small harmonic linear perturbations about the steady flow. This assumption allows the equations to be transformed to the frequency domain. The resulting linear equations require significantly less computational effort to solve (1 to 2 orders of magnitude faster than time-marching methods). Here, an efficient and robust method for solving the time-linearised Navier-Stokes equations is presented. The formulation of the linearised equations is similar to the methods presented by Clark & Hall [2] and Sbardella & Imregun [3].

K.C. Hall et al.(eds.),
Unsteady Aerodynamics, Aeroacoustics and Aeroelasticity of Turbomachines, 437–448.

The main difference between the current method and the previous methods is the use of GMRES with preconditioning instead of pseudo-time-stepping to solve the linearised equations. This was found to be a very efficient and robust method.

2. Flow Model

The two-dimensional Reynolds-averaged Navier-Stokes (RANS) equations with the Spalart & Allmaras one-equation turbulence model [4] are used to model the unsteady flow. The flow is assumed to be fully turbulent and no transition model is included. The turbulence model was chosen by the author and previous researchers [2, 3] because of its ability to accurately model the flow at a reasonable computational effort [5]. Better turbulence models do exist, but the effort required to solve their equations is significantly greater and prohibits their use for design calculations. The unsteady flow equations for a moving control volume can be written

$$\frac{\partial}{\partial t}\int_{\vartheta(t)} \mathbf{U}\, d\vartheta \;+\; \oint_{S(t)} \mathbf{H}\, dS \;=\; \int_{\vartheta(t)} \mathbf{S}\, d\vartheta \tag{1}$$

where $\mathbf{U}$ is the vector of conserved variables, ϑ is the control volume, S is the control surface, $\mathbf{H}$ is the flux of conserved variables at the control surface, t is time, and $\mathbf{S}$ is the vector of source terms due to the turbulence model.

The flow domain is discretised by a multi-block structured grid, and the flow equations are discretised using a cell-centered finite-volume scheme. The discretised flow equations can be written

$$\frac{d}{dt}\left[\mathbf{U}\,\vartheta\right] + \sum_{i=1}^{4} \mathbf{H}_i\, S_i = \mathbf{S}\,\vartheta, \tag{2}$$

or

$$\mathbf{R} = \frac{d\mathbf{U}}{dt} = -\frac{1}{\vartheta}\left[\sum_{i=1}^{4} \mathbf{H}_i\, S_i + \mathbf{U}\frac{d\vartheta}{dt}\right] + \mathbf{S}, \tag{3}$$

where $\mathbf{U}$ is the vector of the cell-averaged conserved variables, ϑ is the volume of the cell, S_i is the area of a cell interface between two cells, and $\mathbf{H}_i$ is the average flux through a cell interface. The inviscid flux is determined by reconstructing the flow states at both sides (typically called left and right) of the cell interface using MUSCL interpolation with a modified van Albada limiter [7]. The flux at the interface can be estimated from the left and right states using one of the following upwind schemes: Roe's approximate Riemann solver [8], AUSMDV [9], an exact Riemann solver [10], and EFM [11]. The spatial derivatives required for the viscous fluxes are calculated by an application of the divergence theorem [12].

The boundary conditions applied at the wall, on the periodic boundaries, and at the far-field boundaries are the same as applied by the previous researchers [2, 3]. It should be stated that the exact (for uniform flow) non-reflecting boundaries described by Giles [6] has been implemented at the far-field boundaries. The implementation and verification of this boundary condition required significant effort.

3. Linearisation and Transformation to Frequency Domain

The governing flow equation is transformed to the frequency domain by assuming that the prescribing motion of grid points is harmonically oscillating about their steady-state positions

$$\mathbf{x} = \overline{\mathbf{x}} + \Re\{\tilde{\mathbf{x}} e^{\jmath\omega t}\} \tag{4}$$

and the resulting unsteady cell-averaged perturbations are also harmonically oscillating about its steady-state values

$$\mathbf{U} = \overline{\mathbf{U}} + \Re\{\tilde{\mathbf{U}} e^{\jmath\omega t}\}. \tag{5}$$

The discretised time derivative of the flow solution, $\mathbf{R}$ (Eqn. 3) is linearised by performing a first-order Taylor expansion about the steady-state flow values, steady-state grid position, and zero grid velocity.

$$\frac{d\mathbf{U}}{dt} = \mathbf{R}(\mathbf{U}, \mathbf{x}, \dot{\mathbf{x}}) \tag{6}$$

$$\mathbf{R} \approx \frac{\partial \mathbf{R}}{\partial \mathbf{U}} \mathbf{\Delta U} + \frac{\partial \mathbf{R}}{\partial \mathbf{x}} \mathbf{\Delta x} + \frac{\partial \mathbf{R}}{\partial \dot{\mathbf{x}}} \mathbf{\Delta \dot{x}}. \tag{7}$$

Note that it is assumed that the time-derivative of the flow solution at the steady-state condition,

$$\overline{\mathbf{R}} = \mathbf{R}(\overline{\mathbf{U}}, \overline{\mathbf{x}}, 0) = 0. \tag{8}$$

Substituting Eqs. 7, 4, 5 into Equation 6 and dropping the $e^{\jmath\omega t}$ term gives the following result

$$\begin{aligned} \left[\jmath\,\omega - \frac{\partial \mathbf{R}}{\partial \mathbf{U}}\right] \tilde{\mathbf{U}} &= \frac{\partial \mathbf{R}}{\partial \mathbf{x}} \tilde{\mathbf{x}} + \frac{\partial \mathbf{R}}{\partial \dot{\mathbf{x}}} \jmath\omega \tilde{\mathbf{x}} \\ &\approx \Delta\mathbf{R}(\overline{\mathbf{U}}, \overline{\mathbf{x}} + \tilde{\mathbf{x}}, 0) + \jmath\,\Delta\mathbf{R}(\overline{\mathbf{U}}, \overline{\mathbf{x}}, \omega\,\tilde{\mathbf{x}}) \end{aligned} \tag{9}$$

where

$$\Delta\mathbf{R}(\mathbf{U}, \mathbf{x}, \dot{\mathbf{x}}) = \mathbf{R}(\mathbf{U}, \mathbf{x}, \dot{\mathbf{x}}) - \overline{\mathbf{R}}. \tag{10}$$

The right hand side of the linearised flow equation can be easily determined by calculating the change in $\mathbf{R}$ from the steady-state due to perturbing the grid by the amplitude of the grid motion and also calculating the change in $\mathbf{R}$ due to setting the grid velocity equal to the amplitude of the maximum velocity of the grid motion. The partial derivative of $\mathbf{R}$ with respect to the flow solution required on the left hand side of the equation is equal to

$$\frac{\partial \mathbf{R}}{\partial \mathbf{U}} = -\frac{1}{\vartheta} \sum_{i=1}^{4} \frac{\partial \mathbf{H}_i}{\partial \mathbf{U}} S_i + \frac{\partial \mathbf{S}}{\partial \mathbf{U}}. \tag{11}$$

The Jacobians required are calculated numerically and the Jacobian of the flux calculation includes the action of MUSCL and the limiter. Note that some of the flux schemes (AUSMDV and the exact Riemann solver) used here are not strictly differentiable for some input flow states. However, for the cases to be presented it was possible to obtain accurate solutions using numerically calculated derivatives of these fluxes.

4. Solution Method

The steady-state solution is found by implicitly time-stepping the unsteady flow equations (Eqn. 1) until the steady-state residual has been reduced several orders of magnitude. Local time-stepping is used to increase the rate of convergence. The traditional method [2, 3] of solving the time-linearised flow equations (Eqn. 9) is to add pseudo-time derivatives to the left side of the equations. The equations then have a similar form to the unsteady flow equations and hence the same method can be employed to solve them. Instead of the traditional pseudo-time-stepping, the current scheme uses GMRES with preconditioning to solve the linearised flow equations.

The Generalized Minimum RESidual (GMRES) [13] can be used to solve large, sparse and non-symmetric linear systems. GMRES belongs to the class of Krylov based iterative methods. Consider the linear system

$$\mathbf{A}\mathbf{x} = \mathbf{b} \tag{12}$$

where $\mathbf{A}$ is a square non-singular $n \times n$ complex matrix, and $\mathbf{b}$ is a complex vector of length n. Let $\mathbf{x}_0 \in \mathcal{C}^n$ be an initial guess for this linear system and $\mathbf{r}_0 = \mathbf{b} - \mathbf{A}\mathbf{x}_0$ be its corresponding residual. The GMRES algorithm builds an approximation of the solution of Equation 12 under the form

$$\mathbf{x}_l = \mathbf{x}_0 + \mathbf{V}_l \mathbf{y} \tag{13}$$

where $\mathbf{V}_l$ is an orthonormal basis for the Krylov space of dimension l

$$\mathcal{K}_l = \text{span}\left\{\mathbf{r}_0, \mathbf{A}\mathbf{r}_0, \ldots, \mathbf{A}^{l-1}\mathbf{r}_0\right\}, \tag{14}$$

where $\mathbf{y}$ belongs to $\mathcal{C}^l$. The vector $\mathbf{y}$ is determined so that 2-norm of the residual $||\mathbf{r}_l||_2$ is minimal over $\mathcal{K}_l$. The 2-norm is defined as

$$||\mathbf{x}||_2 = \sqrt{\sum_{i=1}^{n} |x_i|^2}. \tag{15}$$

For more information about GMRES see Saad [13].

The convergence rate of Krylov subspace methods is highly dependent on the condition number of the matrix $\mathbf{A}$. The smaller the condition number, the better the convergence. Preconditioning can be used to reduce the condition number of the linear system. The current scheme uses ILU(p) [13] to right precondition the linear system. The preconditioner is calculated by performing an incomplete Gaussian elimination. The method is incomplete because the non-zero pattern on the preconditioner is determined by the non-zero pattern of the original matrix and the level of fill p. For inviscid cases, a level of fill $p = 1$ gave the best performance and for viscous cases $p = 3$. In order to construct the preconditioner, it is necessary to explicitly determine and store the governing matrix of the linearised flow equation (Eqn. 9).

5. Test Cases

In order to verify that a computational method is accurately solving the given equations for real profiles where no analytical solution exists, it is necessary to compare results with previous numerical work. Most of the test cases shown are of Standard Configuration 10 mainly due to the quality, quantity and availability of previous numerical solutions. Unfortunately this is an Euler test case, but many features of the code (correct Euler formulation, correct far-field boundary treatment, and correct treatment of shocks) can be examined by this case. In order to verify the correct formulation of the linearised Navier-Stokes equations and the turbulence model, Standard Configuration 11 is examined.

5.1 Standard Configuration 10

Standard configuration 10 [14] is a two-dimensional compressor cascade of a modified NACA0006 profile at a stagger angle of 45 degrees with a gap to chord ratio of 1.0. The unsteady inviscid pressure response due to the blades harmonically pitching about their mid-chord position is sought.

Solutions for Case 1 (inlet Mach number $M_1 = 0.7$, inlet flow angle $\beta_1 = 55.0^o$, reduced frequency $\omega^* = 0.5$ based on chord and interblade phase angle $\sigma = 0$) are shown in Fig. 1. The solutions were calculated using Roe's scheme. The comparison with the previous numerical work is very good and the current method appears to give the correct answer for this case.

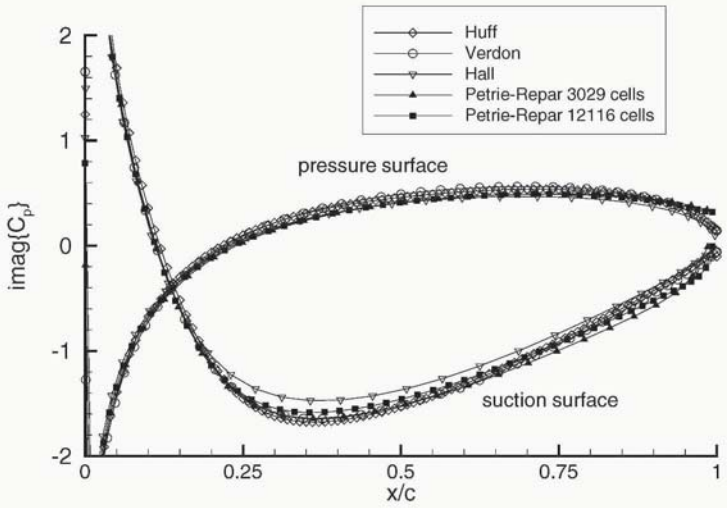

Figure 1. Imaginary unsteady pressure coefficients for Standard Configuration 10 Case 1: $M_1 = 0.7$, $\beta_1 = 55.0^o$, $\omega^* = 0.5$ and $\sigma = 0^o$

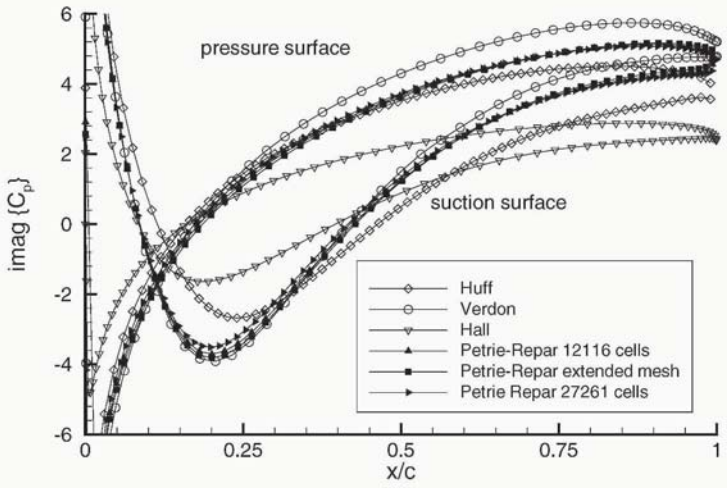

Figure 2. Imaginary unsteady pressure coefficients for Standard Configuration 10 Case 6: $M_1 = 0.7$, $\beta_1 = 55.0^o$, $\omega^* = 1.5$ and $\sigma = 90^o$

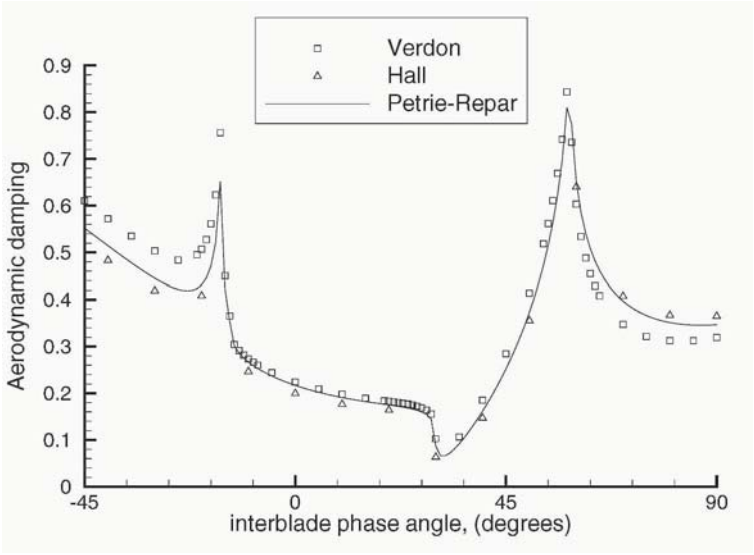

Figure 3. Aerodynamic damping for Standard Configuration 10: $M_1 = 0.7$, $\beta_1 = 55.0^o$ and $\omega^* = 0.5$. Solution calculated on a grid with 27261 cells

Solutions for Case 6 ($M_1 = 0.7$, $\beta_1 = 55.0^o$,$\omega^* = 0.5$, $\sigma = 90^o$) are shown in Fig. 2. These solutions were also calculated using Roe's scheme. This case is significantly more challenging than Case 1 because it is at a resonant condition at the downstream far-field as the sum of the acoustic waves here form planar waves which are travelling in a direction perpendicular to the axis. Conversely, for Case 1 where $\sigma = 0$, planar waves are formed in both far-fields, which are travelling parallel to the axis, and a one-dimensional treatment is sufficient to ensure non-reflection of waves at these boundaries. The difficulty of Case 6 is evident in the fact that there is no consensus between the previous solutions. The solutions are similar but one would expect a better agreement (as achieved for Case 1) for such a well defined problem. Solutions from the current method are shown at two different grid resolutions and also for an extended mesh which has the same grid resolution as the mesh with 12116 cells but with the far-field boundaries located two chord length from the profile as opposed to one chord length for the other meshes. Note that the solutions from the current method are independent of grid resolution and the location of the far-field boundaries. Also note that a higher grid resolution than Case 1 was required to achieve grid convergence for this case. The fact that the current solutions are independent of far-field boundary location suggests that the non-reflecting boundary condition has been correctly implemented. Further verification of this can be seen in the good comparison of the aerodynamic

damping versus interblade phase angle with previous work shown in Fig. 3, particularly the prediction of the peaks at resonant conditions.

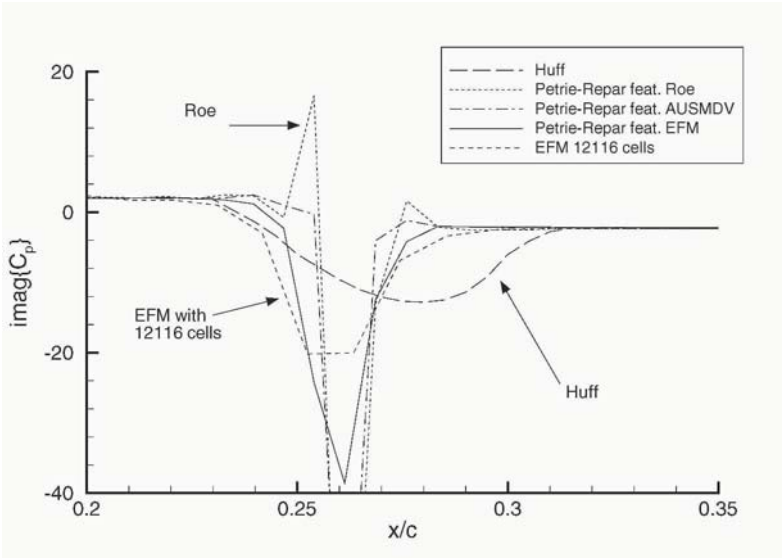

Figure 4. Imaginary unsteady pressure coefficients on the suction surface near the shock for Standard Configuration 10 Case 17: $M_1 = 0.8$, $\beta_1 = 58.0^o$, $\omega^* = 0.5$ and $\sigma = 0^o$. All simulations performed on a grid with 27261 cells unless stated otherwise

Solutions for Case 17 ($M_1 = 0.8$, $\beta_1 = 58.0^o$, $\omega^* = 0.5$ and $\sigma = 0$) are shown in Fig. 4. The inlet Mach number is higher for this case than the previous two cases and causes a shock to form on the suction surface at approximately $x/c = 0.25$. Solutions calculated with Roe's scheme, AUSMDV and EFM at a high grid resolution (27261 cells) are shown. For each solution shown, the same flux scheme was used for the the steady-state and linear solution. The Roe solution exhibits unphysical peaks in the solution near the shock. This is probably due to lack of numerical dissipation at the high grid resolution. These peaks are still present in the AUSMDV solution but are significantly smaller. The peaks are not present in the EFM solution due to the highly dissipative nature of the scheme. The conclusion is made that for high resolution Euler calculations, EFM is the better choice because its solutions at high grid resolution are less likely to exhibit unphysical noise and the extra dissipation of the scheme only has a small affect on the accuracy of the solution [10].

The shape of the shock impulse (unsteady pressure response due to motion of shock) predicted by Huff is wider with a lower peak than that predicted by the current method. This is because Huff used a pitching amplitude of $\alpha_0 = 2.0^o$, and the current method uses a very small amplitude ($\alpha_0 = 1.0 \times 10^{-6\ o}$)

in order to calculate the linear response. An EFM solution at a lower grid resolution (12216 cells) is also shown and it can be seen that grid convergence has not been achieved. However, the work done on the blade by the shock impulse does converge. The aerodynamic dampings calculated by EFM solutions on grids with 3029, 12216 and 27261 cells were 0.2122, 0.2344 and 0.2340 respectively. The validity of using linearised unsteady analysis for flows with shocks for flutter investigations was recognized by Lindquist and Giles [16].

5.2 Standard Configuration 11

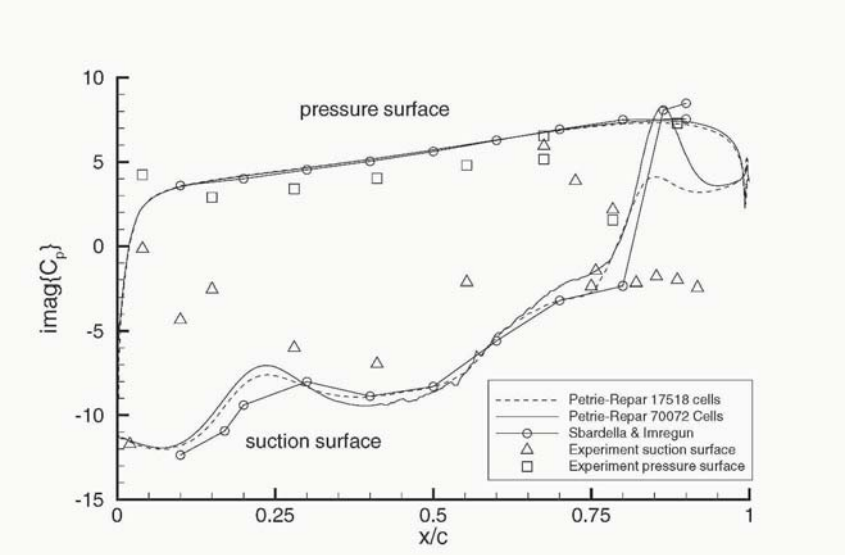

Figure 5. Imaginary unsteady pressure coefficients for Standard Configuration 11 test case

Standard Configuration 11 [15] is a two-dimensional turbine cascade. An off-design transonic condition is examined which is characterized by a separated flow region on the suction side with detachment immediately downstream of the leading edge and re-attachment at approximately 30 percent chord. A shock is also present on the suction surface at approximately 80 percent chord. The inflow conditions are: $\beta_1 = -34.0^o$ and inlet Reynolds number is 1.4×10^6. The isentropic Mach number at the exit $M_2 = 0.99$. The imaginary unsteady pressure response due to harmonic bending normal to chord with $\omega^* = 0.309$ and $\sigma = 180^o$ is shown in Fig. 5. Solutions are shown at two mesh resolutions (17518 and 70072 cells) with the height of the first grid line above the profile equal to $h/c = 2.0 \times 10^{-5}$ ($y^+ = 1.15$) and $h/c = 1.0 \times 10^{-5}$ ($y^+ = 0.58$) respectively. AUSMDV was used to calculate

the fluxes because the dissipative behavior of EFM in a boundary layer makes it unsuitable for viscous flows [7]. AUSMDV is preferred to Roe's scheme because it is less susceptible to noise near shocks at high grid resolutions (see Fig. 4). The agreement between the current solution and the previous numerical work [3] is good. Note that grid convergence was not achieved where the flow separated and at the shock. Experimental data [15] is also shown and the disparity on the suction surface is probably due to the failure of the two-dimensional flow model to model accurately the three-dimensional separated flow.

6. Computational Efficiency and Robustness

The calculations were performed on a personal computer with two Intel Pentium IV processors (jobs run in serial mode) with a clock speed of 1.7GHz. The computational effort required for some of the test cases presented in this paper are shown in Table 1. In terms of computational time, it can be seen that the current scheme is very efficient. The memory requirements are large but not unreasonable for a modern personal computer. However, if the current scheme is to be extended to three-dimensions, a supercomputer or a cluster of PCs would be necessary to deliver the required memory.

Table 1. Computational effort required for various test cases

Problem	Equations	Flux	cells	CPU (seconds)	Memory (Mb)
SC10 Case 17	Euler	EFM	3029	4.8	52.6
SC10 Case 17	Euler	EFM	12116	32.2	209
SC10 Case 17	Euler	EFM	27261	113	678
SC11	RANS	AUSMDV	17518	75	559
SC11	RANS	AUSMDV	70072	793	3000

The linearised solutions to the Standard Configuration 11 test case described above, using various flux schemes but all based on the same steady-state solution (AUSMDV) are shown in Fig. 6. The fact that it was possible to obtain accurate solutions when the flux scheme used to calculate the steady-state solution is different to the scheme used by the unsteady linearised solution is a good demonstration of the robustness of GMRES with preconditioning. Hall and Clark [17] stated that for transonic flows with shock capturing, the discretised perturbation equations should be a faithful linearisation of the discretised unsteady nonlinear equations used to compute the steady flow. Moreover, Hall & Clark could not obtain converged linearised solutions in the vicinity of a res-

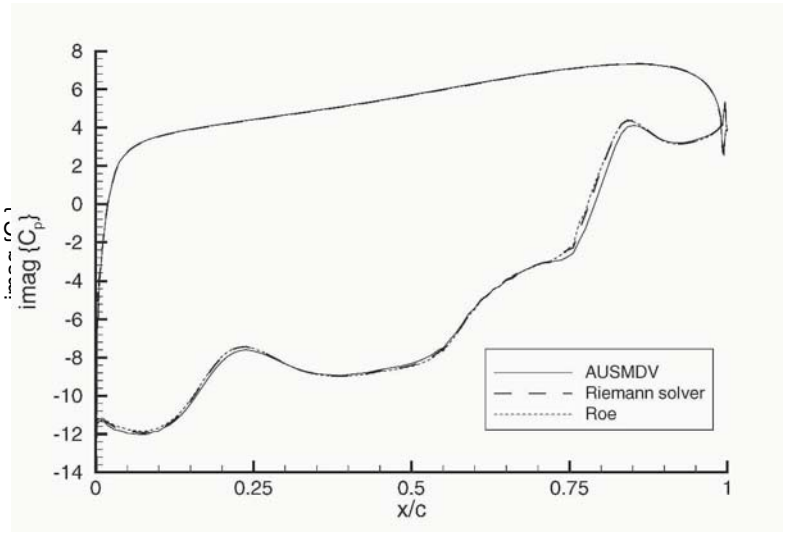

Figure 6. Solutions to Standard Configuration 11 using various upwind schemes

onant interblade phase angle when pseudo-time-stepping was employed. The author also encountered similar difficulties when using pseudo-time-stepping. However when GMRES was employed it was possible to find solutions for all interblade phase angles. Note the aerodynamic dampings shown in Fig. 3 are calculated at one degree intervals.

7. Summary

A linearised Navier-Stokes flow solver which includes the Spalart & Allmaras turbulence model that is suitable for flutter investigations has been presented. Various flux schemes were tested and EFM gave the best results for Euler calculations and AUSMDV gave the best results for viscous calculations. GMRES with preconditioning was used to solve the unsteady linearised flow equations in a robust and efficient manner. A three-dimensional version of this method is currently being developed.

References

[1] S. Weber, M.F. Platzer: "A Navier-Stokes Analysis of the Stall Flutter Characteristics of the Buffum Cascade". Journal of Turbomachinery. **122**, 2000, pp. 769-776.

[2] W.S. Clark, K.C. Hall: "A Time-Linearized Navier-Stokes Analysis of Stall Flutter". Journal of Turbomachinery. **122**, 2000, pp. 467-476.

[3] L. Sbardella, M. Imregun: "Linearised Unsteady Viscous Turbomachinery Flows Using Hybrid Grids". Journal of Turbomachinery. **123**, 2001, pp. 568-582.

[4] P.R. Spalart, S.R. Allmaras: "A One-Equation Turbulence Model for Aerodynamic Flows". In Proceedings of 30^{th} Aerospace Sciences Meeting & Exhibit. 1992, AIAA-92-0439.

[5] J. E. Bardina, P. G. Huang, T. J. Coakley: "Turbulence Modeling Validation, Testing, and Development". NASA Technical Memorandum 110446, April 1997.

[6] M. Giles: "Non-Reflecting Boundary Conditions for the Euler Calculations". AIAA Journal. **28**, 1990, pp. 2050-2058.

[7] I.A. Johnston: "Simulation of Flow Around Hypersonic Blunt-Nosed Vehicles for the Calibration of Air Data Systems". Ph.D. Thesis. Department of Mechanical Engineering. University of Queensland. Australia. 1999.

[8] P.L. Roe: "Approximate Riemann Solvers, Parameter Vectors, and Difference Schemes". Journal of Computational Physics. **43**, 1981, pp. 357-372.

[9] Y. Wada, M.-S. Liou: "A Flux Splitting Scheme with High-Resolution and Robustness for Discontinuities". AIAA Paper 94-0083, Jan. 1994.

[10] P. J. Petrie-Repar: "Numerical Simulation of Diaphragm Rupture". Ph.D. Thesis, University of Queensland, Australia, 1998.

[11] D. I. Pullin: "Direct simulation methods for compressible inviscid ideal-gas flow". Journal of Computational Physics **34** pp. 231–244, 1979.

[12] P. A. Jacobs: "Single-block Navier-Stokes Integrator" NASA CR-187613, ICASE Interim Report 18, 1991.

[13] Y. Saad: "Iterative Methods for Sparse Linear Systems". SIAM, 2003.

[14] T.H. Fransson, J.M. Verdon: "Updated Report on Standard Configurations for Unsteady Flow Through Vibrating Axial-Flow Turbomachine Cascades". Report. Royal Institute of Technology, Stockholm, Sweden. URL: http://www.egi.kth.se/ekv/stck.

[15] T.H. Fransson, M. Jöcker, A. Bölcs, P. Ott. "Viscous and Inviscid Linear/Nonlinear Calculations Versus Quasi 3D Experimental Cascade Data for a New Aeroelastic Turbine Standard Configuration". Journal of Turbomachinery. **121**, 1999, pp. 717-725.

[16] D. R. Lindquist, M. B. Giles: "Validity of Linearized Unsteady Euler Equations with Shock Capturing". AIAA Journal **32**(1), pp. 46-53, January 1994.

[17] K.C. Hall, W.S. Clark: "Calculation of Unsteady Linearized Euler Flows in Cascades Using Harmonically Deforming Grids". In Proceedings of Unsteady Aerodynamics, Aeroacoustics and Aeroelasticity of Turbomachines and Propellers. Editor: H.M. Atassi. University of Notre Dame. 1991.

OPTIMIZED DUAL-TIME STEPPING TECHNIQUE FOR TIME-ACCURATE NAVIER-STOKES CALCULATIONS

Mikhail Nyukhtikov
Moscow Institute of Physics and Technology
Moscow, Russia

Natalia V. Smelova, Brian E. Mitchell, D. Graham Holmes
General Electric Global Research Center
Niskayuna, NY USA

Abstract This paper presents an optimized discretization of the time derivative term for the dual-time stepping method. The proposed discretization is second order accurate and has a lower level of dissipation and dispersion errors than the conventional non-optimized second order discretization. Sample calculations demonstrate that the optimized scheme requires approximately 45-50% less time steps per unsteady cycle compared to the standard non-optimized scheme to resolve an unsteady flow within a certain margin of amplitude error. The number of time steps per cycle can be reduced by 10-15% to keep the phase error less than a certain level when the optimized scheme is used. Since time-accurate calculations are expensive, the proposed approach leads to significant savings of computational time and resources.

1. Introduction

Flows in the turbomachinery environment are inherently unsteady. Physical phenomena like vortex shedding, wake/blade row interaction, tip leakage etc. can be modeled correctly only by time-accurate non-linear methods. A number of such methods were developed over the past few years. One of them, the dual-time stepping method [Jameson, 1991], is widely used and is favored for its convergence properties and its ease of implementation. It employs well-known convergence acceleration techniques like multigridding, false time marching, and residual smoothing. It also has been shown [Melson et al., 1993] that this method allows an implicit treatment of the real time derivative and this removes the upper stability limit from the size of the time step. However, the

K.C. Hall et al.(eds.),
Unsteady Aerodynamics, Aeroacoustics and Aeroelasticity of Turbomachines, 449–459.

consideration of the stability limit is not sufficient because the dissipation and dispersion errors also limit the size of the time step.

This paper focuses on the development of a new optimized time derivative discretization, which has a better dissipation and dispersion properties as compared to conventional non-optimized discretization. This new discretization allows larger time steps (hence, reduced computational time) for a given level of numerical error. The technique for constructing a low-dissipation and low-dispersion scheme [Tam and Webb, 1993, Hu et al., 1994] is based on introducing more than the minimum required number of points to the discretization stencil. The coefficients for these extra points are determined by minimizing the dissipation and dispersion errors. Note that the introduction of extra points increases the memory requirements.

In this paper, a second order accurate discretization of the time derivative is considered. The optimized scheme with low dissipation and dispersion errors is constructed by introducing only one additional point. A detailed description of the optimization process is provided. The paper also presents test problems, which demonstrate the overall improvements and speedup.

2. Technical approach

For simplicity, the analysis is performed for the one-dimensional wave equation given by

$$\frac{\partial u}{\partial t} + c\frac{\partial u}{\partial x} = 0. \tag{1}$$

Applying the dual-time stepping technique, a fictitious time, τ , is introduced, and equation (1) is rewritten in the form

$$\frac{\partial u}{\partial \tau} + \frac{\partial u}{\partial t} + c\frac{\partial u}{\partial x} = 0 \tag{2}$$

or

$$\frac{\partial u}{\partial \tau} + R^*(u,t) = 0. \tag{3}$$

The derivative with the respect to the real time, t, is discretized as

$$\left(\frac{\partial u}{\partial t}\right)^{n+1} = \frac{a_1 u^{n+1} + a_2 u^n + a_3 u^{n-1} + a_4 u^{n-2} + ... + a_{m+2} u^{n-m}}{\Delta t}, \tag{4}$$

where Δt is the physical time step, and the superscript n denotes the solution at physical time $t = n\Delta t$. Equation (3) is marched in fictitious time, τ, to reach a pseudo-steady state, which advances the solution forward in time from $t = n\Delta t$ to $t = (n+1)\Delta t$. In order to speed up the convergence of the residual $R^*(u)$ to zero, acceleration techniques like local time stepping and multigridding are usually incorporated.

It is a common practice [Melson et al., 1993] to use a three-point backward formula to discretize the time derivative term, $\partial u/\partial t$, i.e.

$$\Big(\frac{\partial u}{\partial t}\Big)^{n+1} = \frac{3u^{n+1} - 4u^n + u^{n-1}}{2\Delta t}, \tag{5}$$

which is second order accurate in time and unconditionally stable. It can be shown that discretizations higher than second order accurate are only conditionally stable which makes them not practical. To improve the quality of the discretization (5) an optimization technique for constructing low-dissipation and low-dispersion schemes [Tam and Webb, 1993,Hu et al., 1994] is applied.

Consider a Fourier representation of the solution, u, given by

$$u(\tau, t, x) = \sum_l u_l(\tau) \exp[i(\omega_l t - k_l x)], \tag{6}$$

where $i = \sqrt{-1}$. Substituting (4) and (6) into (1) yields an approximation of the dispersion relation for the wave equation (1). This is given by

$$\frac{1}{\Delta t}(a_1 + a_2 \exp(-i\omega\Delta t) + a_3 \exp(-2i\omega\Delta t) + a_4 \exp(-3i\omega\Delta t) + ...) - ick = 0, \tag{7}$$

or

$$\omega^* - ck = 0, \tag{8}$$

where $\omega^* = -i[a_1 + a_2 \exp(-i\omega\Delta t) + a_3 \exp(-2i\omega\Delta t) + a_4 \exp(-3i\omega\Delta t) + ...]/\Delta t$ is a numerical approximation of the exact frequency, ω. Equation (6) can be presented in the form

$$u(\tau, t, x) = \sum u_l(\tau) \exp(i\omega_l t) \exp(-Re[i\omega_l^* x/c]) \exp(-iIm[i\omega_l^* x/c]). \tag{9}$$

From equation (9) the dissipation (amplitude) and dispersion (phase) error are estimated by the equations

$$\epsilon_{ampl} = Re[i\omega^*\Delta t - i\omega\Delta t], \tag{10}$$

$$\epsilon_{phase} = Im[i\omega^*\Delta t - i\omega\Delta t]. \tag{11}$$

Optimized schemes can be constructed by introducing more points to the discretization stencil (4) than the minimum number of points required to maintain the order of accuracy. These extra points are used to minimize the dissipation and dispersion errors given by (10) and (11).

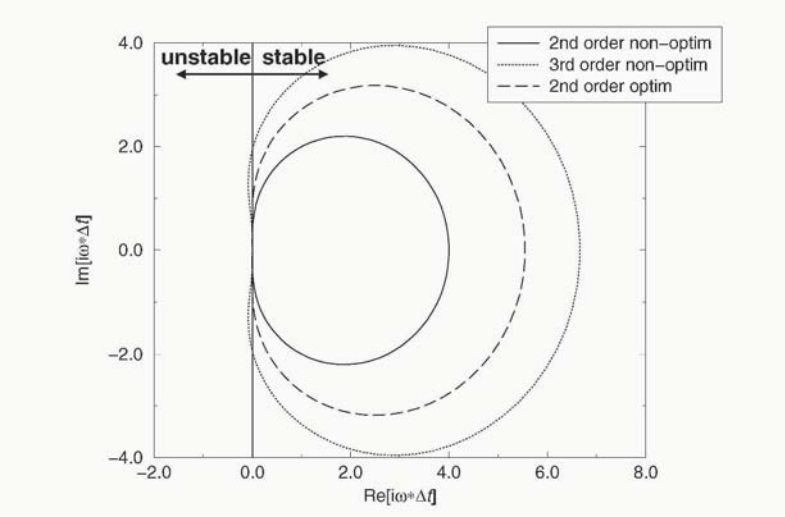

Figure 1. Stability plot

In this paper, a four point second order optimized scheme is constructed. The coefficients, $a_i, i = 1, ..., 4$, for this scheme are determined from the accuracy condition given by

$$\begin{aligned} a_1 &= 1.5 - a_4 \\ a_2 &= -2 + 3a_4 \\ a_3 &= 0.5 - 3a_4 \end{aligned} \tag{12}$$

that is obtained by expanding the solution, u, in equation (4) into a Taylor series and keeping all the terms up to the second order. The free parameter, a_4, is found subject to constraints on the amplitude and phase errors,

$$\begin{aligned} -0.001 < \epsilon_{ampl} < 0.002,\ \omega\Delta t < 0.7 \\ \epsilon_{phase} < 0.005,\ \omega\Delta t < 0.3 \end{aligned} \tag{13}$$

where the limits are set to keep the dissipation and dispersion errors smaller than those of the non-optimized second order scheme. The resulting coefficients are given in Table 1. Figure 1 shows the stability plots and Fig. 2 shows the dissipation and dispersion errors. Note, that if $Re(i\omega^*\Delta t) < 0$, then the scheme is unstable (see equation (9)). While the non-optimized second order scheme is unconditionally stable, the non-optimized third order scheme is only conditionally stable. The optimized scheme is weakly unstable, however the level has been minimized, and the lower limit was chosen to avoid instability on a typical turbomachinery problem.

Table 1. Coefficients for time derivative discretization

Discretization	a_1	a_2	a_3	a_4
2nd order	1.5	-2.0	0.5	0.0
3rd order	1.83	-3.0	1.5	0.33
2nd order optimized	1.69	-2.58	1.08	-0.19

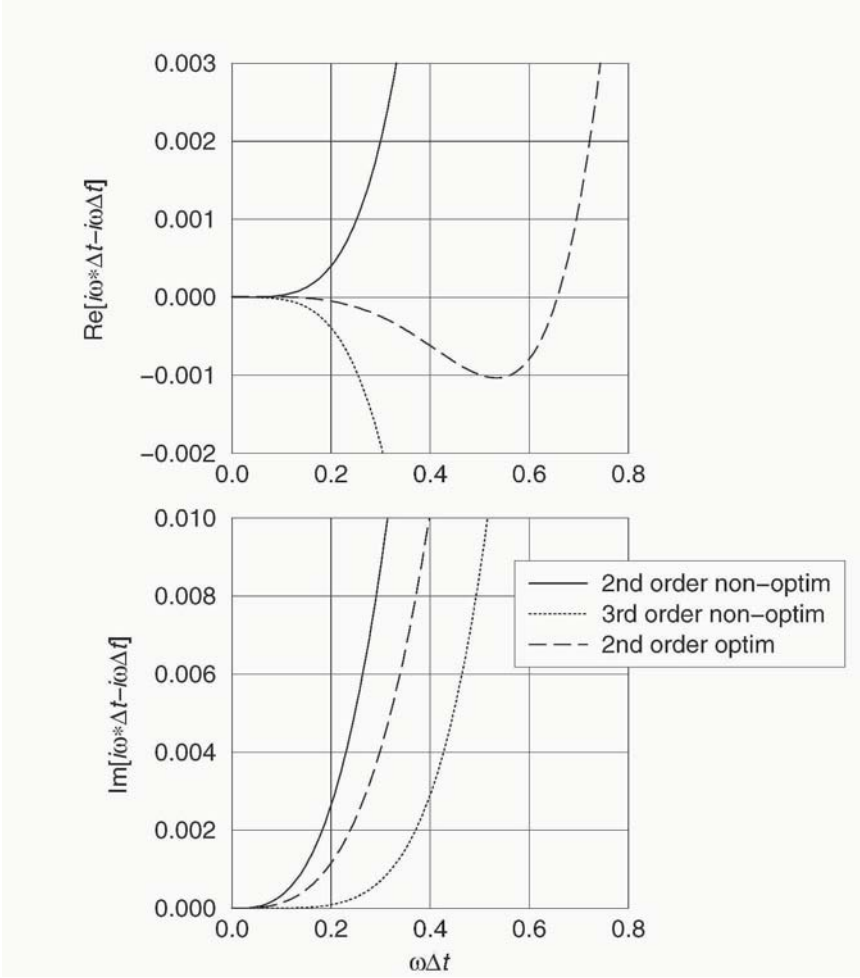

Figure 2. Dissipation and dispersion errors

3. CFD code

The described optimized time discretization has been implemented and tested in an internal GE code. The main features of this code [Holmes et al., 1997] can be summarized as follows:

- Multiblock structured meshes
- Dual-time stepping for unsteady flow simulations
- Phase lag boundary conditions
- Multigrid and local time stepping for convergence acceleration
- Adaptive 2nd/4th order (JST) dissipation
- $k - \omega$ model for turbulence modeling

4. Numerical results

The first calculation considered is the propagation of an entropy wave in a periodic duct. The flow is subsonic and inviscid. The initial flow is uniform. At the inlet plane, an entropy wave is specified that convects downstream with frequency such that the expected wave length is approximately six times smaller than the length of the duct. At the exit, non-reflecting boundary conditions are applied that allow all the outgoing waves to leave the computational domain. The calculations are performed with non-optimized and optimized second order temporal discretizations. The number of time steps per unsteady period is varied from 10 to 90. We also perform a calculation with an excessively large number of time steps per period to obtain a solution independent of the size of the time step. This solution is used to compute errors for the calculations with larger time steps. All inner iteration loops for all calculations are fully converged. The grid size is 250 by 50 which is sufficiently fine to resolve the specified wave. Figure 3 shows the density distribution along the duct for the both optimized and non-optimized schemes. Figures 4 and 5 show the amplitude and phase errors at the points located at the middle and the exit of the duct. These plots demonstrate that in order to achieve a certain level of the amplitude error one needs approximately twice as many time steps per period for a calculation with non-optimized discretization compared to the optimized one. To maintain the same phase error the number of time steps per period can be reduced by 15% when the optimized discretization is used.

Next, we consider a wake/blade row type calculation where the blade row is a rotor of a three-dimensional high pressure compressor. The wake is modeled by specifying a vorticity wave at the inlet. Again, calculations are performed

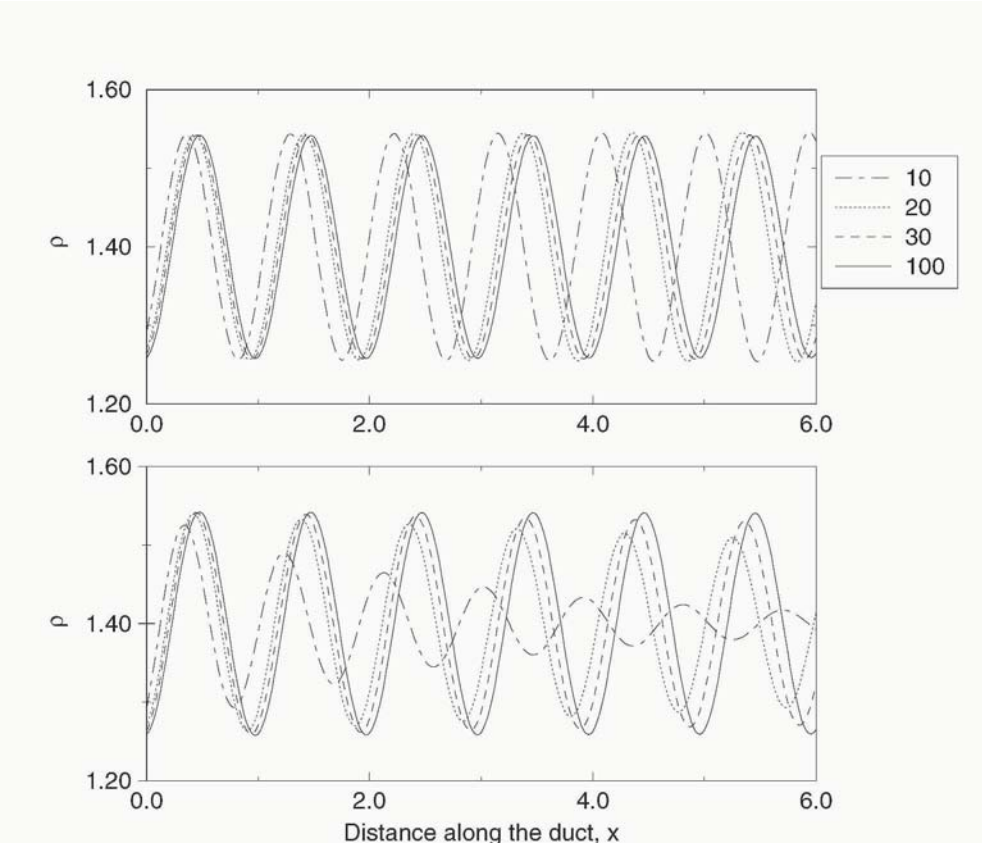

Figure 3. Density distribution along a periodic duct. Calculations with optimized (upper graph) and non-optimized (lower graph) schemes. The legend indicates the number of the time steps per unsteady cycle

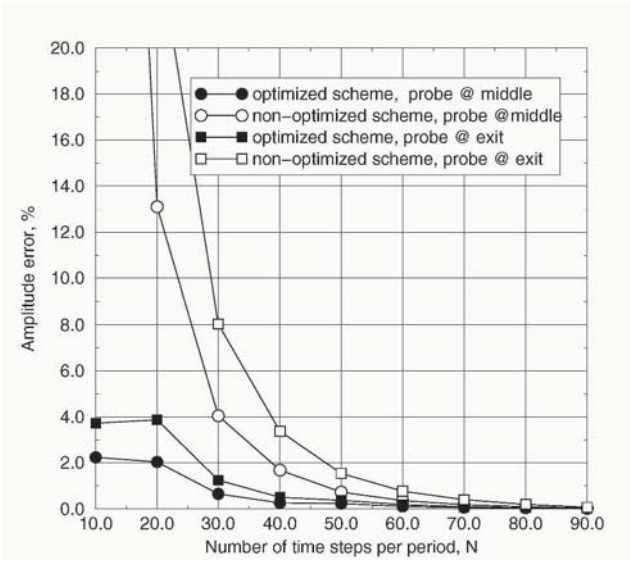

Figure 4. Periodic duct. Amplitude error

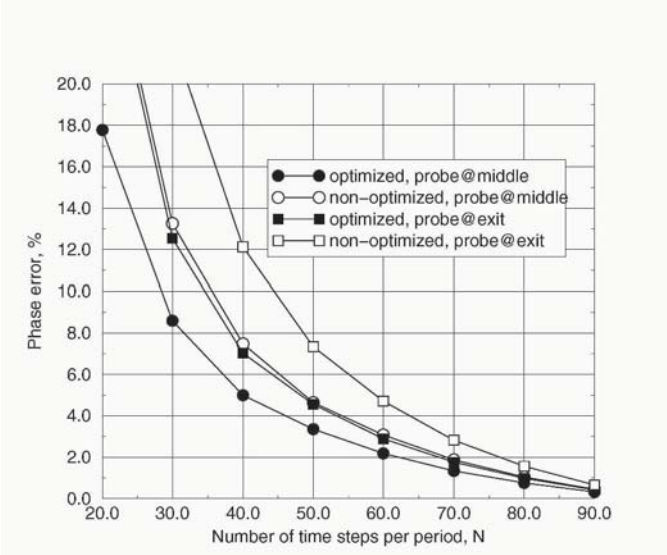

Figure 5. Periodic duct. Phase error

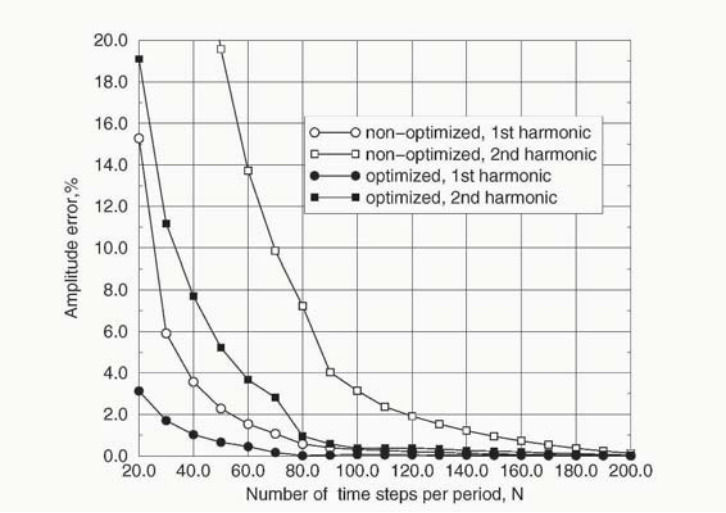

Figure 6. Three-dimensional compressor. Amplitude error

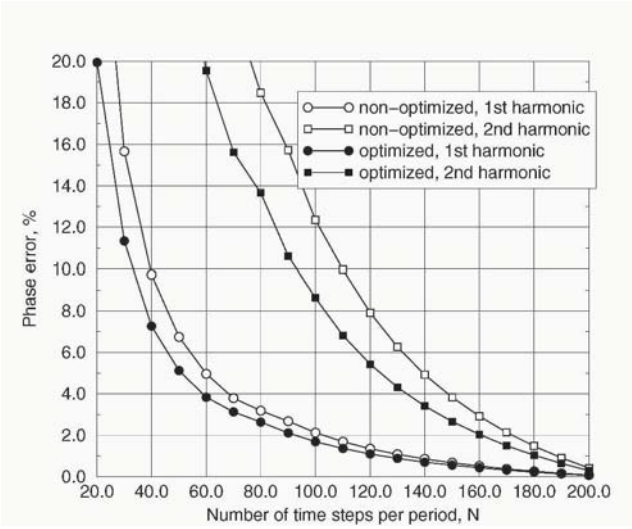

Figure 7. Three-dimensional compressor. Phase error

for a range of time steps. All inner loops are completely converged. Several monitor points are selected throughout the computational domain. Once a periodic state is reached, the amplitude and phase errors are computed at these points for the first two harmonics. Static pressure errors are computed relative to a solution obtained with 250 time steps per period. Figures 6 and 7 show the amplitude and phase errors at a point located at the midspan between the blades. Again, the optimized discretization requires less time steps per period to achieve a certain level of an error compared to the non-optimized one. Note that a finer time step is required to achieve convergence of the second harmonic compared the first harmonic. Overall, the optimized scheme performs as well in this three-dimensional case as it does in a simple duct case.

5. Summary and conclusions

In this paper, a new optimized second order discretization of the time derivative is applied to the dual-time stepping technique. This new discretization uses an extra point in the discretization stencil, but it has a lower level of the dissipation and dispersion errors compared to the standard non-optimized second order scheme. Higher than second order schemes are considered as well. However, these discretizations are only conditionally stable and for this reason they are not used.

It has been shown that the new optimized second order scheme allows 45-50%(10-15%) less time steps per unsteady period while resolving the unsteady flows to the required level of amplitude(phase) error. This can lead to a significant reduction of computational time especially for expensive non-linear calculations.

Acknowledgments

This work was jointly sponsored by GEAE and GE Global Research. The authors are grateful to the General Electric Company for permission to publish this work. The authors are grateful to Dr. Scott Hunter for his useful comments on a draft of the paper.

References

Jameson, A., Time Dependent Calculation Using Multigrid, with Application to Unsteady Flows Past Airfoils and Wings, AIAA Paper 91-1596, 1991.

Hu, F. Q., Hussaini, M. Y., and Manthey, J., Low-Dissipation and Dispersion Runge-Kutta Schemes for Computational Acoustics, NASA Report, 1994.

Holmes, D. G., Mitchell, B. E., and Lorence, C. B., Three Dimensional Linearized Navier-Stokes Calculation for Flutter and Forced Response, Presented at the 8th ISUAAAT Conference, Sweden, 1997.

Melson, N. D., Sabetrik, M. D., and Atkins, H. L., Time-accurate Navier-Stokes Calculations with Multigrid Acceleration. Presented at the 6th Copper Mountain Conference on Multigrid Methods, Copper Mountain, Colorado, April 4-9, 1993.

Tam, C. K. W. and Webb, J. C., Dispersion-Relation-Preserving Schemes for Computational Acoustics. *Journal of Computational Physics*, 107:262–281, 1993.

VII

EXPERIMENTAL UNSTEADY AERODYNAMICS

EXPERIMENTAL AND NUMERICAL STUDY OF NONLINEAR INTERACTIONS IN TWO-DIMENSIONAL TRANSONIC NOZZLE FLOW

Olivier Bron[1,2], Pascal Ferrand[1], and Torsten H. Fransson[2]

bron@energy.kth.se, Pascal.Ferrand@ec-lyon.fr, fransson@energy.kth.se

[1] *L.M.F.A., Ecole Centrale, Lyon, France*

[2] *Heat and Power Technology, Royal Institute of Technology , Stockholm, Sweden*

Abstract A prerequisite for aeroelastic stability prediction in turbomachines is the understanding of the fluctuating aerodynamic forces acting on the blades. Unsteady transonic flows are complex because of mutual interactions between travelling pressure waves, outlet disturbances, shock motion, and fluctuating turbulent boundary layers. Complex phenomena appear in the shock/boundary layer region and produce phase lags and high time harmonics, which can give a significant contribution to the overall unsteady lift and moment, and therefore affect flutter boundaries, cause large local stresses, or even severely damage the turbomachine.

This paper is concerned with the understanding of phenomena associated with travelling waves in non-uniform transonic flows and how they affect the unsteady pressure distribution on the surface as well as the far field radiated sound. In similitude with turbomachines potential interaction, the emphasis was put on the unsteady interaction of upstream propagating acoustic waves with an oscillating shock in a 2D nozzle flow. Both numerical and experimental studies are carried out and compared with each other. Results showed that the unsteady pressure distribution results from the superposition of upstream and downstream propagating pressure waves, which are partly reflected or absorbed by the oscillating shock. Beside, the phase angle shift underneath the shock location was found to linearly increase with the perturbation frequency, which can be critical regarding aeroelastic stability since it might have a significant impact on the phase angle of the overall aerodynamic force acting on the blade and shift the aerodynamic damping from stable to exciting.

Keywords: Unsteady flow, shock motion, Shock Boundary Layer Interaction, Nozzle flow

K.C. Hall et al.(eds.),
Unsteady Aerodynamics, Aeroacoustics and Aeroelasticity of Turbomachines, 463–481.

Introduction

Transonic flows about streamlined bodies are strongly affected, particularly near the shock location, by unsteady excitations. Experimental and computational studies [1, 2] have shown that the unsteady pressure distribution along the surface of an airfoil or a cascade blade in unsteady transonic flow exhibits a significant bulge near the shock location. Tijdeman and Seebass [3] reported that the unsteady pressure bulge and its phase variation resulted from non-linear interaction between the mean and unsteady flows. This non-linear interaction causes a shift in the shock location, which produces the observed large bulge in the unsteady pressure distribution. Studies [4] on choked flutter have shown that, in unsteady transonic flows around a single airfoil, the shock motion, and thus the pressure distribution along the surface, can be critical regarding to the self-exciting oscillations of the airfoil. It was also shown that the mean flow gradients are of high importance regarding the time response of the unsteady pressure distribution on the airfoil surface. Beside, numerical computations [5] pointed out that the exact location of the transition point could strongly affect the prediction of stall flutter. Further studies [6] suggested that this sharp rise in the unsteady pressure distribution was due to the near sonic condition, and that the near-sonic velocity acts as a barrier they identified as acoustic blockage preventing acoustic disturbances from propagating upstream in a similar way to the shock in transonic flows. A transonic convergent-divergent nozzle experimentally investigated by Ott et al [7] was thereafter used as a model to investigate the non-linear acoustic blockage. Analytical and numerical computations [8, 9, 10, 11] were then carried out to analyze and quantify the upstream and downstream propagation of acoustic disturbances in the nozzle.

Similarly, in order to focus the present analysis on essential features, the investigation has been carried out in a simple geometry such as a 2D convergent divergent nozzle. Special influences of leading and trailing edges, and interblade row region interactions are therefore avoided.

1. Experimental model

1.1 Test facility

The test section was designed highly modular to be able to insert different test objects, so called 'bumps', in a 100x120mm rectangular channel as sketched in figure 1(a). A continuous air supply is provided by a screw compressor driven by a 1MW electrical motor and capable of reaching a maximum mass flow up to 4.7 kg/s at 4 bar. A cooling system allows a temperature range from 30^oC to 180^oC. The adjustment of different valves also allows the exper-

imentalist to control independently the mass flow and the pressure level in the test section in the respective range of $M_i = 0.1 - 0.8$ and $Re = \frac{\rho_{air} U_\infty d}{\nu_{air}}$ = 1.87 10^4 - 1.57 10^6 with $d = 0.26$m, ρ_{air}=0.54-4.48 kg/m^3 and $\nu_{air} = 1.5$ 10^{-5} m^2/s.

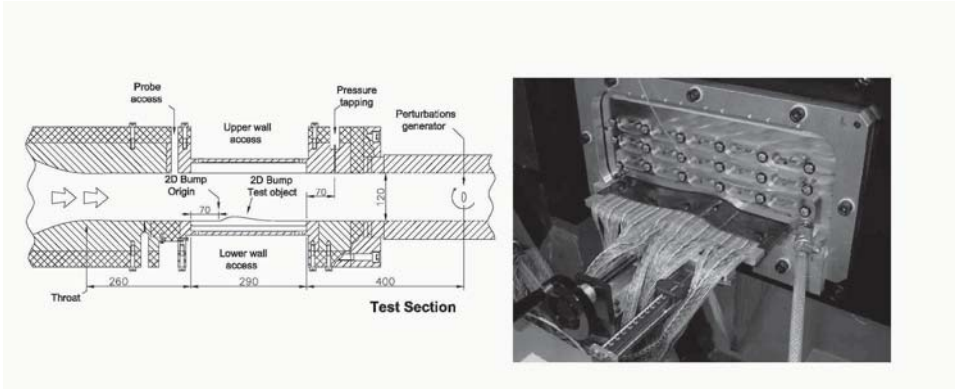

(a) Modular test section (b) Traverse mechanism for 2D bump

Figure 1. Transonic wind tunnel test section facility

1.2 Test object and instrumentation

The investigated test object consists of a long 2D bump, presented in figure 1(b), which can slide through the width of the test section using the traverse mechanism and inflated O-ring sealing system . The nozzle geometry thus consists of a 100mm wide and 120mm high flat channel with a 10.48mm maximum thickness and 184mm long 2D bump on the lower wall. The beginning of the curvatures was chosen as the origin of the X-axis (x=0mm). The Y-axis and Z-axis were set to be aligned with the channels's width and height respectively to form an orthogonal basis. The profile coordinates of the bump are presented in table A.1.

The bump is equipped with one row of 100 hot film sensors, and three staggered rows of 52 pressure taps each. The traverse mechanism fixed on the side window allows the displacement of both the pressure tap rows and the hot film sensors through the width of the channel. As a result, by sliding the 2D bump and successively position each rows of pressure taps at the same location in the channel will provide a spatial resolution measurements of 1.5mm for pressure measurements. Unsteady pressure measurements were performed using fast response Kulite transducers glued in protective pipes. Each pipe was designed with a locking device so that it could be inserted in any of the already instrumented pressure hole located underneath the sliding 2D bump.

1.3 Unsteady perturbation generator

With the aim at simulating potential interaction in turbomachines, the "quasi steady" shock wave was put into oscillations using a rotating elliptical cam placed at x=625mm in the reference system of the bump. A DC motor was used to rotate the cam up to 15,000RPMs in order to generate pressure perturbations up to 500Hz. The rotating speed was monitored using an optical encoder located directly on the shaft of the motor. Rotating speed fluctuations and time drift were measured under $\pm 0.024\%$ in the worst case. Furthermore, a TTL pulse generated by the motor was used as a reference signal during unsteady pressure measurements and Schlieren visualizations in order to correlate both measuring techniques.

1.4 Measuring techniques

Steady state pressure measurements were performed using a 208-channels 'low speed' data acquisition system. The scanners used feature a pressure range of $\pm 100kPa$ relative to atmosphere with an accuracy of $\pm 0.042\%$ full scale. Taking into account the digital barometer, the overall accuracy for steady state pressure measurements is about $\pm 43.5Pa$. The sampling frequency and sampling time were respectively set to 10Hz and 200s in order to 'capture' the lowest frequencies.

Additionally, a 32-channels high frequency data acquisition and storage system was used for **unsteady pressure measurements**. Accounting for the resonance frequency of the capillarity pipes between the bump surface and the transducer, the sampling frequency was set to 8kHz with a low pass filter at 4kHz to avoid bias effects. Each channel was connected to a fast response Kulite transducer and individually programmed to fully use the 16bit AD conversion. A static calibration of all fast response transducers was performed prior and after the measurements in order to reduce the systematic error related to the drift of the sensitivity and offset coefficients. Furthermore, a dynamic calibration was performed on all pressure taps in order to estimate the damping and time delay of propagating pressure waves through the capillarity tubes. The unsteady pressure measurements were thereafter corrected to account for the above estimated damping and phase-lag.

Finally, a **conventional Schlieren system** connected to a high speed CCD camera was used to monitor the shock motion throughout the whole test section height up to 8kHz. A special feature of the camera allows the display of the TTL signal position directly onto the pictures for referencing purpose during later post treatment. The sampling frequency and shutter speed of the camera were optimally set up depending on the perturbation frequency in order to obtain approximately 20 pictures per unsteady cycle (up to 500Hz). The spatial

accuracy based on the camera resolution and optical system was estimated to be around $\pm 0.33mm$. However, it should be reminded that the processed image is an integration of density gradients throughout the channel's width.

1.5 Acquisition procedure and data reduction

Steady state operating flow conditions were set up by adjusting the inlet total pressure, inlet total temperature, and outlet static pressure. Both stagnation pressure and temperature were measured in the settling chamber using a total pressure probe and a T-type thermocouple which gave an accuracy of $\pm 0.7K$ on the temperature reading. The outlet static pressure was measured using a pressure tap located on the upper and side walls at x=290mm. Unsteady operating flow conditions were thereafter estimated by measuring the change in back pressure between the extreme positions (vertical and horizontal) of the downstream rod and then setting the averaged value order to match the steady state operating point. The experimental operating conditions are summarized in table 1.

Table 1. Operating conditions during steady and unsteady pressure measurements

	P_t^{in} [kPa]	T_t^{in} [K]	P_s^{out} [kPa]	M^{in} [-]	$\dot{Q_m}$ [kg/s]
Estimated accuracy	$\pm 43.5Pa$	$\pm 0.7K$	$\pm 43.5Pa$	± 0.001	$\pm 0.03kg/s$
Steady State OPs*	160.09	303.1	106.07	0.702	3.66
Unsteady measurements**					
• Vertical Rod	160.10	303.3	103.76	0.692	3.73
• Horizontal Rod	160.29	303.4	108.00	0.688	3.73
• Averaged	160.19	303.35	105.88		
Unsteady conditions:	$A_p = \pm 2.12$kPa		F_p=50,100,250,500Hz		

*Without elliptical rod **With elliptical rod in extreme position

Once the operating conditions were set up, the acquisition procedure for unsteady pressure measurements basically consisted in sliding the 2D bump throughout the width of the channel and record the transducer output voltage together with TTL reference signal for each of the operating conditions summarized in table 1. Schlieren visualizations were performed at the very same operating conditions. As the resolution of the CCD camera decreases with the frame rate, a translation device was used in order to focus the image onto the region of interest in the test section. As a result, shock motion were recorded throughout the whole channel's height.

The data reduction for unsteady pressure measurements consisted of, first,

converting the output voltages from the transducers into pressure signals using the coefficients obtained during the static calibration. An ensemble average (EA) of the time-serie data was then performed for each channel using the reference TTL signal from the motor. The obtained single unsteady cycle hence represents an average of all unsteady cycles. Thereafter, a Discrete Fourier Serie Decomposition (DFSD) was performed on the EA signal computed previously and the amplitude and phase angle of the few first harmonics were evaluated. Additionally, a Fast Fourier Transform (FFT) was performed on the entire time fluctuating signal to evaluate all frequency components. At this point, the transfer function (TF) throughout each capillarity tube was evaluated depending on the respective amplitude of the fundamental and finally, both the DFSD components (amplitude and phase of all harmonics) as well as the FFT signal (amplitude only) were corrected using the damping and phase lag values evaluated at the corresponding frequency.

The data reduction procedure for high speed Schlieren visualizations consisted in extracting the instantaneous shock position at different location of the channel's height, perform an EA to obtain a single unsteady cycle and conduct an harmonic analysis on the resulting time-serie signal.

Finally, all data was made dimensionless by dividing the amplitude of each harmonic of the DFSD on pressure by the amplitude of the fundamental at the outlet, and subtracting the phase angle of the outlet pressure signal for each harmonic respectively. As a result, the data issued from harmonic analysis presented in this paper actually corresponds to the pressure amplification and phase lag relative to a reference at the outlet.

2. Numerical model

2.1 CFD tool

Simulations were performed using the computational model referenced as PROUST [12] and developed to simulate steady and unsteady, viscous and inviscid flows. The fully three-dimensional unsteady, compressible, RANS equations are solved. The space discretization is based on a MUSCL finite volume formulation. The convective fluxes are evaluated using an upwind scheme based on Roe's approximate Riemann solver, and the viscous terms are computed by a second order centered scheme. The turbulence closure problem is solved using Wilcox k-ω two equations model and fully accounts for the effect of the boundary layer (BL) separation which originates at the shock foot location. Compatibility relations are used to account for physical boundary conditions. One-dimensional numerical boundary conditions are implemented by retaining the equations associated to the incoming characteristics and fixing the wave velocity to zero to prohibit propagation directed into the computa-

tional domain. The resulting semi discrete scheme is integrated in time using an explicit five steps Runge-Kutta time marching algorithm.

2.2 Numerical domain

The computed configuration is the experimental 2D nozzle previously described. The numerical domain was however extended 70mm upstream and 164mm downstream of the bump in order to avoid numerical interaction with the boundaries. Steady state simulations were performed on both 2D and 3D structured H-grids in order to achieve a good understanding of the mean flow structures. The respectively meshes comprise 150x84 and 150x84x35 nodes with adapted grid density both around the shock location and in upper, lower and side wall BLs (containing respectively 33, 28 and 26 nodes). Unsteady simulations were however only performed on the 2D mesh due to computation time restriction. Both RANS and Euler unsteady computations were performed for comparison purposes.

2.3 Steady flow conditions

For RANS computations, the fluid is modelled as a viscous perfect gas. The specific heat ratio equals κ=1.4 and the perfect gas constant is R=287 J/kg/K. The laminar dynamic viscosity and the thermal conductibility are assumed constant and respectively equal μ=1.81 10^{-5} kg/m/s and k=2.54 10^{-2} m.kg/K/s^3. The inlet conditions in the free stream are such that the stagnation pressure, P_t^{inlet}, and the stagnation temperature, T_t^{inlet}, equal respectively 160kPa and 303K. A fully developed 7mm thick BL profile computed over a flat duct is specified as inlet condition. The outlet static pressure was adjusted in order to match the experimental shock configuration. The numerical operating conditions are summarized in table 2.

Table 2. Numerical operating conditions

	P_t^{in} [kPa]	T_t^{in} [K]	P_s^{out} [kPa]	M^{in} [-]	$\dot{Q_m}$ [kg/s]
Steady state simulations:					
• 3D RANS	160	303	108	0.695	3.93
• 2D RANS	160	303	110	0.693	3.99
• 2D Euler	160	303	115	0.683	4.02
Unsteady simulations*:	$A_p = \pm 2\% P_s^{out} = \pm 2.2$ kPa		F_p=100, 500, 1000Hz		

*2D RANS OP

2.4 Unsteady flow conditions and data reduction

The shock motion was imposed by sinusoidal downstream static pressure plane fluctuations. The amplitude and frequency of the perturbations are summarized in table 2 and the corresponding reduced frequency are presented in table 3. The reduced frequency based on the BL thickness is considered small enough to justify a quasi-steady response of the turbulence that is compatible with the turbulent model used.

Table 3. Numerical reduced frequency

	100Hz	500Hz	1000Hz	100Hz	500Hz	1000Hz
	(Based on $L_{bump} = 184mm$)			(Based on $\delta_{BL} = 7mm$)		
k_1	0.5	2.5	5	0.019	0.095	0.19
k_2	0.46	1.16	2.33	0.017	0.044	0.089

NB:$k_i = \frac{2\pi f L}{U_i}$ with $U_1 = 231.2m/s$ or $U_2 = 248.3m/s$

The data reduction consisted in performing an harmonic analysis on both the unsteady pressure distribution and the shock motion. Similarly to experiments, the amplitude of each harmonic was divided by the amplitude of the fundamental at the outlet, and the phase angle value at the outlet reference location was subtracted to all signals, for each harmonic respectively.

3. Results and discussion

3.1 Steady state results

The steady state shock wave in the 2D nozzle is presented in figure 3.1 for experimental visualization and viscous numerical simulations (at mid channel plane for the 3D RANS simulation). Although a fairly good agreement on the shock location and structure is achieved, the experimental shock position could only be matched by raising up the outlet static pressure value in the numerical simulations. For the same back pressure value, the simulations would position the shock more downstream in the diffusor. Although there might be a real probability that the $k-\omega$ turbulent model underestimates the level of losses, it cannot, by itself, explain the differences in the shock location. A more probable explanation involves the thickening of the side wall BLs and the resulting change in the effective section area, which would act like a slight convergent and magnify the pressure gradient. As the back pressure is manually setup, the pressure right downstream of the shock is then higher and the shock moves upstream.

Using the continuity equation at the outlet ($\dot{Q}_m = \rho_2 V_{x_2} S_2$), the reduction of section area due to BL thickening can be estimated for numerical simulations by calculating the change of section necessary to obtain the experimental mass flow under the same numerical outlet conditions. For the 2D RANS simulation, in which no side wall BL is specified, the change of section area was estimated around $9.44cm^2$, equivalent to a BL with a displacement thickness of 3.9mm on each side wall. For the 3D RANS, which already features outlet side wall BLs, the change of section area was estimated around $7.63cm^2$ and is equivalent to an increase of the displacement thickness of 1.73mm on each side wall BL.

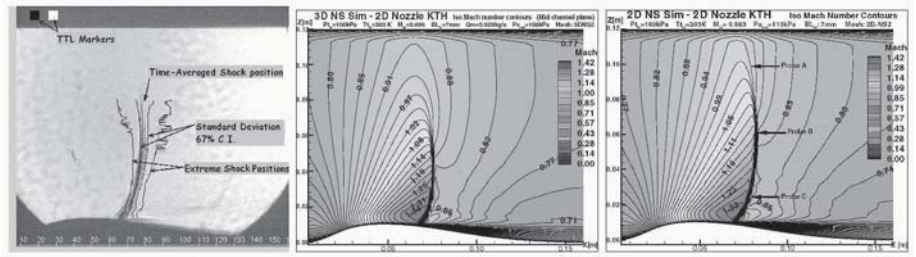

(a) Schlieren (Ps_{out}=106kPa) (b) 3D RANS (Ps_{out}=108kPa) (c) 2D RANS (Ps_{out}=110kPa)

Figure 2. Steady state shock structure in 2D nozzle

The steady state pressure distribution at mid channel (y=50mm) over the 2D bump surface is plotted in figure 3 for experimental results and viscous numerical simulations. Although the curves collapse fairly well regarding the shock location, they differ downstream of it. Indeed, experimental results present a smoother pressure recovery, which denotes a change of local curvatures (towards a more convex surface) usually due to a separated flow region. This phenomenon is even stronger closer to the wall (see pressure distribution at y=10mm) and denotes a large BL thickening or a separation of the flow in the corners. Probably due to larger side wall BLs and the interaction with the shock, the pressure rise occurs more upstream in the region close to the side walls.

In figure 4 are presented the streamlines from experimental visualization and 3D RANS calculation. As mentioned previously, the side wall BLs start thickening right downstream of the shock and a 15mm large and 60mm long separation appears in both corners. In comparison, the 3D RANS predicts a

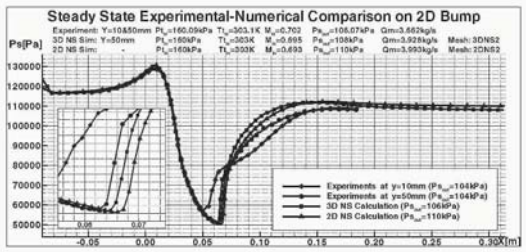

Figure 3. Steady state pressure over 2D bump

Table 4. Separated region location

	X_{sep} [mm]	X_{reat} [mm]	L_{sep} [mm]
Oil visu	67	101	34
3D RANS	68.5	82.0	13.6
2D RANS	70.2	100.2	30

much lower separated region, both in the corner and at mid channel. Again, this can be an effect of mismatched inlet boundaries or an important underestimation of the losses by the turbulent model. The size of the separated region, measured at mid channel, is presented in table 4. Whereas the 2D RANS calculation presents a fairly good estimation of the separated region, it is noteworthy that the 3D RANS simulation actually gives a much worth prediction. A possible reason might simply be the underestimation of the side wall BL thickening.

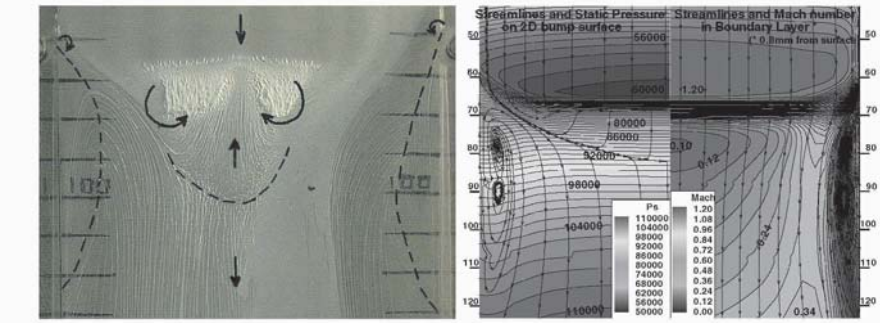

(a) Oil-paint (Ps_{out}=106kPa) (b) 3D RANS (Ps_{out}=108kPa)

Figure 4. Steady state streamlines over 2D bump

3.2 Unsteady results

3.2.1 Numerical-Experimental comparison on unsteady pressure distribution. The amplitude (normalized by outlet value) and phase angle of the unsteady pressure distribution is plotted in figure 5 for a perturbation frequency of 100Hz. A pressure amplification of factor three can be observed downstream of the shock location for both experimental and RANS calcula-

tion results. It is interesting to note that this amplification is not observed in the Euler simulation and might thus originate viscous or turbulent effects, or even possibly the Shock Boundary Layer Interaction (SBLI).

The analysis of the phase angle distribution is facilitated by considering the behaviour of travelling pressure waves in duct flows. Similarly to potential interaction in turbomachines, outlet static pressure fluctuations propagate upstream at a relative velocity of |c-U|. As long as the propagating speed is unchanged, the slope of the phase angle also remains constant, which is the case in the outflow region. However, in the vicinity downstream of the shock, the phase angle stops decreasing and even increases, which would actually correspond to a downstream propagating pressure wave.

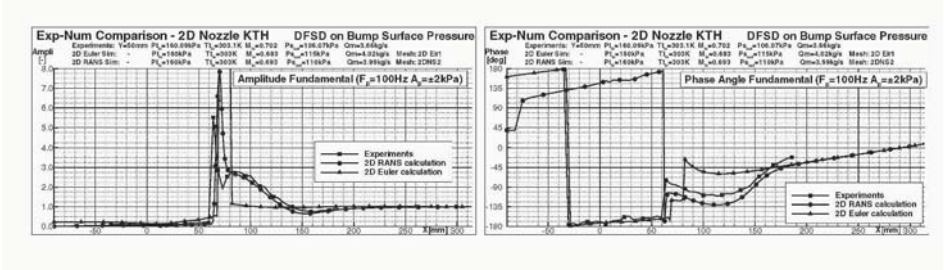

Figure 5. DFSD on unsteady pressure distribution over 2D bump for F_p=100Hz

At higher perturbation frequency (Fp=500Hz on figure 6), the pressure amplification for both experimental and 2D RANS simulation exhibits an attenuation downstream of the shock whereas the phase angle distribution presents an important phase shift (about 160^o) at the same location (x=95mm). Furthermore the same "increasing phase angle" behaviour is still observed downstream of the shock. It is noteworthy that the Euler simulation differs both in the amplitude and phase distribution and does not present the same characteristics.

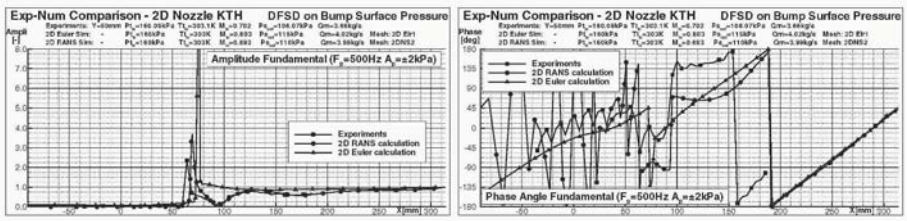

Figure 6. DFSD on unsteady pressure distribution over 2D bump for F_p=500Hz

Generally, a fairly good agreement was achieved between experiments and turbulent computations. However, although the phase angle distribution for experimental measurements and 2D RANS simulation are very similar, there seems to be an "offset" between the two distributions. This may be explained by the location of the experimental reference on the side wall. As the pressure perturbations are generated by the rotating ellipse and propagate upstream in the test section, there might be a possibility of a phase shift between the lower and side wall pressure measurements as the flow is non uniform in the diffusor downstream of the shock.

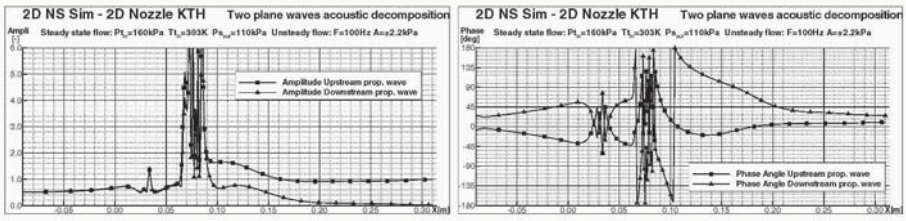

Figure 7. Upstream and downstream propagating plane waves decomposition

Considering the above observation on phase shift (increasing phase angle in the vicinity of the shock) it is believed that the unsteady pressure distribution at this location results from the superposition of an upstream and downstream travelling wave with respective varying amplitudes and phase angles. Assuming that only plane waves can propagate in the nozzle at 100Hz, a one dimensional acoustic decomposition (see equation 1) was performed on the 2D RANS numerical results using the isentropic flow velocity and sound speed on the bump surface.

$$P(x,t) = \mathbf{A_{up}} \quad e^{i\left(\omega t + \frac{\omega (x - x_{out})}{|c-U|} + \mathbf{\Phi_{up}}\right)} + \mathbf{A_{dwn}} \quad e^{i\left(\omega t - \frac{\omega (x - x_{out})}{|c+U|} + \mathbf{\Phi_{dwn}}\right)} \tag{1}$$

The amplitude and phase distributions of the respective travelling pressure waves are plotted in figure 7. According to the present decomposition, the amplitude $\mathbf{A_{up}}$ and phase angle $\mathbf{\Phi_{up}}$ of a single upstream travelling wave should be constant since time and spatial fluctuations are correlated in travelling waves. This is typically the case in the outflow region (from x=230mm to 310mm) where the amplitude and phase angle were found fairly constant for both upstream and downstream propagating waves. At the outlet plane for instance, the acoustic field is mainly composed by upstream propagating wave since the amplitude of downstream propagating waves is nearly zero.

As suspected in the region downstream of the shock, the decomposition revealed the presence of both upstream and downstream propagating waves with

respective amplitude 1.7 and 0.8. The relative phase angle distribution is more delicate to understand. For upstream propagating wave, the phase distribution tends to increase in the vicinity of the shock. This might be explained by the fact that the relative propagating velocity |c-U| tends toward zero in the vicinity of the shock. The wave length thus also tends toward zero locally, which is interpreted as an increase of the phase in the decomposition algorithm. Concerning the downstream propagating waves, it is not yet clear why the phase distribution is decreasing between x=80mm and x=210mm. It is assumed that the decomposition model is not fully accurate in the region and that other phenomena are not yet taken into account.

3.2.2 Unsteady pressure distribution at different channel heights.

Considering the fairly good agreement between experiments and 2D RANS simulations, a complementary analysis of the unsteady pressure distribution was conducted within the numerical domain at different positions in the channel's height. In addition to the upper and lower walls, three other locations were selected as illustrated in figure 2(c): the SBLI region (probe C), the middle of the shock (probe B), and the region where the sonic line meets the shock (probe A).

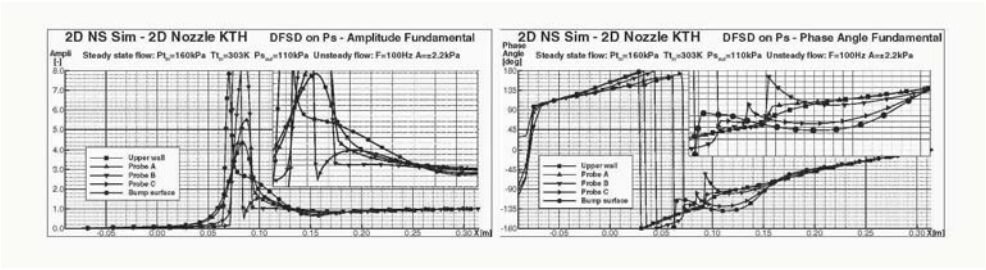

Figure 8. DFSD on unsteady pressure distribution over 2D bump for F_p = 100Hz

At low perturbation frequency (100Hz), the highest pressure amplification occurs in the BL on the upper and lower walls. Although not located in the BL, a slight amplification occurs downstream of the shock at the location of probe A and C whereas the pressure amplification in the middle of the channel (probe B) is very similar to the one observed in Euler computation. Beside, the phase angle distribution exhibits the behaviour described previously concerning the increasing phase angle downstream of the shock exclusively for the location where a shock occurs. It is noteworthy that this phenomenon is most pronounced in the middle of the channel although no pressure amplification was noticed. It thus seems as the observed phenomenon on the phase angle is

rather due to the presence of the shock wave than to viscous or turbulent effects.

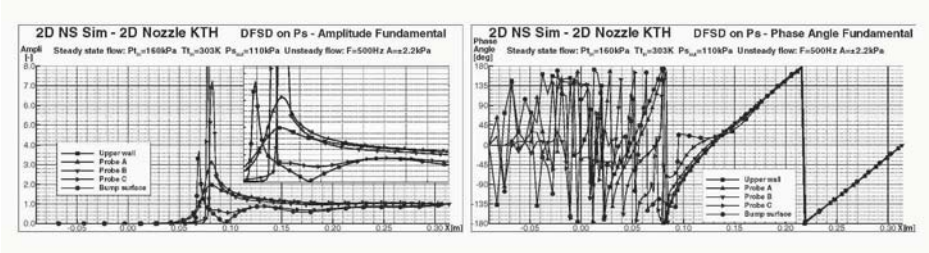

Figure 9. DFSD on unsteady pressure distribution over 2D bump for F_p = 500Hz

At higher perturbation frequency (500Hz), a pressure attenuation can be observed close to the bump surface whereas a slight amplification still occurs at other location in the channel. Surprisingly, the increasing phase angle behaviour only occurs on the bump surface whereas the phase angle distribution reflects a single upstream propagating wave behaviour at all other locations.

The particular amplitude and phase angle distribution is not yet clearly understood and might be related to the lower amplitude of the motion of the shock, its inertia to oscillate, or the smaller wave length of the perturbation at higher frequencies.

3.2.3 Shock motion. The amplitude and phase angle of the shock motion throughout the channel's height are presented in figure 10 and 11 respectively for the perturbation frequencies 100Hz and 500Hz. A fairly good agreement is achieved between experiments and numerics regarding both the amplitude and phase distribution of the unsteady shock motion. For both frequencies, the amplitude of shock motion increases with the height of the channel. It is noteworthy that the same trend is observed also in the Euler simulation. The amplitude of motion of the shock is thus related to the mean flow gradients rather than to the SBLI. Beside, the amplitude clearly decreases with the frequency. Assuming that the shock has a certain inertia to oscillate or to respond to a back pressure variation, the decreasing amplitude of motion of the shock at higher frequencies is then probably due to shorter perturbation wave length although the amplitude of perturbation remains the same.

On the other hand, the shock motion phase angle slightly differs both between the two frequencies and the two numerical calculations. At low frequency, the phase angle seems to be constant throughout the channel height, which corresponds to a "rigid" motion between the foot and the top of the shock. At higher frequency however, there is an important phase lag (up to

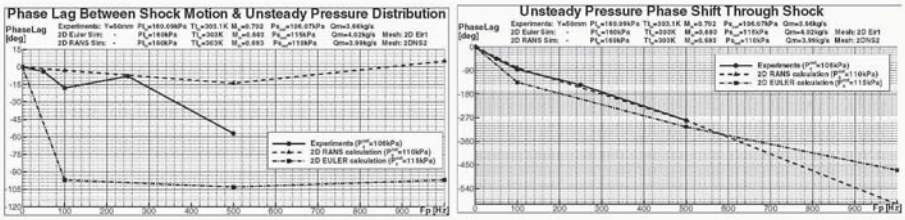

Figure 10. DFSD on shock motion over 2D bump for F_p = 100Hz

90^o for experiments) between the foot and the top of the shock. The "head" of the shock seems to oscillate with a certain time lag (delay) compared to the foot. This tendency can be observed both on experimental visualization and 2D RANS simulation, but not on Euler calculation where the phase angle is still constant throughout the channel height. This effect might be related to the higher propagation speed within the BL than in the free stream. As a result, the pressure perturbations reach the foot of the shock slightly in advance in the SBLI region. The same behaviour should theoretically also be seen at lower frequencies, but since the wave propagation speed is the same, the perturbations wave length is longer and thus the phase lag between perturbations in the BL and in the free stream is lower.

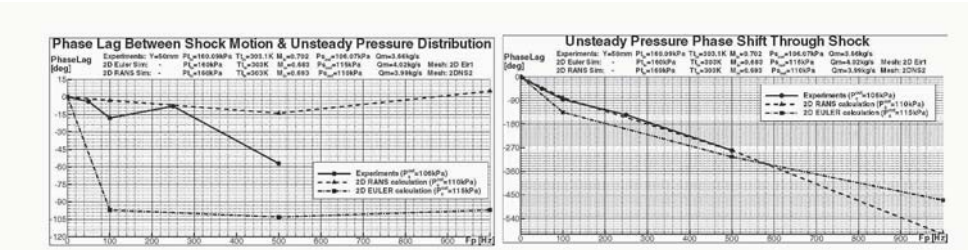

Figure 11. DFSD on shock motion over 2D bump for F_p=500Hz

3.2.4 Relation between unsteady pressure and shock motion. The phase lag between unsteady pressure distribution over the bump and the shock motion (closest from the bump) has been calculated and plotted in figure 12 as a function of the perturbation frequency. Experimental results show an increasing phase lag with the perturbation frequency, meaning that the shock response with a certain increasing time delay with the perturbation frequency. For numerical simulation however, the trend is not as clear and further calculations

should be performed in order to clearly define a tendency.

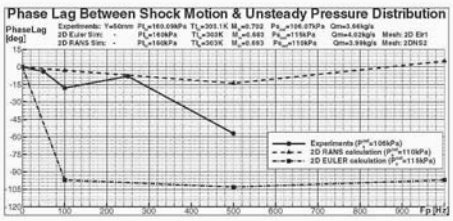

Figure 12. Phase Lag between Ps & Shock

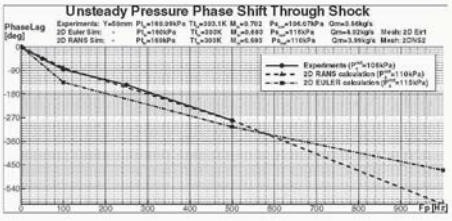

Figure 13. Phase shift through shock

Additionally, the unsteady pressure phase angle jump through underneath the shock location was plotted as a function of the perturbation frequency in figure 13. A fairly good agreement was found between experimental pressure measurements and 2D RANS numerical simulation. This unsteady pressure phase shift, which seems to increase linearly with the perturbation frequency, is extremely important considering aeroelastic stability prediction. Indeed, the unsteady aerodynamic load on an airfoil is directly influenced by the value of the phase shift and the overall stability of the airfoil might change from stable to unstable (and vice versa) for a certain value of this phase shift.

3.2.5 Unsteady separated region motion. The unsteady motion of the separated zone was evaluated as a function of the shock motion for the 2D RANS numerical simulation, and is presented in figure 14 for two perturbation frequencies (100Hz and 500Hz). The advantage to display the separation versus the shock motion is to be able to see both the amplitude of motion and the phase lag between the separation/reattachment and the shock oscillations. Clearly, the separation oscillates with the same amplitude and nearly in phase with the shock wave. This behaviour does not seem to change with the frequency and confirms the idea of a shock induced separation. On the other hand, the reattachment seems to oscillate with a much larger amplitude and a certain phase lag with the shock. Both the amplitude and phase lag seem to be related to the perturbation frequency. It is however not possible to state upon a clear tendency and further calculation as well as experimental measurement should be performed.

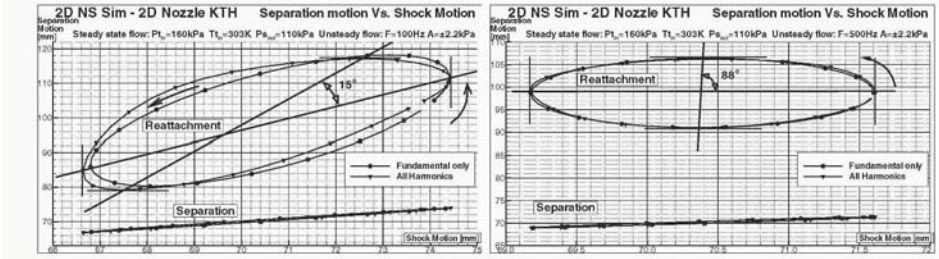

Figure 14. Separated region motion for 2D RANS calculations

4. Summary

Unsteady pressure measurements and high speed Schlieren visualizations were conducted together with 2D RANS and Euler numerical simulations over a convergent divergent nozzle geometry in order to investigate the Shock Boundary Layer interaction. A fairly good agreement between experiments and numerical simulations was obtained both regarding the unsteady pressure distribution and shock motion.

Results showed that the unsteady pressure distributions, both on the bump and within the channel, result from the superposition of upstream and downstream propagating waves. It is believed that outlet pressure perturbations propagate upstream within the the nozzle, interact in the high subsonic flow region according to the acoustic blockage theory, and are partly reflected or absorbed by the oscillating shock, depending on the frequency of the perturbations. The amplitude of motion of the shock was found to be related to the mean flow gradients and the local wave length of the perturbations rather than to the shock boundary layer interaction. The phase angle between unsteady pressure distribution on the bump and the shock motion for experimental results was found to increase with the perturbation frequency. However, no clear tendency could be defined for numerical results.

At last, but not least, the phase angle "jump" underneath the shock location was found to linearly increase with the perturbation frequency. The phase shift is critical regarding aeroelastic stability since it might have a significant impact on the phase angle of the overall aerodynamic force acting on the blade and shift the aerodynamic damping from stable to exciting.

Acknowledgments

The authors wish to thank the Swedish Energy Agency (STEM) for its financial support over the project, as well as the Center for Parallel Computers

(PDC) and the National Informatic Center of Superior Education (CINES) for the CPU resources allowed.

References

[1] DAVID S.S., MALCOM G.N. *Experiments in unsteady transonic flows* AIAA/ASME/ASCE/AHS 20th Structure, Structural Dynamics and Material Conference AIAA paper 79-769, pp. 417-433St. Louis, M.O., 1979

[2] ATASSI H.M., FANG J., FERRAND P. *A study of the unsteady pressure of a cascade near transonic flow condition* ASME paper 94-GT-476, June 1994

[3] TIJDMAN H., SEEBASS R. *Transonic flow past oscillating airfoils* Annual Review of Fluid Mechanics, vol. 12, 1980, pp. 181-222

[4] FERRAND P. *Etude theorique des ecoulements instationnairs en turbomachine axiale. Application au flottement de blocage* State thesis, Ecole Centrale de Lyon, 1986

[5] EKATERINARIS J., PLATZER M. *Progess in the Analysis of Blade Stall Flutter* Symposium on Unsteady Aerodynamics and Aeroelasticity of Turbomachines, Tanida and Namba Editors, Elsevier, September 1994, pp. 287-302

[6] ATASSI H.M., FANG J., FERRAND P. *Acoustic blockage effect in unsteady transonic nozzle and cascade flows* Symposium on Unsteady Aerodynamics and Aeroelasticity of Turbomachines, Tanida and Namba Editors, Elsevier, September 1994, pp. 777-794

[7] OTT P. *Oszillierender Senkrechter VerdichtungsstoSS in einer Ebenen Düse* Ph.D. Thesis at Ecole Polytechnique Federale de Lausanne; These No 985 (1991); 1992

[8] FERRAND P., ATASSI H.M., AUBERT S. *Unsteady flow amplification produced by upstream or downstream disturbances* AGARD, CP 571, January 1996, pp. 331.1-31.10

[9] FERRAND P., ATASSI H.M., SMATI L. *Analysis of the non-linear transonic blockage in unsteady transonic flows* AIAA paper 97-1803, Snowmass, Col. USA, 1997

[10] FERRAND P., AUBERT S., ATASSI H.M. *Non-linear interaction of upstream propagating sound with transonic flows in a nozzle* AIAA paper 98-2213, Toulouse, 1998

[11] GEROLYMOS G. A., BRUS J.P. *Computation of Unsteady Nozzle Flow due to Fluctuating Back-Pressure using Euler Equations* ASME Paper No. 94-GT-91

[12] SMATI L. *Contribution au développement d'une méthode numérique d'analyse des écoulements instationnaires. Applications aux turbomachines* PhD, ECL, France, 1997

Appendix: Two dimensional bump coordinates

Table A.1. Two-dimensional bump profile coordinates

x*	thickness*	x	thickness	x	thickness	x	thickness
-70.00	0.00	26.29	7.50	61.11	9.82	95.94	4.92
-56.51	0.00	29.19	8.39	64.01	9.56	98.84	4.47
-43.11	0.00	32.09	9.07	66.92	9.25	101.96	4.01
-29.72	0.00	34.99	9.59	69.82	8.91	107.25	3.29
-16.39	0.00	37.90	9.97	72.72	8.54	117.22	2.16
-5.13	0.00	40.80	10.24	75.62	8.13	131.71	1.02
3.45	0.06	43.70	10.40	78.52	7.70	146.34	0.37
9.78	1.01	47.60**	10.47	81.43	7.25	160.98	0.09
14.33	2.53	49.50	10.46	84.33	6.79	175.61	0.01
17.58	3.89	52.41	10.38	87.23	6.32	190.24	0.00
20.48	5.18	55.31	10.24	90.13	5.85	204.88	0.00
23.39	6.41	58.21	10.05	93.04	5.38	220.00	0.00

*Coordinates in mm. **Throat located at x=47.6mm.

INTERACTION BETWEEN SHOCK WAVES AND CASCADED BLADES

Shojiro Kaji
Department of Aerospace Engineering
Teikyo University
1-1 Toyosato-dai, Utsunomiya 320-8551
Japan
kaji@koala.mse.teikyo-u.ac.jp

Takahiro Suzuki
Department of Aeronautics and Astronautics
University of Tokyo
7-3-1 Hongo, Bunkyo-ku, Tokyo 113-8656
Japan

Toshinori Watanabe
Department of Aeronautics and Astronautics
University of Tokyo
7-3-1 Hongo, Bunkyo-ku, Tokyo 113-8656
Japan
watanabe@aero.t.u-tokyo.ac.jp

Abstract Interaction between a sonic boom and cascaded blades is studied numerically. The incident sonic boom is modeled by a finite amplitude N wave with a short rising time, and the time dependent transonic cascade flow with a passage shock inside is solved. Detailed mechanism on reflection and transmission of a sonic boom by the cascade and unsteady aerodynamic force exerted on blades are elucidated. The peak amplitude of the unsteady blade force is the same order of magnitude as the pressure amplitude of the incident sonic boom.

Keywords: sonic boom, cascaded blades, interaction, supersonic transport, numerical analysis

K.C. Hall et al.(eds.),
Unsteady Aerodynamics, Aeroacoustics and Aeroelasticity of Turbomachines, 483–491.

1. Introduction

In this century, a new era of supersonic transport (SST) is in prospect where a great number of SST is introduced concurrently with subsonic transport. Then, there will be an increasing possibility for subsonic transport of encountering a sonic boom of supersonic transport. In such an occasion shock waves due to a sonic boom of SST are swallowed in an engine inlet and interact with fan rotor blades and stator vanes. In another occasion a sonic boom may invade into the engine cowl from the rear side.

Another example of interaction of shock waves and cascaded blades can be found in an innovative concept of a pulse detonation engine (PDE) combustor combined with a turbine engine. In this case shock waves due to a detonation combustor hit upon turbine nozzle vanes and blades. The strength of shock waves for a PDE combustor reaches more than 200 dB in pressure amplitude. Again we have a strong motivation to investigate the interaction between shock waves and cascaded blades.

The purpose of the present paper is to investigate numerically the impact of a sonic boom produced by SST on the engine fan rotor of subsonic transport. The same problem was treated in the last symposium analytically by use of the semi-actuator disk model for cascaded blades [1]. The results obtained in the analysis showed that (1) the amplitude of the transmitted N wave across the cascade passage shock increases over the incident N wave, (2) the pressure fluctuation at the cascade passage shock has a discontinuous character, and (3) unsteady aerodynamic force exerted on blades by a sonic boom becomes strong in the direction of chord. The numerical approach taken in this paper enables to check the validity of the semi-actuator disk model and give more detailed interaction mechanism.

Similar analyses have been made from different view points. Paynter et al. [2] needed the rear end boundary condition for numerical analysis of an engine air intake. They solved the flow field including the cascade to determine the reflection coefficient of sound waves. Freund et al. [3] investigated experimentally the reflected pressure fluctuation for the disturbance incident upon an engine compressor. Dorney [4] analyzed numerically the effect of sound waves incident upon a viscous transonic cascade.

2. Numerical Method

A sonic boom is produced by a supersonic airplane because of its volume and aerodynamic forces. Its waveform is very much complicated near the airplane, however, in the distant field the waves are naturally weakened and coalesced to be a so-called N-wave, i.e., the combination of a bow shock and an end shock. The detailed waveform and strength will be dependent, therefore, on the difference of flight altitudes of the SST and the subsonic transport in

question. Numerical simulation of the sonic boom of Concorde at various altitudes [5] indicates that at 40,000 ft the maximum amplitude of the sonic boom reaches as high as 100 Pa. This value corresponds to about 0.5strength should be increased as the speed and size of airplane increases. For example, as we go from Mach 2 to Mach 3 the sonic boom strength increases by 15 next generation SST of 300 ton class, it increases by about 20 Therefore, the strength of a sonic boom encountered at altitudes of subsonic transport should be 1

In the present analysis a numerical approach is taken based on the two-dimensional Euler equation.

$$\frac{\partial U}{\partial t} + \frac{\partial F}{\partial x} + \frac{\partial G}{\partial y} = 0 \tag{1}$$

where

$$U = \begin{pmatrix} \rho \\ \rho u \\ \rho v \\ e \end{pmatrix} \quad F = \begin{pmatrix} \rho u \\ p + \rho u^2 \\ \rho uv \\ (e+p)u \end{pmatrix} \quad G = \begin{pmatrix} \rho v \\ \rho uv \\ p + \rho v^2 \\ (e+p)v \end{pmatrix} \tag{2}$$

$$e = \rho\varepsilon + (u^2 + v^2)/2 \tag{3}$$

$$p = \rho RT \tag{4}$$

In the actual analysis, the basic equations are transformed into the generalized coordinate system $\xi = \xi(x, y), \eta = \eta(x, y)$.

To capture shock waves the upwind type TVD scheme by Harten-Yee is adopted. For time integration, the LU-ADI scheme is used. The Newton iteration method is applied to the non-steady calculation in order to ensure time accuracy. For the boundary conditions in case of steady calculation, the total pressure, the total temperature and the circumferential velocity are specified at the inlet, and the static pressure is fixed at the exit.

For the non-steady calculation, the nonreflecting boundary condition of the Thompson type is applied. For the incident N-wave, the physical conditions are specified at the inlet boundary. The finite amplitude, one-dimensional isentropic wave can be described by

$$\begin{aligned} u - u_1 = \pm \int_{\rho_1}^{a} \frac{a}{\rho} d\rho &= \pm \frac{2a_1}{\gamma - 1} \left[\left(\frac{\rho}{\rho_1} \right)^{\frac{\gamma-1}{2}} - 1 \right] \\ &= \pm \frac{2a_1}{\gamma - 1} \left[\left(\frac{p}{p_1} \right)^{\frac{\gamma-1}{2\gamma}} - 1 \right] \end{aligned} \tag{5}$$

where u is the velocity, a the velocity of sound, p the pressure, and ρ the density, and the subscript indicates the steady state condition before the wave arrives. The plus sign indicates the progressing wave and the minus sign represents the retreating wave.

From the above equation, once the pressure is given, the density and the induced velocity are obtained. During the period of the incident N-wave, the total pressure and the total temperature are not fixed but the static pressure, density and velocity are given in accordance with the above relation of the N-wave. After the entrance of the N-wave, the total pressure and the total temperature are fixed again at the inlet. In order to simulate a realistic sonic boom, we introduce a start up time(or rising time) of 0.1ms for the shock wave to gain the peak pressure.

The combination of grids of H-type in the upstream and downstream fields and those of O-type near the region of cascaded blades is adopted. The blades have the tip section profile used in the NASA Quiet Engine Fan Program B. At the design condition the inlet Mach number is 1.2 and the exit Mach number is 0.853.

3. Results and Discussion

Figure 1 shows the pressure contours of the steady state cascade flow (Δp = 333Pa). This flow field corresponds to the case of the back pressure of 75,000 Pa. The inlet Mach number is 1.2 and the exit Mach number is 0.605. The inlet flow angle is 57.6 deg., and the exit flow angle is 52.35 deg. At the leading edge we have oblique shocks, and in the cascade passage a normal shock. Interaction between a sonic boom and cascaded blades is studied based on this steady condition. In order to save computational region as well as time we chose the incident N wave of a short period of 8 ms. In reality the sonic boom induced by SST may have a longer period of 200 ms, we thought the interaction between the shock and cascaded blades should be essential, but the period of two shocks may not be so important in the phenomena. This tendency has been suggested by the semi-actuator disk analysis.

The maximum static pressure amplitude of the N wave given at the inlet boundary is selected to be 325 Pa. This value corresponds to the increase of relative total pressure of 1013 Pa, 1% of the atmospheric pressure. In this case the maximum amplitude of the absolute total pressure is 1.19%, and the static pressure is 0.78% of the steady value, respectively.

Hereafter we investigate the pressure variation history along the grid points indicated in Fig.2. The points from 1 to 15 locate in the upstream field, those from 15 to 25 locate in the cascade passage, and points from 25 and greater locate in the downstream field.

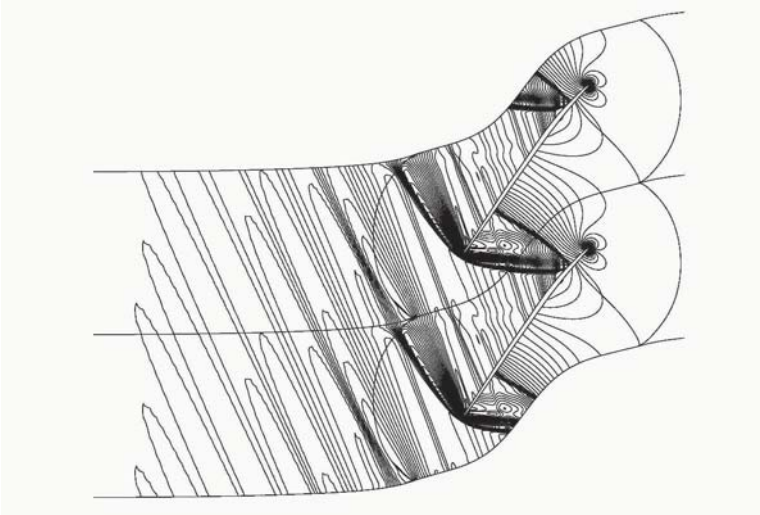

Figure 1. Steady Pressure Contour (Δp:333Pa)

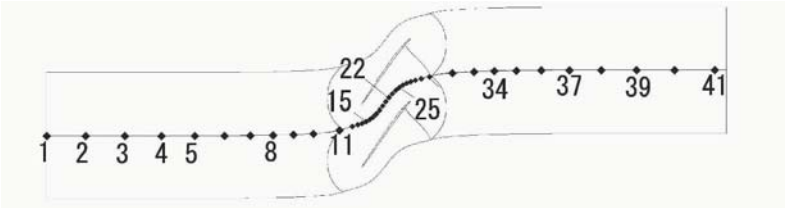

Figure 2. Calculation Grid and Pressure Monitoring Stations

Figures 3 (a) to (e) show the results of pressure variation history for the incident N-wave of period of 8ms. From the pressure history at the position 1, we can clearly recognize the incident N-wave followed by a little bit smaller N-wave reflected back by the cascade at the leading edge plane. At positions 4, 6 and 8 the reflected wave complicates the pressure signal significantly. Figures 3 (c) and 3 (d) show the pressure signals in front of and behind the passage shock, respectively. We see that high frequency components appear on the pressure signals behind the passage shock. Those components are probably due to various types of resonance in the cascade passage. Further we go downstream the pressure signals seem to recover the N-shape as the transmitted wave.

Figure 4 shows the history of the non-steady aerodynamic force acting on blades during the passage of the N-wave. We see that at the passage of the front shock of the N-wave, the aerodynamic force once drops sharply then increases to have a peak. During the passage of the expansion portion of the N-wave, the

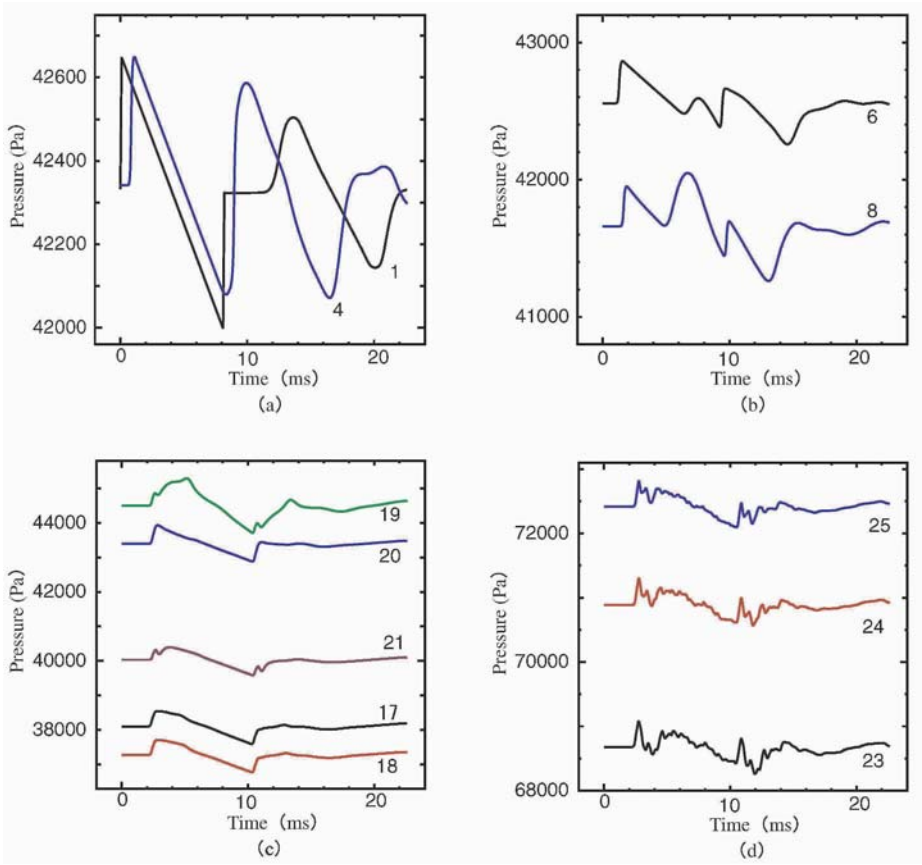

aerodynamic force increases gradually. At the passage of the end shock of the N-wave, the sharp variation of the aerodynamic force repeats again. The sharp variation can be explained as follows: First, the incident shock wave hits upon the suction side of blades reducing the aerodynamic force. Then, the shock wave reflected at the suction side propagates downstream and hits upon the pressure side of blades increasing the aerodynamic force.

Figures 5 (a) to (d) show the blade surface pressure distribution along chord as measured by the perturbation from the steady state condition. We focus on the short period of the passage of the front shock, i.e., from 2.4ms to 3.0ms. The non-steady aerodynamic force experiences a sharp variation during this period. From 2.4ms to 2.6ms the suction side surface pressure increases because of the incident shock wave. The pressure side surface pressure does not change during this time period. Then at 2.8ms the high pressure wave is diffracted around the trailing edge thus increasing the pressure side surface pressure near the trailing edge. In addition to this effect, at 3.0ms and after the pressure wave reflected at the suction side of a blade arrives at the pressure

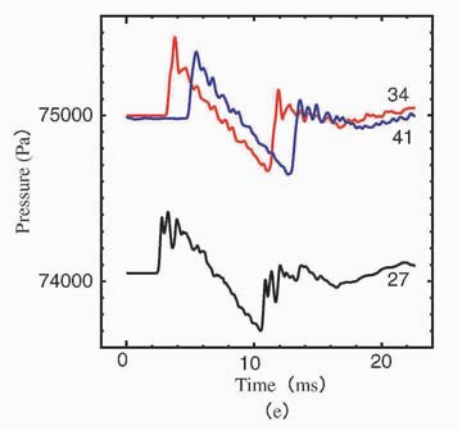

Figure 3. Pressure Variation History at Each Station

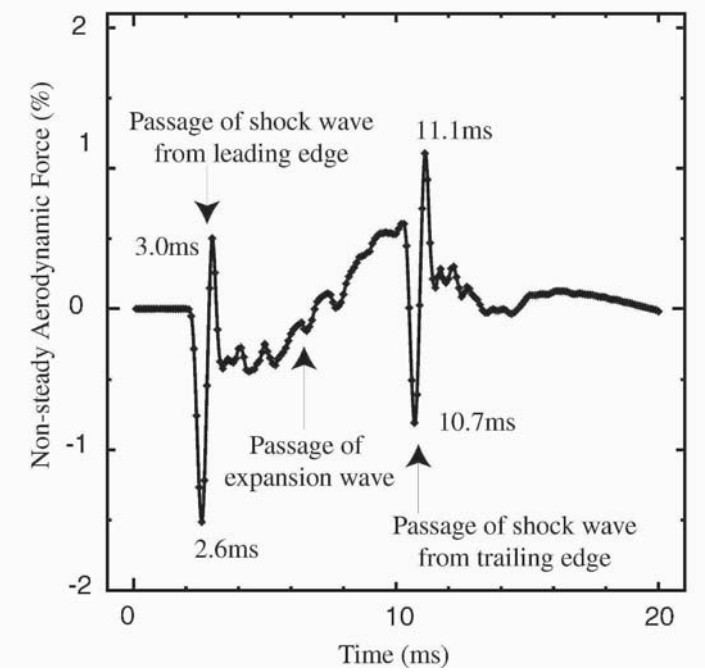

Figure 4. Non-steady Aerodynamic Force (8ms period)

side of the adjacent blade increasing the whole level of the pressure side surface pressure. These behaviors of surface pressure clearly explain the variation of the non-steady aerodynamic force acting on blades.

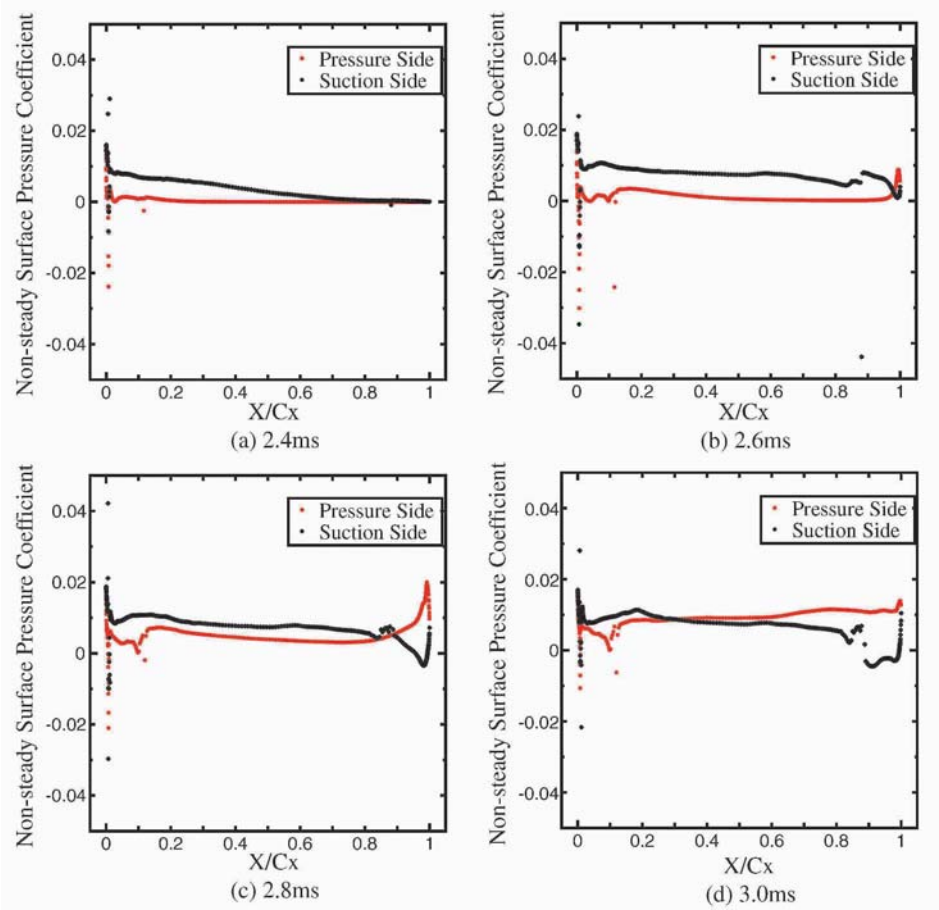

Figure 5. Surface Pressure Distribution

The maximum amplitude of the non-steady aerodynamic force reaches 1.51% of the steady state aerodynamic force for the incident N-wave having the amplitude of 1% of the steady state static pressure. Thus we can conclude that the amplitude of the non-steady aerodynamic force is of the same order of magnitude as the pressure amplitude of the incident N-wave.

4. Conclusions

Interaction between a sonic boom and a transonic cascade of blades is studied numerically. The main results obtained can be summarized as follows.

1 For an incident N wave, the reflected N wave and the transmitted N wave are clearly observed.

2 After passing through the passage shock the increase in the N wave amplitude which has been suggested by the semi-actuator disk analysis is not clearly observed.

3 By the incidence of a sonic boom the aerodynamic force once drops sharply then rises to attain the peak pressure. The mechanism is the process such that first the incident shock wave hits upon the suction side of a blade then be reflected to hit upon the pressure side of the adjacent blade.

4 The maximum amplitude of the unsteady aerodynamic force reaches 1.51% of the steady state aerodynamic force for the incident N wave having the amplitude of 1% of the steady state static pressure.

References

[1] Kaji, S., "Interaction of Sonic Boom and Engine Fan Rotor", *Proc. 9th ISUAAAT*, Sep. 2000, pp.362-374.

[2] Paynter, G. C., Clark, L. T., and Cole, G. L., "Modeling the Response from a Cascade to an Upstream Acoustic Disturbance", *AIAA J.*, Vol.38, No.8, Aug. 2000.

[3] Freund, D. and Sajben, M., "Experimental Investigation of Outflow Boundary Conditions Used in Unsteady Inlet Flow Computations", AIAA paper 97-0610.

[4] Dorney, D. J., "Unsteady Acoustic Wave Propagation in a Transonic Compressor Cascade", AIAA paper 96-0246.

[5] "Study on Advanced Aircraft Technology Development" Report No. 1204, SJAC, 2001.

MEASURED AND CALCULATED UNSTEADY PRESSURE FIELD IN A VANELESS DIFFUSER OF A CENTRIFUGAL COMPRESSOR

Teemu Turunen-Saaresti
Lappeenranta University of Technology
Laboratory of Fluid Dynamics
Teemu.Turunen@lut.fi

Jaakko Larjola
Lappeenranta University of Technology
Laboratory of Fluid Dynamics
Jaakko.Larjola@lut.fi

Abstract An unsteady experimental and numerical investigation was conducted to a centrifugal compressor with a vaneless diffuser. The unsteady static pressure was measured at the diffuser inlet and outlet at three different circumferential positions. Also a time-accurate numerical simulation was carried out. The whole compressor was modeled. Turbulence was modeled with the low Reynolds number $k - \epsilon$ turbulence model. The measurements were made in operation points near the surge, near the choke and at the design operation point of the compressor. The numerical simulations were conducted at the design operation point and at the operation point near the choke. The gathered numerical and experimental unsteady pressures were compared with each other.

Keywords: Unsteady pressure, centrifugal compressor, vaneless diffuser

1. Introduction

The fbw field inside a radial compressor is highly three-dimensional and unsteady. The wakes from the blades of the impeller and the non-axisymmetry of the volute causes a circumferentially varying fbw field in the diffuser. The fbw field in the vaneless diffuser is examined by measuring unsteady pressure at the inlet and outlet of the diffuser and analyzing the whole compressor numerically.

K.C. Hall et al. (eds.),
Unsteady Aerodynamics, Aeroacoustics and Aeroelasticity of Turbomachines, 493–503.

The simultaneous solution of the three-dimensional unsteady Navier-Stokes equations in the impeller and volute requires a large amount of a computational resources. Previously Fatsis et al. [1] have carried out three dimensional unsteady flow calculation of the impeller using Euler solver. Hillewaert and Van den Braembussche [2] have carried out the same simulation with the inclusion of a steady volute calculation. Koumoutsos et al. [3] have conducted viscous three-dimensional unsteady flow calculation to the centrifugal compressor stage with vaned diffuser but the volute was not modeled.

In this paper, the time-accurate simulation was conducted to the whole compressor and the unsteady static pressure was measured at the diffuser inlet and outlet at three different circumferential positions. In the time-accurate simulation, the computational mesh describing the rotational part of the compressor was rotated. The connection between the stationary and the rotating part of the mesh was handled by using the sliding mesh technique. The grid lines between the impeller blocks and the stator block were discontinuous, so a mass conserving interpolation was made at every time step [4]. At first, a time-averaged solution was calculated for the starting point of the time-accurate simulation. Then, using dual time-stepping, in which a pseudo-time integration was performed inside every physical time step, the time-accurate calculation was performed. This way the time history could be taken into account. Turbulence was modeled with the Chien's $k-\epsilon$ model [5]. A parallel computation with six processors was used to achieve a tolerable computational time. The convergence was speeded up with the multigrid method.

The unsteady static pressure measurements were made with Kulite XTC-190 pressure transmitter and the data was collected with a Tektronix oscilloscope connected to the computer. The unsteady pressure was measured within the time of ten rotations of the impeller. The measuring frequency was 1 MHz. Three sets of data were collected at each measuring point. The exact rotation speed of the rotor was measured at the same time.

2. Test Compressor

The modeled and measured compressor is a one-stage radial compressor. The compressor is driven directly by a 175 kW high-speed electric motor that is supplied with variable frequency AC-current by a 200 kW inverter. No gearbox is needed because of the single shaft construction, and the use of an inverter allows variable speed control from zero RPM to full speed. Active magnetic bearings are used in the rotor. The compressor has a mass flow rate of 1.574 kg/s, pressure ratio 2.01, and rotational speed 21640 RPM at the design operation point, and it produces a 50-kPa vacuum at the inlet.

The impeller has 7 full blades and 7 splitter blades with 30° backsweep at the trailing edge measured from the radial direction. The diameter of the

impeller is 309 mm. The diffuser is vaneless and the overhung volute has a circular cross-section. The area of the cross-section of the volute is designed for a constant static pressure along the circumference at the design operation point. More detailed information about the test facilities and the simulated compressor are presented in Ref. [6].

3. Instrumentation

The experiments were conducted in the Laboratory of the Fluid Dynamics at Lappeenranta University of Technology. The layout of the test facility can be seen in Fig. 1. The test stand allows the measurement of ambient pressure, temperature and humidity, mass flow, inlet total pressure and temperature, outlet total pressure and temperature, rotational speed and input power. The compressor can be monitored on-line with the help of an in-house developed data acquisition program.

The unsteady static pressure inside the vaneless diffuser was measured using Kulite XTC-190 miniature transducer. The pressure transducer is mounted to the shroud wall in the diffuser inlet and to the hub wall in the diffuser outlet. The unsteady pressure was also measured at three different circumferential angles 78°, 168° and 348° in the diffuser inlet and outlet (see Fig. 2).

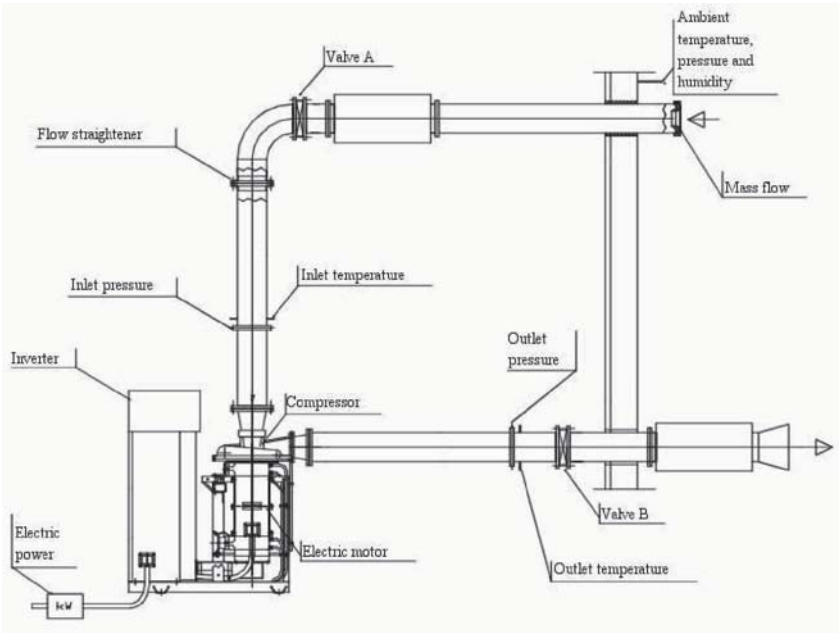

Figure 1. The compressor test facility

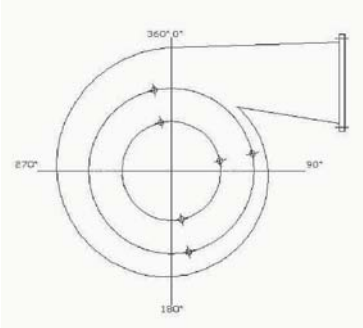

Figure 2. The location of the unsteady pressure transducers

4. Numerical Methods and Boundary Conditions

The computational grid of the compressor is divided to 33 blocks and the number of the computational cells is 618,496. The surface grid of the compressor is shown in Fig. 3. Every second grid line is visible. Tip clearance is not modeled. The topology of the grid has been made in such way that the all blocks except the ones in the volute and exit cone contain clustering near to the walls (Fig. 4).

The inflow boundary conditions for the numerical simulation are given at beginning of the inlet pipe, which is located 1.05 meters above the impeller leading edge. Total enthalpy, mass flow and flow direction at the inlet are defined. The pressure is extrapolated from the flow field and the density is iterated with the help of the total enthalpy and the pressure. The velocity distribution is uniform and the intensity of the turbulence and the dimensionless turbulent viscosity are defined at the inlet plane. The distributions of the velocity and the quantities of the turbulence start to develop before the leading edge of the impeller since the inlet pipe is long. The outflow boundary conditions are given at the end of the outlet pipe 1.60 meters downstream of the end of the volute. The static pressure is given at the outlet to define the pressure level of the solution.

The numerical solver Finflo has been used to carry out the simulations. Finflo is a Navier-Stokes solver developed at Helsinki University of Technology. The Reynolds averaged Navier-Stokes equations are solved by a Finite-Volume method. The code utilizes Roe's Flux-difference splitting, and convergence is accelerated by a multigrid method. More details can be found in Refs. [7] and [8]. The parallelization of the code is based on the Message Passing Interface (MPI) standard [9]. The computational domain is divided into groups of blocks and the boundaries between the groups are updated using MPI. The number of cells in the groups should be equal in order to get the

best benefit from the parallelization. On the other hand, the different groups can contain different amounts of block, which makes it easy to assign the same number of grid cells to each processor to ensure an equal division of the computational workload. [10]. Time-accurate simulation is based on a three-level fully implicit second order time-integration method. This method is described in [11]. The inner iterations are made at every time step. The number of the inner iterations is chosen to get convergence for each time step. In our case, 25 seems to be enough. In this case, the time step is $1\mu s$, which has been found to be small enough to get a solution. The rotor of the compressor is rotated 0.13° at every time step. The connection between the stationary and the rotating part of the mesh is handled by using a sliding mesh technique. The grid lines between the impeller blocks and the stator block are discontinuous, thus a mass conserving interpolation is made at every time step.

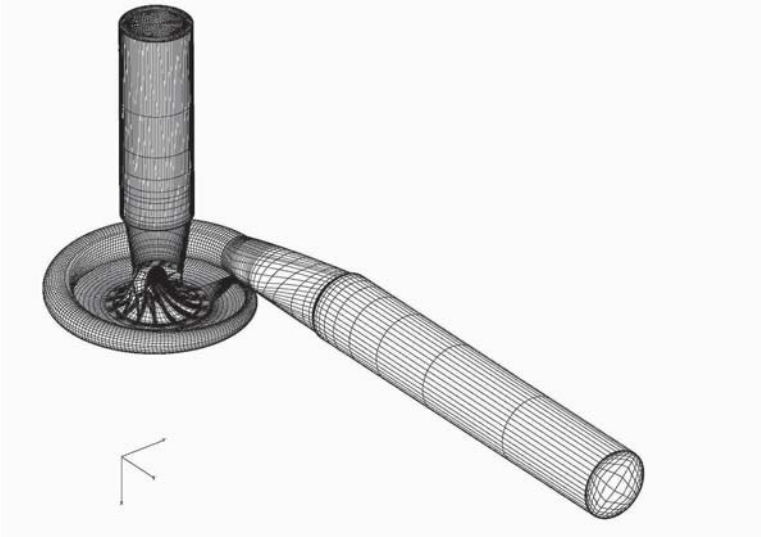

Figure 3. The surface grid of the compressor. Every second grid line is visible

5. Analysis of Time-Dependent Data

The measured data was collected with the measuring frequency of 1 MHz. 30000 data points were collected, which is a 0.03 s period of time. This is 10.8 rotations of the impeller. Three measurements were made at each measuring point and at each operation condition. The measured data was phase averaged over ten rotations of the impeller, and three different sets of measured data were compared to each other to ensure the regularity of the achieved pressure variations. In this case, phase averaging means that the 10 impeller rotations-

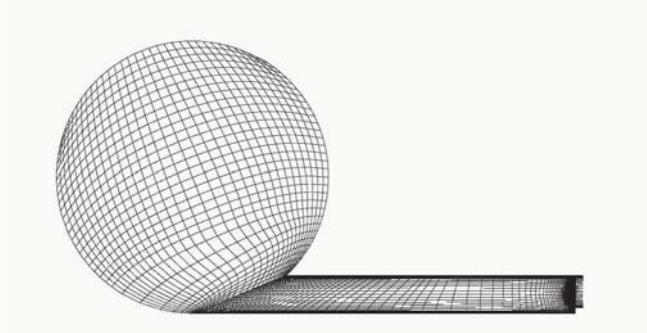

Figure 4. The computational grid of the volute and the diffuser at the 360-degree circumferential position

long measured data were cut in ten 1-rotation-long pieces with the help of the measured rotation speed. Then the measured pressure data points at the same position of the impeller were averaged. The fast Fourier transform (FFT) was made to examine pressure fluctuations in the frequency plane.

The time step used in the computational calculations was $1\mu s$. 11600 time steps were calculated, which is about four rotations of the impeller. The data was collected from the last full rotation of the impeller. The data was taken only at every 10th time step. Even when the data was collected from the last rotation of the impeller and from every 10th time step, the amount of achieved data was over 5 Gb. Static pressures were collected from the calculated data at the same location where the measurements were made. A FFT was also made for the calculated data.

6. Results

6.1 Unsteady pressure at the diffuser inlet

The measured pressure spectra at the diffuser inlet are presented in Fig. 5. The results from different operation points and different circumferential angles are shown. At the operation point near the surge, one can see small variation of the pressure at the blade passing frequency (about 5050 Hz) at every circumferential angle. The amplitude of the pressure variation is about 200 Pa. At the circumferential angle 168° and 348° one can also see the pressure variations at the frequency of every second blade (about 2525 Hz). The amplitude of the pressure variation is larger at the circumferential angle 168° than at the circumferential angle 348°.

At the design operation point, the amplitude of the pressure variations are largest at the frequency of every second blade. The amplitude is a little bit larger at the circumferential angle 168° than at the other circumferential angles. No clear pressure variation is seen at the blade passing frequency.

At the operation point near the choke, larger amplitude of the pressure variations is seen at the circumferential angle $168°$. The frequencies of the variations are the blade passing frequency and the frequency of the every other blade. The larger pressure variation is also seen at the circumferential angle $348°$, and at the blade passing frequency. One can also notice that there are smaller pressure fluctuations at the multiplex frequencies of the rotational speed at every operation point. These fluctuations get larger when the flow through the compressor is increased (see Fig. 5).

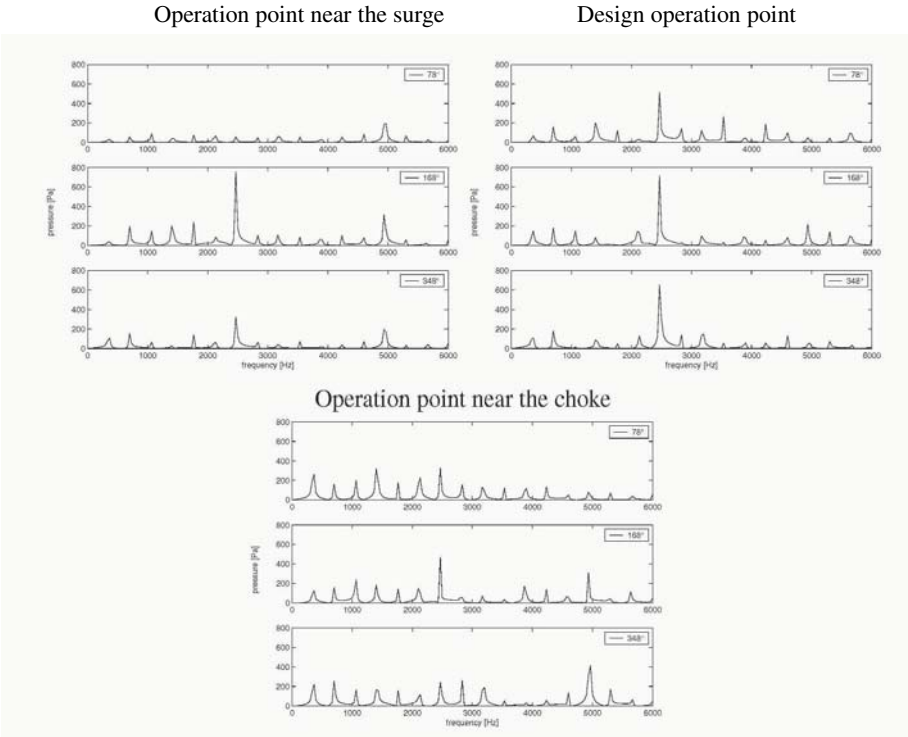

Figure 5. Measured pressure spectra at different circumferential angles at the diffuser inlet

The calculated pressure spectra are presented in Fig. 6. The results from the design operation point, the operation point near the choke, and the different circumferential angles are shown. At the design operation point, one can clearly see pressure variation at the blade passing frequency and at the frequency of every second blade. The amplitude of the pressure variation is largest at the circumferential angle $168°$ and at the frequency of every second blade. The magnitude of the amplitude is the same in the measured and in the calculated pressure spectrum at the frequency of every second blade. On the other hand,

pressure variation is not seen in the measured spectrum at the blade passing frequency (see Fig. 5).

There are larger pressure variations at the multiplex frequency of the rotation speed at the operation point near the choke. The largest amplitude of the pressure variations is seen at the frequency of every second blade and at the circumferential angles 78° and 348°. These are not seen in the measured pressure spectra (see Fig. 5). Larger amplitude of pressure variations is also seen at the blade passing frequency in the calculated spectra. This is also seen in the measured spectra at the circumferential angles 168° and 348°.

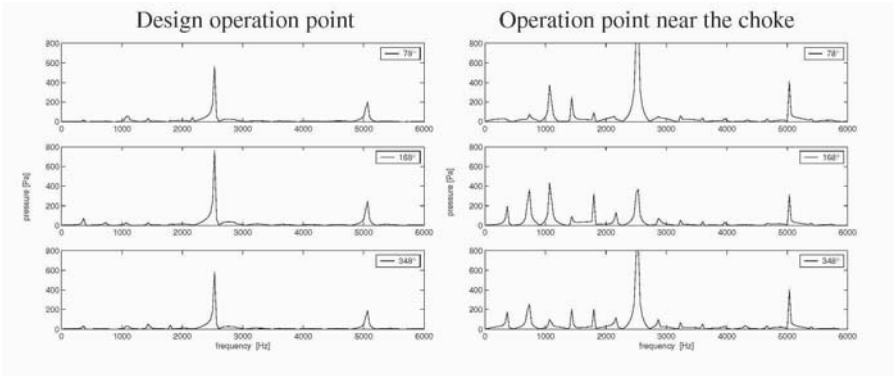

Figure 6. Calculated pressure spectra at different circumferential angles at the diffuser inlet

6.2 Unsteady pressure at the diffuser outlet

The measured pressure spectra at the diffuser outlet are presented in Fig. 7. The results from different operation points and different circumferential angles are shown. At the operation point near the surge, the largest amplitude of the pressure variation is seen at the circumferential angle 348°. However, the largest amplitude of the pressure variation at the diffuser inlet is seen at the circumferential angle 168° (see Fig. 5). There is no large amplitude of pressure variation at the blade passing frequency at the diffuser outlet. On the other hand, pressure variations at the blade passing frequency are visible at the diffuser inlet.

At the design operation point the largest amplitude of the pressure variation is seen at the frequency of every second blade (see Fig. 7). This is also seen at the diffuser inlet, but the amplitude is larger.

At the operation point near the choke the largest amplitude of the pressure variation is seen at the frequency of every second blade and at the circumferential angle 168°. This is also seen at the diffuser inlet.

The calculated pressure spectra are presented in Fig. 8. The results from the design operation point, the operation point near the choke and different circum-

ferential angles are shown. The pressure variation can be seen at the passing frequency of every second blade at the design operation point. The amplitude of the pressure variation decreases when the circumferential angle increases. The magnitude of the pressure variation in the measured data is equal to the magnitude of the pressure variation in the calculated data at the circumferential angles $168°$ and $348°$. Small amplitude of the pressure variation is also seen both in the measured and in the calculated data at the blade passing frequency.

At the operation point near the choke, the behavior of the pressure is similar to the behavior of the pressure at the diffuser inlet. Only the amplitude of the pressure variations is smaller. The calculated data shows large amplitude pressure variations at the frequency of every second blade at the circumferential angles $78°$ and $348°$, which are not seen in the measured pressure spectra.

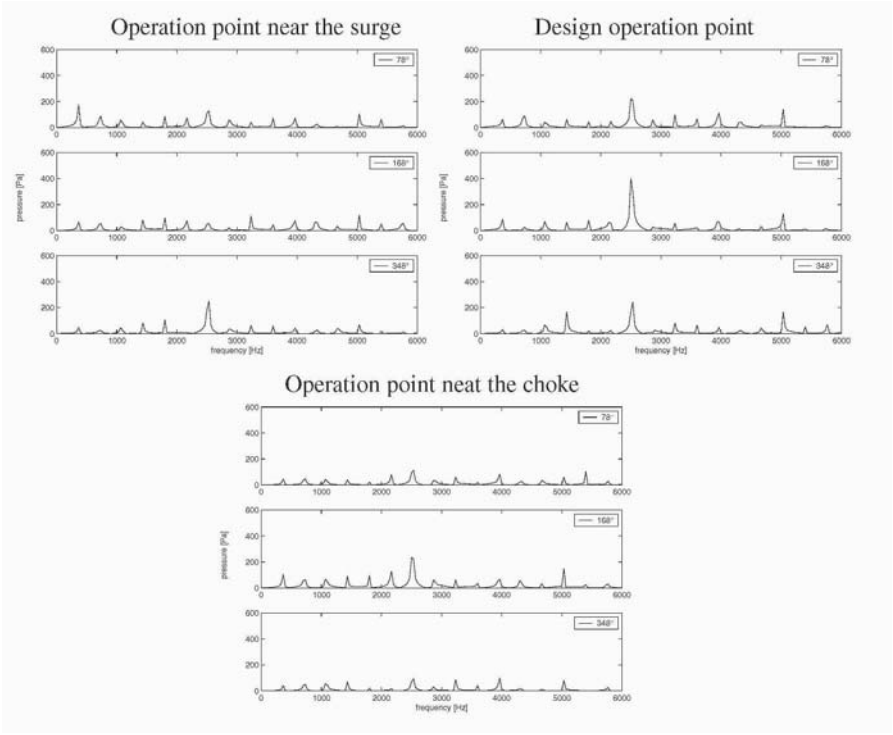

Figure 7. Measured pressure spectra at different circumferential angles at the diffuser outlet

7. Conclusions

An unsteady fbw field in the vaneless diffuser of a centrifugal compressor was investigated. Unsteady static pressure was measured at the diffuser inlet and outlet at different circumferential angles. A time-accurate numer-

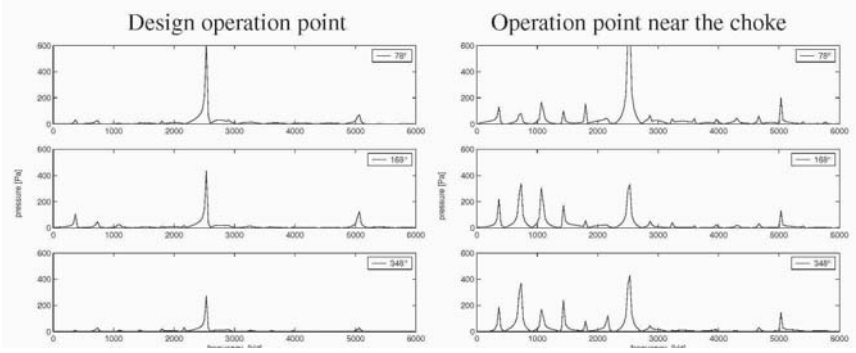

Figure 8. Calculated pressure spectra at different circumferential angles at the diffuser outlet

ical simulation was conducted to the tested compressor. A FFT was made to the measured and calculated static pressure. The provided pressure spectra were analyzed, and the measured and calculated data were compared with each other.

It can be concluded that most of the pressure variations lay at the passing frequency of every second blade. Pressure variations did not vanish in the diffuser and were visible at the diffuser outlet. However, the amplitude of the pressure variations decreased in the diffuser. It can be also concluded that the measured pressure variations were largest at the design operation point.

The time-accurate calculations showed quite good agreement with the measured data. Agreement was very good at the design operation point, even though the computational grid was not dense enough in the volute and exit cone. The time-accurate calculation over-predicted the amplitude of the pressure variations in the operation point near the choke.

Acknowledgments

The authors wish to thank the National Technology Agency (TEKES), High Speed Tech Oy Ltd and Sundyne Corporation for financing this research. CSC-Scientific Computing Ltd provided the computer resources for the numerical work. The authors also wish to thank the Laboratory of Applied Thermodynamics at Helsinki University of Technology and Finfb Oy Ltd for their kind cooperation.

References

[1] Fatsis, A., Pierret, S., Van den Braembussche, R. (1997). Three-Dimensional Unsteady Flow and Forces in Centrifugal Impellers with Circumferential Distortion of the Outlet Static Pressure. Journal of Turbomachinery, Vol. 119, pp. 94-102.

[2] Hillewaert, K., Van den Braembussche, R., A. (1999). Numerical Simulation of Impeller-Volute Interaction in Centrifugal Compressors. Journal of Turbomachinery, Vol 121, pp. 603-608.

[3] Koumoutsos, A., Tourlidakis, A., Elder, R., I. (2000). Computational Studies of Unsteady Flows in a Centrifugal Compressor Stage. Proceedings of the Institution of Mechanical Engineers, Part A: Journal of Power and Energy, Vol. 214, No. 6, pp 611-633.

[4] Rai, M. (1986). A Relaxation Approach to Patched.-Grid Calculations with the Euler Equations. Journal of Computational Physics, Vol. 66, No. 1, pp 99-131.

[5] Chien, K. (1982). Predictions of Channel and Boundary-Layer Flows with a Low-Reynolds-Number Turbulence Model. AIAA Journal, Vol. 20, No 1. pp 33-38.

[6] Reunanen, A. (2001). Experimental and Numerical Analysis of Different Volutes in a Centrifugal Compressor. Lappeenranta, Lappeenranta University of Technology, Acta Universitatis Lappenrantaensis 118. Diss.

[7] Siikonen, T., Pan, H. (1992). An Application of RoeŠs Method for the Simulation of Viscous Flow in Turbomachinery. In: Hirch et al. (eds) Computational Fluid Dynamics '92, Vol.2, Proceeding of the First European Computational Fluid Dynamics Conference, Brussels, Sept. 7-11, 1992. Elsevier Science Publishers B.V. pp. 635-641.

[8] Siikonen, T. (1995). An Application of RoeŠs Flux-Difference Splitting for the $k - \epsilon$ Turbulence Model. International Journal for Numerical Methods in Fluids, Vol 21, pp. 1017-1039.

[9] Message Passing Interface Forum. (1994). ŚMPI: A message-passing interface standard.Š, Technical Report CS-94-230, Computer Science Dept., University of Tennessee, Knoxville, TN.

[10] Rautaheimo, P., Salminen, E., Siikonen, T. (1996). Parallelization of a Multi-Block Navier-Stokes Solver. In Proceedings of the ECCOMAS Congress, Paris, Sept.

[11] Hoffren, J. (1992). Time-Accurate Schemes for a Multi-Block Navier-Stokes Solver. Report A-14, Helsinki University of Technology, Laboratory of Aerodynamics, ISBN 951-22-1350-8.

DPIV MEASUREMENTS OF THE FLOW FIELD BETWEEN A TRANSONIC ROTOR AND AN UPSTREAM STATOR

Steven E. Gorrell, William W. Copenhaver
U.S. Air Force Research Lab
Propulsion Directorate
Wright-Patterson AFB, Ohio

Jordi Estevadeordal
Innovative Scientific Solutions, Inc.
Beavercreek, Ohio

1. Introduction

The use of a planar non-intrusive measurement techniques such as Digital Particle Image Velocimetry (DPIV) have made it possible to investigate many aspects of unsteady flows previously considered difficult due to the effect of a measurement probe on the flow field, or too time consuming because of the pointwise nature of Laser Doppler Velocimetry or Laser Transit Anemometry. Furthermore, time-accurate CFD codes are being developed and are now commonly used to simulate compressors and investigate complex unsteady flow phenomenon.

In this paper, DPIV measurements made in a transonic compressor stage are used to investigate interactions between an upstream stator and a downstream transonic rotor. In particular, the interaction between the rotor bow shock and the wake shed from the upstream stator are explored and offered as a test case for unsteady CFD comparison.

Blade-row interactions are known to have a significant impact on the aeromechanical and aerodynamic performance of compressors. For example, Sanders and Fleeter [1] have shown shock-induced rearward forcing to elicit significant upstream surface-pressure amplitudes and a complicated forcing environment that contributes to High Cycle Fatigue (HCF). Numerous low speed and high speed experimental and numerical investigations [2], [3], [4], [5], [6], [7] have revealed how some blade row interactions improve stage pressure ratio and efficiency while others are detrimental to performance.

K.C. Hall et al.(eds.),
Unsteady Aerodynamics, Aeroacoustics and Aeroelasticity of Turbomachines, 505–519.

Previous experiments using pointwise velocimetry techniques have been used to better understand the three-dimensional geometry of rotor shocks [8], wake recovery [4], wake-shock interactions [9], [10], and for steady CFD code comparison [11].

2. Stage Matching Investigation Rig

The DPIV measurements were acquired on the U. S. Air Force's Stage Matching Investigation (SMI) rig. It is a high-speed, highly-loaded compressor consisting of three blade-rows: a wake generator, rotor, and stator as shown in Fig. 5. The rig was designed so that the wake generator to rotor axial spacing and the wake generator blade count could be varied. The axial spacings were denoted as "close", "mid", and "far". The mid and far spacings represent typical axial gaps found in operational fans and compressors. However, the current generation of high performance fans and compressors are being designed with the goal of minimizing blade-row spacing in order to increase performance and reduce compressor length and thus weight. The wake generator blade count could be set to 12, 24, or 40, or the rig could be run without any wake generators (identified as the "clean inlet" configuration). Table 1 gives the wake generator to rotor axial spacings normalized by the wake generator chord.

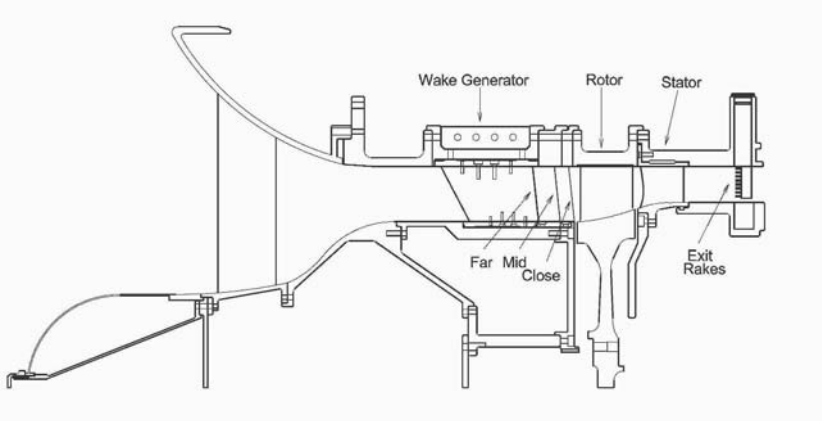

Figure 1. Stage Matching Investigation Rig Layout

2.1 Compressor Stage and Wake Generators

The rotor and stator were designed by Law and Wennerstrom [12]. A summary of the SMI stage aerodynamic design parameters is given in Table 2. The purpose of the wake generators was to create wakes typically found in modern-technology, highly-loaded, low-aspect-ratio fan and compressor front stages. In general, these wakes are turbulent and do not decay as rapidly as

Table 1. Wake Generator-Rotor Axial Spacing

Spacing	ax/c (mean)	ax/c (hub)	ax/c (tip)
Close	0.13	0.10	0.14
Mid	0.26	0.26	0.26
Far	0.55	0.60	0.52

ax = axial spacing
c = wake generator chord

Table 2. SMI Aerodynamic Design Parameters

PARAMETER	ROTOR	STATOR
Number of Airfoils	33	49
Aspect Ratio - Average	0.961	0.892
Inlet Hub/Tip Ratio	0.750	0.816
Flow/Annulus Area, $kg/s/m^2$	195.30	--
Tip Speed, Corrected m/s	341.37	--
M_{REL} LE Hub	0.963	0.820
M_{REL} LE Tip	1.191	0.690
Max D Factor	0.545	0.502
LE Tip Dia., m	0.4825	0.4825

wakes from high-aspect-ratio stages with lower loading. The wake generators were designed with the intent of producing a two-dimensional representation of wakes measured at the exit of a high-pressure-ratio, low-aspect-ratio fan stage reported by Creason and Baghdadi [13]. A two-dimensional representation was desired in order to isolate the effect of different wake parameters during the experiment.

Details of the Wake Generator (WG) design were presented by Gorrell et al. [14]. In summary, the WG's are uncambered symmetric airfoils that do not turn the fbw. They have a small leading edge and a blunt trailing edge. This shape creates a large base drag and no swirl. Solidity is held constant from hub to tip by varying the chord, the intent being to hold spanwise loss and wake width constant.

Calibration of the WG's showed this was the case except near the endwalls. The calibration procedure, instrumentation, and results are found in

Refs. [15] and [16]. From those results, the widening of the wake from close to far spacing was clearly evident. Wake depth was deepest at close spacing and became shallower at mid and far spacing. The wake width was nearly constant from hub to case. This confirmed the intent of the wake generator design to produce a two-dimensional wake profile. The wake is constant in the circumferential and radial directions but not in the streamwise direction. Also evident from rake measurements near the endwalls was the boundary layer growth as the spacing increased from close to far.

From calculated velocity profiles, it was observed that the wake depth was similar at the hub and case and deepest near mid span. Wake decay analyzed by Chriss et al. [16] showed that the SMI wake generator wakes demonstrated similar trends to that compared in the literature.

Due to the blunt trailing edge of the wake generator, its wakes may be wider than what would be produced from a normally cambered stator airfoil, but wake measurements for comparison are not found in the open literature. Regardless of the wake thickness, the loss produced was very near the design intent and well within the range typically found in highly loaded stators.

2.2 SMI Performance

Performance characteristics for the SMI rig are shown in Fig. 5. There was a significant difference in performance between each of the three spacings tested. Both the pressure ratio and efficiency characteristics decreased significantly as the blade-row axial spacing was reduced from far to close. The choking mass flow rate decreased as the blade-row axial spacing was reduced. The difference in pressure ratio, efficiency, and mass flow rate between the far and close spacing configurations was greater than the repeatability documented in Ref. [14]. Therefore it was concluded that the observed change in performance with axial blade-row spacing was real and not due to experimental measurement uncertainty.

3. DPIV System

The DPIV system used to obtain the measurements presented in this paper has been described in detail by Estevadeordal et al. [17]. Figure 5 contains schematics of the optical system. Two frequency-doubled Nd:YAG lasers are employed for instantaneous marking of the seed particles in the flow field. Combined by a polarizing cube or a beam combiner, the beams are directed through sheet-forming optics and illuminate the test section with a 2D plane of thickness $\sim$1 mm. The scattering from the seed particles is recorded on a cross-correlation CCD camera with 1008 x 1018 pixels (Redlake ES1.0). The camera maximum repetition rate is 15 double exposures per second and was set to 10 Hz for synchronization with the laser repetition rate. The time delay between

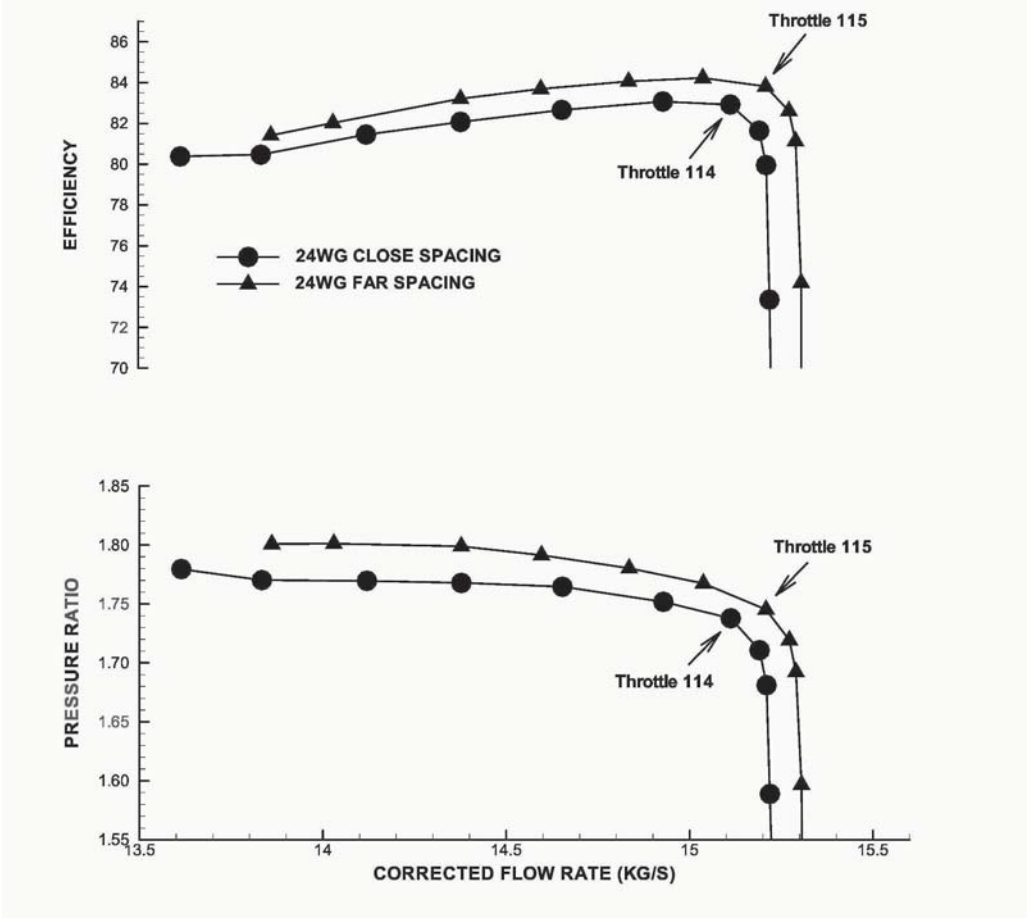

Figure 2. SMI Performance, 24WG's, 100% Corrected Speed

the lasers was typically 2 μsec. For the present experiments where only a small area was to be captured, the camera offered sufficient resolution. A 105-mm Nikon lens was used. The magnification for the present experiments was 17 and 27 pixels/mm which corresponds to a viewing width of 59 mm (close spacing) and 37 mm (far spacing).

The laser-sheet delivery system consists of a probe inserted in an enlarged WG, light-sheet-forming optics, prisms, and probe holders for mounting the optics and for protecting them from contaminated seed materials. To minimize perturbations the modified WG was located two WGs below the WG that was centered at the receiving window. A receiving window made of chemically strengthened glass allowed optical access to the region of interest. Figure 5 shows schematic diagrams of the path for the laser system and the optical probe. Although the path was relatively long, the power required for laser-sheet

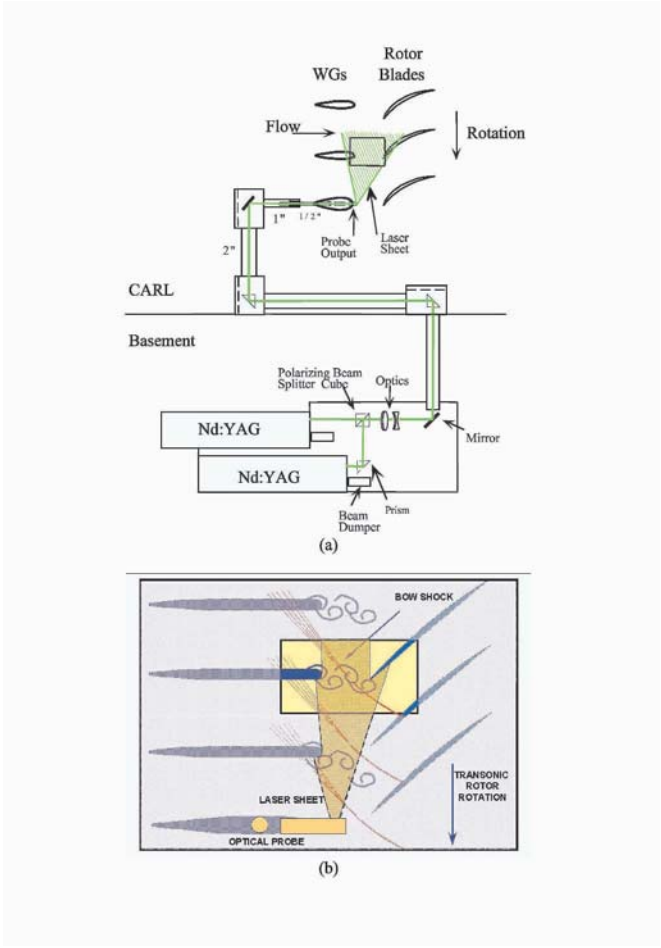

Figure 3. a) Schematic of optical path; b) Schematic of flow features (drawn to scale) showing DPIV delivery and receiving optics

illumination was very low (∼10 mJ/pulse) because of the minimal amount of optics loses. The F stop of the 105 mm lenses was kept at 5.6 for these experiments; this allowed the laser power to be kept low which is important for the safety of the optical components in the optical probe as the beam starts focusing.

The shape of the laser sheet (thickness, width, focal distance) can be changed through various combinations of the spherical-lens focal length, the cylindrical-lens diameter, and the distance between them inside the WG as well as through external optics (a spherical lens) located in the laser path. The spanwise loca-

tion of the laser sheet was changed by rotating the probe (Fig. 5). As shown in this figure, the laser sheet is inclined and not at a constant radius.

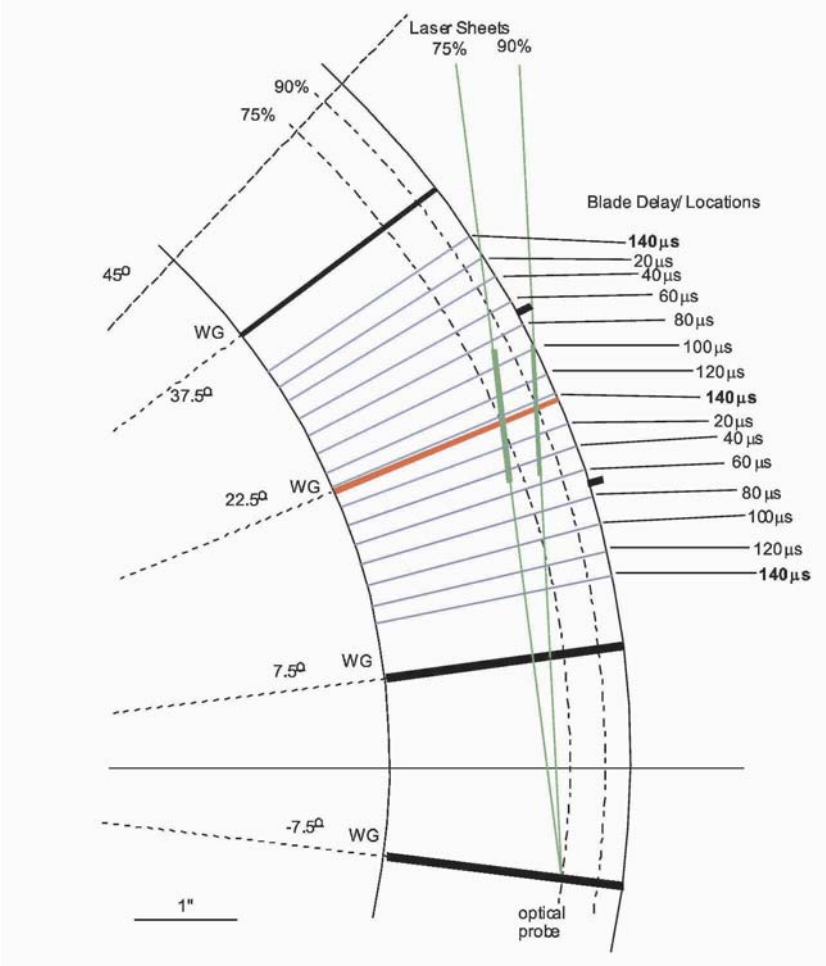

Figure 4. Laser sheet orientation. Blade LE locations are shown at 20 μs intervals with lighter lines. Thicker portions of laser sheets denote DPIV image locations

The length of the probe that was outside the WG could also be changed to provide further flexibility in moving the laser-sheet in the streamwise direction. The probe was set manually before each experiment.

The camera was aligned and focused on the laser sheet prior to each run. It was mounted on a tripod to minimize the effect of rig vibrations. To account for possible motion of the camera with respect to the laser sheet that might occur, the camera was positioned by means of a translation stage that was remotely controlled to allow small corrections in the camera location. Large changes with respect to the laser sheet could produce magnification changes that must

be taken into account. After every experiment, the laser-sheet and camera locations were verified for possible misplacements. In the present experiments, the only change required was slight refocusing, with negligible magnification effects.

The viewing window had the same curvature as the rotor housing (inner housing radius is 241.3 mm), was made of chemically strengthened glass, and had a thickness of 2 mm. The effect of window curvature and thickness was investigated by Copenhaver et al. [18] and found to have a negligible effect for the present CARL setup.

Several options for seeding the high-fbw ($\sim$ 16 kg/s) SMI rig in the CARL facility were evaluated [17], including the use of various seeding units and seed materials. Both local and global seeding was considered. The seed material used was sub-micron-size smoke particles generated from a glycerin and water mixture. During its use in the CARL facility, this system produced sufficient seed when the particles were introduced at the end of the settling chamber, before the contraction, and at the height of the receiving window. The machine can be remotely controlled. The seed material was introduced through a pipe of 50.4-mm diameter located under the contraction entrance.

The rotor one-per-revolution signal was used for triggering the synchronization system. A digital pulse generator (Stanford DG535) and a camera framegrabber (National Instruments PCI-1424) were used.

Once the PIV images have been captured and digitized, the velocity field is obtained using cross-correlation techniques over interrogation domains of the images using DPIV software developed internally. The dimensions of each interrogation domain are dependent on particle density, estimated local velocity gradients, particle-image size, and desired spatial resolution. The peak of the correlation map corresponds to the average velocity displacement within the interrogation spot. An intensity-weighted peak-searching routine is used to determine the location of the peak to sub-pixel accuracy. To improve the signal-to-noise ratio in the correlation maps, a correlation-correction scheme [19] is applied wherein each map is multiplied by its immediate four neighborhoods. An overlapping of 75% is used to include much the same particles in the five maps that are multiplied to yield a single correlation map with lower noise. Zero padding is also employed for adding accuracy. The software includes a grid feature that allows selection of areas of the image to be processed. This permits removal of solid regions such as blades and WGs and also shadows from the processing areas. It also provides a choice of various correlation engines and correlation peak locators and incorporates several improvements to standard (single-pass) PIV techniques such as recursive estimation of the velocity field through a multipass algorithm for increasing resolution. Two passes with interrogation cells overlapping 75% were performed. The interrogation domains are overlapped by three-quarters the domain size to yield more vec-

tors. The overlapping includes new particles in every subregion. Average routines allow for removal of outliers beyond any number of standard deviations. Because of the strong phase-locked flow features, the median offers a valid, robust, and smooth statistical representation of the average velocity field [17].

Many factors are involved in the DPIV uncertainty-calculation process (laser, CCD, seeding, imaging, algorithms, oscilloscope, etc.). The highest uncertainty was found to be associated with the velocity calculation which involves Δx (the displacement in pixels of each interrogation region), Δt (the time interval between the two exposures), and the magnification of the digital image relative to the object (pix/m). The displacement in pixels obtained by peak-locator algorithms can provide sub-pixel accuracy (< 0.1 pixels) after correction for various biases [20]. The Δt was adjusted to yield typical displacements of the main stream > 10 pixels, and the uncertainty is thus < 1%. Values in the wake region, however, may have higher uncertainties due to the lower Δx. The maximum uncertainty in the Δt was calculated from the time interval between the two laser pulses with the aid of an oscilloscope (uncertainty 2%). It was found that this uncertainty increases with lower laser power and with lower Δt. A conservative number for the present experiments, which employed a Δt of about 2 μs and powers around 10 mJ, was found to be 1%. The magnification was measured using images of grids located in the laser-sheet plane to better than 1%. Combining these conservative measurements of uncertainty yields a maximum error of < 2% for the free-stream velocity and $\sim$10% in the wake near the WG area.

4. Results

DPIV results are presented for close and far spacing configurations at 75% span, 100% corrected speed, peak efficiency. Of particular interest is the interaction between the wake generator wake and the rotor bow shock and the effect blade-row axial spacing has on the overall flow field. The median of 50 instantaneous images is plotted as it was found that it provided the clearest image of the flow field.

4.1 Close Spacing

Previous analysis of flow visualization and DPIV results from the SMI rig (Refs. [17], [18], and [21]) have shown that at close spacing vortex shedding from the wake generator trailing edge is phase locked to the rotor blade pass frequency. The main source of the synchronization appears to be the strong pressure perturbation provided by the rotor bow shock to the wake generator trailing edge. At close spacing the instantaneous images of vortex shedding are similar for any given operating condition and blade delay. This is consistent with high response pressure measurements obtained on the wake generator sur-

face, which showed a strong fluctuation in pressure at blade-passing frequency (7.7 kHz). Since the instantaneous DPIV data contains holes in velocity information where seeding was not sufficient to obtain a correlation, it is more informative to look at the average flow field where data intermittency can be minimized. Since the vortex shedding is phase locked to rotor passing, rotor phase locked averaging is possible without destroying the details of the velocity field in this interaction region.

At close spacing DPIV measurements were made at blade delay intervals of 5 μs giving 30 different rotor blade locations for one blade-pass period. Seven of the blade delays are shown in Fig. 5. The rotor bow shock is defined by the large velocity gradient and a change in flow angle toward the shock. Streamlines are drawn near the wake generator to highlight the wake motion at different rotor locations. The wavy motion of the wake is a result of a vortex being shed from the pressure or suction surface of the wake generator. This up and down motion continues as the wake convects downstream and interacts with the rotor bow shock and then is chopped by the rotor blade. Downstream of the rotor bow shock there is an expansion zone due to the flow accelerating around the rotor suction surface.

The DPIV images at blade delay 140 μs and 20 μs illustrates that the shock-wake interaction results in a wider and deeper wake downstream of the shock. At time 20 μs the low velocity region downstream of the shock and within the wake moves up to 18% pitch suggesting that the shock-wake interaction has resulted in an increase in wake width.

From the plot at blade delay 140 μs it is clear that the wake actually splits the shock into two distinct regions above and below the wake. It was also observed that the velocity magnitude at the wake generator trailing edge fluctuates significantly depending on the location of the rotor bow shock. As the shock approaches the wake generator the velocity increases first near the wake generator pressure surface, then on the suction surface. Once the shock is separated and propagates upstream the velocity magnitude decreases. Numerical analysis reported by Gorrell et al. [7] showed that the interaction of the wake generator trailing edge with the rotor bow shock causes the shock to turn more normal to the freestream flow. This phenomenon is also observed in the experimental data presented in Fig. 5.

4.2 Far Spacing

DPIV plots of median velocity at the far spacing configuration are shown in Fig. 5. Due to the limit in laser sheet width, the flow field was not captured near the wake generator trailing edge. The wake shedding frequency is not easily determined as it was at close spacing. Hot wire measurements obtained downstream of the wake generator show the blade-pass frequency of 7.7 kHz

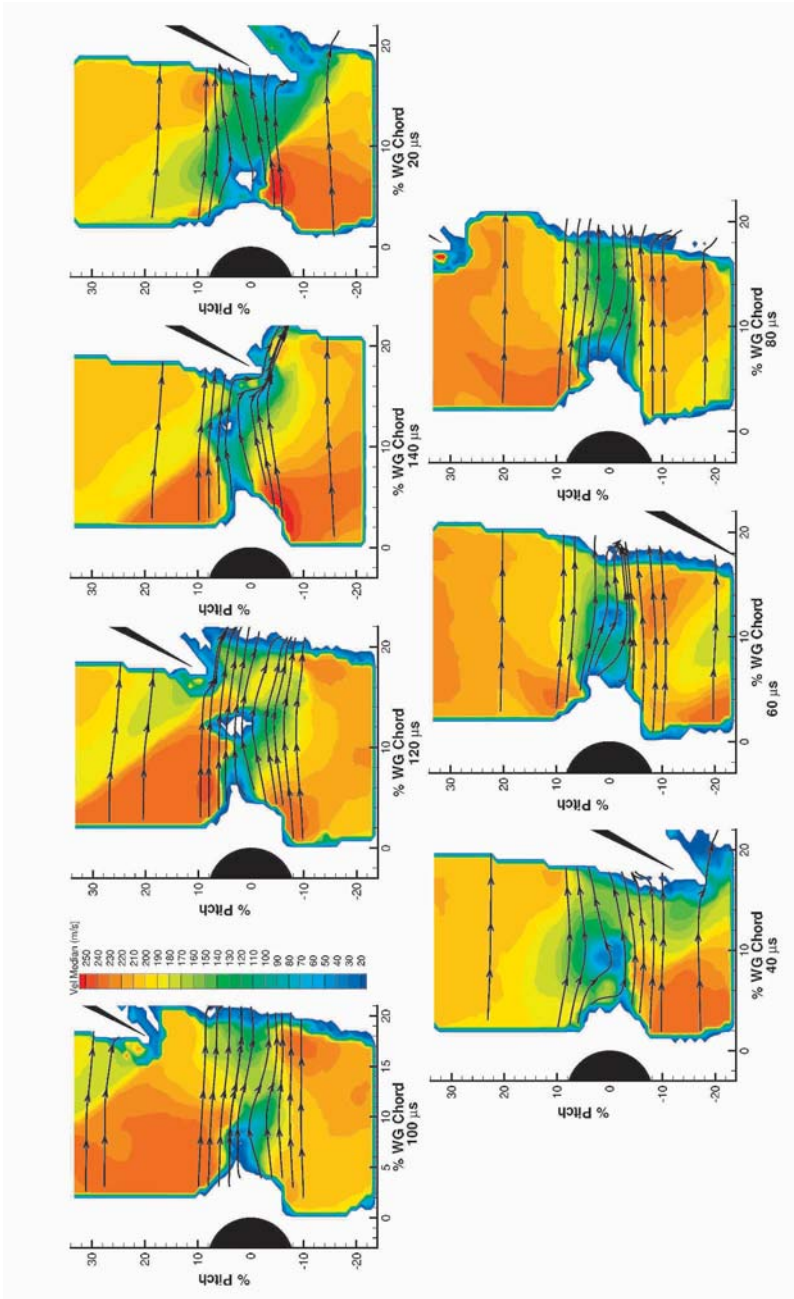

Figure 5. Close spacing, 75% span, median velocity

and another frequency of 8.8 kHz are the most powerful peaks in the spectrum. Further analysis is required to determine the natural shedding frequency of the

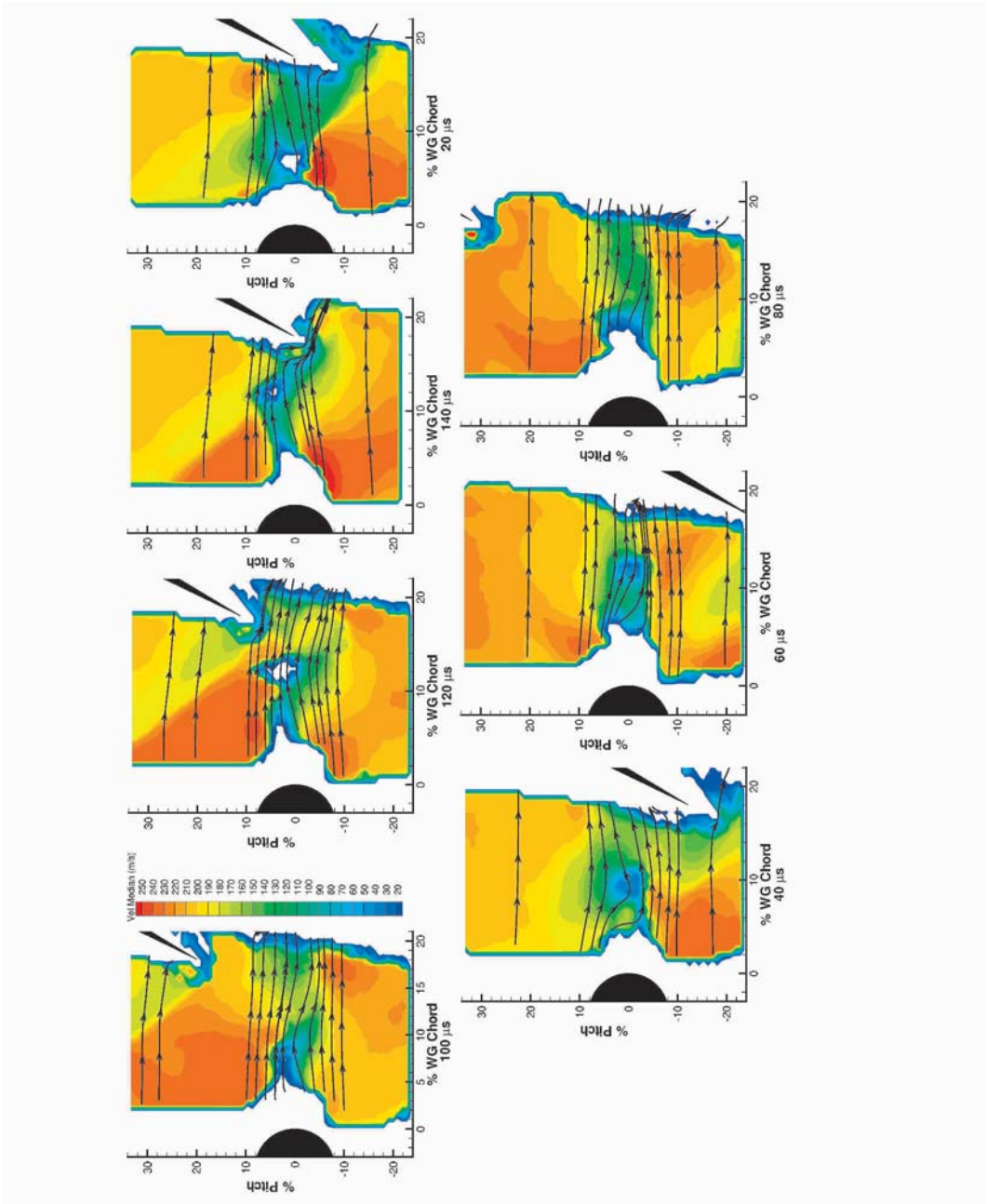

Figure 6. Far spacing, 75% span, median velocity

wake generator. An observation made from the instantaneous flow visualization images (not presented here) suggest a phase locking of the wake shedding to the bow wave perturbation but random motion of the vortices as they convect downstream. At far spacing, two or three shed vortices are present at any given time in the gap between the wake generator and rotor. At close spacing, there is only one vortex present. As a result the averaged instantaneous images at far spacing do not show as clear a view of the wake region as close spacing. Nevertheless, plots of median velocity still illustrate important details of the far spacing flowfield.

Analysis of Fig. 5 shows bands of low and high velocity in the flow field that are a result of the rotor bow shock and expansion zone. At far spacing, the rotor bow shock is not as well defined because it is weaker than at close spacing. This is evident from the peak velocity magnitude observed in the DPIV images. The peak velocity at far spacing is approximately 220 m/s while at close spacing it is 245 m/s. Due to the increased axial gap between the rotor leading edge and wake generator the rotor bow shock has dissipated into more of a bow wave at the location it interacts with the wake generator trailing edge.

The wake generator wake has mixed out more resulting in a wider and shallower wake. The interaction of a weaker wake with a weaker bow shock does not split the rotor bow shock into two clearly defined regions such as was observed at close spacing.

5. Summary

A DPIV system for use in transonic turbomachinery has been described. Results from an experiment conducted in the SMI rig are presented that show the complex flow field associated with the interaction of a downstream transonic rotor with an upstream stator. The effect of changing the axial gap between blade-rows is studied and the DPIV plots are presented as an experimental data set for time accurate CFD validation.

At close spacing, the wake shedding is synchronized with the rotor blade-pass frequency. The interaction of the rotor bow shock and wake generator causes the wake to expand downstream of the shock. The shock is split into two regions above and below the wake. As the shock approaches the wake generator trailing edge, the velocity increases and the shock to turn more normal to the freestream flow.

At far spacing the wake convects downstream in a chaotic fashion. Bands of high and low velocity are evident from the rotor bow shock and expansion waves downstream of the shock. The interaction between the rotor bow shock and wake generator is much weaker than the close spacing interaction. The wake has mixed out more at the location it interacts with the shock and does not split the shock in two nor turn the shock normal to the freestream flow.

Acknowledgments

The wake generators, rotor, and stator were built by Pratt & Whitney. From the CARL group at Wright-Patterson AFB the authors would like to recognize Dr. Herb Law, Robert Wirrig, Ron Berger, Terry Norris, Bill Ullman, and Chris Blackwell for their assistance in gathering the data. The assistance of Dr. Sivaram Gogineni and Dr. Larry Goss of ISSI in setting up the DPIV system is also recognized. Post processing of the results was assisted by Justen England and Nathan Woods. The authors thank the Propulsion Directorate management for supporting the research and allowing the presentation and publication of this paper.

References

[1] Sanders, A. and Fleeter, S. Experimental Investigation of Rotor-Inlet Guide Vane Interactions in Transonic Axial-Flow Compressor. *AIAA Journal of Propulsion and Power*, 16(3):421–430, 2000.

[2] Smith, L. H. Wake Dispersion in Turbomachines. *ASME Journal of Basic Engineering*, (3):668–690, 1966.

[3] Smith, L. H. Wake Ingestion Propulsion Benefit. *AIAA Journal of Propulsion and Power*, 9(1):74–82, 1993.

[4] Van Zante, D. E., Adamczyk, J. J., Strazisar, A. J., and Okiishi, T. H. Wake Recovery Performance Benefit in a High-Speed Axial Compressor. *ASME Journal of Turbomachinery*, 124:275–284, 2002.

[5] Van de Wall, A. G., Kadambi, J. R., and Adamczyk, J. J. A Transport Model for the Deterministic Stresses Associated With Turbomachinery Blade Row Interactions. *ASME Journal of Turbomachinery*, 122:593–603, 2000.

[6] Gorrell, S. E, Okiishi, T. H., and Copenhaver, W. W. Stator-Rotor Interactions in a Transonic Compressor, Part 1: Effect of Blade-Row Spacing on Performance. *ASME Journal of Turbomachinery*, 125:328–335, 2003.

[7] Gorrell, S. E, Okiishi, T. H., and Copenhaver, W. W. Stator-Rotor Interactions in a Transonic Compressor, Part 2: Description of a Loss Producing Mechanism. *ASME Journal of Turbomachinery*, 125:336–345, 2003.

[8] Strazisar, A. J. Investigation of Flow Phenomena in a Transonic Fan Rotor Using Laser Anemometry. *ASME Journal of Engineering for Gas Turbines and Power*, 107:427–435, 1985.

[9] Ottavy, X., Trebinjac, I., and Voullarmet, A. Analysis of the Interrow Flow Field Within a Transonic Axial Compressor: Part 1 - Experimental Investigation. *ASME Journal of Turbomachinery*, 123:49–56, 2001.

[10] Ottavy, X., Trebinjac, I., and Voullarmet, A. Analysis of the Interrow Flow Field Within a Transonic Axial Compressor: Part 2 - Unsteady Flow Analysis. *ASME Journal of Turbomachinery*, 123:57–63, 2001.

[11] Calvert, W. J. Detailed Flow Measurement and Predictions for a Three-Stage Transonic Fan. *ASME Journal of Turbomachinery*, 116:298–305, 1994.

[12] Law, C. H. and Wennerstrom, A. J. Two Axial Compressor Designs for a Stage Matching Investigation. Technical Report AFWAL-TR-89-2005, Air Force Wright Aeronautical Laboratory, WPAFB, OH, 1989.

[13] Creason, T. and Baghdadi, S. Design and Test of a Low Aspect Ratio Fan Stage. AIAA Paper 88-2816, 1988.

[14] Gorrell, S. E., Copenhaver, W. W., and Chriss, R. M. Upstream Wake Influences on the Measured Performance of a Transonic Compressor Stage. *AIAA Journal of Propulsion and Power*, 17(1):43–48, 2001.

[15] Gorrell, S. E. *An Experimental and Numerical Investigation of Stator-Rotor Interactions in a Transonic Compressor*. PhD thesis, Iowa State State University, Ames, Iowa, 2001.

[16] Chriss, R. M, Copenhaver, W. W., and Gorrell, S. E. The Effects of Blade-Row Spacing on the Flow Capacity of a Transonic Rotor. ASME Paper 99-GT-209, 1999.

[17] Estevadeordal, J., Gogineni, S., Goss, L., Copenhaver, W., and Gorrell, S. Study of Wake-Blade Interactions in a Transonic Compressor Using Flow Visualization and DPIV. *ASME Journal of Fluids Engineering*, 124(1):166–175, 2002.

[18] Copenhaver, W., Estevadeordal, J., Gogineni, S., Gorrell, S., and Goss, L. DPIV study of near-stall wake-rotor interactions in a transonic compressor. *Experiments in Fluids*, 33:899–908, 2002.

[19] Hart, R. The Elimination of Correlation Errors in PIV Processing. In *9th International Symposium on Applications of Laser Techniques to Fluid Mechanics*, Lisbon, Portugal, 1998.

[20] Westerweel, J. Fundamentals of Digital Particle Imaging Velocimetry. *Measurement Science and Technology*, 8:1379–1392, 1997.

[21] J., Estevadeordal, Gogineni, S., Goss, L., Copenhaver, W., and Gorrell, S. DPIV Study of Wake-Rotor Synchronization in a Transonic Compressor. AIAA Paper 01-3095, 2001.

UNSTEADY PRESSURE MEASUREMENT WITH CORRECTION ON TUBING DISTORTION

H. Yang, D. B. Sims-Williams, and L. He
School of Engineering, University of Durham, Durham, DH1 3LE, U.K.

Abstract A method of correcting distortion in measured unsteady pressures using a tubing system and off-board pressure transducers is described. This technique involves the frequency domain correction using the known tubing transfer function and not only corrects the amplitude distortion, but also eliminates the phase shift. The technique is demonstrated for surface pressures in a turbomachinery blade flutter case, and for wake measurements for a vortex shedding case.

1. Introduction

In recent years, computational methods for predicting unsteady flow through turbomachines have been fully developed. For the validation of these codes, systematic, accurate, and detailed unsteady pressure experimental data are needed. Most previous measurements are confined to the use of miniature high-response pressure transducers buried in the blade surface (largely on 2D sections) of linear oscillating cascades (Buffum 1993, Carta 1978 and Fleeter, 1977), annular cascades (Bölcs and Körbächer, 1993, Fransson 1990) and rotating machines (Manwaring 1997, Frey 2001, Minkiewicz 1998). Due to the transducer size limitation and airfoil contour preservation as well as expensive cost, only a limited number of unsteady signals can be obtained. Unsteady (static and stagnation) pressure field patterns are not obtained; these could be used to improve understanding of the flow, to identify modeling limitations, and to aid future development for both aeromechanic and aerothermal (e.g. unsteady loss) applications. With embedded transducers, the movement of the blade subjects the transducer to an acceleration, for which an extensive calibration and correction is required. Various installation configurations have been designed to isolate the miniature pressure transducers from the airfoil strain and centrifugal loads to improve the durability. Improved transducer characteristics are desired to diminish temperature sensitivity. In order to provide the required spatial resolution of the unsteady flow measurements at blade sur-

K.C. Hall et al. (eds.),
Unsteady Aerodynamics, Aeroacoustics and Aeroelasticity of Turbomachines, 521–529.

faces, various optical measurement techniques (pressure sensitive paints – PSP, doppler sensors, micromachined fabry-perot pressure sensors and so on) were developed. However, every method requires a complicated optical technique and expensive equipment. These issues can be avoided by using off-board pressure transducers. The blade can be instrumented by detailed static pressure tappings, which are connected to the off-board pressure transducer by the pneumatic tubing. This approach makes economical use of pressure transducers. However, the tubing system, characterized by the tubing length, its internal diameter, and the transducer internal volume, introduces a distortion of the unsteady signals. In the area of turbomachinery aeroelasticity, this distortion of the unsteady signal was generally either neglected because of low frequencies and short tubing lengths (He & Denton, 1991), or it simply was corrected for phase lag and amplitude attenuation for a certain tubing length (Bell and He, 2000). In the present work, a correction method is used which is more generally applicable in that it corrects phase lag and amplitude for all frequencies using a measured transfer function for each tube.

In contrast to the low reduced frequencies for blade flutter, in the case of forced response, higher frequencies associated with higher order modes can be excited. Even for the low modes of blade flutter applications, higher flow velocities at more realistic conditions require high physical frequencies to reach realistic reduced frequencies. If off-board pressure transducers are used to measure unsteady signals, these signals will be distorted by the pressure measurement system, and a correction must be performed. In the present paper, a tubing transfer function approach involving a frequency domain correction is described, typical transfer functions are presented, and the correction technique is demonstrated for the tubing system in isolation, for surface pressures in a turbomachinery blade flutter case, and for wake measurements for a vortex shedding case.

2. Theory of Tubing Transfer Function Approach

The tubing transfer function approach presented in this paper is based on a technique originally employed for wall pressure measurements in wind engineering by Irwin et al. (1979). This technique was subsequently applied for multi-hole probe measurements by Sims-Williams and Dominy (1998a) and by Hooper and Musgrove (1991).

The unsteady pressure signal propagates from the pressure tapping to the off-board pressure transducer via the tubing between them. The signal can be amplified by resonance effects at particular frequencies and will be attenuated by viscous effects at higher frequencies. There will also be a time-lag for the pressure signal to reach the transducer which will result in an increasing phase

offset at higher frequencies. This frequency-dependent tubing response can be characterized by a transfer function. Once the transfer function of a given tubing system is known, then it is possible to correct for the tubing distortion. This technique requires that the system obeys the principal of linear superposition so that an unsteady signal can be decomposed into multiple frequency components, and this has been confirmed.

To utilize this approach, the tubing transfer function of the pressure measuring system must be known in advance, and this can be obtained experimentally. A test unsteady pressure signal including a range of frequencies is recorded by a reference pressure transducer directly and by another pressure transducer via a tubing length used for actual unsteady pressure measurements. Fast Fourier Transforms (FFTs) of both the undistorted and distorted signals are computed. The complex tubing system transfer function $TF(f)$ is expressed as:

$$TF(f) = \frac{B(f)}{A(f)} \tag{1}$$

where $A(f)$are the complex Fourier coefficients of the pressure measured by the reference transducer, and $B(f)$ are the complex Fourier coefficients of the distorted pressure.

When aerodynamic measurements are later recorded, an FFT of the (distorted) signal is performed in order to obtain the Fourier coefficients in the frequency domain of the distorted signal ($B(f)$). The known transfer function is then used to infer the Fourier coefficients of the signal prior to distortion ($A'(f)$):

$$A^{'}(f) = \frac{B(f)}{TF(f)} \tag{2}$$

The corrected coefficients $A^{'}(f)$ are then transformed back to the time domain using an inverse FFT in order to obtain a corrected pressure signal with the effect of tubing distortion eliminated. Both amplitude and phase distortions are removed, the latter being essential if multiple simultaneous signals are to be compared.

3. Implementation Issues

A block diagram of the apparatus used in measurements of TTF of a static pressure tapping and the pneumatic tubing is presented in Fig. 1.

A swept sine wave is generated which covers the range of frequencies of interest, and this is fed to an audio amplifier and loudspeaker. For the blade flutter case, the frequency range used was 0.1 Hz to 50 Hz, with a sweep period 0.75 second when logging sets of 2048 samples at 800 Hz. The loudspeaker produces pressure fluctuations with roughly the same wave forms as the input voltage. The loudspeaker is connected to a small cavity via a short rubber tube

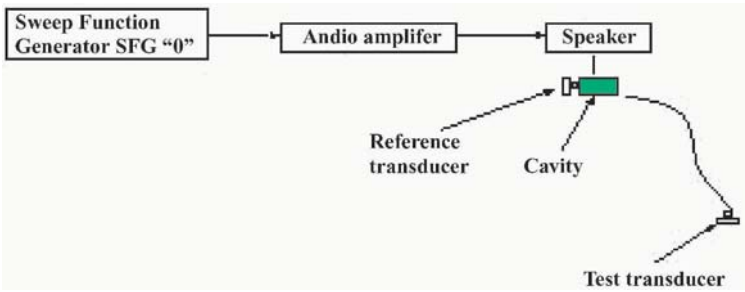

Figure 1. Correction apparatus

to isolate mechanical vibrations. A reference pressure transducer is directly connected to the small cavity and used to record the pressure inside the cavity. A static pressure tapping used in the unsteady pressure measurement (0.3 mm diameter for blade flutter case) is also connected to the cavity. A length of plastic tube is used to connect the static pressure tapping with the other (off-board) pressure transducer as would be done for the aerodynamic measurements.

In the blade flutter case, the reference transducer (type: Sensym 113LP01d-PCB, -1-+1 mbar range) uses the ambient pressure as a reference, and the test transducer (type: Sensym 142C01D, 0-1 psi range) uses the total pressure of the setting chamber of the wind tunnel as a reference, which is the same as that in unsteady pressure measurements. The tubing system includes the transducer's internal volume, the connector, the Portex plastic tubing, and the brass tube with six static tappings– the tapping style for the blade flutter case.

The definition used to calculate the complex transfer function is:

$$TF(f) = \frac{1}{M} \sum_{j=1}^{M} [(B(f))_j / (A(f))_j] \tag{3}$$

where M is the number of sets used to average $TF(f)$. The Fourier coefficients $A(f)$ and $B(f)$ are defined above.

In order to obtain smooth transfer function desired for correcting pressure signals, M, can be greater than 20. A Hanning window function is used to reduce the effect of the finite data length, which has been found to improve the quality of the results.

4. Examples

Figure 2 shows a typical example of the measured tubing transfer function for a tubing length used in the measurement of unsteady pressures in an os-

cillating cascade. In this case a slight amplification can be seen over the frequency range of interest, indicating a resonant peak at a higher frequency. The phase distortion is more significant due to the importance of the relative phase of surface pressure fluctuations and the vibration of the blade.

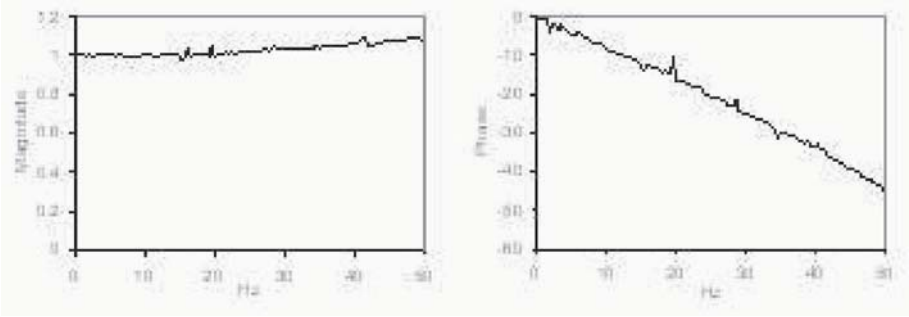

Figure 2. Transfer Function of the measurement system for the blade flutter case (brass tube, 180mm x 1mm Portex tubing and connector)

Figure 3 shows the transfer function for a single tube of a 5-hole probe used to make measurements in the wake of a bluff body exhibiting vortex shedding. Small tube diameters near the probe head and a longer tubing length results in a system in which viscous attenuation dominates over any resonant effects.

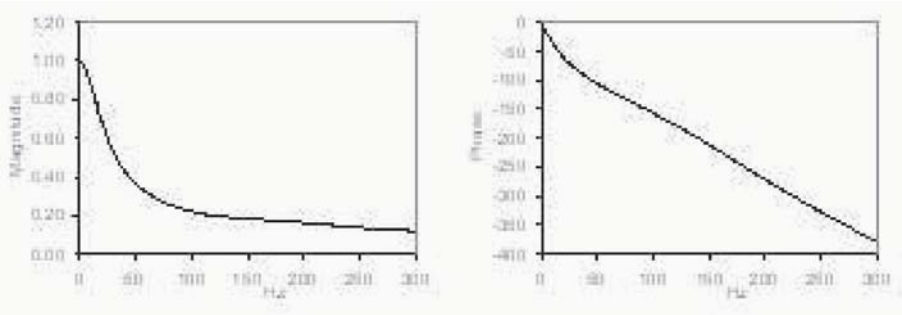

Figure 3. Transfer Function of the measurement system for the vortex shedding case (5 hole probe, 0.75mm Portex tubing and connector)

Figure 4 shows the effectiveness of the transfer function correction method in reconstructing an original reference signal from a distorted one. The tubing system of Fig. 3 was subjected to a 100Hz saw waveform using the transfer function measurement apparatus. Significant phase lag and attenuation relative to the reference signal is clearly apparent in the uncorrected signal and the increased attenuation of higher harmonics alters the waveform shape. The previously measured transfer function was then used to infer the original signal

and this is labeled "corrected" in Fig. 4. This can be seen to closely match the original reference signal.

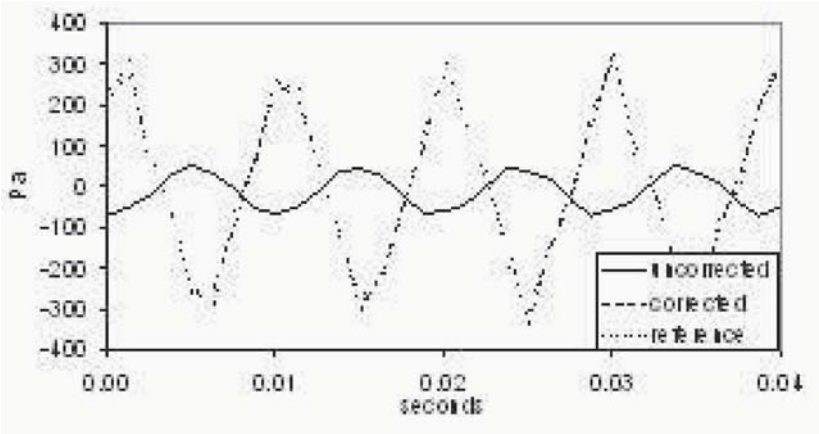

Figure 4. Effect of transfer function correction with single hole of a 5-hole probe (100Hz saw wave)

The requirement for miniaturization of pneumatic probes makes the use of off-board transducers particularly attractive, however, traditionally this has been assumed to limit the probe to steady-state measurements only. By using transfer function correction, it is possible to use a conventional pneumatic probe to make time-accurate measurements. To validate the use of transfer function correction for probe measurements, the 5-hole probe used above was mounted adjacent to a single element hot-wire probe in the wake of a bluff body exhibiting vortex shedding at frequency of 58 Hz. The agreement between the hot-wire and pneumatic probe with transfer function correction was similar to the level of agreement between two hot-wire probes at the same spacing in the same flow. Further details can be found in Sims-Williams and Dominy (1998b).

Because probes are generally used to make measurements at different locations in the flow-field sequentially, some form of synchronization is required in order to obtain instantaneous flow-field data. In cases where the unsteadiness is imposed externally (eg: forced vibration), or where it is coupled with some mechanical oscillation (eg: aeroelasticity), this may be accomplished using triggered sampling from the mechanical motion. For cases of self-excited aerodynamic unsteadiness, this is more difficult. The unsteady reconstruction technique of Sims-Williams and Dominy (2000) uses a signal from a stationary reference probe, and a complex convolution in the frequency domain, to effectively synchronize probe measurements made sequentially. This provides a more robust determination of relative phase than simply using triggered sam-

pling, and this makes the technique appropriate even for weakly periodic flow-fields. Figure 5 shows the instantaneous vorticity field in the wake of a "Gurney Flap" high lift device on the trailing edge of an inverted airfoil. By producing a series of these images vortex shedding can be clearly observed.

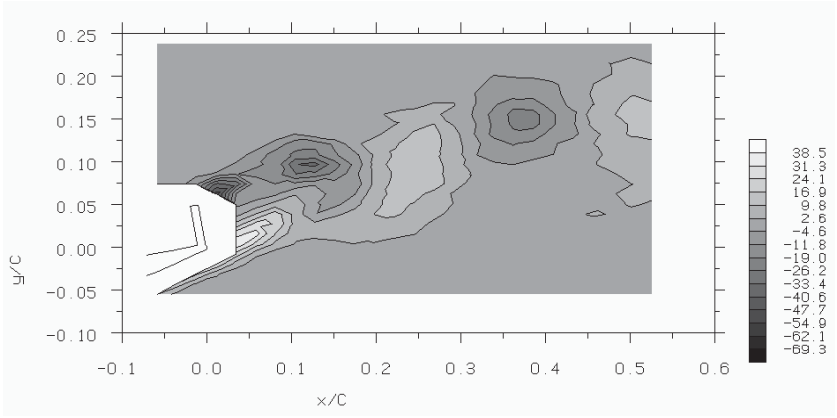

Figure 5. Instantaneous non-dimensional vorticity in the wake of a Gurney Flap

Unlike other methods of unsteady flow-field measurement, the use of a pressure probe allows the observation of static and stagnation pressure, as well as velocity. Figure 6 illustrates the instantaneous stagnation pressure field corresponding to Fig. 5. An issue of interest regarding the understanding/interpretation of unsteady results is the decoupling between stagnation pressure (*the measure of loss for steady flow only*) and entropy (*the measure of loss in general*). This has been observed computationally for a LP turbine cascade subject to incoming unsteady wakes (He, 1992, 1996) and has been observed computationally and experimentally adjacent to the wake of bluff bodies exhibiting vortex shedding (Sims-Williams and Dominy 1998b). In Fig. 6, packets of stagnation pressure deficit corresponding to the shed vortices can be observed, but importantly, it is also possible to see regions where the stagnation pressure coefficient is greater than unity. As discussed above, in an unsteady flow, instantaneous stagnation pressure and entropy become uncoupled. The frequency of the shedding in this case was approximately 300Hz. Further details of this work on Gurney flap vortex shedding may be found in Sims-Williams et al. (1999) and Sims-Williams (2001).

The upper limit on the frequency response, which can be obtained for multi-hole probes using transfer-function correction, is restricted both by the level of correction required (which results in a deterioration in signal to noise ratio), and by time required for the flow around the head of the probe to develop (since the assumed sensitivity of the probe is based on a steady-state calibration).

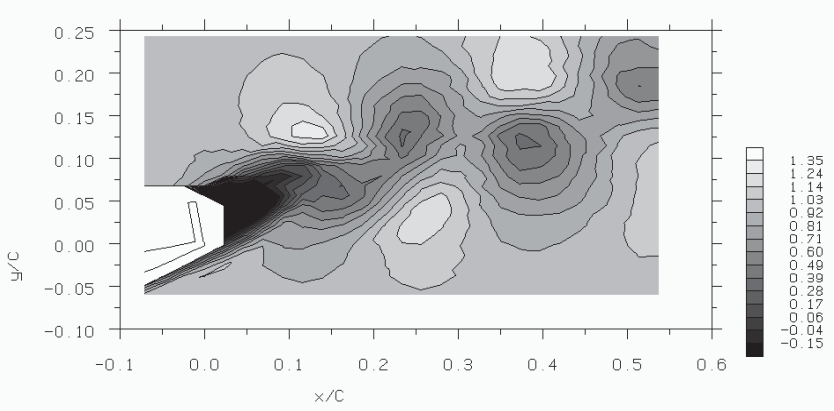

Figure 6. Instantaneous stagnation pressure coefficient in the wake of a Gurney Flap

For typical multi-hole probes used in low-speed applications, these two factors both suggest a similar upper limit in the region of 1000Hz.

References

[1] Bell, D.L. and He, L., 2000, Three-Dimensional Unsteady Flow for an Oscillating Turbine Blade and the Influence of Tip Leakage, *Journal of Turbomachinery*, Vol. 122, pp. 93–101.

[2] Buffum, D.H. and Fleeter, S., 1993, Wind Tunnel Wall Effects in a Linear Oscillating Cascade, *Journal of Turbomachinery*, Vol. 115, pp. 147–156.

[3] Bölcs, A. and Körbächer, H., 1993, Periodicity and Repetitivity of Unsteady Measurements of an Annular Turbine Cascade at off design Flow Conditions, ASME 93-GT-107.

[4] Carta, F.O. and St. Hilaire, A.O., 1978, Experimentally Determined Stability Parameters of a Subsonic Cascade Oscillating Near Stall, *Journal of Engineering for Power*, Vol. 100, pp. 111–120.

[5] Fleeter, S., Novick, A.S., Riffel, R.E. and Caruthers, J.E., 1977, An Experimental Determination of the Unsteady Aerodynamics in a Controlled Oscillating Cascade, *Journal of Engineering for Power*, Vol. 99, pp. 88–96.

[6] Fransson, T. H., 1990, Analysis of Experimental Time-Dependent Blade Surface Pressures from an Oscillating Turbine Cascade with the Influence-Coefficient Technique, ASME 90-GT-225.

[7] Frey, K.K. and Fleeter, S., 2001, Oscillating Airfoil Aerodynamics of a Rotating Compressor Blade Row, *Journal of Propulsion and Power*, Vol. 17, pp. 232–239.

[8] He, L., 1992, Stagnation Pressure-Entropy Decoupling on a High Load LP Turbine Cascade, Unpublished work, Whittle Laboratory, Cambridge University.

[9] He, L., 1996, Time-marching Calculations of Unsteady Flows, Blade Row Interaction and Flutter, Unsteady Flows in Turbomachines, Lecture Series 1996-05, von Karman Institute for Fluid Dynamics, Brussels, Belgium.

[10] He, L. and Denton, J.D., 1991, An Experiment on Unsteady Flow Over an Oscillating Airfoil, ASME paper 91-GT-181.

[11] Hooper, J.D. and Musgrove, A.R., 1991, Multi-Hole Pressure Probes for the Determination of the Total Velocity Vector in Turbulent Single-Phase Flow, 4th International Symposium Transport Phenomena in Heat and Mass Transfer, The University of New South Wales, Sydney, Australia, ed. JA Reizes, July, 1991.

[12] Irwin, H.P.A.H., Cooper, K.R. and Girard, R., 1979, Correction of Distortion Effects Caused by Tubing Systems in Measurements of Fluctuating Pressures, *Journal of Industrial Aerodynamics*, Vol. 5, pp. 93–107.

[13] Manwaring, S.R., Rabe, D.C., Lorence C.B. and Wadia, A.R., 1997, Inlet Distortion Generated Forced Response of a Low-Aspect-Ratio Transonic Fan, *Journal of Turbomachinery*, Vol. 119, pp. 665–676.

[14] Minkierwicz, G. and Russler, P., 1998, Unsteady Aerodynamics in Transonic Compressor Rotor Blade Passages, AIAA 98-3897.

[15] Sims-Williams, D.B., 2001, *Self-Excited Aerodynamic Unsteadiness Associated with Passenger Cars*, PhD Thesis, School of Engineering, University of Durham, Durham.

[16] Sims-Williams, D.B. and Dominy, R.G., 1998a, Experimental Investigation into Unsteadiness and Instability in Passenger Car Aerodynamics, SAE Paper 980391 in Developments in Vehicle Aerodynamics (SAE SP-1318), 1998.

[17] Sims-Williams, D.B. and Dominy, R.G., 1998b, The Validation and Application of a 5 Hole Pressure Probe with Tubing Transfer Correction for Time-Accurate Measurements in Unsteady Flows, Second MIRA International Conference on Vehicle Aerodynamics, Coventry, 20-21 October, 1998.

[18] Sims-Williams, D.B. and Dominy, R.G. 2000, The Reconstruction of Periodic Pressure Fields from Point Measurements, SAE Paper 1999-01-0809 in SAE Transactions 2000.

[19] Sims-Williams, D.B., White, A.J. and Dominy, R.G., 1999, Gurney Flap Aerodynamic Unsteadiness, *Sports Engineering*, (1999) 2, pp. 221–233.

VIII

AEROTHERMODYNAMICS

UNSTEADY 3D NAVIER-STOKES CALCULATION OF A FILM-COOLED TURBINE STAGE WITH DISCRETE COOLING HOLE

Th. Hildebrandt, J. Ettrich
NUMECA Ingenieurbüro, D-90530 Wendelstein
Thomas.Hildebrandt@numeca.de

M. Kluge, M. Swoboda, A. Keskin, F. Haselbach, H.-P. Schiffer
ROLLS ROYCE Deutschland, Eschenweg 11, D-15287 Dahlewitz, Germany
Marius.Swoboda@rolls-royce.com

Abstract Every modern high-pressure turbine needs a highly sophisticated cooling system. The most frequently used cooling method of to date is film cooling, characterized by a high degree of interaction between the main flow and the cooling flow. Therefore the effects of film cooling have to be taken into account in the aerodynamic design of film cooled high-pressure turbines.

Using modern commercial turbomachinery oriented CFD-methods, the modeling of film cooling holes can be achieved by various numerical methods of different complexity. The so-called source term modeling is fast and easy to apply, but cannot provide very detailed flow information. In contrast, the discretization of every single cooling hole represents a very complex approach, but provides more in-depth information about the cooling pattern. The efforts of full-scale modeling need to be balanced against the more detailed and accurate results. In addition to the complex geometries of film cooled turbines, the flow phenomena are highly unsteady, thus requiring a CPU intensive time dependent numerical approach.

The present paper is focused on a detailed investigation of the unsteady flow field in a film cooled high-pressure turbine stage. An unsteady 3D Navier-Stokes calculation is applied to the entire stage configuration including a full discretization of all the cooling holes.

Nomenclature

M = Blowing rate
v = Velocity (m/s)

K.C. Hall et al.(eds.),
Unsteady Aerodynamics, Aeroacoustics and Aeroelasticity of Turbomachines, 533–549.

p = Pressure (Pa)
Ma = Mach Number
Re = Reynolds Number
ρ = Density (kg/m^3)

Subscripts
c = cooling
$1, 2$ = Inlet,exit conditions
t = total
is = isentropic

Abbreviations
NGV = Nozzle Guide Vane

1. Introduction

In order to obtain maximum thermodynamic cycle efficiency a high temperature level is required in the high pressure (HP) turbines of modern environmentally friendly gas turbines. The temperature level there is usually by far higher than the maximum allowable temperature of even the most advanced materials. Therefore, every modern HP turbine needs a sophisticated cooling system. From a variety of available cooling methods film cooling emerged as today's standard cooling method. Relatively cool compressor air is injected through numerous holes and slots on the blade and endwall surfaces of a HP-turbine. Apart from the desired influence of the injected cooling air on the heat transfer coefficients of the blade and endwall surfaces, the cooling jets have a considerable effect on the main flow as well (Benz (1994), Hildebrandt et.al. (2001), Vogel (1997)). As a consequence, the effects of film cooling have to be taken into account in the aerodynamic design of a HP turbine.

Modern commercial Navier-Stokes solvers provide the designer in the turbomachinery environment with a variety of options to simulate the flow inside the blade passage of a film-cooled turbine. The CFD modeling of film cooling holes can be achieved by various numerical methods of different complexity. The numerical technique of source term modeling is the fastest and least complex method to introduce the effects of film cooling into a 3D Navier-Stokes calculation of a turbine. This method is computationally least expensive and easy to apply, making it well suitable for the fast turn-around times, which are required in the modern design processes. The cooling flow is taken into account by a distribution of various sources of mass, momentum and energy on the blade and endwall surfaces. In contrast, the full modeling of every single cooling hole represents the most complex approach. Using this method every cooling hole, including the cooling air plenum is discretized. Obviously, turn-

around times and engineering efforts are by far higher if compared to the source term method. The reward of applying this method to a film-cooled turbine is a high amount of very detailed flow information.

The complex flow phenomena of film cooling are apparently time dependent themselves, and additionally, highly influenced by the unsteady rotor-stator interaction of the adjacent blade rows. The impinging wakes of a preceding blade row are periodically altering the local cooling efficiency along the blade surfaces of the succeeding turbine rotor. Vice versa, the circumferentially changing backpressure induced by a succeeding blade row can lead to considerable fluctuations in blade pressure distribution and shock location. The local blowing rate given by

$$M = \frac{\rho_c v_c}{\rho_1 v_1} \tag{1}$$

is a function of the local velocity ratio, hence depending strongly on the pressure gradient between the plenum and the local ejection position on the blade surface. Therefore, a periodically fluctuating blade pressure distribution leads directly to an equivalently fluctuating local film cooling efficiency. Therefore Unsteadiness is crucial if the focus is on very detailed cooling flow phenomena.

The present paper is focused on a detailed investigation of an unsteady flow field in a film cooled high-pressure turbine stage. The flow is simulated using an unsteady 3D Navier-Stokes calculation of the entire turbine stage of a nozzle guide vane and rotor configuration including a full modeling of all single cooling holes.

2. Computational Method

Within the frame of the presented computations a commercial CFD systems has been employed. FINE/Turbo, developed by NUMECA Int. S.A (NUMECA (2002)), is a specialized CFD package for all sort of turbomachinery applications. The package includes grid generation, the flow solver and a post processing software. All program modules are embedded into a turbomachinery specific environment.

The numerical scheme solves the 3D Reynolds-averaged Navier-Stokes equations (RANS) on general structured non-orthogonal multi-block grids. The flexibility of the structured grids is greatly enhanced by use of so-called "Full Non Matching Connections", a technique, which allows to arbitrarily connect grids block of different grid topologies or point numbers to each other.

The numerical algorithm incorporated into FINE/Turbo is an explicit four stage Runge-Kutta scheme (Jameson and Baker (1984)). A variety of convergence acceleration techniques are employed, such as implicit residual smoothing, dual time stepping and full multigrid. Space integration is performed us-

Table 1. Design Data of the MT-1 Turbine

Aero-/Thermodynamics			
Blade Number NGV / Rotor	n	32 / 60, 64*	[-]
Mass Flow, Inlet	m_1	17.49	[kg/s]
Rotational Speed	ω	9.500	[RPM]
Exit Mach Number	Ma_2	0.98	[-]
Reynolds Number	Re_2	2.8e6	[-]
Gas-to-Wall Temperature Ratio		1.54	

ing a second order cell-centered finite volume discretization with second and fourth order artificial dissipation. Coarse grid calculations can be carried out in an automatic way on every coarser grid level.

A number of turbulence models are available within FINE/Turbo. In the scope of the present work the algebraic turbulence model of Baldwin and Lomax (1978) has been chosen. All solid walls have been treated as fully turbulent. The authors are well aware that a simple turbulence model and the assumption of fully turbulent boundary layers cannot capture sufficiently accurate the quite complex turbulent structures typical for film cooling. With the main objectives of this study in mind, comparing a fully discretized film cooling geometry with a source term approach, the use of a somewhat simpler model seemed justified and effective. Moreover, new experimental data suggest (Ardey (1998)) that in film cooling simulations the use of any eddy viscosity turbulence model is questionable due to the extreme anisotropic nature of turbulence in these cases.

3. The MT-1 Single Stage HP Turbine

The MT-1 single stage HP-turbine, which had been investigated in the present study, is described in detail in (Kluge et.al. (2003)). Table 1 summarizes some basic geometrical and aerodynamic specifications of the design data of the TATEF turbine stage.

In order to carry out unsteady CFD simulations with an acceptable computational effort the domain scaling method had been applied. There, it is desirable to obtain a small common integer factor as a blade number ratio between NGV and rotor. The original blade number of the rotor had been increased from 60 to 64 enabling to perform a time-dependent periodic computation with one stator passage and two rotor passages meshed. Usually the error, which results from changing the solidity, is acceptable, if the change in blade pitch is less than 10%, which is the case herein.

Table 2. Numerical Boundary Conditions

Aero-/Thermodynamics			
Inlet, NGV	p_{t_1}	461.000	[Pa]
	Direction	axial	
	T_{t_1}	444.4	[K]
Inlet, Front cavity	p_{t_1}	943.000	[Pa]
	Direction	axial into Plenum	
	T_{t_1}	271	[K]
Inlet, rear cavity	p_{t_1}	682.000	[Pa]
	Direction	axial into Plenum	
	T_{t_1}	272	[K]
Outlet	p_2 (rad. eq.)	142.100 Hub	[Pa]
Walls: all NGV, rotor hub & blade	T_w imposed	288.5 / 333	[K]
Walls: all other	Adiabatic		

4. Numerical Boundary Conditions

These types of inlet and exit boundary conditions are typical for turbomachinery cases. There was some uncertainty about the specification of the wall boundary conditions. As a best possible assumption, the thermal wall boundary conditions had been set to a constant wall temperature inside the entire NGV as well as on the rotor blade surface and hub. All other walls within the domain were treated as adiabatic. Considering the very short measurement times (approx. 500ms) this simplification seems justified.

5. Computational Grid

The numerical domain was discretized using a structured multi-block grid. Compared to an unstructured tetrahedral approach structured grids usually provide a higher numerical accuracy. Consequently, emphasis was laid on a high grid quality in order to minimize numerical errors, particularly inside the cooling holes and their immediate vicinity. The grid in these regions is locally highly refined. This high level of refinement would have led to an overall number of grid points, far beyond any reasonable limits. In order to reduce the problem size coarser grid blocks are located around the highly resolved grid regions. The coarse and fine grid areas are connected by means of a non-congruent block-to-block connection using a fully conservative interpolation technique. The application of this technique in film cooling configurations had been described by Hildebrandt (2001).

Around the blades as well as in the front and rear plenum and inside the cooling holes HOH-topologies had been applied (Fig.1, Fig. 2). The grid is composed of 651 grid blocks with a total number of 2.1 Mio. Grid points.

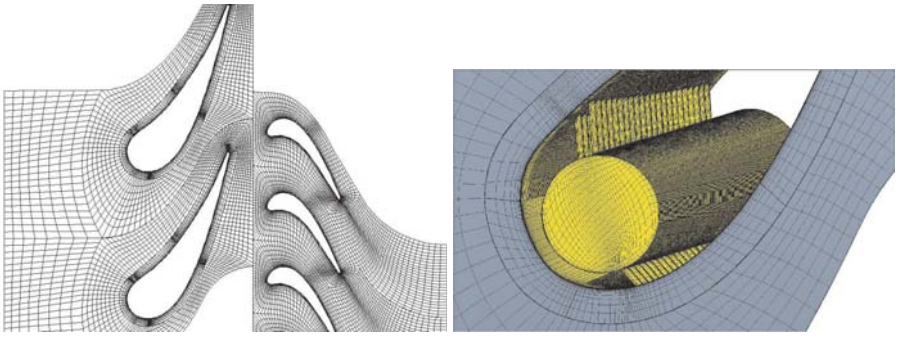

(a) Blade-to-Blade View (b) Plenum with Cooling Holes

Figure 1. Numerical Grid

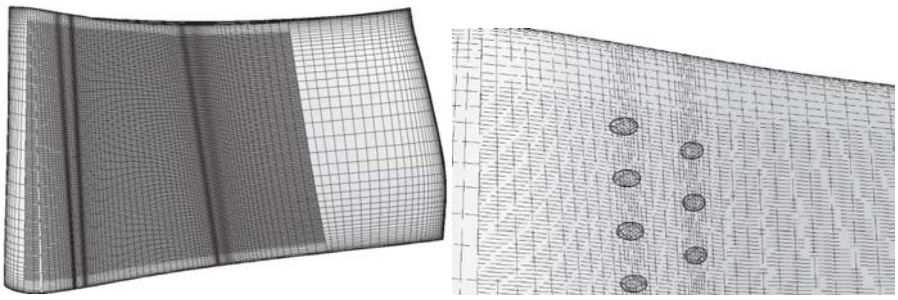

(a) Blade-to-Blade View (b) Plenum with Cooling Holes

Figure 2. Numerical Grid on NGV Surface

About 75% of the grid points are located in the immediate vicinity of the cooling holes. The refined areas around the rows of cooling holes are visible in Fig.2. These areas are resolved about four times finer in each spatial direction than the surrounding regions of the main flow.

The non-dimensional wall distance y+ varies typically around 1 and 2, depending on the local flow conditions. The laminar sub-layer, important for any prediction of wall shear stress or heat transfer, is therefore well captured.

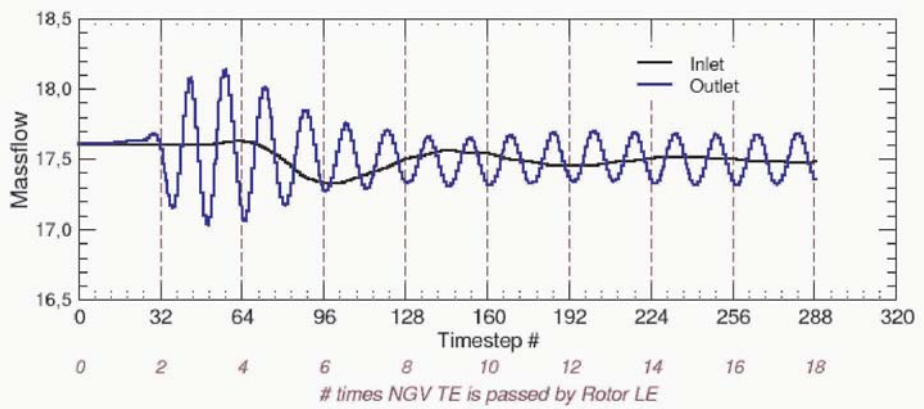

Figure 3. Mass Flow Convergence History

Table 3. Resource requirements

	Source Term	Full Discretization
Iterations for full convergence	6.200	10.000
Grid points	1.500.000	2.100.000
Blocks	16	651
Relative CPU time	1.0	2.4
Relative RAM	1.0	1.55

6. Computational Performance

All computations were carried out on a single processor PC at 1800 MHz, running under LINUX. Starting from a steady state solution the unsteady computation took about 18 times to pass the rotor leading edge behind the NGV trailing edge in order to achieve a satisfactory periodical behaviour. The unsteady mass flow was taken as a convergence criteria (Fig.3). The total CPU time was in the order of 20 days, requiring about 1 GB of RAM. The overall level of convergence was slightly fluctuating around three orders of magnitude reduction in the total RMS residual.

The unsteady calculations were carried out using the domain scaling technique. The rotor pitch was brought from 60 to 64 blades, allowing to mesh two rotor blades with the same periodicity as one NGV pitch. For convergence acceleration dual time stepping was used. The rotor turning was resolved by 32 discrete angular positions for one rotor pitch.

7. Comparison Full Discretization/ Source Term Approach

Apart from the human effort of meshing 120 additional cooling holes, the source term approach requires considerably less computational resources. The larger RAM requirements are obvious, considering the higher number of grid cells and blocks. In addition, the CPU time increases over-proportionally since the coupling between the main flow and the cooling jets is much stronger in case of the fully discretized approach. Here, convergence is slowed down due to the slow propagation from the main flow through the holes into the plenum.

8. Results

Blade Pressure Distribution

The blade pressure distribution, given as isentropic Mach number (Fig. 4) in the NGV at 50% span compares the results of the steady and unsteady results of both the source term approach and the fully discretized cooling holes as well as experiments.

Quite interestingly, although the unsteady results are fluctuating within a hardly visible range, the time average deviates significantly from the steady calculation performed by using a mixing plane approach. The differences occur mainly in three areas.

First, all the pressure peaks around the emerging cooling jets are by far more dominant in the unsteady calculation than in the steady results. Here, any influence from the downstream rotor can be excluded since the location of the cooling holes is upstream of the sonic throat. The pressure peaks are particularly significant in case of the fully meshed cooling holes, and less obvious in the source term results. These pressure over- and undershoots originate in a quasi stagnation of the main flow immediately in front of the cooling jet. After a severe deceleration, the main flow is forced around the cooling jet resulting in a strong acceleration. In such a case the cooling jet behaves very much like a solid obstacle in the flow, characteristic for cylindrical cooling holes (Hildebrandt, Ganzert, Fottner (2000)). Strong interactions between the emerging cooling jets and the main flow occur. These interactions lead to a complicated system of vortices (Vogel (1997)), which are prone to self-excited unsteadiness.

The second region of interest is around the exits of the second row of cooling holes located at the pressure side at around (x/lax = 0.5). The cooling holes on the pressure side are arranged in two double rows. In the steady calculation, a strong peak occurs, which corresponds to the first set of holes of the second rows, while the effects from the second part of the double row is barely visible. In contrast, the time accurate solution produces the dominant velocity peak

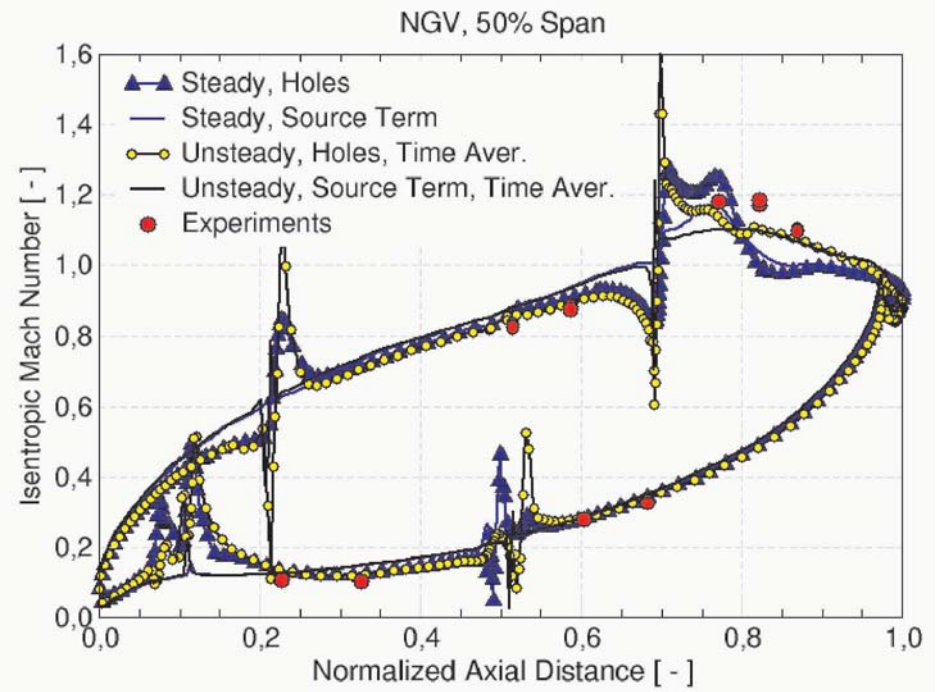

Figure 4. Isentropic Mach Number Distribution NGV 50% Span

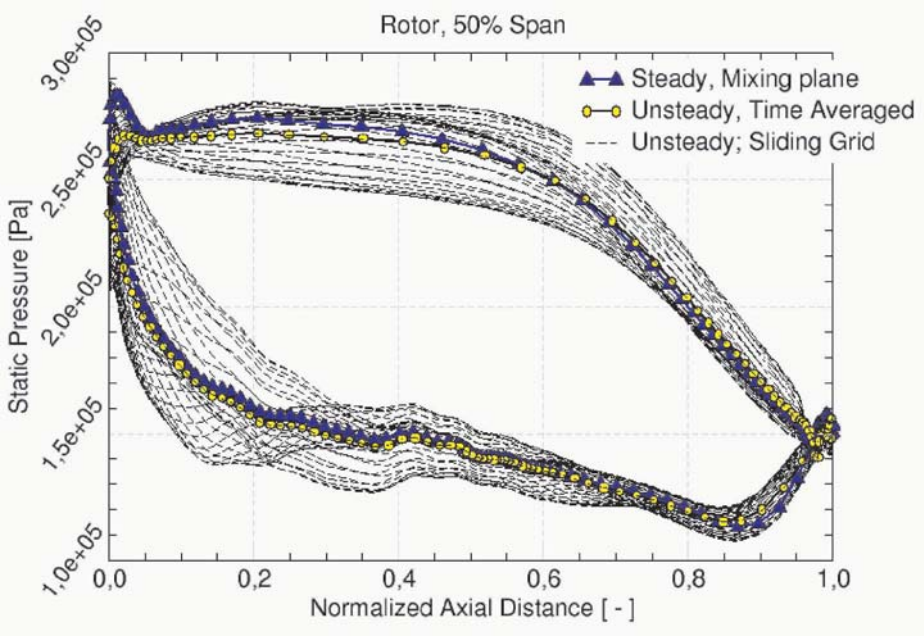

Figure 5. Blade Pressure Distribution Rotor 50% Span

around the position of the second set of cooling holes in the double row. The unsteadily computed jets of the first row are apparently by far stronger than their counterparts from the steady solution. The strong peak visible for the first cooling hole row on the suction side gives also evidence to this. Consequently, the stronger unsteady jet of the first line of holes forces the main flow away from the blade surface, which results in a much less severe interaction between the main flow and the jets emerging from the second line of holes. Again this effect is by far less pronounced, but still detectable in case of the source term approach. Here, the cooling jets are always weaker than in case of the fully discretized holes. The steady source term calculation hardly shows any sign of the cooling jets in the isentropic Mach number distribution.

Third, the second row of cooling holes on the suction side have the most visible effect on the main flow, recognizable by a strong pressure under- and overshoot. The location (x/lax = 0.7) is close to the peak Mach-Number of the main flow. Hence, the jets are emerging into a region of low pressure, resulting in a high local blowing rate. The succeeding shock (x/lax = 0.75) is less pronounced in the unsteady time-averaged calculation. The unsteady shock fluctuations are smeared out by the time-averaging. Since there are hardly any differences between source term approach and the discretized cooling holes, it is obvious that this phenomena is not connected to any film cooling effects.

The blade pressure on the rotor surface is given for all the unsteady time steps, the unsteady time average and the steady computation (Fig. 5). Naturally, the time dependent fluctuations inside the rotor are by far more dominant, forced by the impinging wakes from the upstream NGV. The differences between the time averaged and the steady results is largest at the rotor leading edge. It is this region, which suffers most from the numerical simplifications necessary for a mixing plane approach. The range of the time dependent fluctuations is large throughout nearly the complete blade. However, approaching the trailing edge, the fluctuations are damped out, showing hardly any influence on the rotor exit Mach number.

Heat Transfer Coefficients

The heat transfer on the blade surfaces is expressed by the Nusselt number

$$Nu = \frac{L}{k} \frac{q}{T_2 - T_w}. \tag{2}$$

Similar to the blade pressure distribution the unsteady effects are less obvious in the NGV. There, the most significant phenomena are taking place on the suction side close to the leading edge. The ejecting cooling flow interacts with the main flow, triggering time dependent separations of the main flow immediately behind the NGV leading edge. The obvious discontinuity at around 50% normalized axial distance (x/lax = 0.5) on the NGV suction surface is caused by the connection of a very fine grid to the relatively coarse surrounding grid. The high gradients of the quite sensitive Nusselt number are smeared out on the coarser grid, causing a discontinuity if plotted along the blade surface.

The overall level of the Nusselt number along the uncooled rotor blade surface is by far smaller compared to the cooled NGV. Unsteady effects are dominant throughout the entire blade passage (Fig. 7). The range of the time dependent Nusselt number can reach more than three times the level of the steady or time averaged calculation questioning the reliability of steady heat transfer calculations in multistage configurations.

The hot streaks of uncooled flow and the cooling jets emerging from the NGV enter the rotor passage in an alternating way (Fig. 8). In cases where relatively cool air from the jets impinges on the rotor blade surface the Nusselt number changes its sign, indicating a heat flux from the rotor into the flow (Fig.7).

Flow Details

In contrast to a less labour- and CPU-intensive set-up with source terms (Kluge et.al. (2003)) the meshing of every single cooling hole, including the plenum provides a much higher level of detailed information. Since the local

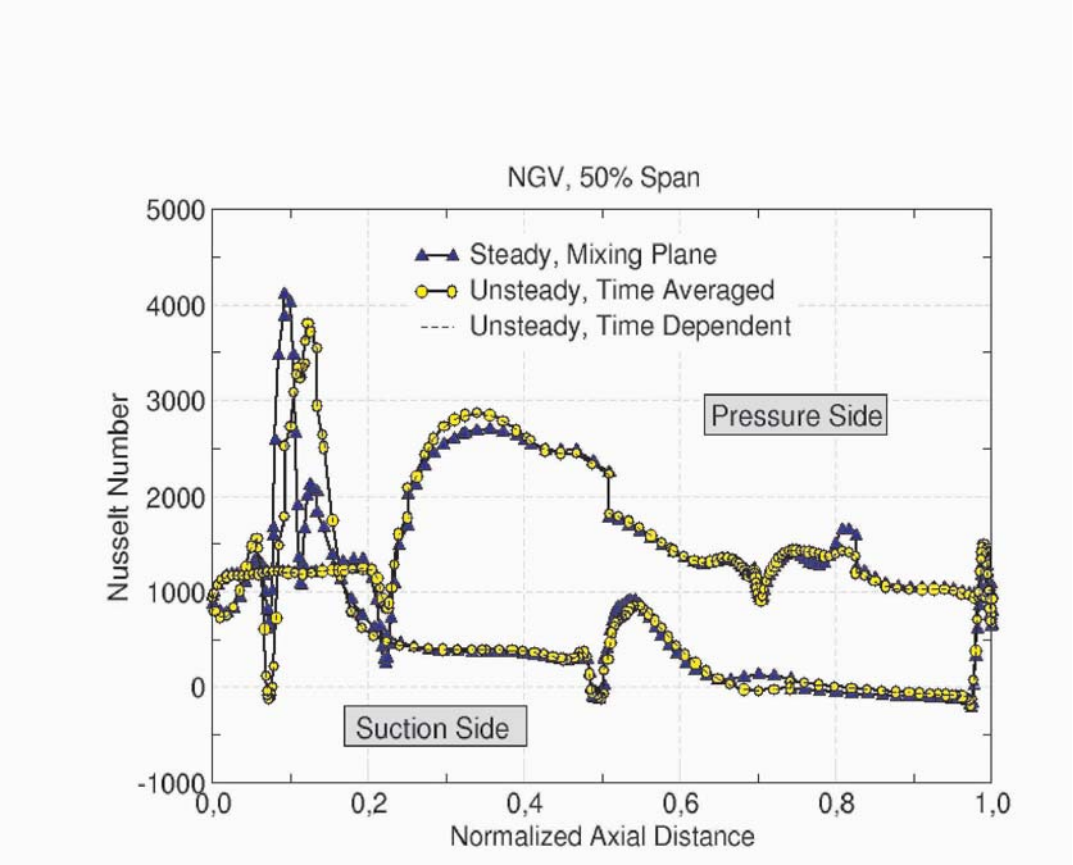

Figure 6. Nusselt Number Distribution, NGV 50% Span

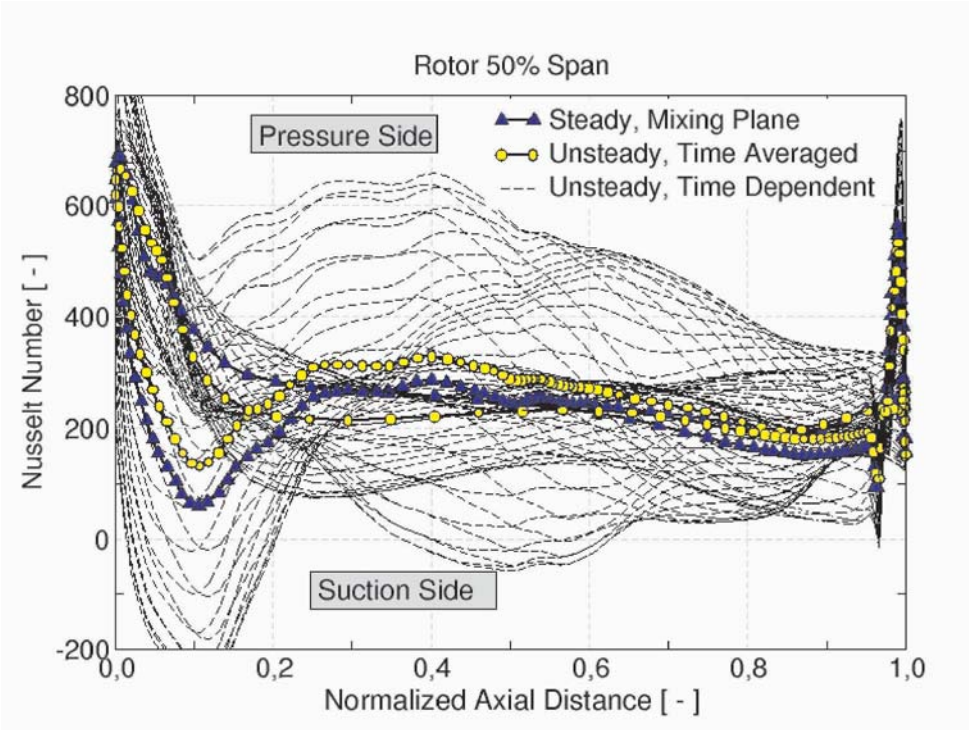

Figure 7. Nusselt Number Distribution, Rotor 50% Span

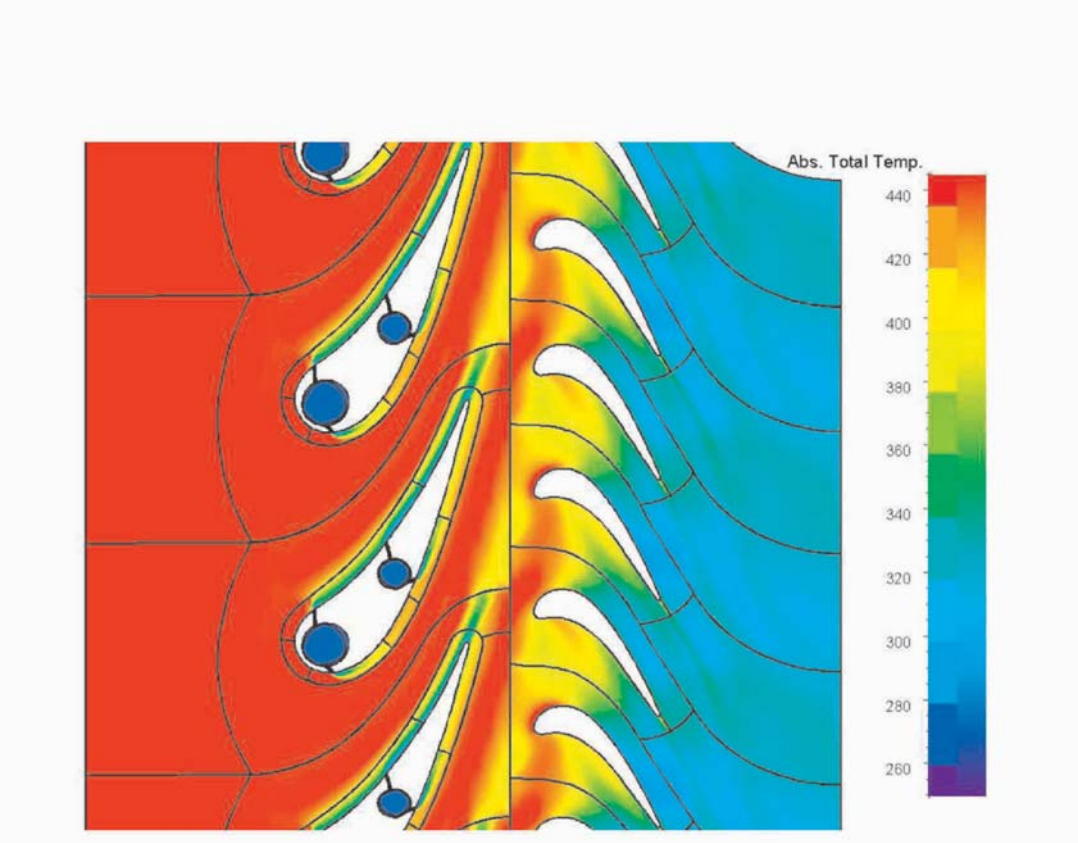

Figure 8. Absolute Total Temperature Distribution, Rotor 50% Span

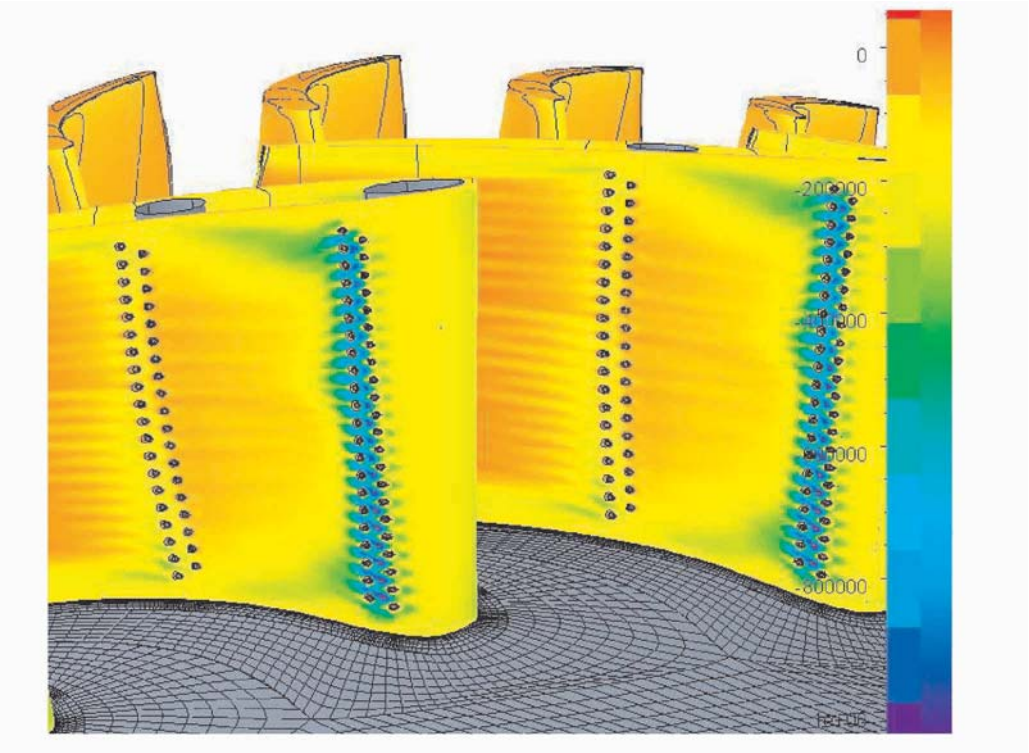

Figure 9. Heat Transfer Coefficient in NGV

flow conditions at the cooling hole exits are not longer a fixed boundary condition as in the source term approach, the local blowing rate has the freedom to adapt itself according to the local flow conditions. Consequently, the local blowing rate varies from hole to hole, obvious in the distribution of the heat transfer coefficient in Figure 9.

The cooling flow enters the blade passage in a typical flow pattern (Fig. 10). In dependence on the inclination angle, the local blowing rate and the shape of the cooling hole, the emerging jet acts much like a solid obstacle. The incoming boundary layer of the main flow rolls up into a horseshoe vortex, causing a counter-rotating kidney vortex behind the jet. (Hildebrandt et.al. (2002), Wilfert (1994)). This vortex configuration is responsible for the hot gas entrainment beneath the cool air, a distinct and undesired feature of cylindrical cooling holes.

Conclusions

Unsteady calculations of a transonic film cooled turbine stage where the cooling holes and the cold air plenum is discretized represent a high level

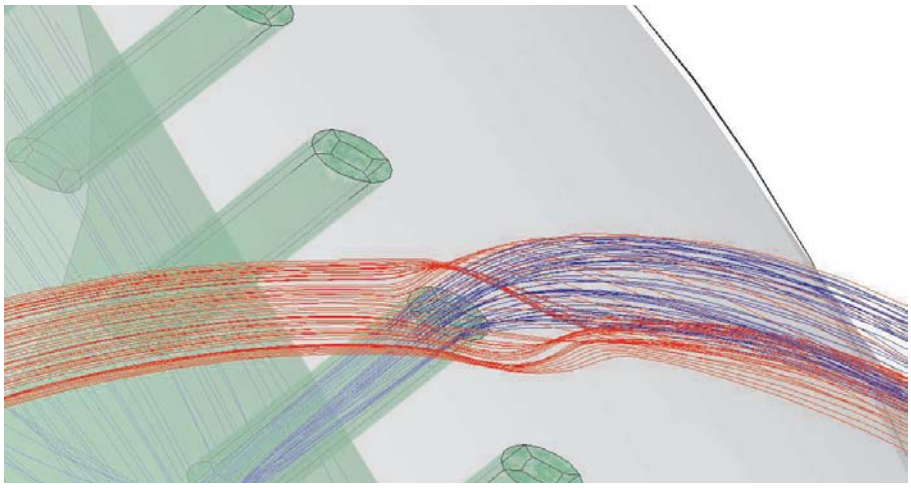

Figure 10. Vortex Configuration at Cooling Flow Exit

of very detailed information from the flow. Clearly, on the downside of this approach are the high CPU requirements and the quite labour intense pre-processing. Both limitations prohibit the use of such a method in the frame of the daily design work in industry, which is characterized by short turn around times. The source term approach, presented in Kluge et. al. (2003) is more suitable in such an environment, but suffers not only from a lack of detailed flow information, but more important from an uncertainty in the specification of the correct boundary condition for the source terms. Here, a full discretization offers the advantage that no boundary conditions are necessary on the exit surface of the cooling holes as long as the plenum is taken into account. However, the boundary conditions for the plenum are relatively straightforward to obtain. An option is proposed to combine these two approaches. First, a set of fully discretized simulations are conducted for typical configurations and operating conditions. From these results, boundary conditions for the source term approach can be derived in order to calibrate the source term boundary conditions. But even then, the immediate vicinity of the cooling holes will be better captured using a full discretization of holes and plenum.

Acknowledgements

The reported work was carried out under the contract of the European Commission as part of the BRITE EURAM project contract number BRPR-CT-97-0519, Project number BE97-4440 (TATEF).The authors wish to acknowledge the financial support as well as the contributions from ALSTOM POWER,

FIAT AVIO, ITP, SNECMA, TURBO-MECA, MTU AeroEngines, ROLLS-ROYCE Plc. and ROLLS ROYCE DEUTSCHLAND.

References

Ardey, S., (1998): 'Untersuchung der aerodynamischen Effekte von Vorderkanten-Kühlluftausbl an einem hochbelasteten Turbinengitter', Ph.D. Thesis, University of the German Armed Forces Munich, Germany.

Baldwin, B.S.; Lomax H., (1978): 'Thin Layer Approximation and Algebraic Model for Separated Turbulent Flow', AIAA Paper 78-0257

Benz, E. (1994): 'Entwicklung und Erweiterung von grundlegenden Ansätzen zur numerischen Berechnung turbulenter Unter- und Überschallströmungen in Gasturbinen', Ph.D. Thesis, University Karlsruhe, Germany

Hildebrandt, Th.; Ganzert, W., Fottner, L. (2000): 'Systematic Experimental and Numerical Investigations on the Aerothermodynamic of a Film Cooled Turbine Cascade with Variation of the Cooling Hole Shape Part II', ASME Paper 00-GT-298

Hildebrandt, Th.; (2001): 'CFD Simulation Filmgekühlter Turbinen', VDI-GET 2001, Düsseldorf, Germany

Jameson, A.; Baker, T.J.; (1984): 'Multigrid Solution of the Euler Equations for Aircraft Configurations', AIAA Paper 84-0093

Kluge, M.; Swoboda, M.; Keskin, A.; Haselbach, F.; Schiffer, H.-P., Hildebrandt, Th.; Ettrich, J. (2003): 'Unsteady 3D Navier-Stokes Calculation of a Film-Cooled Turbine Stage, - Cooling Flow Modeling via Source Term Approach'

NUMECA Int. S.A; (2002), FINE/Turbo User Manual, V. 5.3, Brussels, Belgium

Vogel, D.T.; (1997): 'Numerische Untersuchung des Mischungsverhaltens von Filmkühlstrahlen in Turbinenströmungen', DLR-Report 96-35, Institut für Antriebstechnik, DLR Cologne, Germany

Wilfert, G.; Fottner, L.; (1994): 'The Aerodynamic Mixing Effect of Discrete Cooling Jets with the Mainstream Flow on a Highly Loaded Turbine Cascade', ASME Paper 94-GT-235

ANALYSIS OF UNSTEADY AEROTHERMODYNAMIC EFFECTS IN A TURBINE-COMBUSTOR

Horia C. Flitan and Paul G. A. Cizmas
Department of Aerospace Engineering, Texas A&M University
College Station, Texas 77843-3141
horiaf@plano.tamu.edu and cizmas@tamu.edu

Thomas Lippert and Dennis Bachovchin
Siemens Westinghouse Power Corporation
Pittsburgh, Pennsylvania

Dave Little
Siemens Westinghouse Power Corporation
Orlando, Florida

Abstract This paper presents a numerical investigation of the unsteady transport phenomena in a turbine-combustor. The flow and combustion are modeled by the Reynolds-averaged Navier-Stokes equations coupled with the species conservation equations. The chemistry model used herein is a two-step, global, finite rate combustion model for methane and combustion gases. The governing equations are written in the strong conservation form and solved using a fully implicit, finite difference approximation. This numerical algorithm has been used to investigate the airfoil temperature variation and the unsteady blade loading in a four-stage turbine-combustor. The numerical simulations indicated that *in situ* reheat increased the turbine power by up to 5.1%. The turbine combustion also increased blade temperature and unsteady blade loading. Neither the temperature increase nor the blade loading increase exceeded acceptable values for the turbine investigated.

Keywords: Turbine-combustor, *in situ* reheat, unsteady flow, turbine flow

1. Introduction

In the quest to increase the thrust-to-weight ratio and decrease the thrust specific fuel consumption, turbomachinery designers are facing the fact that

K.C. Hall et al.(eds.),
Unsteady Aerodynamics, Aeroacoustics and Aeroelasticity of Turbomachines, 551–566.

the combustor residence time can become shorter than the time required to complete combustion. As a result, combustion would continue in the turbine, which up to recently has been considered to be undesirable. A thermodynamic cycle analysis demonstrates performance gains for turbojet engines with turbine-burner [Sirignano and Liu, 1999]. Even better performance gains for specific power and thermal efficiency are predicted for power generation gas-turbine engines when the turbine is coupled with a heat regenerator.

The process of combustion in the turbine is called *in situ* reheat and the turbine in which combustion takes place is called turbine-burner. The fuel is commonly injected in the turbine-burner through the vanes. Several challenges are, however, associated with the combustion in the turbine-burner: mixed subsonic and supersonic flows; flows with large unsteadiness due to the rotating blades; hydrodynamic instabilities and large straining of the flow due to the very large three-dimensional acceleration and stratified mixtures [Sirignano and Liu, 1999]. The obvious drawback associated with the strained flows in the turbine-burner is that widely varying velocities can result in widely varying residence time for different flow paths and as a result there are flammability difficulties for regions with shorter residence times. In addition, transverse variation in velocity and kinetic energy can cause variations in entropy and stagnation entropy that impact heat transfer. The heat transfer and mixing may be enhanced by increasing interface area due to strained flows.

Turbine aerodynamics might be drastically modified by strong exothermic combustion processes in a turbine-burner. Thermal expansion due to combustion could significantly change the pressure variation and the shock strength and location. As a result, the blade loading would be modified. There is evidence on a low pressure turbine without *in situ* reheat, that the temperature non-uniformities can generate strong entropic and vortical waves. These waves produced excitations large enough to generate unsteady loadings and stresses on the 5th stage of a low pressure turbine, sufficient to cause high-cycle fatigue failures of a disk/blade/tip-shroud system mode crossing [Manwaring and Kirkeng, 1997]. The danger of high-cycle fatigue is even more imminent for a turbine-burner because larger temperature non-uniformities are likely to produce stronger entropic and vortical waves.

Experimental data for conventional (*i.e.*, without *in situ* reheat) gas-turbines have shown the existence of large radial and circumferential temperature gradients downstream of the combustor [Dills and Follansbee, 1979, Elmore et al., 1983]. These temperature non-uniformities, called hot streaks, have a significant impact on the secondary flow and wall temperature of the entire turbine. Since the combustor exit flow may contain regions where the temperature exceeds the allowable metal temperature by 260-520^{o}C [Butler et al., 1989], understanding the effects of temperature non-uniformities on the flow and heat transfer in the turbine is essential for increasing vane and blade durability. It

is estimated that an error of $55^{\circ}\mathrm{C}$ in predicting the time-averaged temperature on a turbine rotor can result in an order of magnitude change in the blade life [Graham, 1980, Kirtley et al., 1993].

Temperature non-uniformities generated by the upstream combustor can be amplified in a turbine-burner. Consequently, it is expected that not only the secondary flow and wall temperature be affected but also the blade loading due to the modified pressure distribution. Temperature non-uniformities in a turbine-burner can also affect the location of hot spots on airfoils and as a result can impact on the internal and film cooling schemes.

There are extensive experimental [Whitney et al., 1980, Schwab et al., 1983, Stabe et al., 1984, Butler et al., 1989, Sharma et al., 1992, Shang et al., 1995] and numerical [Rai and Dring, 1990, Krouthen and Giles, 1988, Takahashi and Ni, 1991, Shang and Epstein, 1996, Dorney et al., 2000, Dorney et al., 1999] results for the influence of temperature non-uniformities on the flow and heat transfer in a conventional turbine. To the best knowledge of the authors, however, there are no data available in the open literature for the effect of *in situ* reheat on turbine-burners. The objective of this paper is to investigate the effects of *in situ* reheat on the unsteady aerothermodynamics in a multi-stage turbine-combustor. This numerical simulation is crucial for the development of turbine-burners which, in spite of their challenges, can provide significant performance gains for turbojet engines and power generation gas-turbine engines.

The next section presents the physical model used for the simulation of flow and combustion in the turbine-combustor. The governing equations and the chemistry model are presented. The third section describes the numerical model. This section includes information about the grid generation, boundary conditions, numerical method and parallel algorithm. The results are presented in the fourth section.

2. Physical Model

The flow and combustion through a multi-row turbine-burner with arbitrary blade counts is modeled by the Reynolds-averaged Navier-Stokes equations and the species conservation equations. To reduce the computational time, the flow and combustion are modeled as quasi-three-dimensional. This section will present the details of the governing equations and the chemistry model.

Governing Equations

The unsteady, compressible flow through the turbine-combustor is modeled by the Reynolds-averaged Navier-Stokes equations. The flow is assumed to be fully turbulent and the kinematic viscosity is computed using Sutherland's law. The Reynolds-averaged Navier-Stokes equations and species conserva-

tion equations are simplified by using the thin-layer assumption [Isvoranu and Cizmas, 2002].

In the hypothesis of unity Lewis number, both the Reynolds-averaged Navier-Stokes and species equations can be written as [Balakrishnan, 1987]:

$$\frac{\partial Q}{\partial \tau}+\frac{\partial F}{\partial \xi}+\frac{\partial G}{\partial \eta}=\frac{\sqrt{\gamma_\infty}M_\infty}{Re_\infty}\frac{\partial S}{\partial \eta}+S_{ch}. \tag{1}$$

Note that equation (1) is written in the body-fitted curvilinear coordinate system (ξ,η,τ).

The state and flux vectors of the Reynolds-averaged Navier-Stokes equations in the Cartesian coordinates are

$$q^{ns}=\begin{bmatrix}\rho\\ \rho u\\ \rho v\\ e\end{bmatrix},\ f^{ns}=\begin{bmatrix}\rho u\\ \rho u^2+p\\ \rho uv\\ (e+p)\,u\end{bmatrix},\ g^{ns}=\begin{bmatrix}\rho v\\ \rho uv\\ \rho v^2+p\\ (e+p)\,v\end{bmatrix}.$$

The state and flux vectors of the species conservation equations in the Cartesian coordinates are

$$q^{sp}=\begin{bmatrix}\rho y_1\\ \rho y_2\\ \vdots\\ \rho y_N\end{bmatrix},\ f^{sp}=\begin{bmatrix}\rho u y_1\\ \rho u y_2\\ \vdots\\ \rho u y_N\end{bmatrix},\ g^{sp}=\begin{bmatrix}\rho v y_1\\ \rho v y_2\\ \vdots\\ \rho v y_N\end{bmatrix}.$$

Further details on the description of the viscous terms and chemical source terms are presented in [Cizmas et al., 2003].

Chemistry Model

The chemistry model used herein to simulate the *in situ* reheat is a two-step, global, finite rate combustion model for methane and combustion gases [Westbrook and Dryer, 1981, Hautman et al., 1981]

$$\begin{gathered}CH_4+1.5O_2\rightarrow CO+2H_2O\\ CO+0.5O_2\rightarrow CO_2.\end{gathered} \tag{2}$$

The rate of progress (or Arrhenius-like reaction rate) for methane oxidation is given by:

$$q_1=A_1\exp\left(E_1/R_M/T\right)[CH_4]^{-0.3}\,[O_2]^{1.3}\,, \tag{3}$$

where $A_1=2.8\cdot 10^9\ s^{-1}$, $E_1/R_M=24360\ K$. The reaction rate for the CO/CO_2 equilibrium is:

$$q_2=A_2\exp\left(E_2/R_M/T\right)[CO]\,[O_2]^{0.25}\,[H_2O]^{0.5} \tag{4}$$

with $A_2 = 2.249 \cdot 10^{12} \left(m^3/kmol\right)^{0.75} s^{-1}$ and $E_2/R_M = 20130\ K$. The symbols in the square brackets represent local molar concentrations of various species. The net formation/destruction rate of each species due to all reactions is:

$$\hat{\dot{w}}_i = \sum_{k=1}^{N_r} \mathcal{M}_i \nu_{ik} q_k,$$

where ν_{ik} are the generalized stoichiometric coefficients. Note that the generalized stoichiometric coefficient is $\nu_{ik} = \nu_{ik}^{''} - \nu_{ik}^{'}$ where $\nu_{ik}^{'}$ and $\nu_{ik}^{''}$ are stoichiometric coefficients for species i in reaction k appearing as reactant or as a product. Additional details on the implementation of the chemistry model can be found in [Isvoranu and Cizmas, 2002].

3. Numerical Model

The numerical model used herein is based on an existing algorithm developed for unsteady flows in turbomachinery [Cizmas and Subramanya, 1997]. The Reynolds-averaged Navier-Stokes equations and the species equations are written in the strong conservation form. The fully implicit, finite-difference approximation is solved iteratively at each time level, using an approximate factorization method. Three Newton-Raphson sub-iterations are used to reduce the linearization and factorization errors at each time step. The convective terms are evaluated using a third-order accurate upwind-biased Roe scheme. The viscous terms are evaluated using second-order accurate central differences. The scheme is second-order accurate in time.

Grid Generation

The computational domain used to simulate the flow inside the turbine-combustor is reduced by taking into account flow periodicity. Two types of grids are used to discretize the flow field surrounding the rotating and stationary airfoils, as shown in Fig. 1. An O-grid is used to resolve the governing equations near the airfoil, where the viscous effects are important. An H-grid is used to discretize the governing equations away from the airfoil. The O-grid is generated using an elliptical method. The H-grid is algebraically generated. The O- and H-grids are overlaid. The flow variables are communicated between the O- and H-grids through bilinear interpolation. The H-grids corresponding to consecutive rotor and stator airfoils are allowed to slip past each other to simulate the relative motion.

Discretization of Governing Equations

The transport of chemical species is modeled by the mass, momentum, energy and species balance equations. These gas-dynamics and chemistry

governing equations are solved herein using a fully decoupled implicit algorithm. Further discussions on the coupled vs. decoupled algorithms for combustion problems can be found in [Eberhardt and Brown, 1986, Yee, 1987, Balakrishnan, 1987, Li, 1987]. A correction technique has been developed to enforce the balance of mass fractions. The governing equations are discretized using an implicit, approximate-factorization, finite difference scheme in delta form [Warming and Beam, 1978]. The discretized operational form of both the Reynolds-averaged Navier-Stokes (RANS) and species conservation equations, combined in a Newton-Raphson algorithm [Rai and Chakravarthy, 1986], is:

$$\begin{aligned}&\left[I+\frac{\Delta\tau}{\Delta\xi}\left(\Delta_\xi\left(A^-\right)^p+\nabla_\xi\left(A^+\right)^p\right)\right]\left[I+\Delta\tau\frac{c}{p_\infty}\sqrt{\frac{p_\infty}{\rho_\infty}}C^p_{i,j}+\frac{\Delta\tau}{\Delta\eta}\left(\Delta_\eta\left(B^-\right)^p+\nabla_\eta\left(B^+\right)^p-\right.\right.\\&\left.\left.\frac{\sqrt{\gamma_\infty}M_\infty}{Re}\delta_\eta\left(Y\right)^p\right)\right]\left(Q^{p+1}_{i,j}-Q^p_{i,j}\right)=-\left(1.5Q^p_{i,j}-2Q^n_{i,j}+0.5Q^{n-1}_{i,j}\right)-\frac{\Delta\tau}{\Delta\xi}\left(\hat{F}^p_{i+\frac{1}{2},j}-\hat{F}^p_{i-\frac{1}{2},j}\right)\\&-\frac{\Delta\tau}{\Delta\eta}\left(\hat{G}^p_{i,j+\frac{1}{2}}-\hat{G}^p_{i,j-\frac{1}{2}}\right)+\sqrt{\gamma_\infty}M_\infty Re^{-1}\frac{\Delta\tau}{\Delta\eta}\left(S^p_{i+\frac{1}{2},j}-S^p_{i-\frac{1}{2},j}\right)+\left(S^p_{ch}\right)_{i,j}\end{aligned}\tag{5}$$

where A and B are the flux Jacobian matrices $A = \partial F/\partial Q$, $B = \partial G/\partial Q$. The Y and C matrices are $Y = \partial S/\partial Q$ and $C = \partial S_{ch}/\partial Q$. Note that the flux Jacobian matrices are split into $A = A^+ + A^-$, where $A^\pm = P\Lambda^\pm P^{-1}$. Λ is the spectral matrix of A and P is the modal matrix of A. The spectral matrix Λ is split into $\Lambda = \Lambda^+ + \Lambda^-$, where the components of Λ^+ and Λ^- are $\lambda_i^- = 0.5(\lambda_i - |\lambda_i|)$ and $\lambda_i^+ = 0.5(\lambda_i + |\lambda_i|)$, respectively [Steger and Warming, 1981]. The same flux vector splitting approach is applied to the matrix B. In equation (5), Δ, ∇ and δ are forward, backward and central differences operators, respectively. Q^p is an approximation of Q^{n+1}. At any time step n, the value of Q^p varies from Q^n at first internal iteration when $p = 0$, to Q^{n+1} when integration of equation (5) has converged. Additional details on the implementation of the inter-cell numerical fluxes and on the Roe's approximate Riemann solver are presented in [Cizmas et al., 2003].

Boundary Conditions

Two classes of boundary conditions must be enforced on the grid boundaries: (1) natural boundary conditions, and (2) zonal boundary conditions. The natural boundaries include inlet, outlet, periodic and the airfoil surfaces. The zonal boundaries include the patched and overlaid boundaries.

The inlet boundary conditions include the specification of the flow angle, average total pressure and downstream propagating Riemann invariant. The upstream propagating Riemann invariant is extrapolated from the interior of the domain. At the outlet, the average static pressure is specified, while the downstream propagating Riemann invariant, circumferential velocity, and entropy are extrapolated from the interior of the domain. Periodicity is enforced by matching flow conditions between the lower surface of the lowest H-grid of a row and the upper surface of the top most H-grid of the same row. At the airfoil surface, the following boundary conditions are enforced: the "no slip"

condition, the adiabatic wall condition, and the zero normal pressure gradient condition.

For the zonal boundary conditions of the overlaid boundaries, data are transferred from the H-grid to the O-grid along the O-grid's outermost grid line. Data are then transferred back to the H-grid along its inner boundary. At the end of each iteration, an explicit, corrective, interpolation procedure is performed. The patch boundaries are treated similarly, using linear interpolation to update data between adjoining grids [Rai, 1985].

4. Results

This section presents selected the results of the numerical simulation of unsteady transport phenomena inside a four-stage turbine-combustor. The section begins with a description of the geometry and flow conditions, followed by a brief discussion of the accuracy of numerical results. The last part of this section presents the effects of *in situ* reheat on the unsteady flow and blade loading.

Geometry and Flow Conditions

The blade count of the four-stage turbine-combustor requires a full-annulus simulation for a dimensionally accurate computation. To reduce the computational effort, it was assumed that there were an equal number of airfoils in each turbine row. As a result, all airfoils except for the inlet guide vane airfoils were rescaled by factors equal to the number of airfoils per row i divided by the number of airfoils per row one. An investigation of the influence of airfoil count on the turbine flow showed that the unsteady effects were amplified when a simplified airfoil count 1:1 was used [Cizmas, 1999]. Consequently, the results obtained using the simplified airfoil count represent an upper limit for the unsteady effects.

The inlet temperature in the turbine-combustor exceeds 1800 K and the inlet Mach number is 0.155. The inlet flow angle is 0 degrees and the inlet Reynolds number is 194,000 per inch, based on the axial chord of the first-stage stator. The values of the species concentrations at inlet in the turbine-burner are: $y_{CO_2} = 0.0775$, $y_{H_2O} = 0.068$, $y_{CO} = 5.98 \cdot 10^{-06}$, $y_{H_2} = 2.53 \cdot 10^{-07}$, $y_{O_2} = 0.1131$, $y_{N_2} = 0.7288$ and $y_{Ar} = 0.0125$. The rotational speed of the test turbine-burner is 3600 RPM.

The unsteady effects of *in situ* reheat will be investigated by comparing the turbine without combustion against three cases of fuel injection in the turbine-combustor. Pure methane will be injected at the trailing edge of the first vane in all the cases of *in situ* reheat presented herein. The injection velocity and pressure, methane temperature and injection slot dimension are presented in Table 1.

Table 1. Parameters of fuel injection

Parameter	*Case 1*	*Case 2*	*Case 3*
Injection velocity [m/s]	270.6	270.6	77
Pressure [bar]	14.88	14.88	14.88
Temperature [K]	313	590	313
Injection slot size [mm]	0.54	0.54	1.36

Accuracy of Numerical Results

Currently there are no experimental data available for the validation of numerical simulation of transport phenomena in a turbine-combustor. To validate the accuracy of the numerical results corresponding to the governing equations used, it was necessary to show that the results were independent of the grid which discretizes the computational domain. The verification of grid independence results was presented in [Isvoranu and Cizmas, 2002], where a one-stage turbine-combustor was simulated. Note that the grids were generated such that, for the given flow conditions, the y^+ number was less than 1. Approximately 20 grid points were used to discretize the boundary layer regions.

Following the conclusions of accuracy investigation presented in [Isvoranu and Cizmas, 2002], the medium grid was used herein, since it provides the best compromise between accuracy and computational cost. This grid has 53 grid points normal to the airfoil and 225 grid points along the airfoil in the O-grid, and 75 grid points in the axial direction and 75 grid points in the circumferential direction in the H-grid. The stator airfoils and rotor airfoils have the same number of grid points. The inlet and outlet H-grids have each 36 grid points in the axial direction and 75 grid points in the circumferential direction. The grid is shown in Fig. 1, where for clarity every other grid point in each direction is shown.

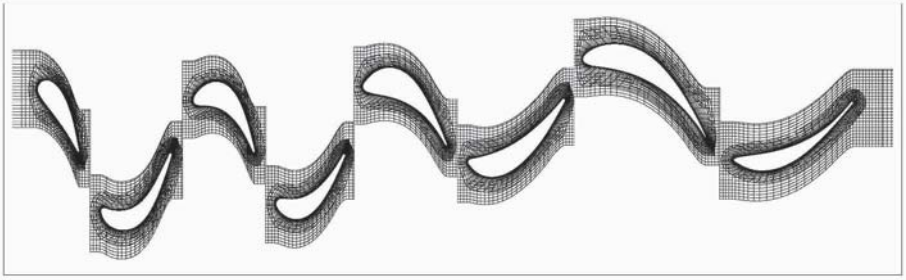

Figure 1. Detail of the medium grid (every other grid point in each direction shown)

Unsteady Temperature Variation

The results presented in this paper were computed using three Newton subiterations per time-step and 2700 time-steps per cycle. Here, a cycle is defined as the time required for a rotor to travel a distance equal to the pitch length at midspan. To ensure time-periodicity, each simulation was run in excess of 80 cycles.

The variation of total enthalpy for the three *in situ* reheat cases and for the no combustion case is shown in Fig. 2. The abscissa indicates the axial location. S1 denotes stator 1, R1 denotes rotor 1, etc. The total enthalpy is calculated at inlet and outlet of each row. Depending on the row type, that is, stator or rotor, the total enthalpy is calculated using either the absolute or the relative velocity. The switch between using absolute or relative velocities generates discontinuities between rows. As shown in Fig. 2, for all fuel injection cases the total enthalpy increases compared to the no combustion case. The largest enthalpy increase is located on the first rotor, where most of the combustion takes place. The combustion and heat release continue throughout the second stator and rotor, as indicated by the total enthalpy variation shown in Fig. 2.

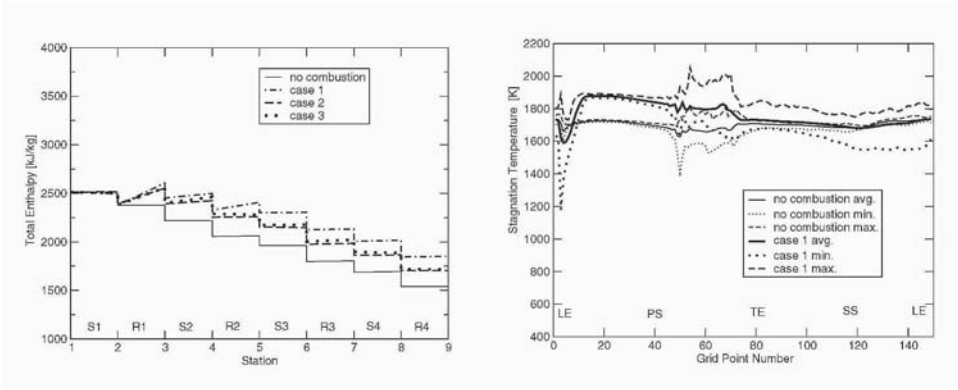

Figure 2. Variation of averaged total enthalpy (absolute or relative)

Figure 3. Variation of stagnation temperature along first row of rotors for the case without combustion and case 1 of *in situ* reheat

The stagnation temperature variation along the first row of rotors is strongly influenced by the *in situ* reheat, as shown in Fig. 3. Figure 3 shows the averaged, minimum and maximum stagnation temperature for the flow without combustion and for case 1 of flow with combustion. On the pressure side, the averaged temperature of case 1 is approximately 180 K larger than the no combustion case temperature. At the leading edge, however, the averaged temperature of case 1 is approximately 70 K lower than in the no combustion case. On the suction side, the averaged temperature of case 1 is slightly higher than

in the no combustion case. On most of the suction side, the averaged temperature of case 1 is approximately 15 to 20 K larger than the no combustion case temperature.

The averaged temperature indicates that combustion takes place on the pressure side of the rotor airfoil. The existence of small regions where the averaged temperature of the case with combustion is lower than the average temperature of the case without combustion indicates that combustion is not completed. Consequently, the low enthalpy of the fuel injected reduces locally the airfoil temperature. The maximum temperature of the case with combustion is larger than the maximum temperature of the no combustion case over the entire airfoil. On the pressure side, the minimum temperature of the case with combustion is larger than the minimum temperature of the case without combustion. On most of the suction side, however, the minimum temperature of the case with combustion is smaller than the minimum temperature of the case without combustion, indicating that the unburned, cold fuel injected is affecting this region.

Unsteady Force Variation

The fuel injection in the turbine-combustor results in the modified the tangential forces in the turbine, as shown in Table 2. *In situ* reheat decreased tangential force F_y on the first blade row but increased tangential force on the subsequent rows. Since the tangential force decrease on the first stage is smaller than the increase on the subsequent stages, the power of the turbine-combustor increased for all cases with combustion. Although the variation of the averaged blade force F_{tot} is rather small, as shown in Table 2 and Fig. 4, the power increase of approximately 5% is significant.

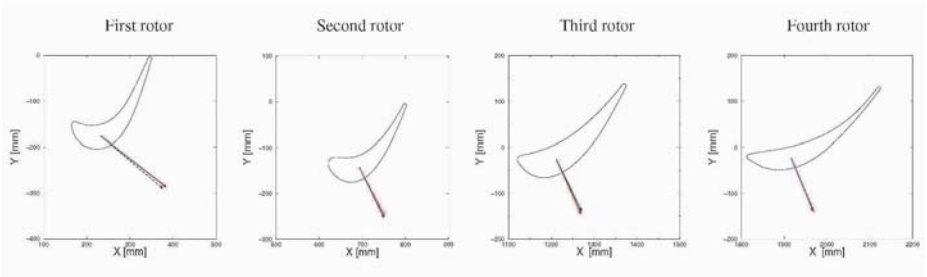

Figure 4. Averaged force on rotors, F_{tot}

The time variation in of the rotor blade tangential forces, shown in Fig. 5, indicates that the largest amplitudes occur in the last rotor row and the smallest amplitudes occur in the first rotor row. This conclusion is valid for every combustion or no combustion case.

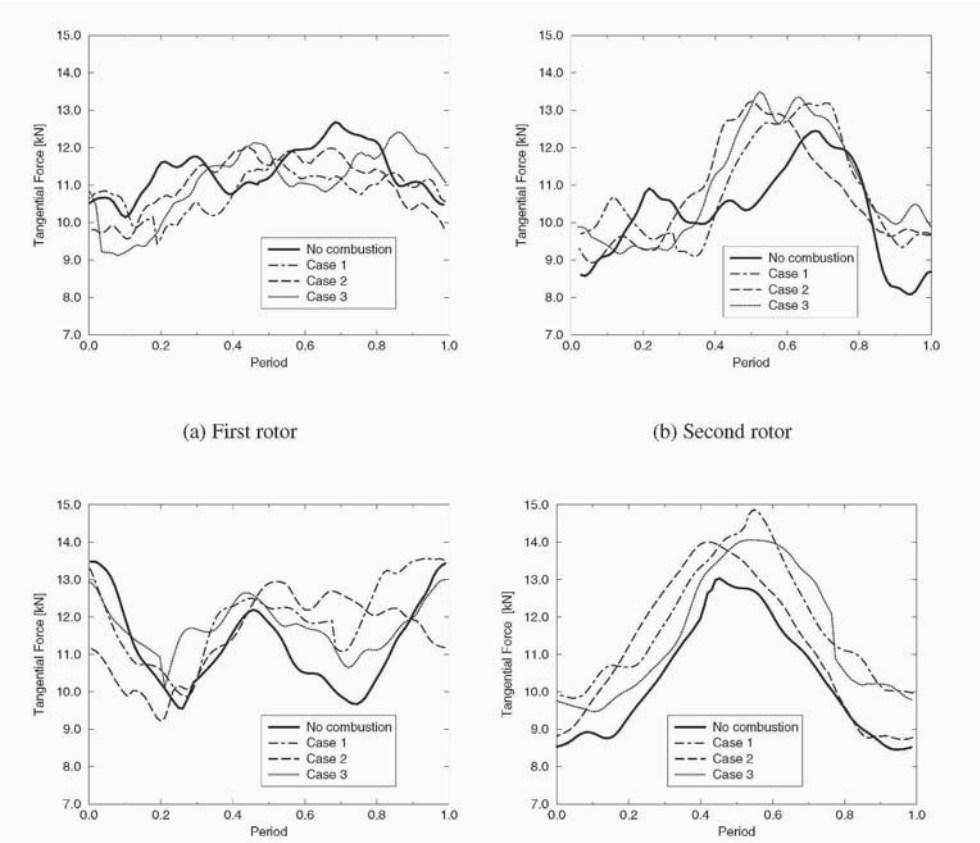

Figure 5. Variation of tangential forces on the rotors

Table 2. Forces on blades

	No Combustion	*Case 1*	*Case 2*	*Case 3*
F_{tot1} [kN]	18.28	18.21	18.71	18.67
α_1 [deg]	38.4	36.4	36.1	36.3
F_{y1} [kN]	11.36	10.81	11.03	11.05
F_{tot2} [kN]	11.87	12.27	12.17	12.31
α_2 [deg]	60.3	61.7	61.9	62.7
F_{y2} [kN]	10.31	10.81	10.74	10.94
F_{tot3} [kN]	12.62	13.19	12.75	13.08
α_3 [deg]	62.2	65.0	63.9	63.8
F_{y3} [kN]	11.17	11.95	11.45	11.73
F_{tot4} [kN]	11.41	13.03	12.31	12.58
α_4 [deg]	65.5	65.5	65.7	66.1
F_{y4} [kN]	10.38	11.85	11.21	11.51

Table 3. Power increase

	Case 1	*Case 2*	*Case 3*
Power increase [%]	5.1	2.8	4.6

A phase shift caused by fuel injection is visible for the first and second rotor blades. The larger unsteadiness within the second rotor makes this phenomenon more clearly distinguishable in Fig. 5(b). The patches of burning mixture and the reduced degree of mixedness are the probable causes for this tangential force phase shift in the upstream region.

Figure 6 shows the fast Fourier transform of the tangential forces. They have been nondimensionalized by the average tangential force obtained in the case without fuel injection. The blades of the fourth rotor are excited the most. This excitation occurs at the first blade passing frequency (BPF), which is 1920 Hz. For the rest of the blades, the excitation due to the second BPF is comparable in amplitude to the excitation of the first BPF. Except for first rotor in case 1 and third rotor in case 3, the fuel injection has the effect of increasing the excitation of the first BPF. The largest amplitude increase is 216% and occurs on the third row blades in case 2. The unsteady force, however, is approximately 50% of the maximum amplitude value that occurs on the fourth rotor blade at BPF.

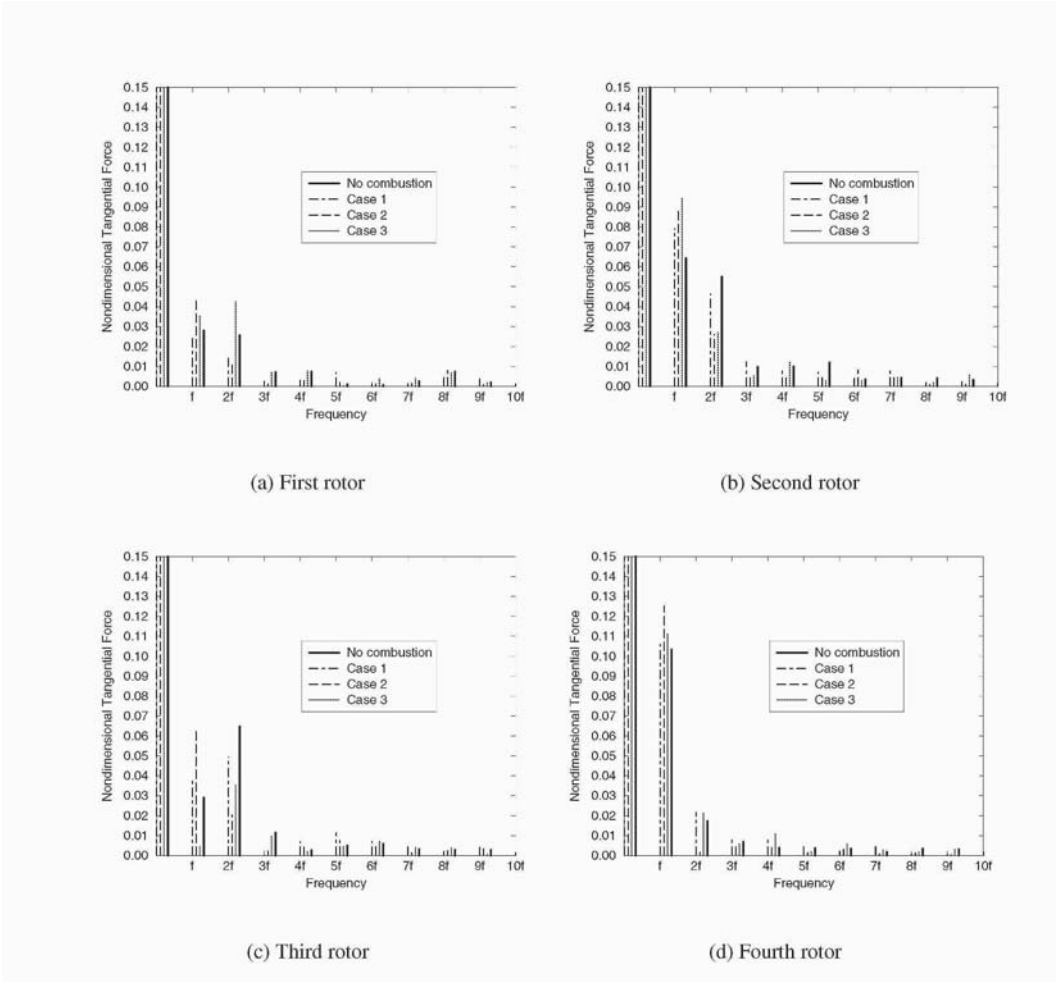

Figure 6. Fast Fourier transform of tangential forces

5. Conclusions

The complexity of the transport phenomena in a multi-stage turbine-combustor makes it one of the most challenging numerical simulation problems. The large unsteadiness and straining of the flow along with the wide range of velocity variation lead to a widely spread of local characteristic time scales for flow and combustion, which strongly impacted the on-going reactions. As a first step in the numerical simulation of the *in situ* reheat, a two-reaction chemistry mechanism has been considered.

The numerical simulation was used to predict the airfoil temperature variation and the unsteady blade loading in a four-stage turbine-combustor. The *in situ* reheat decreased the power of the first stage, but increased more the power of the following stages. The power of the turbine increased between 2.8% and 5.1%, depending on the parameters of the fuel injection. The largest excitation of the four-stage turbine-combustor corresponded to the rotor of the fourth stage, with or without combustion. The highest excitation corresponded to the first blade passing frequency, for all cases analyzed.

Acknowledgments

This work was funded by the National Energy Technology Laboratory of the Department of Energy (DOE). The authors gratefully acknowledge the support of Mr. Charles Alsup, the DOE project manager. The authors also appreciate the support of the Texas A&M Supercomputing Center and the Super-Computing Science Consortium $(SC)^2$ who generously provided access to the computing resources of the Pittsburgh Supercomputing Center.

References

Balakrishnan, A. (1987). Application of a flux-split algorithm to chemically relaxing, hypervelocity blunt-body flows. In *22nd Thermophysics Conference*, Honolulu, Hawaii. AIAA. AIAA Paper 87-1578.

Butler, T. L., Sharma, O. P., Joslyn, H. D., and Dring, R. P. (1989). Redistribution of an inlet temperature distortion in an axial flow turbine stage. *Journal of Propulsion and Power*, 5:64–71.

Cizmas, P., Flitan, H., and Isvoranu, D. (2003). Numerical prediction of unsteady blade loading in a turbine-combustor. In *8th National Turbine High Cycle Fatigue Conference*. Universal Technology Corporation, Monterey, CA.

Cizmas, P. G. A. (1999). Transition and blade count influence on steam turbine clocking. Technical report, Texas Engineering Experiment Station, College Station, Texas.

Cizmas, P. G. A. and Subramanya, R. (1997). Parallel computation of rotor-stator interaction. In Fransson, Torsten H., editor, *The Eighth International Symposium on Unsteady Aerodynamics and Aeroelasticity of Turbomachines*, pages 633–643, Stockholm, Sweden.

Dills, R. R. and Follansbee, P. S. (1979). Use of thermocouples for gas temperature measurements in a gas turbine combustor. Technical report, National Bureau of Standards. Special Publication 561.

Dorney, D. J., Gundy-Burlet, K. L., and Sondak, D. L. (1999). A survey of hot streak experiments and simulations. *International Journal of Turbo and Jet Engines*, 16(1):1–15.

Dorney, D. J., Sondak, D. L., and Cizmas, P. G. A. (2000). Effects of hot streak/airfoil ratios in a high-subsonic single-stage turbine. *International Journal of Turbo and Jet Engines*, 17(2):119–132.

Eberhardt, S. and Brown, K. (1986). A shock capturing technique for hypersonic, chemically relaxing flows. In *24th Aerospace Sciences Meeting*, Reno, Nevada. AIAA. AIAA Paper 86-0231.

Elmore, D. L., Robinson, W. W., and Watkins, W. B. (1983). Dynamic gas temperature measurement system. Technical report, NASA. Contractor Report 168267.

Graham, R. W. (1980). Fundamental mechanisms that influence the estimate of heat transfer to gas turbine blades. *Heat Transfer Engineering*, 2(1):39–47. also published as ASME Paper 97-HT-43.

Hautman, J., Dryer, F. L., Schug, K. P., and Glassman, I. (1981). A multiple-step overall kinetic mechanism for the oxidation of hydrocarbons. *Combustion Science and Technology*, 25:219–235.

Isvoranu, D. D. and Cizmas, P. G. A. (2002). Numerical simulation of combustion and rotor-stator interaction in a turbine-combustor. In *The Ninth International Symposium on Transport Phenomena and Dynamics of Rotating Machinery (ISROMAC-9)*, Honolulu, Hawaii.

Kirtley, K. R., Celestina, M. L., and Adamczyk, J. J. (1993). The effect of unsteadiness on the time-mean thermal loads in a turbine stage. SAE Paper 931375.

Krouthen, Bjorn and Giles, Michael B. (1988). Numerical investigation of hot streaks in turbines. In *24th AIAA/SAE/ASME/ASEE Joint Propulsion Conference*, Boston, Massachusetts. AIAA Paper 88-3015.

Li, C. P. (1987). Chemistry-split techniques for viscous reactive blunt body flow computations. In *25th Aerospace Sciences Meeting*, Reno, Nevada. AIAA. AIAA Paper 87-0282.

Manwaring, S. and Kirkeng, K. (1997). Forced response vibrations of a low pressure turbine due to circumferential temperature distortions. In *Proceedings of The 8th International Symposium on Unsteady Aerodynamics and Aeroelasticity of Turbomachines*, pages 379–392, Stockholm, Sweden.

Rai, M. M. (1985). Navier-Stokes simulation of rotor-stator interaction using patched and overlaid grids. In *AIAA 7th Computational Fluid Dynamics Conference*, Cincinnati, Ohio. AIAA Paper 85-1519.

Rai, M. M. and Chakravarthy, S. (1986). An implicit form for the Osher upwind scheme. *AIAA Journal*, 24:735–743.

Rai, M. M. and Dring, R. P. (1990). Navier-Stokes analyses of the redistribution of inlet temperature distortions in a turbine. *Journal of Propulsion and Power*, 6(3):276–282. also published as AIAA Paper 87-2146.

Schwab, J. R., Stabe, R. G., and Whitney, W. J. (1983). Analytical and experimental study of flow through and axial turbine stage with a nonuniform inlet radial temperature profile. In *19th AIAA/SAE/ASME Joint Propulsion Conference*, Seattle, WA. AIAA Paper 83-1175.

Shang, T. and Epstein, A. H. (1996). Analysis of hot streak effects on turbine rotor heat load. In *International Gas Turbine and Aeroengine Congress*, Birmingham, UK. ASME Paper 96-GT-118.

Shang, T., Guenett, G. R., Epstein, A. H., and Saxer, A. P. (1995). The influence of inlet temperature distortion on rotor heat transfer in a transonic turbine. In *31st AIAA/ASME/SAE/ASEE Joint Propulsion Conference*, San Diego, CA. AIAA Paper 95-3042.

Sharma, O. P., Pickett, G. F., and Ni, R. H. (1992). Assessment of unsteady flows in turbomachines. *Journal of Turbomachinery*, 114(1):79–90. also published as ASME Paper 90-GT-150.

Sirignano, W. A. and Liu, F. (1999). Performance increases for gas-turbine engines through combustion inside the turbine. *Journal of Propulsion and Power*, 15(1):111–118.

Stabe, R. G., Whitney, W. J., and Moffitt, T. P. (1984). Performance of a high-work low aspect ratio turbine tested with a realistic inlet radial temperature profile. In *20th AIAA/SAE/ASME Joint Propulsion Conference*, Cincinnati, OH. AIAA Paper 84-1161.

Steger, J. L. and Warming, R. F. (1981). Flux vector splitting of the inviscid gasdynamic equations with application to finite-difference methods. *Journal of Computational Physics*, 40:263–293.

Takahashi, R. K. and Ni, R. H. (1991). Unsteady hot streak migration through a 1-1/2 stage turbine. In *27th AIAA/SAE/ASME/ASEE Joint Propulsion Conference*, Sacramento, CA. AIAA Paper 91-3382.

Warming, R. F. and Beam, R. M. (1978). On the construction and application of implicit factored schemes for conservation laws. *SIAM-AMS Proceedings*, 11:85–129.

Westbrook, C. K. and Dryer, F. L. (1981). Simplified reaction mechanisms for the oxidation of hydrocarbon fuels in flames. *Combustion Science and Technology*, 27:31–43.

Whitney, W. J., Stabe, R. G., and Moffitt, T. P. (1980). Description of the warm core turbine facility and the warm annular cascade facility recently installed at NASA Lewis Research Center. Technical report, NASA. Technical Memorandum 81562.

Yee, H. C. (1987). Construction of explicit and implicit symmetric schemes and their applications. *Journal of Computational Physics*, 68:151–179.

IX

ROTOR STATOR INTERACTION

STATOR-ROTOR AEROELASTIC INTERACTION FOR THE TURBINE LAST STAGE IN 3D TRANSONIC FLOW

Romuald Rzadkowski
Institute of Fluid-Flow Machinery, Polish Academy of Sciences
80-952 Gdansk, ul. Fiszera 14, Polish Naval Academy
z3@imp.gda.pl

Vitaly Gnesin, Luba Kolodyazhnaya
Department of Aerohydromechanics, Institute for Problems in Machinery
Ukrainian National Academy of Sciences 2/10 Pozharsky st., Kharkov 310046, Ukraine
gnesin@ipmach.kharkov.ua

Abstract A three-dimensional numerical analysis for aerodynamic unsteady forces and flutter parameters of the last stage steam turbine 13K215 rotor blades have been presented. The low frequency excitation was simulated for a 94 rotating blades with 54 nozzles. It was assumed that the pressure behind the rotor blades is changing in the circumferential direction. The flutter parameters of this stage were calculated.

Keywords: unsteady forces, inviscid flow, rotor blades, stator blades

1. Introduction

The classical and partial integration flutter analysis (Bakhle et al. 1992, He 1994; Moyround et al. 1996, Rzadkowski 1998, Rzadkowski and Gnesin 2000, 2001, He and Ning 1998, Bendiksen 1998, Gnesin et al. 2000, 2001, Carstens and Belz 2000) take into consideration only the rotor blades. The stator blades are modelled by the interblade phase angle of the rotor blades as the initial condition.

Hall and Silkowski 1997 can be cited as one of a few papers investigating into the effect of neighbouring blade rows. Namba and Ishikawa 1983 give an analytical study on contra-rotating annular cascades with oscillating blades. For the first time the coupled solution of an aeroelastic problem for turbine

K.C. Hall et al. (eds.),
Unsteady Aerodynamics, Aeroacoustics and Aeroelasticity of Turbomachines, 569–580.

stage with vibrating blades was presented by Rzadkowski and Gnesin 2002 for uniform distribution of the pressure behind the rotor blade.

In this paper a three-dimensional numerical analysis for aerodynamic unsteady forces of the last stage steam turbine 13K215 rotor blades have been presented for non-uniform pressure distribution behind the rotor blades.

The numerical calculation of the 3D transonic flow of an ideal gas through turbomachinery blade rows moving relatively one to another without taking into account the blades oscillations is presented.

An ideal gas flow through the mutually moving stator and rotor blades with periodicity on the whole annulus is described by the unsteady Euler conservation equations, which are integrated using the explicit monotonous finite-volume difference scheme of Godunov-Kolgan and moving hybrid H-H grid.

It was assumed that the pressure behind the rotor blades is changing in the circumferential direction (measured by the angle around the axis of rotation of the turbine). For circumferential angle ($\alpha \in (0, 90^\circ)$ p_2=6000 Pa, $\alpha \in (90^\circ, 180^\circ)$ p_2=7500 Pa, $\alpha \in (180^\circ, 270^\circ)$ p_2=9000 Pa, $\alpha \in (270^\circ, 360^\circ)$ p_2=7500 Pa. The unsteady forces acting on the ith rotor blades, in axial, tangential and radial directions were found.

2. Aerodynamic Model

An ideal gas flow through the mutually moving stator and rotor blades with periodicity on the whole annulus is described by the unsteady Euler conservation equations, which are integrated using the explicit monotonous finite-volume difference scheme of Godunov-Kolgan and moving hybrid H-H grid.

The algorithm proposed allows calculate unsteady forces of the turbine stages with an arbitrary pitch ratio of stator and rotor blades.

The 3D transonic flow of inviscid non-heat conductive gas through an axial turbine stage is considered in the physical domain, including the nozzle cascade (NC) and the rotor wheel (RW), rotating with constant angular velocity. In general case both NC and RW have an unequal number of blades of the arbitrary configuration (see Figures 1). Taking into account the flow unperiodicity from blade to blade (in the pitchwise direction) it is convenient to choose the calculated domain including all blades of the NC and RW assembly, the entry region, the axial clearance and the exit region. Each of passages is dicretized using H-type grid for stator domain and hybrid H-H grid for rotor domain (Rzadkowski and Gnesin 2002). Here outer H-grid remains stationary during the calculation, while the inner H-grid is rebuilt in each iteration by a given algorithm, so that the external points of the inner grid remain unmoved, but the internal points (on the blade surface) move according to the blade motion.

It is assumed that the unsteady flow fluctuations are due to both the rotor wheel rotation and to prescribed blade motions, and the flows far upstream

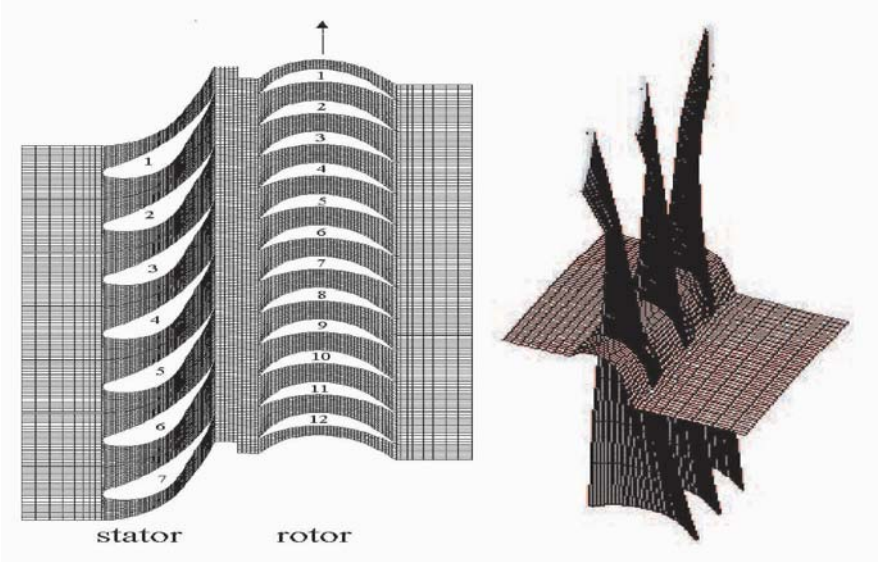

Figure 1. The calculated domain

and far downstream from the blade row are at most small perturbations of uniform free streams. So, the boundary conditions formulation is based on one - dimensional theory of characteristics, where the number of physical boundary conditions depends on the number of characteristics entering the computational domain (Gnesin and Rzadkowski 2000).

In the general case, when axial velocity is subsonic, at the inlet boundary initial values for total pressure, total temperature and flow angles are used, while at the outlet boundary only the static pressure has to be imposed. Non-reflecting boundary conditions can be used, i.e., incoming waves (three at inlet, one at the outlet) have to be suppressed, which is accomplished by setting their time derivative to zero.

3. Structure Model

The structure rotor blades model is based on a modal approach of the coupled fluid-structure problem (Bathe and Wilson 1976, Rzadkowski 1998). The first step of the modal approach consists of solving the problem of the natural mode shapes and eigenvalues without damping and in a vacuum. Then the displacement of each blade can be written as a linear combination of the first N modes shapes with the modal coefficients depending on time. Taking into account the orthogonality property of the mode shapes the equation of motion reduces to the set of independent differential equations relatively to modal coefficients of natural modes. The modal forces are calculated for each iteration

with the use of the instantaneous pressure field calculated form the flow code (Gnesin and Rzadkowski 2000).

4. Numerical Results

The numerical calculations presented below were carried out for the stage of the turbine with rotor blades length of 0.765 m. The number of stator blades is equal to 56, the number of rotor blades is equal to 96. The stator to rotor blade number ratio of 56:96 (7:12). All geometrical parameters of the blade are presented in Rzadkowski 1998.

It was assumed that the pressure behind the rotor blades is changing in the circumferential direction (measured by the angle around the axis of rotation of the turbine). For circumferential angle $\alpha \in$ (0, 90°) p_2=6000 Pa, $\alpha \in$ (90°, 180°) p_2=7500 Pa, $\alpha \in$(180°, 270°) p_2=9000 Pa, $\alpha \in$ (270°, 360°) p_2=7500 Pa (see Figures 2 pressure = $p_2/(\rho_k a_k^2)$,$\rho_k a_k^2$ =9467 Pa). The unsteady forces acting on the ith rotor blades, in axial, tangential and radial directions were found.

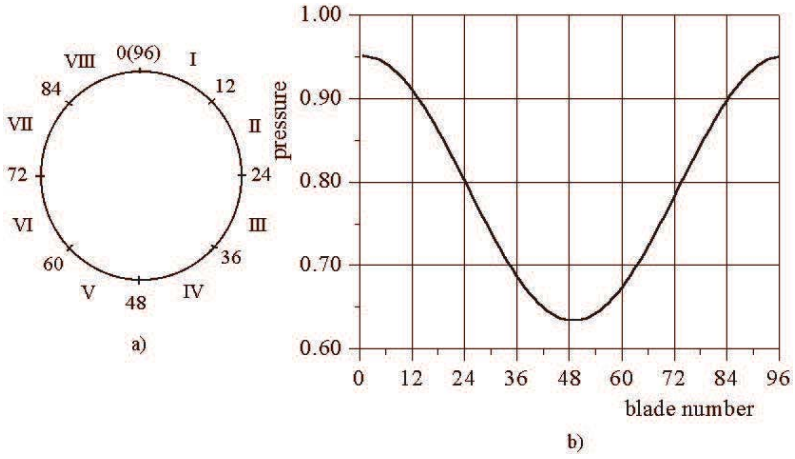

Figure 2. The pressure distribution behind the rotor wheel

The numerical and experimental verification of the numerical code is presented in Rzadkowski and Gnesin 2000.

The numerical calculations have been made using the computational H-grid of 11*24*60 grid points for each stator passage and 11*14*60 grid points for each rotor passage.

One of the important aspects of stator-rotor interaction is the effect of the blade response with taking into account the excitation caused by the flow uniformity and excitation due to blades oscillations.

The blade vibrations are defined with taking into account the first ten natural modes shapes of rotating blade. The values of natural frequencies and the mechanical damping coefficients $h_i = 2\omega_i\xi_i$, are given in Table 1. The modal damping coefficients were assumed (Rzadkowski 1998): ξ_1 = 0.00075, ξ_2 = 0.00094, ξ_3 = 0.0011, $\xi_3 = \xi_4 = \xi_{10}$.

Table 1. Natural frequencies and mechanical damping coefficients of the rotating rotor blade L=0.765 m

Mode Number	1	2	3	4	5	6	7	8	9	10
ω_i Hz	99	160	268	297	398	598	680	862	1040	1124
h_i Hz	0.149	0.304	0.62	0.8	1.23	2.1	2.65	3.7	4.89	5.73

The unsteady force is the unperiodic function in time. The forces acting on the various blades differ one from another. We are using here the term the unsteady modal force which is equal along the blade length and correspond to the particular mode shape. This is disadvantage of the modal superposition calculations, where modal force averaged along the length of the blades is calculated. After the start regime, there began the coupled vibrations where unsteady forces in the turbine stage are the result of continuous interaction between gas flow, rotation of the rotor wheel and blades vibration. So, it is impossible to separate the unsteady effects caused by the external excitation and the unsteady effects due to blades vibration.

Figures 3 - 4 shown the unsteady modal forces corresponding to the 1st, 2nd, 4th and 8th modes for the 1st blades. Generally the low frequency excitation is predominant.

Figures 5a, b present the modal components of the unsteady modal force corresponding to the first mode. The high frequency excitation appeared for 2800 Hz and is equal to 1 % of the steady force A_o=27.5 [N]. The low frequency excitation caused by non-uniform pressure distribution is 158 % of A_o for frequency 50 Hz (see Figure 5b).

Figures 6a, b present the modal components of the unsteady modal force corresponding to the second mode. The high frequency excitations appeared for 2800 Hz and is equal to 2% of the steady force A_o=35.5 [N]. The low frequency excitation is 38 % of A_o for frequency 50 Hz (see Figure 6b).

Figures 7a, b present the modal components of the unsteady modal force corresponding to the fourth mode. The high frequency excitations appeared for 2800 Hz and is equal to 2 % of the steady force A_o=27.0 [N]. The low frequency excitation is 78 % of A_o for frequency 50 Hz (see Figure 7b).

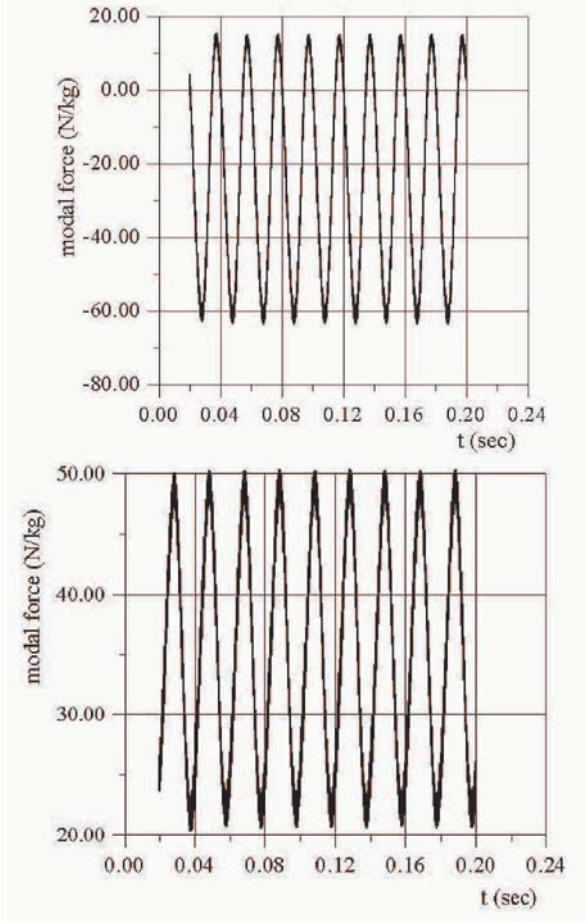

Figure 3. The unsteady modal forces of the 1st, 2nd modes

Figures 8a, b present the modal components of the unsteady modal force corresponding to the 8th mode. The high frequency excitations appeared for 2800 Hz and is equal to 5 % of the steady force A_o= 6.8 [N]. The low frequency excitation is 600 % of A_o for frequency 50 Hz (see Figure 8b).

It should be noted that only first four modes bring their contribution to the blade motion. The low frequency unsteady forces caused by non-uniform pressure distribution are higher in comparison to the high frequency excitations.

The modal coefficients of the 1st blade motion corresponding to the 1st, 2nd, 4th and 8th modes shape have been shown in Figures 9 -12.

The unsteady amplitude of the first mode (see Figure 9) has frequency 73 Hz (99 Hz the natural frequency) and the frequency closes to 100 Hz. The

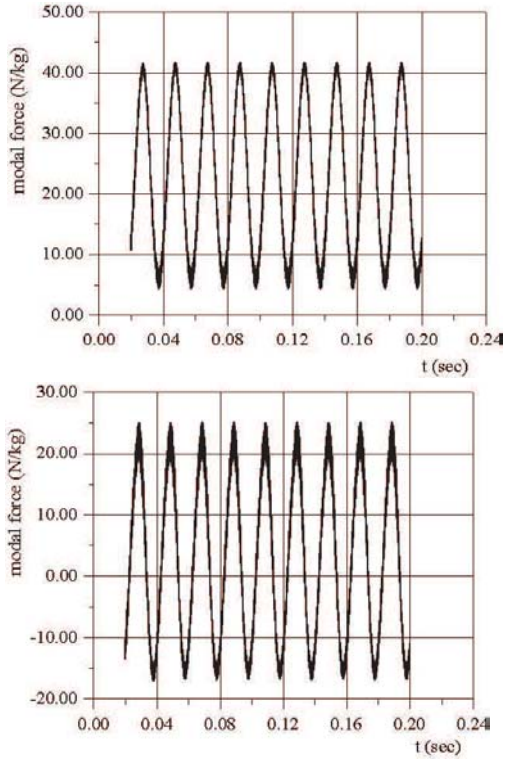

Figure 4. The unsteady modal forces of the 4th , 8th modes

unsteady amplitude of the second mode (see Figure 10) has frequency 70 Hz and 157 Hz (160 Hz the natural frequency).

The unsteady amplitude of the fourth mode (see Figure 11) has frequencies 77 Hz and 280 Hz (297 Hz the natural frequency). The unsteady amplitude of the 8th mode (see Figure 12) has frequencies 77 Hz (862 Hz the natural frequency).

The spectrum includes mainly the blade oscillation frequencies closed to their natural ones (not multiple to the rotation frequency).

5. Conclusions

A partially - integrated method based on the solution of the coupled aerodynamic and structure problem is used for calculation of the unsteady 3D flow through a turbine stage with taking into account the rotor blades oscillations. The paper has investigated the mutual influence of both outer nonuniform distribution of the pressure behind the rotor blade and rotor blades rotation and oscillations. The interblade phase angle of blades oscillations depends not

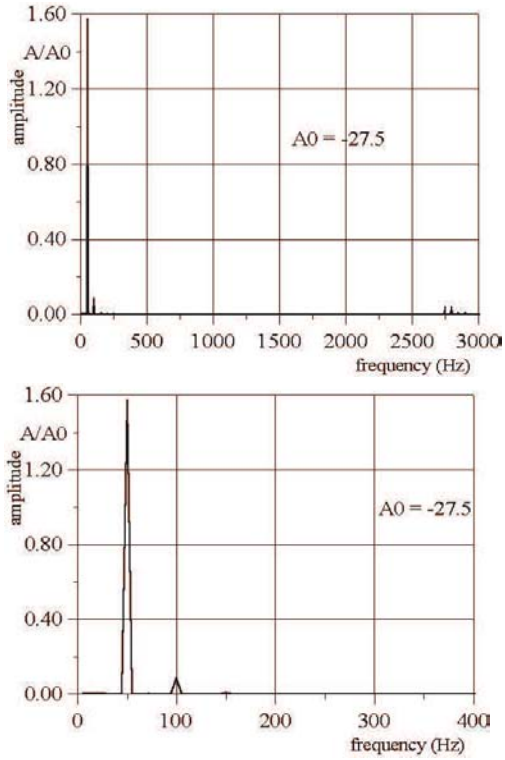

Figure 5. The amplitude-frequency spectrum for the modal force of the 1st mode

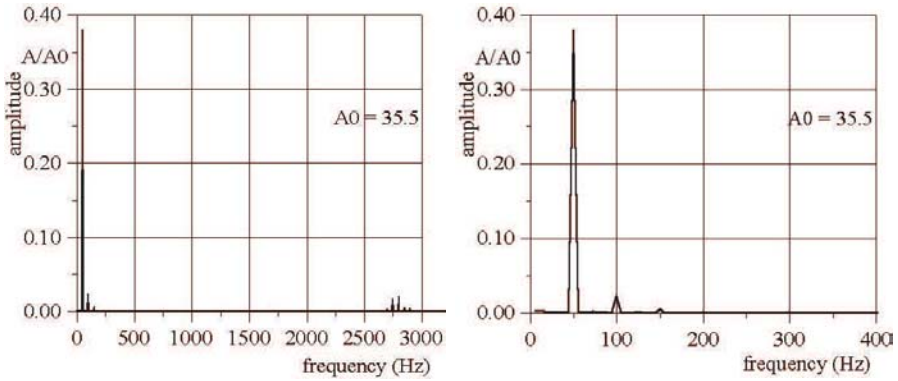

Figure 6. The amplitude-frequency spectrum for the modal force of the 2nd mode

only on unsteady forces lag but on the blade natural frequencies, as well. The low frequency unsteady forces caused by non-uniform pressure distribution are higher in comparison to the high frequency excitations. It has shown that

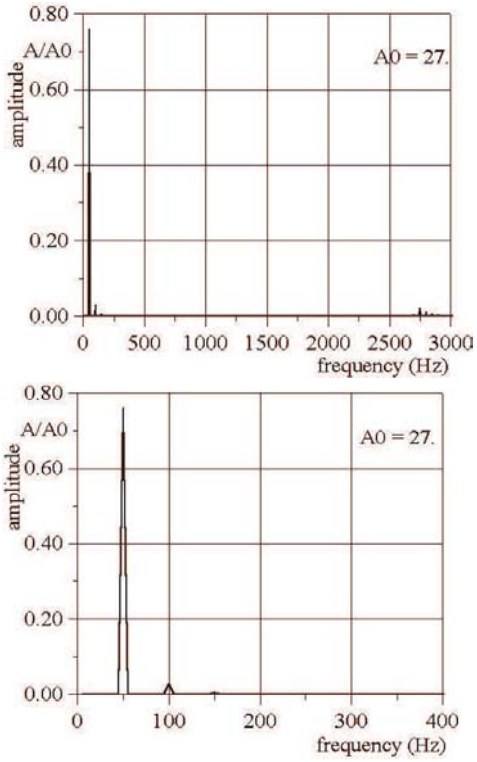

Figure 7. The amplitude-frequency spectrum for the modal force of the 4th mode

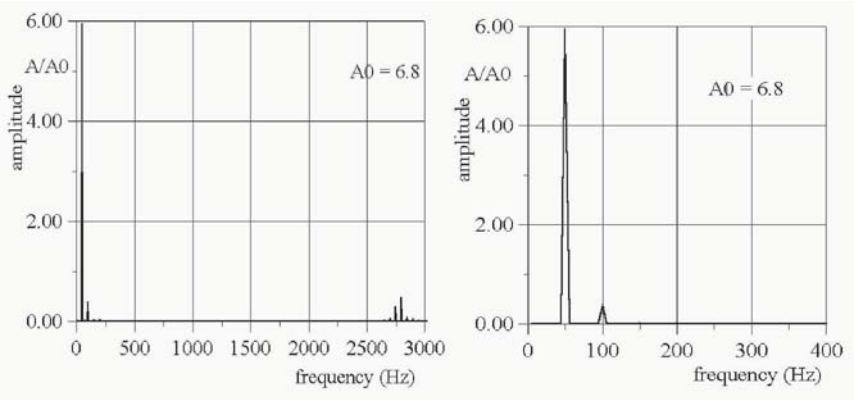

Figure 8. The amplitude-frequency spectrum for the modal force of the 8th mode

amplitude-frequency spectrum includes the harmonics with frequencies which are not multiple to the rotation frequency.

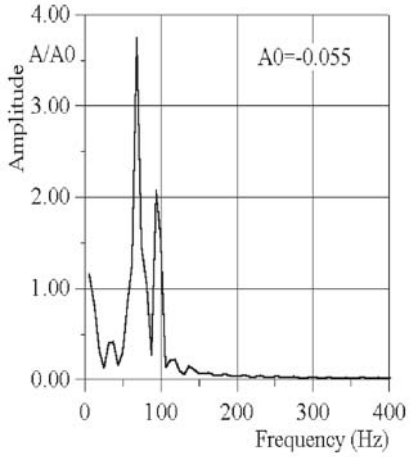

Figure 9. Amplitude-frequency spectrum of the blade oscillations by 1st mode

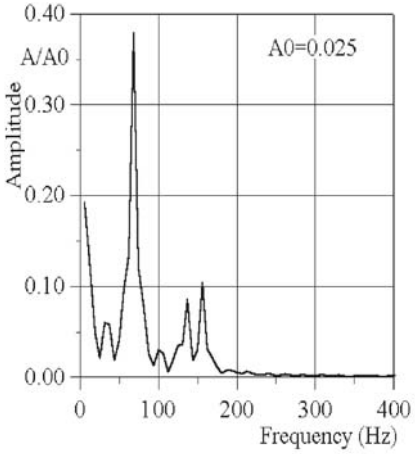

Figure 10. Amplitude-frequency spectrum of the blade oscillations by 2nd mode

References

Bakhle, M.A., Reddy, T.S.R., and Keith T.G. (1992). Time Domain Flutter Analysis of Cascades Using a Full-Potential Solver, AIAA J. vol.30, No 1, p.163.

Bathe K., Wilson E. (1976). Numerical Methods in Finite Element Analysis, Prentice-Hall, Inc., Englewood Cliffs, New Jersey.

Bendiksen O. (1998). Nonlinear blade vibration and flutter in transonic rotors, Proc. of IS-ROMAC – 7, The 7^{th} Intern. Symp. on Transport Phenomena and Dynamics of Rotating Machinery, 22-26 February, Honolulu, Hawaii, USA, 664.

Carstens V., Belz J. (2000). Numerical investigation of nonlinear fluid-structure interaction in vibrating compressor blades, ASME paper 2000-GT-0381, 2000.

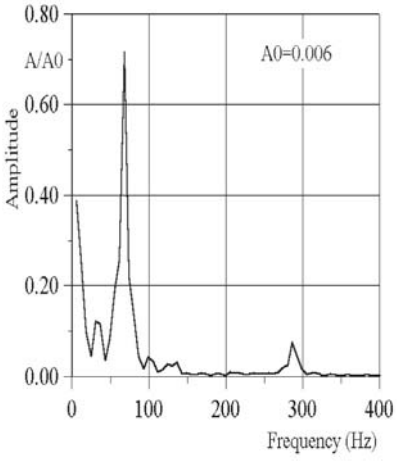

Figure 11. Amplitude-frequency spectrum of the blade oscillations by 4th mode

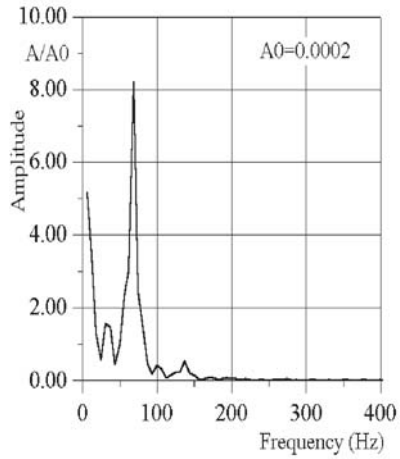

Figure 12. Amplitude-frequency spectrum of the blade oscillations by 8th mode

Chew J.W., Marshall J.G., Vahdati M. and Imregun M. (1998). Part-Speed Flutter Analysis of a Wide-Chord Fan Blade, T.H. Fransson(ed.), Unsteady Aerodynamics and Aeroelasticity of Turbomachines, Kluwer Academic Publishers, Printed in the Netherlands. 707-724.

Gnesin V., Rzadkowski R. and Kolofyazhnaya, L., V. (2000). A coupled fluid-structure analysis for 3D flutter in turbomachines, ASME paper 2000-GT-0380.

Gnesin V., and Rzadkowski R. (2000). The theoretical model of 3D flutter in subsonic, transonic and supersonic inviscid flow, Transactions of the Institute of Fluid-Flow Machinery, No. 106, 45-68.

Gnesin V., Rzadkowski R. (2001). Aeroelastic behaviour of the last stage steam turbine blades. Part II. Coulped fluid-structure oscillations harmonic oscillations, Transactions of the Institute of Fluid-Flow Machinery, No 108, 73-94.

Gnesin V., Rzadkowski R. and Kolodyazhnaya, L., V. (2000). A coupled fluid-structure analysis for 3D flutter in turbomachines, ASME paper 2000-GT-0380.

Hall, K.C. and Silkowski, P.D. (1997). The Influence of Neighbouring Blade Rows on the Unsteady Aerodynamic Response of Cascades, ASME Journal of Turbomachinery, 119,85-93.

He L. (1994). Integration of 2D fluid/structure coupled systems for calculation of turbomachinery aerodynamic, aeroelastic instabilities, Journal of Computational Fluid Dynamics. **3**, 217.

He L. and Ning W. (1998). Nonlinear harmonic analysis of unsteady transonic inviscid and viscous flows, unsteady aerodynamics and aeroelasticity of turbomachines, Proceedings of the 8^{th} International Symposium held in Stockholm, Sweden, 14-18 September, 183-189.

Moyroud F., Jacquet-Richardet G., and Fransson T. H. (1996). A modal coupling for fluid and structure analysis of turbomachine flutter application to a fan stage, ASME Paper 96-GT-335, 1-19.

Namba, M. and Ishikawa, A. (1983). Three-dimensional Aerodynamic Characteristics of Oscillating Supersonic and Transonic ĕnnular Cascades, ASME J. of Engineering for Power 105,138-146.

Rzadkowski R., Gnesin V. (2000). The numerical and experimental verification of the 3D inviscid code, Transactions of the Institute of Fluid-Flow Machinery, No. 106, 2000, 69-95.

Rzadkowski R., Gnesin V. (2002). 3D Unsteady Forces of the Transonic Flow Through a Turbine Stage with Vibrating Blades, ASME Paper GT-2002-300311.

Rzadkowski R. (1998). Dynamics of steam turbine blading. Part two: Bladed discs, Ossolineum, WrocŠaw-Warszawa.

EFFECTS OF STATOR CLOCKING IN SYSTEM OF ROWS STATOR-ROTOR-STATOR OF THE SUBSONIC AXIAL COMPRESSOR

N.M. Savin, V.E. Saren
The Central Institute of Aviation Motors
Aviamotornaya st. 2, Moscow, 111116, Russia *

Abstract Results of researches of blade rows unsteady interaction in the three-rows stage of the axial compressor are presented with the purpose of definition the gas-dynamical mechanism of clocking effects in system of rows stator-rotor-stator. Experiments were carried out on the large-dimensional low-speed compressor with measurements of stationary and unsteady flow parameters. Mutual circumferential position of stator rows, axial gaps and numbers of blades in rows are varied. Results of measurements are compared to calculation of flow parameters, received on the half-analytical theory of potential-vortical interaction of the airfoil cascades and by numerical simulation of averaged on Reynolds 2-D unsteady Navier-Stokes equations.

Keywords: Subsonic compressor,clocking effect

1. Introduction

Perfection of modern axial turbomachines demands already at a design stage of the account of unsteady interaction of rotors and stators. As have shown researches of last years, this circumstance is connected not only to a traditional problem of resonant blade vibrations, but also with influence of unsteadiness on the time-averaged gasdynamical characteristics of turbomachines. The level of periodic pressure pulsations in a flowing path of the axial turbomachine, designed on specified parameters, is determined by aerodynamic loading of the rows, axial gaps between them and the relation of numbers blades (or pitches) in rotors and stators.

*Work is executed at financial support of International scientific and technical centre (ISTC), the grant number 672.2.

K.C. Hall et al. (eds.),
Unsteady Aerodynamics, Aeroacoustics and Aeroelasticity of Turbomachines, 581–601.

One of displays of the mutual influence of rows on their flow is the effect of a mutual circumferential position of stators and (or) rotors (clocking effect). As have shown the first experiments at a transonic compressor stage with IGV [1,2] and on 4-stages turbine [3,4], at typical axial gaps between rows and equal (or multiple) numbers of vanes in stators their mutual circumferential position essentially influences on a flow in rotor [1,2], and also on efficiency of stags [3,4].

According to the further experimental researches on turbines [5,6] change of efficiency at change of a mutual circumferential position of stators, having equal numbers of vanes, achieves 0,5 %. Detailed researches of a typical subsonic stage of the high pressure compressor [7,8] have shown, that appropriate change of efficiency achieves 1,5 %. Thus the level of stagnation pressure pulsation in an absolute flow changes twice. The done work changes a little bit, and change of efficiency is provided, mainly, due to change of useful work [7,8].

From theoretical methods of research of effect of mutual circumferential position of stators have received application a half-analytical method of potential-vortical interaction of mutually moving cascades [1,2,9-11] and a method of direct numerical integration of averaged on Reynolds 2-D unsteady Navier-Stokes equations, closed by this or that model of turbulence [3,4-8]. First of the specified methods is based on the most simple quasi-steady model of an incompressible flow and allows to describe qualitative features of investigated flow. This method theoretically predicted influence of a mutual circumferential position of stators on a flow of the located between them rotor before performance of the first experiments.

Numerical methods are widely used by various authors, however for a task unsteady interaction of rotors and stators demand significant computing resources. Besides it is necessary to recognize that for similar tasks there are not clear requirements to construction of calculation grid zones, and also influence of used model of turbulence on accuracy of description of the unsteady vortical wakes dissipation. By that less, in overwhelming majority of the mentioned above works calculation and experimental data are compared.

Thus, available theoretical and experimental results allow to consider optimization of a mutual circumferential position of blade rows in an axial turbomachine as an effective control mean of unsteady interaction of rotors and stators for decrease of losses and pressure pulsations.

In given paper results of theoretical and the experimental researches are presented, executed on the large-dimensional compressor, which was specially created in CIAM for research of effects of unsteady interaction of blade rows of the axial compressor. The work was executed at financial support of the International Science and Technology Centre (ISTC), the Grant No.672-98. The first results, received on this compressor, were reported on previous ISUAAAT

Symposium in Lyons [12]. As against the experiments executed earlier at modelling stages of the axial compressor [1,2,7,8], on the created compressor the complex research was carried out, including flow laser anemometry between rows and digital processing of results of measurements of instant values of static pressure on the rotor case and on the stator vanes and also stagnation pressure between rows and behind a compressor. Researches are carried out at various axial gaps between rows and various numbers of blades in rows.

The basic attention in the paper is given to statement of the research problem, the developed measurement technique and the analysis of the results, allowing to reply on the questions, connected to use in the practical purposes of effect of a mutual circumferential position of stators in system of compressor rows stator-rotor-stator.

2. Methods and means of research

Experimental installation and measurements

Experimental installation includes the researched compressor, consisting of inlet guide vanes (IGV), rotor (R) and stator (S). The compressor has a cylindrical flowing path and is designed as a typical stage of the low-speed compressor on the following parameters: external diameter $Dc = 1.2m$, hub/tip ratio diameter $\overline{d}_1 = 0.8$, relative maximal airfoil thickness $\overline{C}_{max} = 10\%$, frequency of the R rotation $n = 2000rot/min$, the R tip speed $U_{tip} = 125m/s$, air flow rate $G = 30.8kg/s$, flow coefficient $\phi = 0.5$, loading coefficient $\psi = 0.32$, total pressure ratio $\pi_t = 1.055$, efficiency $\eta_{ad} = 0.90$, inlet and outlet flow angles $\alpha_1 = \alpha_3 = 90^{\circ}$, a degree of reaction $\tau = 0.8$. Flowing path and measurements are shown on Fig.1.

In initial assembly the compressor has numbers of blades IGV, R and S equal, accordingly, 36, 38, 36. The construction of the compressor allows to change over a wide range axial gaps between blade rows from 5 up to 90mm (from 0.05 up to 0.93 lengths of an axial projection of the R blade) and numbers of vanes in stators. During experiment independent turn of the IGV and S is carried out, that allows to measure circumferential distortion of a flow field and their change owing to mutual shift of the stators. The IGV vanes, having a symmetric airfoil, are located along an axis of the compressor with a zero incidence angle.

At experimental researches the measurements were made, allowing to receive average on time gasdynamical parameters of the compressor, and also structure of unsteady flow outside of and inside blade rows R and S. Unsteady values of pressure were measured with the help of high-response sensors "Endevco" on the R case in 6 points, on the suction and pressure surfaces S vanes in 12 points and in a flow behind the R and S on mean radius (see Fig.1).

Flow velocity was measured with the help of two-component laser anemometer (LDA) on mean radius in an axial gap between R and S.

Technique of experiment and data processing

The experimental information on a flow structure in the compressor at various circumferential positions of stator rows was obtained as follows. On a constant operation mode of the compressor on the given frequency of the R rotation and the air flow rate by circumferential shift of IGV relative S the relative mutual circumferential position of stators (parameter ν) is changed from 0 (some starting position of stators) up to 1 (shift of IGV relative S on one full pitch of stator vanes H_{st}) with the pitch $\Delta\nu = 0,1$. In turn at each of 11 values ν_i by simultaneous circumferential shift of IGV and S value of the relative circumferential position of stators (parameter Y_{st}) is changed from 0 up to 1 with the pitch $\Delta Y_{st} = 0,1$. Thus, the received files of measured parameters provided the information on their circumferential distortion and on their change in dependence on mutual stators position.

At measurements by high-response sensors the information on change of flow parameters on time within 1 second with phase synchronization of measurements with the help of the R blade passing frequency (BPF) mark was provided. After amplification of electric signals of sensors and their transformation to physical values with the help of analog-digital converters measured parameters entered in a digital kind to PC. Frequency of interrogation of high-response sensor made 19,2kHz, that at BPF 1,2kHz provided 15 measurements on the period of BPF. It is enough received volume of the experimental information for obtaining of change of flow parameters as in steady (connected with stators), and rotating (connected with a rotor) systems of references by results of measurements by high-response sensors in the steady system of reference, realized in experiment. The technique of recalculation of the measured parameters for their representation in rotating system of reference is described in [12,14]. For allocation of a periodic signal the indications of sensors were averaged on ensemble on 114 periods of BPF (3 revolutions of R). Random flow pulsations were determined by subtraction of periodic components of pulsations from the measured values. It is necessary to notice, that random pulsations are caused not only by flow turbulence, but also small deviations in geometry of the R blades and operation mode of the compressor.

Any flow parameter $\Pi(r, x, y, t, \nu)$ (for example, pressure, velocity and etc.) generally is the function, dependent from radial r, axial x and circumferential y coordinates of a considered point, time t and a mutual circumferential position of stators ν. For reception of integrated estimations of interactions of rows effects by results of experiment or calculation at fixed values r, x and ν were determined the following generalized parameters:

$(\Pi)_t$ – averaged on time value Π;

$< \Pi >_t$ – mean root square (RMS) deviation of Π from its average on time value $(\Pi)_t$;

$((\Pi)_t)_y$, $(< \Pi >_t)_y$ – averaged on period H (pitch of stators or rotor) values $(\Pi)_t$ and $< \Pi >_t$;

$< \Pi >_y$, $<< \Pi >_t>_y$ – RMS deviations of values $(\Pi)_t$ and $< \Pi >_t$ from their averaged values $((\Pi)_t)_y$ and $(< \Pi >_t)_y$ on circumferential period H.

Averaged on circumferential period H values $((\Pi)_t)_y$ and $(< \Pi >_t)_y$ characterize some stationary flow, obtained by averaging of real unsteady flow, and RMS deviations $< \Pi >_y$ and $<< \Pi >_t>_y$ determines a level of unsteady interactions of mutually moving rows and for the isolated row of identical blades $< \Pi >_y$ and $<< \Pi >_t>_y$ are equal to zero. The specified parameters may be determined in the R and S systems of reference. Conformity between the parameters, determined in different systems of reference, is given in [14].

Calculation Methods

Flow calculations were carried out on a design operation mode of the compressor for 2D-flow in system of cascades IGV-R-S on mean radius. From the measured radial distributions of stagnation pressures and temperatures on a path of the compressor, given on Fig.2, it is visible that flow radial distortion is not great, and flow on the mean section on blade height is representative enough for the characteristic of flow in all compressor.

In the theory of potential-vortical interaction of cascades it is supposed that vortical wakes behind cascades in relative movement are given as universal velocity distribution in automodel area. In details specified theory is described in works [10,11] and used in [9].

At numerical flow simulation averaged on Reynolds Navier-Stokes equations were used, closed by two-parametrical (q, ω) model of turbulence. Features of the calculating scheme and construction of the grids are described in [13]. In the given work conditions of periodicity were imposed on the bottom and top borders of the calculating area, containing accordingly 18, 19, 18 airfoils in the IGV, R, S cascades at full simulation of conditions of experiment or 1, 1, 1 airfoils at the simplified flow simulation. In the latter case the general number of grid units has made 12700 at the minimal size of a cell at an airfoil, equal to $1,5 \times 10^{-3} mm$. The step of integration on time was equaled $T/3800$, where period $T = h_R/u$, h_R is the R cascade pitch. Calculations were executed by V.G. Krupa.

The basic advantage of numerical simulation in comparison with the model of potential-vortical interaction consists in an opportunity of a direct estimation of influence of row unsteady interaction on time-averaged gasdynamical characteristics. From comparison of experimental and calculated circumferen-

tial distributions of time-averaged stagnation pressures at the compressor exit for an optimum point ($U_{tip} = 125m/s$, $\phi = 0,5$) on Fig.3 it is visible, that the calculated data are close to experimental.

It is necessary to note, that attempts of the simplified calculations by replacement of the real relation of numbers of blades in the rows 18¸ 19¸ 18 on simplified 1¸ 1¸ 1 resulted in essential deviations of calculated values from experimental. Therefore all calculations, for which comparisons with experiment are presented, were received for real relation of numbers of blades.

The purpose and volume of experiments

The purposes of a series of the experiments, executed in work, are the determination of influence of axial gaps between rows and numbers of IGV vanes on unsteady flow parameters of the R blades and an experimental estimation of influence of unsteadiness on losses in the compressor. Practical result of the analysis is definition of optimization criteria of mutual circumferential position of stators.

Axial gaps Δ_{12} (between IGV and R) and Δ_{23} (between R and S) at researches of the clocking effect are chosen, recognizing that according to Refs. [1,2,7,8,9,12], the source of the clocking effect in system of rows IGV-RK-S is change of flow in the R at mutual circumferential shift of the IGV and S. As criteria of an estimation of a unsteadiness level and clocking effect the generalized parameters were used:

$(< \Gamma_R >_t)_\nu$ – averaged on mutual circumferential position of stators ν ($0 \le \nu \le 1$) of RMS deviation on time t of velocity circulation on the R blade $\Gamma_R = \Gamma_R(t)$;

$<< \Gamma_R >_t >_\nu$ – RMS deviation $< \Gamma_R >_t$ from $(< \Gamma_R >_t)_\nu$ for all mutual circumferential position of stators. Values $(< \Gamma_R >_t)_\nu$ and $<< \Gamma_R >_t >_\nu$ were calculated under the theory of potential-vortical interaction for cascades on mean radius of the compressor at various combinations of axial gaps Δ_{12} and Δ_{23} in a wide range of their change from 5 up to 60mm (from 0,05 up to 0,62 from the R blade axial projection length).

By results of calculations 2 assembly of the compressor were chosen for research, providing essentially various levels of parameter $<< \Gamma_R >_t >_\nu$ at close values of parameter $< \Gamma_R >_t$, i.e. essentially various levels of clocking effect at close values of flow unsteadiness on the R blades:

1-st compressor assembly – $\Delta_{12} = \Delta_{23} = 15mm$ ($\overline{\Delta}_{12} = \overline{\Delta}_{23} = 0,15$), $<< \Gamma_R >_t >_\nu = 41\%$, $(< \Gamma_R >_t)_\nu = 4,2\%$;

3-th compressor assembly – $\Delta_{12} = 60mm$, $\Delta_{23} = 5mm$ ($\overline{\Delta}_{12} = 0,62$, $\overline{\Delta}_{23} = 0,05$), $<< \Gamma_R >_t >_\nu = 15\%$, $(< \Gamma_R >_t)_\nu = 4,3\%$;

Besides the specified configurations of the compressor, for which experiment was carried out at numbers of blades 36-38-36, **2-nd compressor as-**

sembly was executed at numbers of blades 18-38-36. By a calculated estimation reduction of numbers of the IGV vanes in 2 times results in increase of common flow unsteadiness on the R blades, however considerably reduces clocking effect.

3. Results of research

Overall compressor parameters

On Fig.4 changes on a stators pitch of total pressure upon mean radius before R and static pressure upon the case behind R, measured in axial gaps at 1-st assembly of the compressor on the design operating mode at $U_{tip} = 125m/s$, $\phi = 0,5$. Thus, in the researched compressor R blades work in conditions of the disturbed flow on an input owing to wakes behind the IGV vanes and on an output owing to potential influence upwards on a flow of the S vanes. Displacement on a phase of these disturbances by mutual circumferential shift of the IGV and S (changes of parameter ν), is the basic source of clocking effect.

Change of the overall parameters in 1-st assembly of the compressor in dependence on a mutual circumferential position of stators is presented on Fig.5. Change of efficiency makes $0,8 \div 1,0\%$ and this change, basically, is connected to change of a total pressure ratio. At other assemblies of the compressor change of efficiency on ν did not exceed $0,5\%$ and is commensurable with a margin error its definitions during experiment. It gives the basis to consider 1-st assembly of the compressor with identical number vanes in stator rows and with identical axial gaps $\overline{\Delta}_{12} = \overline{\Delta}_{23} = 0,15$ the optimal on clocking effect on overall characteristics of the compressor.

Structure of unsteady flow in system of rows stator-rotor-stator of the axial compressor

Rotor blade flow

The R flow analysis is based on measurements of static pressure pulsations on the R case with the help of 6 high-response sensors, uniformly distributed along an axis of the compressor within of an axial projection of the R blade from a leading (the sensor No.1) up to trailing (the sensor No.6) edges of R (see Fig.1).

On Fig.6 as illustration distributions on a R blade pitch (the sensor No.4, $X = 0,6$) of values $\Delta P(y,t) = P(y,t) - ((P)_t)_y$, where $P(y,t)$ is static pressure in a point of measurement are presented. Static pressure is expressed in the R system of reference and thus, corresponds to its blade to blade distribution at the various moments of time at fixed mutual circumferential position of the IGV and S ($\nu = 0$). Axis Oy is directed opposite to R rotation. The difference of the maximal and minimal values of ΔP reflects difference of

static pressure on pressure and suction surfaces of the R blade, a little bit distinguished (to reduction) from true owing to leakages in a radial clearance.

The analysis of results of measurements has shown, that time-averaged values of static pressure difference $\Delta(P)_t = (P)_t - ((P)_t)_y$ practically do not depend on ν for all investigated compressor assemblies 1, 2 and 3. Thus, averaged on time parameters of relative flow in the R do not depend on unsteady interaction of rows. The unsteady part of static pressure thus rather essentially depends on axial gaps, numbers of vanes in stators and their mutual circumferential position. Fluctuations of $\Delta P(y,t)$ on time for various sensors make $10-20\%$ from it time-averaged value $\Delta(P)_t$. These fluctuations characterize unsteady interaction in system of rows stator-rotor-stator.

For an estimation of influence of ν on an unsteady part of static pressure distribution and, hence, on aerodynamic loading on the R blades the value was used

$$\Gamma(t) = \frac{R_y(t) - (R_y)_t}{(R_y)_t} \cdot 100\%,$$

where $R_y(t)$ is instant value of the linear circumferential aerodynamic load, acting on the R blade, and $(R_y)_t$ is it averaged on time value. Necessary for definition $R_y(t)$ the difference of static pressure on the R blade was determined on measurements of static pressure on the case by sensors No.1-6. Examples of such measurements are submitted on Fig.6. Further, after project of the local loading determined thus on a circumferential direction, total loading was calculated as result of integration on 6 values of the local loading, received on each of sensors.

As illustrations on Fig.7 dependences of $\Gamma = \Gamma(t)$ for compressor assemblies 1 and 3 are presented at values $\nu = 0$ and $0,6$. The similar data, received for all assemblies and various values ν show, that the circumferential aerodynamic loading, acting on the R blade, has on the period significant fluctuation from 5 up to 10% from its averaged on time loading. Thus the amplitude of fluctuations of loading is essentially various for various values ν, in particular for assembly 1. Thus, overall aerodynamic interaction of the R with IGV and S at their mutual circumferential shift is changed significantly.

Velocity fi elds behind the rotor

Research of a velocity field behind R is based on laser flow anemometry in an axial gap between R and S and calculation of viscous flow by the numerical simulation of averaged on Reynolds 2-D unsteady Navier-Stokes equations.

Influence of mutual circumferential shift of the IGV and S on time-averaged and unsteady parameters of a vortical wake is illustrated on Fig.8, where for three compressor assemblies the measured distributions on the R pitch of time-averaged relative velocities behind $R\,|(\boldsymbol{W})_t|\,/W_{av}$ and their RMS deviations on time $< \boldsymbol{W} >_t$ for two values of $\nu = 0;\ 0,5$ are presented. It is visible

that distributions of $|(\boldsymbol{W})_t| / W_{av}$ practically coincide at $\nu = 0$ and $\nu = 0,5$. Thus, averaged on time flow parameters of the R blades do not depend from unsteady aerodynamic interactions of R with IGV and S.

Apparently on Fig.8 that unsteadiness of a velocity vector in a vortical wake behind R, estimated in the value $< \boldsymbol{W} >_t$, first, it is rather significant especial in the field of a vortical wake where it achieves 25% and more, and, second, essentially changes at mutual circumferential shift of the IGV and S. As one would expect, for assembly 1 of the compressor stronger influence of circumferential shift of stators on structure of unsteady vortical wakes behind R, than for assemblies 2 and 3, is observed. Besides assembly 3 differs more a high level of unsteadiness in a flow core and less expressed clocking effect, that is connected to strong potential influence of the S upwards on a stream owing to small ($\overline{\Delta}_{23} = 0,05$) an axial gap between R and S.

On Fig.9 the data on measurements $(W)_t$, shown on Fig.8 for the assemble 1, are compared to results of direct numerical simulation (see item 2). Apparently, calculation well is coordinated to experiment in a flow core and considerably differs in the zone of vortical wake.

As a whole the received data testify that at a rotor-stator interaction flow velocity pulsations appear behind the R, especially significant in the zones of vortical wakes. From here it is necessary to expect that stators clocking most essentially may affect on value $<< w >_t>_y$, which determines RMS deviation on the R pitch of RMS deviation on time of a velocity vector. Really, dependence from ν value $<< w >_t>_y$, presented on Fig.10 for various compressor assemblies, shows essential influence of stators clocking on velocity pulsations in vortical wakes, in particular for assembly 1. The detailed description of structure of vortical wakes behind R blades is given in [15, 16].

Pressure pulsations behind R

Measurements of stagnation pressure pulsations were made by the insert probes, equipped with high-response sensors, on mean radius in an axial gap behind R and on an exit from the compressor. By results of static and dynamic calibrations receivers of probes are insensitive to a flow angles $\pm 15^{\circ}$ and have the uniform amplitude-freauency characteristic up to frequency 20kHz.

For an estimation of influence of the R and stators interaction on a level of stagnation pressure pulsations P_{t2} (behind R) and P_{t3} (behind S) values were used

$$SP_{t2} = \sqrt{\frac{[< (P_{t2})_t >_y]^2 + [<< P_{t2} >_t>_y]^2}{\left[(< P_{t2} >_t)_y\right]^2}},$$

$$SP_{t3} = \sqrt{\frac{\left[\left(< P_{t3} >_t\right)_y\right]^2 + [<< P_{t3} >_t >_y]^2}{[< (P_{t3})_t >_y]^2}},$$

where P_{t2} and P_{t3} are expressed in the stator system of reference. It is easy to notice, that for isolated R and S values SP_{t2} and SP_{t3} are equal to zero and are nonzero for interactive rows. SP_{t2} and SP_{t3} were determined both for periodic $(SP_{t2,3})_p$ and for random $(SP_{t2,3})_r$ pressure pulsations. Thus in expressions for SP_{t2} and SP_{t3} denominators are determined in both cases by a periodic part of pressure pulsations.

Dependences of values SP_{t2p}, SP_{t2r} and also SP_{t3p}, SP_{t3c} from parameter ν are presented on Fig.11 for assembly 1. Apparently, behind R the periodic part of stagnation pressure pulsations, caused by vortical wakes, considerably surpasses random component and essentially depends from ν. On an exit from the compressor, on the contrary, random component has essentially increased concerning periodic component, which poorly depends from ν. The similar result is received also for assembly 2.

Undoubtedly the received data testify to evolution of vortical wakes behind R, which dissipate during mixture.

The increase of random pulsations concerning periodic pulsations on all compressor assemblies is shown also for static pressure p, which pulsations were measured on mean radius on the S vanes. Measurements were carried out by 12 high-response sensors, which were allocated in regular intervals along suction and pressure surfaces of the next S vanes (on 6 sensors on one vane) from leading up to trailing edges.

As an illustration on Fig.12 dependence from ν value is presented

$$\lambda\,(\nu) = \frac{< p >_t}{\Delta(p)_t}$$

for the sensors No. 4, located on middle of a S vane chord from the suction and pressure sides. Here $\Delta\overline{p} = (p_{p.s.})_t - (p_{s.s.})_t$ is difference of time-averaged static pressure. The value λ is presented for assembly 1 both for periodic (λ_p), and for random (λ_r) components of pressure pulsations of p.

Apparently from Fig.12, both on suction and pressure sides of the S vanes random pressure pulsations practically do not depend from ν and surpass periodic pulsations, for which dependence from ν remains appreciable.

The important conclusion follows from results of measurement of value $\Delta(p)_t$ for various mutual circumferential positions of stators. Dependences from ν of $\Delta(p)_t$ are presented on Fig.13 (assembly 1) for 5 pairs of sensors, where sensor No.1 and No.6, accordingly, concern to vicinities of leading and trailing edges of the S vanes. The received data show that as distributed and

overall averaged on time aerodynamic loading on the S vanes practically does not depend on a mutual circumferential positions of the IGV and S vanes.

4. On influence of stators clocking on losses of total pressure in a compressor

The results of the presented above analysis of a flow in system of rows IGV-R-S allow to make the conclusion, concerning observably in experiments [3-8] dependence of total pressure losses in a compressor stage from stators clocking ν.

As follows from the experimental data received here, the parameter ν does not influence on averaged on time aerodynamic characteristics of the R and S. At the same time the unsteady (periodic) part of velocity circulation on the R blades rather considerably may depend on a mutual circumferential position of stators. In this connection in works [5-8] the assumption was stated, that influence ν on losses of total pressure in a stage is caused by dissipation of the free vortexes, descending with R blades at change on them of velocity circulation. The results received in the given work directly allow to compare dependences from ν intensity of free vortexes and losses of total pressure.

According to Thomson theorem running intensity of free vortexes γ behind an airfoil at the moment of time t in a point of a wake with arc coordinate s, counted from a leading edge of an airfoil, is equal

$$\gamma\left(s,t\right)=-\frac{1}{v\left(s\right)}\frac{\partial\Gamma}{\partial t}\,|_{\tau}\quad,\quad\tau=t-\int\limits_{0}^{s}\frac{ds}{v\left(s\right)},$$

where $v(s)$ is velocity of free vortexes drift, $\Gamma(t)$ is velocity circulation on an airfoil. From here the measure of free vortexes intensity ε may be expressed by the formula

$$\varepsilon=\sqrt{\frac{1}{T}\int\limits_{0}^{T}\left[\frac{\partial\Gamma}{\partial t}\right]^{2}dt},$$

where T is the period of a flow pulsation on the R blades.

The value $\varepsilon(\nu)$ may be calculated according to experiment, which illustration is given on Fig.7. Function $\Gamma(t)$ thus is determined as a result of the decision of the Cauchy-Lagrange equation concerning of velocity discontinuity on an airfoil pressure and suction sides at value of pressure difference known from experiment [16].

In turn the value of total pressure losses behind R is determined according to measurements by probes of the stagnation pressure, located behind the R and S, by calculation of value

$$\Delta P_t = \left((P_{t2})_t\right)_y - \left((P_{t3})_t\right)_y$$

As shows experiment, as against time-averaged aerodynamic loadings on the R and S, values ΔP appear essentially dependent from ν in particular for the assembly 1.

For the specified assembly on Fig.14 dependences are presented

$$\mu(\nu) = \frac{\varepsilon(\nu) - (\varepsilon)_\nu}{(\varepsilon)_\nu} \quad , \quad \lambda(\nu) = \frac{\Delta P_t(\nu) - (\Delta P_t)_\nu}{(\Delta P_t)_\nu}.$$

The received data show that in spite of the fact that $\Gamma(t)$ is determined for peripheral section of the R blades, and value ΔP_t was measured on mean radius, character of dependences $\mu = \mu(\nu)$ and $\lambda = \lambda(\nu)$ are close. Areas ν, appropriate to the lowered (increased) values of free vortexes intensity coincide with areas of the lowered (increased) values of total pressure losses behind the R.

It is necessary to notice that this result specifies also a source of the additional losses, caused a rotor-stator interaction in axial turbomachines.

5. Conclusions

The received results allow to formulate the following conclusions.

1 The presented experimental installation and the technique of data processing developed by authors allow to carry out complex researches of unsteady flows, in particular, effects of a rotor-stator interaction in the subsonic axial compressors.

2 Researches of flow properties show the following: – the rotor-stator interaction in a subsonic axial turbomachine at mean level of axial gaps ($\sim$15–25% of rotor blade pitch) does not influence on time-averaged aerodynamic loadings on blades and structure of vortical wakes behind them;

– total pressure losses in a flow, caused a rotor-stator interaction, are bound up with additional losses owing to dissipation of free (periodic) vortexes in wakes behind blades.

3 Stator clocking effects in system of rows stator-rotor-stator of the axial compressor are bound up with influence of a mutual circumferential position of stators on unsteady aerodynamic characteristics of a rotor. The effects are most significant at equal number of stators vanes and essentially depend on axial gaps between rows. Stators clocking may serve as an effective practical control facility a level of the rotor-stator interaction in axial turbomachines.

References

[1] Saren, V.E. (1994) Some Ways of Reducing Unsteady Blade Loads Due to Blade Row Hydrodynamic Interaction in Axial Flow Turbomachines, *Second International Conference EAHE*, Pilsen, Czech Republic, pp.160 - 165.

[2] Saren, V.E. (1995) Relative Position of Two Rows of an Axial Turbomachine and Effects on the Aerodynamics in a Row Placed Between Them, *Unsteady Aerodynamics and Aeroelasticity of Turbomachines*, Elsevier, pp.421 - 425.

[3] Huber F.W., Johnson P.D., Sharma O.P. et ol. (1995) Performance Improvement Through Indexing of Turbine Airfols. Part 1. Experimental Investigation, *ASME Paper* No. GT-27.

[4] Griffin L.W. , Huber F.W. and Sharma O.P. (1995) Performance Improvement Through Indexing of Turbine Airfols. Part 2. Numerical Simulation, *ASME Paper* No. GT-28.

[5] 5 Dorney D.J. and Sharma O.P. (1996) A Study of Turbine Performance Increases Through Airfoil Clocking, *AIAA Paper* No.2816.

[6] 6 Hohn W. (2001) Numerical and Experimental Investigation of Unsteady Flow Interaction in a Low Pressure Multistage Turbine, *XV Intern. Sump. On Airbreathing Engines*, Sept. 2-7, Bangalore, India.

[7] 7 Saren V.E., Savin N.M., Dorney D.J., Zacharias R.M. (1997) Experimental and Numerical Investigatin of Unsteady Rotor-Stator Interaction on Axial Compressor Stage (with IGV) Performance, *Unsteady Aerodynamics and Aeroelasticity of Turbomachines*: 8 th Intern. Symp., Stockholm, Dordrecht et al.: Kluwer, P. 407-416.

[8] 8 Saren V.E., Savin N.M., Dorney D.J., Sondak D.L. (1998) Experimental and Numerical Investigatin of Airfoil Clocking and Inter-Blade-Row Gap Effects on Axial Compressor Performance, *International Journal of Turbo and Jet Engines*, 15, P. 235-252.

[9] 9 Savin N.M. and Saren V.E (2000) Hydrodynamic Interaction of the Blade Rows in the Stator-Rotor-Stator System of an Axial Turbomachine, *Fluid Dynamics.* Vol.35, _3, pp. 145-158.

[10] 10 Saren V.E. (1971) On Hydrodinamical Interaction of Cascades of Profiles in Potential Flow, Izv. ÇS of USSR, > GG, _4, pp.75-84.

[11] 11 Judin V.À. 1981 Calculation of Hydrodinamical Interaction of Cascades of Profiles with account of wakes, *Aeroelasticity of Turbomachines Blades. Tras. of the CIAM*, _953, pp.52-66.

[12] 12 Saren V.E., Savin N.M., Krupa V.G. (2000) Experimental and Computional Research of a Flow Structure in a Stator-Rotor-Stator System of an Axial Compressor, *The 9th Internaional Symposium on Unsteady Aerodynamics, Aeroacoustics and Aeroelasticity of Turbomachines (ISUAAAT)*, Lyon, France, September 4-8, pp.494 - 502.

[13] 13 Ivanov M.. Ja, Krupa V.G., Nigmatullin R.Z. (1989) Implicit High Accuracy S.K. Godunov Scheme for Integration of Navier-Stokes Equations, *Journal of Calculating Mathematic and Mathematical Physic*, vol.29, No.6.

[14] 14 Saren V.E., Savin N.M., Krupa V.G., Petrovitchev A.M. (2001) Influence of a Rotor-Stator Interaction on the Steady and Unsteady Characteristics of the Axial Compressor, *Paper from the XV ISABE*, Bangalore, India.

[15] 15 Saren V.E and Smirnov S.A. (2003) Unsteady Vortical Wakes behind Mutually Moving Rows of Axial Turbomachine, *Thermophysics and Aerodynamics*, Vol.10, No.2.

[16] 16 Saren V.E, Smirnov S.A. (2003) Structure of Unsteady Vortical Wakes behind Blades of Mutually Moving Blade Rows of an Axial Turbomachine, *The 10th Internaional Symposium on Unsteady Aerodynamics, Aeroacoustics and Aeroelasticity of Turbomachines (ISUAAAT)*, Durham, North Carolina, USA, Sept. 7-11.

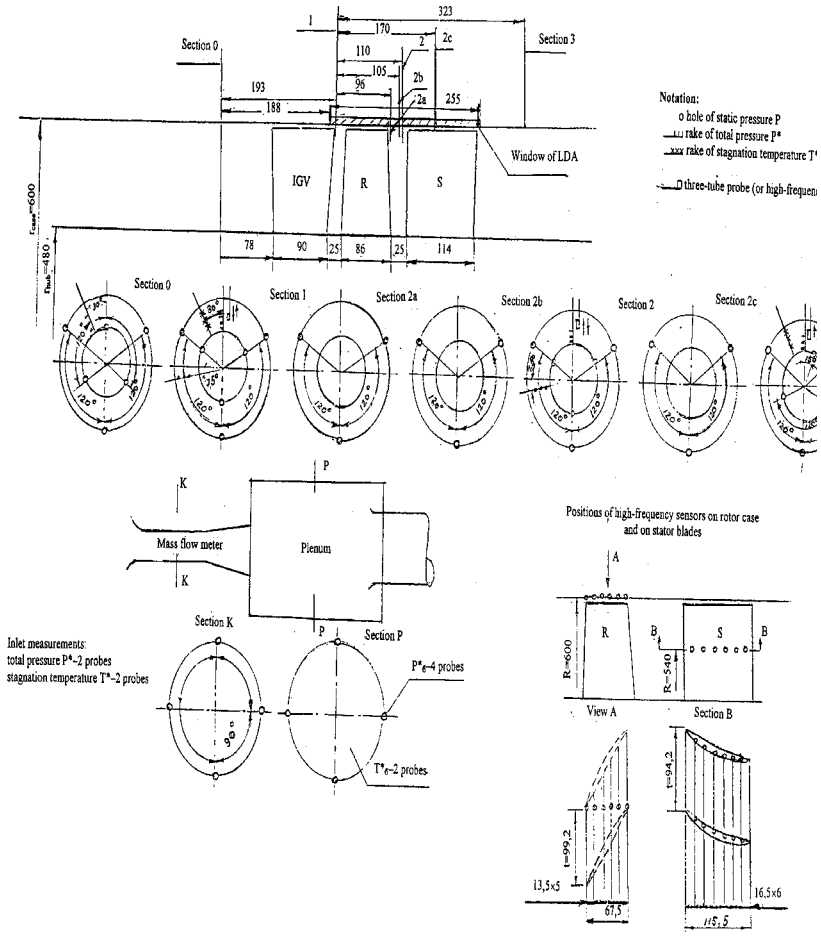

Figure 1. Compressor flow path and measurements

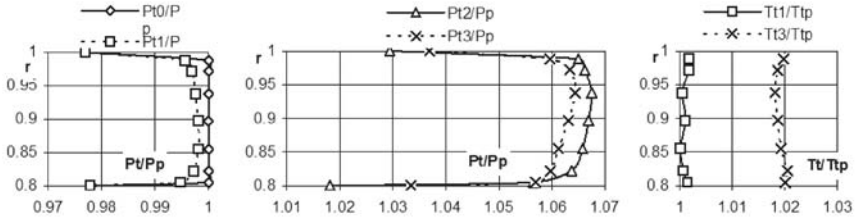

Fig.2 Radial distributions of stagnation pressure Pt and temperature Tt along flow path.

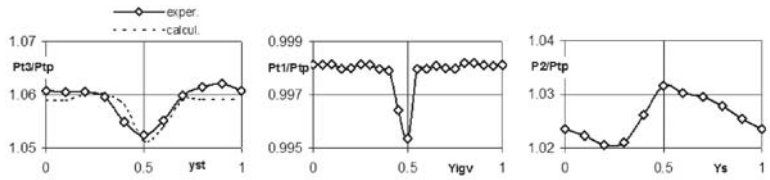

Fig.3 Comparison of experimental and numerical pitch-wise distribution of stagnation pressure behind S.

Fig. 4 Pitch-wise distributions of total pressure before R (left) and static pressure after R (right).

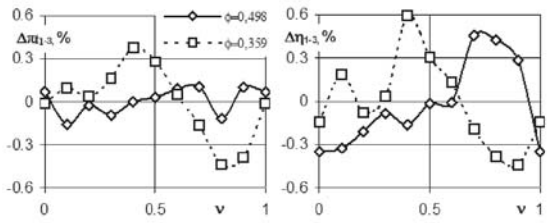

Fig.5 Change of total pressure ratio and efficiency depending on mutual circumferential position of stators ν.

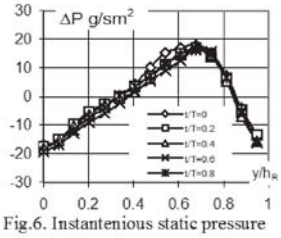

Fig.6. Instantenious static pressure distributions along rotor pitch for sensor №4

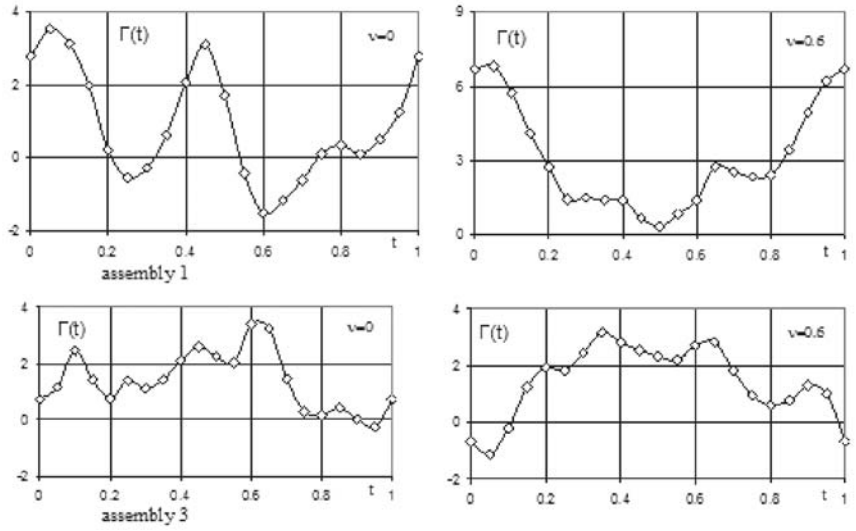

Fig. 7. Time variations of velocity circulation T.

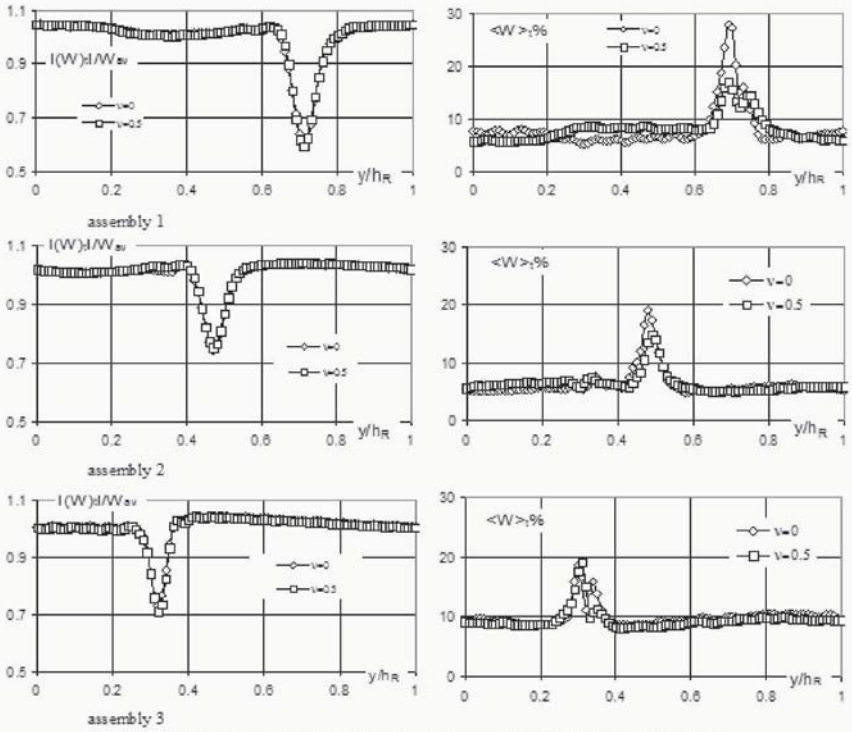

Fig.8. Structure of vortical wakes behind R blade

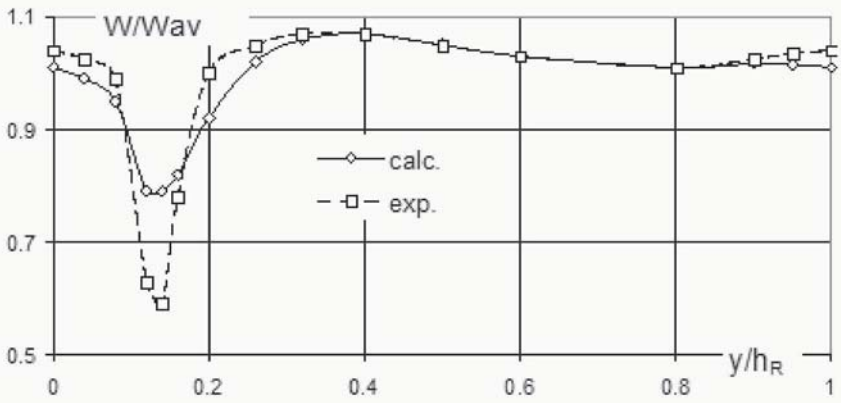

Fig.9.Pitch-wise distributions of flow velocity behind R. Assembly 1.

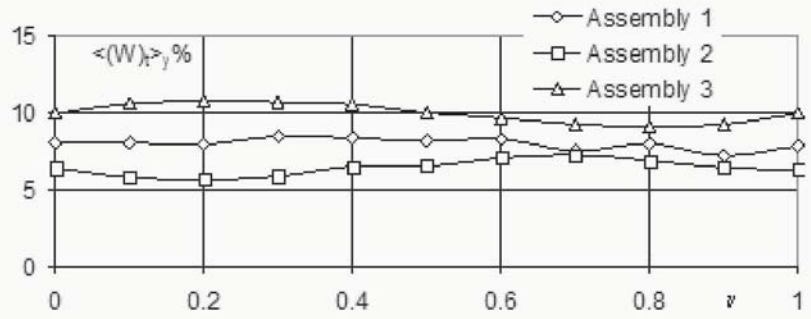

a) Measure of circumferential distortion of time-average flow

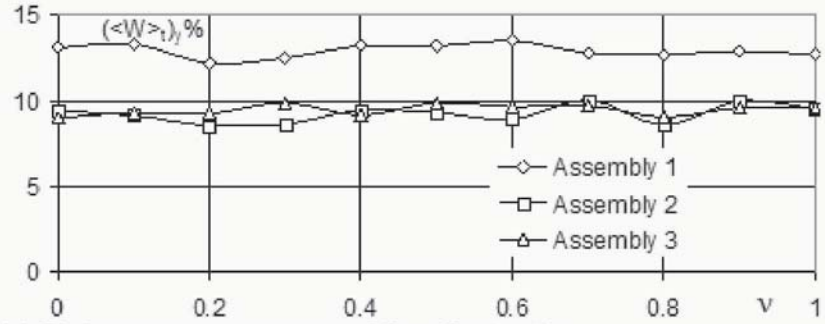

b) Pitch-average measure of flow fluctuation

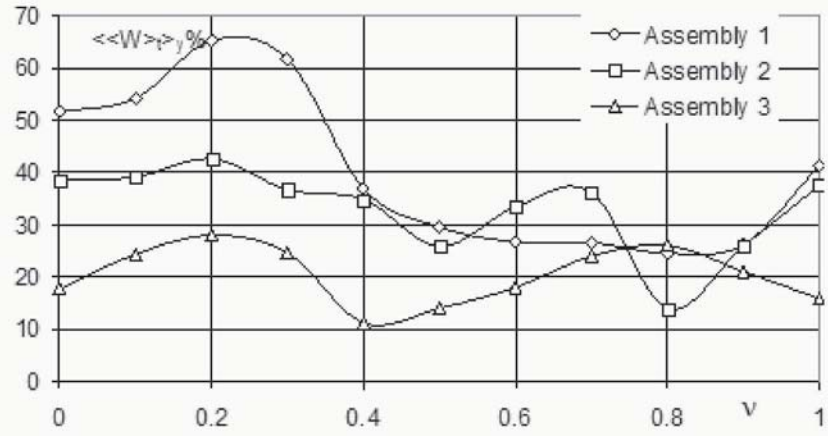

c) Measure of circumferential distortion of flow fluctuation

Fig.10. Influence of mutual clocring positions of stators on relative flow velocity behind rotor.
Design operating mode: n=2000 rpm. Gcorr=30.8kg/s.

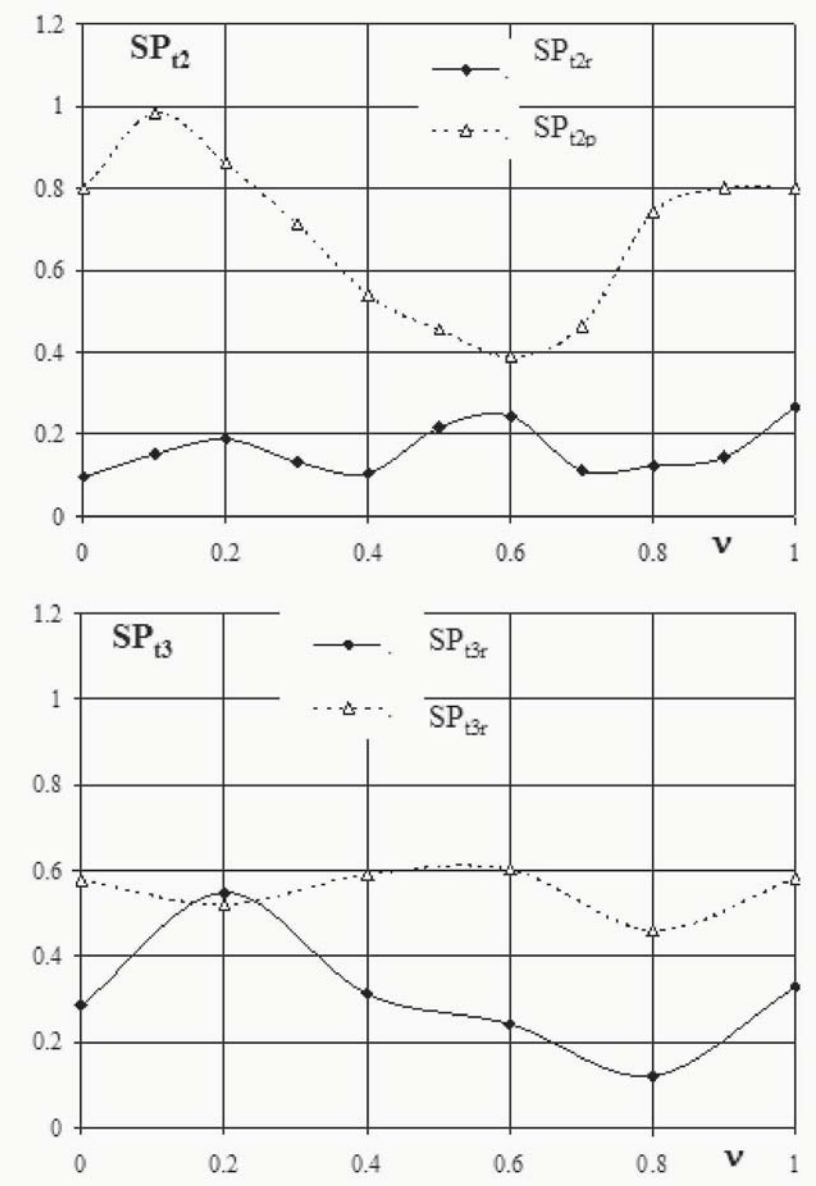

Fig.11.Unsteadiness of tital pressure before and after S

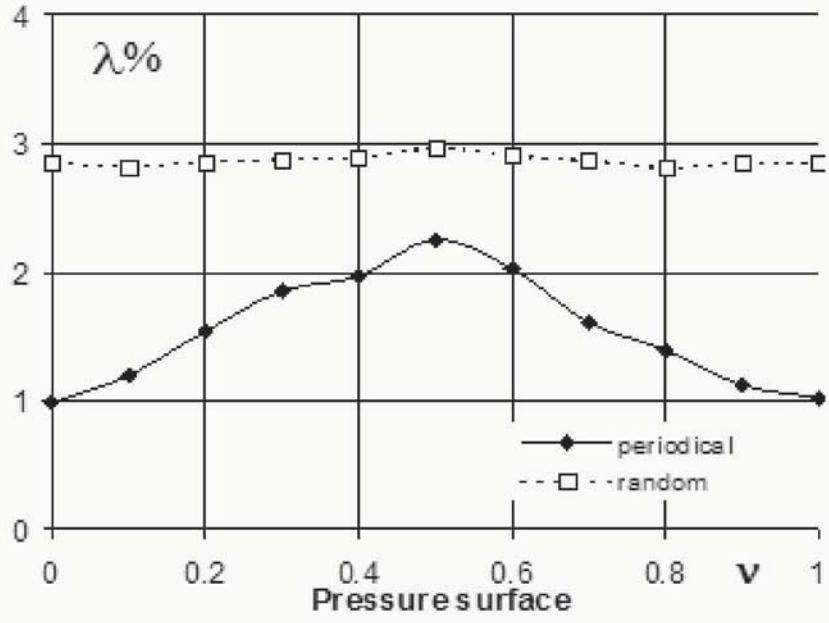

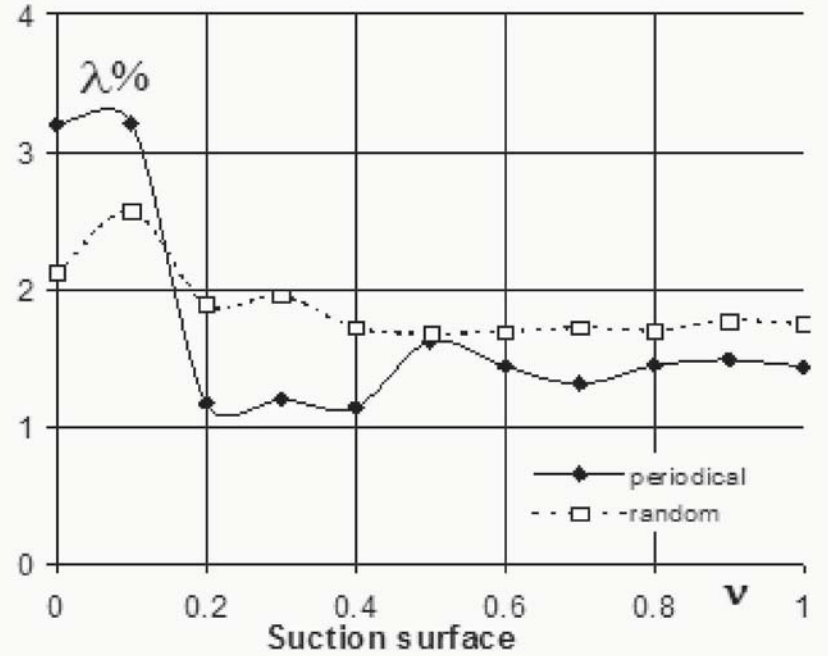

Fig.12.Static pressure pulsation on the S vanes. assembly 1

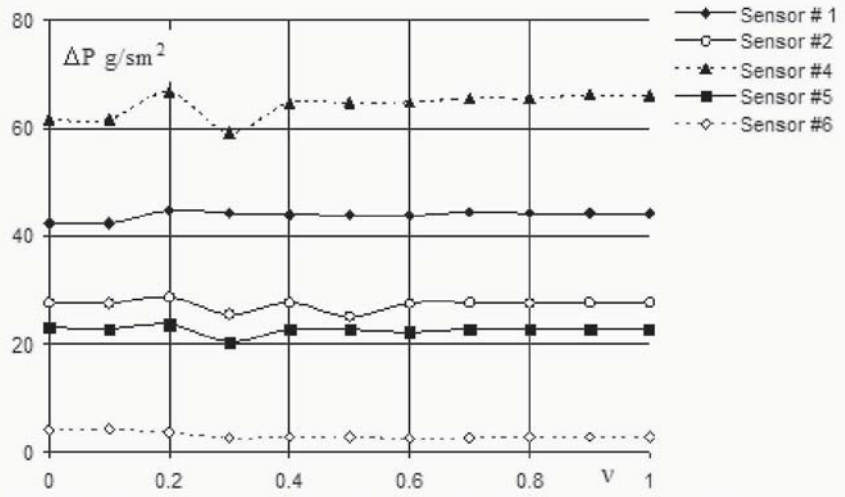

Fig.13. Time-averaged loading on the S vanes. Assembly 1.

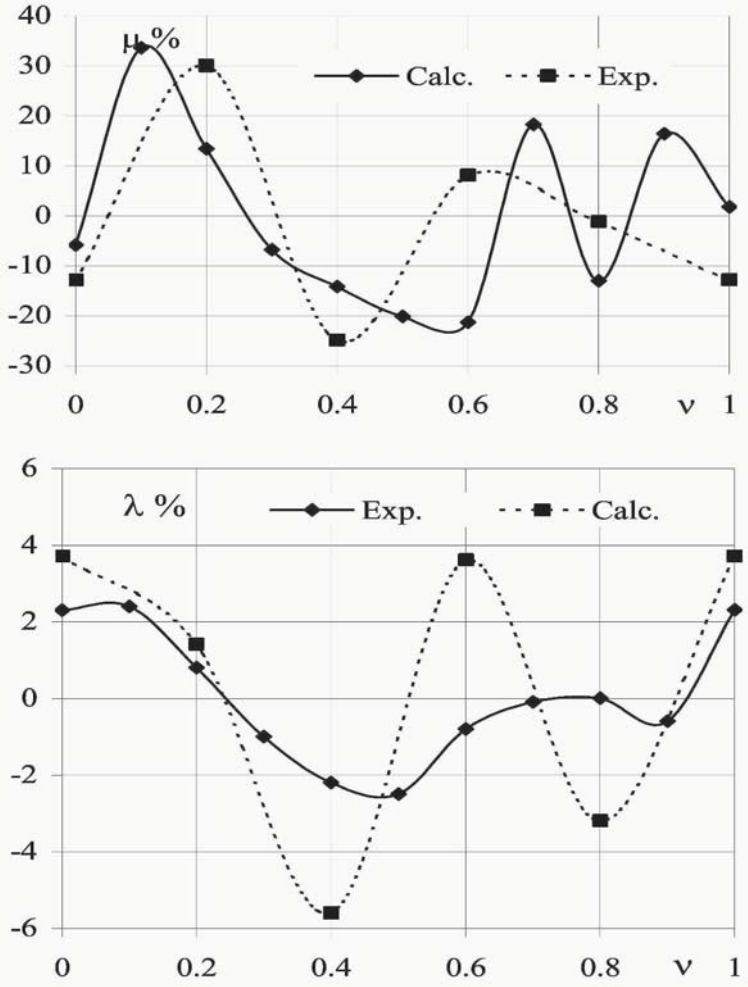

Fig.14.Comparison of dependences from ν intencity of free vortexes μ losses behind R λ. Assemble 1.

ROTOR-STATOR INTERACTION IN A HIGHLY-LOADED, SINGLE-STAGE, LOW-SPEED AXIAL COMPRESSOR: UNSTEADY MEASUREMENTS IN THE ROTOR RELATIVE FRAME

Unsteady Measurements in the Rotor Relative Frame

O. Burkhardt, W. Nitsche,
Technical University of Berlin
Institute of Aeronautics and Astronautics
Marchstr. 12, Sekr. F2, 10587 Berlin, Germany

M. Goller, M. Swoboda, V. Guemmer,
Rolls-Royce Deutschland Ltd. and Co. KG
Eschenweg 11, 15827 Dahlewitz, Germany

H. Rohkamm, and G. Kosyna
Technical University of Braunschweig, Pfleiderer-Institute
Langer Kamp 6, 38106 Braunschweig, Germany

Abstract Unsteady measurements were performed on rotor and stator blades of a highly-loaded 1.5-stage, low-speed axial compressor cascade using dynamic skin-friction measurement techniques. The project focusses on advanced 3D compressor blade design and has the potential to improve tip-clearance flow control at high loading by introducing different advanced unsteady measurement techniques. As an alternative to typical hot films, a novel surface hot wire with a better dynamic response was used. This device is capable of measuring the effects of unsteady aerodynamics in turbo machinery components. The results show the influence at different operating points (mass flow) and rotor-stator interactions on the boundary layer transition development using statical values as well as analysis functions such as power spectrum and correlation. In addition, preliminary results of the unsteady boundary layer development at rotating stall are being presented.

Keywords: Rotor-stator interaction; Unsteady aerodynamics; Boundary layer transition; Measurements in rotating frame.

K.C. Hall et al. (eds.),
Unsteady Aerodynamics, Aeroacoustics and Aeroelasticity of Turbomachines, 603–614.

1. Introduction

The boundary-layer transition process on turbo machine blades is mainly influenced by periodically incoming wakes, generated by an upstream blade row. Investigation by Adamczyk [1] has shown that the total pressure loss of a compressor blade row can be reduced if the incoming wakes mix out after rather than before the following blade row. Preliminary measurements, e.g. [2], were carried out using simple and suitable set ups to investigate interactions between rotating and stationary blade rows. Traversable bars with diameters of 3 mm placed in front of a linear stator cascade were used to simulate and investigate wake-induced transition. In the last few years measurements were directly conducted on real turbo machines with single or multi-stage blade rows. Detailed boundary layer measurements on stator vanes were done using surface hot film sensors. However, until now simultaneous data acquisition using a high number of sensors has never been carried out, especially on rotor blades due to the complexity of the setup. Such measurements were performed in this project using a telemetry-system and a 16-channel miniature constant-temperature anemometry ring.

2. Setup

Low-Speed Axial Compressor

All measurements were performed on the highly-loaded, single-stage, low-speed axial compressor shown in Figure 1. The test stage is designed with custom tailored CDA profiles and uses an inlet guide vane (IGV) to ensure that the inlet swirl to the following stage is truly representative of middle stage of a high-pressure compressor [3]. The axial compressor has a maximum capacity of $\dot{m}$=9 kg/s at a speed of n=2800 rpm. The rotor consists of 43 blades, while the stator and the inlet guide vane use 45 vanes. The rotor as well as the stator blade chord is l=75 mm and the aspect ratio is h/l=1.0. The axial distance between the blade rows is about 50% chord at mid-span. The test section of the compressor has a casing diameter of D_C=600 mm and a hub diameter of D_H=450 mm with parallel annulus lines at constant inner and outer radii. The maximum motor power is P_{max}=58 kW and allows a free-stream velocity of U=60 m/s. The measured compressor performance characteristics are presented in Figure 2. The diagram shows three different trend lines of the static pressure ratio and the efficiency η due to a mass flow variation. In addition, the operating points of interest are marked in the diagram.

Measurement Techniques

Data Acquisition. For measurements of periodically unsteady conditions in the cascade, a phase-locked ensemble average technique was used. This technique was proposed by Lakshminarayana et al. [4]. Data acquisition was carried out using a shaft encoder coupled with the rotor shaft to get a trigger-impulse. In the case of the present measurements sensor-signals were recorded 200 times using sample rates up to n=1024 and a scanning frequency of f=20 kHz. The ensemble-averaged sensor signals were analyzed using the AC-output voltages representing quasi wall-shear stress fluctuations. Statistical values of root-mean-square (rms) and skewness (μ_3), as well as analysis functions such as power spectra and cross-correlation, were used to analyze the data.

Surface Hot Wire. As an alternative to a surface hot film, a new flush mounted hot wire with a better dynamic response was used for measurements on a stator vane for the experimental project part. The surface hot wire (SHW) is a thermal-resistive sensor, which is directly welded over a tiny cavity, flush-mounted to the surface [5]. The device offers a promising technique for skin friction measurements on compressor blades. The sensor design considerably reduces the heat conduction into the substrate and, therefore, yields an improved signal-to-noise ratio and a higher frequency response compared to a common surface hot film. Figure 3 shows a sketch of the sensor. A platinum-coated, 5 μm diameter tungsten wire is used as sensor element while a 30 μm copper-layer serves as substrate. The bonded sensor element has a resistance of approximately R=5.5 Ω and is positioned several wire diameters above the wall. The array is very flexible and allows for easy attachment onto curved surfaces.

Blade Instrumentation. The measurements on rotor and stator were conducted at blade mid-span using Senflex hot film arrays. 16 and 25 single sensors were applied along the streamwise direction of a rotor and stator blade, respectively. In addition, a stator vane was equipped with a 16 single sensor surface hot wire array during the first experiment (see Figure 4). All sensors were operated in the constant-temperature mode with typical overheat ratios. The sensors on the rotor blade were adjusted using miniature anemometry-circuits. 16 electric circuits were designed on a ring-shaped printed circuit board (PCB) and implemented on the rotor disk (Figure 5). The integrated telemetry-system was used for a cable-less data transfer as well as a power supply for the 16-channel miniature constant-temperature anemometry ring.

3. Results

The results shown in this paper include a comparison of the thermal-resistive techniques used, and shows the influence of mass flow and rotating speed on the boundary layer transition position on the compressor blades. These techniques also give detailed information of the unsteady boundary layer development on rotor and stator blades at $\dot{m}$=6.4 and 5.85 kg/s, as well as at near stall conditions.

Surface Hot Wire Application

Figures 6 and 7 compare the skewness distribution on stator vanes at the compressor design point ($\dot{m}$=6.82 kg/s) using hot film and hot wire techniques. The figures are plotted as Campbell-diagrams (t-s-diagram) over a time span of t=2 ms, corresponding to four wake periods. The results show a good concordance of both transition lines, which indicates the point of μ_3=0 at streamwise positions between x/c=30-40%. The transition lines are clearly modulated by the periodically incoming wakes generated by the up-stream rotor. The results from individual measurements at two stator vanes show slight changes in position, as well as expansion of the lines. These results imply a good performance of the novel hot wire technique used for unsteady measurements on turbo machine components.

Boundary Layer Transition shifting

A general overview of the mass flow and speed of rotation influence on the axial-compressor rows are given in the Figures 8 and 9. The results show the streamwise transition development at 3 different rotating speed frequencies over a range of mass flows ($\dot{m}$). The results indicate clear up-stream shifting of the transition due to a throttling of the machine and a corresponding mass flow decrease. Additionally, Figure 8 shows a good correlation of the data of both thermal-resistive sensors used for unsteady measurements on the stator vanes.

Position of Unsteady Boundary Layer

Compressor at maximum efficiency ($\dot{m}$=6.4 kg/s). The next figures describe the development of the unsteady boundary layer along the rotor and stator blades at maximum compressor efficiency (η_{max}) using t-s-diagrams of the bridge output voltage e and the skewness μ_3 (Figures 10, 11) as well as line plots of e, rms and μ_3(Figures $12-15$). The boundary layer on compressor blades can be described by two typical paths, which occur periodically: the wake-induced path with the regions A, B, and C, and the path between two wakes that consists of the regions A, D, E and F. The laminar region (A) occurs at the leading edge of the blade and becomes transitional downstream (E, F).

The beginning of the transition is dominated by a calmed region (D) along the non-wake induced path. This region causes a delay of the transition process in the transitional region E and is generated by turbulent spots in the transitional region (B). Further downstream a turbulent region can be identified for x/c >63%. Line plots through the two paths are shown in the Figures 12 and 13 for the rotor, which compare, among other things, the beginning of by-pass transition. At the wake induced region the incoming wakes cause instabilities, which generate turbulent spots and, therefore, results in an earlier induced transition (Fig. 13: x/c=38%).

Line plots for a stator vane along the two typical paths are shown in the Figures 14 and 15. The distributions were measured using the surface hot wire technique. The transition points (μ_3=0) show different positions along the two paths due to the incoming wakes, induced by the IGV stage.

Compressor at reduced mass flow ($\dot{m}$=5.85 kg/s). The consequences of a mass flow reduction on rotor and stator are shown in Figures $16 - 23$. The rotor blade Campbell-diagrams of quasi wall-shear stress (e) and skewness indicate that transition above a separation bubble that begins at x/c=25% chord has occured, see Figures 16,17. A turbulent reattachment takes place between x/c=70-75% and is clearly modulated by the IGV-wakes. In the line plots (Figures 18,19) the beginning of the separation area is indicated by a local rms-maximum. The global maximum at 60% chord, on the other hand, describes the region of laminar-turbulent transition. A typical zero-skewness (transition point) could not be detected due to the sensor positions that are directly placed on the wall. The mass flow reduction causes free-stream conditions which are similar to an increase of the angle of incidence. This leads to a destabilization of the boundary layer and results in a separation due to a local pressure increase.

Turbulent boundary layer reattachment can be identified by means of looking at cross-correlations of the last few array sensors, see Figure 20. The presented correlations use the last sensor of the array for reference. The results show no correlation with the sensor at x/c= 67% but a clear amplitude-increase and a positive time shift at 89.1% chord, which indicates a reattached boundary layer. The correlation at x/c=74.1% shows an increased amplitude tendency but no significant amplitude peak due to the sensor position, which is near the reattachment line.

While the rotor boundary layer is separated above a blade region of approximately 40-50% of the chord, investigations on the stator vane (Figures 21 and 22) reveal that the boundary layer remains attached and turns turbulent between x/c=20-40%, modulated by the incoming wakes.

Compressor at Stall. A Rotating stall is characterized by one or more cells of reduced, and often reversed, flow travelling with an angular velocity which is much smaller than that of the rotor stages. While a few investigations of stator vanes have been carried out in the past, simultaneous surface sensor measurements on rotor blades were performed for the first time. Figure 23 shows ensemble averaged power spectra at 6 different streamwise positions at the rotor blade with an excited blade frequency at f=1665Hz. It can be seen that the frequency does not dominate in each spectrum due to highly unsteady flow conditions.

A sequence of instantaneous boundary layer distributions at the stator is shown in Figure 24. Due to the stall cells moving with a reduced angular velocity compared to the rotating speed, it appears that the boundary layer phenomena results in a backwards movement in the t-s-diagrams. A common transition mode such as by-pass transition or the transition above a laminar separation bubble will not arise. The boundary layer development along the chord is controlled by turbulence effects generated near the leading edge.

4. Summary

The results presented in this paper were obtained in a highly-loaded, 1,5-stage, axial low-speed compressor. Typical wake and non-wake induced paths, as well as regions of laminar, transitional, and turbulent boundary layer flows were periodically detected on rotor and stator blades using surface sensor array techniques. In particular, the results obtained by the novel surface hot wire imply that the technique has the potential for shear stress measurements in unsteady flows. Investigations of the boundary layer development on a rotor blade were obtained by means of a telemetry system and miniature constant-temperature anemometry fixed to the rotor. Using such a data acquisition system, it can be shown that the boundary layer at the design point and at maximum efficiency is based on a by-pass process. A mass flow reduction causes a laminar boundary layer separation in connection with a transition above a bubble, as well as a turbulent reattachment near the trailing edge.

Acknowledgments

The reported work was performed within the AdComB research project that is funded by the 5^{th} European Framework. The project has been supported by Rolls-Royce Deutschland Ltd. and Co. KG, and carried out at the Pfleiderer-Institute of the Technical University of Braunschweig. The 16-channel miniature constant-temperature anemometry ring used for the measurements at the rotor blade was developed by the M. Baumann engineer-bureau.

References

Adamczyk, J.J.,"Wake Mixing in Axial Compressors" *ASME 96-GT-29*, 1996

Swoboda M., Teusch R., Guemmer V., Fottner L., Wenger U., "Experimental Investigation of Boundary Layer Transition in Compressor Cascades at Unsteady Flow Conditions", *STAB Proceedings*, 1998, pp. 474-482

Rohkamm, H., Wulff, D., Kosyna, G., Saathoff, H., Stark, U., Gümmer, V., Swoboda, M., Goller, M., "The Impact of Rotor Tip Sweep on the Three- Dimensional Flow in a Highly-Loaded Single-Stage Low-Speed Axial Compressor: Part-II Test Facility and Experimental Results", 5th European Conference on Turbomachinery - Fluid Dynamics and Thermodynamics, Prague, Czech Republic, 18.-21. March 2003.

Lakshminarayana B., "A Method of Measuring Three-Dimensional Rotating Wakes Behind Turbomachinery Rotors", *Journal of Fluids Engineering*, June 1974, Vol. 96, pp. 87-91

Sturzebecher, D., Anders, S., Nitsche, W., "The Surface Hot-Wire as a Means of Measuring Mean and Fluctuating Wall Shear Stress", *Experiments in Fluids*, Vol. 31, 2001, pp. 294-301

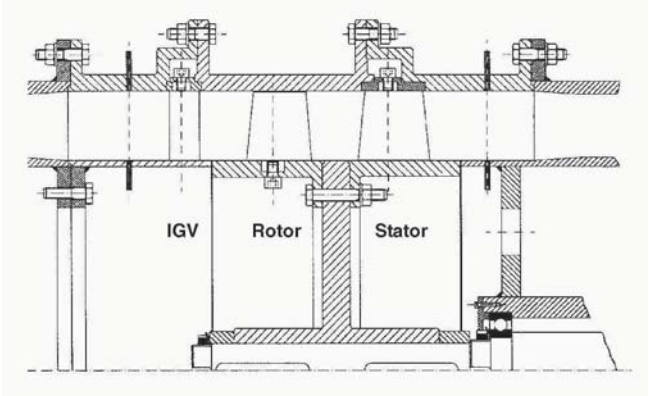

Figure 1. Measurement set up

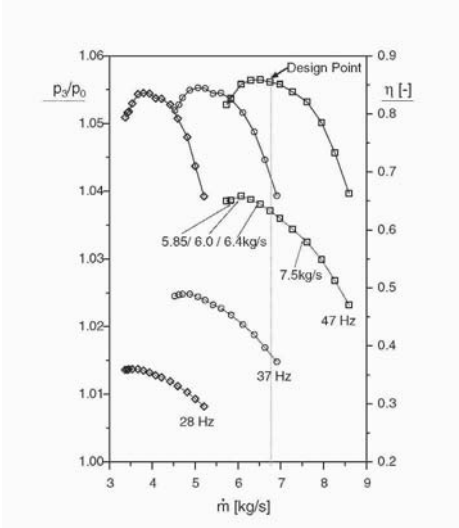

Figure 2. Performance characteristics of the axial compressor

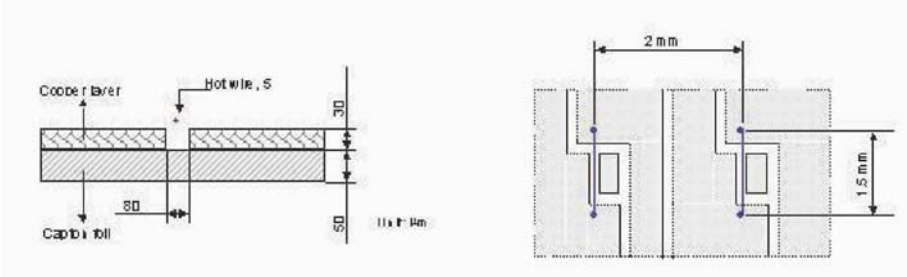

Figure 3. The surface hot wire

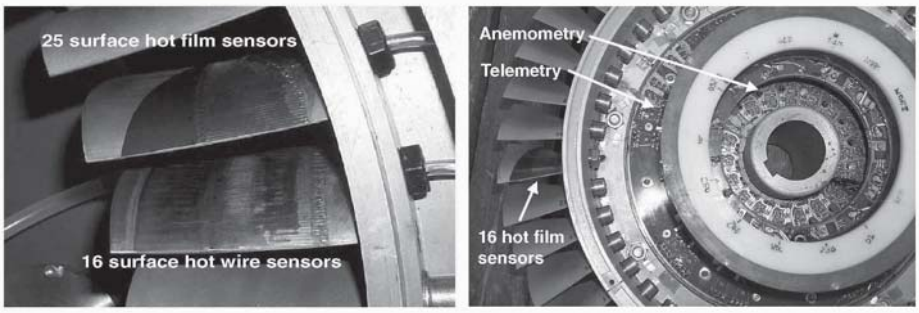

Figure 4. Instrumented stator vanes

Figure 5. Rotor with anemometry-circuits and telemetry transmitting-component

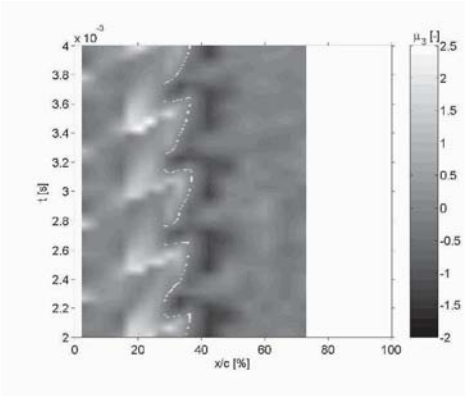

Figure 6. $t - s$ diagram of the skewness, measured with a hot wire array

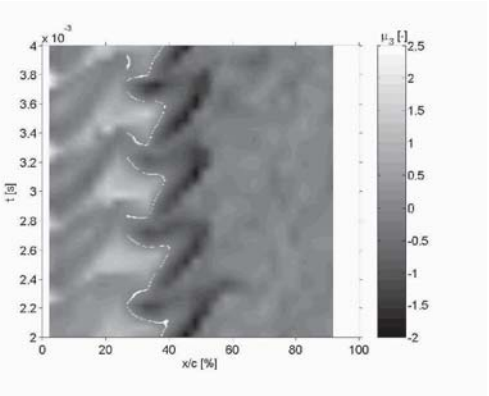

Figure 7. $t - s$ diagram of the skewness, measured with hot films

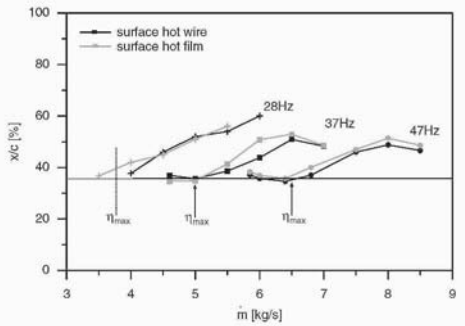

Figure 8. Stator vane: influence of mass flow and rotation speed

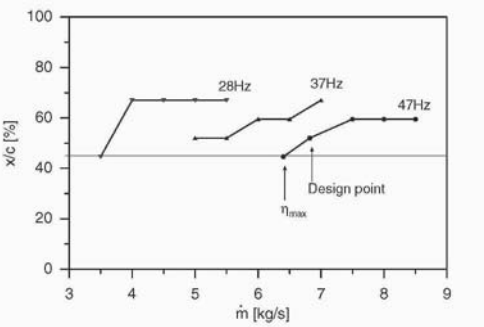

Figure 9. Rotor blade: influence of mass flow and rotation speed

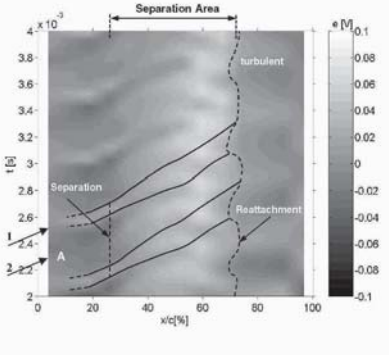

Figure 10. Rotor: Campbell-diagram quasi wall shear stress e[V], $\dot{m}$ = 6.4kg/s

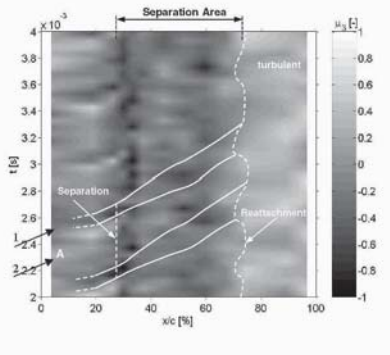

Figure 11. Rotor: Campbell-diagram skewness μ_3[-], $\dot{m}$ = 6.4kg/s

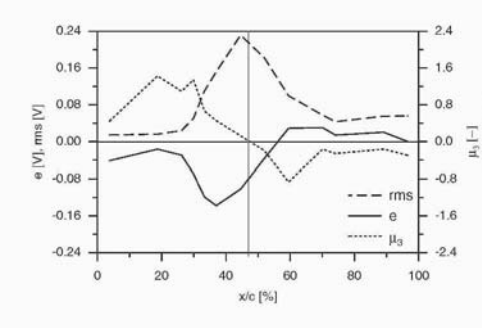

Figure 12. Rotor: e, rms, and μ_3 line plots non-wake induced path ($\dot{m}$ = 6.4kg/s)

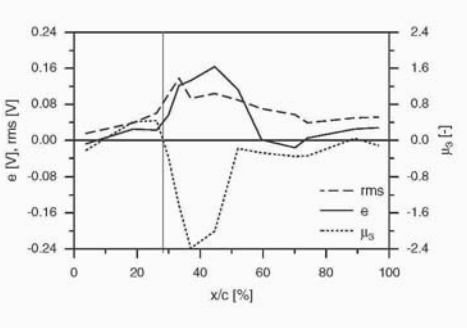

Figure 13. Rotor: e, rms, and μ_3 line plots wake induced path ($\dot{m}$ = 6.4kg/s)

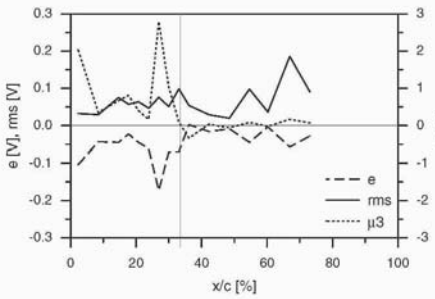

Figure 14. Stator: e, rms, and μ_3 line plots at non-wake induced path ($\dot{m}$ = 6.4kg/s)

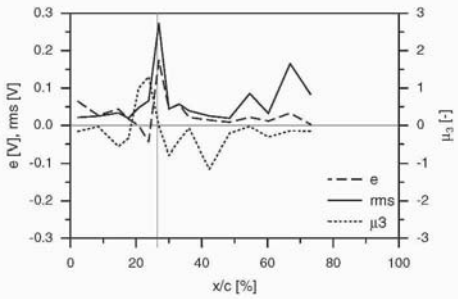

Figure 15. Stator: e, rms, and μ_3 line plots at wake induced path ($\dot{m}$ = 6.4kg/s)

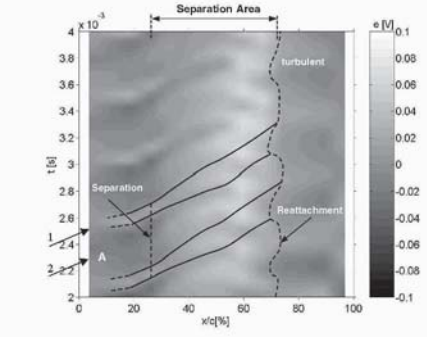

Figure 16. Rotor: Campbell-diagram of quasi wall shear stress (m = 5.85kg/s)

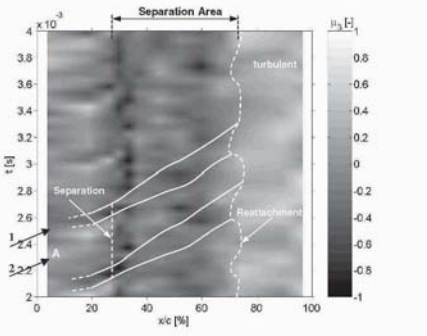

Figure 17. Rotor: Campbell-diagram of the skewness (m = 5.85kg/s)

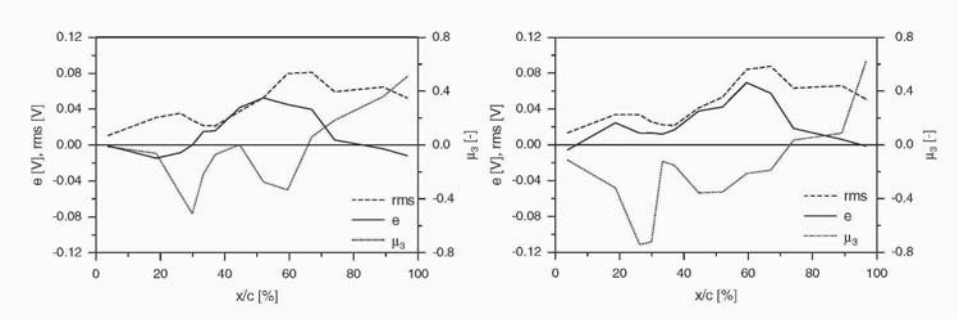

Figure 18. Rotor: e, rms, μ_3 line plots at non-wake induced path ($\dot{m}$ = 5.85kg/s)

Figure 19. Rotor: e, rms, μ_3 line plots at wake induced path ($\dot{m}$ = 5.85kg/s)

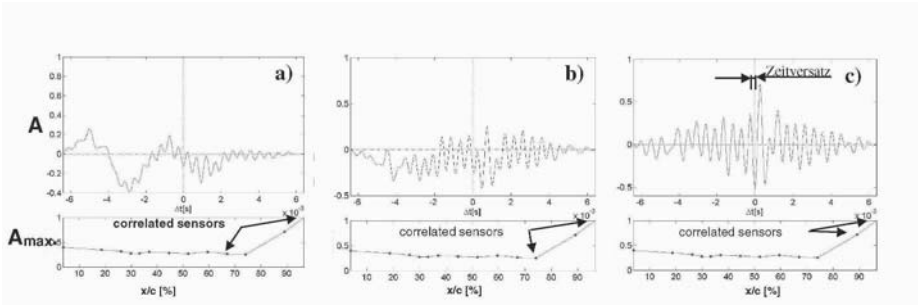

Figure 20. Correlation response of different rotor sensors: Validation of turbulent reattachment

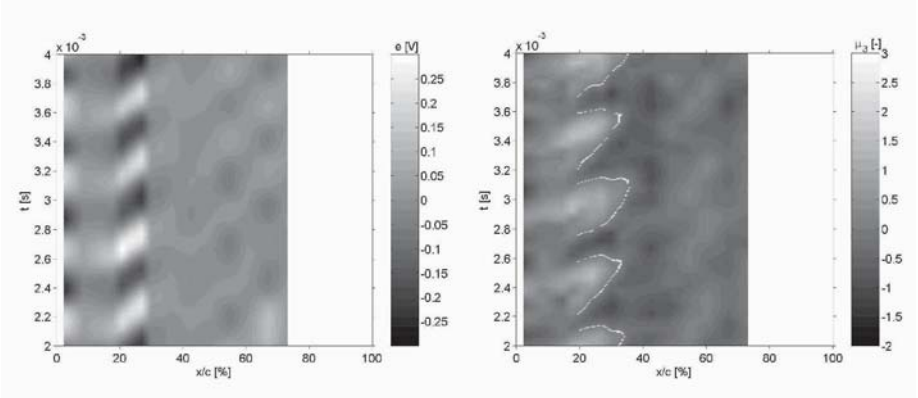

Figure 21. Stator: Campbell-diagram quasi wall shear stress ($\dot{m}$ = 5.85kg/s)

Figure 22. Stator: Campbell-diagram skewness ($\dot{m}$ = 5.85kg/s)

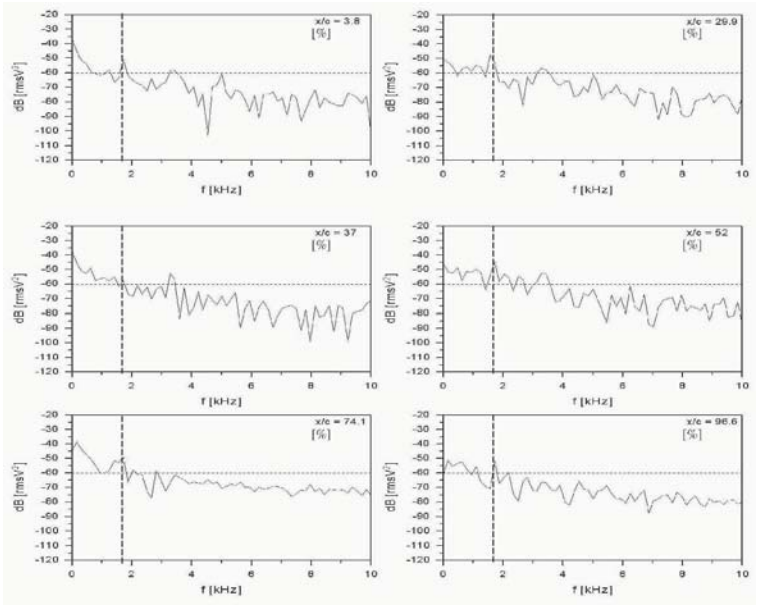

Figure 23. Rotor at stall: power spectra at different streamwise positions

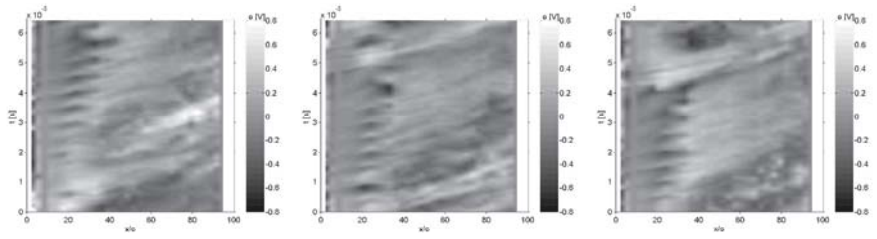

Figure 24. Stator at stall: t-s-diagram sequence

TWO-STAGE TURBINE EXPERIMENTAL INVESTIGATIONS OF UNSTEADY STATOR-TO-STATOR INTERACTION

Indexing Effect

Jan Krysinski
Institute of Turbomachinery, Technical University of Lodz
krysinski@p.lodz.pl

Robert Blaszczak Jaroslaw
Institute of Turbomachinery, Technical University of Lodz
blaszczk@p.lodz.pl

Antoni Smolny
Institute of Turbomachinery, Technical University of Lodz
asmo1948@p.lodz.pl

Abstract The results of the stator-to-stator clocking effect in a two-stage low-pressure turbine are presented. The main goal is focused on a detailed investigation of the shape and its position of the stator wake after the first stage and the correlation between different parameters including acoustic signal levels. The numerical calculations confirmed the image of the flow field obtained during the measurements.

Keywords: axial turbine, clocking effect, measurements, flow field, acoustics

1. Introduction

In order to improve performance and prediction methods accuracy for multistage axial turbomachines, understanding of the unsteady flow is essential. A number of experimental and numerical studies have been carried out in recent years to investigate these flow phenomena [e.g. Arnone et al. 2000, 2002; Dorney et al. 1999, Eulitz 2000; Haldeman et al., 2003; He et al. 2002, Howel et al. 2001, Huber 1996, Hummel 2002; Jouini et al. 2003; Reinmoeller et al.

K.C. Hall et al.(eds.),
Unsteady Aerodynamics, Aeroacoustics and Aeroelasticity of Turbomachines, 615–626.

2002, Saren et al. 2002]. The experimental work presented herein is the continuation of our earlier studies, starting from mid-nineties [e.g. Krysinski et al. 1995 - 2002; Smolny, Blaszczak 1997] and it is still in progress at the Institute of Turbomachinery (Technical University of Lodz, Poland). The objective of the present test program is to experimentally investigate vane-indexing effects (so called also the clocking effects) on the performance of the two-stage low-pressure turbine test rig. Special clocking mechanisms were designed to allow the first stage vanes to be moved circumferentially relative to the second stage vanes independently of the casing. This allows changing the clocking positions of the first and the second stator vanes during the tests without stopping the turbine and dismantling it. Herein, some unsteady flow measurement results, wall pressure above the rotor blades and the external characteristics for different circumferential positions of the stator vanes are described.

2. Facility

The series of tests were conducted on the two-stage low-pressure model turbine with the eddy-current brake. The layout of the turbine test rig is presented in Fig. 1. A two-fan set with a specially equipped control system provided a continuous and strictly constant airflow to the test rig. The inlet air parameters during the tests presented here were as follows: total pressure p_{t0} = 15.668 $\pm$ 0.003 kPa, total inlet temperature T_{t0} = 318 $\pm$ 2 K, mass flow rate m = 3.565 $\pm$ 0.005 kg/s (n = 49.2 Hz) to m = 3.730 $\pm$ 0.005 kg/s (n = 30 Hz) - variations were due to the clocking effect. During the tests the rotational speed n was in the range 25.00 to 58.33 Hz (1500 rpm to 3500 rpm). Variation of the speed n at the working point was less then 0.02 Hz (1 rpm) during every measurement session. Fig. 2 shows the cross section of the test rig with the main measuring planes and Fig. 3 shows the performance curves of the machine.

The turbine geometry with some indexing positions of the first stator vane (pos. 5 $\Rightarrow$ x/T = 0.0 $\Rightarrow$ identical circumferential position of both stators) is presented in Fig. 4. For tests presented herein both identical stators have 16 constant-section cylindrical vanes with the trailing edge inclined to the radial direction at an angle of 22 deg. Both identical rotors have 96 twisted blades. This atypical machine with a very clear stator wake presence is an interesting case from the numerical point of view. A more detailed description of the test facility geometry and the unsteady flow measurement can be found in our earlier studies [Krysinski et al. 1995 - 2002, Smolny, Blaszczak 1997].

3. Instrumentation

The external characteristic experimental data (rotational speed, torque, power, e.g. Fig. 3) were obtained for 28 different clocking positions of the two stators (relative range about 2.5 based on the vane pitch) with high-accuracy eddy-

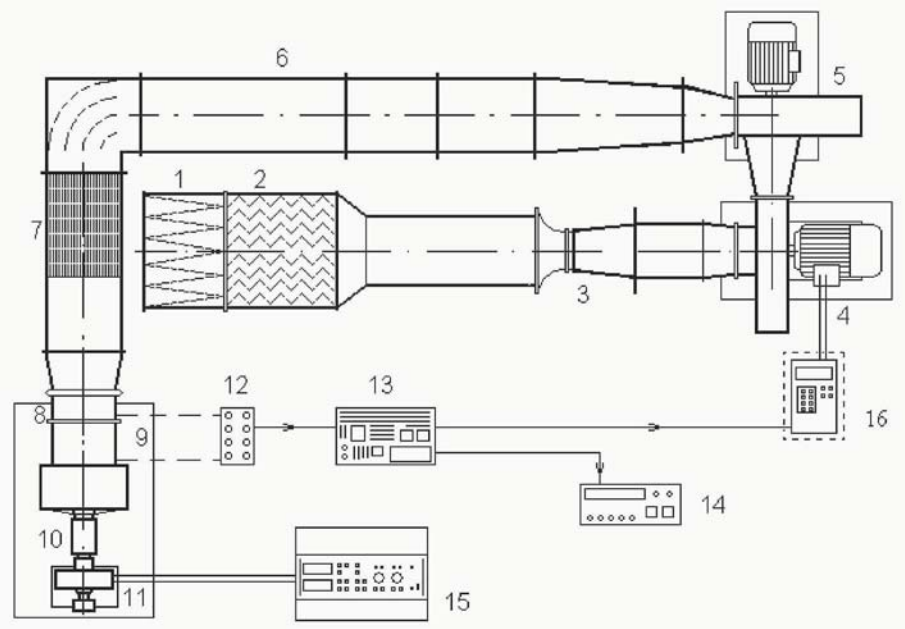

Figure 1. Layout of the TM-3 turbine test rig (Technical University of Lodz, Poland) 1) Air filter 2) Noise silencer 3) Venturi tube 4) Fan1 5) Fan2 6) Air-duct 7) Honey-comb straightener 8) Inlet ring 9) Turbine 10) Shaft 11) Eddy-current brake 12) Inlet/outlet control pressure transducers 13) Converter controller 14) DMM 15) Eddy-current brake control system 16) Current converter

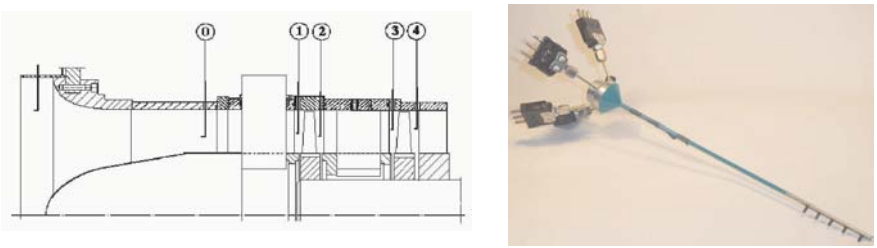

Figure 2. Turbine cross-section with the main measuring planes and the temperature probe

current brake controlling system. Additional pressure and temperature kiel-head probes (Fig. 2) fixed at the inlet and outlet section of the turbine were used. In this case two stator fixed together were moved every 1/12 of the pitch performing 1000 measurements in every position, next the clocking position was changed by 1/6 of the pitch, the stators again were fixed and the operation was repeated until all indexing range was passed.

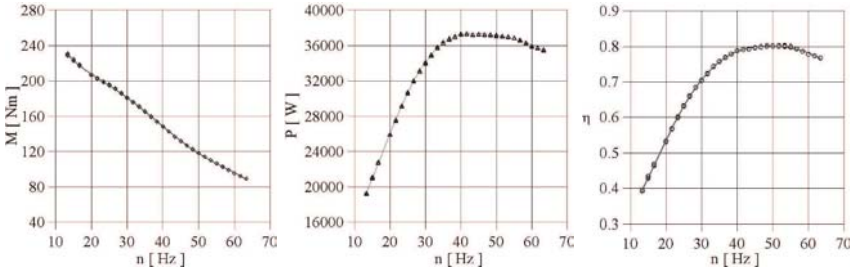

Figure 3. Performance curves of the turbine (torque, power and efficiency) obtained for the design clocking position x/T = 0.0

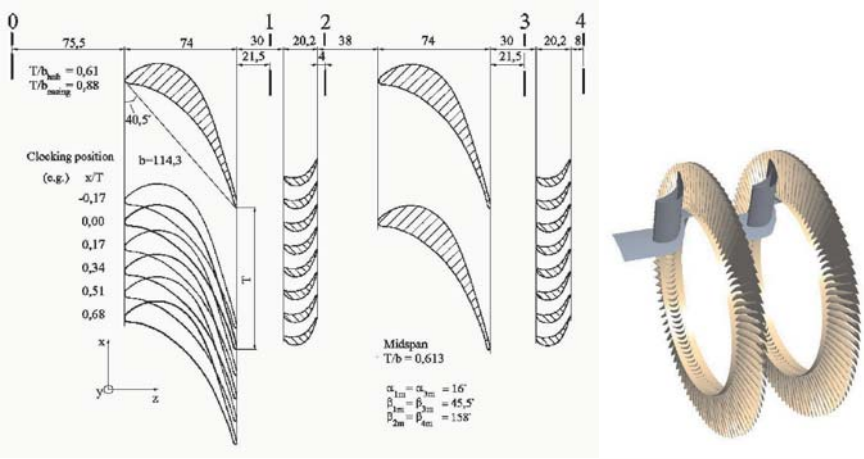

Figure 4. Turbine geometry with some clocking positions presented [Krysinski et al., 1999]

The basic flow parameters (e.g. pressures, temperatures, flow vectors, turbulence levels) after the annular cascades in each main measuring plane (0, 1, 2, 3, 4 - Fig.2) were surveyed before the measuring session using classical methods and the tests confirmed the results obtained from earlier sessions [Smolny, Blaszczak 1997; Krysinski et al. 1999-2002].

During tests presented in this paper supplementary measurements were performed. To find out if there is any influence of the indexing effect on leakage flow above the rotor blades, the pneumatic signals with the help of unsteady pressure transducers were received (Fig. 6b). The data from the pressure transducer were simultaneously recorded by the digital multimeter (DC part of the signal) and the transient recorder (AC part of the signal) to obtain the maximum resolution. The data acquisition was triggered by a photocell located at the hub of the rotor.

Unsteady pressure was sampled in a one-time window with a digital resolution of 256 points at a sampling frequency of 240 kHz. After one rotor rev-

Figure 5. Turbine stator vanes with glue-on probes for boundary layer measurements

olution, the next time-window was recorded, until 256 of these time-windows were stored.

The triggering and data acquisition systems for the thermoanemometric measurements were the same. For vane boundary layer phenomena identification glue-on hot-film probes were used. The results presented here were performed on the suction side of the vanes at the midspan of the flow channel. Additionally, to find the correlation between hot-film signals and inside noise level another tests were performed including acoustic measurements with the help of $1/4$" microphones perpendicularly connected to the vane surface tap tubing. The method was similar to the one used by [Sabah, Roger 2001]. The data from glue-on hot-film sensor and the microphone were sampled simultaneously at 50 kHz and next, recorded by a digital data acquisition system.

More details about data treatment methods can also be found in [Smolny, Blaszczak 1996, 1997].

Figure 6. Rotor geometry (a) and the position (b) of the unsteady pressure transducer (c)

4. Experimental results

A lot of the unsteady 3D flow measurements using three-sensor hot-wire probes were presented in earlier papers [Krysinski et al. 1999 - 2002].

Based on earlier tests one could observe that there were no significant differences after the first stator and the first rotor while indexing the airfoils. It was clearly visible how the first stator wakes pass through the first rotor and change their circumferential position downstream. The small flow-blocking effects (according to the vane clocking) observed during earlier tests were neutralised by keeping the inlet/outlet pressure ratio at the same level with an especially prepared control system (Fig. 1, pos. 13). Significant changes were observed inside the flow passing the second stage, especially after the second vane. New test results showed again visible differences due to the clocking effect when compared to the situation when two stators were at the design position (x/T = 0.0), especially it is showed for highly loaded machine (Fig. 7).

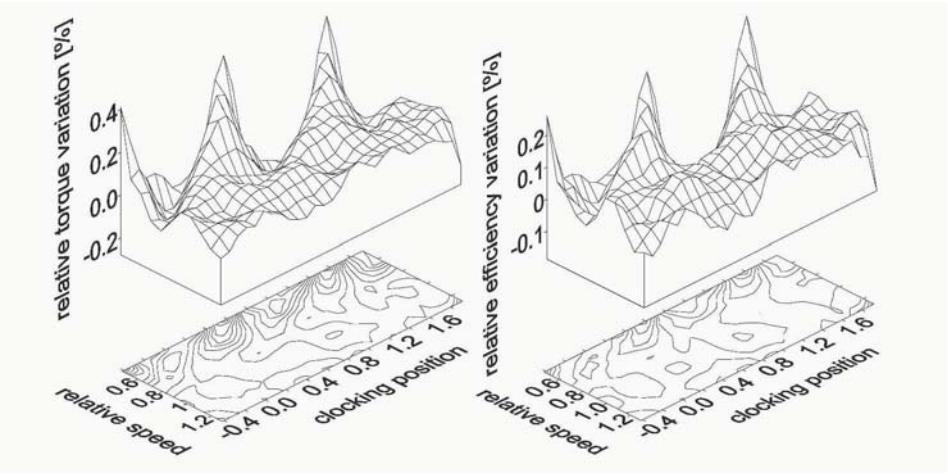

Figure 7. Measured relative torque and efficiency versus clocking position and rotational speed

Periodic and random components of unsteady pressure above the first rotor for rotational speed n = 42 Hz are presented in Fig. 8. The presence of the position of the preceding stator is clearly visible for the periodic component. The minimum value of the periodic component is related to the situation when the stator wake (secondary flow structures) flows inside the testing zone (nearby transducer position) and the maximum value is obtained when the inside vane channel flow is passing by. Due to the low level of the measured pressure and the low frequency resolution of the pressure transducer the tests above the second rotor were not performed. In this case the clocking effect phenomena are hardly to measure using standard instrumentation.

Fig. 9 shows a comparison of the relative random (e_r/E) and periodic (e_p/E) components of thermoanemometric signals measured on the suction sides of the first stator and the second stator vanes with a help of glue-on hot-film sensors. The results are similar for both vanes. The rapid grow of the signal is

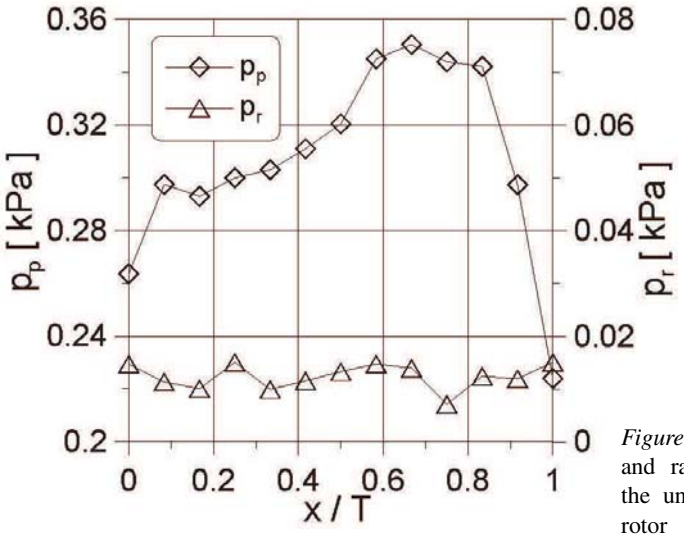

Figure 8 RMS of periodic and random components of the unsteady pressure above rotor

clearly visible due to the laminar-turbulent transition zone. The beginning of this phenomenon on the surface of the second stator vane starts earlier and is characterised by higher RMS values. The end of the zone is almost at the same place and its position is related to the inlet conditions. A detailed flow measurement data comparison is beyond the scope of this paper and will be discussed in another paper.

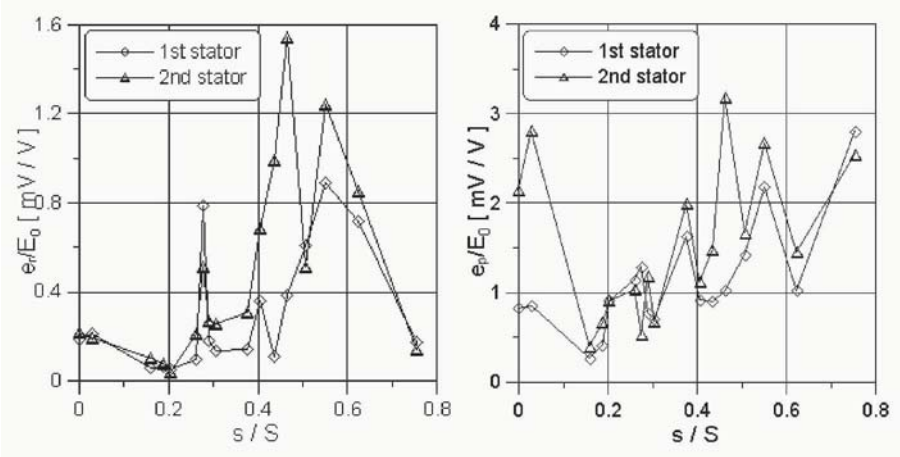

Figure 9. Relative random (er/E, left) and periodic (ep/E, right) components of the glue-on hot-films measured on the suction sides of the first stator and the second stator vanes (direction z - along the main axis of the turbine, Z = 74 mm, Fig. 4)

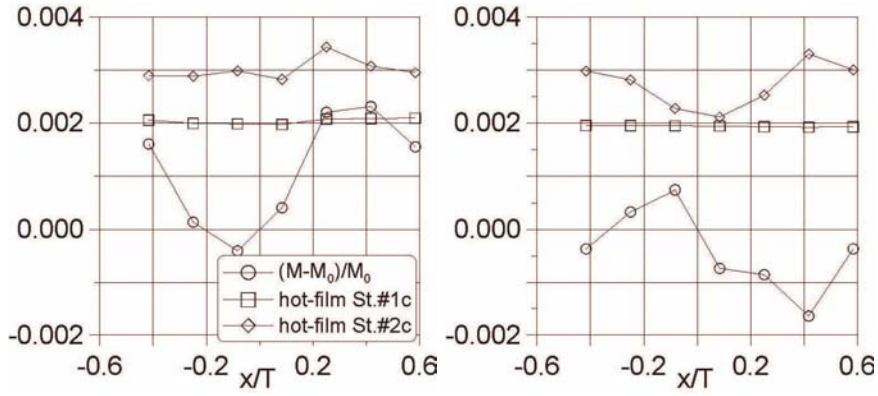

Figure 10. Results of the glue-on hot-film signals analysis compared to the variation of the torque of the turbine for the same clocking positions

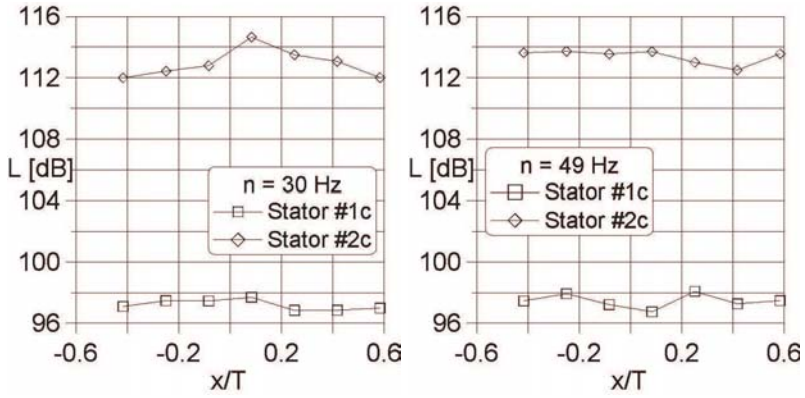

Figure 11. Noise level measured at the leading edge of the vane vs. clocking position

Fig. 10 shows the results of the glue-on hot-film signals analysis from two stators compared to the variation of the torque of the turbine for the same clocking positions. The position of the sensor was at the leading edge of the vane and in the middle of the flow channel height. Additionally acoustic measurements with the microphone connected pneumatically to the pressure tap nearby the hot-film sensor were performed. The results are shown in Fig. 11. Small variations of the measured values are visible but they are not clearly correlated to the overall performance changes. This due to the fact that the most important performance changes are present nearby the hub and the casing. In this case more detailed tests along the flow channel height are necessary.

The next figure (Fig. 12a) shows differences of the thermodynamic turbine efficiency versus height of the flow channel position at different rotational

speeds. The differences are visible for all speeds and the shape of the curves is similar showing the visible drop in the near the walls regions, especially nearby the hub. From earlier studies it is known that the turbulence level is very high in these regions [Krysinski et al. 2001]. Fig. 12 b and c show the efficiency changes due to the clocking effect at different flow channel heights. The variations in the region near the hub are about 1 %. Along the height of the flow channel the variations of the turbine efficiency are phase shifted. This shift makes the overall efficiency variation to be small and not clearly visible. If the shift does not exist (that means across the flow channel height the efficiency obtains maximum value at the same clocking position) for the nominal rotating speed we will obtain the efficiency benefit about 0.6 %.

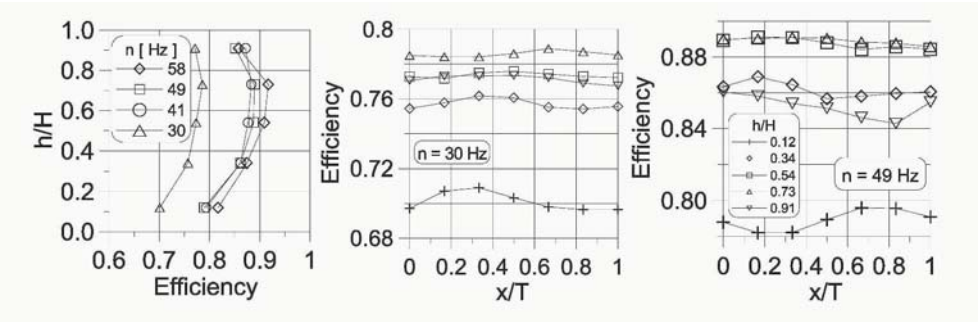

Figure 12. Measured thermodynamic turbine efficiency along the height of the flow channel for different rotational speeds (left) and for different clocking positions (middle and right)

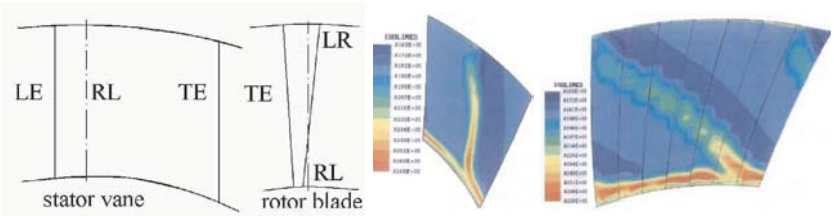

Figure 13. a) Stator and rotor leading edge (LE) and trailing edge (TE) compared to the radial direction (RL) b) Results of the numerical calculation downstream the first stator and the first rotor

5. Conclusions

Two-stage low-pressure turbine at the Institute of Turbomachinery (Technical University of Lodz, Poland), was prepared for experimental investigations of the stator-to-stator clocking effect. Special attention was directed into machine work conditions and strictly constant inlet conditions, especially inlet/outlet pressure ratio. The changes due to the flow blocking effect were re-

duced with the help of special inlet condition control system. Continuation of earlier experimental investigations of the stator-to-stator interaction has been performed in the axial gaps, on the vane profile and outer casing.

The results of precise measurements of the power and torque output differed slightly according to the stator-to-stator clocking position. Only for the lowest rotational speed the effect of the clocking position was very clearly visible on overall performance. That gave the conclusion that it was very hard to find out the influence of the clocking position measuring and considering only the external characteristics, especially for the case of not highly loaded turbine.

The flow parameters downstream the first turbine stage showed similarities for the different clocking positions. The stator vane wake could be clearly observed also after the rotor. With the improved resolution of the measuring system even the thermal wake after the first stator was observed (Krysinski et al. 1999).

The exit flow of the second stator was strongly influenced by the clocking position of the first stator. The differences of the flow parameters became smaller downstream the second stage due to the strong flow mixing phenomena inside the second rotor but the time-averaged values downstream the turbine showed significant differences relative to the first stage and when compared with different clocking positions. The results showed that the presented phenomena are very complicated. The first stator wakes do not pass directly inside the second stator flow channel or directly impinge the noses of the second stator vanes as other authors presented it. The wakes start immediately to rotate inside the first stator-rotor axial gap and next downstream the turbine. As a result they interact strongly with the channel boundary layers not only at hub and casing regions but also on both surfaces (suction and pressure side) of the following stator vanes.

Parallel to presented results the numerical calculations of the flow were performed to understand unsteady flow behaviour in multistage machines and to determine the clocking effect more deeply. Fig.13 shows the geometrical position of the leading and trailing edges of the turbine blading as well some numerical results. The numerical models showed the good accordance with the experimental results. They show also the wake variations, especially nearby the hub region where the wake is strongly shifted. The numerical codes need more and more sophisticated data to be improved. The data presented in this paper provide the community with an understanding of the effects that indexing airfoils can have on the overall turbine efficiency giving the vision of a future turbomachinary performance improvement. The new design with less rotor-to-stator blading number ratio is prepared to find out the influence of the clocking effect for other geometries of the machines working at similar conditions.

Nomenclature

b = chord length [m]
m = mass flow rate [kg/s]
n = rotational (shaft) speed [Hz]
p = pressure [Pa]
T = vane pitch [m], temperature [K]
x = coordinate along circumferential direction [m]
y, h = coordinate along radial direction [m]
z = coordinate along axial direction [m]
α = circumferential (pitchwise) flow angle (absolute frame) [deg]
β = circumferential (pitchwise) flow angle (relative frame) [deg]

Subscripts and Superscripts

0 = inlet conditions
1 = downstream the first stator
2 = downstream the first rotor
3 = downstream the second stator
4 = downstream the second rotor
m = design (metal)
t = total (stagnation)

References

Arnone A., Marconcini M., Pacciani R. (2000): On the Use of Unsteady Methods in Predicting Stage Aerodynamic Performance. ISUAAAT'2000, Lyon, France, pp. 24- 46.

Arnone A., Marconcini M., Pacciani R., Schipani, Spano E. (2002): Numerical Investigation of Airfoil Clocking in a Three-Stage Low-Pressure Turbine. Trans. of the ASME, J. of Turbomachinery, Jan. 2002, Vol. 124 pp. 61-68.

Dorney D.J., Sondak D.L., Cizmas P.G.A., Saren V.E., Savin N.M. (1999): Full-Annulus Simulations of Airfoil Clocking in a 1-1/2 Stage Axial Compressor. ASME 99-GT-023.

Eulitz F. (2000): Modeling and Simulation of Transition Phenomena in Unsteady Turbomachinery Flow. ISUAAAT'2000, Lyon, France, pp. 332-337.

Haldeman C.W., Krumanaker M.L., Dunn M.G. (2003): Influence of Clocking and Vane/Blading Spacing on the Unsteady Surface Pressure Loading for a Modern Stage and One-Half Transonic Turbine. ASME GT2003-38724.

He L., Chen T., Wells R.G., Li Y.S., Ning W. (2002): Analysis of Rotor-Rotor and Stator-Stator Interferences in Multi-Stage Turbomachines. Trans. of the ASME, J. of Turbomachinery, Oct. 2002, Vol. 124, pp. 564-571.

Howell R.J., Ramesh O.N., Hodson H.P., Harvey N.W., Schulte V. (2001): High Lift and Aft-Loaded Profiles for Low-Pressure Turbines. Trans. of the ASME, J. of Turbomachinery, Apr. 2001, Vol 123, pp. 181-188.

Huber F.W., Johnson P.D., Sharma O.P., Staubach J.B., Gaddis S.W. (1996): Performance Improvement Through Indexing of Turbine Airfoils: Part 1 - Experimental Investigation. ASME J. of Turbomachinery, Vol. 118, pp. 630-635.

Hummel F. (2002): Wake-Wake Interaction and Its Potential for Clocking in a Transonic High-Pressure Turbine. ASME J. of Turbomachinery, Vol. 124, pp. 69-635.

Jouini D.B.M., Little D., Bancalari E., Dunn M., Haldeman C., Johnson P.D. (2003): Experimental Investigation of Airfoil Clocking Impacts on Aerodynamic Performance in a Two Stage Turbine Test Rig. ASME GT2003-38872.

Krysinski J., Smolny A., Blaszczak J.R., Gallus H.E., Walraevens R., Mertens B. (1995): Axial Two-Stage Turbine Test Rig For Unsteady Flow Measurements. SYMKOM'95, Int. Symp. CMP Pč 108, Lodz, p.99.

Krysinski J., Gallus H.E., Smolny A., Blaszczak J.R. (1999): Stator Wake Clocking Effects on 3D Unsteady Flows In a Two-Stage Turbine. 3rd EuroConf. On Turbomachinery, IMechE, C557/017/99. Vol. A, pp. 323-332, London, UK.

Krysinski J., Smolny A., Blaszczak J.R., Gallus H.E. (2000): 3D Unsteady Flow Experimental Investigations in a Two-Stage Low-Pressure Turbine. ISUAAAT'2000, Lyon, France, pp. 515-523.

Krysinski J., Blaszczak J.R., Smolny A. (2001): Stator Clocking Effect on Efficiency of a Two-Stage Low-Pressure Model Turbine. 4th European Conference on Turbomachinery: Fluid Dynamics and Thermodynamics, ATI-CST090/01, pp. 1045-1051, Firenze, Italy.

Krysinski J., Blaszczak J.R., Smolny A. (2002): Efficiency Improvement Through Indexing Of Stators Of A Two-Stage Turbine. HEFAT2002, KJ2, Kruger Park, South Africa.

Reinmoeller U., Stephan B., Schmidt S., Niehuis R. (2002): Clocking Effects ina a 1.5 Stage Axial Turbine - Steady and Unsteady Experimental Investigations Supported by Numerical Simulations. Trans. of the ASME, J. of Turbomachinery, Jan. 2002, Vol. 124, pp. 52-60.

Saren V.E., Savin N.M., Krupa V.G. (2000): Experimental and Computational Research of a Flow Structure in a Stator-Rotor-Stator System of an Axial Compressor. ISUAAAT'2000, Lyon, France, pp. 494-502.

Saren V.E., Savin N.M. (2000): Hydrodynamic Interaction of a Stator-Rotor-Stator System of an Axial Turbomachine. Fluid Mechanics 3/2000, UDK 533.6.011.34, Russian Academy of Sciences, Moscow, pp. 145-158 (in Russian).

Smolny A., Blaszczak J.R. (1996): Boundary Layer and Loss Studies on Highly Loaded Turbine Cascade. CP-571/4, AGARD.

Smolny A., Blaszczak J.R. (1997a): Experimental Investigations Of Unsteady Flow Fields In A Two-Stage Turbine. 2nd EuroConf. on Turbomachinery, Antwerp, Belgium.

Swirydczuk J., Gardzilewicz A. (2002): Analysis of the Stator-Rotor Interaction in the TM-3.00 Turbine. Institute of the Fluid Flow Machines of the Polish Academy of Sciences. Internal Report 2764/02 (in Polish), Gdansk.